STRUCTURE AND BONDING 114

Series Editor D. M. P. Mingos
Volume Editors K. A. Müller · A. Bussmann-Holder

Superconductivity in Complex Systems

Springer

114
Structure and Bonding

Series Editor: D. M. P. Mingos

Superconductivity in Complex Systems

Volume Editors: K. A. Müller, A. Bussmann-Holder

Springer Berlin Heidelberg New York

The series *Structure and Bonding* publishes critical reviews on topics of research concerned with chemical structure and bonding. The scope of the series spans the entire Periodic Table. It focuses attention on new and developing areas of modern structural and theoretical chemistry such as nanostructures, molecular electronics, designed molecular solids, surfaces, metal clusters and supramolecular structures. Physical and spectroscopic techniques used to determine, examine and model structures fall within the purview of Structure and Bonding to the extent that the focus is on the scientific results obtained and not on specialist information concerning the techniques themselves. Issues associated with the development of bonding models and generalizations that illuminate the reactivity pathways and rates of chemical processes are also relevant.
As a rule, contributions are specially commissioned. The editors and publishers will, however, always be pleased to receive suggestions and supplementary information. Papers are accepted for *Structure and Bonding* in English.
In references *Structure and Bonding* is abbreviated *Struct Bond* and is cited as a journal.

Springer WWW home page: http://www.springeronline.com
Visit the SB content at http://www.springerlink.com

ISSN 0081-5993 (Print)
ISSN 1616-8550 (Online)

ISBN-13 978-3-540-23124-0
DOI 10.1007/b12231

Series Editor

Professor Dr. Michael P. Mingos

Principal
St. Edmund Hall
Oxford OX1 4AR, UK
michael.mingos@st-edmund-hall.oxford.ac.uk

Volume Editors

Professor Dr. Dr. h.c. mult.
K. Alex Müller

Physik-Institut
der Universität Zürich
Winterthurer Str. 190
8057 Zürich, Switzerland
kam@physik.unizh.ch

Priv.-Doz. Dr.
Annette Bussmann-Holder

Max-Planck-Institut
für Festkörperforschung
Heisenbergstr. 1
70569 Stuttgart, Germany
A. Bussmann-Holder@fkf.mpg.de

Editorial Board

Preface

In this volume of the Springer Series "Structure and Bonding" superconductivity in unconventional systems is reviewed with emphasis on cuprate superconductors, however one additional contribution to the superconductivity of alkali-doped fullerides A_3C_{60} has also been included. Even though in this latter compound the evidence for phonon mediated pairing is well manifested, the problem to be solved lies in the fact that the Coulomb repulsion is of the same order of magnitude as the vibronic energy, whereas the A_2C_{60} and A_4C_{60} are insulators, the A_3C_{60} is a superconductor. Treating both energy scales on the same footing, an interesting interplay between Coulomb and phonon contributions results which enables electron (hole) pairing locally. The important phonon contribution is shown to arise from an intramolecular Jahn-Teller vibration which stabilizes the local pairs and overcomes the Coulomb repulsion for the A_3C_{60}.

The problem with cuprates is more complex since here pairing via phonon exchange is strongly debated. In addition the conventional pairing mechanism in the sense of the Bardeen-Cooper-Schrieffer (BCS) theory can be ruled out, as the very enhanced superconducting transition temperatures are not attainable without use of unreasonable parameters. The complexity of cuprates is enhanced due to the doping dependent phase diagram which not only change from an antiferromagnetic insulator to a metallic superconductor, but also exhibits regimes where charge and/or spin ordering is observed, typically characterized by the appearance of a pseudogap. The antiferromagnetism of the parent compounds has frequently been taken as evidence that a purely electronic mechanism is the origin for the hole pairing. Also the near vanishing isotope effect on the superconducting transition temperature T_c at optimum doping has supported a non-phononic mechanism, even though a substantial isotope effect appears when approaching the antiferromagnetic regime. The support of purely electronic pairing models was further increased by the observation that the superconducting gap function is of $d_{x^2-y^2}$ symmetry, which is hard to achieve within a phonon mediated pairing model. However, more detailed experiments give clear evidence that the symmetry of the pairing function is not that simple and especially bulk sensitive experiments have to be contrasted with surface sensitive ones. Obviously a pure $d_{x^2-y^2}$ symmetry order parameter is incompatible with the experimental observations and a substantial s-wave

component has to be present. Also the role of lattice displacements is crucial to superconductivity as outlined in the present volume.

A very specific aspect of exotic superconductivity in cuprates is played by the inherent heterogeneity of these compounds which reflects itself in the coexistence of locally distorted areas with the regular lattice. The role played by this heterogeneity is reviewed by one of the authors (K. A. M.) where various experimental findings are summarized which all yield stringent evidence that inhomogeneity is crucial to the pairing mechanism. Since most of the experimental data test lattice responses, a substantial involvement of the lattice in the pairing mechanism must be considered. Consistent with these observations are new isotope experiments where unconventional isotope effects as e.g. on the London penetration depth are reported. Such effects neither find an explanation within conventional phonon mediated BCS theory nor within any purely electronic pairing model. Here ideas related to the Jahn-Teller effect, polaron, bipolaron formation and preformed pair models are the only way out to obtain any isotope effect and again underline the special role played by specific lattice vibrations. Obviously also neutron scattering data support this point of view since strong phonon anomalies are observed in the superconducting regime only. The transfer of spectral weight at special momentum values to other regions in the Brillouin zone signals the local character of the lattice vibration and establishes that average properties are less relevant to superconductivity. This is also related to the short coherence length of the Cooper pairs which reflects the local character of the pairing potential.

A detailed neutron scattering analysis of the crystal-field spectra reveals evidence that the doping induced charge distribution is inhomogeneous and tends to appear in clusters thus leading to charge rich and charge poor areas. These experiments are also able to test directly the opening of the pseudogap where a huge mass reversed isotope effect is observed on the corresponding temperature T*. Also this effect implies that the lattice plays a dominant and unconventional role at least for the pseudogap state, but if this is considered to be the onset of local pair formation, it also points to a relevant role of special lattice distortions to superconductivity. A detailed analysis of the quasiparticle dynamics by femto second spectroscopy supports the picture of inherent heterogeneity since two relaxation times are observed which suggest that quasiparticles obeying different time scales coexist. The finding supports the idea of Jahn-Teller polaron formation and real space pair formation. Similarly the analysis of electron paramagnetic resonance data convincingly supports a polaronic picture where here a three spin polaron state is required in order to obtain agreement with experiment. Theoretically a two-component approach has been analysed which indicates that strong enhancements of the superconducting transition temperature are obtained as soon as the interaction between the two components is switched on. An additional enhancement factor stems from polaronic coupling as long as this is not too strong, which then favours localisation and a breakdown of superconductivity. The inhomogeneity is attributed here to strong anharmonicity in the electron-phonon

interaction which enables and stabilizes coexisting ground states. Charge rich and poor areas coexist and define new length scales which are incommensurate with the regular lattice. An extended account is also given of a scenario where local pairs coexist with itinerant electrons by means of which interesting crossovers between a BCS regime and a Bose-Einstein condensation are obtained. Finally a chemists point of view is presented where superconductivity is attributed to the coexistence of flat and steep electronic bands. While the flat bands give rise to local pairs, the steep bands provide them with mobility. Some conventional superconducting systems are analysed but also results for MgB_2 are presented where special emphasis is put on the role played by the smaller gap.

The current volume of Structure & Bonding is certainly biased concerning the pairing mechanism in exotic superconductors, since models based on purely electronic mechanisms are not included even though briefly reviewed in one of the contributions. It seems, however, to be timely to stress two issues which have long been ignored in these systems: the role of heterogeneity and the role of the lattice. While the former could be substantiated by new high resolution time and local probe experiments, the latter are known to be the key in conventional superconductors, but have been mostly ruled out for the compounds considered in this volume. The accumulating experimental evidence for their central role has been summarized in this issue. Last but not least it should be noted that the discovery of high temperature superconductivity in cuprates originated from the idea that Jahn-Teller polaron formation could cause a sufficiently attractive pairing potential to support high temperature superconductivity.

Stuttgart and Zürich, January 2005 Annette Bussmann-Holder
K. Alex Müller

Contents

Struct Bond (2005) 114: 1–11
DOI 10.1007/b101015

Essential Heterogeneities in Hole-Doped Cuprate Superconductors

K. A. Müller (✉)

Physics Institute, University of Zürich, 8057 Zürich, Switzerland

Abstract An expanded review of recent pertinent experiments in hole-doped cuprates is presented [1]. These include photoemission, inelastic neutron scattering, EXAFS, PDF, electron paramagnetic resonance and susceptibility data. For doping concentrations below optimum all are compatible with Jahn-Teller bipolaron formation at the pseudogap temperature T*, with a simultaneous presence of fermionic quasi-particles. The theoretically derived superconductivity onset and maximum T_c at optimal doping agree quantitatively with observation. Very large isotope effects at T* for lower doping support the vibronic character of the ground state.

Keywords High T_c superconductivity · Jahn-Teller effect · Lattice effects · Isotope effects

List of Abbreviations

ARPES	Angle resolved photoemission electron spectroscopy
EPR	Electron paramagnetic resonance
ESR	Electron spin resonance
EXAFS	Extended X-ray absorption fine spectroscopy
JT	Jahn-Teller
LTO	Low temperature orthorhombic
LTT	Low temperature tetragonal
NQR	Nuclear quadrupole resonance
PDF	Pair distribution function
T*	Pseudogap formation temperature
XANES	X-ray absorption near edge spectroscopy

1
Local Distortions

The essential structure of high T_c superconductors is well represented by Tokura's [2] picture of donor/acceptor/inert layers bracketing a CuO_2 sheet conductor. The many body wave function in the material is vibronic, i.e. includes both nuclear and electronic parts. For a single ion with the degenerate ground state

$$\Psi = \sum_i \psi_n^i \psi_e^i \tag{1}$$

without being in the adiabatic slaving limit and i=2,3. The many body nuclear part ψ_n^i is probed in neutron scattering experiments, while the electronic part ψ_e^i is probed by photoemission. There are, in general, two types of excitation energies that are doping dependent. This "vibronic" picture, in the sense of an interplay between the electronic charge and the ionic lattice structure, is a major theme of this review.

Photoemission (ARPES) data by Lanzara et al. [3] clearly show a common feature in different high temperature superconductors, that is a signature of the lattice playing a role. The quasi-particle energies vs (rescaled) wave vector plots for Bi2212, Bi2201 and LSCO show a kink, while NCCO does not show any such behaviour (Fig. 1).

The kink occurs near 70 meV at a characteristic wave vector half in the Brillouin zone and indicates two different group velocities. They are due to two different quasi-particles, one of fermionic character, and the other of more bosonic character at more negative energies.

Probing the other part of the wave function in Eq. (1), inelastic neutron scattering by Egami and collaborators [4] shows that LO phonon spectra in YBCO and LSCO change significantly with oxygen doping concentrations in $YBa_2Cu_3O_{6+x}$ from x=0.2 to 0.93 (Fig. 2).

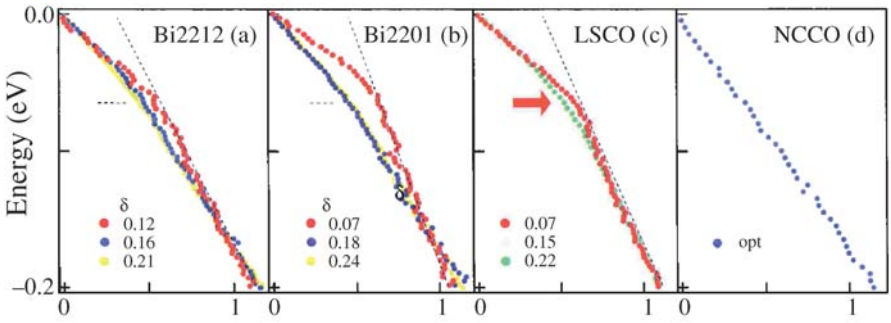

Fig. 1a–d The quasi-particle dispersions vs the rescaled momentum k′ for three p-type material systems (nodal direction): **a** Bi2212; **b** Bi2201; **c** LSCO. The *arrow* indicates the frequency values obtained by inelastic neutron diffraction data. The dispersions are compared with: **d** n-type superconductor NCCO along ΓY. The *dotted lines* are a guide to the eye obtained fitting, the linear part with a linear function [3]

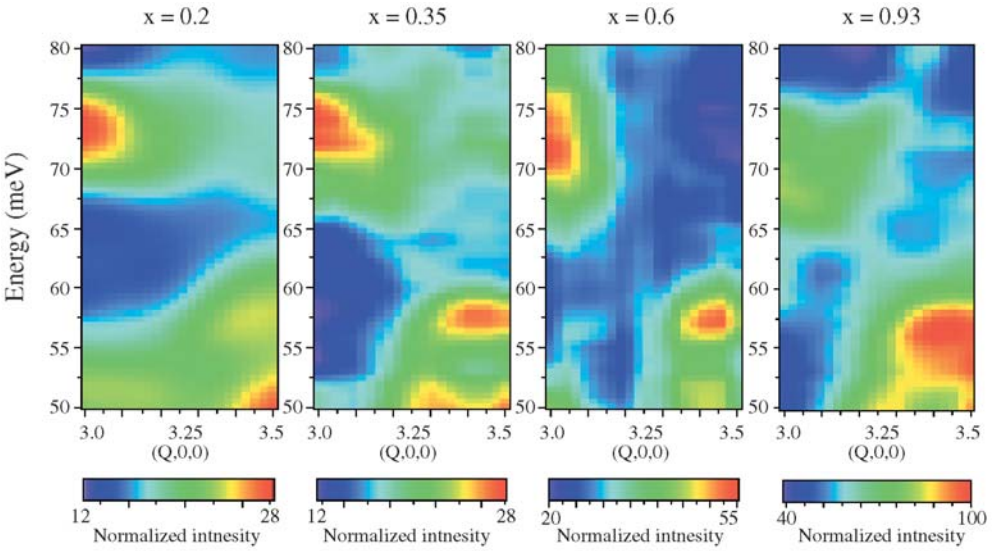

Fig. 2 Composition dependence of the inelastic neutron scattering intensity from YBCO single crystals with x=0.2, 0.35, 0.6 and 0.93, at T=10 K [4]

There is a distinct feature in the dispersion at 60–80 meV that also occurs in the Brillouin zone along a particular wave vector. The intensity of the excitation above the anomaly changes significantly in favour of the one below it. This reflects the change of the ratio of the two types of quasi-particles present.

While structure clearly is expected to play a role, there was already early evidence by EXAFS measurements of Bianconi et al. [5] that this lattice structure is locally varying. They suggested in x=0.15 LSCO that nano domains occurred, with alternating bands of "stripes", separating charge-rich and charge-poor regions. The stripes consist of distorted unit cell bands (D) of width ~8 Å and undistorted unit cell bands (U) of width ~16 Å (Fig. 3).

The U regions are locally LTO like, while the D regions have LTT like CuO_6 octahedra, relatively tilted by about 16°, and with bonds relatively closer in length. We note that the distorted octahedral are similar to a "Q_2" type local mode, familiar in the Jahn-Teller effect, a point we will return to later.

Lattice inhomogeneities are associated with the local patterns of octahedral tilts, or more generally, with a pair distribution (111) of such tilts as found by the Billinge group [6] (PDFs). They find from neutron diffuse scattering, that for LSCO, the x=0.1 data corresponding to "3° tilts" can in fact be reproduced by combinations of heavily (5°) and untilted (0°) octahedra. They support qualitatively the existence of two different lattice conformations in stripes as indicated in Fig. 3.

EPR data by Kochelaev et al. [7] show that in LSCO distortions exist (Fig. 4). They have been successfully modelled as a 3-spin polaron, again associated with dynamic "Q_2" like Jahn-Teller distortions.

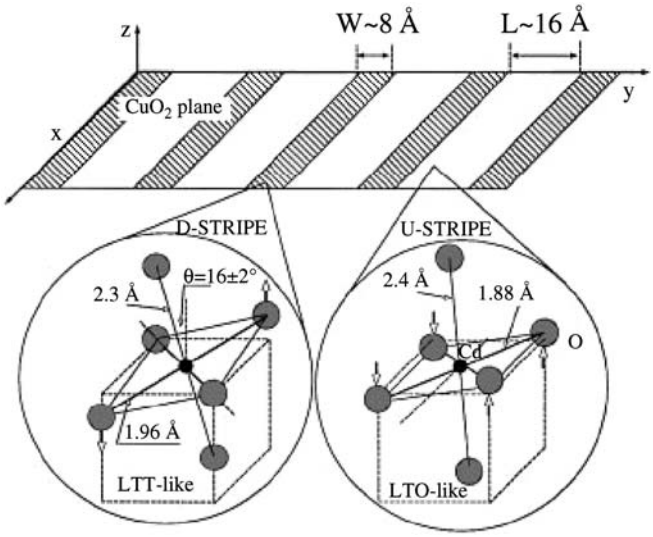

Fig. 3 Stripe formation at T* for $La_{2-x}Sr_xCuO_4$, x=0.15. Pictorial view of the distorted CuO_6 octahedra (*left side*) of the "LTT type" assigned to the distorted (D stripes) of width ≈8 Å and of the undistorted octahedra (U stripes) of width L≈16 Å. The superlattice of quantum stripes of wavelength λ=L+W is shown in the *upper part* [5]

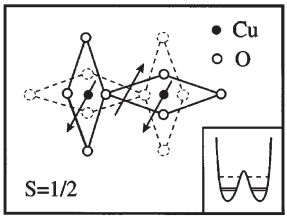

Fig. 4 Three-spin magnetic polaron which is regarded as the EPR active centre in the CuO_2 plane. The Jahn-teller distorted polaron has two degenerate configurations as indicated by the *dashed lines*. The inset shows the corresponding double-well potential with the excited vibronic states (*dashed lines*) and the ground state split by tunnelling (*solid lines*) [7]

In short, a variety of probes, including neutron scattering, PDF, ESR and EXAFS show that structural modes are important at various *finite wave vector* values, involving combinations of JT distortions.

2 Pairing

The intersite JT correlations can in fact, lead to a finite wave vector $q_c=2\pi/d$ pairing interaction, with a small pair size and short coherence length, $d \lesssim \xi$.

Kabanov and Mihailovic [8] have introduced a model compatible with these experiments, and to an interaction with a coupling constant of the form

$$g(q) = g_0[(q - q_c)^2 + \Gamma^2]^{1/2} \tag{2}$$

that is resonant in the wave vector. A group theoretical analysis showed that one can have coupling between $q \neq 0$ phonons and two-fold degenerate electron states including spins (Fig. 5) all with the resonant coupling structure of Eq. (2). By symmetry there are four coupling terms as shown in Panel 1. In front of each is a Pauli matrix σ_i, due to the twofold degeneracy of the state. The first term results from the coupling to the breathing mode. The second and third are due to the interaction to the x^2–y^2 and xy JT modes, and the fourth with the s_z matrix is due to the magnetic interaction. Measurements of the ratios of the g_1 and g_2 JT-coupling constants vs the magnetic coupling g_3 would settle the long standing discussion on the importance of lattice displacements as compared to the magnetic origin of the HTS in the cuprates.

Panel 1: Interaction between phonons $k \neq 0$ and twofold degenerate electronic states (a $k \neq 0$ Jahn-Teller effect)

$$\begin{aligned} H_{\text{int}} = & \sum_{l,s} \sigma_{0,l} \sum_{k_0=1}^{4} \sum_{\vec{k}} g_0(k_0, \vec{k}) \exp[i\vec{k}\,l] (b_{\vec{k}}^{+} + b_{-\vec{k}}) \\ & + \sum_{l,s} \sigma_{3,l} \sum_{k_0=1}^{4} \sum_{\vec{k}} g_1(k_0, \vec{k}) (k_x^2 - k_y^2) \exp[i\vec{k}\,l] (b_{\vec{k}}^{+} + b_{-\vec{k}}) \\ & + \sum_{l,s} \sigma_{1,l} \sum_{k_0=1}^{4} \sum_{\vec{k}} g_2(k_0, \vec{k}) k_x k_y \exp[i\vec{k}\,l] (b_{\vec{k}}^{+} + b_{-\vec{k}}) \\ & + \sum_{l,s} \sigma_{2,l} S_{z,l} \sum_{k_0=1}^{4} \sum_{\vec{k}} g_3(k_0, \vec{k}) k_x k_y \exp[i\vec{k}\,l] (b_{\vec{k}}^{+} + b_{-\vec{k}}) \end{aligned}$$

where $g_i(k_0, \vec{k}) = \dfrac{g_0\sqrt{\pi\gamma^2}}{[(k - k_0)^2 + \gamma^2]}$ and the Pauli matrices $\sigma_{i,j}$ represent the degenerate electronic states.

We note here that Weisskopf had shown for classical superconductors, that

$$\Delta \approx E_F \lambda / \xi \tag{3}$$

where λ is the screening length. This implies that the superconducting gap/temperature $\Delta \approx T_c$ is high when the correlation length ξ is small. Thus a small-pair model can be a high-T_c model.

In fact, if pairs are small, then superconductivity can be established through some kind of percolation, with pair size l_P smaller than the coherence length, and bigger than the lattice scale a:

$$a < \xi < l_P \tag{4}$$

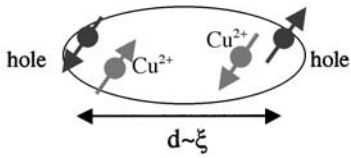

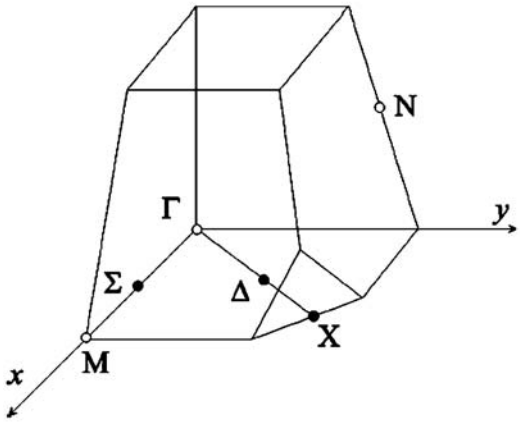

Fig. 5 The intersite Jahn-Teller pairing interaction. The Brillouin zone (BZ) of $La_{2-x}Sr_xCuO_4$ corresponding to the tetragonal phase with point group D_{4h} is shown below [8]

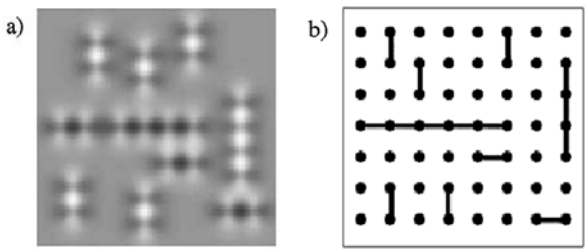

Fig. 6 **a** The amplitude of the lattice deformation caused by pairs described by the mesoscopic Jahn-Teller model. The picture corresponds to a "snapshot" at 6% doping at T=0 K. **b** The bond percolating model describing situation a [9]

The picture that emerges is of Jahn-Teller induced mesoscopic pairs, that fluctuate and percolate [9]. A further development of these ideas (Fig. 6) yields quantitatively:

1. An understanding of the minimum coherence length observed
2. The right percentage of holes for the onset of cuprate superconductivity (~6%)

3 Pseudogap

Returning to structure, we consider the pseudogap temperature T* as where the local distortions begin to occur. Work by Bussmann-Holder et al. [10] has shown that the bands of different symmetries $x^2–y^2$, $3z^2–r^2$ can be coupled dynamically by tilting octahedra. The model yields both a T_c, and a pseudogap temperature T*. The pseudogap formation drastically reduces the energy separation between charge and spin levels, from ~2 eV to the ~meV level.

There are also other related analyses [11] based on the JT polarons combining to form bipolarons, whose binding energy is found to fall as 1/x with doping. So the temperature doping phase diagram would show a bipolaron formation temperature T*(x) that decreases with doping x, and is above another negative-slope characteristic temperature, where bipolarons cluster to form stripes. The decreasing T* line would nearly meet the increasing superconducting T_c phase boundary at the optimum doping, i.e. maximum temperature T_c^{max} for superconductivity.

The local structure and its formation temperature T* can be probed by XANES methods, when an X-ray photon ejects an electron from the Cu^{2+} and the electron waves interact with the O^{2-} neighbours. Plots in an early paper by

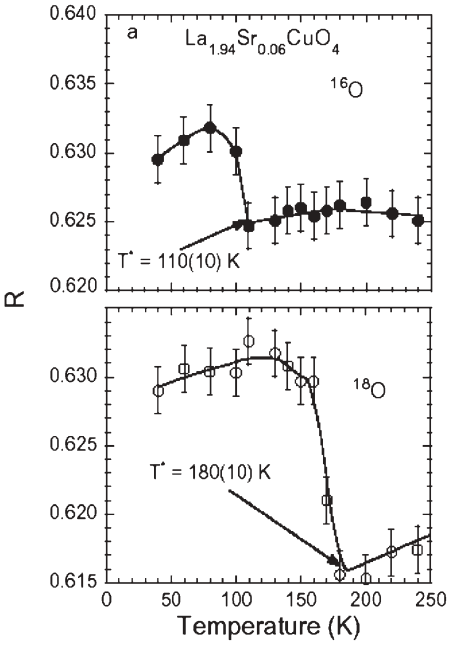

Fig. 7 The oxygen isotope effect on the charge-stripe ordering temperature T* in $La_{1.94}Sr_{0.06}CuO_4$ and the doping dependence of T*. The temperature dependence of the XANES peak intensity ratio R for the ^{16}O and ^{18}O samples of $La_{1.94}Sr_{0.06}CuO_4$ [12]

Lanzara et al. [12] show fluorescence counts vs phonon energy, with features that are linked to the neighbouring La/Sr, and in-plane oxygen. NQR is another important probe of local structure, as used by Imai and collaborators [13].

The temperature-dependence of the XANES peak intensity ratio shows a dip at T*~110 K, that is associated with stripe formation. Since this technique probes only oxygen neighbours, it is a site specific way to investigate effects of isotopic substitutions. In fact there is a large isotope effect, with $^{16}O \rightarrow ^{18}O$ substitution causing a rise to T*~180 K (Fig. 7). The dynamics of the stripes is exponentially dependent on the oxygen mass due to the polaronic character of the quasiparticles. The compound with the heavier ^{18}O then requires a larger thermal energy to "melt" the stripes at T* into single polarons.

Several techniques can be used to probe the T* vs doping curve for La and the techniques like XANES, NQR and EPR probe widely different time scales (10^{-13} s, 10^{-7} s, 10^{-9} s). Nonetheless, the data fall on the same curve below $T_c^{\max}$.

A quantitative confirmation of the XANES results in Fig. 7 are the inelastic time-of-flight, neutron scattering measurements by Rubio Temprano et al. [14]

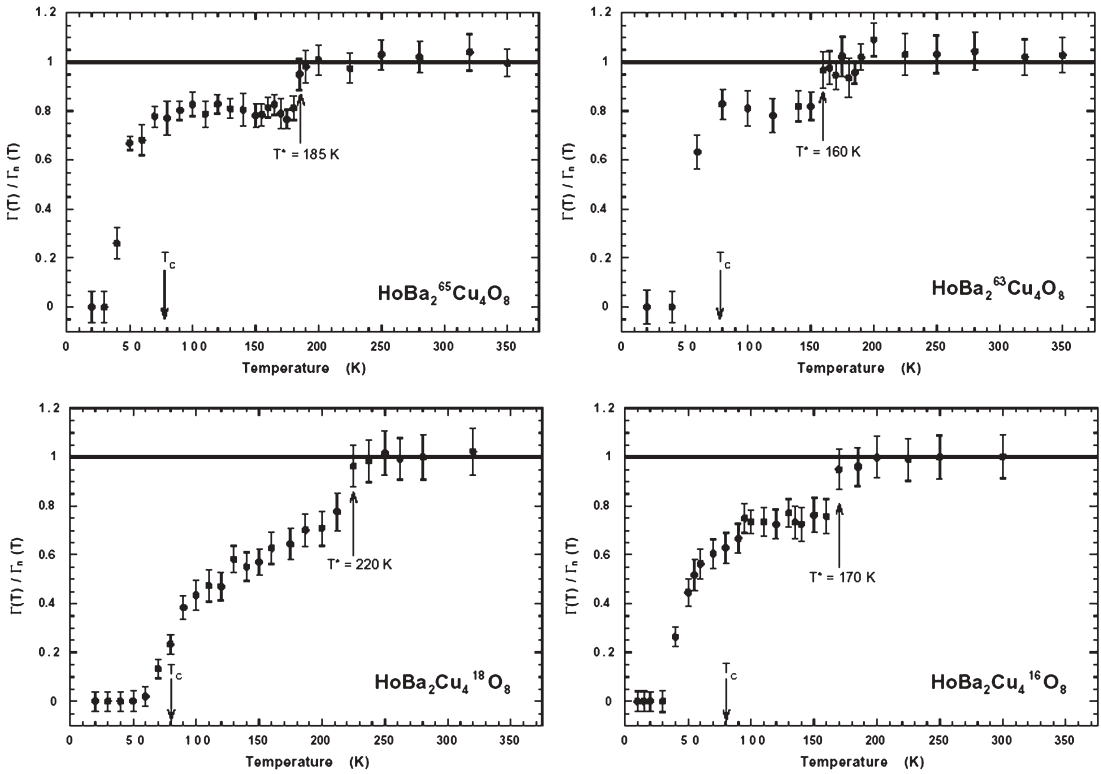

Fig. 8 Temperature dependence of the reduced linewidth observed for both copper and oxygen isotope substituted $HoBa_2Cu_4O_8$. The *solid line* represents the normal state linewidth were the linear term expected by the Korringa law has been subtracted

that substitute for yttrium. This work on the isotopic series $HoBa_2{}^{(n)}Cu_4{}^{(p)}O_8$ where n=63, 65 and p=16, 18, reveals a large T* isotope effect for oxygen (α_0^*=–2.2) and an even larger value for copper (α_{Cu}^*=–4.9) (Fig. 8 [14]). Thus *both* copper and oxygen dynamics play a role in stripe formation of YBCO, on a scale of ~10^{-12} s, that cannot be accounted for by magnetic interactions.

The oxygen isotope shift reflects the JT interaction whereas the Cu isotope effect is ascribed to the so-called "umbrella" mode in which a Cu motion is present due to the lack of inversion symmetry at the planar Cu site. This is because of the pyramidal oxygen coordination of Cu in YBCO. Indeed, later results for Ho in LSCO yielded a similar oxygen isotope shift for T* but none between Cu^{63} and Cu^{65} samples [15]. In LSCO the Cu is octahedrally coordinated and only the quadrupolar JT modes can be active; the inversion symmetry precludes an asymmetric Cu motion. In conjunction, the T_c in LSCO is about half the one in YBCO of 92 K at maximum doping, that is the coupling to the umbrella mode in YBCO is responsible for about half of the superconductivity, the other half appears to come from the JT mode with the same strength as in LSCO.

4 Most Recent Advances

Both, photoemission and EPR have substantially contributed very recently to the understanding of the microscopic behaviour of the cuprates, deepening the so far described insights. The former technique probes the wave vector particle dispersion as a function of energy. Referring to Fig. 1, no isotope effect has been found for small energies below (0,0), marking the Fermi level. However, for the larger energies below the characteristic knee in the dispersion substantial and doping dependent effects have been observed by Lanzara et al. [16]. The isotope independent part near the Fermi energy is ascribed to metallic quasi particles and the other may be related to polarons. This confirms the presence of two kinds of particles one of fermionic and the other of polaronic character.

Directly related to these observations are the EPR results of Shengelaya et al. [17]. In lightly doped LSCO, using Mn^{2+} as a probe, two EPR lines are detected, a narrow and a broad one. The width of the narrow one is oxygen isotope independent, whereas the broad one is isotope dependent. The former line is assigned to Mn^{2+} ions sited in metallic regions of the sample and the broad to those near single polarons. Upon cooling, the narrow one grows exponentially in intensity whereas the broad one nearly disappears. The activation energy deduced from the exponential behaviour of the narrow EPR line is 460 (50) K, independent of the hole doping between 1% and 6%, the range of the experiments. The experimental activation energy is within experimental error the same as deduced from Raman and inelastic scattering from bipolarons. Therefore it is suggestive that bipolaron formation is the elementary process for the aggregation of metallic regions, as Fig. 6 shows. This finding has as well a

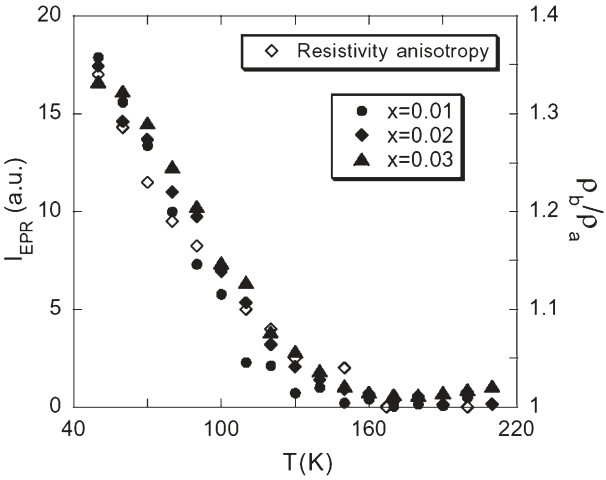

Fig. 9 Temperature dependence of the narrow EPR line intensities in $La_{2-x}Sr_xCu_{0.98}Mn_{0.02}O_4$ and of the resistivity anisotropic ratio in $La_{1.97}Sr_{0.03}CuO_4$ [17]

macroscopic consequence, because the EPR intensity follows the same temperature dependence as the in-plane resistivity anisotropy in LSCO for the same doping range (Fig. 9). The same temperature behaviour of the microscopic EPR and macroscopic resistivity anisotropy shown is astounding.

5 Concluding Comments

Most theories of cuprate superconductors use the machinery of highly correlated conducting matter, and in them the lattice is taken as rigid at the outset. The many experiments of quite different character outlined here tell a quite different story, especially if the time scale of a particular experiment is sufficiently short. The heterogeneity becomes manifest in a clear manner. For all of them, the vibronic character of the ground state is present in a consistent way. This, however, was the concept which led to the discovery of HTS cuprates [18]. Finally it should be noted that the JT bipolaron quasi-particles include high correlations as well, which is often overlooked.

Acknowledgements A. Bussmann-Holder edited this manuscript in a substantial way based on an earlier version [1].

References

1. A shorter version lacking figures has appeared in: Bishop AR, Shenoy SR, Sridhar S (eds) (2003) Intrinsic multiscale structure and dynamics in complex electronic oxides. World Scientific, p 1
2. Tokura Y, Arima T (1999) Jpn J Appl Phys 29:2388
3. Shen ZX, Lanzara A, Ishihara S, Nagaosa N (2002) Phil Mag B 82:1349; Lanzara A, Bogdanov PV, Zhou X, Kellar SA, Feng DL, Liu ED, Yoshida T, Eisaki H, Fujimori A, Kishio K, Shimoyama JI, Noda T, Uchida S, Hussain Z, Shen ZX (2001) Nature 412:510
4. Petrov Y, Egami T, McQueeney RJ, Yethiraj M, Mook HA, Dogan F (2000) cond-mat/0003414; McQueeney RJ, Petrov Y, Egami T, Yethiraj M, Shirane G, Endoh Y (1999) Phys Rev Lett 82:628; Chung JH, Egami T, McQueeney RJ, Yethiraj M, Arai M, Yokoo T, Petrov Y, Mook HA, Endoh Y, Tajima S, Frost C, Dogan F (2003) Phys Rev B 67:014517
5. Bianconi A, Saini NL, Lanzara A, Missori M, Rosetti T, Oyanagi H, Yamaguchi H, Oka K, Itoh T (1996) Phys Rev Lett 76:3412
6. Bozin ES, Billinge SJL, Kwei GH, Takagi H (1999) Phys Rev B 59:4445
7. Kochelaev BI, Sichelschmidt J, Elschner B, Lemor W, Loidl A (1997) Phys Rev Lett 79:4274
8. Mihailovic D, Kabanov VV (2001) Phys Rev B 63:054505
9. Mihailovic D, Kabanov VV, Müller KA (2002) Europhys Lett 57:254
10. Bussmann-Holder A, Müller KA, Micnas R, Büttner H, Simon A, Bishop AR, Egami T (2001) J Phys Cond Mat 13:L169
11. Müller KA, Zhao GM, Conder K, Keller H (1998) J Phys Cond Mat 10:291
12. Lanzara A, Zhao GM, Saini NL, Bianconi A, Conder K, Keller H, Müller KA (1999) J Phys Cond Mat 11:L541
13. Hunt AW, Singer PM, Thurber KR, Imai T (1999) Phys Rev Lett 82:4300
14. Rubio Temprano D, Mesot J, Janssen S, Conder K, Furrer A, Mutka A, Müller KA (2000) Phys Rev Lett 84:1990
15. RubioTemprano D, Mesot J, Janssen S, Conder K, Furrer A, Sokolov A, Trounov V, Kazakov SM, Karpinski J, Müller KA (2001) Eur Phys J B 19:R5
16. Lanzara A (2004) Nature (submitted)
17. Shengelaya A, Bruun M, Kochelaev BI, Safina A, Conder K, Müller KA (2004) Phys Rev Lett (submitted)
18. Bednorz JG, Müller KA (1988) Adv Chem 100:757, Nobel Lecture

Struct Bond (2005) 114: 13–69
DOI 10.1007/b101016

Two-Component Scenarios for Non-Conventional (Exotic) Superconductors

Roman Micnas[1] (✉) · Stanislaw Robaszkiewicz[1] · Annette Bussmann-Holder[2]

[1] Institute of Physics, A. Mickiewicz University, 85 Umultowska St., 61-614 Poznan, Poland
rom@alpha.amu.edu.pl
[2] Max-Planck-Institute for Solid State Research, Heisenbergstr. 1, 70569 Stuttgart, Germany

Abstract The possibility of superconductivity is analyzed within models where two components are present. Here both components may be non-superconducting on their own, but become superconducting when coupled to each other. Also the possibility exists that only one system is superconducting and induces via coupling superconductivity in the second component. Another scenario is that the physical properties of the considered systems are totally different: while one is assumed to consist of itinerant fermions, the second may consist of preformed pairs, "hard core bosons". All scenarios are shown to lead to superconductivity where different pairing symmetries are possible. Typically two superconduct-

ing gaps are observed, and enhancements of the superconducting transition temperature T_c as compared to BCS theory are a consequence. The consequences for other superconducting characteristics but also for the normal state are investigated and possible applications to new non-conventional high temperature superconductors discussed.

Keywords High temperature superconductivity · Unconventional electron-lattice interactions · Boson fermion model · Two component superconductivity

List of Abbreviations

BCS	Bardeen Cooper Schrieffer
d	d-wave symmetry
KT	Kosterlitz Thouless
LP	Local Pair
MFA	Mean-field approximation
s	s-wave symmetry
s*	Extended s-wave symmetry
T^*	Pseudogap temperature
T_c	Superconducting transition temperature

1 Introduction

The discovery of superconductivity in mercury by Kammerlingh Onnes in 1911 was not expected theoretically and remained an unsolved problem for about half a century. Only in 1957 Bardeen, Cooper and Schrieffer (BCS) [1] suggested that the virtual exchange of phonons may give rise to an effective attractive electron-electron interaction and a superconducting ground state. This theory is based on amazingly many simplifying assumptions which are hardly ever fulfilled in realistic systems: the Fermi surface is approximated by a sphere with a single band, the phonons are structureless, i.e. Einstein oscillators, the crystalline lattice is replaced by an oscillating continuum, the Coulomb interaction is replaced by a constant, the electron-lattice coupling is weak, etc. In spite of all these simplifications the theory has been extremely successful and applied to many compounds, and mostly the predictions made by BCS have been verified experimentally. With the increasing number of superconducting systems, deviations from BCS theory were observed experimentally which have been explained within extensions of the theory as, e.g., strong coupling Eliashberg theory [2], the Allen-Dynes approach [3], and many more approaches [4–6]. However the main assumptions of the BCS theory of electron-electron attraction due to virtual exchange of phonons have mostly remained the basis of all its extensions.

In this review we concentrate on systems which consist of two components, both of which may be superconducting on their own, both may be non superconducting, one may be a superconductor while the other is a conventional metal or insulator, one subsystem consists of preformed pairs (bosons), while

the other consists of itinerant electrons. The diverse scenarios are investigated and the consequences for the superconducting as well as the normal state explored.

The review is organized in the following way: in the next section the two-band model is introduced followed by an introduction of the standard case. Extensions of this are presented in the following section where first the case of *induced* superconductivity is discussed and then the competition and/or coexistence of different gap symmetries is analyzed. Possible sources of how to enhance the superconducting transition temperature are detailed consecutively, where especially the role played by *unconventional* electron-lattice coupling is addressed. Consequences of these couplings are shown to arise in unusual isotope effects. After this, the emphasis is on the coexistence of local electron pairs and itinerant electrons. The generalities of such a scenario are outlined first, followed by solutions for anisotropic superconductivity in terms of the phase diagram and the superfluid characteristics. Phase fluctuation effects, pairing correlations and the pseudogap are finally analyzed. Finally, the results are summarized and possible applications discussed.

2
The Two-Band Model

2.1
The Standard Case

Very shortly after the work by BCS [1] two papers discussed independently of each other the possibility that superconductivity may not arise in a single band, but may be a consequence of two overlapping bands in the vicinity of the Fermi surface where a pairwise exchange of electrons between the two bands takes place via a phononic mechanism [7, 8]. In spite of the fact that effectively s and d bands or s and p bands or various other bands may contribute to the two-band model, effective density of states in the vicinity of the Fermi surface are introduced in addition to average matrix elements for phonon mediated transitions. The starting point for this two-band model is the generalized BCS Hamiltonian:

$$H = H_1 + H_2 + H_3 \tag{1}$$

$$H_1 = \sum_{k,\sigma} [E_1(\vec{k}) - \mu_1)\, a^+_{k,\sigma}\, a_{k,\sigma} + (E_2(\vec{k}) - \mu_2)\, b^+_{k,\sigma}\, b_{k,\sigma}] \tag{1a}$$

$$H_2 = -\frac{1}{V} \sum_{k \neq g} [V_1\, a^+_{k\uparrow}\, a^+_{-k\downarrow}\, a_{-g\downarrow}\, a_{g\uparrow} + V_2\, b^+_{k\uparrow}\, b^+_{-k\downarrow}\, b_{-g\downarrow}\, b_{g\uparrow}] \tag{1b}$$

$$H_3 = -\frac{1}{V} \sum_{k \neq g} [V_{12}(a^+_{k\uparrow}\, a^+_{-k\downarrow}\, b_{-g\downarrow}\, b_{g\uparrow} + b^+_{k\uparrow}\, b^+_{-k\downarrow}\, a_{-g\downarrow}\, a_{g\uparrow}] \tag{1c}$$

Here V is the volume and the terms in H_1 are the momentum k, g dependent kinetic energies E_i (i=1, 2) and chemical potentials μ_i of the two bands considered, where electron creation and annihilation operators of the two bands are denoted by a^+, a in band 1 and b^+, b in band 2, respectively, with spin index σ. H_2 contains the effective attractive *intraband* pairing potentials given by V_i, whereas H_3 corresponds to pairing interactions V_{12} stemming from *interband* pair scattering. Even though the attractive interactions can be due to any type of interactions, it is assumed that they are phonon mediated. Obviously the above Hamiltonian implies that the coupled components are characterized by two order parameters and a term that admits for pairwise exchange between both. A scenario like this has long been searched for after the introduction of the two-band model and its extensions [9–13], and has been believed to be realized in many conventional superconductors; however an unambiguous identification of a two-gap structure, which is a consequence of the model, could only be obtained in Nb-doped $SrTiO_3$ [14]. Only very recently, it has been shown that the new high temperature superconductor MgB_2 is characterized by two gaps with very different values of the individual gap energies [15–21]. In high temperature superconducting cuprates this question is still open even though many experimental facts point to a realization of such a scenario.

In order to derive the superconducting properties of the Hamiltonian in Eq. (1), it is convenient to apply a Bogoliubov transformation [22] to the Fermi operators according to

$$\begin{aligned} a_{k\uparrow} &= u_k^{(a)}\alpha_{k1} + v_k^{(a)}\alpha_{-k0}^+ \qquad & b_{k\uparrow} &= u_k^{(b)}\beta_{k1} + v_k^{(b)}\beta_{-k0}^+ \\ a_{k\downarrow} &= u_k^{(a)}\alpha_{k0} - v_k^{(a)}\alpha_{-k1}^+ \qquad & b_{k\downarrow} &= u_k^{(b)}\beta_{k0} - v_k^{(b)}\beta_{-k1}^+ \end{aligned} \tag{2}$$

The transformed Hamiltonian then reads

$$H = U + H_0 + H_1 + H_2 + H_3 + H_4 + H_5 \tag{3}$$

$$U = 2\sum_k [\varepsilon_1(\vec{k})v_k^{(a)2} + \varepsilon_2(\vec{k})v_k^{(b)2}), \quad \varepsilon_i = E_i - \mu_i \tag{3a}$$

$$H_{0\alpha} = \sum_k \Omega_1(\vec{k})[\alpha_{k1}^+\alpha_{k1} + \alpha_{k0}^+\alpha_{k0}] \tag{3b}$$

$$H_{1\alpha} = \sum_k [\varepsilon_1(\vec{k})\{u_k^{(a)2} - v_k^{(a)2} - \Omega_1(\vec{k})\}]\{\alpha_{k1}^+\alpha_{k1} + \alpha_{k0}^+\alpha_{k0}\} \tag{3c}$$

$$H_{2\alpha} = \sum_k 2\varepsilon_1(\vec{k})u_k^{(a)}v_k^{(a)}[\alpha_{k1}^+\alpha_{-k0}^+ + \alpha_{-k0}\alpha_{k1}] \tag{3d}$$

$$\begin{aligned} H_{3\alpha} = -\frac{1}{V}\sum_{k,g} u_k^{(a)}v_k^{(a)}[\alpha_{-k0}\alpha_{-k0}^+ - \alpha_{k1}^+\alpha_{k1}][V_1 u_g^{(a)}v_g^{(a)}(\alpha_{-g0}\alpha_{-g0}^+ - \alpha_{g1}^+\alpha_{g1}) \\ + V_{12}u_g^{(b)}v_g^{(b)}(\beta_{-g0}\beta_{-g0}^+ - \beta_{g1}^+\beta_{g1})] \end{aligned} \tag{3e}$$

$$H_{4\alpha} = -\frac{1}{V}\sum_{k,g} u_k^{(a)} v_k^{(a)} [\alpha_{-k0}\alpha_{-k0}^{+} - \alpha_{k1}^{+}\alpha_{k1}] [V_1(u_g^{(a)2} - v_g^{(a)2})(\alpha_{g1}^{+}\alpha_{-g0}^{+} + \alpha_{-g0}\alpha_{g1}) + V_{12}(u_g^{(b)2} - v_g^{(b)2})(\beta_{g1}^{+}\beta_{-g0}^{+} - \beta_{-g0}\beta_{g1})] \tag{3f}$$

$$H_{5\alpha} = -\frac{1}{V}\sum_{k,g} [u_k^{(a)2}\alpha_{k1}^{+}\alpha_{-k0}^{+} - v_k^{(a)2}\alpha_{-k0}\alpha_{k1}] \{V_1(u_g^{(a)2}\alpha_{-g0}\alpha_{g1} - v_g^{(a)2}\alpha_{g1}^{+}\alpha_{-g0}^{+}) + V_{12}(u_g^{(b)2}\beta_{-g0}\beta_{g1} - v_g^{(b)2}\beta_{g1}^{+}\beta_{-g0}^{+})\} \tag{3g}$$

All terms of $H_{i\beta}$ (i=1–5) in Eq. (3) analogous to those in α have to be added to the above Hamiltonian, whereby all terms referring to the first band have to be replaced by those of the second band and vice versa. In Eq. (3) the renormalized energies of the elementary excitations $\Omega_i(\vec{k})$ have been introduced. These together with $u^{(a,b)}$, $v^{(a,b)}$ have to be determined. A convenient method to do this, is to consider the thermodynamic potential [23]:

$$\Psi = \Psi_0 - \frac{1}{k_B T}\sum_{p\geq 1}(-1)^p \int_0^{1/k_B T} dt_1 \ldots dt_p < S'(t_1) \ldots S'(t_p) > \tag{4}$$

where $< >$ is the statistical average and

$$S'(t) = e^{H_0 t} S' e^{-H_0 t} \tag{5}$$

The thermodynamic potential in the zero order approximation is then given by

$$\Psi_0 = U - 2k_B T \sum_k \sum_{i=1,2} \ln\left[1 + \exp\left(-\frac{\Omega_i(\vec{k})}{k_B T}\right)\right] \tag{6}$$

Following [24] and introducing the Fermi functions $f_i(k)$=1/[1+exp($\beta\Omega_i(k)$] (β=1/$k_B T$) one obtains for the first order in S':

$$\Psi = \Psi_0 + 2\sum_{\substack{k,\, i=1,2\\ a,\, b}} [\varepsilon_i(\vec{k})(u_k^{(a,b)2} - v_k^{(a,b)2}) - \Omega_i(\vec{k})][1 - f_i(\vec{k})] - \frac{1}{V}\sum_{\substack{k,\, i=1,2\\ a,\, b}} V_i u_k^{(a,b)} v_k^{(a,b)} [1 - 2f_i(\vec{k})] - 2\frac{1}{V}\sum_{k,g} V_{12}[u_k^{(a)} v_k^{(a)}(1 - 2f_1(\vec{k}))][u_g^{(b)} v_g^{(b)}(1 - 2f_2(\vec{g}))] \tag{7}$$

The parameters of the problem are calculated by requiring that terms appearing in second order in S' are fully compensated, whereas the asymptotic higher order approximations for $S' \to \infty$ do not contribute further to the thermodynamic potential. As a result the following solutions are obtained:

$$u_k^{(a)} = \sqrt{\left[\frac{1}{2}\left(1 + \frac{\varepsilon_1(\vec{k})}{\Omega_1(\vec{k})}\right)\right]}, \quad v_k^{(a)} = \sqrt{\left[\frac{1}{2}\left(1 - \frac{\varepsilon_1(\vec{k})}{\Omega_1(\vec{k})}\right)\right]}$$
$$u_k^{(b)} = \sqrt{\left[\frac{1}{2}\left(1 + \frac{\varepsilon_2(\vec{k})}{\Omega_2(\vec{k})}\right)\right]}, \quad v_k^{(b)} = \sqrt{\left[\frac{1}{2}\left(1 - \frac{\varepsilon_2(\vec{k})}{\Omega_2(\vec{k})}\right)\right]} \tag{8}$$

$$\Omega_i(\vec{k}) = \sqrt{\varepsilon_i(\vec{k})^2 + \Delta_i^2}$$

$$\Delta_1 = \frac{V_1}{V}\sum_k u_k^{(a)} v_k^{(a)} [1 - 2f_1(\vec{k})] + \frac{V_{12}}{V}\sum_k u_k^{(b)} v_k^{(b)} [1 - 2f_2(\vec{k})]$$
$$\Delta_2 = \frac{V_2}{V}\sum_k u_k^{(b)} v_k^{(b)} [1 - 2f_2(\vec{k})] + \frac{V_{12}}{V}\sum_k u_k^{(a)} v_k^{(a)} [1 - 2f_1(\vec{k})] \tag{9}$$

Consequently the thermodynamic potential adopts the following form:

$$\Psi = \sum_{k,i=1,2} [\varepsilon_i(\vec{k}) - \Omega_i(\vec{k})] - [2k_BT \sum_{k,i=1,2} \ln[1 + \exp(-\Omega_i(\vec{k})/k_BT)]$$
$$+ \frac{V}{V_1}\Delta_1 \frac{\Delta_1 - \frac{V_{12}}{V_2}\Delta_2}{1 - \frac{V_{12}^2}{V_1 V_2}} + \frac{V}{V_2}\Delta_2 \frac{\Delta_2 - \frac{V_{12}}{V_1}\Delta_1}{1 - \frac{V_{12}^2}{V_1 V_2}} \tag{10}$$

The gap equations can now be derived:

$$\Delta_1 = \frac{V_1}{2V}\sum_k \frac{\Delta_1}{\Omega_1(\vec{k})} \tanh\left[\frac{\Omega_1(\vec{k})}{2k_BT}\right] + \frac{V_{12}}{2V}\sum_k \frac{\Delta_2}{\Omega_2(\vec{k})} \tanh\left[\frac{\Omega_2(\vec{k})}{2k_BT}\right] \tag{11}$$

$$\Delta_2 = \frac{V_2}{2V}\sum_k \frac{\Delta_2}{\Omega_2(\vec{k})} \tanh\left[\frac{\Omega_2(\vec{k})}{2k_BT}\right] + \frac{V_{12}}{2V}\sum_k \frac{\Delta_1}{\Omega_1(\vec{k})} \tanh\left[\frac{\Omega_1(\vec{k})}{2k_BT}\right] \tag{12}$$

The critical temperature T_c is then defined by the condition $\Delta_1, \Delta_2 \to 0$ to yield:

$$\Delta_1 = \frac{V_1}{2V}\sum_k \frac{\Delta_1}{\varepsilon_1(\vec{k})} \tanh\left[\frac{\varepsilon_1(\vec{k})}{2k_BT_c}\right] + \frac{V_{12}}{2V}\sum_k \frac{\Delta_2}{\varepsilon_2(\vec{k})} \tanh\left[\frac{\varepsilon_2(\vec{k})}{2k_BT_c}\right]$$
$$\Delta_2 = \frac{V_2}{2V}\sum_k \frac{\Delta_2}{\varepsilon_2(\vec{k})} \tanh\left[\frac{\varepsilon_2(\vec{k})}{2k_BT_c}\right] + \frac{V_{12}}{2V}\sum_k \frac{\Delta_1}{\varepsilon_1(\vec{k})} \tanh\left[\frac{\varepsilon_1(\vec{k})}{2k_BT_c}\right] \tag{13}$$

Upon replacing the summations by integrals and introducing the density of states at the Fermi energy like

$$N_{i,i=1,2}(0) = \frac{1}{8\pi^3} \iint_{E_F} \frac{dS_i}{|\, grad_k E_i(\vec{k})} \tag{14}$$

dimensionless coupling constants are defined by $\lambda_1 = N_1(0)V_1$, $\lambda_2 = N_2(0)V_2$, $\lambda_{12} = \sqrt{N_1(0)N_2(0)}\,V_{12}$ from which, together with Eq. (13) the implicit equation for T_c is given by

$$\int_0^{\hbar\omega} \frac{1}{\varepsilon} \tanh\left[\frac{\varepsilon}{2k_B T_c}\right] d\varepsilon = \frac{1}{2}\left[\lambda_1 + \lambda_2 \pm \sqrt{(\lambda_1 - \lambda_2)^2 + 4\lambda_{12}^2}\right] / [\lambda_1\lambda_2 - \lambda_{12}^2] \tag{15}$$

i.e.

$$k_B T_c = 1.14\hbar\omega \exp(-1/\lambda) \tag{16}$$

$$1/\lambda = \frac{1}{2}\left[\lambda_1 + \lambda_2 \pm \sqrt{(\lambda_1 - \lambda_2)^2 + 4\lambda_{12}^2}\right] / [\lambda_1\lambda_2 - \lambda_{12}^2] \tag{17}$$

The sign in front of the root in Eq. (17) has to be chosen such that λ is positive. At this point it has to be emphasized that in the final derivation of T_c already a number of approximations have been introduced which might be rather unrealistic for real systems: i) the gap parameters have been taken to be independent of k; ii) it has been assumed that a single (Einstein) phonon energy is involved in the pairing which is the same for both bands; iii) the density of states at E_F has been assumed to be constant; iv) the interband scattering potential is the same for pair exchanges between band 1 and 2 and vice versa; v) finally both band energies are identical. In spite of these approximations a variety of predictions are obvious from the modeling: i.e. the gap to T_c ratios do not agree with BCS predictions, the isotope effect differs from the one in conventional BCS theory, the penetration depth could be anisotropic, in tunneling experiments two gaps should be detected, the specific heat jump at T_c is modified like

$$\Delta c_V = \frac{V}{(k_B T_c)^2} \sum_{i=1,2} N_i(0) \left(\frac{d\Delta_i^2}{d\,\dfrac{1}{k_B T_c}} \right)_{T=T_c} \tag{18}$$

When analyzing the above results limiting solutions are obvious: in the case of V_{12} being zero the gap equations are decoupled and basically two values for T_c, i.e. T_{ci}, are obtained: Here the smaller value of V_i defines the lower bound of T_{ci}. Thus upon cooling the system of independent electrons, system 1 will become superconducting at T_{c1}, whereas further cooling will drive subsystem 2 into the superconducting state at T_{c2} (if $V_1 > V_2$). In this case the values for the gaps can be derived analytically in the limit $T \to 0$: $\Delta_1 = 2\hbar\omega \exp(-1/\lambda_1)$, $\Delta_2 = 2\hbar\omega \exp(-1/\lambda_2)$,

$\Delta_1/\Delta_2=\exp(1/\lambda_2-1/\lambda_1)$. However, as soon as V_{12} is finite, both gaps vanish simultaneously at a single transition temperature, as given in Eq. (16). In the special case of $V_{12}^2/(V_1V_2)=1$ the equation for T_c simplifies to: $T_c=1.14\hbar\omega \exp[-1/(\lambda_1+\lambda_2)]$ and the gaps become

$$\Delta_1(0) = 2\hbar\omega \left[\frac{V_{12}}{V_2}\right]^{\frac{\lambda_2}{\lambda_1+\lambda_2}} \exp\left[-1/(\lambda_1+\lambda_2)\right]$$
$$\Delta_2(0) = 2\hbar\omega \left[\frac{V_{12}}{V_1}\right]^{\frac{\lambda_1}{\lambda_1+\lambda_2}} \exp\left[-1/(\lambda_1+\lambda_2)\right] \tag{19}$$

A similar simplification is achieved if one assumes that the densities of states in the two bands differ considerably, i.e. one being much larger than the other, a situation which probably applies to systems with d-electron bands. Here, however, the analytical derivation is not given since this can be done easily from the knowledge of the above derived expressions. It is important to note that superconductivity in the two-band model is much more robust than in the conventional BCS model, as here even repulsive interband interactions lead to enhancements of the superconducting transition temperature and the neglected Coulomb repulsion is more easily compensated.

2.2 Induced Superconductivity

An interesting case of the above model has been studied by Kresin and Wolf and collaborators [24–30], where they assume that one of the two subsystems is not superconducting at all (*normal*), but may become superconducting under the influence of the second (*intrinsically* superconducting) component. Here two possibilities arise: superconductivity in the *normal* band can be induced either via charge transfer through the interband interaction term V_{12} or by tunneling. The tunneling can easily be incorporated in the Hamiltonian equations (Eq. 1) by adding the term [31]

$$H_T = \sum_{k,g} (T_{k,g}^{(a,b)} a_k^+ b_g + T_{g,k}^{(b,a)} b_g^+ a_k) \tag{20}$$

to the Hamiltonian. This leads to an important modification of the gap equations, i.e.

$$\Delta_1 = \frac{V_1}{2V}\sum_k \frac{\Delta_1}{\Omega_1(\vec{k})}\tanh\left[\frac{\Omega_1(\vec{k})}{2k_BT}\right] + \frac{V_{12}}{2V}\sum_k \frac{\Delta_2}{\Omega_2(\vec{k})}\tanh\left[\frac{\Omega_2(\vec{k})}{2k_BT}\right]$$
$$+ \Gamma_{1,2}^{(a,b)}\sum_k \frac{\Delta_2}{\Omega_2(\vec{k})}\tanh\left[\frac{\Omega_2(\vec{k})}{2k_BT}\right] \tag{21}$$

$$\Delta_2 = \frac{V_{12}}{2V}\sum_k \frac{\Delta_1}{\Omega_1(\vec{k})}\tanh\left[\frac{\Omega_1(\vec{k})}{2k_BT}\right] + \Gamma_{1,2}^{(a,b)}\sum_k \frac{\Delta_1}{\Omega_1(\vec{k})}\tanh\left[\frac{\Omega_1(\vec{k})}{2k_BT}\right] \tag{22}$$

with the definition $\Gamma_{1,2}^{(a,b)}=|T^{(a,b)}|^2N_2(0)$, $\Gamma_{2,1}^{(b,a)}=|T^{(b,a)}|^2N_1(0)$ [4]. In view of the fact that system 2 is *normal*, the first term appearing in the equation for Δ_1 is missing in the one for Δ_2. This means explicitly that superconductivity is *induced* in this band where two terms contribute to it: the first term in Eq. (22) arises from charge transfer, while the second is equivalent to the MacMillan tunneling proximity model [4]. This is possible only, if the two subsystems are spatially separated and tunneling of Cooper pairs becomes possible. A realization of this idea can be found in layered compounds where, e.g., one layer is a metal while the other one is an insulator. Here the cuprate superconductors are likely candidates and also MgB_2 could represent a realization of these ideas.

Similar to the two-band model with two intrinsically superconducting subsystems the *induced* two-band model also admits for limiting cases which are analytically solvable. In the weak coupling limit, i.e. $\lambda_1 \ll \varpi/2\pi$, where $\varpi=\langle\omega^2\rangle^{1/2}$ is a typical phonon frequency, the gap equations can be reduced to a single one by inserting Δ_2 into the equation for Δ_1 [28]. This procedure leads to the appearance of new terms in Δ_1 which stem from the intrinsic pairing of the *a* carriers, the two-band channel, and the intrinsic proximity channel. A new feature appears in addition to the above mentioned ones, which is mixed in character since phonon mediated transitions from *a* to *b* are followed by proximity tunneling from *b* to *a* and vice versa. In case that the tunneling term is small, i.e. $\Gamma=\Gamma_{12}+\Gamma_{21}\ll 1$ the critical temperature is given by [29]

$$\begin{aligned} T_c &= T_{c1}\exp(f) \\ f &= \frac{\lambda_{12}\lambda_{21}}{\lambda_1^3} + \frac{1}{16}\left[2\frac{\lambda_{12}}{\lambda_1} - 1\right]\frac{\Gamma_{12}}{T_{c1}}, \end{aligned} \tag{23}$$

where $\lambda_{12}, \lambda_{21}$ are interband couplings. Such a case is realized when the spatial separation between the two subsystems is large. Obviously, in the limit $\Gamma_{12}=0$ and $\lambda_{12}, \lambda_{21} \ll \lambda_1$ the BCS results are obtained. In the opposite limit, when the separation between the two layers becomes very small corresponding to $\Gamma \gg \varpi$,

$$\begin{aligned} T_c &= T_{c1}\left[\frac{T_{c1}}{1.14\varpi}\right]^{\beta} \\ \beta &= \frac{\Gamma_{12}}{\Gamma_{21}}\left[1 - \frac{\lambda_{12}}{\lambda_1}\frac{\Gamma}{\Gamma_{12}}\right] \end{aligned} \tag{24}$$

Since the above results have been derived in the weak coupling limit, and setting $\lambda_{12}=0$, the tunneling effect always leads to a depression of T_c as compared to the isolated *a* system, i.e. $T_c<T_{c1}$. In the strong coupling limit, i.e. λ_1 large

corresponding to $2\pi T_c \gg \varpi$, and neglecting terms proportional to $\lambda_{12}\lambda_{21}$, the expression for T_c is given by [29]

$$T_c \approx \varpi / 2\pi [\tilde{\lambda}]^{1/2} \tag{25}$$

$$\tilde{\lambda} = \frac{\lambda_1 + \lambda_{12} \dfrac{\Gamma_{21}}{\pi T_c}}{1 + \dfrac{\Gamma_{21}}{\pi T_c + \Gamma_{21}} + 2\mu_1}$$

When the interband phonon mediated term is set equal to zero, then T_c will be depressed by the proximity effect, whereas the mixed term, which combines the tunneling channel with the phonon mediated one, stabilizes superconductivity and always enhances T_c [3, 31].

In the intermediate coupling regime and in the limit of small λ_{21}, the tunneling channel is the relevant one, which supports an increase in the density of states in system 2 and consequently depresses T_c as compared to T_{c1}. Oppositely, large values of λ_{21} reverse this effect and together with terms proportional to $\lambda_{ij}\Gamma_{ij}$ $(i,j=1,2)$ strengthen superconductivity. Results from the numerical calculations [29] in this regime are shown in Fig. 1.

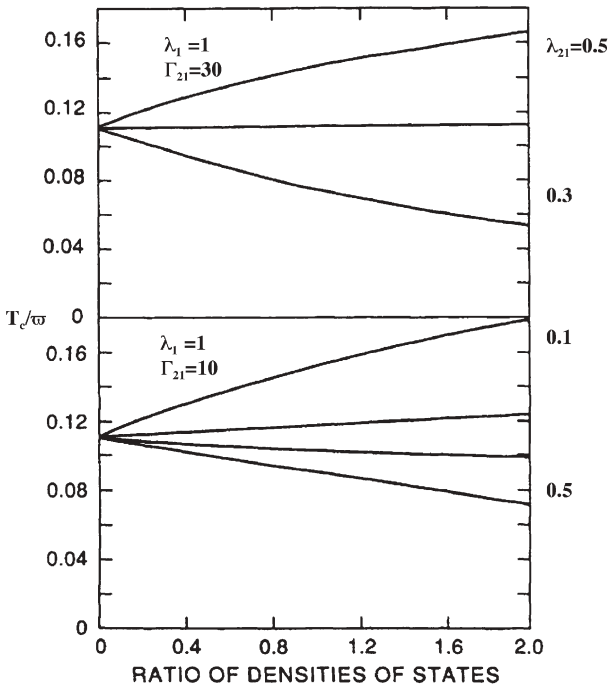

Fig. 1 T_c/ϖ as a function of the ratios of the density of states for various model parameters

The model has been applied to various superconductors and specific applications have been made for $YBa_2Cu_3O_7$. On the basis of Eqs. (21) and (22) the temperature dependence of the density of states for stoichiometric $YBa_2Cu_3O_7$ has been calculated (Fig. 2a), where at low energies no contributions to it exist [30]. The first peak is observed when the lower gap value is reached and a second one at higher energies, signaling the opening of the higher gap, which is attributed to the CuO planes. Here, the energy gaps are determined in close analogy to the BCS formalism as appearing at the peak positions. The energy gaps at T=0 K can thus be derived and their corresponding ratio to T_c be determined. These are Δ_1=3 T_c and Δ_2=0.8 T_c, respectively [30]. Their temperature dependencies are shown in Fig. 2b, where strong deviations from conventional BCS superconductors are observed since over a broad regime the dependence on T is very weak, to become strong only in the very vicinity of T_c.

In summarizing the results of induced superconductivity within the two-band model, the important aspects are that besides of the fact that two channels are available to induce superconductivity in the *normal* subsystem 2, an additional channel is opened where both, phonon mediated processes and tunneling act cooperatively. Even though the pure proximity effect induces superconductivity in channel 2, it acts destructively on T_c. The pure phonon processes also induce superconductivity but support higher T_c's as compared to the T_c of the isolated system 1. The same effect is observed for the combined action of phonon and tunneling since here a pair in 1 is transferred to 2 via the phonon mechanism and then scattered back to 1 via the proximity effect. Finally, it should be mentioned that magnetic impurities [29], induced in subsystem 2, have the interesting effect of leading to gapless superconductivity in channel 2, however, with finite order parameter Δ_2.

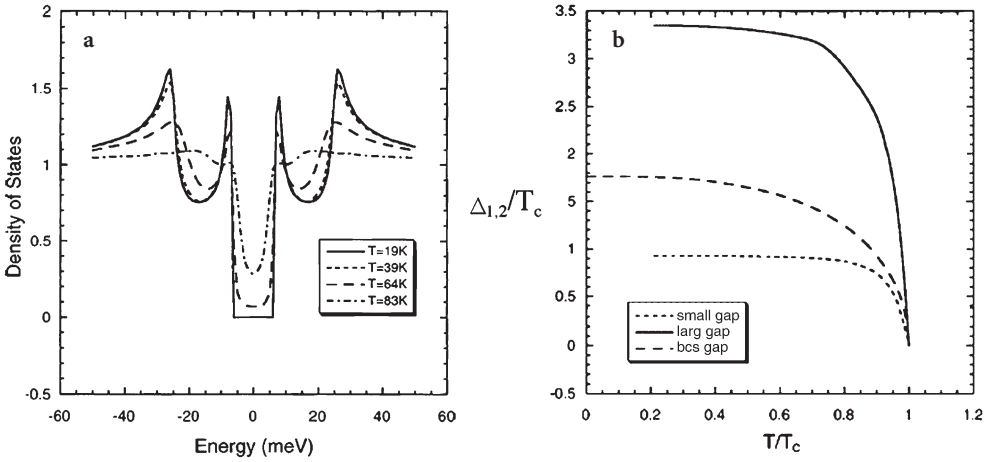

Fig. 2 **a** (Left panel). Temperature dependence of the density of states of stoichiometric $yBa_2Cu_3O_7$. **b** (Right panel). Temperature dependence of the energy gaps Δ_1/T_c, Δ_2/T_c together with the same for an ordinary BCS superconductor [30]

3
Extensions of the Two-Band Model

3.1
Motivation

Cuprate superconductors [32] are one of the very first systems, where various experiments give evidence that the superconducting order parameter is of d-wave symmetry. On the other hand, experiments testing properties along the c-axis seem to support an s-wave order parameter. The situation here is obviously much more complex than discussed above and the two-band model requires extensions to account for these observations. Also it has been pointed out by various authors that it is important to consider two components in these materials, since experimentally two different time and length scales have been observed (for further details see the articles by D. Mihailovic, T. Egami and K. A. Müller in this volume). An additional complication arises in cuprates due to the fact that superconductivity appears on doping the antiferromagnetic parent compounds. Since these are insulating half-filled band systems, it is stringent that a large Hubbard repulsion at the copper site is present which prevents it from being metallic. This fact together with a missing isotope effect on T_c at optimum doping [33–35] (the various isotope effects are discussed in the review by H. Keller, and, in part by A. Furrer, this volume) has been taken as evidence that more complex pairing interactions than phononic mechanisms have to be considered [see, e.g., 36–38]. Especially strong electron correlations have been favored as microscopic origin of the hole pairing mechanism [39–42]. Also the unexpected large values of T_c give clear evidence that a pure BCS or strong coupling approach is insufficient. Thus the origin of superconductivity in these materials is still strongly debated and remains controversial.

It is argued in the following that a two-component approach carries much of the physics observed in these materials, although in a more complicated fashion than within the simple two-band model introduced in the beginning (this topic is also addressed in the contribution by S. Deng et al. in this volume, although with emphasis on chemical aspects). This paragraph is subdivided into sections where first the two-band model is discussed extended to incorporate different pairing symmetries and realistic band structures. The second section deals with lattice effects which differ from conventional electron-phonon interaction models, since higher order electron-phonon interactions are included [43–45] and treated within the Lang-Firsov approximation [46]. In the following paragraph, the consequences of these terms on isotope effects and pseudogap formation are discussed.

3.2
Gap and Order Parameter Symmetry

The starting point is again the two-band model, although extended to account for different order parameter symmetries which are a consequence of the effective pairing interaction. The origin of the electron-electron (hole-hole) attraction is not the focus here. It can be a phonon mechanism as well as a consequence of strong electronic correlations. However, since the final results are thought to be applicable to cuprate superconductors, the relevant electronic bands are the copper d-states and the oxygen p-states [47]. The attractive interactions are analogue to the two-band model, but extended to take into account their momentum k dependence. The electron creation and annihilation operators are differentiated according to the predominance of the p-d hybridized bands as p and d states. The two bands which are of relevance, are the in-plane copper-oxygen band (*d-band*) and the out-of-plane copper-oxygen band (*c-band*). The Hamiltonian is given by [47, 48]

$$H = H_0 + H_1 + H_2 + H_{12} \tag{26}$$

$$H_0 = \sum_{k_1\sigma} \xi_{k_1} c^+_{k_1\sigma} c_{k_1\sigma} + \sum_{k_2\sigma} \xi_{k_2} d^+_{k_2\sigma} d_{k_2\sigma} \tag{26a}$$

$$H_1 = -\sum_{k_1 k_1' q} V_1(k_1, k_1')\, c^+_{k_1+q/2\uparrow}\, c^+_{-k+q/2\downarrow}\, c_{-k_1'+q/2\downarrow}\, c_{k_1'+q/2\uparrow} \tag{26b}$$

$$H_2 = -\sum_{k_2 k_2' q} V_2(k_2, k_2')\, d^+_{k_2+q/2\uparrow}\, d^+_{-k_2+q/2\downarrow}\, d_{-k_2'+q/2\downarrow}\, d_{k_2'+q/2\uparrow} \tag{26c}$$

$$H_{12} = -\sum_{k_1 k_2 q} V_{12}(k_1, k_2)\, \{c^+_{k_1+q/2\uparrow}\, c^+_{-k_1+q/2\downarrow}\, d_{-k_2+q/2\downarrow}\, d_{k_2+q/2\uparrow} + h.c.\} \tag{26d}$$

where H_0 is the kinetic energy of the bands i=1, 2 with band energy, ξ_k. ε_i denotes the position of the c and d band with creation and annihilation operators c^+, c, d^+, d respectively, and μ is the chemical potential. The pairing potentials $V_i(k_i, k_i')$ are assumed to be represented in factorized form like $V_i(k_i, k_i')$= $V_i(\varphi_{k_i}, \psi_{k_i'})$, where φ_{k_i}, ψ_{k_i}, are cubic harmonics for anisotropic pairing which yields for dimension D=2 and on-site pairing: φ_{k_i}=1, ψ_{k_i}=1, extended s-wave: φ_{k_i}=cos$k_x a$+cos$k_y b$=γ_{k_i}, and d-wave: φ_{k_i}=cos$k_x a$–cos$k_y b$=η_{k_i} where a, b are the lattice constants along x and y directions; throughout this chapter $a \neq b$. By performing a BCS mean-field analysis of Eqs. (1) those transform to

$$H_{red} = \sum_{k_1\sigma} \xi_{k1}\, c^+_{k_1\sigma}\, c_{k_1\sigma} + \sum_{k_2\sigma} \xi_{k_2}\, d^+_{k_2\sigma}\, d_{k_2\sigma} + \overline{H}_1 + \overline{H}_2 + \overline{H}_{12} \tag{27}$$

$$\begin{aligned} \overline{H}_i = &-\sum_{k_i'} [\Delta_{k_i'}\, c^+_{k_i'\uparrow}\, c^+_{-k_i\downarrow} + \Delta^*_{k_i'}\, c_{-k_i'\downarrow}\, c_{k_i\uparrow}] \\ &+ \sum_{k_i, k_i'} V_i(k_i, k_i')\, \langle c^+_{k_i\uparrow}\, c^+_{-k_i\downarrow}\rangle\, \langle c_{-k_i'\downarrow}\, c_{k_i'\uparrow}\rangle \end{aligned} \tag{27a}$$

where (i=1, 2)

$$\overline{H}_{12} = -\sum_{k_1,k_2} [V_{12}(k_1,k_2)\langle c^+_{k_1\uparrow} c^+_{-k_1\downarrow}\rangle d_{-k_2\downarrow} d_{k_2\uparrow} + V_{12}(k_1,k_2)\langle d_{-k_2\downarrow} d_{k_2\uparrow}\rangle c^+_{k_1\uparrow} c^+_{-k_1\downarrow}$$
$$+ V^*_{12}(k_1,k_2)\, d^+_{k_2\uparrow} d^+_{-k_2\downarrow}\langle c_{-k_1\downarrow} c_{k_1\uparrow}\rangle + V^*_{12}(k_1,k_2)\, c_{-k_1\downarrow} c_{k_1\uparrow}\langle d^+_{k_2\uparrow} d^+_{-k_2\downarrow}\rangle$$
$$- V_{12}(k_1,k_2)\langle c^+_{k_1\uparrow} c^+_{-k_1\downarrow}\rangle\langle d_{-k_2\downarrow} d_{k_2\uparrow}\rangle - V^*_{12}(k_1,k_2)\langle c_{-k_1\downarrow} c_{k_1\uparrow}\rangle\langle d^+_{k_2\uparrow} d^+_{-k_2\downarrow}\rangle] \tag{27b}$$

and for i=2 c is replaced by d. $\xi_{k_i}=\varepsilon_i+\varepsilon_{k_i}-\mu$, where μ is the chemical potential. Here it is assumed that $\langle c^+_{-k_1+q/2\uparrow} c^+_{-k_1+q/2\downarrow}\rangle=\langle c^+_{k_1\uparrow} c^+_{-k_1\downarrow}\rangle\delta_{q,0}$ and equivalently for the d operators. In addition the following definitions are introduced:

$$\Delta^*_{k_i} = \sum_{k_i} V_i(k_i,k_i')\langle c^+_{k_i\uparrow} c^+_{-k_i\downarrow}\rangle \tag{28}$$

together with $A^*_{k_1}=\sum_{k_2} V_{12}(k_1,k_2)\langle d^+_{k_2\uparrow} d^+_{-k_2\downarrow}\rangle$, $B^*_{k_2}=\sum_{k_2} V_{12}(k_1,k_2)\langle c^+_{k_2\uparrow} c^+_{-k_2\downarrow}\rangle$, and $V^*_{12}=V_{12}$. Applying standard techniques as derived earlier we obtain

$$\langle c^+_{k_1\uparrow} c^+_{-k_1\downarrow}\rangle = \frac{\overline{\Delta}^*_{k_1}}{2E_{k_1}} \tanh\frac{E_{k_1}}{2k_BT} = \overline{\Delta}^*_{k_1}\Phi_{k_1} \tag{29a}$$

$$\langle d^+_{k_2\uparrow} d^+_{-k_2\downarrow}\rangle = \frac{\overline{\Delta}^*_{k_2}}{2E_{k_1}} \tanh\frac{E_{k_2}}{2k_BT} = \overline{\Delta}^*_{k_2}\Phi_{k_2} \tag{29b}$$

with $E^2_{k_2}=\xi^2_{k_2}+|\,\overline{\Delta}_{k_2}|^2$, $\overline{\Delta}_{k_2}=\Delta_{k_2}+B_{k_2}$ and $E^2_{k_1}=\xi^2_{k_1}+|\overline{\Delta}_{k_1}|^2$, $\overline{\Delta}_{k_1}=\Delta_{k_1}=\Delta_{k_1}+A_{k_1}$, which results in the self-consistent set of coupled equations

$$\overline{\Delta}_{k_1} = \sum_{k_1'} V_1(k_1,k_1')\overline{\Delta}_{k_1'}\Phi_{k_1'} + \sum_{k_2} V_{1,2}(k_1,k_2)\overline{\Delta}_{k_2}\Phi_{k_2} \tag{30a}$$

$$\overline{\Delta}_{k_2} = \sum_{k_2'} V_2(k_2,k_2')\overline{\Delta}_{k_2'}\Phi_{k_2'} + \sum_{k_1} V_{1,2}(k_1,k_2)\overline{\Delta}_{k_1}\Phi_{k_1} \tag{30b}$$

from which the temperature dependencies of the gaps and the superconducting transition temperature have to be determined. If the interactions V are constants, the resulting gaps are momentum independent corresponding to the results obtained earlier. A more interesting case is obtained by assuming the following general momentum dependence of the intraband interactions $V_i=g^{(i)}_0+g^{(i)}_\gamma\gamma_k\gamma_{k'}+g^{(i)}_\eta\eta_k\eta_{k'}$, where as already outlined above, the first term yields onsite pairing, the second extended s-wave pairing and the last term d-wave pairing. In the calculation it is assumed that V_1 is proportional to g_0 while V_2 is determined by either g_0 or by g_η. In addition the two bands considered are 1-dimensional in the case of the c band while the d-related band is 2-dimensional with the following dispersion: $\varepsilon_{k_2}=-2t(\cos k_x a+\cos k_y b)$. Also, it is assumed

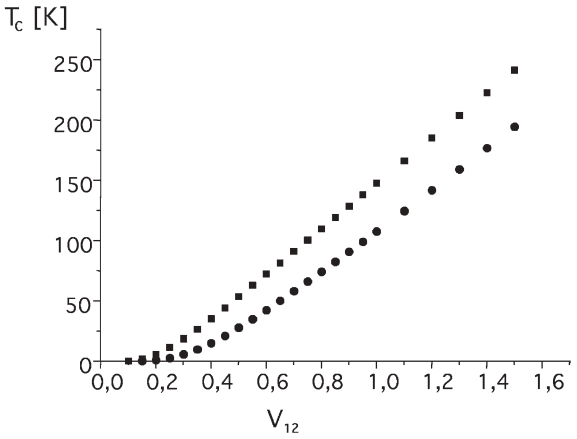

Fig. 3 The dependence of the superconducting transition temperature on the interband coupling V_{12} for the case of both, V_1 and $V_2 \sim g_0$ (*circles*) and the case where $V_1 \sim g_0$, $V_2 \sim g_\eta$ (*squares*)

in all cases discussed later that the values for the intraband interactions are chosen such that both bands separately do not exhibit superconductivity, specifically, $V_1 = V_2 = 0.01$, where $V_1 = \widetilde{V}_1 N_c$, $V_2 = \widetilde{V}_2 = N_d$. Within this scenario the self-consistent set of equations is solved numerically as a function of $V_{12} = \widetilde{V}_{12}\sqrt{N_c N_d}$, where N_c, N_d are the density of states of c and d band, respectively. The results are shown in Fig. 1 where both cases $V_1 \sim g_0$, $V_2 \sim g_0$ and $V_1 \sim g_0$, $V_2 \sim g_\eta$ are considered. Obviously small values of V_{12} are sufficient to induce superconductivity in both channels. With increasing V_{12} dramatic enhancements of T_c are obtained such that T_c easily exceeds 100 K. Interestingly the d-wave component in the two component systems has an additional T_c-increasing factor which increases with increasing interband coupling (Fig. 3). This finding clearly shows that a mixed order parameter symmetry favors superconductivity, as opposed to two onsite pairing interactions.

The related superconducting energy gaps are shown in Fig. 4 where $V_{12} = 0.5$. Here again the effect of considering onsite couplings only depresses the gaps as compared to s/d-wave coupled gaps, and in addition a stronger anisotropy of the two gaps is observed within the mixed order parameter system as compared to the one with identical order parameters. In Fig. 5 the ratios of the gaps with respect to T_c are shown as a function of T_c for the mixed order parameter case only. Interestingly the s-wave gap ratio is close to the BCS ratio, slightly increasing with increasing T_c. The corresponding ratio of the d-wave gap is enhanced as compared to a one band approach and remains nearly constant as function of T_c with a slight decrease at small T_cs. The gap vs temperature behavior is comparable to the conventional two-band model and follows a BCS type temperature dependence.

In summarizing this paragraph it can be concluded that the two-band model with different pairing symmetries bears new features as compared to the con-

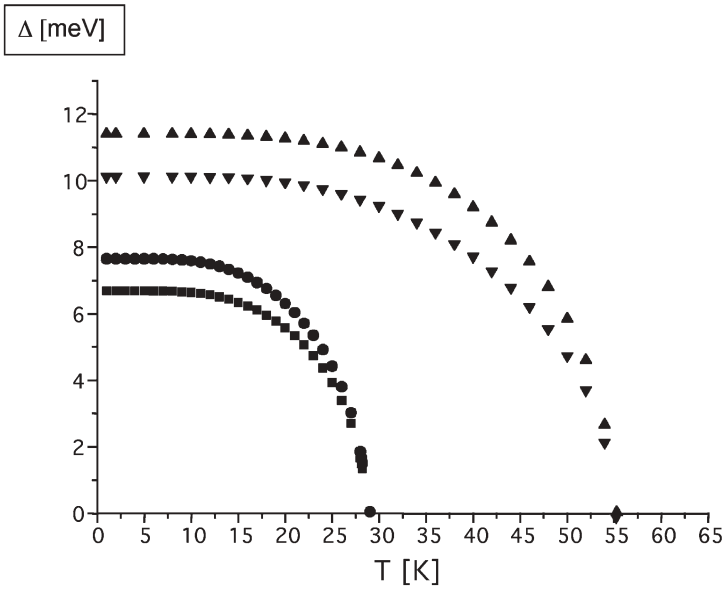

Fig. 4 Temperature dependencies of the superconducting gaps. *Squares and circles* refer to *s+s* gaps while *down and up triangles* are derived for *s+d* gaps

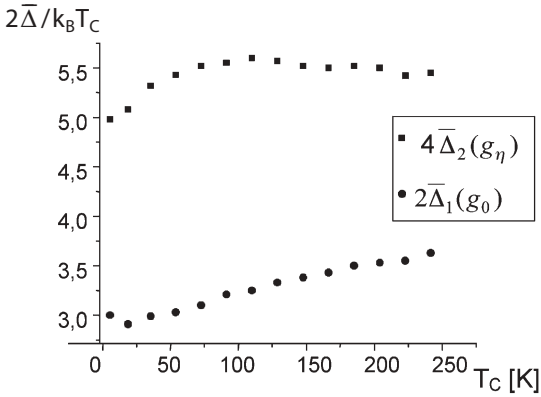

Fig. 5 The ratios of the maximal gaps over T_c vs T_c. The parameters used for this calculation are the same as given in [47]

ventional one and the induced pairing model. The enhancements in T_c in a mixed order parameter model are nearly twice of those of two isotropic order parameters even if the individual components are not superconducting on their own. Including the possibility that either of the bands is superconducting (see the above section) has been tested numerically. In this case T_c is further enhanced by a superconducting s-wave channel whereas the d-wave component

has a minor effect on this increase. Also the inclusion of second nearest neighbor hopping in the *d*-band dispersion has been tested. This also seems to be quite irrelevant for the magnitude of T_c within the above modeling.

3.3 Unconventional Lattice Effects and the Phase Diagram of Cuprates Within the Two-Band Model

The two-band model has originally been developed on the basis that *intraband* as well as *interband* interactions are mediated by the virtual exchange of phonons. However, in cuprate superconductors the role played by the lattice is unclear. Conventional electron-phonon coupling can nearly be ruled out to contribute to the pairing mechanism. In addition, the phase diagram of high temperature superconducting copper oxides exhibits, as a function of hole doping, an unusual richness. It shows antiferromagnetism in the undoped or lightly doped regime, a bad or strange metal state follows with increasing doping with charged stripe formation [50]. Superconductivity with unexpectedly high transition temperatures sets in with increasing doping. In the overdoped regime a normal metallic behavior is observed.

The understanding of this complexity is at present very incomplete and only few concepts exist to address the full range of experimentally observed properties. Specifically, the antiferromagnetic properties have challenged theoreticians to explain the pairing and the phase diagram in terms of purely electronic models based on spin fluctuation mechanisms; see [37–42]. In these approaches the onset temperature T^* of the so-called pseudogap opening is identified as a spin gap temperature, even though various recent experiments have revealed a giant oxygen and copper isotope effect on T^* [51–53]. These findings point to strong lattice effects being important in the pseudogap formation. Correlated with the above mentioned isotope results are experimental results obtained from EXAFS [54], inelastic neutron scattering [55, 56] NMR [57] and EPR [58], which all show that strong anomalies in the lattice take place at T^*. Thus, in order to model high-temperature superconductors and understand their phase diagram, a pure electronic mechanism is insufficient. Rather the interaction between spin, charge and phonons (lattice) has to be properly included. Another crucial issue, which is also debated experimentally, is the correlation between T^* and T_c. While various approaches exist, which invoke the striped phase as destroying superconductivity [59], others assume that the striped phase supports superconductivity and leads to enhancements of T_c [60]. Also it is strongly debated how to locate the phase separating T^* and T_c. While tunneling data from [61] support a coincidence between the optimum T_c and T^*, other tunneling data [62], find that T^* is larger than T_c at the optimum doping. This controversial issue has the important consequence, that the first mentioned tunneling data suggest that a quantum critical point [63] (QCP) exists inside the superconducting phase, while the latter data give no evidence for this scenario.

It is shown the QCP seems unlikely to be realized in HTSC, but that – if there is any QCP at all – this point should lie at the onset of the superconducting phase in accordance with a 2D/3D crossover scenario of the quantum critical XY model [64], and possibly show a second QCP when superconductivity and the striped phase are destroyed in the overdoped regime.

In the following the starting point are the antiferromagnetic parent compounds of cuprate superconductors. The relevant two components, which will be discussed below, are attributed, as before, to the CuO_2 planes and the Cu $d_{3z^2-r^2}$ and O p_z orbitals perpendicular to the planes[48, 49, 65]. In the undoped state the physics of the planes can be cast into a pure spin $^1/_2$ antiferromagnetic Heisenberg model. Doping has very dramatic consequences since all energy scales are destabilized. Since the large Hubbard U at the copper site prevents the holes from occupying d-orbitals, in a scenario that neglects Cu-O covalency, the oxygen ion p-orbitals will be occupied by the doped holes. This leads to a stabilization of the oxygen ion $2p^6$ instability and an energy gain at the oxygen ion lattice site [66]. As a consequence and in order to achieve a low energy state, the hole spin aligns anti-parallel with respect to the nearest neighbor copper ion to form a spin singlet state [67]. In addition hole doping induces a strong electron-phonon coupling to a Q_2-type Jahn-Teller distortion [68–70] which leads to a substantial localization of the singlet state and renders it ineffective for superconductivity. This localization is even more enhanced through the antiferromagnetic background where hopping of the singlet is possible only through energetically unfavorable spin flips or triplet formation. Consequently it has to be concluded that the spin related in-plane channel provides a stable low-energy state [67].

The out-of-plane component carries a "ferroelectric" type character with strong electron phonon interactions. Here an instability to a charge ordered state is inherent. Since, without doping, the two components discussed above are orthogonal, no interaction between them is possible. However, when the structure is distorted this orthogonality is violated and they start to interact. For instance, if the Cu-O-Cu bond angle deviates from 180° by buckling or tilting, the in-plane and c-axis phonon modes become coupled [54, 71–75]. These distortions occur due to changes in the chemical bonding by doping, and play an important role, as will be shown below. Such distortions are usually local, rather than collective, and can be static as well as dynamic. It is important to point out that a two component scenario has been considered by others before to be of relevance in understanding the physics of cuprates [13, 76–81].

In order to describe the coupling between the two components, new hopping elements have to be introduced which admit for processes like hopping from $d_{x^2-y^2}$–p_z, p_z–$d_{3z^2-r^2}$, $d_{3z^2-r^2}$–p_x, p_y, etc. (It should be noted here that band structure calculations point to the possibility that the Cu 4 s states are more likely occupied than the $d_{3z^2-r^2}$-states [82]. This is, however, for the following considerations, of no importance.) In addition, strongly anharmonic interactions between in-plane and c-axis phonons take place [83]. It is important to emphasize that these anharmonic interaction terms give rise to spatial modulations of the ionic

displacement coordinates which – in turn – can induce nanoscale inhomogeneity [84, 85]. The electronic response to these modulations is strong and dynamic charge ordering a consequence to be discussed later. Assuming for simplicity that the in-plane states can be described by a single already strongly *p-d* hybridized band and making the same simplification for the c-axis electronic states, the system can be modeled by the following Hamiltonian [48, 49, 86]:

$$H = \sum_{i,\sigma} E_{xy,i}\, c^{+}_{xy,i,\sigma} c_{xy,i,\sigma} + \sum_{j,\sigma} E_{z,j}\, c^{+}_{z,j,\sigma} c_{z,j,\sigma} + \sum_{i,j,\sigma,\sigma'} T_{xy,z}[c^{+}_{xy,i,\sigma'}\, c_{z,j,\sigma'} + h.c.] + \sum_{i,j} \widetilde{T}_{xy}\, n_{xy,i\uparrow}\, n_{xy,j\downarrow} + \sum_{i,j,\sigma,\sigma'} \widetilde{V}_C\, n_{i,\sigma} n_{j,\sigma'} + \sum_{i,j,\sigma,\sigma'} V_{pd}\, n_{i,\sigma} n_{j,\sigma'} \tag{31}$$

Here $c^{+}c{=}n$ is the in-plane (xy), c-axis (z) electron density at site i, j with energy E and spin index σ. $T_{xy,z}$ is the hopping integral between plane and c-axis orbitals, and $\widetilde{T}$ is the in-plane spin singlet hopping integral from which a d-wave symmetry of the superconducting order parameter would result. V_C as well as V_{pd} are density-density interaction terms referring to plane/c-axis and in-plane elements. The phonon contributions have already been incorporated in Eq. (31), where all energies are given by renormalized quantities:

$$E_{xy,i} = [\xi_{xy,i} - \{\widetilde{\Delta}^{\star} + f(xy,z)\}] \tag{32a}$$

$$E_{z,j} = [\xi_{z,j} - \{\Delta^{\star} + f(z,xy)\}] \tag{32b}$$

$$T_{xy,z} = [t_{xy,z} - \sqrt{\widetilde{\Delta}^{\star}\,\Delta^{\star}}]\exp(-\Phi_T^{xy,z}) \tag{32c}$$

$$\widetilde{T}_{xy} = \left(t_{pd}^2 \frac{\widetilde{U}_d - (E_{xy,i} - E_{z,j})}{(E_{xy,i} - E_{z,j})[\widetilde{U}_d - (E_{xy,i} - E_{z,j})]} - \widetilde{\Delta}^{\star}\right)\exp(-\Phi_T^{xy,z}) \tag{32d}$$

$$\widetilde{U}_d = U_d - \widetilde{\Delta}^{\star} \tag{32e}$$

$$V_C = V_C - \sqrt{\widetilde{\Delta}^{\star}\,\Delta^{\star}} \tag{32f}$$

$$V_{pd} = \widetilde{\Delta}^{\star} + \sqrt{\widetilde{\Delta}^{\star}\Delta^{\star}} \tag{32g}$$

In Eqs. (32) the ξ are the unrenormalized band energies, $f(xy, z)$, $f(z, xy)$ are higher order electron-phonon interaction energies caused by anharmonicity, and $\widetilde{\Delta}^{\star}, \Delta^{\star}$ are level shifts due to intraband electron-phonon coupling with

$$\Delta^{\star} = |\gamma_z(q_0)|^2\, \hbar\omega_{q_z} \tag{33}$$

and an equivalent expression for $\widetilde{\Delta}^{\star}$, where ω, γ is the phonon mode energy and the dimensionless electron-phonon coupling [87, 88] which is proportional to $\sqrt{M}$, M being the ionic mass. From the above equations it is obvious that both energy bands experience a level shift, and a strong suppression of the

onsite Coulomb repulsion U_d takes place. Similarly the Coulomb correlations V_C are reduced and additional phonon driven density-density interactions (proportional to V_{pd}) appear which lead to its further reduction. This hybridization term is a consequence of electron-phonon interactions only, and favors the hopping between in-plane and out-of-plane orbitals. Another important observation is the exponential suppression of the in-plane related hopping integral (proportional to t_{pd}) where

$$\Phi_T = \frac{1}{2N} \sum_q f(q) |\gamma|^2 \coth \frac{\hbar \omega_q}{2k_B T} \tag{34}$$

with $f(q)$ a function of the scattering angle [46]. From the structure of Eqs. (32) it becomes clear that two instabilities should be observed in this coupled system: in the charge channel (c-axis, z), a charge density wave (CDW) instability could set in, while in the spin channel (ab-plane, xy) a transition to a spin density wave state (SDW) could occur which has also been reported experimentally [89]. A stabilization of both these instabilities is obtained through the coupling between both components (proportional to $f(xy,z)$, $f(z,xy)$, $T_{xy,z}$, V_C, V_{pd}) which are dominated by anharmonic interactions present in these compounds [91]. The effect of doping is to shift the "spin" gap state towards the Fermi level and to provide mobility of it through dispersion. The charge related channel has Fermi liquid like properties, is highly mobile and located in the very near vicinity of the Fermi energy. Here the charge gap shifts the states towards the other singlet related band and takes away dispersion to reduce the mobility. Since both effects combine to drive the charge and spin channels together, interband processes are easily facilitated. (An approximate band scheme is shown in Fig. 6.) It is just this interband coupling which is driven by buckling/tilting which has, in addition to the single particle gaps, an important enhancement effect on T_c. In analogy with [87], the two transition temperatures can be calculated. The higher (charge instability) temperature is identified with the onset temperature

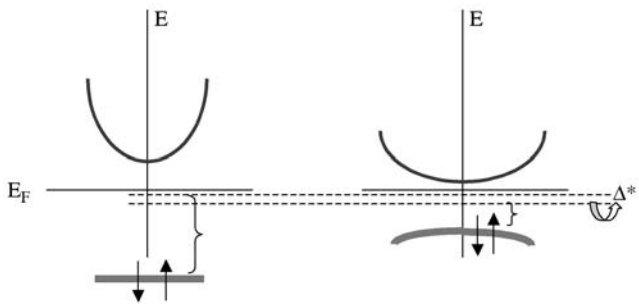

Fig. 6 The schematic energy level structure of the charge and spin related components. The *grey line* refers to the spin channel, the *black line* to the charge level. The *left panel* shows the energy level structure in the absence of the pseudogap Δ*, while the *right panel* shows the effect of Δ* on the level position and dispersion

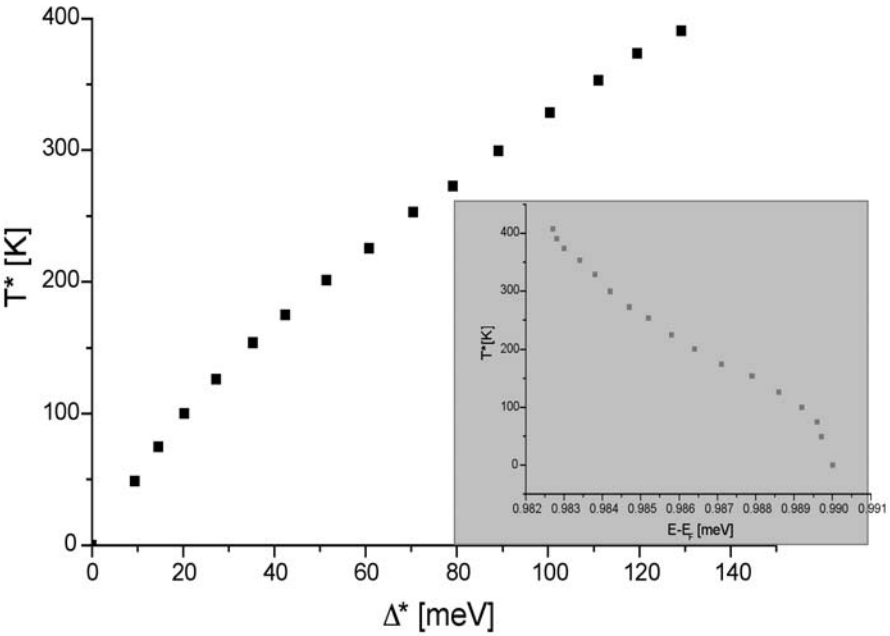

Fig. 7 T^* plotted as function of the phonon induced energy gap (c-axis) proportional to Δ^*. The *inset* shows T^* as function of doping proportional to $E–E_F$ (E_F=Fermi energy)

of stripe (i.e., charge/lattice inhomogeneity) formation T^*. In Fig. 7 T^* is shown as a function of the phonon induced electronic gap Δ^*.

In order to figure out the effect of the band renormalization on superconductivity the Hamiltonian in Eq. (31) is recast into an effective Hamiltonian analogue to Eq. (26), where now c-operators are used instead of the previously used notations c, d:

$$
\begin{aligned}
H_{eff} = & \sum_k E_{xy,k}\, c^+_{xy,k,\sigma}\, c_{xy,k,\sigma} + \sum_k E_{z,k}\, c^+_{z,k,\sigma}\, c_{z,k,\sigma} \\
& + \sum_{k_1,k_1',q} V_1(k_1,k_1')\; c^+_{xy,k_1+q/2\uparrow}\, c^+_{xy,-k_1+q/2\downarrow}\, c_{xy,-k_1'+q/2\downarrow}\, c_{xy,k_1'+q/2\uparrow} \\
& + \sum_{k_2,k_2',q} V_2(k_2,k_2')\; c^+_{z,k_2+q/2\uparrow}\, c^+_{z,-k_2+q/2\downarrow}\, c_{z,-k_2'+q/2\downarrow}\, c_{z,k_2'+q/2\uparrow} \\
& + \sum_{k_1,k_2,q} V_{12}(k_1,k_2)\,[c^+_{xy,k_1+q/2\uparrow}\, c^+_{xy,-k_1+q/2\downarrow}\, c_{z,-k_2+q/2\downarrow}\, c_{z,k_2+q/2\uparrow} + h.c.]
\end{aligned}
\tag{35}
$$

Here the effects of the Coulomb interactions are included in the effective interaction constants V. It is most important here that the spin/charge related gaps $\Delta^*, \tilde{\Delta}^*$ act on the single particle energies. The mixing of both components is not only through the effective interaction V_{12}, which stems from buckling/tilting, but also through the site energies (terms proportional to f in Eq. 32).

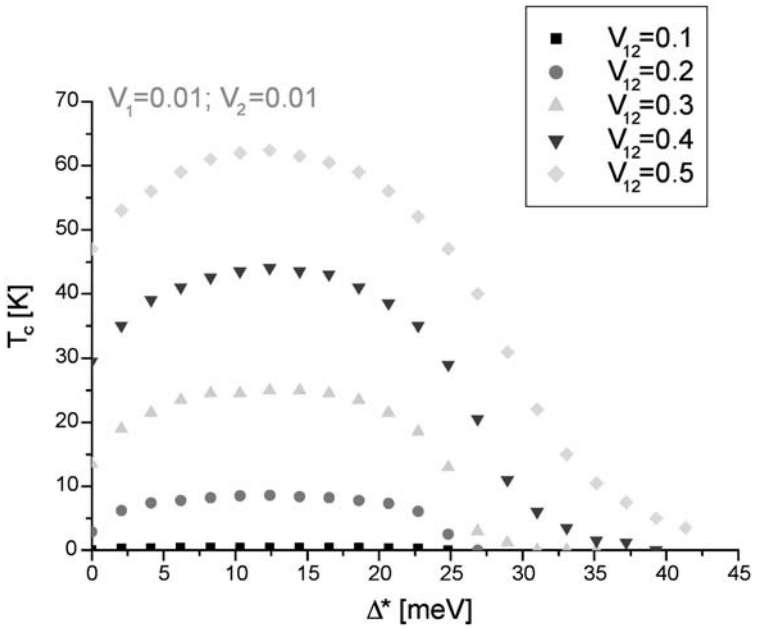

Fig. 8 The superconducting transition temperature T_c as a function of Δ^* for different values of the inter-component coupling V_{12}

Equation (35) can be solved in complete analogy to the methods used earlier to yield the gap equations and the corresponding superconducting transition temperature T_c. Starting point is again the assumption that the two components when uncoupled are not superconducting, i.e., $V_1 = V_2 = 0.01$ are too small to create a paired state. With relatively small interband coupling, V_{12}=0.1 the system remains non-superconducting. When including the effect of the T^* related gap Δ^*, superconductivity appears already at rather small values of Δ^*, but the corresponding T_c remains small. Keeping V_1, V_2 unchanged, but increasing the interband interaction V_{12} (see Fig. 8) and incorporating the effect of Δ^* yields a rapid increase in T_c which readily approaches the experimentally observed values.

As discussed previously, the in-plane spin related channel supports a d-wave superconducting order parameter, while the charge channel leads to an s-wave superconducting state. Here both contributions are mixed, leading to the scenario developed earlier and an additional T_c enhancing effect. The crucial effects played by the lattice, as emphasized here, point to the pivotal role played by the atomic structure.

From the above calculations the phase diagram can now be calculated, since T^* is known as function of the Fermi energy and T_c is know as function of Δ^*. This makes it possible to relate T_c and T^* simultaneously to the doping level and to derive the corresponding phase diagram. The results are shown in Fig. 9.

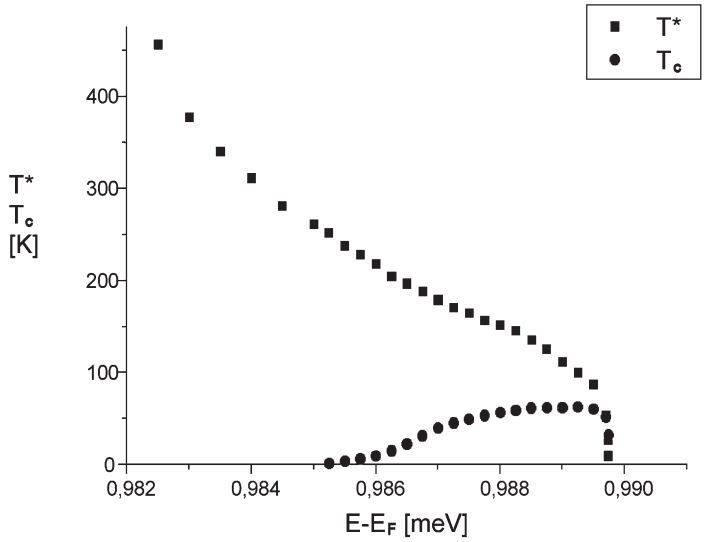

Fig. 9 The phase diagram of cuprates as a function of doping which is here simulated by varying the Fermi energy. *Circles* refer to the superconducting transition temperature T_c, while *squares* denote the charge ordering temperature T^*. The results are obtained for both order parameters being of s-wave symmetry, but do not change qualitatively for mixed pairing symmetries

It is obvious from Fig. 9 that the maximum T_c at optimum doping is smaller than the corresponding T^*. The two temperature scales vanish simultaneously in the overdoped regime which means that a quantum critical point within the superconducting regime is not existent in the present scenario.

Importantly the present scenario establishes a direct connection between T_c and T^* and the superconducting gap and the pseudogap, and yields mixed pairing symmetries. In Fig. 10 the calculated dependencies of $2\Delta_{sc,max}(d)/kT_c$ and $2\Delta_{sc,max}(s)/kT_c$ on T^*/T_c are shown, where the d-wave component is related to in-plane pairing while the s-wave component is related to the out-of-plane pairing. These dependencies are approximately linear. As a function of doping the relative s-wave component increases.

Concluding this chapter, it has been shown, that the analysis of a two-component model of high temperature superconducting copper oxides yields two inherent instabilities related to a d-wave spin governed channel in the CuO_2 planes and an s-wave charge channel stemming from out-of-plane elements. Both components are coupled by buckling/tilting of the CuO_2 planes. The coupling between these elements occurs through incipient spin and charge density wave instabilities and leads to high temperature superconductivity with mixed s- and d-wave pairing symmetry. The predicted pseudogap temperature T^* is always greater than T_c, so there is no quantum critical point within the superconducting region in the present modeling. The effect of the lattice is crucial,

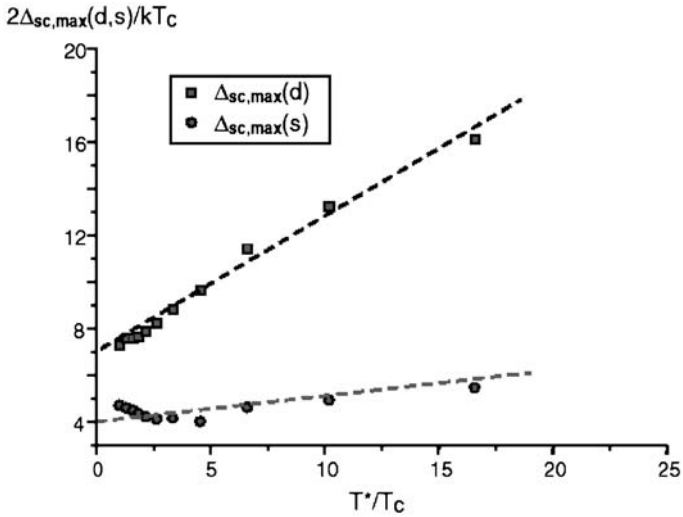

Fig. 10 $2\Delta_{sc,max}$(s,d) as functions of T^*/T_c for doping levels >0.986 (E-E_F). The *lines* are guides to the eye. Note that the s-wave component gains weight with increasing doping

since the electron-phonon coupling induces a level shift in the single particle energies together with an exponential reduction of the in-plane hopping integral. The level shift (proportional to Δ^*) leads to an enhancement of T_c as long as the coupling is not too strong. However, upon increasing the electron-phonon coupling further, localization sets in which is accompanied by a rapid depression of T_c.

3.4 Isotope Effects in a Two-Component Model

The hole pairing mechanism in cuprate superconductors has rapidly been ruled to be conventional, not only because of the high superconducting transition temperatures but also because of the missing isotope effect on T_c at optimum doping. However, with decreasing doping it has been shown that the isotope effect recovers [91–96] and even exceeds the BCS value at the boundary to the antiferromagnetic regime [97]. In addition various unexpected other isotope effects have been reported like, e.g., one, already mentioned before, on the pseudogap formation temperature T^* [51–53], which is huge and has the "wrong" sign, i.e., T^* increases with increasing isotope mass, an isotope dependence of the plane copper NQR frequency [98], and an isotope effect on the London penetration depth λ_L [99–103], which should be absent in all conventional theories including the two-band model and any purely electronic model.

In this section it will be shown, that the unconventional electron-phonon couplings considered above provide an explanation for these observations and that polaronic coupling is their origin. While all previous sections dealt with

results obtained on a mean field level, the isotope effect on T^* can only be obtained by going beyond this level and looking for exact solutions of the nonlinear model equations [104]. Here it is meant that exact solutions for the lattice displacement fields modified by the electron-phonon interaction are investigated, which give rise to "extra" dynamics on top of the ordinary phonon spectrum [54, 73, 74, 105–107]. Such solutions have no analytical analogue but are obtained numerically only. The displacement fields are always anomalous with respect to the oxygen ion while the Cu ion displacements, when dealing with the CuO_2 planes, are harmonic [104]. Typical oxygen ion displacements in the planes are shown in Fig. 11. Correlated with these extra dynamics are modulations in the charge distribution which have to be calculated by inserting the local spatial solutions for the displacements into a CDW type gap equation [87, 88, 108, 109] which in turn yields the spatial variation of the charge distribution. A similar variation in the induced electronic gap is observed as in the induced displacement field by means of which charge rich and charge poor areas can be defined. In terms of cuprate superconductors these results can be interpreted also as areas where spin dynamics dominate (charge poor) and areas where the doped holes lead to an accumulation of charge (Fig. 12).

A possible isotope effect on this charge ordering phenomenon is investigated by substituting the ^{16}O mass by its isotope ^{18}O and solving the nonlinear

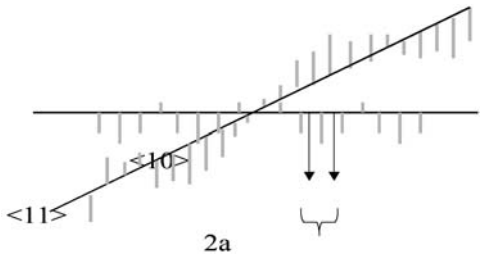

Fig. 11 In-plane oxygen ion displacements along the ⟨11⟩ and ⟨10⟩ direction. The displacements are "on-top" of the phonon dynamics and correspond to solutions of the nonlinear problem which have been obtained numerically

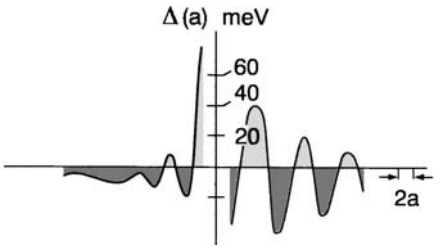

Fig. 12 Induced modulations of the electronic energy gap as function of lattice constants along the ⟨11⟩ direction

equations again numerically. Then, in turn, the solutions are inserted into the gap equations, where an increase in the induced gap is observed [104]. Since T^* is identified as the temperature at which charge ordering occurs, the results show that an increase in the oxygen ion mass leads to an increase in the electronic gap which corresponds to an increase in T^*. However, a direct comparison with experiments is hard to achieve as spatial variations are considered whereas in the experiments integrated quantities are observed. Qualitatively one can, however, estimate the effect of the isotope substitution on T^* by integrating the spatial solutions. This method gives an estimate of $T^*(^{16}O)$ as function of $[T^*(^{18}O)\text{-}T^*(^{16}O)]$ (Fig. 13). Obviously, the smaller T^* the smaller is the isotope shift. For large values of T^* substantial enhancements in $T^*(^{18}O)$ are obtained which are in approximate agreement with experimental data.

The issue of the isotope effect on T_c as function of doping has been addressed in [110], where it was shown that the density of states of the specific structural elements of cuprates is differently modified by the isotopic substitution. Also the site dependent isotope effect could be explained within this framework. The same topic has been investigated in [111], where another approach based on a Landau free energy model has been introduced.

Very recently it has been shown for the first time by direct methods using low energy muon spin rotation (LEμSR) [103] that the London penetration depth is isotope dependent. The results clearly show, that λ_L increases by a few percent when ^{16}O is replaced by ^{18}O. Theoretically, an isotope effect on T_c and the in-plane effective mass has been considered within a (bi)polaronic model [112]. Also it has been noted that a violation of the Migdal theorem and/or nonadiabatic effects could induce this isotope dependence [113]. Another in-

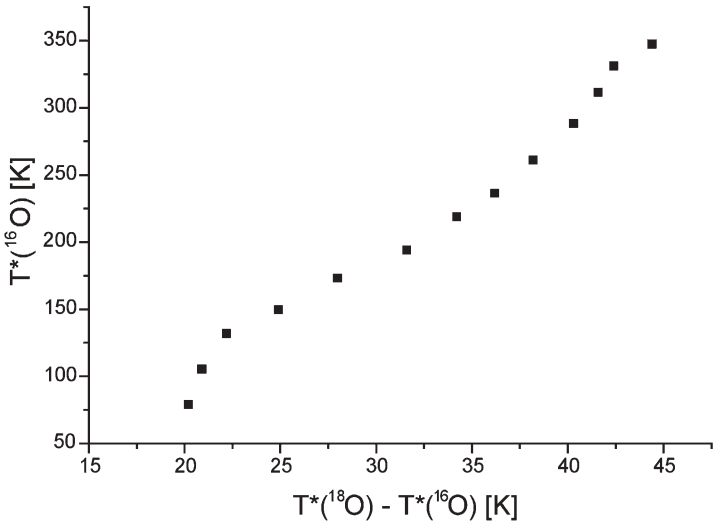

Fig. 13 Isotope effect on T^*: $T^*(^{16}O)$ as a function of $[T^*(^{18}O)-T^*(^{16}O)]$

terpretation has been given in terms of impurity scattering [114] which leads to new scaling relations. In line with the previously developed picture for cuprates it can be shown that the observed isotope effect can be a consequence of polaronic coupling within the two component scenario [115]. The details of the polaronic coupling are now explicitly given by [46]

$$\overline{H}_0 = \sum_{k_i\sigma} \xi_{k_i} c^+_{k_i\sigma} c_{k_i\sigma} + \sum_q \hbar\omega_q b^+_q b_q + \frac{1}{\sqrt{2N}} \sum_{q,\sigma,k_1} \gamma_i(q)\, c^+_{k_i+q\sigma} c_{k_i\sigma} (b_q + b^+_{-q}); \; i = 1, 2 \tag{36}$$

where the consequences for the two bands are, as shown before, different since ξ_{k_z} is renormalized as defined in Eq. (32a), whereas $\xi_{k_{xy}}$ experiences an additional exponential narrowing: $\tilde{\xi}_{k2} = \left[\varepsilon_{k_x,k_y} \exp\left(-\frac{1}{2N} \sum_q |\gamma|^2 \coth \frac{\hbar\omega_q}{2k_BT} \right) - \tilde{\Delta}^* \right]$ (the notations used here are the same as those used earlier). In the above equations b^+, b are phonon creation and annihilation operators with energy ω, γ is the dimensionless electron-phonon coupling [29]. The in-plane electronic dispersion is of tight-binding form, i.e., $\varepsilon_{k_x,k_y} = -2t[\cos k_x a + \cos k_y b]$ with $a \neq b$ to account for the orthorhombicity and t being the nearest neighbor hopping integral. The penetration depth λ_L is anisotropic as a consequence of the two-channel superconductivity and is obtained from the superfluid stiffness ρ_S via the relation

$$\lambda_L^{-2} = (16\pi e^2/\hbar^2 c^2)\rho_s \tag{37}$$

The superfluid stiffness is calculated within linear response theory through the relation between the current and the induced transverse gauge field [116]:

$$\rho_s^\alpha = \frac{1}{2V} \sum_k \left\{ \left(\frac{\partial \tilde{\xi}_{k\alpha}}{\partial k_\alpha} \right)^2 \frac{\partial f(E_{k\alpha})}{\partial E_{k\alpha}} + \frac{1}{2} \frac{\partial^2 \tilde{\xi}_{k\alpha}}{\partial k_\alpha^2} \left[1 - \frac{\tilde{\xi}_{k\alpha}}{E_{k\alpha}} \tanh \frac{E_{k\alpha}}{2kT} \right] \right\} \tag{38}$$

where $E_k = \sqrt{\tilde{\xi}_k^2 + \overline{\Delta}_k^2}$, $f(E_{k\alpha})$ is the Fermi function, and $\overline{\Delta}$ as defined earlier. The penetration depth can thus be calculated for the two channels (in-plane d-wave, s-wave along the c-axis) where the renormalizations arising from gap coupling and polaronic effects are fully taken into account. The results for the isotope effect on the in-plane penetration depth are shown as a function of polaronic coupling in Fig. 14, where the insert shows the dependence of T_c on the isotope effect and the coupling. The interband interactions are kept constant for the two cases investigated and the intraband interactions are, as noted, too small to induce superconductivity in the individual channels. The relevant regime of γ reproducing the experimental findings is indicated by the shaded areas and lies between $0.4 < \gamma < 1.1$, which corresponds to small to intermediate couplings and is too small to account for bipolaron formation [112]. The temperature dependence of the normalized ${}^{18}\lambda_{ab}$ and ${}^{16}\lambda_{ab}$, i.e, $[{}^{18}\lambda_a - {}^{16}\lambda_{ab}]/{}^{16}\lambda_{ab}$, is derived from Eq. (38) together with the self-consistent gap (Eqs. 30a,b) and is shown in

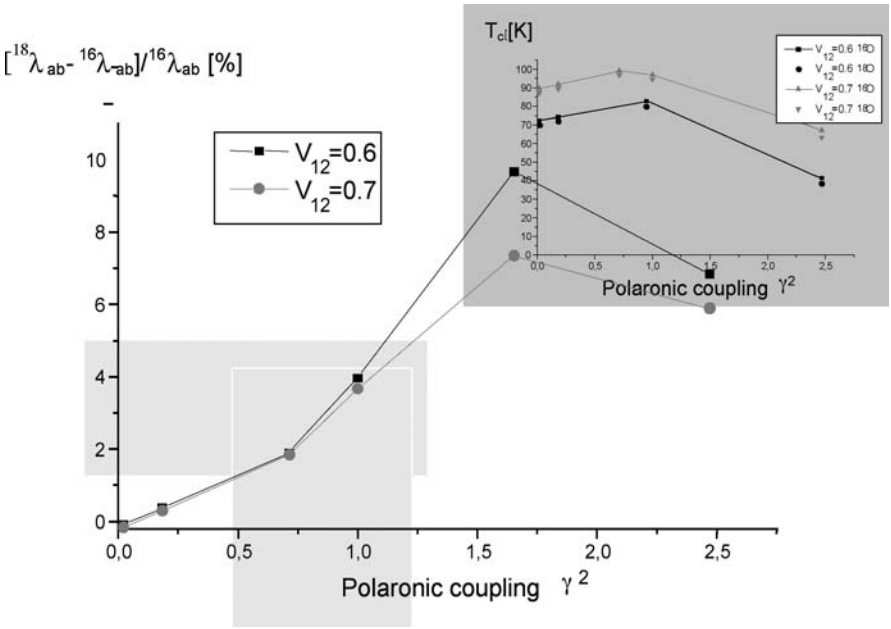

Fig. 14 Relative change in the in-plane penetration depth with oxygen isotope replacement $[^{18}\lambda_{ab} - {}^{16}\lambda_{ab}]/{}^{16}\lambda_{ab}$ as a function of polaronic coupling γ^2. The *inset* shows the isotope dependence of T_c as a function of γ^2. In both figures the *interband* coupling is 0.6, 0.7, respectively, as indicated in the figure and both *intraband* couplings are 0.01. The *shaded areas* correspond to the experimentally relevant regime

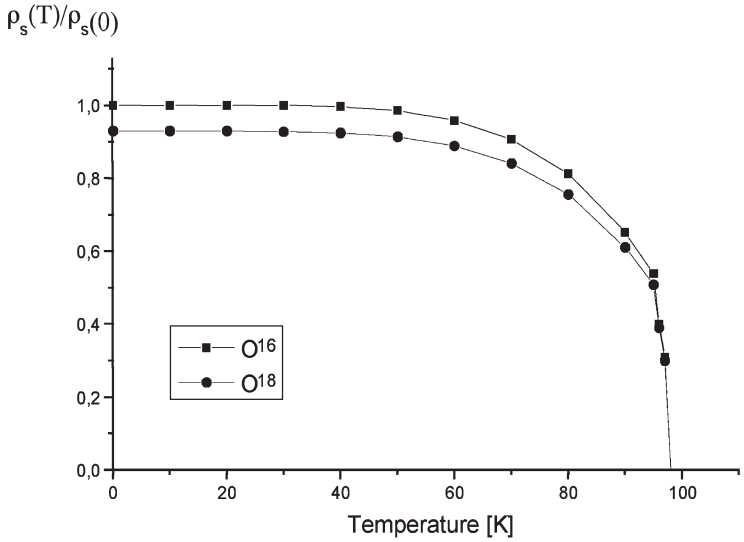

Fig. 15 Calculated temperature dependence of the normalized in-plane penetration depth $\lambda^2_{ab}(0)/\lambda^2_{ab}(T)$ for ^{16}O (*squares*) and ^{18}O (*circles*) with polaronic coupling γ^2=1. and V_{12}=0.7

Fig. 15 for the case of γ^2=1. The results are in good agreement with experimental data [102, 103]. Also the isotope effect on the c-axis penetration depth and the anisotropy of λ, i.e., λ_{ab}/λ_c have been investigated where the former is shown in Fig. 16 while the anisotropy is shown as the insert to Fig. 17. Obviously, within the coupling regime discussed above, the isotope effect on λ_c is very small and nearly negligible while the anisotropy can be substantial and seems to diverge for small couplings.

Since for many experiments single crystals are rarely available, a dependence of the ratio λ_{ab}/λ_c for an oxygen isotope effect could be experimentally more meaningful. Our results are shown in Fig. 17 for two different interband couplings. As before, it is observed that the interband coupling strength does not affect the overall behavior. More interestingly, the isotope effect now reverses sign as compared to the in-plane penetration depth but remains rather small in the experimentally relevant regime. The last result together with the one on the c-axis penetration depth have not been measured so far and are suggested for future experimental tests.

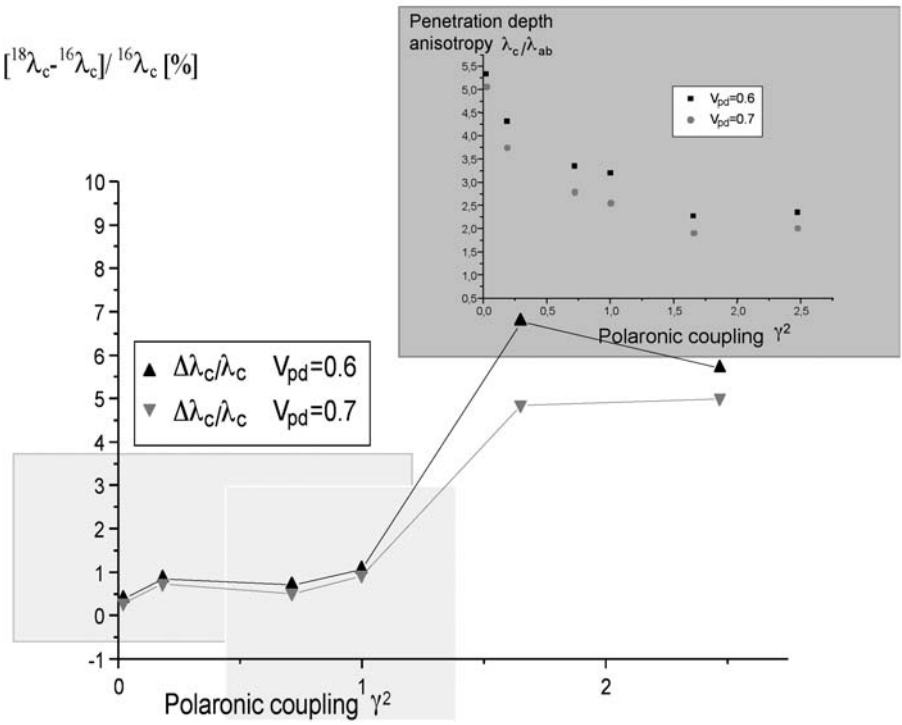

Fig. 16 Isotope induced relative change in the c-axis penetration depth $[^{18}\lambda_c - ^{16}\lambda_c]/^{16}\lambda_c$ as a function of polaronic coupling for two different interband coupling strengths (V_{12}=0.6 – *black line and symbols*; V_{12}=0.7 – *grey line and symbols*). The *insert* shows the anisotropy ratio λ_c/λ_{ab} as a function of the coupling. The *shaded areas* are those which are relevant to the experimental results on the inplane penetration depth

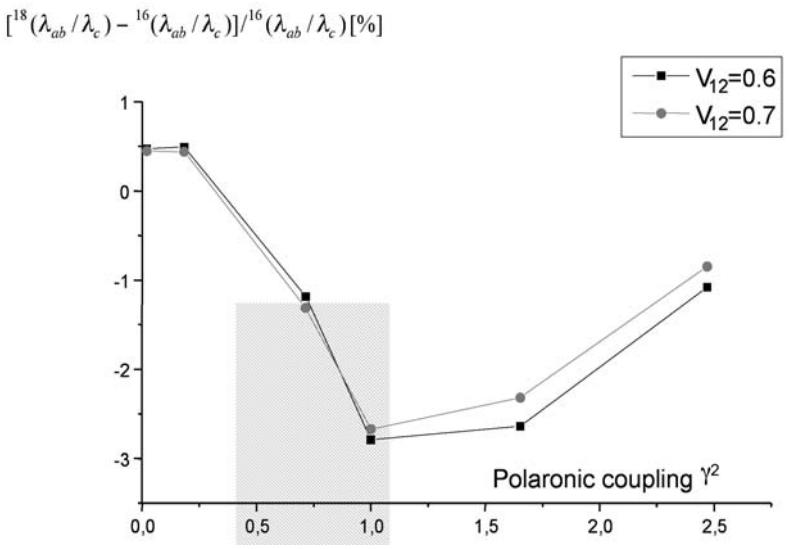

Fig. 17 Isotope dependence of the relative change of λ_{ab}/λ_c as a function of polaronic coupling for interband interactions V_{12}=0.6 (*black symbols and line*), 0.7 (*grey symbols, line*). The *shaded area* corresponds to one which is experimentally relevant

4
Superconductivity in a Two-Component Model with Local Electron Pairs

Due to the complexity of the model of coexisting preformed pairs and itinerant electrons we restrict ourselves in the following discussion of this model to purely electronic aspects, by means of which isotope effects are not accounted for and anomalous lattice effects are neglected. Further numerical studies of the model are planned where the important lattice contributions will be incorporated.

4.1
Introduction

In classical BCS-like superconductors and also two-band superconductors with finite interband interactions, the electron (hole) pairing temperature T_c coincides with the formation of a coherent macroscopic quantum state. It has been argued frequently that the pair formation could be independent of temperature of the long-range coherence and occur at much higher temperatures than the superconducting T_c. In the case of strong electron-phonon interaction the carriers can form small polarons. Typically the strong lattice deformation is sufficient to attract another of these objects to combine into pairs which have Bose character and can eventually condense into a superfluid state [117]. The result is the formation of a macroscopic coherent quantum state of q=0 eigen-

states of hard-core bosons on a lattice. Materials exhibiting such behavior should have paired electrons already in the normal state. Besides strong electron-lattice interaction effects, an attractive Hubbard term could also give rise to the above scenario, where the source of this attractive interaction has to be detailed and can arise from all kinds of couplings.

The existence of local pairs has been established in a variety of different compounds [117–119]; however, the observation of pure bipolaronic superconductivity is debated. The reasoning for this has frequently been attributed to the fact that those compounds are mostly half-filled band systems which have the tendency to form charge ordered ground states [120, 121]. The discovery of new superconductors which neither fit into the conventional BCS scheme nor in the two-band model [42, 119, 122, 123] has re-invoked the picture of preformed pairs as origin of exotic superconductivity. These new superconductors typically have several electronic bands in the vicinity of E_F, which are either d or f in character with the tendency towards localization, i.e., they are rather flat than dispersed, which is a prerequisite for local pairing since the electronic wave function is highly localized. In particular, such a localization can occur in systems where the electron-phonon coupling constant $\lambda \geq 1$ [124, 125]. The theory of local pairs has been worked out considerably [112, 119, 121, 126] and many properties, observed in exotic superconductors have been predicted within this scheme, like, e.g., non-monotonic variation of T_c with the concentration; extremely high values of the upper critical field H_{c2} and its nonstandard variation with temperature, non-exponential variation of the specific heat with temperature; effects of collective modes in the superconducting state; strong influence of magnetic as well as nonmagnetic impurities, etc. These results have mostly been obtained by considering a single narrow band corresponding to the scenario of carriers being only local pairs (hard-core charged bosons) [119, 121, 124]. An extension of these ideas takes into account that two components are mostly relevant in realistic systems, i.e., wide band electrons and narrow band electrons which interact with each other. This mixture of interacting charged bosons (local electron pairs with charge $e^*=2e$) and fermions can exhibit properties intermediate between pure bipolaronic superconductivity and BCS-like superconductivity [117, 119, 127, 128]. It can also give insight into the problem of single band systems with short range attraction in the intermediate coupling regime, where bound and ionized pairs coexist. Its various versions have been analyzed as a two-component modeling of high temperature superconductors [42, 128, 129]. A similar model has been used to describe superfluidity in atomic Fermi gases, where the bosons are associated with a Feshbach resonance and can mediate a resonance s-wave superfluidity [130–132].

4.2 The Model of Coexisting Local Pairs and Itinerant Electrons

The effective Hamiltonian describing coexisting electron pairs (hard-core bosons "b") and itinerant electrons ("c") is given by [133]:

$$H = \sum_{k,\sigma} (\varepsilon_k - \mu) c^+_{k,\sigma} c_{k,\sigma} + 2 \sum_i (\Delta_0 - \mu) b^+_i b_i - \sum_{ij} J_{ij} b^+_i b_j + \sum_{k,q} [V_q(k)\, c^+_{k+q/2,\uparrow} c^+_{-k+q/2,\downarrow} b_q + h.c.] + H_C \tag{39}$$

Here ε_k refers to the band energy of the c-electrons with momentum k and spin σ, Δ_0 measures the relative position of the local pair level with respect to the bottom of the c-electron band, μ is the chemical potential which ensures that the total number of particles is constant, i.e,

$$n = \frac{1}{N} [\sum_{k,\sigma} \langle c^+_{k,\sigma} c_{k,\sigma} \rangle + 2 \sum_i \langle b^+_i b_i \rangle] = n_c + 2 n_B \tag{40}$$

where n_c is the concentration of c-electrons, and n_B is the number of local pairs per site. J_{ij} is the pair hopping integral, H_C denotes the Coulomb interaction terms and $V_q(k)$ is the coupling constant between the two components. The operators for local pairs b^+_i, b_i obey the commutation rules for hard-core bosons (the Pauli spin 1/2 commutation rules), which exclude multiple occupancy of a given pairing center: $[b_i, b^+_j]=(1-2n_i)\delta_{ij}$, $[b_i, b_j]=0$, $(b^+_i)^2=(b_i)^2=0$, $b^+_i b_i + b_i b^+_i = 1$, $n_i = b^+_i b_i$. For on-site pairs the relations $b^+_i = d_{i\uparrow}{}^+ d_{i\downarrow}{}^+$, $b_i = d_{i\downarrow} d_{i\uparrow}$, $2b^+_i b_i = \sum_\sigma d_{i\sigma}{}^+ d_{i\sigma}$ hold (where $d_{i\sigma}{}^+ d_{i\sigma}$ operate in the subspace with single occupancies excluded). For the analysis of the properties for $T \le T_c$, in the following the q-dependence of the inter-component coupling V will be neglected for small q, i.e. $V_q(k) = V_0(k) = I\phi_k/\sqrt{N}$. With this definition the interaction between the singlet pair of c-electrons B^+_q and the hard core bosons b_q becomes

$$H_1 = \frac{1}{\sqrt{N}} \sum_q I [B^+_q b_q + b^+_q B_q] \tag{41}$$

where

$$B^+_q = \sum_k \phi_k\, c^+_{k+q/2,\uparrow} c^+_{-k+q/2,\downarrow} \tag{42}$$

is the singlet pair creation operator of the c-electron subsystem and I is the coupling constant. The pairing symmetry on a 2D square lattice is determined by the k-dependence of ϕ_k, which is constant (=1) for on-site pairing (s), $\phi_k = \gamma_k = \cos(k_x) + \cos(k_y)$ for extended s-wave (s^*), and $\phi_k = \eta_k = \cos(k_x) - \cos(k_y)$ for $d_{x^2-y^2}$-wave pairing (d). In general, one can consider a decomposition $I\phi_k = g_0 + g_s\gamma_k + g_d\eta_k$, with appropriate coupling parameters for different symmetry channels. The appropriate symmetry form factors for 3D lattices can also readily be determined.

The superconducting state of the model can be characterized by two order parameters:

$$x_0 = \sum_k \phi_k \langle c^+_{k\uparrow} c^+_{-k\downarrow} \rangle, \quad \rho^x_0 = \frac{1}{2N} \sum_i \langle b^+_i + b_i \rangle \tag{43}$$

The following analysis of the model is within the BCS mean-field approximation (BCS-MFA) and linear response theory, but keeping in mind that further theoretical extensions are required in this complex many-body problem. However, for the evaluation of the superconducting critical temperature these extensions are already incorporated, i.e., the Kosterlitz-Thouless theory will be used in 2D and the T-matrix approach in 3D. Within the BCS-MFA and in the limit H_C=0, the following set of self-consistent equations is obtained:

$$x_0 = -\frac{1}{N} \sum_k \frac{I\phi_k^2 \rho_0^x}{2E_k} \tanh \frac{E_k}{2k_B T} \tag{44}$$

$$\rho_0^x = -\frac{Ix_0 - J_0 \rho_0^x}{2\Delta} \tanh \frac{\Delta}{k_B T} \tag{45}$$

$$n_c - 1 = -\frac{1}{N} \sum_k \frac{\varepsilon_k - \mu}{E_k} \tanh \frac{E_k}{2k_B T} \tag{46}$$

$$2n_B - 1 = -\frac{\Delta_0 - \mu}{\Delta} \tanh \frac{\Delta}{k_B T} \tag{47}$$

where the quasiparticle energy of the c-electron subsystem is given by:
$E_k = \sqrt{\bar{\varepsilon}_k^2 + \overline{\Delta}_k^2}$, $\bar{\varepsilon}_k = \varepsilon_k - \mu$, $\overline{\Delta}_k^2 = I^2 \phi_k^2 (\rho_0^x)^2$, $\Delta = \sqrt{(\Delta_0 - \mu)^2 + (-I|x_0| + J_0 \rho_0^x)^2}$, $J_0 = \sum_{i \neq j} J_{ij}$.

For the 2D square lattice the c-electron dispersion is of the form $\varepsilon_k = \widetilde{\varepsilon}_k - \varepsilon_b = -2t[\cos(k_x) + \cos(k_y)] - 4t_2 \cos(k_x)\cos(k_y) - \varepsilon_b$, where t, t_2 are nearest and next-nearest-neighbor (nn, nnn) hopping integrals and $\varepsilon_b = \min \widetilde{\varepsilon}_k$ with the lattice spacing set to unity. The case of a quasi 2D electron spectrum is discussed below. It is important to mention that the energy gap in the c-band is caused by the non-zero Bose condensate amplitude ($|\langle b \rangle| \neq 0$), and well defined Bogoliubov quasiparticles can exist in the superconducting state. The free energy of the system reads

$$F/N = -\frac{2k_B T}{N} \sum_k \ln[2\cosh(E_k/2k_B T)] - k_B T \ln[2\cosh(\Delta/k_B T)] + C \tag{48}$$

with

$$C = -\varepsilon_b + \Delta_0 + \mu(n_c + 2n_B) - 2\mu - 2I|x_0|\rho_0^x + J_0(\rho_0^x)^2 \tag{49}$$

The energy spectrum of the system is characterized by E_k and Δ. The order parameters and chemical potential can also be obtained by minimizing the free energy with respect to them, i.e.,

$$\frac{\partial F}{\partial x_0} = 0, \quad \frac{\partial F}{\partial \rho_0^x} = 0, \quad \frac{\partial F}{\partial \mu} = 0$$

and yield Eqs. (44)–(47). These equations have to be solved simultaneously with the condition that the total number of particles is $n=n_c+2n_b$. The superfluid stiffness is derived in analogy to Eq. (38) and is, in the case $J_{ij}=0$, [133]:

$$\rho_s^x = \frac{1}{2N}\sum_k \left\{ \left(\frac{\partial \varepsilon_k}{\partial k_x}\right)^2 \frac{\partial f(E_k)}{\partial E_k} + \frac{1}{2}\frac{\partial^2 \varepsilon_k}{\partial k_x^2}\left[1 - \frac{\bar{\varepsilon}_k}{E_k}\tanh\frac{E_k}{2k_BT}\right]\right\} \tag{50}$$

where similar equations hold for ρ_s^y, ρ_s^z. In the local limit the London penetration depth λ_L can be expressed by $\lambda^{-2} \propto (16\pi e^2/\hbar^2 c^2)\rho_s$. It is also of interest to derive the BCS condensate density of c-electrons which is given by

$$n_0(T) = \frac{1}{N}\sum_k \left(\frac{\bar{\Delta}_k}{2E_k}\tanh\frac{E_k}{2k_BT}\right)^2 \tag{51}$$

and the pair correlation length

$$\xi^2 = \sum_k |\nabla \varphi_k|^2 \Big/ \sum_k |\varphi_k|^2 \tag{52}$$

where $\varphi_k = \bar{\Delta}_k/(2E_k)$. The mean-field transition temperature (T_c^{MFA}), at which the gap vanishes, yields an estimation of the c-electron pair formation temperature [134]:

$$1 = \left[J_0 + \frac{I^2}{N}\sum_k \phi_k^2 \frac{\tanh\left(\dfrac{\bar{\varepsilon}_k}{2k_BT_c^{\mathrm{MFA}}}\right)}{2\bar{\varepsilon}_k}\right]\frac{\tanh\left[\dfrac{\Delta_0-\mu}{k_BT_c^{\mathrm{MFA}}}\right]}{2(\Delta_0-\mu)} \tag{53}$$

$$n = 2 - \tanh\frac{\Delta_0-\mu}{k_BT_c^{\mathrm{MFA}}} - \frac{1}{N}\sum_k \tanh\frac{\bar{\varepsilon}_k}{2k_BT_c^{\mathrm{MFA}}} \tag{54}$$

In Eq. (53) $I^2/2(\Delta_0-\mu)$ can be interpreted as the pairing interaction mediated by the local pairs and the factor $\tanh[\Delta_0-\mu)/k_BT]$ is due to the hard-core nature of the bosons.

Due to fluctuation effects, the superconducting phase transition temperature is lower than the one obtained within BCS-MFA theory. In 2D, T_c can be derived within the Kosterlitz-Thouless (KT) theory for 2D superfluids, which describes the transition in terms of vortex-antivortex pair unbinding [135]. Using the KT relation for the universal jump of the (in-plane) superfluid density ρ_s at $T_c=T_c^{\mathrm{KT}}$ [135, 136], one obtains

$$\frac{2}{\pi} k_B T_c^{\mathrm{KT}} = \rho_s(T_c^{\mathrm{KT}}) \tag{55}$$

Consequently T_c^{KT} has to be derived from a set of four self-consistent equations (Eqs. 55, 50, 44–47) whereas in the weak coupling limit ($|I_0|/2D \ll 1$, $J_0=0$, D is the half band-width, $I=-|I_0|$) the relation $T_c^{\mathrm{KT}}/T_c^{\mathrm{MFA}} \to 1$ if $|I_0|/2D \to 0$ is obtained. It is important to emphasize that the sign of I can be positive as well as negative. For $I>0$ the order parameters exhibit opposite signs, whereas for $I<0$ they both have the same sign. In 3D the superconducting transition temperatures derived within the T-matrix approach are given below.

The phase diagrams and superfluid properties of the model defined by Eq. (39) are discussed in the following. In the absence of interactions and depending on the relative concentration of c-electrons and local pairs, three physically different regimes can be distinguished (Fig. 18):

For $n \leq 2$ these are:

1. $\Delta_0<0$: at $T=0$ all available electrons form local pairs ($2n_b \gg n_c$). This limit is the local pair regime (LP).
2. $\Delta_0>0$: the c-electron band is filled up to the Fermi level $\mu=\Delta_0$ and the remaining electrons form local pairs. Obviously here a coexistence of local pairs and c-electrons is observed ($0<2n_b$, $n_c<2$) corresponding to a mixed regime (LP+E).
3. $\Delta_0>0$: the Fermi level is below Δ_0 and at $T=0$ all available electrons are in c-states ($n_c \gg 2n_b$). This limit corresponds to c-regime or the weak-coupling ("BCS"-like) regime (E).

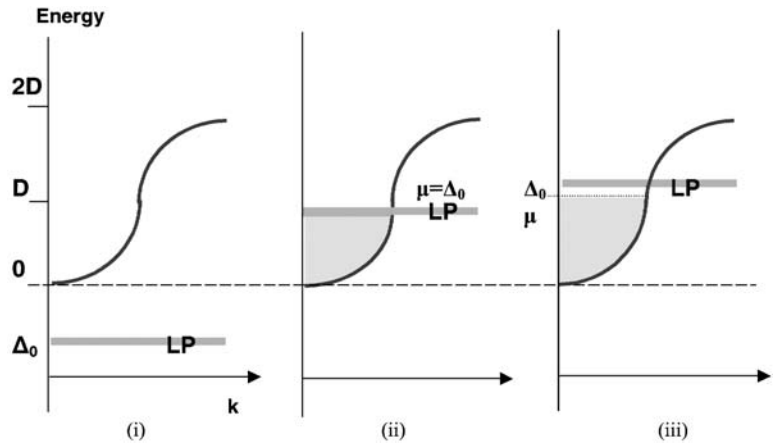

Fig. 18 The relative position of the local pair (LP) level Δ_0 with respect to the bottom of the wide band electrons in the absence of any interaction effects: (i) $\Delta_0<0$: In the ground state only LP states are occupied; (ii) $0<\Delta_0=\mu$: In the ground state both, local pairs and wide band electron states are occupied; (iii) $\mu<\Delta_0$. In the ground state only single particle states of wide band electrons are occupied

For $|I_0|\neq 0$ in case 2 superconductivity is a consequence of the interchange between local pairs and *c*-electron pairs. The *c*-electrons become "polarized" into Cooper pairs and local pairs gain mobility by decaying into *c*-electron pairs. In this intermediate regime neither the usual BCS picture nor the LP approach apply, and superconductivity has a "mixed" character. The system shows here features which are intermediate between both limits. This concerns the energy gap in the single electron excitation spectrum, the gap to T_c ratios, the critical fields, the Ginzburg ratio κ, as well as the normal state properties. In case 1 the local pair mobility is provided through virtual excitations into empty *c*-electron states. This mechanism gives rise to long range hopping of local pairs (which is analogous to the RKKY interaction for the s-d mechanism in the magnetic equivalent). The superconducting properties resemble those of a pure bipolaronic superconductor, especially if $J_{ij}\neq 0$. In case 3 the situation is similar to that of a BCS superconductor: Cooper pairs of *c*-electrons are exchanged via virtual transitions into local pairs. This mechanism can be particularly effective in the presence of additional attractive interactions among the *c*-electrons.

4.3 Phase Diagram and Critical Temperatures

A study of the phase diagrams and the superfluid properties of the model Eq. (39) for different pairing symmetries including s, extended s (s*) and $d_{x^2-y^2}$-wave symmetries for 2D and quasi 2D lattices has been performed in [133, 134]. The generic phase diagram for $t_2=0$ and d-wave symmetry is shown in Fig. 19 as a function of the LP level Δ_0; n is fixed here and two different values of $|I_0/D|$ ($D=4t$) have been used.

A sharp drop in the superfluid stiffness and in T_c^{KT} takes place when the bosonic level reaches the bottom of the *c*-electron band and the system moves to the LP limit. In the opposite limit, i.e., the BCS-like regime, T_c^{KT} is asymptotically close to T_c^{MFA}, with a narrow fluctuation regime. Between both T_c^{KT} and T_c^{MFA}, phase fluctuations are of importance and a pseudogap in the *c*-electron spectrum develops. In this region the normal state properties will show non-Fermi liquid behavior [137]. In Fig. 20 the phase diagram, is shown as a function of the total number of carriers for given value of $\Delta_0/D=0.25$. The regime between the MFA and KT transition temperatures, where a pseudogap develops, decreases in magnitude with decreasing inter-subsystem coupling $|I_0|$. Simultaneously the superconducting mixed region shrinks as can also be observed in Fig. 20. The dependences of T_c^{MFA} and T_c^{KT} on the local pair level Δ_0 for d-, s*- and s-wave symmetry are shown in Fig. 21a–c, respectively. In all cases a sharp drop in the KT transition temperature takes place when the LP level reaches the bottom of the *c*-electron band. For extended s-wave pairing $T_c^{\mathrm{KT}}\propto\rho_s(0)$ if $\Delta_0<0$. The non-monotonous behavior of T_c for the extended s-wave paring and $n>1$ reflects the fact that in a single band model this pairing is realized for low electron (hole) densities if $t_2=0$.

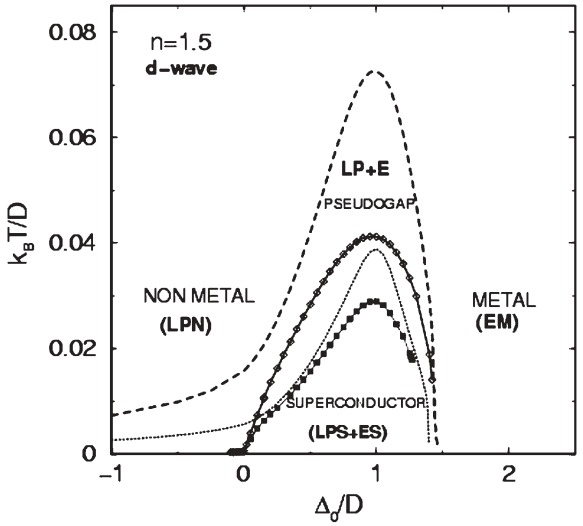

Fig. 19 Phase diagram of the induced pairing model for $d_{x^2-y^2}$-wave symmetry. The parameters used are n=1.5, I=–$|I_0|$, J_{ij}=0, D=4t. The *dashed line* corresponds to the BCS-MFA transition temperature, the *line with diamonds* represents the KT temperature for $|I_0|/D$=0.25. The *dotted line* and the *line with full squares* show the BCS-MFA and KT transition temperatures for $|I_0|/D$=0.15. LPN – normal state of LPs; EM – electronic metal; LPS+ES – (mixed) superconducting state

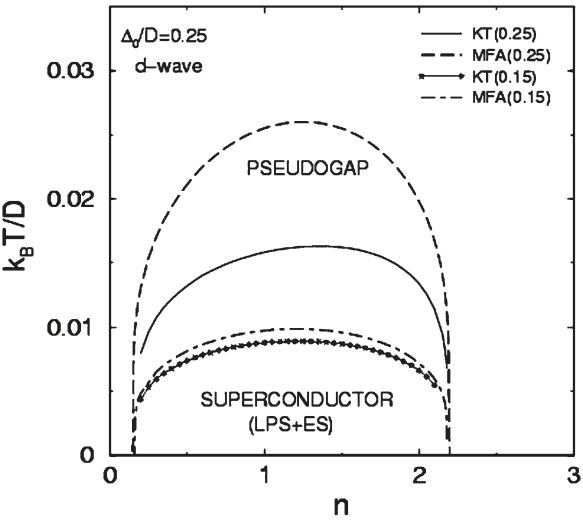

Fig. 20 Phase diagram of the induced pairing model (for d-wave symmetry) as a function of the total number of carriers n and fixed value of Δ_0/D=0.25. The two values of the inter-subsystem couplings, used in the figure, are indicated in there. Here and in Figs. 21–31 $|J_{ij}|$=0

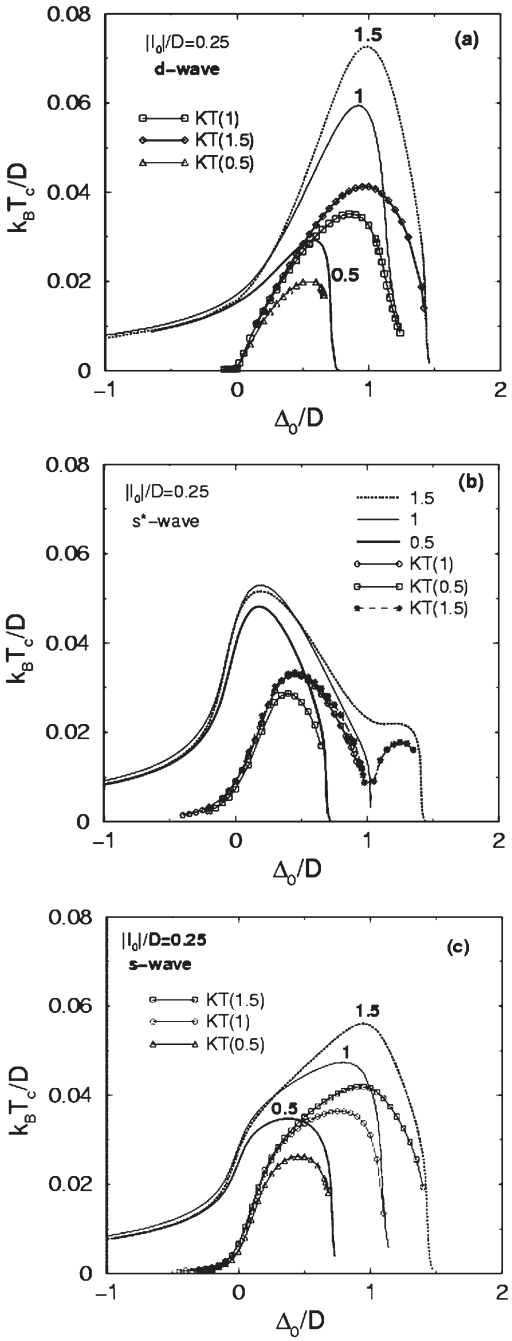

Fig. 21 The transition temperatures T_c^{MFA} and T_c^{KT} as functions of Δ_0/D for several fixed values of n as indicated in the figures with $|I_0|/D$=0.25 and t_2=0: **a** $d_{x^2-y^2}$-wave symmetry; **b** extended s-wave symmetry; **c** s-wave symmetry

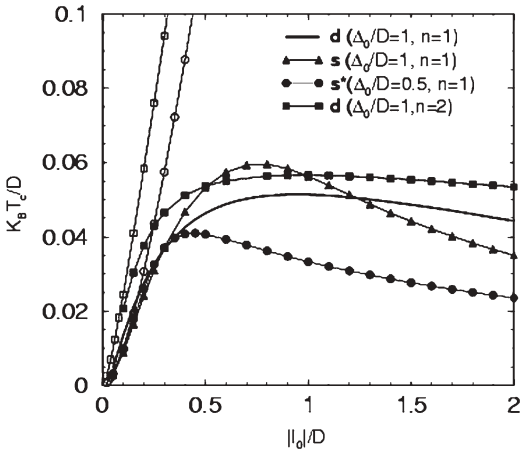

Fig. 22 Temperatures T_c^{MFA} and T_c^{KT} as functions of $|I_0|/D$ for various types of pairing for a 2D lattice (t_2=0). The *lines with full symbols and the thick solid line* denote the KT transition temperatures. The *line with empty squares* is T_c^{MFA} for d-wave pairing (Δ_0/D=1, n= 2), while the *line with open circles* is T_c^{MFA} for s*-wave pairing (Δ_0/D=0.5, n= 1)

The region between T_c^{MFA} and T_c^{KT}, where the system can exhibit a pseudogap, expands with increasing intersubsystem coupling $|I_0|/D$, which is shown in Fig. 22. As observed previously [133], the coupling dependencies of T_c^{MFA} and T_c^{KT} are qualitatively different, except for $|I_0|/D \ll 1$. T_c^{MFA} is an increasing function of $|I_0|/D$ for all pairing symmetries, whereas T_c^{KT} vs $|I_0|/D$ first increases, then passes a through a round maximum to finally decrease (analogous to the attractive Hubbard model). The position of the maximum appears at intermediate values of $|I_0|/D$ and depends on the pairing symmetry as well as on the values of Δ_0 and n. For large $|I_0|/D$, T_c^{KT} is close to the upper bound of the phase ordering temperature which is given by $\pi\rho_s(0)/2$.

Including the effect of a finite next-nearest-neighbor (nnn) hopping integral t_2 in the evaluation of T_c yields a substantial enhancement of T_c^{MFA} as long as the sign of t_2 is opposite to the one of t (Fig. 23). Also d- and s-wave pairings are supported by the nnn hopping term, however for smaller values of n_c. If both hopping parameters have the same sign T_c^{MFA} is reduced as compared to the case where t_2=0. In the case that the hopping parameters have opposite signs, both, T_c^{MFA} and T_c^{KT}, shift to lower values of Δ_0/D, and, in addition, the LP regime increases which is consistent with the fact that the fermionic bound states are favored for t_2<0.

The above results clearly point to the importance of including the next-nearest-neighbor hopping in the calculation of T_c when considering a scenario of coexisting local pairs and *c*-electrons.

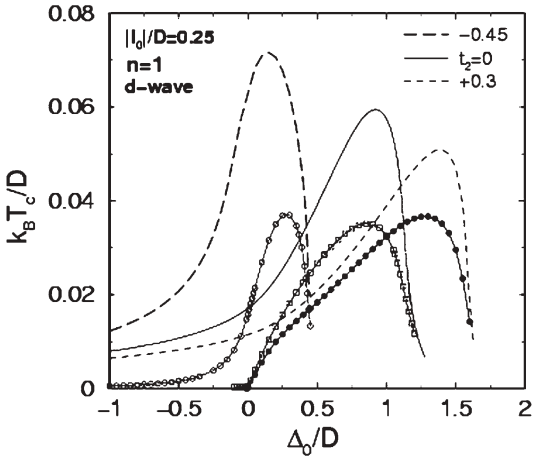

Fig. 23 The effect of t_2 on the transition temperatures T_c^{MFA} (*lines*), T_c^{KT} (*lines with symbols*) for d-wave pairing. The variation of t_2 together with the parameters used, are indicated in the figure

4.4 Superconducting Characteristics and Crossover from Weak-Coupling to Local Pair Regime

The system of coexisting local pairs and itinerant electrons exhibits the limiting behaviors discussed above. Depending on the choice of parameters and the number of pairs and *c*-electrons, the system can exhibit different kinds of superconducting behavior ranging from weak-coupling ("BCS-like) to local pair like. Interestingly a new regime is possible in this scenario, which is neither BCS nor LP like: this is the regime where LPs and *c*-electrons contribute equally well to the pairing and superconductivity is of mixed character. The superfluid characteristics as a function of n at fixed Δ_0 and as a function of Δ_0 at fixed n are shown in Figs. 24–28. In the case of n fixed and <2, the superconducting properties evolve from LP to mixed and finally to weak-coupling with varying LP level. If n>2, the situation is reversed, i.e., "BCS" to mixed to LP.

In Fig. 24 the evolution of the order parameters, the concentrations of *c*-electrons and LPs, the chemical potential, the gap related parameter in the fermionic spectrum and the superfluid density in the superconducting ground state are shown as a function of Δ_0/D with n fixed. In particular, Fig. 24b shows that the superfluid stiffness $\rho_s(0)$ in the mixed and LP regimes is smaller than the fermionic gap amplitude $\Delta_F(0)$, in contrast to the "BCS"-like limit. Especially the pair correlation length ξ and the gap ratios are affected by this crossover which is shown for the correlation length in Fig. 25 where in Fig. 25a n=1 and Δ_0/D is varied, while in Fig. 25b Δ_0/D is given whereas n is varied. Here the pairing symmetries are also of importance since for extended s-wave symmetry ξ increases smoothly from the LP limit to the "BCS" like regime while in the case

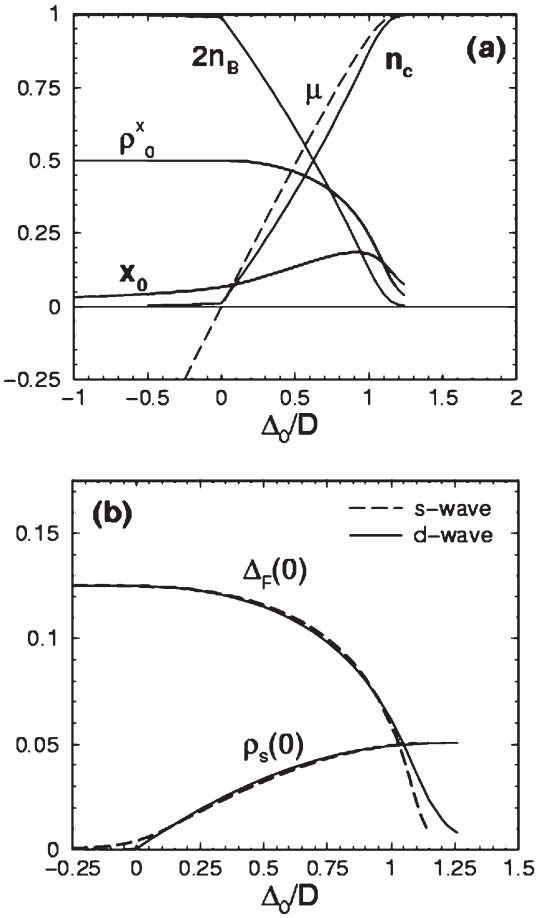

Fig. 24 **a** Variation of n_c (concentration of *c*-electrons), n_B (concentration of LPs), superconducting order parameters ρ_0^x, x_0 and the chemical potential μ/D at T=0 as functions of Δ_0/D, for n=1, $|I_0|/D$=0.25, t_2=0, J_0=0, *d*-wave pairing. **b** $\Delta_F(0)/D$ and $\rho_s(0)/D$ vs Δ_0/D for the same parameters where $\Delta_F=|I_0|\rho_0^x$

of d-wave symmetry an anomaly in ξ is observed when Δ_0 passes the bottom of the *c*-electron band which is a consequence of the existence of nodal quasiparticles for $\Delta_0>0$.

An analogous calculation has been performed for the variation of the T_c to gap ratios again as a function of Δ_0/D and n, where as above, in the first case n is constant while in the latter Δ_0/D is fixed (Figs. 26 and 27). Also here the pairing symmetries are crucial for these ratios, where the energy gap for the *c*-electrons is defined by E_g=2 max $\overline{\Delta}_k$ if the chemical potential is within the band for s- and d-wave pairing, and E_g=2 min E_g for extended s-wave pairing, or if μ is below the bottom of the band. In the weak-coupling regime the ratios approach the BCS values (0.57 for s and extended s-wave symmetry and 0.47

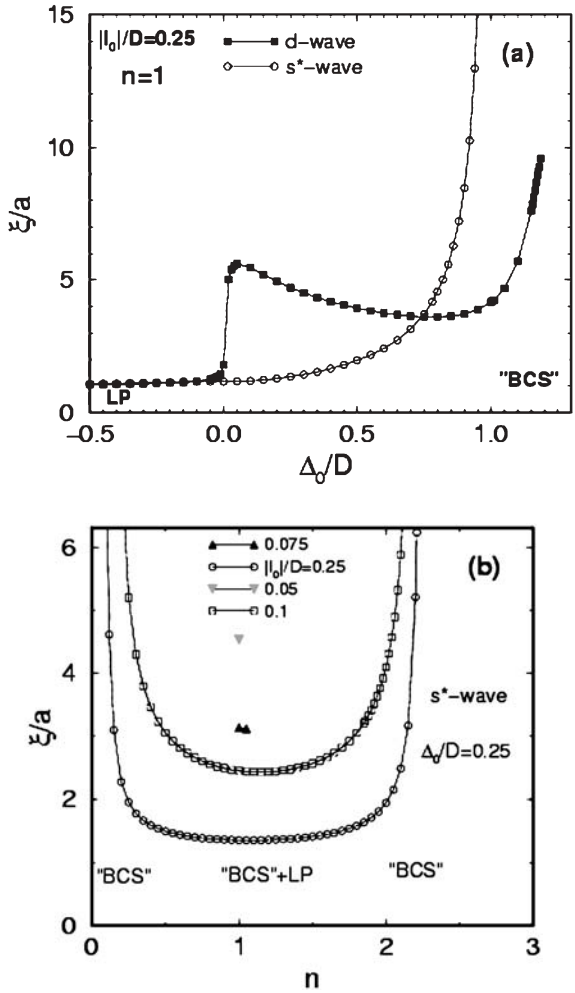

Fig. 25 **a** Pair radius of the *c*-electrons as a function of Δ_0/D for $|I_0|/D$=0.25, n=1, t_2=0 and extended s-wave and d-wave symmetries. In the case of d-wave symmetry the calculations were done at small but finite temperature. **b** Pair radius of *c*-electrons as a function of n for Δ_0/D=0.25 and some fixed values of $|I_0|/D$ for extended s-wave symmetry and t_2=0

for d-wave symmetry) and decrease with increasing concentration of LPs. In the regime, where predominantly LPs exist, the ratios approach zero. A sharp anomaly is observed for d-wave pairing when Δ_0=0.

Since the mixed regime is the most interesting one, this has been analyzed in deeper detail. It is observed here that when the LP level is lowered and reaches the bottom of the fermionic band, the effective attraction between *c*-electrons becomes strong as it varies like $I^2/(2\Delta_0-2\mu)$ and $\mu\approx\Delta_0$. Here the density of fermions is small and formation of preformed *c*-electron pairs sets in.

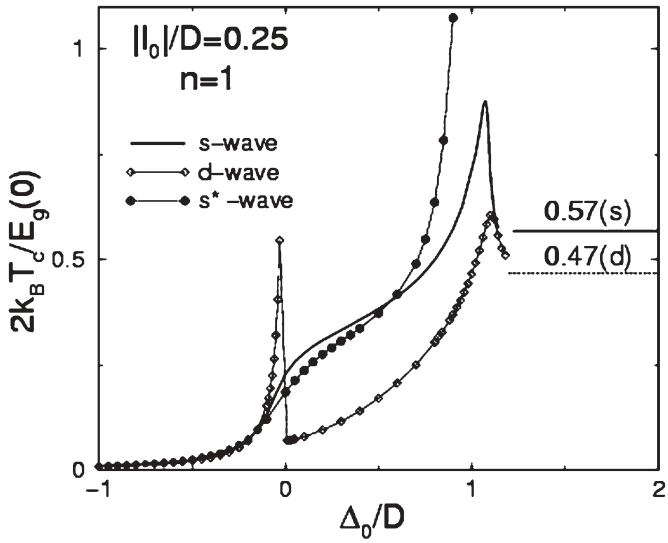

Fig. 26 $2k_BT_c^{MFA}/E_g(0)$ as a function of Δ_0/D for various pairing symmetries and n=1, $|I_0|/D$= 0.25, t_2=0

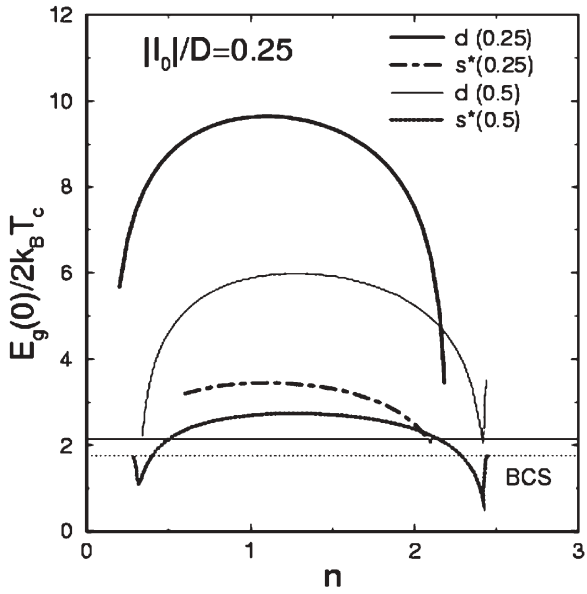

Fig. 27 $E_g(0)/2\ k_BT_c^{MFA}$ as a function of total carrier concentration n for d-wave and extended s-wave symmetries for $|I_0|/D$=0.25, t_2=0 and two values of Δ_0/D=0.25 and 0.5 as indicated in the figure. The *two straight lines* correspond to weak coupling BCS results for d-wave (*full line*) and s-wave pairing (*dotted line*), respectively

This, however, is accompanied by the opening of a gap in the single-particle spectrum, independent of the pairing symmetry, where half of the binding energy of these preformed pairs essentially scales with T_c^{MFA}. Such a behavior is an indication of a rearrangement of the normal state occurring at T_c^{MFA} when $\Delta_0<0$, since bound states with zero center of mass momentum of *c*-electrons are formed [133, 138]. The transition temperature to the superconducting state is always much lower than the *c*-pair formation temperature and quickly vanishes with $|\Delta_0/D|$. In this case the superconducting state consists of a mixture of coexisting (composite) bosons: preformed *c*-electron pairs and LPs.

The superconducting properties are strongly dependent on the total number of carriers and in general three different types of density driven crossovers can occur with increasing n: 1. for $2\geq\Delta_0/D\geq 0$ the weak coupling ("BCS"-like) behavior changes to the "mixed" regime and then again to weak coupling; 2. $\Delta_0/D>2$ weak coupling directly changes to that of LPs; 3. $\Delta_0/D<0$ the reversed behavior is seen as compared to 2., i.e., LP→weak coupling.

The density driven crossovers are shown in Fig. 25b for the correlation length and in Fig. 27 for the gap to T_c ratio. It is important to emphasize again that in the mixed regime a strong increase in the gap ratios takes place accompanied by a substantial and sudden decrease of the *c*-electron pair radius. Here ξ is only weakly dependent on n and is of the order of a few lattice constants only. Only when the LP level is located deeply below the bottom of the *c*-electron band, the system remains in the LP regime for any $n\leq 2$ and ξ is small (about of the order of a the lattice constant). Here for s and extended s-wave pairing as well as

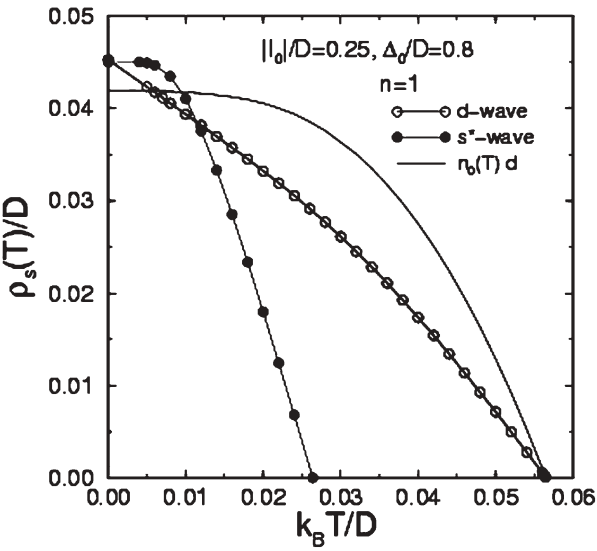

Fig. 28 Temperature dependencies of the superfluid density ρ_s for d- and extended s-wave pairing and the BCS condensate density of the *c*-electrons n_0 (for d-wave) with $|I_0|/D=0.25$, $\Delta_0/D=0.8$, $n=1$

for d-wave pairing symmetry the gap ratios tend to the BCS value at the mixed-"BCS" boundary (Fig. 27) while they strongly increase in the mixed region. Here the d-wave symmetry favors even higher ratios as compared to extended s-wave.

If Δ_0 is fixed but n is varied, superconductivity in the mixed regime seems to be not very sensitive to the pairing symmetry. Here n_c remains almost constant whereas n_b increases with n. The chemical potential in this mixed regime is nearly pinned around Δ_0, being an increasing function of n.

In Fig. 28 the superfluid and BCS-condensate densities are shown as functions of temperature. A clear difference in the behavior of the superfluid density is observed when comparing d-wave symmetry with extended s-wave symmetry. While in the former case a linear in T-behavior is observed at low temperatures, it is nearly independent of T for the latter case in the same temperature regime. The c-electron condensate density follows mostly a BCS T-dependence.

Within the KT scenario the T_c^{KT} vs zero temperature phase stiffness $\rho_s(0)$ dependencies have been calculated for d-wave and extended s-wave symmetries in order to reproduce the Uemura plots [139] (Figs. 29 and 30). For fixed n but with varying position of the LP level a linear dependence of T_c^{KT} with $\rho_s(0)$ is obtained which is a consequence of the separation of energy scales for the pairing and phase coherence in the proximity of the nonmetallic LP regime. Such a linear scaling is, however, not present within the MFA approach (Fig. 30). If Δ_0/D is fixed and n is varied, this linear relation is not obtained as long as the hopping among c-electrons is allowed for nearest neighbors only [133]. (The

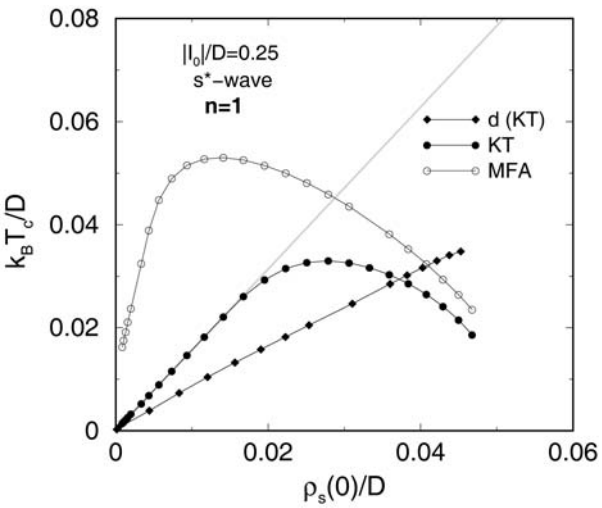

Fig. 29 Uemura-type plots $k_B T_c^{KT}/D$ vs ρ_0/D for d-wave and extended s-wave symmetries with control parameter Δ_0/D and n=1, $|I_0|/D$=0.25, t_2=0. Δ_0/D varies fom –0.4 to 0.85 and from –0.1 to 0.8 for extended s-wave and d-wave pairing, respectively. The *straight line* gives an estimate for the upper bound of the phase ordering temperature $\pi\rho_s(0)/2$. The corresponding dependence of T_c^{MFA} for extended s-wave pairing is indicated by the curve with *open circles*

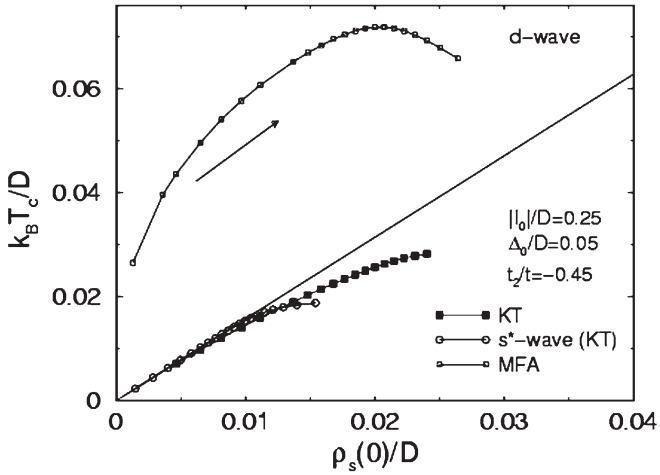

Fig. 30 Uemura-type plots $k_B T_c^{KT}/D$ vs $\rho_s(0)/D$ for d-wave and extended s-wave symmetry with control parameter n and $|I_0|/D=0.25, \Delta_0/D=0.05$, $t_2=-0.45t$. The increase in n is marked by the *arrow*. $n\in[0.1, 2]$ for extended s-wave and $n\in[0.2, 2]$ for d-wave symmetry. The analogous plot for T_c^{MFA} and $d_{x^2-y^2}$ symmetry is represented by *open squares* with $n\in[0.05, 2.2]$. As before, the *straight line* yields the upper bound on the phase ordering temperature

straight line in Figs. 29 and 30 represents an upper bound for the phase ordering temperature, i.e., $\pi\rho_s(0)2$.) Including, however, a finite second nearest neighbor hopping integral t_2, with t_2 opposite in sign to t, yields the Uemura plots with a linear scaling at low superfluid stiffness again for both d-wave and extended s-wave symmetry. As a matter of fact, for low c-electron concentrations, there exists the possibility to form bound states, and the chemical potential in the superconducting phase can move below the bottom of the bare electronic band. In this case, the superconducting state is a consequence of LPs and preformed pairs of c-electrons.

4.5 Effects of Weak Interlayer Coupling

The properties of the model of coexisting local pairs and itinerant c-electrons have, up to now, been considered within a two-dimensional case. Effects of quasi-two-dimensionality can be incorporated by modifying the c-electron dispersion to allow for an inter-planar hopping element, i.e., $\varepsilon_k=-2t[\cos(k_x)+\cos(k_y)]-4t_2\cos(k_x)\cos(k_y)-2t_\perp\cos(k_z)-\tilde{\varepsilon}_b$, where $t_\perp$ is the inter-planar hopping amplitude, and the bottom of the band is shifted to $\tilde{\varepsilon}_b-4t-4t_2-2t_\perp$. In the special case that $t_2=0$ and $t_\perp/t\leq 0.01$, the inter-planar hopping has nearly no influence on T_c^{MFA}. Results of the numerical calculation are shown in Fig. 31 where T_c^{MFA} for d-wave symmetry is plotted as function of n with Δ_0 constant. The investigation of T_c^{MFA} at constant n but Δ_0 variable yields similar results [133]. The

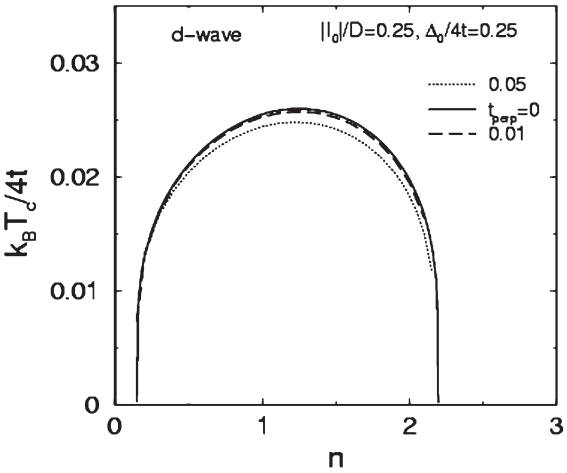

Fig. 31 Effect of the interplanar hopping $t_\perp/t$ on $k_B T_c^{\mathrm{MFA}}$ with varying n for d-wave symmetry and t_2=0. The *curves* correspond to different ratios of $t_\perp/t$ as indicated in the figure

influence of the weak interplanar hopping is in both cases very small and justifies to work in the 2D space.

The effects of a weak interlayer coupling on the calculated superconducting transition temperatures [140, 141] are discussed in the following. In the KT theory the 2D correlation length behaves as follows for $T>T^{\mathrm{KT}}$: $\xi(T)= a\exp(b/\sqrt{T/T^{\mathrm{KT}}-1})$, where $b\approx 1.5$ and a is the size of the vortex core. If U_c is the coupling energy per unit length between the planes and $U_c \ll T^{\mathrm{KT}}$, then the actual T_c can be estimated by calculating the energy needed to destroy phase coherence between two regions of size $\approx\xi^2$ in different planes, i.e., $T_c \approx \bar{c}U_c[\xi(T_c)/a]^2$, where $\bar{c}$ is the interplanar distance. The resulting equation for T_c can be solved asymptotically:

$$T_c = T^{\mathrm{KT}}\left(1+\frac{4b^2}{\ln^2(T^{\mathrm{KT}}/\bar{c}U_c}\right) \tag{56}$$

Therefore T_c is only weakly dependent on the interplanar distance $\bar{c}$ and is close to T^{KT}, if $U_c \ll T^{\mathrm{KT}}$. In the presence of the interplanar coupling there is no discontinuous jump in ρ_s but a crossover from 2D like to 3D like (XY) behavior occurs.

4.6 Superfluid Transition from the Pseudogap State in 3D

In this last section, results obtained by going beyond the BCS-MFA in the isotropic 3D case are presented. Of interest here is the evaluation of the superconducting transition temperature from the pseudogap state. This can be

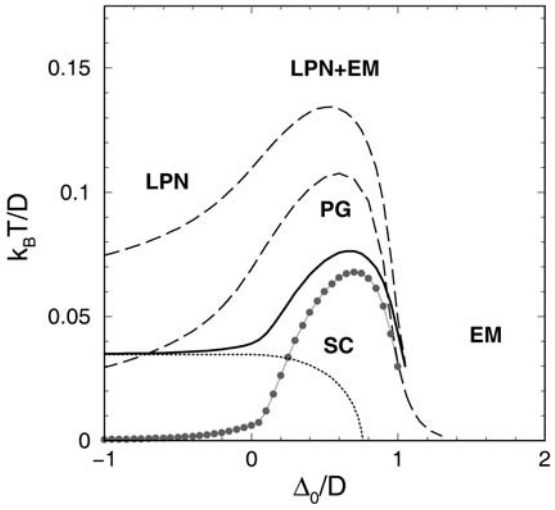

Fig. 32 Phase diagrams of the hard-core boson-fermion model as a function of Δ_0/D for s-wave pairing and an sc lattice with n=0.5, $|I_0|/D$=0.5, D=6 t. The transition temperatures, derived within the T-matrix approach, are for two values of J (J_0/D=0.1: *solid line*, J_0=0: *solid line with symbols*). The *dashed curves* correspond the BCS-MFA transition temperatures (J_0/D=0.1: *upper curve*, J_0=0: *lower curve*). The *dotted line* is the RPA result for J_0/D=0.1, $|I_0|$=0. LPN: normal state of predominantly LPs; EM: electronic metal; SC: superconducting state (LPS+ES); PG: pseudogap regime

analysed by applying the generalized T-matrix approach adapted to a two-component boson-fermion model [142], and it includes pairing fluctuations and bosonic self-energy effects. This approach is an extension of the pairing fluctuation theory of the BCS-Bose-Einstein crossover [143, 144] developed previously for a one-component fermion system with attractive interactions. The numerical results presented in Fig. 32 are for s-wave pairing and a 3D sc lattice assuming the tight-binding dispersions for fermions and bosons to be of the following form:

$$\varepsilon_k = D(1 - \tilde{\gamma}_k),\ D = zt;\ J_q = J_0\,\tilde{\gamma}_q,\ J_0 = zJ,\ \tilde{\gamma}_q = [\cos k_x + \cos k_y + \cos k_z]/3,\quad z = 6$$

The results are shown for both cases, with and without the direct hopping of LPs J_{ij}. Except for the c-regime, the calculated T_cs are much lower as compared to BCS-MFA results (which are given by Eq. 53), and if J=0 T_c is strongly depressed as soon as the LP level is close to the bottom of the electronic band. In the pseudogap region the electronic spectrum is gapped, and the pseudogap parameter at T_c for Δ_0>0 essentially measures a mean square amplitude of the pairing field (of the "c" electrons). The values of the pseudogap parameters at T_c are comparable to the zero temperature gap values in the fermionic spectrum beyond the c-regime.

With the direct hopping J_0/D=0.1, which corresponds to m_B=10m_F (m_B, m_F=boson, fermion mass), the hard-core bosons can undergo a superfluid transition even without the inter-subsystem coupling $|I_0|$. For the case $|I_0|$=0 the approach reduces to the random phase approximation for hard-core bosons and the critical temperature is determined by [121]

$$(1 - 2n_B)^{-1} = \frac{1}{N}\sum_q \coth\frac{E_q^0}{2k_BT_c} \tag{57}$$

where E_q^0=$J_0(1-\tilde{\gamma}_q)(1-2n_B)$ together with the constraint n=n_c+2n_B, n_c=1–$(1/N)\sum_k \tanh(\bar{\varepsilon}_k/2k_BT_c)$, 2μ=$2\Delta_0$–$J_0(1-2n_B)$. The solution (for a parabolic dispersion of the bosons) is shown in Fig. 32 by the dotted line. As can also be seen there, in the presence of finite boson-fermion coupling $|I_0|$ the transition temperature is much enhanced in the mixed regime.

In the self-consistent T-matrix approach the fluctuations of the order parameter are included at the Gaussian level. Nevertheless it is interesting to observe that the phase diagram for J_0=0, shown in Fig. 32 displays similar regimes as that of Figs. 19 and 21c determined from BCS and KT theories in 2D discussed earlier. It is worthwhile to note that in both cases, the shapes of the dependence of T_c on Δ_0/D are qualitatively similar for J_0=0. Proceeding from the regime of predominantly c-electrons to that of predominantly LPs T_c first sharply increases with decreasing Δ_0, going through a maximum inside the mixed regime, to decrease then and being suppressed when the LP level reaches the bottom of the c-band, where the system enters the LP regime.

4.7
Summary of the Model of Coexisting Local Pairs and c-Electrons

Superconductivity as result of the coexistence of local pairs and itinerant electrons has been studied, where the coupling between the two components is due to a charge exchange mechanism. The cases of 2D, quasi 2D and 3D lattices were considered. In the analysis MFA-BCS and linear response theory were applied. In addition, the KT scenario has been used for the study of phase fluctuation effects on the superconducting transition temperature in 2D and the self-consistent T-matrix approach for pairing fluctuations in 3D. The superconducting characteristics of the system have been found to be strongly dependent on the relative position of the local pair level with respect to the bottom of the c-electron band and the total number of carriers n. As a consequence the model exhibits not only the limiting cases of weak coupling and pure LP superconductivity, but also the interesting, intermediate regime where the properties are mixed. Typically and independently of the pairing symmetry, it is observed that T_c^{KT} is substantially smaller than T_c^{MFA} in the mixed and LP regime. Similarly, T_c in 3D is strongly reduced as compared to T_c^{MFA} due to pairing fluctuations.

The main results can be summarized as follows:

1. In the mixed regime the mechanism of induced superconductivity (at constant Δ_0) is not very sensitive to the pairing symmetry; n_c is nearly constant and n_b increases with n. The chemical potential in the superconducting phase remains almost pinned around Δ_0.
2. Well defined Bogoliubov quasiparticles can exist in the superconducting ground state. However, above T_c (in the mixed regime) local pairs coexist with itinerant fermions, and the normal state properties deviate from Fermi liquid behavior [137].
3. The T_cs as calculated beyond BCS-MFA within the T-matrix approach in 3D and in the KT scenario for 2D show crucial effects of pair fluctuations (and phase fluctuations) in the mixed and LP regimes.
4. In the mixed regime, for temperatures between T_c^{MFA} and T_c^{KT}, the system exhibits a pseudogap in the c-electron spectrum, which develops into a real gap when moving to the LP regime. For $\Delta_0<0$, the LPs coexist with preformed c-electron pairs which have a binding energy $E_b/2 \propto T_c^{\mathrm{MFA}}$, and the system will show nodeless behavior even for $d_{x^2-y^2}$-wave pairing symmetry.
5. As long as only nearest neighbor hopping in the c-electron band is considered, d-wave pairing and also on-site s-wave pairing are favorable as compared to extended s-wave pairing at high concentrations of c-electrons, while in the small concentration regime extended s-wave can be realized. Inclusion of second nearest neighbor hopping terms t_2 (with reversed sign as compared to t) can enhance T_c, and, moreover, it supports d-wave symmetry for smaller values of n_c.
6. The existence of nodal quasiparticles for d-wave pairing (beyond the LP regime) gives rise to a linear in T relationship in the superfluid density which is absent for the other here considered pairing symmetries. The normalized superfluid stiffness as a function of normalized temperature shows only a weak dependence on the total carrier concentration.
7. The gap to T_c ratios differ substantially from weak coupling BCS predictions and are especially enlarged over the BCS value when d-wave symmetry is realized.
8. The Uemura type plots, i.e., the T_c vs zero-temperature phase stiffness $\rho_s(0)$ are obtained for s, extended s- and d-wave symmetry within the KT scenario. The Uemura scaling $T_c \propto \rho_s(0)$ is a consequence of the separation of energy scales for pairing and phase coherence. Such a scaling is not realized within the BCS-MFA.

Relations to experimental results for high temperature superconducting copper oxides are especially interesting concerning ARPES experiments, from which a pseudogap has been suggested with features related to truncations of the Fermi surface around the corners caused by the formation of preformed pairs (bosons) with charge 2e. Along the diagonals these features are absent thus indicating the existence of unpaired "normal" electron states [145, 146]. In the two-component model such a situation is realized when LPs and c-electrons

coexist in the mixed regime. The linear in T dependence of the superfluid stiffness has been observed experimentally in cuprates and also in other superconductors (e.g., organic superconductors). This points to a d-wave order parameter symmetry and the existence of nodal quasiparticles. The Uemura plots and the scaling $T_c \propto \rho_s(0)$ reported for cuprates and organic superconductors can be reproduced within the present model for extended s and d-wave order parameters. In the model the gap ratios are not universal for all pairing symmetries and can deviate strongly from BCS predictions. This feature is also observed in several other exotic superconductors.

5 Conclusions

In this review a two-component model for superconductivity has been analyzed within different scenarios. Above, the two-band model is considered where pairing takes place in both bands simultaneously and interband interactions provide the possibility of a pairwise exchange between both bands. The model has been introduced as a generalization of the BCS model and distinctly different features as compared to the BCS theory have been obtained, concerning the gap to T_c ratio, the isotope effect, the critical fields, specific heat etc. The realization of a two band superconductor has long been searched for and been believed to be realized many times, however without a direct probe of the two gap features. Until now only two systems have been discovered, i.e., $SrTiO_3$ [14] and MgB_2 [15–21] where these gaps could be seen. In the cuprates there is some evidence for its realization, but hidden beyond a strong d-wave order parameter.

Extensions of the two-band model in its simplest form have been considered consecutively (see above) where specifically the idea of having a superconducting state in one band only whereas the second band exhibits induced superconductivity has been analyzed in detail. Including tunneling in this approach yields the possibility to open a second channel where electron pairs are scattered via interband effects into the nonsuperconducting component and tunnel back into the first channel. This model is thought to apply to layered structures where the interlayer distance triggers the tunneling process. It is, however, observed that the tunneling part does not yield a T_c enhancement effect but mostly counteracts superconductivity.

The other alternative scenario for the two-band model is based on the assumption that both components are not superconducting on their own but only via interband interactions. These interactions are crucial in enhancing T_c, and when taking into account that the pairing potentials of both bands might have different symmetries an additional support for superconductivity is obtained. Incorporating in such a model electron-lattice interaction effects in a polaronic manner leads to strong renormalizations of all energy scales and the opening of pseudo-gaps in both bands. While a level shift in the one-dimensional band occurs, an additional exponential narrowing effect sets in in the two-dimen-

sional band. These effects yield a reasonable explanation for unusual isotope effects, especially on the superfluid stiffness, whereas solutions obtained beyond a mean-field level provide an explanation for the isotope effect on the pseudo-gap opening temperature T^*.

Finally, the two component model consisting of itinerant electrons and local electron pairs (hard-core bosons) is discussed, where the coupling between both systems is due to charge exchange. Such a model provides a new scenario for both, the normal and the superconducting state properties. The normal state can exhibit non-Landau Fermi liquid properties and a new type of superconductivity can develop, which is neither BCS like not pure LP like but has a mixed character. In this case the LPs scatter into *c*-electrons and vice versa, thus providing a new pairing mechanism. As discussed above, depending on the location of the local pair level with respect to the wide band or the total carrier concentration, the model can exhibit several kinds of crossovers between the weak coupling, the mixed and the LP regimes. In the most interesting mixed regime a pseudo-gap is realized and dramatic deviations from both the BCS limit and the LP limit properties are obtained. A variety of experimental results can be related to this regime and applications to exotic superconductors are possible.

Acknowledgement It is a pleasure to acknowledge many useful discussions with A. R. Bishop, H. Büttner, O. Dolgov, V. Z. Kresin and the other authors of this book. We would like to express our thanks to A. Simon for a critical reading of the manuscript. R. M. acknowledges support from the Foundation for Polish Science. S. R. and R. M. also acknowledges partial support from the State Committee for Scientific Research (KBN Poland), Project No. 1 P03B 084 26.

References

1. Bardeen J, Cooper l, Schrieffer J (1957) Phys Rev 108:1175
2. Eliashberg GM (1960) Zh Eksperim i Teor Fiz 38:966; (1960) 39:1437 ([English translation: (1960) Soviet Phys-JETP 11:696; (1961) Soviet Phys-JETP 12:1000]
3. Allen P, Dynes R (1975) Phys Rev B 12:905
4. McMillan W (1968) Phys Rev 175:537
5. Scalapino D (1969) In: Parks R (ed) Superconductivity. Marcell Dekker, New York, p 449
6. Anderson PW (1959) J Phys Chem Solids 11:26
7. Suhl H, Matthias B, Walker L, (1959) Phys Rev Lett 3:552
8. Moskalenko V (1959) Fiz Metal Metallov 8:503
9. Kondo J (1963) Prog Theor Phys 29:1
10. Geilikman B, Zaitsev R, Kresin V (1967) Fiz Tverd Tela (Leningrad) 9:693 [(1966) Sov Phys Solid State 9:542]
11. Kresin V (1973) J Low Temp Phys 11:519
12. Geilikman B, Kresin V (1974) In: Kinetic and nonstationary phenomena in superconductors. Wiley, New York, pp 34, 80
13. Robaszkiewicz S, Micnas R, Ranninger J (1987) Phys Rev B 36:180; Chakraverty BK (1993) Phys Rev B 48:4047
14. Binning G, Baratoff A, Hoenig H, Bednorz G (1980) Phys Rev Lett 45:1352

15. Amy Y, Liu Y, Mazin II, Kortus J (2001) Phys Rev Lett 87:087005
16. Szabo P, Samuely P, Kazmarzik J, Klein T, Marcus J, Fruchart D, Miraglia S, Marcenat C, Jansen AGM (2001) Phys Rev Lett 87:137005
17. Giubileo F, Roditchev D, Dacks W, Lamy R, Thanh DX, Klein J, Miraglia S, Fruchart D, Marcus J, Monod P (2001) Phys Rev Lett 87:177008
18. Pavarini E, Dasgupta I, Jepsen O, Andersen OK (2001) Phys Rev Lett 87:047003
19. Bouquet R, Fisher RA, Phillips NE, Hinks DG, Jorgensen JD (2001) Phys Rev Lett 87: 047002
20. Uchiyama H, Shen KM, Lee S, Damascelli A, Lu DH, Feng DL, Shen Z-X, Tajima S (2002) Phys Rev Lett 88:157002
21. Souma S, Machida Y, Sato T, Takahashi T, Matsui H, Wang S-C, Ding H, Kaminski A, Campuzzano JC, Sasaki S, Kadowaki K (2003) Nature (London) 423:65
22. Bogoliubov NN (1958) Zh Eksp Teor Fiz 34:58; Bogoliubov NN, Tolmachev VV, Shirkov DV (1958) In: A new method in the theory of superconductivity. Izv Akad Nauk SSSR, Moscow
23. Bloch C, Dominisis C (1958) Nucl Phys 7:459
24. Kresin V, Wolf S (1990) Physica C 169:476
25. Kresin V, Wolf S, Deutscher G (1992) J Phys C 191:9
26. Kresin V, Wolf S (1990) Phys Rev B 41:4278
27. Kresin V (1987) Sol St Comm 63:725; Kresin V, Wolf S (1987) Sol St Comm 63:1141
28. Kresin V, Wolf S (eds) (1987) Novel superconductivity. Plenum, New York
29. Kresin V, Wolf S (1992) Phys Rev B 46:6458
30. Adrian SD, Wolf SA, Dolgov O, Shulga S, Kresin VZ (1997) Phys Rev B 56:7878
31. Cohen MH, Falicov L, Phillips J (1962) Phys Rev Lett 8:316
32. Bednorz JG, Müller KA (1986) Z Phys B 64:189
33. Franck JP (1994) In: Ginsberg DM (ed) Physical properties of high temperature superconductors IV. World Scientific, Singapore, pp 189–293
34. Zech D, Conder K, Keller H, Kaldis E, Müller KA (1995) In: Ruani G (ed) Anharmonic properties of high-T_c superconductors. World Scientific, Singapore, p 18
35. Zech D, Conder K, Keller H, Kaldis E, Müller KA (1996) Physica B 219/220:136
36. Dagotto E, Riera J, Chen YC, Moreo A, Nazarenko A, Alcaraz F, Ortolani F (1994) Phys Rev B 49:3548; Dagotto E (1994) Rev Mod Phys 250:763
37. Scalapino DJ (1995) Phys Rep 250:329
38. Schrieffer JR, Wenig XG, Zhang SC (1989) Phys Rev B 39:11663
39. Schmitt-Rink S, Varma CM, Ruckenstein AE (1988) Phys Rev Lett 60:2793; Trugman SA (1988) Phys Rev B 37:1597
40. Anderson PW (1987) Science 235:1196
41. Kivelson SA, Rokhsar DS, Sethna JP (1987) Phys Rev B 35:8865
42. Micnas R, Robaszkiewicz S (1997) In: Kaldis E, Liarokapis E, Müller KA (eds) High temperature superconductivity: 10 years after the discovery. NATO ASI series E, vol 343, (1997) Kluwer Academic, p 31 and references therein
43. Bussmann-Holder A, Bishop AR (1991) Phys Rev B 44:2473
44. Bussmann-Holder A, Simon A, Büttner H (1989) Phys Rev B 39:12340
45. Bussmann-Holder A, Bishop AR, Batistic I (1991) Phys Rev B 43:13728
46. Lang IG, Firsov YA (1963) Sov Phys JETP 16:1301
47. Bussmann-Holder A, Micnas R, Bishop AR (2004) Eur Phys J B 37:345
48. Bussmann-Holder A, Müller KA, Micnas R, Büttner H, Simon A, Bishop AR, Egami T (2001) J Phys Cond Mat 13:L169
49. Bussmann-Holder A, Bishop AR, Büttner H, Egami T, Micnas R, Müller KA (2001) J Phys Cond Mat 13:L545

50. Zaanen J, Gunnarson O (1989) Phys Rev B 40:7391; Zaanen J (1998) J Phys Chem Sol 59:1769; Tranquada JM, Sternlieb BJ, Axe JD, Nakamura Y, Uchida S (1995) Nature (London) 375:561
51. Lanzara A, Zhao G, Saini NL, Bianconi A, Conder K, Keller H, Müller KA (1999) J Phys Cond Mat 11:L545
52. RubioTemprano D, Mesot J, Janssen S, Conder K, Furrer A, Sokolov A, Trounov V, Kazakov SM, Karpinski J, Müller KA (2001) Eur Phys J B 19:R5
53. RubioTemprano D, Mesot J, Janssen S, Conder K, Furrer A, Mutka H, Müller KA (2000) Phys Rev Lett 84:1999
54. Bianconi A, Saini NL, Rossetti T, Lanzara A, Perali A, Missori M, Oyanagi H, Yamaguchi Y, Nishihara Y, Ha DH (1996) Phys Rev B 54:12018
55. McQueeney RJ, Petrov Y, Egami T, Yethiraj Y, Shirane G, Endoh Y (1999) Phys Rev Lett 82:628
56. Chung JH, Egami T, McQueeney RJ, Yethiraj Y, Arai M, Yokoo T, Petrov Y, Mook H, Endoh Y, Tajima S, Frost C, Dogan F (2003) Phys Rev B 67:014517
57. Alloul H, Ohno T, Mendels P (1989) Phys Rev Lett 63:1700
58. Shengelaya A, Keller H, Müller KA, Kochelaev BI, Conder K (2001) Phys Rev B 63:144513
59. Markiewicz RS, Kusko C, Kidami V (1999) Phys Rev B 60:627 and references therein; Zhang SC (1997) Science 275:1089
60. See, e.g., [53] and Nazarenko A, Moreo A, Dagotto E, Riera J (1996) Phys Rev B 54:R768
61. Deutscher G, Dagan Y (2000) J Supercond 13:699
62. Kugler M, Fischer Ø, Renner C, Ono S, Ando Y (2001) Phys Rev Lett 86:4911–4914; Renner CH, Fischer O (1995) Phys Rev B 51:9208
63. Perali A, Castellani C, DiCastro C, Grilli M (1996) Phys Rev B 54:16216; Millis AJ, Sachdev S, Varma CM (1988) Phys Rev B 37:4975; Micnas R, Robaszkiewicz S (1992) Phys Rev B 45:9900; Micnas R, Robaszkiewicz S, Kostyrko T (1995) Phys Rev B 52:6863
64. Schneider T (1997) Acta Phys Polon A91:203; Schneider T, Singer JM (2001) J Supercond 13:789
65. Bussmann-Holder A, Bishop AR (1997) Phil Mag B 76:887
66. Bussmann A, Bilz H, Roenspiess R, Schwarz KH (1980) Ferroelectrics 25:343
67. Zhang FC, Rice TM (1988) Phys Rev B 37:3759
68. Müller KA (1999) J Supercond 99:1
69. Ishihara S, Egami T, Tachiki M (1997) Phys Rev B 55:3163; Petrov Y, Egami T (1998) Phys Rev B 58:9485
70. Lanzara A, Bogdanov PV, Zhou XJ, Kellar SA, Feng DL, Lu ED, Yoshida T, Eisaki H, Fujimori A, Kishio K, Shimoyama J-I, Noda T, Uchida S, Hussain Z, Shen Z-X (2001) Nature (London) 412:510
71. Chmaissen O, Jorgensen JD, Short S, Knizhnik A, Eckstein Y, Shaked H (1999) Nature (London) 397:45
72. Tranquada JM, Axe JD, Ichikawa M, Moodenbaugh AR, Nakamura Y, Uchida S (1997) Phys Rev Lett 78:338
73. Perali A, Bianconi A, Lanzara A, Saini NL (1996) Sol St Comm 100:181
74. Bianconi A (1994) Sol St Comm 89:933
75. Ohta Y, Tohyama T, Maekawa S (1991) Phys Rev B 43:2968
76. Gor'kov LP, Sokol AV (1987) JETP Lett 46:420; Little WA, Holcomb MJ (2000) J Supercond 13:695
77. Robaszkiewicz S, Micnas R, Ranninger J (1987) Phys Rev B 36:180
78. Mihailovic D, Müller KA (1997) In: Kaldis E, Liarokapis E, Müller KA (eds) High temperature superconductivity: 10 years after the discovery. NATO ASI series E, vol. 343. Dordrecht: Kluwer Academic, p 243; Müller KA, Keller H (1997) In Proc. NATO ASI.

Material aspects of High-T_c superconductivity: 10 years after the discovery. Kluwer; Müller KA (2002) Phil Mag B 82:279
79. Perali A, Castellani C, DiCastro C, Grilli M, Piegari E, Varlamov AA (2000) Phys Rev B 62:R9295
80. Mihailovic D, Mertelj T, Müller KA (1998) Phys Rev B 57:6116; Stevens CJ, Smith D, Chen C, Ryan RF, Podobnik D, Mihailovic D, Wagner GA, Evetts JE (1997) Phys Rev Lett 78:2212
81. Richardson CF, Ashcroft NW (1997) Phys Rev B 55:15130
82. Andersen OK, Liechenstein AI, Rodriguez O, Mazin II, Jepsen O, Antropov VP, Gunnarson O, Gopalan S (1991) Physica C 185/189:147
83. Bussmann-Holder A (2000) J Supercond 13:773
84. Bussmann-Holder A, Bishop AR (1997) Phys Rev B 56:5297
85. Bussmann-Holder A, Büttner H, Simon A, Bishop AR (2000) Phil Mag B 80:1955
86. von Szczepanski KJ, Becker KW (1992) Z Phys B 89:327
87. Rice MJ, Strässler S, (1977) Sol St Comm 13:125
88. Chan S-K, Heine V (1973) J Phys F Met Phys 3:795
89. Sharma RP, Ogale SB, Zhang ZH, Liu RJ, Chu WK, Boyed Veal, Zheng H, Vekatesan T (2000) Nature (London) 404:736
90. Mihailovic D, McCarty KF, Ginley DS (1993) Phys Rev B 47:8910
91. Crawford MK, Farneth WE, Harlow RL, McCarron EM, Miao R, Chou H, Huang Q (1992) In: Bar-Yam Y, Egami T, Mustre-de-Leon J, Bishop AR (eds) Lattice effects in high-T_c superconductors. World Scientific, Singapore New Jersey London Hong Kong, p 531
92. Franck JP, Jung J, Mohamed M-AK, Gygax S, Sproule GI (1992) Physica B 169:697; (1991) Phys Rev B 44:5318
93. Franck JP, Hnatiw A, Yu MK, Gygax S, Soerensen G, Altendorf E, Irwin JC (1992) In: Bar-Yam Y, Egami T, Mustre-de-Leon J, Bishop AR (eds) Lattice effects in high-T_c superconductors. World Scientific, Singapore New Jersey London Hong Kong, p 148
94. Franck JP (1994) In: Ginsberg S (ed) Physical properties of high T_c superconductors IV. World Scientific, Singapore New Jersey London Hong Kong, p 189
95. Zech D, Keller H, Conder K, Kaldis E, Liarokapis E, Poulakis N, Müller KA (1994) Nature (London) 371:681
96. Zech D, Conder K, Keller H, Kaldis E, Müller KA (1996) Physica B 219/220:136
97. Crespi VH, Cohen ML, Penn DR (1991) Phys Rev B 43:12921; Crespi VH, Cohen ML (1991) Phys Rev B 44:4712; (1993) Phys Rev B 48:398
98. Mali M, Roos J, Keller H, Karpinski J, Conder K (2002) Phys Rev B 65:184518
99. Zhao G-M, Hunt MB, Keller H, Müller KA (1997) Nature (London) 385:236
100. Hofer J, Conder K, Sasagawa T, Zhao G, Willemin M, Keller H, Kishio K (2000) Phys Rev Lett 84:4192
101. Khasanov R, Shengelaya A, Conder K, Morenzoni E, Savic IM, Keller H (2003) J Phys Cond Mat 15:L17
102. Khasanov R, Eshchenko DG, Luetkens H, Morenzoni E, Prokscha T, Suter A, Garigianov N, Mali M, Roos J, Conder K, Keller H: cond-mat/0305477; (2004) Phys Rev Lett 92:057602
103. Khasanov R, Shengelaya A, Morenzoni E, Angst M, Conder K, Savic IM, Lampakis D, Liarokapis E, Tatsi A, Keller H (2003) Phys Rev B 68:220506
104. Bussmann-Holder A, Simon A, Büttner H, Bishop AR (2000) Phil Mag B 80:1955; Bussmann-Holder A, Bishop AR (1991) Phys Rev B 44:2853; (1997) Phys Rev B 56:5279
105. Saini NL, Oyanagi H, Lanzara A, Di Castro D, Agrestini S, Bianconi A, Nakamura F, Fujita T (2001) Phys Rev B 64:132510

106. Lanzara A, Saini NL, Bianconi A, Duc F, Bordet P (1999) Phys Rev B 59:3851
107. Saini NL, Lanzara A, Bianconi A, Oyanagi H (1998) Phys Rev B 58:11768
108. Kivelson S (1983) Phys Rev B 28:2653
109. Lepine Y (1983) Phys Rev B 28:2659
110. Bussmann-Holder A, Bishop AR, Genzel L, Simon A (1997) Phys Rev B 55:11751
111. Schneider T, Keller H (1992) Phys Rev Lett 69:3374
112. Alexandrov AF, Mott NF (1994) Int J Mod Phys 8:2075
113. Grimaldi C, Capelluti E, Pietronero L (1998) Europhys Lett 42:667
114. Schneider T (2003) Phys Rev B 67:134514
115. Bussmann-Holder A, Micnas R, Bishop AR (2004) Phil Mag 24:1257
116. Micnas R, Tobijaszewska B (2002) J Phys Cond Mat 14:9631
117. Robaszkiewicz S, Micnas R, Ranninger J (1987) Phys Rev B 36:180
118. Lakkis S, Schlenker C, Chakravarty BK, Buder R, Marezio M (1976) Phys Rev B 14:1429; Chakravarty BK, Sienko MT, Bonnerot J (1978) Phys Rev B 17:3781; Onoda M, Takahashi T, Nagasawa H (1982) J Phys Soc Jpn 51:3868; Onoda M, Nagasawa H (1983) J Phys Soc Jpn 52:2231
119. Micnas R, Ranninger J, Robaszkiewicz S (1990) Rev Mod Phys 62:113
120. Alexandrov AS, Ranninger J (1981) Phys Rev B 23:1796; (1981) Phys Rev B 24:1164
121. Robaszkiewicz S, Micnas R, Chao KA (1981) Phys Rev B 23:1447; (1981) Phys Rev B 24:1579, 4018; Micnas R, Robaszkiewicz S (1992) Phys Rev B 45:9900; Micnas R, Robaszkiewicz S, Kostyrko T (1995) Phys Rev B 52:6863
122. Anderson PW, Yu CC (1985) In: Bassini F, Tosi MP (eds) Proceedings of the international school of physics "Enrico Fermi", course no. LXXXIX. North Holland, Amsterdam, p 767
123. Moizhes BY, Drabkin IA (1983) Fiz Tverd Tela (Leningrad) 25:1974 [(1983) Sov Phys Solid State 25:1139
124. Alexandrov AS, Ranninger J, Robaszkiewicz S (1986) Phys Rev B 33:4526
125. Alexandrov AS (1983) Zh Fiz Khim 57:273 [(1985) Russ J Phys Chem 57:167]; Alexandrov AS, Elesin VF (1985) Izv Akad Nauk SSSR 49:326; Alexandrov AS, Elesin VF, Kabanov VV (1984) Zh Eksp Teor Fiz 86:1973 [(1984) Sov Phys JETP 59:1125]
126. [123] and references therein; Kulik IO (1984) Physica 126B:280
127. Ranninger J, Robaszkiewicz S (1985) Physica 135B:468
128. Friedberg R, Lee TD (1989) Phys Rev B 40:6745; Friedberg R, Lee TD, Ren HC (1990) Phys Rev B 42:4122; (1992) Phys Rev B 45:10732; Bar-Yam Y (1991) Phys Rev B 43:359; (1991) Phys Rev B 43:2601
129. Wilson JA, Zahir A (1997) Rep Prog Phys 60:941; Domanski T, Ranninger J (2001) Phys Rev B 63:134505
130. Chiofalo ML, Kokkelmans SJJMF, Milstein JN, Holland MJ (2002) Phys Rev Lett 88: 090402
131. Ohashi Y, Griffin A (2002) Phys Rev Lett 89:130402
132. Milstein JN, Kokkelmans SJJMF, Holland MJ (2002) Phys Rev A 66:0436004
133. Micnas R, Robaszkiewicz S, Bussmann-Holder A (2002) Phys Rev B 66:104516 and references therein
134. Micnas R, Robaszkiewicz S, Bussmann-Holder A (2003) Physica C 387:58; Micnas R, Robaszkiewicz S, Bussmann-Holder A (2004) J Supercond 17:27
135. Kosterlitz JM, Thouless DJ (1973) J Phys C 6:1181; Kosterlitz JM (1974) J Phys C 7:1046; Nelson DR, Kosterlitz JM (1977) Phys Rev Lett 39:1207
136. Denteneer PJH, Guozhong A, Van Leeuwen JMJ (1993) Phys Rev B 47:6256
137. Ranninger J, Robin JM, Eschrig M (1995) Phys Rev Lett 74:4027; Ranninger J, Robin JM (1996) Sol St Comm 98:559; (1996) Phys Rev B 53: R11961; Devillard P, Ranninger J (2000) Phys Rev Lett 84:5200

138. In [131] the formation of two-body bound states for continuum fermions is discussed in detail using the *T*-matrix formalism and s-wave pairing
139. Uemura YJ, Le LP, Luke GM, Sternlieb BJ, Wu WD, Brewer JH, Riseman TM, Seaman CL, Maple MB, Ishikawa M, Hinks DG, Jorgensen JD, Saito G, Yamochi H (1991) Phys Rev Lett 66:2665; Uemura YJ, Le LP, Luke GM, Sternlieb BJ, Brewer JH, Carolan JF, Hardy WN, Kallono R, Kempton JR, Kiell RF, Kreitzman SR, Mulhern P, Riseman TM, Williams DLl, Yang BX, Uchida S, Takaki H, Gopalakrishnan J, Sleight AW, Subramanian MA, Chien CL, Cieplak MZ, Xiao Gang, Lee VY, Statt BW, Stronach CE, Kossler WJ, Yu XH (1989) Phys Rev Lett 62:2317; Uemura YJ, Keren A, Le LP, Luke GM, Wu WD, Kubo Y, Manako T, Shimakawa Y, Subramanian M, Gobb Jl, Markert JT, (1991) Nature (London) 352:605; Uemura YJ (1997) Physica C 282/287:194; Larkin MI, Kinkhabwala A, Uemura YJ, Sushko Y, Saito G (2001) Phys Rev B 64:144514
140. Castro Neto AH (2000) Phys Rev B 64:104509
141. Hikami S, Tsuneto T (1980) Prog Theor Phys 63:387; Loktev VM, Turkovskii V (2003) Phys Rev B 67:214510
142. Micnas R (2003) unpublished
143. Micnas R et al. (1995) Phys Rev B 52:16223
144. Chen Q, Kosztin I, Janko B, Levin K (1999) Phys Rev B 59:7083; Kosztin I, Chen Y, Kao Y-J, Levin K (2002) Phys Rev B 61:11662
145. Geshkenbein VB, Ioffe LB, Larkin AI (1997) Phys Rev B 55:3173
146. Perali A, Castellani C, Di Castro C, Grilli M, Piegari E, Varlamov AA (2000) Phys Rev B 62:R9295

Struct Bond (2005) 114:71–101
DOI 10.1007/b101017

Superconductivity in Alkali-Doped Fullerides

O. Gunnarsson[1] (✉) · J.E. Han[2] · E. Koch[1] V.H. Crespi[3]

[1] Max-Planck-Institut für Festkörperforschung, 70506 Stuttgart, Germany
O.Gunnarsson@fkf.mpg.de, *E.Koch@fkf.mpg.de*
[2] Department of Physics, The Pennsylvania State University, University Park, PA 16802-6300, USA and Department of Physics, The State University of New York at Buffalo, Buffalo, NY 14260, USA
jonghan@buffalo.edu
[3] Department of Physics, The Pennsylvania State University, University Park, PA 16802-6300, USA
crespi@phys.psu.edu

Abstract Alkali-doped fullerides differ in important respects from conventional superconductors. In the latter $\omega_{ph} \ll W$, where ω_{ph} and W are the phononic and electronic energy scales, respectively . Retardation effects are therefore believed to reduce drastically the effects of the Coulomb repulsion, allowing the phonon induced attraction to drive superconductivity. For the alkali-doped fullerides, on the other hand, $\omega_{ph} \sim W$. We discuss retardation effects extensively, and argue that these effects should not drastically reduce the Coulomb repulsion, raising questions about how superconductivity is possible. It is then important to treat the Coulomb repulsion and the electron-phonon interaction on an equal footing, rather than treating the Coulomb repulsion as a small empirical parameter μ^*, as is done for conventional superconductors. For this reason we use the dynamical

mean-field theory. We find that the interplay between the electron-electron and electron-phonon interactions is crucial, leading to a so-called local pairing, where the electrons tend to pair on the molecules. This results from the important phonons being intramolecular Jahn-Teller phonons. This local pairing helps forming a coherent superconducting state and it makes the superconductivity quite resistant to the Coulomb repulsion. It also explains the strong doping dependence in these systems.

Keywords Alkali-doped fullerides · Retardation effects · Local pairing

List of Abbreviations and Symbols

$A(\omega)$	Electron spectral function
a	Lattice parameter
$N(0)$	Density of states per spin at the Fermi energy
t	Hopping integral
T	Temperature
T_c	Superconductivity transition temperature
U	Coulomb repulsion between two electrons on the same molecule in a solid
U_0	Coulomb repulsion between two electrons on a free molecule
W	Band width
α	Isotope effect
$\beta \equiv 1/T$	Inverse temperature
Γ	Effective electron-electron interaction
Δ	Superconductivity gap
λ	Dimensionless electron-phonon coupling
$\lambda(0)$	Penetration depth
μ^*	Coulomb pseudopotential
ξ_{GL}	Ginzburg-Landau coherence length
$\rho^{\rm loc}$	Spectral function of $\chi^{\rm loc}$
$\rho_0^{\rm loc}$	Spectral function of $\chi_0^{\rm loc}$
τ	Imaginary time
χ	Pairing susceptibility
$\chi^{\rm loc}$	Local pairing susceptibility
$\chi_0^{\rm loc}$	Local pairing susceptibility for independently propagating electrons (holes)
ω_{ph}	Phonon frequency

1 Introduction

The fullerenes, e.g., C_{60}, were discovered in 1985 by Kroto et al. [1]. The C_{60} molecule immediately attracted a lot of interest because of its appealing symmetric form. Due to the extremely small amounts of fullerenes available, however, little progress could be made. This changed completely when Krätschmer et al. [2] in 1990 discovered how to produce C_{60} in large quantities. Very soon Haddon et al. [3] found that intercalation of alkali metal atoms into solid C_{60} leads to a metallic behavior. Soon afterwards it was discovered by Hebard et al. [4]

and several other groups [5–8] that some of these alkali-doped C_{60} compounds are superconducting with a transition temperature T_c which at that time was only surpassed by the cuprates. Thus T_c is 33 K for $RbCs_2C_{60}$ [7] and for Cs_3C_{60} under pressure $T_c = 40$ K has been reported [9].

Solid C_{60} is a molecular solid, with a rather weak interaction between the molecules. The molecular levels therefore form narrow, essentially nonoverlapping bands in the solid. In alkali-doped C_{60} compounds a threefold degenerate t_{1u} band is partly occupied. Superconductivity is usually, but not always [10–12], assumed to be due to the electron-phonon interaction [13–15]. The main contribution to the electron-phonon interaction comes from intramolecular phonons, in particular, eight fivefold degenerate H_g modes, which are Jahn-Teller phonons. Essential aspects of the C_{60} superconductors are therefore that they are molecular solids with Jahn-Teller phonons.

The interest in the the fullerides is partly based on their unusual parameter range, which has forced the community to address interesting issues which had earlier been largely ignored. In particular, the ratio between the energy scales for the electronic and nuclear motion is very unusual. For typical metals, the energy scale for the phonons is on the order of $\omega_{ph} \sim 0.01 - 0.1$ eV while the energy scale for the electrons is on the order of $W \sim 10$ eV, i.e., $\omega_{ph}/W \sim 0.001 - 0.01$. The ratio is very small due to the small ratio of the electronic and the nuclear masses. The smallness of this ratio plays a crucial role in many contexts, in particular in the theory of superconductivity.

For fullerides, the phonon energies are very large, extending up to about 0.2 eV. The reason is that the carbon nuclei are light and the C_{60} molecule is stiff. At the same time the conduction electron energy scale of the alkali-doped fullerides is very small, on the order of 1/2 eV. This is due both to the small carrier density and to the molecular solid character of C_{60} which makes hopping between the molecules difficult. Thus we are confronted with the extraordinary situation that the energy scales for the electronic and nuclear motion are comparable, in spite of the small mass ratio between the electrons and the nuclei.

Superconductivity in conventional superconductors is driven by a weak attractive interaction induced by the electron-phonon coupling. The fact that $\omega_{ph}/W \ll 1$ enters crucially in the theory in two ways:

1. These superconductors are normally described in Eliashberg theory, which is based on Migdal's theorem. This theorem states that in a diagrammatic expansion of the electron-phonon interaction, only the lowest order diagram is needed if $\omega_{ph}/W \ll 1$. This provides a tremendous simplification of the theory. Such a simplification, however, is very questionable for the C_{60} compounds [16], since $\omega_{ph}/W \sim 1$.
2. $\omega_{ph}/W \ll 1$ is crucial for the understanding of how the weak phonon induced attraction can lead to superconductivity in spite of the much stronger Coulomb repulsion [17]. This is sometimes explained in a pictorial way as indicated in Fig. 1. As an electron moves through the solid, it attracts the positive nuclei. A second electron moving along the same path feels the

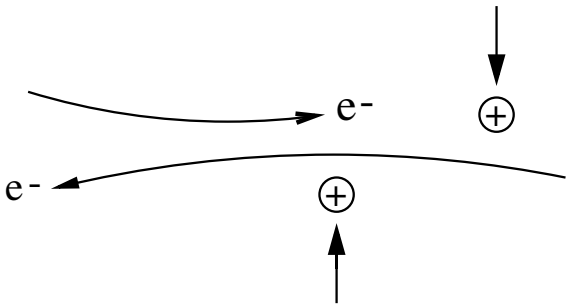

Fig. 1 Schematic picture of the retardation effects

attraction from these nuclei, which leads to an induced weak attractive component of the electron-electron interaction. Simultaneously, the electrons strongly reduce their Coulomb repulsion by staying at a large distance from each other most of the time. For instance, one electron typically arrives at an atom well after the other electron has left, but not so much later that the surrounding nuclei have had time to return to their equilibrium positions. This is possible for a conventional superconductor, because the energy scale is so much smaller for the nuclear motion than for the electronic motion. This leads to a strong reduction of the effective Coulomb repulsion, which is described by the dimensionless Coulomb pseudopotential μ^*. The value of μ^* has usually been treated as a small empirical parameter, and the interest has focused on the electron-phonon interaction.

Since $\omega_{ph}/W \sim 1$ for C_{60}, we expect the retardation effects to be rather small. The Coulomb repulsion between two electrons on the same molecule, $U \sim 1.0 - 1.5\,\text{eV}$ [18], however, is much larger than the phonon induced attraction, on the order of 0.1 eV. The main problem in explaining superconductivity for these systems is therefore to explain why pairing is nevertheless possible. This major complication was not addressed in the early work on superconductivity in alkali-doped C_{60}.

The separation of the electron-electron interaction in an empirical repulsive Coulomb part and an attractive phonon part is somewhat artificial. Below we show that it is important for the understanding of superconductivity in C_{60} compounds to treat the electron-electron and electron-phonon interactions on an equal footing. This has been done by Capone et al. [19] and by Han et al. [20] This leads to a so-called local pairing, where the electrons tend to pair on a molecule, due to the interplay between the Coulomb interaction and the Jahn-Teller effect. This local pairing is helpful in establishing a coherent superconducting state through the solid. We furthermore show that Jahn-Teller phonon and non-Jahn-Teller phonons act in quite different ways. Superconductivity in these systems therefore differs in important ways from conventional superconductors.

There have been several reviews of superconductivity in alkali-doped fullerides. The experimental aspects were emphasized by Ramirez [21] and the theoretical aspects by Gelfand [22] and Gunnarsson [23].

In the next Section we review some of the experimental results. Following that, we describe models we use for studying C_{60} compounds. The retardation effects are then discussed, and it is shown that they are rather small. It is argued that screening effects play a substantial role in reducing the Coulomb pseudopotential. Finally, we avoid the somewhat artificial separation of a Coulomb pseudopotential and treat the electron-electron and electron-phonon interaction on an equal footing by applying the dynamical mean-field theory. This treatment also makes it possible to avoid the assumptions of Migdal's theorem.

2 Experimental Results

There are several classes of C_{60}-based superconductors. Much of the interest has focused on the A_3C_{60} (A = K, Rb, Cs or some combination of these elements). T_c as a function of the lattice parameter a has been determined by a large number of groups [7,8,24–26], and results are shown in Fig. 2. The figure illustrates that T_c varies smoothly with a, with a moderate dependence on the alkali atoms in the compound. The lattice parameter dependence is well understood [7, 8, 27]. The electron-phonon coupling λ depends on intramolecular coupling constants, which are essentially independent of a and on the density of state $N(0)$. As a is increased, the bandwidth is reduced and $N(0)$ is increased. The result is an increase in λ and T_c.

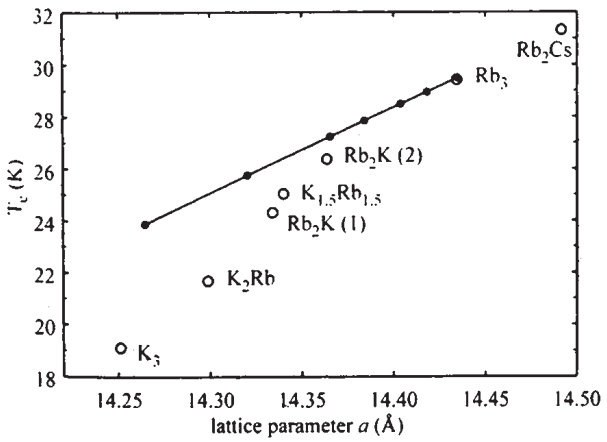

Fig. 2 T_c as a function of the lattice parameter a for the A_3C_{60} superconductors. For Rb_3C_{60} the lattice parameter was varied by changing the pressure, while for $M_xM'_{3-x}C_{60}$ (with M, M′=K, Rb, Cs) the lattice parameter was varied by changing the composition. (after Diederich et al. [26])

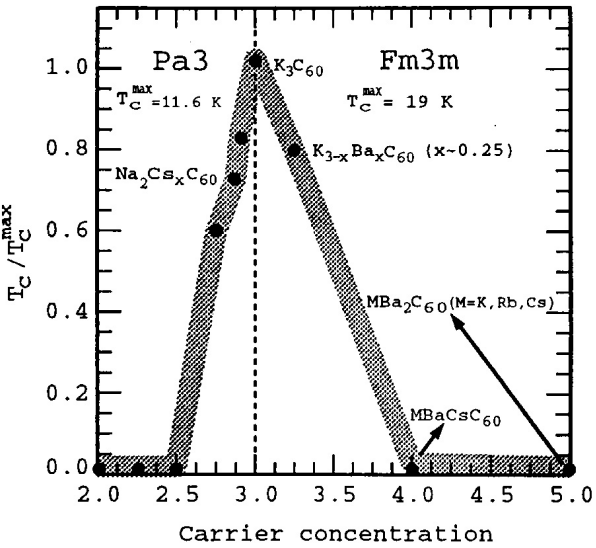

Fig. 3 T_c as a function of C_{60} valence n for the $Na_2Cs_xC_{60}$ ($x \leq 1$, valence ≤ 3) and $K_{3-x}Ba_xC_{60}$ (valence ≥ 3) compounds. T_c is scaled by the T_c (T_c^{max}) of the end members Na_2CsC_{60} and K_3C_{60}. The heavy line is a guide for the eye. Observe the different lattice structures (Pa3 and Fm3m)(after Yildirim et al. [30])

A second class, Na_2AC_{60} (A = K, Rb, Cs or a combination of these), has also attracted much interest due to T_c having an extremely strong dependence on a [28,29]. This strong dependence appears not to be well understood.

The doping dependence of T_c has been studied for the compounds $Na_2Cs_xC_{60}$ ($x = 0.25$, 0.50 and 0.75) [30] and $Rb_{3-x}Ba_xC_{60}$ (x=0.25, 1 and 2) [30–32]. The values of T_c found for these compounds are shown in Fig. 3 as a function of the expected valence $n = 2 + x$ for $Na_2Cs_xC_{60}$ and $n = 3 + x$ for $Rb_{3-x}Ba_xC_{60}$. The figure suggests a rapid drop of T_c when the C_{60} valence deviates from 3, and no superconductivity was observed for valence 2.5 or 4. Similar results have been obtained for Li_xCsC_{60} [33]. Rb_4C_{60} becomes a metal under pressure but no superconductivity has been observed [34].

There has also been a substantial interest in $(NH_3)_4Na_2CsC_{60}$ [35] and $NH_3K_3C_{60}$ [36,37]. In the systems above, the t_{1u} orbital is partly occupied. Superconductivity has furthermore been observed in fullerides where the t_{1g} orbital is starting to be filled, e.g., Ca_xC_{60} ($x \sim 5$) [38], Ba_4C_{60} [39] and Sr_4C_{60} [40]. These systems have been review by Iwasa and Takenobu [41]. Superconductivity has also been found in $Yb_{2.75}C_{60}$ [42], i.e., a rare-earth-doped fulleride.

The superconductivity energy gap Δ is of great interest, since a value of $2\Delta/T_c$ is substantially larger than the BCS value (3.53) indicates that strong-coupling effects are important. For intermediate coupling, it is found that [43] (see also the review of Carbotte [44] for a discussion)

$$\frac{2\Delta}{T_c} = 3.53[1 + 12.5(\frac{T_c}{\omega_{ln}})^2 \ln(\frac{\omega_{ln}}{2T_c})], \tag{1}$$

where ω_{ln} is the logarithmic average phonon frequency. This formula says that the deviation from the BCS result is small if $T_c/\omega_{ln} \ll 1$. The gap has been measured using many different techniques, e.g., point contact [45,46] and break junction [47] tunneling, NMR [48–51], muon spin relaxation [52], optical measurements [47, 53] and photoemission measurements [54, 55]. The data for the ratio $2\Delta/T_c$ obtained from different experiments show a large variation, with many experiments giving results close to the BCS value 3.53 but others giving rather large values on the order of 4.0-4.2. No consensus seems to have been reached.

The isotope effect may provide interesting information about the mechanism for superconductivity. We define the isotope effect as

$$\alpha = -\frac{d\ln T_c}{d\ln M}, \tag{2}$$

where M is the carbon mass. For complete (99%) substitution of ^{12}C by ^{13}C it was found that $\alpha = 0.30 \pm 0.06$ [56] for $K_3C_{60}$and $\alpha = 0.30 \pm 0.05$ [57] or $\alpha = 0.21$ for Rb_3C_{60} [58]. For the alkali phonons no isotope effect was observed with in the experimental accuracy [59,60].

The upper critical field $H_{c2}(0)$ is of interest, since it allows an estimate of the Ginzburg-Landau coherence length ξ_{GL} via [61]

$$H_{c2}(0) = \frac{\phi_0}{2\pi\xi_{GL}^2}, \tag{3}$$

where $\phi_0 = hc/(2e)$. From measurements of dH_{c2}/dT, $H_{c2}(0)$ was deduced using the Werthamer-Helfand-Hohenberg theory, and $\xi_{GL} = 26$ Å was obtained for K_3C_{60} [62]. Based on dc-magnetization measurements, ξ_{GL} was found to be 20 Å for Rb_3C_{60} [63]. The high-field susceptibility gave the values 29 Å to 33 Å [64] and 35 Å [65] for K_3C_{60} and 30 Å [65] for Rb_3C_{60}.

The lower critical field H_{c1} can be used to estimate the penetration depth $\lambda(0)$, using [61]

$$H_{c1} = \frac{\phi_0}{4\pi\lambda(0)^2}\ln(\frac{\lambda(0)}{\xi_{GL}}). \tag{4}$$

In this way, the values $\lambda(0) = 2400$ Å [62] for K_3C_{60} and 2470 [63] and 3700 Å [66] for Rb_3C_{60} were obtained. The penetration depth has also been estimated from μSR [67, 68], optical conductivity [53] and NMR [48]. From the ratio of ξ_{GL}/λ it is clear that A_3C_{60} is a type II superconductor. The magnetic properties of the C_{60} superconductors have been reviewed by Buntar and Weber [69].

The jump in the specific heat at T_c was estimated by Ramirez [70] to be $\Delta C = 68 \pm 13$ mJ/mole-K^2 for K_3C_{60} and by Burkhart and Meingast [71] to be 64±14 and 75±14 mJ/mole-K^2 for K_3C_{60} and Rb_3C_{60}, respectively. The Hebel-Slichter peak was not seen in early NMR measurements [48], but has been seen in μSR [52] and more recent NMR measurements [51].

Table 1 Typical range of experimental values for superconducting parameters of K_3C_{60} and Rb_3C_{60}

Property	K_3C_{60}	Rb_3C_{60}
T_c	19 K	29 K
$\lambda(0)$	2400–8000 Å	2500–8000 Å
ξ_{GL}	26–35 Å	20–30 Å
$\Delta C/T_c$	64-68 mJ/mole-K^2	75 mJ/mole-K^2
$2\Delta/T_c$	3.5-4.3	3.5-4.3
α	0.30	0.21-0.31

Table 1 summarizes the typical range of experimental values for some superconducting parameters (see also Gelfand [22], Hou et al. [72] and Hou et al. [73]).

3 Models

The description of superconductivity in A_3C_{60} requires simple but reasonably realistic models. In such a model, we include the threefold degenerate, partly occupied t_{1u} orbital on each molecule and the hopping between the molecules. We also include the dominating Coulomb interaction between two electrons on the same molecule. This leads to the model

$$H_{el} = \sum_{ij} \sum_{mm'\sigma} t_{im,jm'} \psi^{\dagger}_{im\sigma} \psi_{jm'\sigma} + U \sum_{i} \sum_{(m\sigma)<(m'\sigma')} n_{im\sigma} n_{im'\sigma'}, \tag{5}$$

where the first term describes the hopping and the second term the Coulomb interaction. $\psi_{im,\sigma}$ annihilates an electron on molecule i with orbital quantum number m and spin σ, and $n_{im\sigma} = \psi^{\dagger}_{im\sigma}\psi_{im\sigma}$. Hopping is described in a tight-binding formalism and the effects of orientational disorder [74] are built into the hopping integrals $t_{im,jm'}$ [75, 76]. For the ordered system and $U = 0$, Eq. (5) accurately reproduces the result of a band structure calculation [77]. The important electron-phonon interaction involves the eight intramolecular fivefold degenerate H_g phonons. For simplicity, we introduce one fivefold degenerate H_g mode per molecule and its interaction with the electrons

$$H_{ph} = \omega_{ph} \sum_{i\nu} b^{\dagger}_{i\nu} b_{i\nu} + g \sum_{imm'\sigma\nu} V^{(\nu)}_{mm'} \psi^{\dagger}_{im\sigma} \psi_{im'\sigma} (b_{i\nu} + b^{\dagger}_{i\nu}), \tag{6}$$

where $V^{\nu}_{mm'}$ describes how an electron is scattered from one t_{1u} orbital m' to another orbital m when a phonon ν is created or annihilated. Its precise form is given elsewhere [78, 79]. The dimensionless electron-phonon coupling is given by

$$\lambda = \frac{5}{3} \frac{g^2}{\omega_{ph}} N(0), \tag{7}$$

where $N(0)$ is the density of states per spin at the Fermi energy.

4 Retardation Effects

4.1 Coulomb Pseudopotential and Ladder Diagrams

For conventional superconductors, the high-lying electronic states are usually projected out. In this way one can take into account that the electronic energy scale normally is much larger than the nuclear energy scale. This is often done by summing ladder diagrams [17], as is indicated schematically in Fig. 4. The standard procedure is to use the (statically) screened Coulomb repulsion for the dashed interaction lines [17]. The external lines entering the T-matrix to the left refer to low-lying electronic states which are treated explicitly. The intermediate lines on the right refer to the high-lying states, more than a few phonon energies away from the Fermi energy, which are projected out of the problem. Assuming that the interaction U is independent of $\mathbf{q}$ and ω and that the density of states $N(\varepsilon) \equiv N(0)$ is constant, the diagrams can easily be summed. Introducing $\mu = UN(0)$ and the Coulomb pseudopotential $\mu^* = TN(0)$, where T is the T matrix, one obtains [17]

$$\mu^* = \frac{\mu}{1 + \mu \log(B/\omega_{ph})}, \tag{8}$$

where B is a typical maximum electronic energy, e.g., half the band width or the Fermi energy, and ω_{ph} is the lower cut-off, below which the states are not projected out. If B/ω_{ph} is very large, the unity in the denominator of Eq. (8) can be neglected. Then μ drops out, and $\mu^* \approx 1/\log(B/\omega_{ph})$, independently of the size of U and μ. The corresponding μ^* is small, on the order of $\mu^* = 0.14$ if we assume $\omega_{ph}/B = 0.001$.

For the alkali-doped C_{60} the crucial question is what the appropriate value for the electronic energy scale is. There are two natural choices, namely the half-width $W/2 \sim 0.3\,\text{eV}$ of the partly occupied t_{1u} band or the total half-width of all the subbands, $E_I/2 \sim 15/2\,\text{eV}$ if the π like bands are considered or $E_I/2 \sim 30/2\,\text{eV}$ if both the π and σ like bands are included.

It was initially assumed [13,14] that the relevant energy scale is $E_I \sim 15\,\text{eV}$, since it was argued that the small energy gaps between the subbands should not qualitatively change the physics. The use of Eq. (8) then gives that $\mu^* \sim 0.2$ is only slightly larger than the values believed to be appropriate for conventional superconductors. The early theoretical calculations of $\lambda/N(0)$, like later calcula-

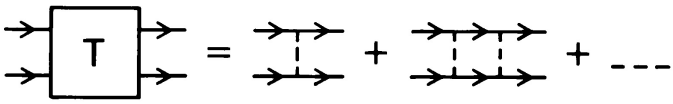

Fig. 4 Ladder diagrams used to describe the reduction of the Coulomb pseudopotential due to retardation effects. The dashed lines represent the Coulomb repulsion, and the full lines the electron Green's function

tions, gave rather small values. $N(0)$ was believed to be large, however. This led to a fairly large value of λ. Together with the rather small value estimated for μ^*, the observed values of T_c seemed to have been explained.

On the other hand, Anderson [80] asserted that the relevant energy scale is the width of the t_{1u} subband. Since this energy is comparable to the phonon energies, the retardation effects are then expected to be small. Anderson therefore argued that μ^* is large, and that the phonon mechanism and retardation effects alone cannot be enough for explaining superconductivity.

The retardation effects have been studied within the framework of summing ladder diagrams in the screened interaction for a model of C_{60} [81]. The matrix elements of the screened Coulomb interaction were calculated in the RPA. A tight-binding approach was used and a long-range Coulomb interaction included. Within this formalism, it was found that the higher subbands are important and that μ^* becomes very small [81]. Below, however, we argue that this is an artifact of summing ladder diagrams in the screened interaction, providing three different types of arguments. We first give some physically intuitive pictures, based on arguments in real space and in frequency space. Finally, we show that the use of ladder diagrams can give very wrong results for a model where we can obtain some exact results.

4.2 Real Space Argument

We first give a real space argument. Figure 1 suggests that a pair of electrons can take advantage of the phonon induced interaction without suffering a strong Coulomb repulsion, since the electrons move much faster than the nuclei. The subband width W describes the movement of the electrons between the molecules, while the total width of all the bands, E_I, describes the motion inside a C_{60} molecule. Due to the large value of E_I, one may then expect that retardation effects play a role for the motion inside a molecule. Such retardation effects are already included in the effective Coulomb interaction U_0 between two electrons on a free C_{60} molecule. The electrons are, nevertheless, not able to avoid each other efficiently when they are on the same molecule. This is reflected by the fairly large $U_0 \sim 3$ eV.

We would expect that retardation effects can effectively reduce μ^* only if the electrons can move rapidly between the molecules. This, however, happens on the energy scale W which is comparable to the phonon energy scale. Therefore the retardation effects should be rather small.

4.3 Frequency Argument

We next give an argument in frequency space, comparing qualitatively the ladder diagrams for the cases when hopping between the molecules is suppressed and allowed, respectively. If retardation effects are crucial for superconductivity, we

expect that they should enter in quite different ways in these two cases. Figure 5 shows the two situations schematically. One difference between the two cases is that if hopping between the molecules is suppressed, the subband width is zero. The matrix elements also differ because of the metallic screening in the case of hopping between the molecules. This difference, however, is not very important for the interband matrix elements [81]. Figure 5 then suggests that the main differences between the two cases are the different energy denominators. Since, however, the subband width is typically rather small compared with the energy difference between the band centers, this difference should not be very important. One would then expect that the ladder diagrams have a similar effect in the two cases [82]. This argument does not say that the ladder diagrams are unimportant, just that their effects should largely be included in the renormalization of U_0 of a free molecule. They should therefore contribute to the reduction of U_0 from its unrenormalized value of about 4 eV to its renormalized value of about 3 eV. This reduction, however, is far too small to explain superconductivity. Similar arguments should also apply to other diagrams.

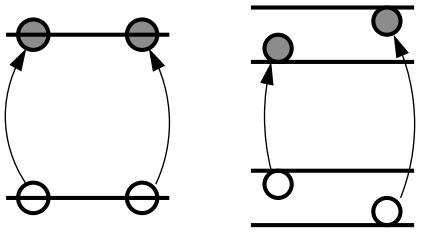

Fig. 5 Schematic representation of electron excitations for the case when hopping to neighboring molecules is suppressed (*left hand side*) and possible (*right hand side*)

4.4 Beyond Ladder Diagrams

Above, we discussed retardation effects within the traditional framework [17] of summing ladder diagrams in the screened interaction. This raises the question about the validity of neglecting other diagrams. For instance, Grabowski and Sham [83] studied the lowest order vertex corrections for the electron gas and found important corrections. It is also possible to construct sets of diagrams, which to a large extent cancel the ladder diagrams [81]. This raises important questions about which diagrams to include.

To address these questions, we have studied a two-band model where some exact results can be obtained [81]. For this purpose we use the Hamiltonian

$$H = \sum_i \sum_{n=1}^{2} \sum_\sigma \varepsilon_n n_{in\sigma} + t \sum_{<ij>} \sum_{n=1}^{2} \sum_\sigma \psi^\dagger_{in\sigma} \psi_{jn\sigma} \tag{9}$$

$$+U_{11} \sum_i \sum_{(n\sigma)<(n'\sigma')} n_{in\sigma}\, n_{in'\sigma'} + U_{12} \sum_i [\psi^\dagger_{i2\uparrow} \psi^\dagger_{i2\downarrow} \psi_{i1\downarrow} \psi_{i1\uparrow} + h.c.],$$

where i is a site index, ε_n the energies of the two levels, t is the hopping integral, U_{11} is the direct Coulomb interaction and U_{12} is the interband scattering. The particularly strong interband scattering between the t_{1u} and t_{1g} bands in C_{60} is of a similar type, namely the excitation of two electrons between two bands.

Consider the limit

$$\Delta\varepsilon \equiv \varepsilon_2 - \varepsilon_1 \gg U_{12}, t \tag{10}$$

$$\frac{1}{2N(0)} \sim \frac{U_{12}^2}{2\Delta\varepsilon} \ll U_{11}. \tag{11}$$

In this limit, the upper subband can be projected out and a new effective Hamiltonian can be obtained, which describes low-energy properties correctly. This process does not generate any new terms for the Hamiltonian at Eq. (9), but it renormalizes the intraband interaction to

$$U_{eff} = U_{11} - \frac{U_{12}^2}{2\Delta\varepsilon}. \tag{12}$$

The renormalization of the intraband interaction is small, since $U_{12}^2/(2\Delta\varepsilon) \ll U_{11}$ (Eq. 10). The properties of this effective Hamiltonian then differ very little from the one-band model, where the upper band was completely neglected. Thus the upper band has little influence on the low energy properties in general and μ^* in particular. For instance, in RPA the screened interaction is $1/[2N(0)]$ in both the one-band and two-band models, if $U_{11}N(0) \gg 1$.

A quite different result is obtained by summing the ladder diagrams in the screened interaction. The screened intraband interaction (Eq. 14) is $\approx 1/[2N(0)]$. The screening of the interband Coulomb interaction U_{12} is negligible in this model and for the limits considered. Summing the ladder diagrams then leads to the effective intraband interaction

$$\frac{1}{2N(0)} - \frac{U_{12}^2}{2\Delta\varepsilon}, \tag{13}$$

where the second term is the correction from the ladder diagrams. In the limit of Eq. (10) this correction is very large and the renormalization of μ^* is important. This is in disagreement with the exact result obtained above, and it shows that the ladder diagrams give incorrect results in this case [81].

The projection method and the summation of ladder diagrams describe similar physics, and for the parameters used here the term treated in the projection approach is also the dominating diagram in the ladder summation. The difference is that in the rigorous projection method, the high energy degrees of freedom were eliminated first, while in the ladder diagram approach the low energy degrees of freedom were treated first, by introducing the metallic screening,

and the high energy degrees of freedom later, by summing the ladder diagrams. There is no rigorous justification for the latter approach.

The subtracted quantity is the same in both cases. This correction term is compared with an intraband Coulomb interaction which is unscreened in one case and screened in the other. The correction term is small compared with the the unscreened interaction but comparable to the screened interaction. In one case the ladder diagrams are therefore unimportant while in the other case they are important. These results should also be of relevance for the retardation effects due to the high-lying states for conventional superconductors.

These results suggest that the summation of ladder diagrams in the screened interaction gives unreliable results for A_3C_{60} and that the renormalization of μ^* due to the higher subbands may not be large. The real space and frequency arguments presented above strongly suggest that this is indeed so.

4.5 Screening

One may ask how much screening effects alone can reduce the Coulomb interaction. In the RPA, the screened interaction can be written as

$$\mathcal{W} = (1 - vP)^{-1}v \tag{14}$$

where $\mathcal{W}$ is a matrix representing the different Coulomb matrix elements, v is the corresponding unscreened matrix elements and P is the polarizability. For the intraband matrix elements, the t_{1u} orbitals dominate the screening, and we can transform to the corresponding basis, neglecting all other orbitals. For small $|\mathbf{q}|$, the diagonal elements of P are related to the density of states $N(0)$ per spin. Since both $N(0)$ and the diagonal elements of v are large, we can assume that the product is much larger than unity. Essentially, the two factors v in Eq. (14) then drop out, and with appropriate assumptions one can then derive [81] that the intraband matrix elements are $\approx 1/2N(0)$. The unrenormalized μ is obtained by multiplying by $N(0)$, giving $\mu \approx 0.5$. Averaging over q gives $\mu \approx 0.4$ [81]. This should be compared with the unscreened result, $UN(0) \sim 1.5 \times 6 = 9$. Within the RPA, screening is therefore very important.

Following the arguments given above, we may assume that there are no renormalization effects due to the higher subbands. If we assume, however, that the arguments behind Eq. (8) apply within the t_{1u} subband, this reduces μ somewhat. The RPA value $\mu = 0.4$ found above is then reduced to $\mu^* \sim 0.3$ [81]. This is then the appropriate value for, e.g., the McMillan formula, while $\mu = 0.4$ is more appropriate for the Eliashberg equation if the t_{1u} band is explicitly included. We emphasize, however, that this is based on RPA screening, and that RPA is questionable for these strongly correlated system.

In the RPA approximation, screening costs kinetic energy. In the limit where a typical Coulomb integral U is large compared with the band width W, the kinetic energy cost of screening is relatively small compared with the potential energy gain, and screening is very efficient in the RPA. This means that as a test

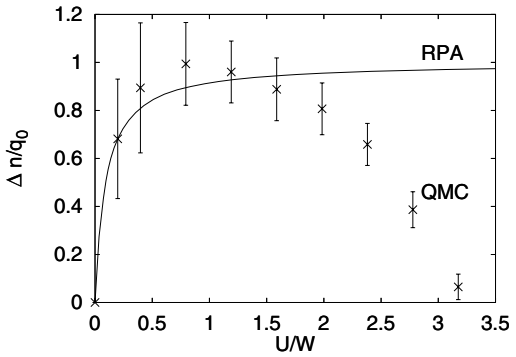

Fig. 6 Screening charge Δn on the site of the test charge ($q = 0.25\,e$) as a function of U/W, extrapolated to infinite cluster size. The *full curve* shows the screening charge in the RPA, obtained from Hartree calculations for the Hamiltonian (15). The *crosses with error bars* give the results of the QMC calculations. The RPA screening remains rather accurate up to $U/W \sim 2$, but fails badly for larger values of U/W. The screening is very efficient for $U/W \sim 0.5 - 2.0$ (after Koch et al. [82])

charge q is introduced on a site 0, almost the same amount of electronic charge moves away from this site, leaving it almost neutral. This argument, however, neglects that when an electron leaves a site, it has to find another site with a missing electron; otherwise there is a large Coulomb energy penalty. While the RPA predicts an extremely efficient screening in this limit, in a correct treatment the screening is very poor. Thus, while the RPA may be rather accurate for small values of U/W, it is qualitatively wrong for large values. It is not clear what happens for intermediate values.

To discuss this, we perform a more accurate calculation. We use the model in Eq. (5) of A_3C_{60}. In addition we include the interaction with an external test charge q on site 0, giving the total Hamiltonian

$$H = H_{el} + qU \sum_{m\sigma} n_{0m\sigma}. \tag{15}$$

The test charge is assumed to interact with the electrons on the same site via the Coulomb integral U. Since we later assume that an electron can be described by a test charge, the interaction of the test charge with other electrons must be U.

A projection Quantum Monte Carlo (QMC) method [84] was used to solve [82] this Hamiltonian. The charge was obtained from the extrapolated estimator. The calculations were performed for clusters with 32, 48, 64, 72 and 108 C_{60} molecules and the results were extrapolated to infinite cluster size. The results are shown in Fig. 6. The RPA is rather accurate for small values of U/W but it fails completely for very large values of U/W, as expected. It remains surprisingly accurate, however, up to rather large values of U/W. Thus the system is rather close to a metal-insulator transition ($U/W \sim 2.5$) before RPA starts to fail badly.

The results suggest that screening effects should be important in reducing the Coulomb interaction and μ^*. For the relevant values of U/W, however, the screening is probably not as efficient as predicted by the RPA. Screening alone may therefore not reduce μ^* to the value 0.4 (0.3) predicted by the RPA, and screening alone may not be sufficient to explain superconductivity. In the next section we show that the so-called local pairing plays an important role in this context.

An efficient screening of the Coulomb repulsion would in general also imply an efficient screening of the electron-phonon interaction. The efficient screening would then probably not help superconductivity very much. The fact that C_{60} is a molecular solid, however, means that the different phonons behave in very different ways, as discussed by Schluter et al. [14]. This can be seen by comparing the intramolecular A_g and H_g phonons. We first observe that the efficient metallic screening is due to a charge transfer between the molecules. When an A_g phonon is excited, all the t_{1u} levels move energetically in the same direction. The system can screen this very efficiently, transferring charge to the molecule where the phonon was excited, until the phonon induced shift is essentially compensated [14]. The situation is quite different for the H_g Jahn-Teller phonons. When a phonon is excited, the t_{1u} levels shift in such a way that the center of gravity is unchanged. This is illustrated in Fig. 7. These shifts cannot be screened by a transfer of charge to the molecule, since this transfer would essentially just shift the center of gravity of the t_{1u} levels. The result is a rather inefficient screening of the H_g phonons [14]. It is therefore possible to have an efficient screening of the Coulomb interaction without the electron-phonon (H_g) interaction being strongly screened. This is one important feature of the alkali-doped C_{60} compounds being molecular solids with Jahn-Teller intramolecular phonons.

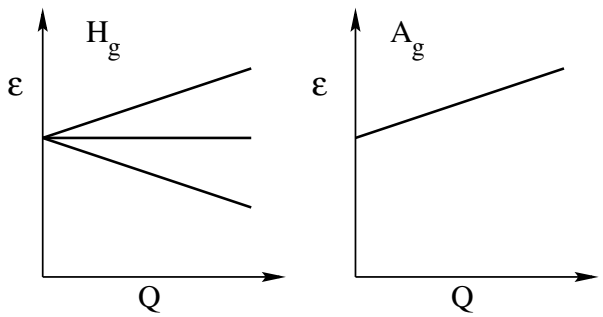

Fig. 7 Schematic illustration of the shifts of the t_{1u} levels as a function of the phonon coordinate Q for one of the H_g modes and for an A_g mode. The figure illustrates that the center of gravity is unchanged for the H_g but not for the A_g mode, and that the A_g, but not the H_g, mode can be screened by a charge transfer to the molecule

5
Local Pairing

There are several important deficiencies in Migdal-Eliashberg theory when treating alkali-doped fullerides. The underlying Migdal's theorem is questionable [16], since $\omega_{ph} \sim W$. Even more important, the theory does not properly incorporate the Jahn-Teller character of the important intramolecular H_g phonons and it only includes the Coulomb repulsion as an empirical Coulomb pseudopotential. We find that exactly the interplay between the Jahn-Teller phonons and the Coulomb repulsion is crucial for the understanding of superconductivity in the fullerides. We therefore study the electron-phonon and electron-electron interactions on an equal footing.

5.1
Model and DMFT Treatment

For this purpose Han et al. [20] studied the model

$$H = H_{el} + H_{phon} \tag{16}$$

where H_{el} (Eq. 5) contains a threefold degenerate t_{1u} level on each molecule, the hopping between the molecules and the Coulomb interaction. The hopping corresponds to a semi-elliptical density of states. H_{phon} (Eq. 6) contains a fivefold degenerate H_g phonon per site and its interaction with the electrons. The model explicitly includes the Jahn-Teller character of the phonons. Below this model is referred to as the $t \times H$ model. We also consider the simplest Jahn-Teller problem, $e \times E$, where a twofold degenerate phonon couples to a twofold degenerate level. As a comparison we consider a non-Jahn-Teller problem, the $a \times A$ model, where a nondegenerate phonon mode couples to a nondegenerate level.

The electron-phonon and electron-electron interactions can be treated on an equal footing by using the dynamical mean-field theory (DMFT) [85]. This approach furthermore avoids the assumptions of Migdal's theorem. In the DMFT, the problem is mapped onto an effective impurity problem, where the impurity is embedded in a host which is determined selfconsistently. The self-energy $\Sigma(\mathbf{q}, \omega)$ is $\mathbf{q}$ independent.

To solve the resulting impurity problem we use the discrete Hubbard-Stratonovich decoupling scheme [86, 87] for the Coulomb interaction terms by introducing auxiliary fields. Monte Carlo sampling is then performed, treating the phonon displacement fields

$$Q_{iv} \equiv (b_{iv}^{\dagger} + b_{iv})/\sqrt{2} \tag{17}$$

and the auxiliary fields on an equal footing [88, 94]. This fully Quantum mechanical treatment of phonons does not make any assumptions about Migdal's theorem or adiabaticity.

We apply a weak perturbation which creates an electron pair

$$\Delta_i = \sum_m \psi^\dagger_{im\uparrow}\psi^\dagger_{im\downarrow}. \tag{18}$$

We introduce the response function (pairing susceptibility)

$$\chi(\tau_1,\tau_2,\tau_3,\tau_4) = \frac{1}{N}\sum_{ijmm'}\langle T_\tau \psi_{im\uparrow}(\tau_1)\psi_{im\downarrow}(\tau_2)\psi^\dagger_{jm'\downarrow}(\tau_3)\psi^\dagger_{jm'\uparrow}(\tau_4)\rangle, \tag{19}$$

where $\langle ...\rangle$ denotes a thermal average, T_τ is a time-ordering operator, τ is an imaginary time, N is the number of sites and $\psi_{im}(\tau)$ is an annihilation operator in the Heisenberg representation. We are interested in the response $\chi(\tau,\tau,\tau',\tau')$ to the perturbation, and a divergence of χ below a temperature T_c signals the onset of superconductivity [89]. We can Fourier transform χ with respect to $\tau_1-\tau_2$ and $\tau_3-\tau_4$ and write down a Bethe-Salpeter equation

$$\chi = (\chi_0^{-1}-\Gamma)^{-1} = (1-\chi_0\Gamma)^{-1}\chi_0, \tag{20}$$

where $\chi_0(\tau_1,\tau_2,\tau_3,\tau_4) = \sum_{\mathbf{k}}\sum_{mm'} G_{mm'}(\mathbf{k},\tau_1-\tau_4)G_{mm'}(-\mathbf{k},\tau_2-\tau_3)/N$, which describes two independently propagating electrons (or holes) at zero net momentum and Γ is an effective interaction. $G_{mm'}(\mathbf{k},\tau)$ is a fully dressed Green's function.

We introduce a local pairing susceptibility

$$\chi^{\mathrm{loc}}(\tau_1,\tau_2,\tau_3,\tau_4) = \sum_{mm'}\langle T_\tau \psi_{m\uparrow}(\tau_1)\psi_{m\downarrow}(\tau_2)\psi^\dagger_{m'\downarrow}(\tau_3)\psi^\dagger_{m'\uparrow}(\tau_4)\rangle, \tag{21}$$

on the impurity site. As in Eq. (20), we construct the Bethe-Salpeter equation for local quantities

$$\chi^{\mathrm{loc}} = [(\chi_0^{\mathrm{loc}})^{-1}-\Gamma^{\mathrm{loc}}]^{-1} \tag{22}$$

$\chi_0^{\mathrm{loc}}(\tau_1,\tau_2,\tau_3,\tau_4) = \sum_{mm'} G^{\mathrm{loc}}_{mm'}(\tau_1-\tau_4)G^{\mathrm{loc}}_{mm'}(\tau_2-\tau_3)$ with a local electron Green function $G^{\mathrm{loc}}_{mm'}(\tau_1-\tau_2) = \sum_{\mathbf{k}} G_{mm'}(\mathbf{k},\tau_1-\tau_2)/N$. Since χ^{loc} and χ_0^{loc} can be calculated within DMFT, we can obtain Γ^{loc}. We assume $\Gamma \approx \Gamma^{\mathrm{loc}}$, which should be a good approximation, since the interaction is dominated by intramolecular phonons and an intramolecular Coulomb repulsion. Since χ_0 can also be calculated within DMFT, χ follows from Eq. (20).

The superconducting instability occurs when the denominator in Eq. (20) becomes singular. This is determined by two factors, χ_0 and Γ. If the system is metallic, χ_0 diverges as $\chi_0(i\omega_n) \sim ZN(0)/(\pi|\omega_n|)$ for Matsubara frequency $\omega_n \to 0$, where Z is the quasi-particle renormalization factor near the chemical potential. Together with an attractive (positive) Γ this leads to a singularity.

5.2 Sum-Rule

We first derive a sum-rule, which allows us to discuss the properties of χ^{loc} and Γ^{loc}. We study $\tau_1=\tau_2$, $\tau_3=\tau_4$ and calculate Fourier transform $\tilde{\chi}^{\mathrm{loc}}$ with respect to $\tau_1-\tau_3$ in the $T\to 0$ limit. This gives

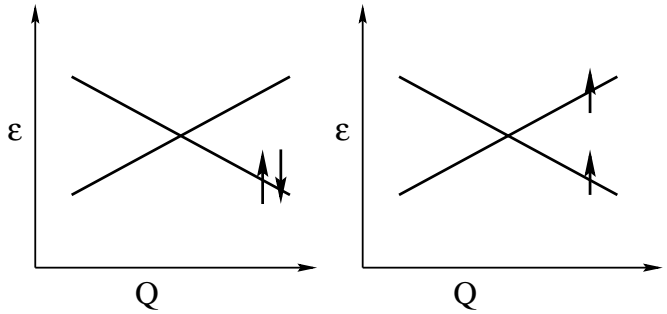

Fig. 8 Schematic illustration of the shifts of the e levels as a function of the phonon coordinate Q for an E phonon. The figure illustrates that the electron-phonon coupling favors a singlet formation

$$\tilde{\chi}^{\rm loc}(i\omega_n) = \frac{1}{2\pi}\int_{-\infty}^{\infty} d\varepsilon \rho^{\rm loc}(\varepsilon)/(i\omega_n - \varepsilon), \tag{23}$$

where

$$\begin{aligned}\rho^{\rm loc}(\varepsilon) \quad &= 2\pi \sum_n |\langle n, N-2| \sum_m \psi_{m\uparrow}\psi_{m\downarrow}|0,N\rangle|^2 \\ &\times \delta(\varepsilon - E_0(N) + E_n(N-2)) + ...\end{aligned} \tag{24}$$

Here $|n,N\rangle$ is the n-th excited state of the system with N electrons and the energy $E_n(N)$. The term shown describes the removal of an electron pair and "..." indicates the addition of an electron pair. We have put the chemical potential $\mu = 0$.

It is now instructive to derive a sum rule for the spectral function $\rho^{\rm loc}(\varepsilon)$ ($\rho^{\rm loc}(\varepsilon) \leq 0$ for $\varepsilon > 0$ and $\rho^{\rm loc}(\varepsilon) \geq 0$ for $\varepsilon < 0$)

$$\frac{1}{2\pi}\int_{-\infty}^{\infty} |\rho^{\rm loc}(\varepsilon)| d\varepsilon = \langle 0,N|A_m + A_p|0,N\rangle, \tag{25}$$

where

$$A_m = \sum_{mm'} \psi^\dagger_{m\downarrow}\psi^\dagger_{m\uparrow}\psi_{m'\uparrow}\psi_{m'\downarrow} \tag{26}$$

first annihilates and then recreates an electron pair and A_p does the opposite.

We first study the simplest Jahn-Teller system, namely the $e \times E$ model at half-filling. Figure 8 illustrates that the coupling to a Jahn-Teller phonon tends to put two electrons in the spin up and spin down orbitals with the same m quantum numbers. For instance, if the Jahn-Teller effect dominates (but λ is not too large), two electrons in the e-level tend to fluctuate between the states

$$\begin{aligned}|1\rangle &= \psi^\dagger_{1\uparrow}\psi^\dagger_{1\downarrow}|0\rangle \\ |2\rangle &= \psi^\dagger_{2\uparrow}\psi^\dagger_{2\downarrow}|0\rangle,\end{aligned} \tag{27}$$

due to the dynamical Jahn-Teller effect. Hopping, on the other hand, tends to favor all states equally. Hopping and the Jahn-Teller effect therefore compete. As

the Coulomb interaction is increased, hopping tends to be suppressed, and the Jahn-Teller effect wins. For simplicity, we consider the limit where U is very large and the electron-phonon coupling λ is very small, taken in such a way the the Jahn-Teller effect wins over hopping. For a half-filled band, the local state then becomes a singlet

$$|0,2\rangle = \frac{1}{\sqrt{2}} \sum_{m=1}^{2} \psi_{m\uparrow}^{\dagger} \psi_{m\downarrow}^{\dagger} |0\rangle. \tag{28}$$

This is due to the dynamical Jahn-Teller effect involving states of the type shown in Fig. 8. This yields

$$A_m |0,2\rangle = A_p |0,2\rangle = 2|0,2\rangle, \tag{29}$$

and the sum rule becomes

$$\frac{1}{2\pi} \int_{-\infty}^{\infty} |\rho^{\mathrm{loc}}(\varepsilon)| d\varepsilon \equiv P = 4, \tag{30}$$

in the limit of a very large U and a finite but a small λ. The existence of a local singlet, Eq. (28), means that the probability for removing two electrons (holes) with the same m quantum number is very large, leading to a large spectral weight $\rho^{\mathrm{loc}}(\varepsilon)$. In contrast, χ_0^{loc} describes independently propagating electrons (holes). As a result, there is a substantial probability that a molecule may not be simultaneously occupied by two electrons with the same m quantum number, and the right hand side of the sum-rule is substantially reduced

$$\frac{1}{2\pi} \int_{-\infty}^{\infty} |\rho_0^{\mathrm{loc}}(\varepsilon)| d\varepsilon \equiv P_0 = 1. \tag{31}$$

The sum-rule in Eq. (30) was derived for the case when λ is finite but very small. For large values of λ, we can use a semiclassical approach [90]. The phonon coordinates are written as

$$Q_1 = q\cos\Theta; \qquad Q_2 = q\sin\Theta \tag{32}$$

For these coordinates, the electron part of the Hamiltonian is diagonalized by

$$\begin{aligned} \psi_{+\sigma} &= \cos\frac{\Theta}{2}\psi_{1\sigma} + \sin\frac{\Theta}{2}\psi_{2\sigma} \\ \psi_{-\sigma} &= -\sin\frac{\Theta}{2}\psi_{1\sigma} + \cos\frac{\Theta}{2}\psi_{2\sigma}. \end{aligned} \tag{33}$$

The ground-state wave function can then be written as

$$|\Psi\rangle = \int dq \int d\Theta f(q,\Theta) \psi_{-\uparrow}^{\dagger} \psi_{-\downarrow}^{\dagger} |q\Theta\rangle, \tag{34}$$

where $|q,\Theta\rangle$ is a phonon state defined by q and Θ and $f(q,\Theta)$ is some function. It then follows that $\langle\Psi|A_{\substack{m\\p}}|\Psi\rangle = 1$ and

$$\frac{1}{2\pi} \int_{-\infty}^{\infty} |\rho^{\mathrm{loc}}(\varepsilon)| d\varepsilon \equiv P = 2, \tag{35}$$

in the limit of a large U and a large λ. For both limits (Eqs. 30 and 35), the two electrons on a molecule are always paired. In the limit at Eq. (30) the two states in Eq. (28) contribute coherently to the sum-rule. In the limit at Eq. (35) this is not the case, since the coherence is destroyed by the phonon state $|q\Theta\rangle$ in Eq. (34). The limit at Eq. (35) is more appropriate for the cases studied here.

Since the sum-rule for $\rho^{\rm loc}(\varepsilon)$ is larger than for $\rho_0^{\rm loc}(\varepsilon)$, $\tilde{\chi}^{\rm loc}$ tends to be larger than $\tilde{\chi}_0^{\rm loc}$ (see Eq. 23). It then follows from Eq. (22) that the effective interaction $\Gamma^{\rm loc}$ tends to be attractive. To illustrate this, we have performed exact diagonalization calculations for finite clusters. Figure 9 compares the Jahn-Teller $e \times E$ problem with the non-Jahn-Teller $a \times A$ problem. In the $e \times E$ case, an increase of U reduces hopping which makes the Jahn-Teller effect more important. As a result, P/P_0 increases. This tends to increase $\chi^{\rm loc}/\chi_0^{\rm loc}$. At the same time spectral weight is shifted upwards in energy, which tends to decrease $\chi^{\rm loc}/\chi_0^{\rm loc}$ (see Eq. 23). The net result is that the ratio is only moderately reduced as U is increased. Counter-intuitively, in molecular solids with Jahn-Teller phonons, Coulomb interactions can in certain respects actually *help* the electron-phonon coupling.

The local pairing and singlet formation can be further illustrated by calculating $\langle S^2 \rangle$, where S is the spin operator for the impurity orbital. Figure 10 shows this quantity divided by its value $\langle S^2 \rangle_0$ for a system with $U = 0$ and $\lambda = 0$. The figure shows how $\langle S^2 \rangle$ is reduced for $U = 0$ compared with its noninteracting value, due to the local singlet formation. As U is increased, $\langle S^2 \rangle$ is further reduced, as the Coulomb interaction reduces hopping and thereby helps the Jahn-Teller phonons to form a local singlet. For $\lambda = 0$, on the other hand, $\langle S^2 \rangle$ increases with U, due to a tendency for the system to form a local moment.

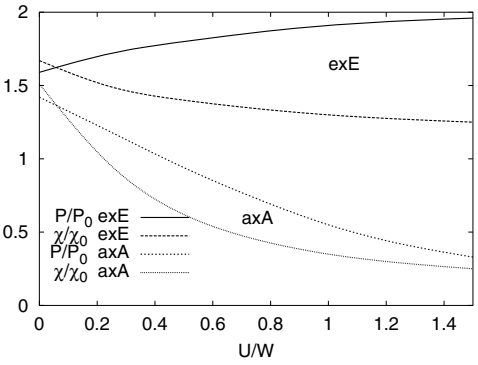

Fig. 9 P/P_0 and $\chi^{\rm loc}/\chi_0^{\rm loc}$ as a function of U/W for the $e \times E$ and $a \times A$ models. The figure illustrates that for the $a \times A$ model, these quantities drop rapidly as U increases. In contrast, for the $e \times E$ model, the pairing susceptibility is very resistant to increasing U. The calculation was performed for an impurity model with five host sites and with $\lambda = 0.6$ (after Han et al. [20])

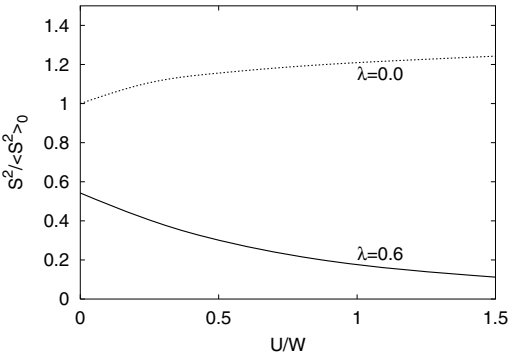

Fig. 10 $\langle S^2\rangle/\langle S^2\rangle_0$ as a function of U/W for $\lambda = 0.6$ and $\lambda = 0$ in the $e \times E$ model. Due to the local singlet formation, $\langle S^2\rangle$ drops quickly for $\lambda = 0.6$, as U is increased, while it grows for $\lambda = 0$

Capone et al. [19] have reached somewhat similar conclusions, analyzing the Fermi liquid parameters instead of the sum-rule used here, and studying a system with doping $n = 2$ and close to a metal-insulator transition.

The behavior of the $a \times A$ model is quite different. The operators A_m (Eq. 26) and A_p can pick up contributions only from components of the ground-state with two or zero electrons. These charge fluctuations are favored by λ but suppressed by U. As U is increased, P/P_0 therefore drops quickly, as does $\chi^{\rm loc}/\chi_0^{\rm loc}$. As a result, the effective interaction Γ quickly becomes repulsive.

Above we have studied the local pairing of the electrons on one molecule. Superconductivity, however, requires the formation of a coherent state throughout the solid. This requires that $(1 - \chi_0\Gamma)$ becomes singular. The behavior of χ_0 is therefore as important as that of Γ. While U in some respects helps the local pairing (Γ), it reduces χ_0, since spectral weight near the chemical potential is transfered to incoherent states at higher energies on order of U. In the following sections we study the combined effects of Γ and χ_0.

5.3
Absence of Coulomb Interaction

Figure 11 shows results for the $U = 0$ case. It shows T_c as a function of λ according to DMFT and Eliashberg theories. To include the renormalization of the phonon frequencies by the electron-phonon interaction, the Eliashberg calculation was performed with a self-consistent phonon Green's function, using a lowest order phonon self-energy. Eliashberg theory is usually expected to overestimate [88] T_c of doped C_{60} because of the violation of Migdal's theorem. Surprisingly, in the $t \times H$ model for $U = 0$, the Eliashberg T_c remains accurate even up to relatively large values of λ. For a small λ, χ_0 goes as $1/(1 + \lambda)$, which renormalizes λ to $\lambda/(1+\lambda)$ in the McMillan equation [91]. For a larger λ, however, χ_0 drops faster in DMFT than in Eliashberg theory. The reason is that as λ is increased, the sys-

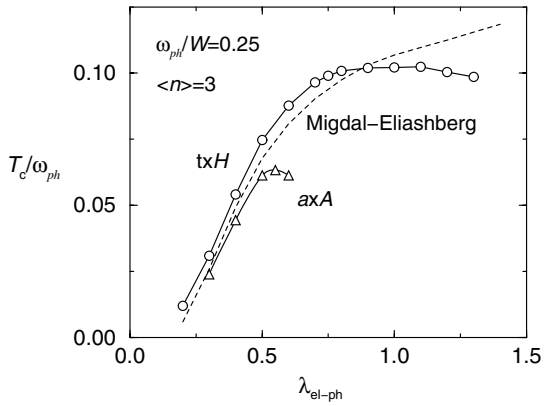

Fig. 11 T_c as a function of λ according to Migdal-Eliashberg (*dashed line*) and DMFT theories for the $t \times H$ (○) and $a \times A$ (△) couplings at half-filling. The parameters are $\omega_{ph}/W = 0.25$ and $U = 0$ (after Han et al. [20])

tem gets close to a metal-insulator transition. A large amount of spectral weight is then transferred away from the chemical potential. As a result, the formation of a coherent state is much less efficient. The DMFT calculation therefore shows a maximum in T_c, which happens at $\lambda \sim 1$. In the $a \times A$ model, the metal-insulator transition happens for a smaller value of λ and therefore Migdal-Eliashberg theory breaks down earlier. It is important to notice that in the cases studied here, Migdal-Eliashberg theory is rather accurate as long as the system is well away from a metal-insulator transition, although $\omega_{ph}/W = 0.25$ is not very small.

5.4 Finite Coulomb Interaction

We next consider a finite U. Figure 12 shows T_c as a function of U for the $t \times H$ and $a \times A$ models. For the $a \times A$ case, T_c drops quickly when U increases, as expected. For the non-Jahn-Teller system, the attractive interaction is quickly canceled by the Coulomb repulsion and for a wide range of U/W the system is a non-superconducting metal. This is illustrated by the effective electron-electron interaction

$$\frac{U_{\text{tot}}}{W} \approx -\frac{\pi}{4}\lambda + \frac{U}{W} = -0.47 + \frac{U}{W}, \tag{36}$$

where the first term is the phonon induced attraction, which for $\lambda = 0.6$ is about $-0.47W$. We would therefore expect superconductivity to be lost when $U/W \sim 0.47$. Figure 12 shows that this actually happens even a little bit earlier.

For the $t \times H$ case, on the other hand, T_c is much more resistant to an increase in U. The discretization error in the QMC solution of the impurity problem leads to an overestimation of T_c for large U, which is about 20 % for $U/W = 1$ and

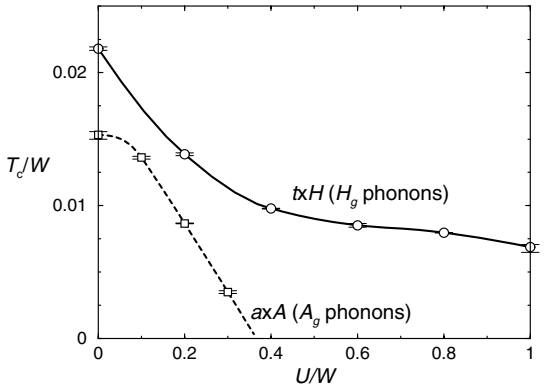

Fig. 12 T_c as a function of U for the $t \times H$ and $a \times A$ models for half-filling. The parameters are $\lambda = 0.6$ and $\omega_{ph}/W = 0.25$. The figure illustrates the important difference between H_g and A_g phonons (after Han et al. [20])

$\lambda = 0.6$ [20]. The reduction of T_c with U is, nevertheless, remarkably slow. The effective interaction between the electrons is given by

$$\frac{U_{\text{tot}}}{W} \approx -0.2 + \frac{U}{W}. \tag{37}$$

Due to strong-coupling effects [79], the phonon induced attraction is weaker than for the $a \times A$ case, and from this type of argument one might have expected superconductivity to have been lost already for $U/W \sim 0.2$. Jahn-Teller phonons, however, help form local pairing and Γ stays attractive, although the net force between the electrons is strongly repulsive. Therefore the superconductivity is expected to exist in the metal right up to the metal-insulator transition.

The effective interaction $v_{eff}(i\omega_n, i\omega_m)$ is defined for a pair of incoming electrons at frequencies $(i\omega_n, -i\omega_n)$ and outgoing electrons at frequencies $(i\omega_m, -i\omega_m)$

$$v_{eff}(i\omega_n, i\omega_m) \equiv -\beta\Gamma^{\text{loc}}(i\omega_n, i\omega_m) \tag{38}$$

The important difference between Jahn-Teller and non-Jahn-Teller phonons is illustrated in Figs. 13 and 14. Figure 13 shows $v_{eff}(i\omega_n, i\omega_m)$ for the $t \times A$ model for $U/W = 0.4$ and $U/W = 0.5$. From the arguments above, we may expect the phonon-induced attractive potential to be somewhat stronger than the Coulomb repulsion for $U/W = 0.4$. The figure shows that $v_{eff}(i\omega_n, i\omega_m)$ is indeed quite negative (attractive) over a small frequency range $\omega_n \approx \omega_m$. For $U/W = 0.5$, $v_{eff}(i\omega_n, i\omega_m)$ is positive (repulsive) over the whole frequency range. This is not surprising, since the Coulomb repulsion is now expected to win over the phonon-induced attraction. Figure 14, on the other hand, shows that for the $t \times H$ model, v_{eff} is strongly attractive over a limited frequency range, even for a large U/W. Indeed, the potential becomes more attractive over some limited range as U is increased. This illustrates that even if the Coulomb repulsion overwhelms the

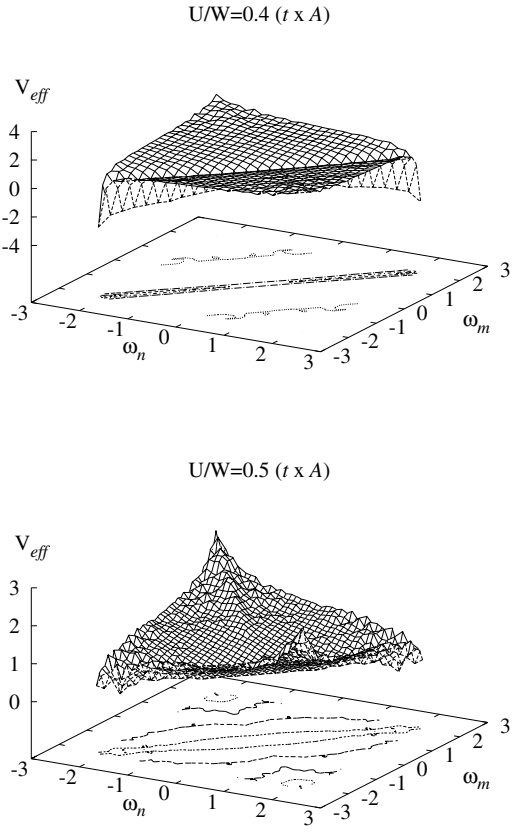

Fig. 13 $v_{eff}(i\omega_n, i\omega_m) = -\beta\Gamma^{\rm loc}(i\omega_n, i\omega_m)$ for the $t \times A$ model for $U/W = 0.4$ at $T/W = 1/80$ (*top*) and $U/W = 0.5$ at $T/W = 1/120$ (*bottom*). The parameters are $\lambda = 0.6$ and $\omega_{ph}/W = 0.25$. The figure illustrates how v_{eff} is negative (attractive) for $\omega_n \approx \omega_m$ and $U/W = 0.4$ but positive (repulsive) for $U/W = 0.5$, where the Coulomb repulsion has won over the phonon induced attraction

phonon-induced attraction, $v_{eff}(i\omega_n, i\omega_m)$ is still attractive, at least for some frequency range, as expected from the local pairing arguments.

5.5 Doping Dependence

As discussed above, T_c drops surprisingly quickly in fullerides when the doping n is changed away from $n = 3$ electrons per C_{60} molecule [30]. Reducing the doping leads to a reduction of the Fermi energy and an increase in the density of states at the Fermi energy [93]. One would then actually expect an increase in λ and T_c according to Eliashberg theory. This has been taken as evidence for an electron-electron mechanism of superconductivity [10]. Fig. 15 shows the doping dependence of T_c in the DMFT. For small U, T_c drops slowly when the doping

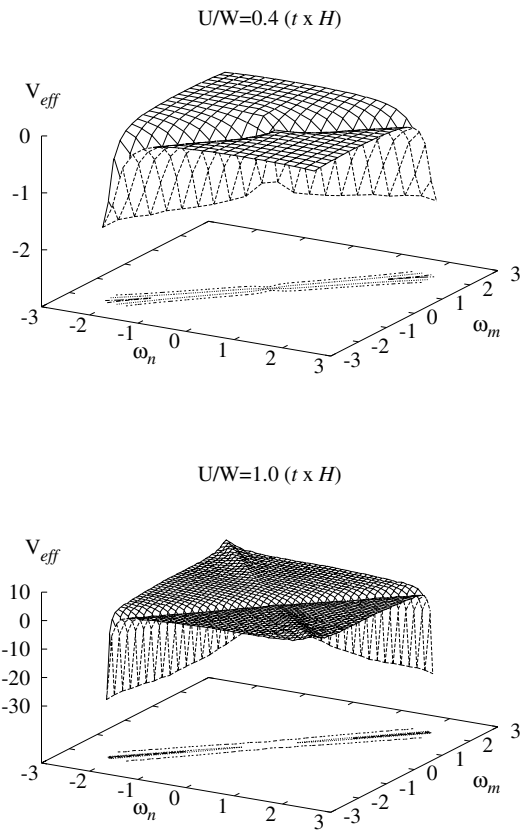

Fig. 14 $v_{eff}(i\omega_n, i\omega_m) = -\beta\Gamma^{\rm loc}(i\omega_n, i\omega_m)$ for the $t \times H$ model for $U/W = 0.4$ at $T/W = 1/60$ (*top*) and $U/W = 1.0$ at $T/W = 120$ (*bottom*). The parameters are $\lambda = 0.6$ and $\omega_{ph}/W = 0.25$. The figure illustrates how v_{eff} is strongly negative (attractive) for $\omega_n \approx \omega_m$ and $U/W = 0.4$ and even more so for $U/W = 1.0$

is reduced until $n \sim 2$ and then starts to drop much faster. Simultaneously, $\Gamma^{\rm loc}$ drops rapidly for $n < 2$, probably because the local pairing is inefficient once $n < 2$. For $U/W > 0.4$, T_c drops very quickly as $n = 2$ is approached from above.

As $n = 2$ is approached, the system approaches a metal-insulator transition [94]. Whether or not the system actually becomes an insulator for $n = 2$, spectral weight is transferred away from the chemical potential. This can be illustrated by studying

$$G(\tau = \beta/2) = \int d\omega \frac{A(\omega)\exp(-\beta\omega/2)}{1 + \exp(-\beta\omega)}, \tag{39}$$

where $\beta = 1/T$ and $A(\omega)$ is the electron spectral function. The exponential functions in the integrand make the integral small for large absolute values of ω and $G(\tau = \beta/2)$ is therefore a measure of $A(\omega)$ for ω close to the chemical potential at $\omega = 0$. Figure 16 shows $G(\tau = \beta/2)$ for different values of U as

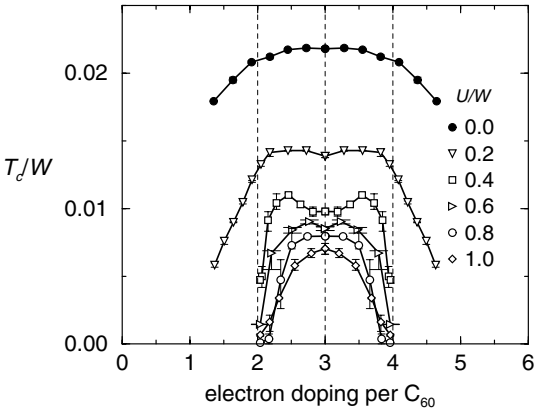

Fig. 15 T_c as a function of doping n for different values of U for $t \times H$ coupling. The parameters are $\omega_{ph}/W = 0.25$ and $\lambda = 0.6$. The figure illustrates the strong doping dependence for $U/W \geq 0.4$

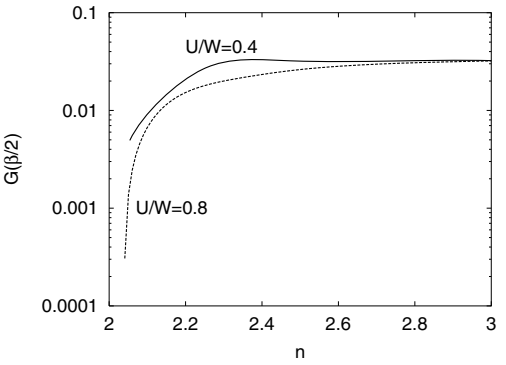

Fig. 16 $G(\tau = \beta/2)$ as a function of doping n for $U/W = 0.4$ and 0.8. The parameters are $\lambda = 0.6$, $\omega_{ph}/W = 0.25$ and $T/W = 1/120$

a function of doping. The rapid drop for $U/W = 0.8$ as $n = 2$ is approached illustrates the large transfer of weight away from the chemical potential. This leads to a reduction of χ_0, which causes a reduction of T_c. Despite strong local singlet formation near $n = 2$ and 4, the weak coherence from the reduced value of χ_0 lowers T_c. The strong doping dependence can therefore be explained within an electron-phonon mechanism, and there is no need to assume an electronic mechanism.

This demonstrates an unexpected failure mode for Eliashberg theory. The problem is not that $\omega_{ph} \sim W$ (cf. Fig. 11), but that the system is close to a metal-insulator transition. As in Fig. 11, T_c drops as the system approaches a metal-insulator transition, which is not properly described in Eliashberg theory. In Fig. 11, this happened as λ was increased for a fixed doping. Here it happens as the doping is changed for a fixed λ.

Capone et al. [19, 92] have calculated T_c as a function of U for $n = 2$ using exact diagonalization for solving the DMFT equations. They considered a smaller value of λ than above, and found superconductivity only in a small range of U values just before the metal-insulator transition occurs. Their explanation of this behavior was based on the large enhancement of the quasiparticle density of states in the DMFT just before the metal-insulator transition takes place.

6 Summary

As discussed in the introduction, the alkali-doped fullerides are very unusual superconductors in the sense that the electron and phonon energy scales are comparable. One may therefore expect the retardation effects, believed to play a crucial role for conventional superconductors, to be rather small for the fullerides. We have given several different types of argument supporting this point of view. This then raises the issue of why superconductivity is possible for the fullerides. We showed that a surprisingly efficient screening should contribute to reducing the Coulomb repulsion and helping superconductivity. In view of the lack of retardation effects, however, there is little justification for treating the Coulomb repulsion as a weak, empirical Coulomb pseudopotential, as is normally done for conventional superconductors. Instead we used the dynamical mean-field theory. This allowed us to treat the electron-electron and electron-phonon interactions on an equal footing and without assuming that Migdal's theorem is valid. We found that local pairing should be important for superconductivity. This mechanism uses the Jahn-Teller character of the phonons and the fact that the dynamical Jahn-Teller effect favors the formation of a low spin state. This leads to a local pairing of the electrons on a molecule and it is helpful for forming a coherent superconducting state throughout the solid. The Coulomb repulsion helps the local pairing, while it hurts the formation of a coherent state, i.e., the propagation of pairs from one molecule to another. The net results is that superconductivity is surprisingly resistant to the Coulomb repulsion, as illustrated in Fig. 12.

It is interesting to ask if the present theory can explain superconductivity in the fullerides quantitatively. The electron-phonon coupling λ has been estimated from photoemission for free C_{60}^- molecules [95] and estimates of the density of states [96]. This leads to $\lambda \sim 1$. However, we also have to take into account the Hund's rule coupling, which counteracts the Jahn-Teller effect. Both effects are measured by the singlet-triplet splitting seen in the insulating compound A_4C_{60} [97]. This splitting is only about 1/3 of the splitting expected from $\lambda = 1$, and it suggests that the Hund's rule coupling cancels about 2/3 of the electron-phonon coupling. We may then implicitly include the Hund's rule coupling by using $\lambda \sim 0.3$. This assumes that the different frequency dependences of the electron-phonon and Hund's rule couplings enter in a similar way in superconductivity and the singlet-triplet splitting. The value U/W has been estimated to

about 1.5-2.5 and W is about 0.6 eV according to band structure calculations [23]. Using $\lambda = 0.3$, $U/W = 1.5$ and $W = 0.6$ eV we obtain $T_c \sim 15 - 20$ K. This is rather close to the experimental results of $T_c = 19$ K for K_3C_{60} and $T_c = 29$ K for Rb_3C_{60}. Given that we have used a ratio U/W at the lower end of the estimated range, our value for T_c is rather small. It is not necessarily unreasonably small, however, given the uncertainty in the parameters and the simplicity of the model.

References

1. Kroto HW, Heath JR, O'Brien SC, Curl RF, Smalley RE (1985) Nature 318:162
2. Krätschmer W, Lamb LD, Fostiropoulos K, Huffman DR (1990) Nature 347:354
3. Haddon RC, Hebard AF, Rosseinsky MJ, Murphy DW, Duclos SJ, Lyons KB, Miller B, Rosamilia JM, Fleming RM, Kortan AR, Glarum SH, Makhija AV, Muller AJ, Eick RH, Zahuraki SM, Tycko R, Dabbagh G, Thiel FA (1991) Nature 350:320
4. Hebard AF, Rosseinsky MJ, Haddon RC, Murphy DW, Glarum SH, Palstra TTM, Ramirez AP, Kortan AR (1990) Nature 350:600
5. Rosseinsky MJ, Ramirez AP, Glarum SH, Murphy DW, Haddon RC, Hebard AF, Palstra TTM, Kortan AR, Zahurak SM, Makhija AV (1990) Phys Rev Lett 66:2830
6. Holczer K, Klein O, Huang S-M, Kaner RB, Fu KJ, Whetten RL, Diederich F (1991) Science 252:1154
7. Tanigaki K, Ebbesen TW, Saito S, Mizuki J, Tsai JS, Kubo Y, Kuroshima S (1991) Nature 352:222
8. Fleming RM, Ramirez AP, Rosseinsky MJ, Murphy DW, Haddon RC, Zahurak SM, Makhija AV (1991) Nature 352:787
9. Palstra TTM, Zhou O, Iwasa Y, Sulewski PE, Fleming RM, Zegarski BR (1995) Solid State Commun 93:327
10. Chakravarty S, Gelfand M, Kivelson S (1991) Science 254:970
11. Chakravarty S, Kivelson S (1991) Europhys Lett 16:751
12. Baskaran G, Tosatti E (1991) Current Sci 61:33
13. Varma CM, Zaanen J, Raghavachari K (1991) Science 254:989
14. Schluter M, Lannoo M, Needels M, Baraff GA, Tomanek D (1992) Phys Rev Lett 68:526; J Phys Chem Solids 53:1473
15. Mazin II, Rashkeev SN, Antropov VP, Jepsen O, Liechtenstein AI, Andersen OK (1992) Phys Rev B 45:5114
16. Pietronero L, Strässler S (1992) Europhys Lett 18:627; Pietronero L, Strässler S, Grimaldi C (1995) Phys Rev B 52:10516; Grimaldi C, Pietronero L, Strässler S (1995) Phys Rev Lett 75:1158; Phys Rev B 52:10530
17. Bogoliubov NN, Tolmachev VV, Shirkov DV (1958) A new method in superconductivity. Consultants Bureau, New York; Morel P, Anderson PW (1992) Phys Rev 125:1263; Schrieffer JR (1964) Theory of superconductivity. Benjamin, New York; Ginzburg VL, Kirzhnits DA (1982) High-temperature superconductivity. Consultants Bureau, New York
18. Lof RW, van Veenendaal MA, Koopmans B, Jonkman HT, Sawatzky GA (1992) Phys Rev Lett 68:3924
19. Capone M, Fabrizio M, Castellani C, Tosatti E (2002) Science 296:2364
20. Han JE, Gunnarsson O, Crespi VH (2002) Phys Rev Lett 90:167006
21. Ramirez AP (1994) Supercond Rev 1:1
22. Gelfand MP (1994) Supercond Rev 1:103
23. Gunnarsson O (1997) Rev Mod Phys 69:575
24. Sparn G, Thompson JD, Huang S-M, Kaner RB, Diederich F, Wetten RL, Grüner G, Holczer K (1991) Science 252:1829

25. Zhou O, Vaughan GBM, Zhu Q, Fischer JE, Heiney PA, Coustel N, McCauley JP Jr, Smith AB III (1992) Science 255:833
26. Diederich J, Schilling JS, Herwig KW, Yelon WB (1997) J Phys Chem Solids 58:123
27. Rosseinsky MJ, Ramirez AP, Glarum SH, Murphy DW, Haddon RC, Hebard AF, Palstra TTM, Kortan AR, Zahurak SM, Makhija AV (1991) Phys Rev Lett 66:2830
28. Tanigaki K, Hirosawa I, Ebbesen TW, Mizuki J, Shimakawa Y, Kubo Y, Tsai JS, Kuroshima S (1992) Nature 356:419
29. Mizuki J, Takai M, Takahashi H, Mori N, Tanigaki K, Hirosawa I, Prassides K (1994) Phys Rev B 50:3466
30. Yildirim T, Barbedette L, Fischer JE, Lin CL, Robert J, Petit P, Palstra TTM (1996) Phys Rev Lett 77:167
31. Yildirim T, Fischer JE, Dinnebier R, Stephens PW, Lin CL (1995) Solid State Commun 93:269
32. Yildirim T, Barbedette L, Fischer JE, Bendele G, Stephens PW, Lin CL, Goze C, Rachdi F, Robert J, Petit P, Palstra TTM (1996) Phys Rev B 54:11981
33. Kosaka M, Tanigaki K, Prassides K, Margadonna S, Brown CM, Lappas A, Fitch AN (1999) Phys Rev B 59:R6628; Margadonna S, Prassides K, Fitch AN, Kosaka M, Tanigaki K (1999) J Am Chem Soc 121:6318
34. Kerkoud R, Auban-Senzier P, Jerome D, Brazovskii S, Lukyanchuk I, Kirova N, Rachdi F, Goze C (1996) J Phys Chem Solids 57:143
35. Zhou O, Fleming RM, Murphy DW, Rosseinsky MJ, Ramirez AP, van Dover RB, Haddon RC (1993) Nature 362:433
36. Rosseinsky MJ, Murphy DW, Fleming RM, Zhou O (1993) Nature 364:425
37. Zhou O, Palstra TTM, Iwasa Y, Fleming RM, Hebard AF, Sulewski PE, Murphy DW, Zegarski BR (1995) Phys Rev B 52:483
38. Kortan AR, Kopylov N, Glarum S, Gyorgy EM, Ramirez AP, Fleming RM, Thiel FA, Haddon RC (1992) Nature 355:529
39. Baenitz M, Heinze M, Lüders K, Werner H, Schlögl R, Weiden M, Sparn G, Steglich F (1995) Solid State Commun 96:539
40. Brown CM, Taga S, Gogia B, Kordatos K, Margadonna S, Prassides K, Iwasa Y, Tanigaki K, Fitch AN, Pattison P (1999) Phys Rev Lett 83:2258.
41. Iwasa Y, Takenobu T (2003) J Phys Condens Matter 15:R495.
42. Özdas E, Kortan AR, Kopylov N, Ramirez AP, Siegrist T, Rabe KM, Bair HE, Schuppler S, Citrin PH (1995) Nature 375:126
43. Mitrovic B, Zarate HG, Carbotte JP (1984) Phys Rev B 29:184
44. Carbotte JP (1990) Rev Mod Phys 62:1027
45. Zhang Z, Chen C-C, Kelty SP, Dai H, Lieber CM (1991) Nature 353:333
46. Jess P, Hubler U, Behler S, Thommen-Geiser V, Lang HP, Güntherodt H-J (1996) Synthetic Metals 77:201
47. Koller D, Martin MC, Mihaly L (1996) Phys Rev Lett 77:4082
48. Tycko R, Dabbagh G, Rosseinsky MJ, Murphy DW, Ramirez AP, Fleming RM (1992) Phys Rev Lett 68:1912
49. Sasaki S, Matsuda A, Chu CW (1994) J Phys Soc Jpn 63:670
50. Auban-Senzier P, Quirion G, Jerome D, Bernier P, Della-Negra S, Fabre C, Rassat A (1993) Synthetic Metals 56:3027
51. Stenger VA, Pennington CH, Buffinger DR, Ziebarth RP (1995) Phys Rev Lett 74:1649
52. Kiefl RF, MacFarlane WA, Chow KH, Dunsiger S, Duty TL, Johnston TMS, Schneider JW, Sonier J, Brard L, Strongin RM, Fischer JE, Smith AB III (1993) Phys Rev Lett 70:3987
53. Degiorgi L, Wachter P, Grüner G, Huang S-M, Wiley J, Kaner RB (1992) Phys Rev Lett 69:2987; Degiorgi L, Briceno B, Fuhrer MS, Zettl A, Wachter P (1994) Nature 369:541; Degiorgi L (1995) Mod Phys Lett B 9:445

54. Gu C, Veal BW, Liu R, Paulikas AP, Kostic P, Ding H, Gofron K, Campuzano JC, Schlueter JA, Wang HH, Geiser U, Williams JM (1994) Phys Rev B 50:16566
55. Hesper R, Tjeng LH, Heeres A, Sawatzky GA (2000) Phys Rev Lett 85:1970
56. Chen C-C, Lieber CM (1992) J Am Chem Soc 114:3141
57. Chen C-C, Lieber CM (1993) Science 259:655
58. Fuhrer MS, Cherrey K, Zettl A, Cohen ML (1999) Phys Rev Lett 83:404
59. Ebbesen TW, Tsai JS, Tanigaki K, Hiura H, Shimakawa Y, Kubo Y, Hirosawa I, Mizuki J (1992) Physica C 203:163
60. Burk B, Crespi VH, Zettl A, Cohen ML (1994) Phys Rev Lett 72:3706
61. Tinkham, M (1996) Introduction to superconductivity. McGraw-Hill, New-York
62. Holczer K, Klein O, Grüner G, Thompson JD, Diederich F, Whetten RL (1991) Phys Rev Lett 67:271
63. Sparn G, Thompson JD, Whetten RL, Huang S-M, Kaner RB, Diederich F, Grüner G, Holczer K (1992) Phys Rev Lett 68:1228
64. Boebinger GS, Palstra TTM, Passner A, Rosseinsky MJ, Murphy DW, Mazin II (1992) Phys Rev B 46:5876
65. Holczer K, Whetten RL (1992) Carbon 30:1261
66. Ramirez AP, Rosseinsky MJ, Murphy DW, as quoted in Ramirez AP (1994) Superconductivity Rev 1:1
67. Uemura YJ, Keren A, Le LP, Luke GM, Sternlieb BJ, Wu WD, Brewer JH, Whetten RL, Huang SM, Lin S, Kaner RB, Diederich F, Donovan S, Grüner G, Holczer K (1991) Nature 352:605
68. Uemura YJ, Lee LP, Luke GM (1993) Synthetic Metals 55/57:2845
69. Buntar V, Weber HW (1996) Superconductor Sci Technol 9:599
70. Ramirez AP, Kortan AR, Rosseinsky MJ, Duclos SJ, Mujsec AM, Haddon RC, Murphy DW, Makhija AV, Zahurak SM, Lyons KB (1992) Phys Rev Lett 68:1058
71. Burkhart GJ, Meingast C (1996) Phys Rev B 54:R6865
72. Hou JG, Crespi VH, Xiang XD, Vareka WA, Briceno G, Zettl A, Cohen ML (1993) Solid Sate Commun 86:643
73. Hou JG, Xiang XD, Crespi VH, Cohen ML, Zettl A (1994) Physica C 228:175
74. Stephens PW, Mihaly L, Lee PL, Whetten RL, Huang S-M, Kaner R, Deiderich F, Holczer K (1991) Nature 351:632
75. Gunnarsson O, Satpathy S, Jepsen O, Andersen OK (1991) Phys Rev Lett 67:3002
76. Mazin II, Liechtenstein AI, Gunnarsson O, Andersen OK, Antropov VP, Burkov SE (1993) Phys Rev Lett 70:4142
77. Gunnarsson O, Erwin SC, Koch E, Martin RM (1998) Phys Rev B 57:2159
78. Lannoo M, Baraff GA, Schlüter M, Tomanek D (1991) Phys Rev B 44:12106
79. Gunnarsson O (1995) Phys Rev B 51:3493
80. Anderson PW (1991) preprint
81. Gunnarsson O, Zwicknagl G (1992) Phys Rev Lett 69:957; Gunnarsson O, Rainer D, Zwicknagl G (1992) Int J Mod Phys B 6:3993
82. Koch E, Gunnarsson O, Martin RM (1999) Phys Rev Lett 83:620
83. Grabowski M, Sham LJ (1984) Phys Rev B 29:6132
84. ten Haaf DFB, van Bemmel HJM, van Leeuwen JMJ, van Saarloos W, Ceperley DM (1995) Phys Rev B 51:353; van Bemmel HJM, van Haaf DFB, van Saarloos W, van Leeuwen JMJ, An G (1994) Phys Rev Lett 72:2442
85. Metzner W, Vollhardt D (1989) Phys Rev Lett 62:324; Jarrell M (1992) Phys Rev Lett 69:168; Georges A, Kotliar G, Krauth W, Rozenberg MJ (1996) Rev Mod Phys 68:13.
86. Blankenbecler R, Scalapino DJ, Sugar RL (1981) Phys Rev D 24:2278
87. Fye RM, Hirsch JE (1988) Phys Rev B 38:433
88. Freericks JK (1994) Phys Rev B 50:403
89. Tahvildar-Zadeh AN, Hettler MH, Jarrell M (1998) Phil Mag B 78:365

90. Bourgoin J, Lanno M (1983) Point defects in semiconductors II. Springer Series in Solid-State Sciences 35. Springer, Berlin Heidelberg New York
91. McMillan WL (1968) Phys Rev 167:331
92. Capone M, Fabrizio M, Tosatti E (2001) Phys Rev Lett 86:5361; (2002) J Phys Chem Solids 63:1555.
93. Gelfand MP, Lu JP (1992) Phys Rev Lett 68:1050
94. Han JE, Koch E, Gunnarsson O (2000) Phys Rev Lett 84:1276
95. Gunnarsson O, Handschuh H, Bechthold PS, Kessler B, Ganteför G, Eberhardt W (1995) Phys Rev Lett 74:1875.
96. Aryasetiawan F, Gunnarsson O, Koch E, Martin RM (1997) Phys Rev B 55:R10165
97. Lukyanchuk I, Kirova N, Rachdi F, Goze C, Molinie P, Mehring M (1995) Phys Rev B 51:3978

Struct Bond (2005) 114: 103–141
DOI 10.1007/b101018

Pairing Mechanisms Viewed from Physics and Chemistry

S. Deng · A. Simon (✉) · J. Köhler

Max-Planck-Institut für Festkörperforschung, Heisenbergstrasse 1, 70569 Stuttgart, Germany
s.deng@fkf.mpg.de, a.simon@fkf.mpg.de, j.koehler@fkf.mpg.de

Abstract Through inspecting the limitations of BCS theory we give a brief review on the microscopic theories of superconductivity. Three basic pairing models have been extracted from the reviewed theories. The flat/steep band model developed from a viewpoint of chemical pairwise interactions is described and explained. The conditions for the occurrence of a flat electronic band within the framework of band theory is discussed together with examples. Characteristic peak-like structures of the electron-phonon coupling, as expected from the model, are shown to occur for conventional superconductors. The functional Psib(Ψ) is introduced to relate chemical pairwise interaction with superconductivity. Investigations on experimental and theoretical low-energy electronic structures of superconductors, from simple elements to complicated cuprates, support our flat/steep band condition.

Keywords Superconductivity · Flat steep band · Pairing mechanism

List of Abbreviations and Symbols

ARPES	Angle-Resolved Photo-Emission Spectroscopy
AS	Assumption
BCS	Bardeen, Cooper, Schrieffer
B-E	Bose-Einstein
BZ	Brillouin Zone
CDW	Charge Density Wave
CI	Configuration Interactions

COHP	Crystal Orbital Hamiltonian Population
DDW	d-Density Wave
dHvA	de Haas van Alphen
DMFT	Dynamic Mean Field Theory
DOS	Density of States
e-p	Electron-phonon
FP	Full Potential
LDA	Local Density Approximation
LMTO	Linear Muffin Tin Orbital
NAFL	Nearly Antiferromagnetic Liquid
RVB	Resonant Valence Bond
TB	Tight Binding
T_c	Superconducting transition temperature
vHs	van Hove Singularity

1 Introduction

Since the discovery of the first superconductor Hg [1], scientists have been trying to explore the microscopic origin of superconductivity. Inspired by the classical work of London [2], earlier efforts tried to establish a relation between superconductivity of the then discovered superconductors and Bose-Einstein (B-E) condensation. To our knowledge, it was Ogg [3] who first proposed that paired electrons in superconductors can be viewed as bosons. Based on similar ideas, Schafroth et al. developed their real space approach to superconductivity [4]. Though it was demonstrated experimentally [5, 6] and theoretically [7, 8] that phonons are involved in superconductivity, it remained unclear why repulsively interacting conduction electrons can be paired until Bardeen, Cooper and Schrieffer developed their milestone BCS theory [9]. The following smooth experimental and theoretical development was interrupted in 1986 with the discovery of high T_c cuprates [10]. Since then a large number of models and scenarios have been proposed, however, up to now with no convergence.

In this review we will first give a brief survey of the most common microscopic theories by summarizing the limitations of BCS theory. In the second part our focus will lie on aspects beyond the BCS theory and in particular on new pairing mechanisms for electrons or holes. In the third part we will turn to a viewpoint of chemistry in order to analyze the origin of pairing. The long established formalism of drawing a line between atoms to describe the singlet electron or hole pair state in a covalent bond serves as a starting point, associating the pairwise attraction between charge carriers of equal sign with a tendency towards their localization. Some superconducting layered rare earth carbide halides are model systems to illustrate and test this idea [11]. They are metallic, however, with slight modifications they become semiconductors. In terms of the electronic band structure, these materials are characterized by highly dispersive bands as well as flat bands at the Fermi level. In our qualita-

tive picture the flat band states are essential in providing electrons (holes) of vanishing velocity, and the presence of steep bands is essential to keep the structure undistorted and to avoid localization. We introduce our flat/steep band model developed by considering the pairwise interaction of electrons (holes) in terms of chemical bonding. The assumptions and the main approximations for this model will be explicitly outlined. Then we will list and explain conditions in the framework of band theory for the occurrence of a flat band. The flat/steep band condition will be tested with the calculated and experimental low-energy electronic structures of superconductors from simple to complex. We present a peak-like structure of the electron-phonon coupling, a result expected from our model when applied to the phonon mediated superconductors. Finally we summarize and discuss our preliminary results to show the relation between chemical pairwise interaction and electron-phonon coupling.

2
BCS Theory and Beyond

BCS theory is a field theoretical approach to an electron-phonon system in which an effective attraction mediated by phonons results in a phase coherent pair condensate [9]. This theory explains many properties of conventional superconductors such as the isotope effect, Meissner effect [12], and the characteristic electronic specific heat, etc. The reduced BCS model Hamiltonian reads

$$H_{BCS} = \sum_{\mathbf{k},\sigma} \varepsilon_{\mathbf{k}} c^{+}_{\mathbf{k}\sigma} c_{\mathbf{k}\sigma} + \sum_{\mathbf{k},\mathbf{k}'} V_{\mathbf{k},\mathbf{k}'} c^{+}_{\mathbf{k}\uparrow} c^{+}_{-\mathbf{k}\downarrow} c_{-\mathbf{k}'\downarrow} c_{\mathbf{k}'\uparrow} , \tag{1}$$

where ε_k is the single electron energy measured relative to the Fermi level and $C^{+}_{\mathbf{k}}$, $C_{\mathbf{k}}$, are the electron creation and annihilation operators, respectively, based on Bloch states specified by wave vector **k** and spin σ. The non-diagonal matrix elements $V_{\mathbf{k},\mathbf{k}'}$ denote the effective electron-electron attraction, which includes the screened Coulomb interaction and the phonon mediated electron-electron interaction; see Fig. 1a. A coherent paired state of electrons appears in this model when the indirect attractive interaction dominates the repulsive Coulomb interaction, i.e., $V_{\mathbf{k},\mathbf{k}'}$ is negative, and superconductivity is possible.

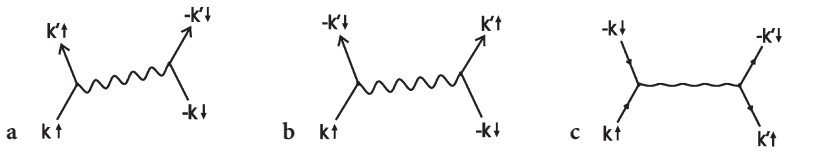

Fig. 1a–c Schematic representations for the pairing mechanisms of electrons: **a** the effective electron-electron (**k**↑,–**k**↓) interactions mediated by phonons, the shown retarded effect was not considered in the original BCS theory; **b** the pairing of electrons mediated by magnon-like or spin fluctuation exchange; **c** the decaying and recombination process of a boson and a pair of electrons

Within BCS theory superconductivity is described as a simultaneous creation and condensation of Cooper pairs instead of a B-E condensation of preformed pairs. The reason is that the size of a Cooper pair given by the coherence length is too large to define it as a composite boson in real space. Within BCS theory the electrons pair in momentum space. The prerequisite of electron (hole) pairing remains necessary [13] even for other so-called exotic [14] superconductors such as organic [15], heavy-fermion [16] and high T_c superconductors [10], where BCS theory is generally thought to be inappropriate or at least needs to be modified. The limitations of BCS theory and its strong coupling extension according to Eliashberg and Migdal [17, 18] can be roughly divided into the following categories.

2.1 Gap Symmetry, Non-Phononic Pairing and Inhomogeneity

1. The superconducting gap or the pair wave function in the BCS model has s-wave symmetry. However, as pointed out in the original work [9c], the possibility of non-zero angular momentum (l≠0), in particular, spin triplet l=1 pairing exists, e.g. the symmetry of the pair wave function in helium-3 [19] is known to be p-like due to spin fluctuation mediated interaction. The gap symmetry of high T_c cuprates and organic superconductors still remains controversial. Although there is clear evidence for gap nodes in hole-doped cuprates and heavy-fermion systems [20] the experimental single particle gap as determined by ARPES measurements is not necessarily identical to the superconducting gap. As pointed out by Randeria et al. [21] the superconducting gap function is different from the single particle energy gap if the chemical potential lies below the bottom of the conduction band, which further complicates the gap problem.
2. In the BCS model, the basis of electron pairing, i.e., the electron-phonon coupling sets a limit to the energy of the electrons which are involved in superconductivity. The energy difference between the electronic states should be less than the phonon energy, $\hbar\omega_D$, where ω_D is the Debye frequency. This limitation was challenged soon after the establishment of BCS theory by considering coupling via quasi-bosons like, e.g., excitons, plasmons etc. [22–25]. In such models, the transition temperature is set by the electronic excitations with frequencies ω_e [23e] which are considerably larger than the Debye frequency ω_D, thus allowing much higher T_cs than within the phononic mechanism.
3. In the original BCS model, band effects were neglected. An important band effect may be the superconducting multi-gap structure as predicted [26, 27] shortly after the establishment of BCS theory. This prediction, actually a two-gap situation, was definitely confirmed for the superconductor MgB_2 [28–30], as will be discussed later. One further multiband effect is the enhancement of T_c even within the BCS framework as first emphasized by Lee and Ihm [31] in their two-band model for the high T_c superconductor

$La_{2-x}(Ba,Sr)_xCuO_4$. Other multiband effects showing up in gap anisotropy, ultrasonic attenuation, thermodynamic critical field, isotope effect etc. due to the inter-band interactions have also been studied, however mainly within the context of high T_c superconductivity [32]. In fact the band effects can be viewed as some kind of "inhomogeneity phenomenon" at the unit cell level, i.e. different types of atoms distribute inhomogeneously within the unit cell and this results in more complicated band structures than assumed in the original BCS model. A detailed discussion on this aspect will be given elsewhere.

The inhomogeneity of a system can be considered as a symmetry breaking which is quantitatively described by an order parameter field [33] such as the magnetization $\mathbf{M}(\mathbf{r})$ for a magnet and the energy gap function $\Delta(\mathbf{r})$ for a superconductor. Long before the discovery of high T_c cuprates it has already been observed that other order parameters may compete or coexist with the superconducting one. Examples include $ErRh_4B_4$ [34] (ferromagnetic order), $ErMo_6S_8$ [34] (antiferromagnetic order), $Gd_xTh_{1-x}Ru_2$ [35] (spin-glass magnetic freezing) and $BaPb_{1-x}Bi_xO_3$ [36] (charge density wave; CDW) etc., which obviously is beyond BCS theory and its strong-coupling extensions. For such superconductors, there has been no simple formula for calculating T_c as derived, e.g., by McMillan [37]. The discovery of high T_c cuprates added a particularly interesting case of a competing, coexisting or even supporting order parameter. The new family of superconductors originates from doping the antiferromagnetic parent insulators such as La_2CuO_4 [38]. Here another possible consequence of electronic inhomogeneity, phase separation, entered the focus of interest. As pointed out by Gor'kov et al. [39] in their two component model for high T_c cuprates, this can happen either dynamically or statically.

The stripe phase as first revealed theoretically within the Hartree-Fock approximation of the Hubbard model [40] and later confirmed by experiments [41] on high T_c cuprates created enormous interest in the problem of spin and charge separation in a superconducting system. Models were proposed to explain high T_c superconductivity on the basis of fluctuating stripes [42] or charge fluctuations [43]. The inhomogeneity observed experimentally at a nano-scale level for high T_c cuprates is due to electronic phase segregation [38, 41]. However, there are indications for chemical phase separation as well [44]. In this case a percolation approach could be appropriate to describe the relevant phenomena as pointed out by Gor'kov et al. [45] for $A_{1-x}B_xMnO_3$ type manganates. More recently high T_c superconductivity has been studied as a quantum critical phenomenon, in which the quantum critical point, defined as a point where various ground states with different symmetries and order parameters coincide at T=0, plays an essential role [46].

2.2 Property of Charge Carriers

A basic limitation of BCS theory is due to its foundation on the Landau Fermi liquid theory [47]. In the framework of Landau's theory, the excitation energy $\varepsilon(\mathbf{k},\mathrm{s})$ of a quasiparticle is

$$\varepsilon(\mathbf{k},\mathrm{s}) = \varepsilon_0(\mathbf{k},\mathrm{s}) + \sum_{\mathbf{k}'\mathrm{s}'} f(\mathbf{k}\mathrm{s},\mathbf{k}'\mathrm{s}')\, n_{\mathbf{k}'\mathrm{s}'} \tag{2}$$

where $f(\boldsymbol{k}\mathrm{s},\boldsymbol{k}'\mathrm{s}')$ is the interaction between the quasiparticles, and $n_{\mathbf{k}'\mathrm{s}'}$ is the occupation number of a quasiparticle state $|\mathbf{k}'s'\rangle$. The description within the quasiparticle picture of interacting Fermions holds only for a well defined quasiparticle:

$$1/\tau \ll |\varepsilon(\mathbf{k},\mathrm{s}) - \mu|, \tag{3}$$

where τ is the lifetime of the quasiparticle, $\varepsilon(\mathbf{k},\mathrm{s})$ is the excitation energy and μ is the chemical potential. The criterion at Eq. (3) was later replaced by a less stringent condition [48],

$$1/\tau \ll \varepsilon_F\,. \tag{4}$$

The above inequality is satisfied by conventional elemental metals or metallic compounds where the quasiparticle quasiparticle interaction is relatively weak. For systems in which the quasiparticles are strongly correlated, or, in case of novel elementary excitations due to special topology, such as low dimensionality, the Fermi liquid description becomes inappropriate. There have been a number of compounds [13, 49], e.g. TiS_2, $Hg_{2.86}AsF_6$, BEDT-TTF, in which the behavior of the charge carriers is difficult to explain within the Fermi liquid theory. For high T_c cuprates, the frequency dependent relaxation rate $1/\tau$ is an important signal for the breakdown of Fermi liquid theory, because it implies a vanishing quasiparticle amplitude. Other experimental evidences have been repeatedly reviewed in the literature [13, 49]. Though there is still controversy concerning this point [50], it is safe to say that Landau's Fermi liquid theory in its unmodified form is not suitable to describe the cuprates. One proposed substitute of Fermi liquid theory to describe the normal state of cuprates is the Luttinger liquid theory [51] in which the inter-particle interactions are treated on the same basis as the one-body kinetic energy. In the Luttinger liquid model there still exists a Fermi surface which encloses a volume equal to that of non-interacting particles. However, this Fermi surface is not related to electron- or hole-like particles. The internal degrees of freedom (spin, charge) of an electron are decoupled, and thus the low-energy elementary excitations of such a special system have two branches. One belongs to the spinon (s=1/2, e=0), the other to the holon (s=0, e=1). Because of this charge-spin separation, the low-energy physics of a Luttinger liquid differs dramatically from that of a Fermi liquid [52].

New theories on high T_c cuprates can be roughly classified into two types (A and B) according to their use of Fermi liquid or other theories and their

relation to BCS theory. Included in the type A are (among others) Anderson's *RVB* theory [53], Varma et al's *marginal Fermi liquid* theory [54], Lee, Wiegmann et al's *gauge* theories [55], Laughlin et al's *flux and anyon* theories [56], Emery et al's *1D stripe* theory [57], Chakravarty and Laughlin's *d-density wave* theory [58]. Within the type B there are the *spin bag* theory of Schrieffer et al. [59], the *spin-polaron* theory initiated by Kamimura, Wood, Mott, et al. [60], the *antiferromagnetic Fermi liquid* theory of Pines et al. [61], the *van Hove singularity* (vHs) scenario pursued by Friedel, Bok, Newns, Markiewicz et al. [62]. The *bipolaron* theory of Alexandrov et al. [63] and the *two component* theory of Ranninger, Micnas et al. [64] do not rely on the Fermi liquid description as other conservative theories of type B. However, the bosons in both theories originate from strong electron-phonon interactions or attractive U. Thus these theories can be considered to lie between the two categories.

The above classification is not strict and complete, because many theories in the list are also based on other considerations, namely, the gap symmetry, pairing mechanism and inhomogeneity. Roughly speaking, the theories in group A are based on a breakdown of the Fermi liquid theory in describing the normal state of high T_c cuprates. In particular, some of these theories (RVB, anyon, etc.) unambiguously advocate that there are no well defined quasiparticles (s=1/2, e=±1) since the relaxation rate $1/\tau$ is close to infinity. In other words, the renormalization constant of the quasiparticles,

$$Z = \left(1 - \frac{\partial \Sigma}{\partial \omega}\right)^{-1}, \tag{5}$$

is set to Z=0, where Σ is the self-energy of a quasiparticle. The elementary excitation is considered to be of collective character or some kind of soliton. In [53b] Anderson listed many experimental evidences for Z=0. Hence he treats the condition as a necessary basis for a correct theory of high T_c cuprates. In his RVB theory, the pairing of charge carriers is determined by the incoherent interlayer hoping $t_\perp$ in two possible processes. One is the so-called superexchange mechanism of magnetic coupling between the copper oxygen planes, which can be described by the following effective Hamiltonian:

$$H_{SE} = \sum_{\mathbf{k}} \lambda_{SE}^{\mathbf{k}} c_{\mathbf{k}\uparrow}^{+}(1)\, c_{-\mathbf{k}\downarrow}^{+}(2)\, c_{-\mathbf{k}\downarrow}(1)\, c_{\mathbf{k}\uparrow}(2), \tag{6}$$

where 1, 2 indicate neighboring layers, $\lambda_{SE}^{\mathbf{k}}$ is the superexchange parameter depending on $t_\perp$ and the energy E_{n} of a virtual high energy intermediate state. The other process is the Josephson like pair hopping described by

$$H_J = \sum_{\mathbf{k}} \lambda_J^{\mathbf{k}} c_{\mathbf{k}\uparrow}^{+}(1)\, c_{-\mathbf{k}\downarrow}^{+}(1)\, c_{-\mathbf{k}\downarrow}(2)\, c_{\mathbf{k}\uparrow}(2), \tag{7}$$

where $\lambda_J^{\mathbf{k}}$ is the tunneling parameter for pairs also depending on $t_\perp$ and E_{n}. The first process involves only a spinon, while the second one only involves the exchange of a holon. Both processes are very different from those considered in the BCS framework. The pairing energy in this model originates physically from the kinetic energy loss due to the confinement of electrons in the Luttinger

liquid. It is claimed by the authors of this theory [53] that it provides reasonable explanations for the unusual normal and superconducting state properties. However, whether there exists really spin-charge separation in the CuO_2 plane has remained very controversial, both theoretically and experimentally [50, 65]. Theoretically the spin-charge separation is not strictly justified in a 2D system as opposed to a 1D system [51, 52], and there have been many alternative explanations for the various anomalous experimental findings. In addition, the inhomogeneity problem of the cuprates is not fully taken into account in this theory, and it has not been developed to the level of the BCS theory for conventional superconductors with respect to the gap equation etc. [66]. The *marginal Fermi liquid*, the *anyon*, and the *gauge* theory have been compared to the *RVB* theory in detail [53b]. The theory developed by Emery el al. [57] is based on an array of 1D stripes and spin-charge separation. The newly proposed *d-density wave* (*DDW*) theory carries characteristics of *staggered flux state* theories [67] and phenomenologically introduces *DDW* as a local order parameter which describes the so-called orbital antiferromagnetism [68]. This theory is interesting, because it naturally includes aspects of inhomogeneity by considering the competition of different order parameters, and the pseudogap is explained as a one-particle gap due to the development of *DDW*. The non-Fermi liquid property of the normal state of high T_c cuprates is suggested to reflect the high temperature behavior of a nearby quantum critical point [46b]. The pairing of charge carriers is caused by the same reason as in many approaches based on the t-J model, namely a nominal Heisenberg exchange.

The theories in the conservative group maintain at least the quasiparticle picture for the charge carriers. For example, in the *spin bag* and *spin polaron* theories the concept of quasiparticles in the traditional sense (having charge ±e, spin 1/2) still holds. In the former case, the *spin bag* is an object centered by a hole and surrounded by a dressing cloud which suppresses the amplitude and twists the quantization axis of the local antiferromagnetic order. The pairing of such *spin bags* is due to reduced exchange energy costs of a two-hole bag as compared to that as a one-hole bag. Though *spin bag* and *spin polarons* are very similar, the concept of *spin polaron* has a much longer history as it dates back to Zener's early work on the *double-exchange* mechanism in manganese oxides [69]. The main difference between *spin bag* and *spin polaron* lies in the fact that the former is based on the one-band Hubbard model [70] while the latter is based on the multiband *t-J* model. Correspondingly, the pairing interaction in the former case depends on the self-exchange energy U, while in the latter case it depends on the effective Heisenberg exchange J involving different orbitals [13]. The one-band Hubbard model is given by

$$H = -t \sum_{\langle i,j\rangle\sigma} (c^{+}_{i\sigma} c_{j\sigma} + H.c.) + U \sum_i n_{i\sigma} n_{i-\sigma}, \tag{8}$$

where U is the on-site Coulomb repulsion, $n_{i\sigma}=c^{+}_{i\sigma} c_{i\sigma}$ is the density operator for electrons at site i, and the summation is performed with respect to the nearest neighbor sites on a square lattice. This model is considered to contain the essential physics of high T_c cuprates [53]. For $U \gg t$, in the strong correlation

limit, the doubly occupied states can be projected out from the Hilbert space through the Schrieffer-Wolff [71] canonical transformation on Eq. (9) [72]. Then one obtains the t-J model,

$$H = -t \sum_{\langle i,j\rangle \sigma} (P_i^{\sigma} c_{i\sigma}^{+} c_{j\sigma} P_j^{\sigma} + H.c.) + J \sum_{\langle i,j\rangle} (S_i \cdot S_j - 1/4\, n_i n_j), \quad (9)$$

where $P_i^{\sigma} = 1 - n_{i,-\sigma}$ is the projection operator which excludes double occupancy, $J = 4t^2/U$ is the nearest neighbor Heisenberg exchange integral, and S_i is the spin operator. Equations (9) and (10) can easily be extended to include the second nearest neighbor interactions or multiband effects as in the *marginal Fermi liquid* [54, 73] and other theories [74]. However, as first shown by Zhang and Rice [75] the higher-energy hybridized orbitals in the multiband models can be completely down-folded [76] to result in an effective one-band model based on the Cu-3 $d_{x^2-y^2}$, O-2 p_{σ} hybrid. In this sense, the concepts of *spin bag* and *spin polaron* are physically connected. The pairing of the *spin polarons* can be mediated through the exchange interaction as shown in Fig. 1b. In the *t-J* model, vertex corrections are suppressed and the exchange interaction is repulsive when the pair wave function has s-symmetry. It can become attractive with p,d symmetry. Because of this reason magnetic mechanisms favor d-wave superconductivity in high T_c cuprates. The existence of spin bipolarons or bound states of two holes, or incoherent pairs as discussed in literature is still controversial. Recent studies do not seem to support the B-E condensation of preformed d-wave pairs [77].

Though the spin fluctuation theory as introduced by Pines et al. [61] belongs to type B, it is not based on simple Fermi liquid theory. In this approach, a new energy scale is set by ω_{sf}, the spin fluctuation energy, which is much smaller than the Fermi energy, above which quasiparticles should be described within the nearly antiferromagnetic Fermi liquid theory (NAFL). In particular, this upper energy scale for the Fermi liquid behavior shrinks with the system approaching a quantum-critical point at $T=0$, where the renormalization factor Z of a quasiparticles is zero [61d].

In NAFL, the dominant interaction between the quasiparticles is caused by the emission and absorption of a collective soft spin. Due to this kind of overdamped spin fluctuation the quasiparticles pair incoherently at the pseudo-gap and coherently at T_c (see Fig. 1b). When considering the spin-fermion coupling, this theory uses the Eliashberg-like ansatz. The generic model Hamiltonian of this theory is also of the one-band Hubbard-type. One of the limitations of this theory is that it is not applicable to the underdoped cuprates, besides some other problems [53b, 61d].

In deriving the gap equation, BCS assumed a density of states (*DOS*) around the Fermi level that is a slowly varying function of energy. This is not realized for most real materials, since there are often peaks near the Fermi level. The vHs scenario [62] emphasizes the role of such peaks in the low-energy physics of a system. That this scenario belongs to the conventional group is obvious, because it is still based on the framework of BCS theory. The origin of the pairing of quasiparticles is not explicitly specified as phonon mediated, and correlation effects

are also considered in the renormalization of quasiparticles in the recent development of this scenario [62e].

Motivated by the experimental findings for $LiTi_2O_4$ and Ti_4O_7 etc. [78], the theory of bipolaronic superconductivity was proposed [63a] shortly after 1980 before the discovery of high T_c materials. This theory is based on the concepts of polarons [79] and bipolaron [78, 80]. Under the condition of $\Delta > W$, where Δ denotes the dissociation energy of a bipolaron and W the polaron band width, the small bipolaron can be stable. As the small bipolaron is a hard core boson, the low-energy physics of a bipolaronic system can not be described by Fermi liquid theory. The superconductivity of such a system occurs due to B-E condensation of bipolarons. In the last few years this theory has been further developed; however, whether it can be applied to the high T_c cuprates is still a controversial matter. The arguments against it from both experimental and theoretical points of view were listed and discussed by Anderson et al. [53b, 81]. Another objection concentrates on the issue of whether or not the itinerant small bipolaron is stable against a decay into two small polarons [82]. In spite of this complication studies on the crossover from BCS to B-E condensation have repeatedly proven that superconductivity of high T_c cuprates falls into the intermediate regime instead of the B-E condensation limit [83].

Soon after the advancement of the bipolaronic theory, Ranninger et al. [64a] considered the possibility of a bipolaron decaying into a pair of electrons and the reverse. They started from a two-component scenario of itinerant (wide band) and local pair electronic states and their mutual hybridization. In fact, such a hybridization had been proposed phenomenologically by Rumer [84] long before the discovery of high T_c superconductivity. The physics behind it even dates back to Anderson's s-d mixing model [85]. By introducing the hybridization term, the final Hamiltonian for this fermion-boson or two-component model reads as

$$H = (zt - \mu) \sum_{i,\sigma} c^+_{i\sigma} c_{i\sigma} - t \sum_{\langle i \neq j \rangle, \sigma} c^+_{i\sigma} c_{j\sigma} + (\Delta_B - 2\mu) \sum_i b^+_i b_i + \nu \sum_i [b^+_i c_{i\downarrow} c_{i\uparrow} + c^+_{i\uparrow} c^+_{i\downarrow} b_i], \tag{10}$$

where z is the nearest-neighbor coordination number of an effective lattice site i, t the bare hopping integral of electrons, μ the chemical potential, c and b the electron and boson operators, respectively, Δ_B is the energy level of the bipolaron and ν the bipolaron fermion exchange coupling constant. The hybridization term schematically shown in Fig. 1c facilitates the bipolaron hopping processes and, in addition, polarizes electrons in the wide band into Cooper pairs, which thus provides an additional channel for the superconducting ground state [64]. The model is discussed in detail by A. Bussmann-Holder et al. in this volume.

Rather similar models have been intensively studied by different groups [39, 86, 87]. It is obvious that the low-temperature physics in this model is determined by the relative concentrations of the fermions and bosons. A local

vibrational mode which strongly couples to the electrons is the origin of the bipolaron formation.

So far we have, by inspecting the gap symmetry, pairing mechanisms, coexistence of competing orders and the low-energy excitation, made a brief survey of the current most common microscopic theories of superconductivity. Among these four aspects the latter two are most fundamental, since the gap symmetry and the pairing mechanism depend on the characteristics of the low-energy excitation of a system. The survey describes a "tree-like" structure for the microscopic theories of superconductivity with *pairing* of charge carriers as the main stem. Remarkably the Ginzburg-Landau equation derived from a purely phenomenological approach implies the result that paired electrons are the charge carriers of the supercurrent [88a]. It became obvious only after Gor'kov introduced the microscopic explanations for this equation [88b, c].

The pairing mechanisms as proposed in these theories can be divided into three classes, which can be illustrated by the following "reactions",

a) $e + X\text{-on} + e \rightarrow B$

b) $e + \Psi + e \rightarrow B$

c) $e + e \rightarrow B$

where B in all cases denotes a Cooper pair in the superconducting state, e represents a fermion (e=±1, s=1/2), X-on means collective bosonic excitations such as phonon, magnon, exciton, etc. Obviously, BCS, spin fluctuation, spin-polaron theories etc. belong to class 1.; Ψ in class 2. represents an intermediate quantum state or states by means of which two electrons (holes) pair. The energy gain in this case is purely a quantum feedback effect associated with the pairing. The RVB theory and the midinfrared scenario [89] are in this category. Case 3. represents a total "reaction" of $e+e \leftrightarrow B'$ [86] and $e+e+B' \leftrightarrow 2B$ where B′ represents a preformed pair (boson) which coexists with fermions e. The bipolaron theory, the two component theories etc. belong to this class.

3
Chemical Bonding and Superconductivity

It is evident from the brief review on current microscopic theories of superconductivity that the pairing of electrons (holes) is a central issue. However, the origins for pairing are quite different among these theories. In many of them explanations are sought within physical concepts like the Fermi and Luttinger liquid concept which do not take into account the specific chemical bonding in a superconductor, a criticism that was raised against BCS theory by Matthias [90]. Indeed, the question of what kind of atoms have to be combined in what kind of structure in order to result in a superconductor is still a matter of serendipity.

An intimate connection between chemical bonding and superconductivity is not too obvious, since the former has an energy scale of nearly two orders larger than the latter. However, early on Bilz drew attention to what he later called dynamical covalency [91]. As exemplified for the then discovered high T_c superconductors of rocksalt- and A15-type the (d+p)π mixing of transition metal d and non-metal p states at the Fermi level is important. The resonance-like enhancement of the non-local dielectric response leads to strong electron-phonon coupling seen as a tendency towards electronic localization by a characteristic lowering of certain phonon frequencies.

Along this line, a model system for superconductivity was found in the 2-D metallic rare earth carbide halides, $RE_2C_2X_2$, mentioned in the introduction [11, 92]. As shown in Fig. 2a quasi molecular C_2 units are surrounded by layers of M atoms followed by layers of X atoms. Such layer packages can be stacked in different ways.

Independent of the stacking sequence the transition temperature to the superconducting state is a smooth function of the size of the metal atom cage around the C_2 unit; see Fig. 2b. Hence, both the origin of the metallic character of the compounds as well as the origin for the electron pairing has to be sought in the chemical bonding within one layer. Strictly speaking the phases $RE_2C_2X_2$ are valence compounds, and they might be expected to be semiconductors. However, due to an overlap of the occupied C_2-π^* states with empty metal d states (backbonding), electronic delocalization arises, similar to the bonding in rare earth carbides or even somewhat similar to the bonding situation in oxocuprates though with a charge transfer in opposite direction. The origin of electron pairing is seen as arising from the presence of C_2-π^* states mixed with M-d states at the Fermi level.

Evidence for the importance of this condition is presented in Fig. 3 [93] which shows T_c values for the superconducting rare earth carbides of REC_2- and RE_2C_3-type, whose electronic balance has been changed by partial metal

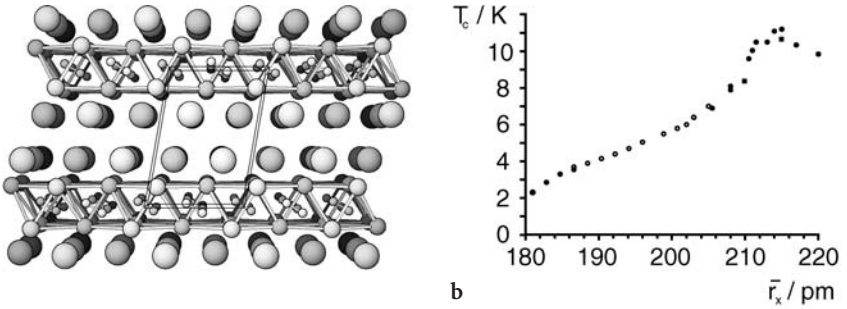

Fig. 2 **a** Projection of the (3 s) layered structures of $RE_2C_2X_2$ along the *b* axis of the monoclinic unit cell (*outlined*). The atoms X, RE, C are drawn with decreasing size. In the 1 s variant the stacking sequence of the layers is different. **b** T_c values for mixed crystals $Y_2C_2Br_{2-x}I_x$ (*circles*), and $Y_2C_2Cl_{2-x}I_x$ (*squares*) plotted vs the mean halide radius r_x. *Open and filled symbols* represent 1 s and 3 s stacking, respectively

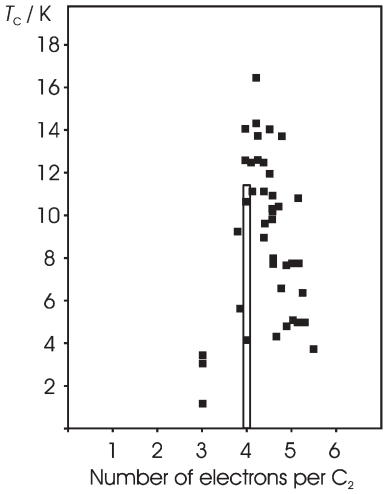

Fig. 3 T_c values of rare earth carbides REC_2, RE_2C_3 and carbide halides $RE_2C_2X_2$, the latter lying within the *open bar*

atom substitution [94]. In spite of different compositions and structures they share the common feature of C_2 units, and the T_c values are plotted vs the number of metal valence electrons transferred to the C_2 units according to the Zintl-Klemm concept. The T_c distribution peaks near a value of four electrons for the C_2 unit which in the ionic limit corresponds to a half-filling of the antibonding C_2-π^* states as in the structurally very different $RE_2C_2X_2$ phases. In a qualitative view, the metallic character of the valence compounds $RE_2C_2X_2$ is due to strong mixing of C_2-π^* and RE-d states, and the pairwise attraction between conduction electrons was associated with their tendency towards localization in the π^* states induced by phonon distortions [11].

Band structure calculations support the qualitative description given for the chemical bonding in $RE_2C_2X_2$ phases and, in particular, reveal flat band regions at the Fermi level of mixed C_2-π^* RE-d character together with highly dispersive bands, see Fig. 4. Inspecting a large number of superconductors including examples such as the A15 phases [95a], one always finds such a characteristic flat/steep band scenario as an obviously *necessary though not sufficient condition* for superconductivity.

A hypothesis was set up that the simultaneous presence of steep and flat band portions at the Fermi level is a kind of "fingerprint" for a metal to become a superconductor [11]. Following this hypothesis, a flat/steep band model for the origin of pairwise coupling of electrons (holes) based on chemical bonding interactions was developed.

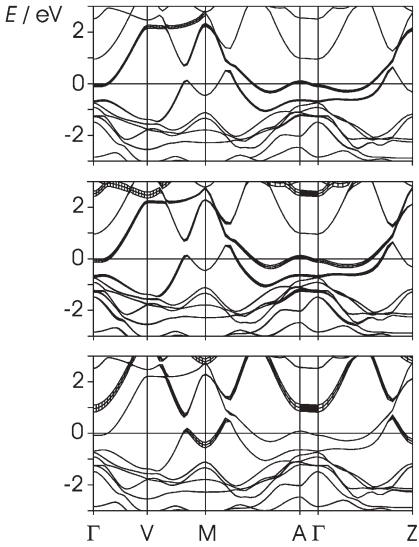

Fig. 4 Representation of the dispersion of the bands for $Y_2Br_2C_2$ in the energy range close to the Fermi level, calculated using the TB-LMTO-ASA method (E_F=0 eV). The prominent orbital contributions to the band structure are indicated in the form of "*fat bands*" (from *top to bottom*: C_2-π*, Y-d_{xz}, Y-$d_{x^2-y^2}$) [11b]

3.1 The Flat/Steep Band Scenario

The flat/steep band model refers to the characteristic electronic structure of the normal state of a superconductor. The flat band [96] is a section of a band which falls into a narrow energy window centered at E_F, where the group velocities of the electrons (holes) approach zero. The steep band is defined as a section of a band crossing the Fermi level with high velocity. The group velocity is defined as

$$\mathbf{v}(\mathbf{k}j) = \frac{1}{\hbar} \nabla_{\mathbf{k}} E(\mathbf{k}j), \tag{11}$$

where k is a composite index of quasi-momentum $\mathbf{k}$ and spin index σ, j is the band index. $E(\mathbf{k}j)$ is the energy of a quasiparticle which is defined as

$$E(\mathbf{k}j) = \varepsilon_{\mathbf{k}} + \sum(\mathbf{k}j, E(\mathbf{k}j)), \tag{12}$$

where $\varepsilon_{\mathbf{k}}$ is the kinetic energy of a free particle relative to the chemical potential μ. $\sum(\mathbf{k}j,\omega)$ is the electron (hole) self-energy through which a single particle Green function can be calculated as

$$G^{-1}(\mathbf{k}j, \omega) = G_0^{-1}(\mathbf{k}j, \omega) - \sum(\mathbf{k}j, \omega), \tag{13}$$

where $G_0(\mathbf{k}j,\omega)$ is the Green function for a non-interacting system,

$$G_0(\mathbf{k}j, \omega) = \frac{1}{\omega - \varepsilon_{\mathbf{k}} + i\delta sgn(\varepsilon_{\mathbf{k}})}. \tag{14}$$

Here δ is a positive small quantity, $sgn(\varepsilon_{\mathbf{k}})$ takes the sign of $\varepsilon_{\mathbf{k}}$. The self-energy $\sum(\mathbf{k}j, \omega)$ of the single particle can, in principle, be divided into two parts,

$$\sum = \sum_1 + \sum_2, \tag{15}$$

where $\sum_1$ is the self-energy due to the so-called external potential of the rigid ion-electron interaction in the spirit of a pseudo-potential approach [97]. $\sum_2$ is the self-energy due to Coulomb interactions and electron-phonon interactions, which can be divided into three groups according to the number of phonon lines occurring in each diagram [98]. The diagrams with more than one phonon line can in most cases be neglected according to the Migdal theorem [18]. In Eqs. (12)–(15) we have followed the tradition of Scalapino [99] for the definition of the electronic self-energy, which may differ from those used by other authors [100], who separate the contributions to the self-energy differently. In the above discussion we have implicitly assumed a Hamiltonian which for the flat/steep band model has the following form [101]:

$$H = H_e + H_{ph} + H_{e-ph}, \tag{16}$$

$$H_e = \sum_{\mathbf{k}} (\varepsilon^c_{\mathbf{k}} - \mu) c^+_{\mathbf{k}} c_{\mathbf{k}} + \sum_{\mathbf{k}} (\varepsilon^d_{\mathbf{k}} - \mu) d^+_{\mathbf{k}} d_{\mathbf{k}} + \sum_{\mathbf{k}} V_{cd}(\mathbf{k})(c^+_{\mathbf{k}} d_{\mathbf{k}} + h.c.), \tag{17}$$

$$H_{ph} = \sum_{\mathbf{q}} \hbar\omega_{\mathbf{q}} (\hat{n}_{\mathbf{q}} + 1/2) + \sum_{\mathbf{q}, \mathbf{q}'} \hbar\Omega_{\mathbf{q}, \mathbf{q}'} (\alpha^+_{\mathbf{q}} \alpha^+_{\mathbf{q}'} + \alpha_{-\mathbf{q}} \alpha_{-\mathbf{q}'}) + \ldots, \tag{18}$$

$$H_{ep} = \sum_{\mathbf{k}, \mathbf{q}} (\gamma^c_{\mathbf{k}, \mathbf{q}} c^+_{\mathbf{k}} c_{\mathbf{k}-\mathbf{q}} + \gamma^d_{\mathbf{k}, \mathbf{q}} d^+_{\mathbf{k}} d_{\mathbf{k}-\mathbf{q}} + \gamma^{cd}_{\mathbf{k}, \mathbf{q}} (c^+_{\mathbf{k}} d_{\mathbf{k}-\mathbf{q}} + d^+_{\mathbf{k}-\mathbf{q}} c_{\mathbf{k}})) \phi_{\mathbf{q}} + \ldots \tag{19}$$

In Eqs. (16)–(19) the electronic band index and the phonon branch index are omitted for simplicity. The annihilation (creation) operators $c(c^+)$ and $d(d^+)$ in Eqs. (17) and (19) refer to the steep and flat band electrons (holes), respectively. The third term in Eq. (17) indicates possible hybridization between both bands. Equation (18) is the phonon Hamiltonian with a two-phonon term explicitly included, where $\hat{n}_{\mathbf{q}}$ is the number operator, $\alpha(\alpha^+)$ the annihilation (creation) operator for phonons, and $\omega_{\mathbf{q}}$, $\Omega_{\mathbf{q},\mathbf{q}'}$ the corresponding $\mathbf{q}$ dependent one-phonon and two-phonon energies. The multi-phonon processes in Eq. (18) may become important for superconductivity in specific cases as already discussed by some authors [32d, 102]. Equation (19) represents the e-p coupling terms for the steep band, the flat band and the hybridization term, where the various γs are the corresponding e-p coupling coefficients. Equation (17) is the fundamental equation in our flat/steep band model.

The similarity between an electron pair in a chemical bond and a Cooper pair can be illustrated by inspecting their wave functions.

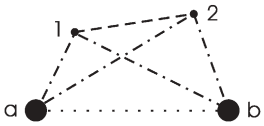

Fig. 5 Paired electrons denoted 1 and 2 in a formal chemical bond between site a and b. The pair state can be singlet or triplet

The approximate wave function of the bonded electron pair as shown in Fig. 5 can be written as

$$\Psi_i = \Psi\chi \tag{20}$$

where i represents the i-th bond, Ψ and χ are the orbital part and spin part, respectively, which can be expressed for the bonding state or attractive interaction as

$$\Psi = \frac{1}{\sqrt{2}}\left(\Phi_a(1)\,\Phi_b(2) + \Phi_a(2)\,\Phi_b(1)\right), \tag{21}$$

where $|\Phi_a\rangle$ and $|\Phi_b\rangle$ are two basis functions centered at a and b, respectively. Due to the fermionic character of electrons the total wave function ψ_i should be anti-symmetric, which requires χ to be in anti-symmetric form,

$$\chi = \frac{1}{\sqrt{2}}\left(\alpha(1)\,\beta(2) - \alpha(2)\,\beta(1)\right), \tag{22}$$

corresponding to a singlet state. For the antibonding state or repulsive interaction Ψ has the anti-symmetric form

$$\Psi = \frac{1}{\sqrt{2}}\left(\Phi_a(1)\,\Phi_b(2) - \Phi_a(2)\,\Phi_b(1)\right), \tag{23}$$

for which χ must be symmetric, which results in a triplet state:

$$\chi = \begin{cases} \alpha(1)\,\alpha(2), \\ \frac{1}{\sqrt{2}}\left(\alpha(1)\,\beta(2) + \alpha(2)\,\beta(1)\right), \\ \beta(1)\,\beta(2). \end{cases} \tag{24}$$

It should be mentioned that the trial wave functions in Eqs. (20)–(24) can be improved by using the linear combinations of other Slater type determinantal functions (CI) [103].

For a system with such bonds, to a first approximation the wave function can be written as

$$\psi = \prod_i \left(u_i|0\rangle + v_i\psi_i\right), \tag{25}$$

where u_i^2 is the unoccupancy of the i-th-bond pair state ψ_i, v_i^2 is the occupancy of this state. The symmetry of ψ depends on ψ_i and its spatial distribution. With a second quantization ψ_i can also be written as $c_{i\uparrow}^{+}c_{i\downarrow}^{+}|0\rangle$, where $|0\rangle$ is the vacuum of a bond pair state. In addition, by assuming a singlet form, which is not necessary, Eq. (25) can be expressed as

$$|\psi\rangle = \prod_i (u_i + v_i c_{i\uparrow}^{+} c_{i\downarrow}^{+})|0\rangle . \tag{26}$$

The comparison with the BCS ground state wave function [9],

$$|G\rangle = \prod_{\mathbf{k}} (u_{\mathbf{k}} + v_{\mathbf{k}} c_{\mathbf{k}\uparrow}^{+} c_{-\mathbf{k}\downarrow}^{+})|0\rangle , \tag{27}$$

clearly indicates similarity of $|\psi\rangle$ and $|G\rangle$. However, the Cooper pair states $c_{\mathbf{k}\uparrow}^{+} c_{-\mathbf{k}\downarrow}^{+}|0\rangle$ in Eq. (27) are all equal-momentum (zero) states, which makes $|G\rangle$ a coherent state. In contrast, $c_{i\uparrow}^{+}c_{i\downarrow}^{+}|0\rangle$ describes a formal bond state, and when the electronic system looses itinerancy, $|\psi\rangle$ describes approximately the electronic state in a typical covalent system with pairwise localized electrons. If we take a covalent solid as one limit and a quasi free electron metal as the other, it is interesting to explore the evolution from $|\psi\rangle$ to $|G\rangle$ and its contribution to $|G\rangle$. In this sense, we talk about the chemical origin for the pairing of electrons.

For metals whose normal-state electronic structure can be well described by the Hamiltonian

$$H_e = \sum_{\mathbf{k}j} (\varepsilon_{\mathbf{k}j} - \mu)\, c_{\mathbf{k}j}^{+} c_{\mathbf{k}j} , \tag{28}$$

superconductivity cannot occur within the formalism expressed by Eq. (28). For superconductivity to occur, one has to include the effect of phonons and consider the e-p coupling as shown in Eqs. (18) and (19), respectively, where the multi-phonon terms can be omitted in most cases. Since the e-p coupling can be treated as a dynamic pseudo Jahn-Teller effect [104], the variation of the chemical bonding [136] must influence the pairwise interaction of the conduction electrons. One has to consider many bond configurations to make $|\psi\rangle$ a correct description of the conduction electrons, which naturally leads to a description of pairing in $\mathbf{k}$ space. The net effect is a *pairwise constraint* acting on the conduction electrons, which manifests itself at low temperatures, where the various scattering probabilities decrease and the pairing becomes coherent as described by $|G\rangle$. Though the constraint varies from material to material, it is expected to be much stronger for superconductors than for non-superconductors. It reduces the kinetic energy of the electrons and leaves its traces on the normal-state single particle electronic structure as flat band around the Fermi level (the origin of the second term in Eq. 17 for a phononic superconductor). It is obvious that different bonding configurations can superimpose with each other when they match in symmetry and energy. This is the physical reason why we have included the third term in Eqs. (17) and (19), respectively, where the third term in Eq. (19) is a phonon assisted hybridization. As the bond

pair wave ψ_i in Eq. (25) and the H_e in Eq. (17) contain the orbital part and spin part, our approach does not exclude a magnetic mechanism, in contrast to other two-component models [64]. In the magnetic case Eqs. (18) and (19) can be neglected. The flat and steep band regions as defined in our model [96] can occur in different bands or one and the same band. Other differences have already been discussed in our earlier work [101]. In principle one or several tightly bonding configurations can dominate in Eq. (25), which will naturally lead to bipolarons in analogy to the model given in [63]. However, this requires very strict conditions such as strong e-p coupling to specific local phonon modes [64]. A too strong pairwise constraint will result in the localization of the involved conduction electrons and induce a structural instability. The occurrence of the steep band and the hybridization term in Eq. (17) counteract this tendency and mobilize the flat band electrons.

Finally, we discuss the main assumptions and approximations employed in the flat/steep band model.

AS1 – there exists a Fermi surface in the system, so our model does not address situations where only collective elementary excitations are possible [53b], or the situation of Higgs-like condensation [58]. As our model describes the evolution from $|\psi\rangle$ to $|G\rangle$, the properties of the quasiparticles vary drastically. Even the extreme case can be addressed, where the Fermi surface is very small, and the quasiparticle may not be well defined.

AS2 – the coexistence of flat and steep bands implies the existence of electronic inhomogeneities in one system. Depending on the relative concentration of charge carriers different orders can arise. In particular, a crystal structure as a basic order is uniquely described by $|\psi\rangle$.

AS3 – the single particle approximation (the second term in Eq. 17) to the state described by $|\psi\rangle$ is used, which might not be a good approximation in the case of a short effective "bond length".

AS4 – as an approach to solve the flat/steep band model, the quasiparticle energy as used in Eq. (11) is replaced by that obtained from the Kohn-Sham equation instead of the single particle Green function, Eq. (13). The Kohn-Sham equation [105] in atomic units reads

$$\left[-\nabla^2 + \sum_n V_n(\mathbf{r} - \mathbf{R}_n) + \int \frac{n(\mathbf{r}')\,d\mathbf{r}'}{|\mathbf{r} - \mathbf{r}'|} + V_{xc}(\mathbf{r})\right] \Psi_{\mathbf{k}j} = \varepsilon_{\mathbf{k}j} \Psi_{\mathbf{k}j}\,, \tag{29}$$

where $V_{xc}(\mathbf{r})$ is the exchange-correlation potential which can only be calculated within the local density approximation (LDA) or its various extensions [100b, 103, 106]. $\varepsilon_{\mathbf{k}j}$ as obtained from Eq. (29) is obviously different from $E(\mathbf{k}j,\omega)$ in Eq. (12). The ω dependence of the quasiparticle energy $E(\mathbf{k}j,\omega)$ describes the dynamics of the quasiparticles and leads to an additional mass normalization and finite life time. Such a replacement has no theoretical justification at all; rather it is justified by the quite good consistence with experimental results [107]. The real band structure of a crystal should be calculated from the Luttinger equation [108]:

$$\left[-\nabla^2 + \sum_n V_n(\mathbf{r}-\mathbf{R}_n) + \int \frac{n(\mathbf{r}')\,d\mathbf{r}'}{|\mathbf{r}-\mathbf{r}'|}\right]\Psi_{\mathbf{k}j} + \int d\mathbf{r}'\,\Sigma_{xc}(\mathbf{r},\mathbf{r}',0)\;\Psi_{\mathbf{k}j}(\mathbf{r}') = \varepsilon_{\mathbf{k}j}\Psi_{\mathbf{k}j}\,, \tag{30}$$

where $\Sigma_{xc}(\mathbf{r},\mathbf{r}',\omega)$ is the exchange-correlation self-energy of the Green function. However, the calculation of $\Sigma_{xc}(\mathbf{r},\mathbf{r}',0)$ is extremely difficult, which limits its practical application.

3.2 The Origin of a Flat Band

As can be seen from Eqs. (11)–(15), except at the Brillouin zone (BZ) center, the flattening of a band originates completely from the self-energy part $\Sigma(\mathbf{k}j,\omega)$, which stems from the static periodic potential, the e-p and the Coulomb interactions. These interactions tend to localize the conduction electrons. In the following discussion we concentrate on the situations as described in **AS4**. In addition, we think that with newly developed approaches such as LDA+U [100b] and LDA+DMFT [106b–c], single particle band theory can grasp the essence of the low-energy electronic structure even in strongly correlated systems. Within such a framework, we studied the origin of a flat band [109] regardless of its position relative to the Fermi level.

By using the Wannier representation [110] of an eigenvector, the eigenvalue of the Hamiltonian $\hat{H}$ can be expressed as

$$E(\mathbf{k}j) = 1/N \sum_{\mathbf{l}} e^{i\mathbf{k}\mathbf{l}} H_j(\mathbf{l})\,, \tag{31}$$

where $H_j(\mathbf{l})=\langle \mathbf{l}_1 j|\hat{H}|\mathbf{l}_2 j\rangle$ with $\mathbf{l}=\mathbf{l}_1-\mathbf{l}_2$ is the hopping integral between lattice site $\mathbf{l}_1$ and $\mathbf{l}_2$, which generally refers to the inter-cell interactions if $\mathbf{l}_1\neq\mathbf{l}_2$ or to the on-site interactions ($\mathbf{l}_1=\mathbf{l}_2$). Using Eq. (31) the group velocity can be expressed as

$$\mathbf{v}(\mathbf{k}j) = \frac{1}{N\hbar}\sum_{\mathbf{l}} i\mathbf{l}e^{i\mathbf{k}\mathbf{l}} H_j(\mathbf{l})\,, \tag{32}$$

which depends on two factors. One, $i\mathbf{l}e^{i\mathbf{k}\mathbf{l}}$, is $\mathbf{k}$ dependent, the other $H_j(\mathbf{l})$ is $\mathbf{k}$ independent. The analysis of the $\mathbf{k}$ dependence of $E(\mathbf{k}j)$ results in a necessary and sufficient condition for a flat band to occur in the BZ, namely *a local inversion center for* $E(\mathbf{k}j)$ *at* $\mathbf{k}$ *with respect to the* $\mathbf{k}$*'s neighborhood.* Based on this general result, a more manageable sufficient condition is derived, namely if there exists an n-th order "pseudo inversion" center at a $\mathbf{k}$ point, then a flat band occurs. Here n-th order pseudo inversion center means that the inversion symmetry holds only for the directions specified by n linearly independent vectors. This condition includes all of the "zero slope" conditions of third order listed by Cracknell [111] as special cases and is more succinct and general. The lower order pseudo inversion center implies that a band is flat only along some special directions.

The **k** independent part $H_j(\mathbf{l})$, which depends on the individual atoms and their chemical bonding, is even more important in determining the physical and chemical properties of a material than the **k** dependent part. The role of $H_j(\mathbf{l})$ in producing a flat band can be demonstrated [109] through finding the relation between $E(\mathbf{k}j)$ and a chemical bonding indicator as follows:

$$E(\mathbf{k}j) = \sum_{\tau L,\, \tau' + \mathrm{T}L'} H_{\tau L,\, \tau' + \mathrm{T}L'} A_{\tau L}^{\mathbf{k}j*} A_{\tau' + \mathrm{T}L'}^{\mathbf{k}j} , \tag{33}$$

where $H_{\tau L, \tau' + \mathrm{T}L'}$ is a Hamiltonian matrix element between the orbital L of atom τ and L' of atom $\tau'+\mathbf{T}$ with **T** being the lattice vector. $A_{\tau L}^{\mathbf{k}j}$ is the eigenvector. The summation term in Eq. (33) can be used as a **k**,*j*-dependent chemical bonding indicator [112] similar to the real space COHP matrix elements [113]. From Eq. (33) the group velocity is calculated as

$$\mathbf{v}(\mathbf{k}j) = \frac{1}{\hbar} \sum_{\tau L,\, \tau' + \mathrm{T}L'} H_{\tau L,\, \tau' + \mathrm{T}L'} \nabla_k (A_{\tau L}^{\mathbf{k}j*} A_{\tau' + \mathrm{T}L'}^{\mathbf{k}j}) , \tag{34}$$

which indicates that *weak covalent bonding* (small $H_{\tau L,\, \tau' + \mathrm{T}L'}$) between the atoms in different unit cells will lead to small **v** and thus produce a flat band. Such a correlation was also mentioned by Hoffmann based on the orbital overlap argument [114]. Molecular or ionic crystals with nearly no covalency between the molecules or ions are typical examples. The bands are indeed rather flat. In the following we give some examples to explain these principles.

3.3 Some Illustration with Actual Superconductors

We chose mercury as the first known superconductor. The metal Hg crystallizes with space group $R\bar{3}m$, and its Patterson group is also $R\bar{3}m$. Figure 6 shows its electronic band structure.

From the listed Wyckoff positions we know that inversion centers exist at a (I'), b (Z), d (L), e (F), respectively. These inversion centers naturally satisfy the third order pseudo inversion center condition. Correspondingly, flat bands should exist at these **k** points, which is consistent with our numerical calculations [96]. It should be pointed out that only flat bands at Z and F points are relevant to superconductivity, because they are close to the Fermi level. The occurrence of a steep band is obvious from Fig. 6. This actually dominates the system. The Fermi surface shown in Fig. 7 indicates the small extension of the flat bands which manifests itself also in the *DOS* curve (Fig. 6), where no peak occurs near the Fermi level.

This is one of the essential differences between the flat/steep band model and the well-known vHs scenario [62], which is thought to be not applicable in this case. In the flat/steep band model the occurrence of flat bands around the Fermi level, in spite of their tiny extension is a signature of strong chemical pairwise constraint on conduction electrons in contrast to, e.g., alkali metals at ambient conditions which lack this feature. The difference of the orbital com-

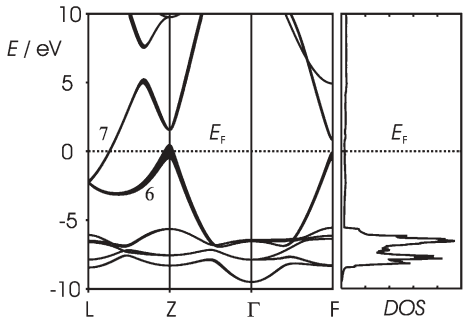

Fig. 6 Band structure calculated for special symmetry directions and the total DOS of Hg. The fatness of the bands illustrates the contribution of the p_z orbital

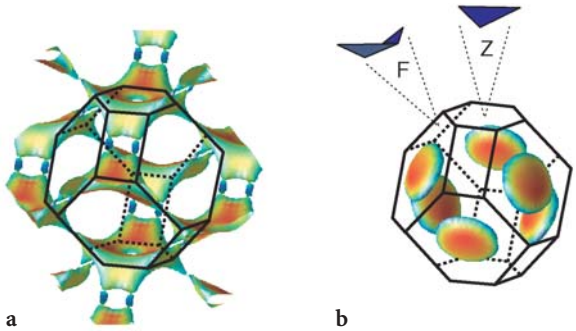

Fig. 7a, b Fermi surface of Hg for: **a** band 6; **b** band 7 (Brillouin zone outlined). The increasing velocity of the electrons is represented by the *change from blue to red*. The isovelocity surface for band 6 around the F and Z points at a value of 0.03 (atomic units) is additionally shown in b. The two features are magnified by a factor of 100; they lie within the range of E_F±0.28 eV

positions of the flat and steep bands can easily be shown with the "fat" band representation as developed in the LMTO method [115].

Out of an overwhelming number of compound superconductors we chose MgB_2 [28–30] to illustrate further the flat/steep band scenario. In Fig. 8a the band structure of MgB_2 calculated with the TB-LMTO method [116] is shown. The fatness of the band indicates the orbital character of some band states. As the Patterson symmetry of MgB_2 is P6/mmm, the condition of a third order pseudo-inversion center is automatically satisfied at Γ, A and M points, respectively. As shown in Fig. 8 the flat band from Γ to A is mainly of σ type, that at M is mainly of π type. As the Γ-A line has C_{6v} symmetry, only a second order pseudo-inversion center exists along this line. The **k** points on this line are all extremal points with respect to directions in the (001) plane, while for the k_z direction there is no pseudo-inversion center, so $\frac{\partial E}{\partial k_z} \neq 0$. However,

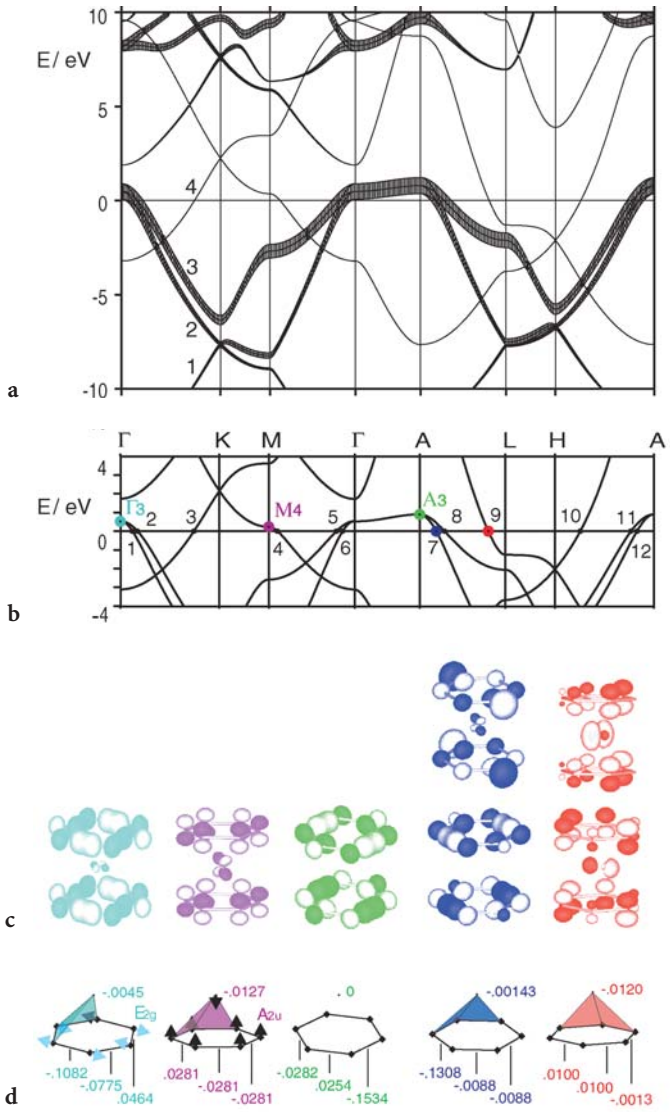

Fig. 8 **a** Band structure of MgB_2 calculated with the TB-LMTO method. Fatness indicates the B-$p_{x,y}$ contribution. Bands are numbered in order of energy. **b** Special points near the Fermi level are denoted as Γ_3, M_4, A_3, points at the Fermi level are numbered 1 to 12. **c** Orbital topologies are shown for selected points with *different shading* for positive and negative lobes at iso-value surfaces drawn at 0.035 (Γ_3), 0.04 (M_4), 0.04 (A_3), 0.04 (7, *bottom*), 0.014 (7, *top*), 0.02 (9, *bottom*), 0.02 (9, *top*). The orbitals for non-special points 7 (*blue*) and 9 (*red*) are represented by their real (*bottom*) and imaginary (*top*) part. Note that only the surfaces shown in c have been calculated by approximating the LMTOs with Slater-like tight-binding bases. **d** The $COHP^{kj}_{R,R'}$ values for the band states Γ_3, M_4, A_3, 7 and 9, representing the bonding (–) and antibonding (+) interactions between nearest neighbor B atoms as well as Mg and B atoms in MgB_2

since the B...B interlayer covalent bonding is rather weak, the z-component of the group velocity, $\frac{\partial E}{\partial k_z}$, is small. Therefore, it is the symmetry and the 2D character of the structure that produce the flat band from Γ to A. The chemical origin of the Fermi states has been studied in detail in our earlier work [112]. The orbital compositions of all the investigated states are given in Table 1. The selected Fermi states numbered in Fig. 8b can be grouped according to their locations. States (1, 6, 7, 12) are on the 2D-1 sheet, while (2, 5, 8, 11) are on the 2D-2 sheet.

As expected and shown in Table 1, the contributions of Mg to these states are nearly negligible and vanish completely at the A point where the two degenerate states are pure B-$2p_{x,y}$ hybrids. The only contribution of Mg to the cylindrical surfaces, see Fig. 9, is – surprisingly – d-like and has the important effect to provide, though little, dispersion to bands along Γ–A.

Neglecting the d-like state the section areas of 2D-1 (Fig. 9) become 1165.5 and 2041.9 Tesla for the de Haas-van Alphen frequencies F_1^0, F_2^0, respectively, to be contrasted to the experimental values of 540 and 1530 Tesla [117]. Inclusion of these states improves the former results to 747 and 1510 Tesla in agreement with earlier results [118], but with the distinction that here a clear assignment of the origin of the improvement can be made. States 3, 4 and M_4 (slightly above E_F) represent states on the 3D-1 sheet, while states 9, 10 are located on the large 3D-2 surface. From Table 1 it is obvious that in both cases a significant contribution to the two surfaces comes from Mg electronic states where a dominating

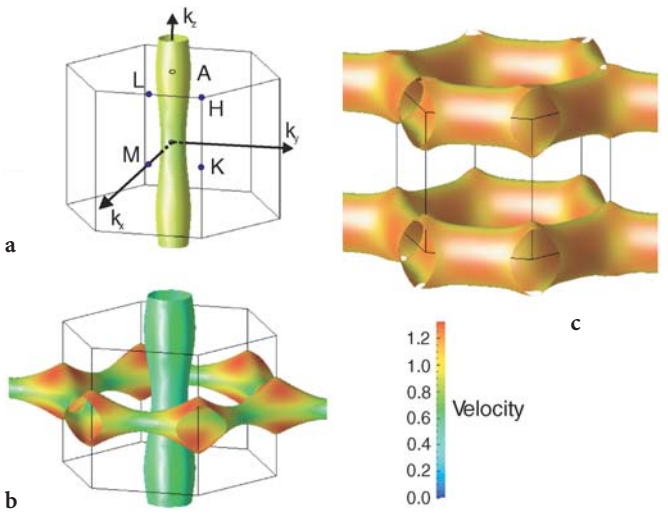

Fig. 9a–c Electronic velocity distribution on the Fermi surface of MgB_2 for: **a** band 3 (2D-1); **b** band 4 (2D-2 (cylinder) and 3D-1); **c** band 5 (3D-2). The BZ together with specific symmetry points are indicated. *Color bar* holds for a–c. According to dHvA measurement the Fermi velocities for the flat bands should be significantly smaller than shown

Table 1 Orbital compositions for band states of MgB_2 denoted in Fig. 9 obtained from TB-LMTO calculations. The values (Mg/B) are given in % for s-, p-, d-like states of Mg and s, p states of B. The "–" sign means 0 or negligible contribution

States	s	$p_x + p_y$	p_z	$d_{x^2-y^2} + d_{xy}$	d_{3z^2-1}	$d_{xz} + d_{yz}$
Γ_3	–/–	–/89.61	–/–	10.39	–	–
1	–/4.17	1.74/83.28	–/–	10.80	–	–
2	–/0.03	4.17/86.23	–/–	9.06	0.50	–
3	–/–	–/–	12.58/62.00	–	–	25.41
M_4	–/–	–/–	–/64.42	–	–	35.57
4	–/–	–/–	7.05/61.82	–	–	31.13
5	–/–	3.63/87.22	–/–	9.16	–	–
6	–/–	1.57/87.65	–/–	10.68	0.09	–
A_3	–/–	–/100.00	–/–	–	–	–
7	–/7.03	–/89.73	0.20/	–	–	3.04
8	–/–	–/93.90	–/–	–	–	6.11
9	25.95/–	17.83/–	–/30.4	25.83	–	–
10	–/–	39.44/–	–/34.33	26.23	–	–
11	–/0.43	–/93.30	0.74/–	–	–	5.53
12	–/7.70	–/89.08	–/–	–	–	3.22

component is again d-like on the hole type 3D-1 sheet, while s-, p- and d-like states contribute to the electron type 3D-2 surface. These results clearly show that Mg is not fully ionized but carries an important covalent character that even dominates the bonding properties between the boron layers and has important impact on the small π gap. To conclude, a flat band in MgB_2 originates from both symmetry and weak covalent bonding and lies close to the Fermi level. The coexistence of flat/steep bands becomes even more clear from the Fermi surface with the scalar velocity field mapped onto it (Fig. 9). MgB_2 is a model compound of the flat/steep band scenario for superconductivity.

On the way from simple to complex the alkali metal fullerides, A_3C_{60} [119], should be mentioned. A chapter in this book by Gunnarsson is dedicated to their detailed discussion. Though seemingly simple salts they face us with quite complex problems starting from the crystal structure with respect to the orientational disorder of the C_{60} fulleride anions [120a]. As a further complication the Coulomb interaction between the conduction electrons is of the order of 1 eV [121b], while the phonon energy can reach the order of ~0.2 eV [121a], and both lie on the energy scale of the conduction band width (~0.5 eV) [121c] indicating a situation close to the Mott-Hubbard transition [121d]. Due to the weak covalent interaction between the anions one expects a global flatness of the conduction band. The recent determination [122] of the band structure of K-doped C_{60} crystalline monolayers with ARPES gives an unambiguous evidence for the flat/steep band condition, as shown in Fig. 10.

Last but not least, the oxocuprate superconductors themselves provide obvious examples for the flat/steep band scenario. Indeed a multiple pattern of

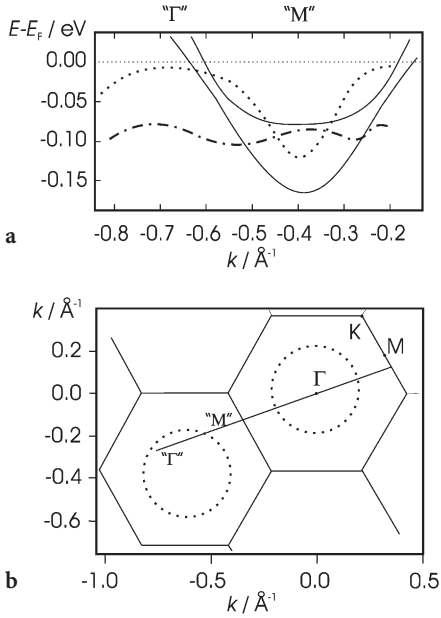

Fig. 10 **a** Band dispersion (*dotted line*) measured on a crystalline K_3C_{60} monolayer. The experimental *dash-dotted* line is preliminarily attributed to a phonon shake-up structure. The *two solid lines* are obtained from pseudo-potential LDA calculations on a model configuration of the K_3C_{60} monolayer. **b** The first Brillouin-Zone of the K_3C_{60} monolayer and the measuring direction for **k** (adapted from [122])

extended flat band regions at the Fermi level together with several highly dispersive bands was observed in p-type cuprates such as $Bi_2(Sr_{0.97}Pr_{0.03})_2CuO_{6+\delta}$ (Bi2201) [123a] and $YBa_2Cu_3O_x$ (YBCO) [123b,c] in agreement with results obtained from LDA calculations [124]. Similar features have also been observed in the n-type superconductor $Nd_{2-x}Ce_xCuO_4$ (NCCO) [125], though the flat band part lies 300 meV below E_F. In the case of the Bi-based cuprates the complicated modulated structures prevent unambiguous results from band structure calculations. However, the ARPES measurement on $Bi_2Sr_2CaCu_2O_{8+\delta}$ (Bi2212) gives clear evidence for an extended flat band at M and a steep band along the Γ-X line [126], as shown in Fig. 11.

The flat/steep band character of the high T_c cuprates appears to be a universal property according to the recent summary of ARPES experiments [127], as, e.g., shown in Fig. 12 for $(La_{2-x}Sr_x)CuO_4$.

It should be mentioned that the existence of a flat band in high T_c cuprates has been considered as an indication for the importance of vHs. However, as we have pointed out the vHs scenario does not include the role of steep band electrons, which are important to ensure structural stability, and also neglects the possible interaction between the two type of electrons which can enhance T_c [31, 64].

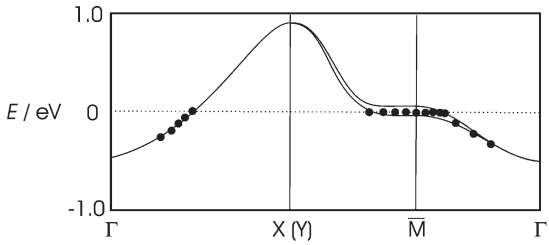

Fig. 11 Experimental dispersion relation (*dots*) of E with **k** near E_F, which indicates a typical flat/steep band character. The *solid lines* illustrate a simple scenario compatible with the experimental data (adapted from [126])

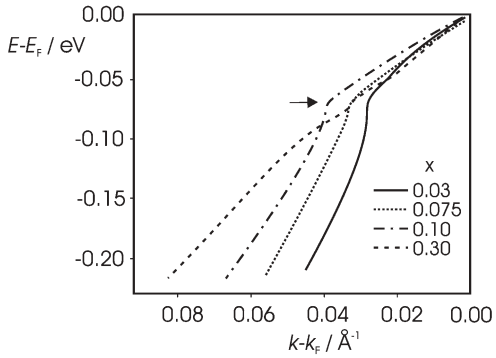

Fig. 12 The experimental dispersion relation of electronic energy E vs wave vector **k** of $(La_{2-x}Sr_x)CuO_4$. The determination with the ARPES technique is performed along the (0,0)–(π,π) nodal direction. The flat band character in the low-energy range is a universal behavior in different families of cuprates. For clarity only part of the original results in [127] are shown here

4
Peak-Like Structure of the e-p Coupling

In the following we focus on situations where the chemical pairwise constraint mainly originates from e-p coupling. In such cases, this constraint can be viewed as a residue of covalent interactions. With an appropriate weak constraint the "formal bond" length for the paired state $|\psi_i\rangle$ in Eq. (20) is rather large whereby the different states $|\psi_i\rangle$ overlap with each other. It has been shown by Scalapino [99] that the dressed electron-ion potential determines not only the band structure but also the e-p coupling constant. Therefore, flat band regions of the bare band structure, as calculated e.g. from LDA, might be indicative for strong e-p coupling. Accordingly, we have the following relation for the parameters in Eq. (19), $\gamma^d \gg \gamma^c, \gamma^{cd}$ and ε^c, $\varepsilon^d \gg V_{cd}$. The last inequality is required, because in the case of too strong hybridization between flat and steep

band, they are not well defined individually. The inequality $\gamma^d \gg \gamma^c, \gamma^{cd}$ implies that there is a peak-like structure for the e-p coupling constant in **k** space. Accordingly, if we consider the bond configuration for a specific $|\mathbf{k}j\rangle$ state, one could expect a similar peak-like structure in **q** space of the phonons, because only a compatible phonon can most effectively change a specific electronic state. This is similar to the Jahn-Teller effect which is always associated with specific distortion modes. Our earlier work [104] based on the extended degenerate perturbation theory has revealed the connection between these two phenomena. The above argument has been corroborated numerically by calculations of the e-p coupling constant.

Our strategy to do such calculations is not directly using the Hamiltonian of Eq. (17); instead we use Eq. (29) to calculate the band structures. Equation (17) is only used to analyze the result. Equations (18) and (19) are incorporated into Eq. (16) by following the approach of Migdal [18], namely by calculating the electronic self-energy as follows:

$$\sum(\mathbf{k}, \omega) = i \sum_{\mathbf{q}, \nu} \int \frac{d\omega'}{2\pi} |g^{\mathbf{q},\nu}_{\mathbf{k},\mathbf{k}-\mathbf{q}}|^2 D(\mathbf{q}, \nu, \omega - \omega') G(\mathbf{k} - \mathbf{q}, \omega') , \tag{35}$$

where $g^{\mathbf{q},\nu}_{\mathbf{k},\mathbf{k}-\mathbf{q}}$ is the e-p matrix element, $G(\mathbf{k}–\mathbf{q},\omega')$ is the electronic Green function as in Eq. (13), $D(\mathbf{q}, \nu, \omega–\omega')$ is the phononic Green function which can be expressed in terms of the phonon self-energy:

$$D^{-1}(\mathbf{q}, \nu, \omega) = D_0^{-1}(\mathbf{q}, \nu, \omega) - \Pi(\mathbf{q}, \nu, \omega) \tag{36}$$

The non-interacting phonon Green function $D_0(\mathbf{q}, \nu, \omega)$ can easily be calculated with the Hamiltonian in Eq. (18) by removing the multi-phonon terms and has the following form:

$$D_0(\mathbf{q}, \nu, \omega) = \frac{2\omega_{\mathbf{q}\nu}}{\omega^2 - \omega^2_{\mathbf{q}\nu} + i\delta} \tag{37}$$

By introducing the e-p spectral function $\alpha^2_{\mathbf{k}}(\Omega)F(\Omega)$ [128], which is defined as

$$\alpha^2_{\mathbf{k}}(\Omega)F(\Omega) = \sum_{\mathbf{q}, \nu} |g^{\mathbf{q},\nu}_{\mathbf{k},\mathbf{k}-\mathbf{q}}|^2 \delta(\varepsilon_{\mathbf{k}-\mathbf{q}} - \varepsilon_F) Im D(\mathbf{q}, \nu, \Omega) , \tag{38}$$

one can write Eq. (35) in the simpler form,

$$\sum(\mathbf{k}, \omega) = \frac{1}{\pi} \int d\Omega \alpha^2_{\mathbf{k}}(\Omega)F(\Omega) L(\omega, \Omega) \tag{39}$$

where $L(\omega, \Omega)$ is a function derived by the replacement of $G(\mathbf{k}–\mathbf{q},\omega')$ in Eq. (35) by $G_0(\mathbf{k}–\mathbf{q},\omega')$, following Migdal, and it has the following form:

$$L(\omega, \Omega) = \int d\omega' \left(\frac{1}{\omega - \omega' + \Omega - i\delta} - \frac{1}{\omega - \omega' - \Omega + i\delta} \right). \tag{40}$$

In deriving Eqs. (39) and (40), it is also assumed that the phonons are not renormalized, namely $ImD(\mathbf{q}, \nu, \Omega)=\pi\delta(\omega_{\mathbf{q}\nu} - \Omega)$. As shown by Allen [128], Eq.(39) can be used for finite temperature if $L(\omega, \Omega)$ is modified accordingly. The self-energy in Eq. (39) is explicitly **k** dependent, which naturally gives an indicator, $\lambda_{\mathbf{k}j}$, to determine the difference among various electronic states in the e-p coupling process. For a common e-p process at low temperature the real part of $\sum(\mathbf{k},\omega)$ is rather small, while $-\partial\sum_r(\mathbf{k},\omega)/\partial\omega|_{\omega=0}$ is relatively large, and the latter is therefore a good parameter to measure the mass renormalization of an electron,

$$\lambda_{\mathbf{k}} = -\partial\sum_r(\mathbf{k}, \omega)/\partial\omega\big|_{\omega=0} = 2\int \frac{d\Omega}{\Omega}\,\alpha^2_{\mathbf{k}}F(\Omega)\,. \tag{41}$$

The average of $\lambda_{\mathbf{k}}$ on the Fermi surface is the dimensionless e-p coupling constant λ, which can be expressed in terms of the e-p spectral function,

$$\lambda = 2\int \frac{d\Omega}{\Omega}\,\alpha^2 F(\Omega)\,. \tag{42}$$

In Eq. (42) λ is identical to the one used in the BCS equation for T_c as well as in the McMillan equation, when expressed as

$$\lambda = N(0)V\,, \tag{43}$$

where $N(0)$ is the electronic density of states per spin at the Fermi level, V is the effective attractive potential mediated by phonons. From Eqs. (38) and (39), one can also decompose λ with respect to the phonon $|\mathbf{q}\nu\rangle$ by integrating out the **k** dependence. The final form of such a decomposition can be simply expressed [128] as

$$\lambda(\mathbf{q},\nu) = \frac{1}{\pi N(0)}\frac{\Gamma_{\mathbf{q}\nu}}{\omega^2_{\mathbf{q}\nu}}, \tag{44}$$

where $\Gamma_{\mathbf{q}\nu}$ is the phonon line width which can be calculated from

$$\Gamma_{\mathbf{q}\nu} = 2\pi\omega_{\mathbf{q}\nu}\sum_{\mathbf{k}}\left|g^{\mathbf{q},\nu}_{\mathbf{k},\mathbf{k}-\mathbf{q}}\right|^2\delta(\varepsilon_{\mathbf{k}-\mathbf{q}} - \varepsilon_F)\,\delta(\varepsilon_{\mathbf{k}} - \varepsilon_F)\,. \tag{45}$$

The e-p matrix elements $\left|g^{\mathbf{q},\nu}_{\mathbf{k},\mathbf{k}-\mathbf{q}}\right|$ in the above equations can be calculated with the linear-response approach [129] or the finite difference method [130]. λ can also be decomposed according to different bands for which the band indices have been omitted in the above equations for brevity. On the basis of $\lambda(\mathbf{q},\nu)$, we defined a *DOS*-like quantity $DOS(\lambda)$ through which one can analyze the distribution of phonon states with respect to the e-p coupling constant λ instead of energy E [104]. $DOS(\lambda)$ is defined as follows:

$$NDOS(\lambda) = \mathrm{V}/(2\pi)^3\sum_{\nu}\int_{BZ}(\lambda - \lambda(\mathbf{q},\nu))\,d^3\mathbf{q}, \tag{46}$$

The main approximation used in deriving the above equations is that the adiabatic parameter ω_D/ε_F is small. By means of λ_k in Eq. (41) and $\lambda(\mathbf{q},\nu)$ in Eq. (44), one can quantitatively analyze the difference between the flat band electrons and steep band electrons in the e-p coupling interactions.

In Fig. 13a,b, we show the $\lambda(\mathbf{q})$ distribution of Hg and MgB_2, respectively. It is obvious that in both cases the e-p coupling constant $\lambda(\mathbf{q})$ has peak-like structures in the corresponding phonon BZs. For Hg, the largest $\lambda(\mathbf{q})$ (~12.4) [104] occurs at $\mathbf{q}=(0.1662,0,0.0749)\frac{2\pi}{a}$ (a result based on a 6×6×6 $\mathbf{q}$-mesh) which is on the Γ–L line. Our earlier calculations showed that the lowest acoustic phonon branch along the Γ–L line is most important for the e-p coupling interactions. It has already been noted [131] that such low-energy phonons are responsible for the low-temperature structural instability of Hg. Again we see an evidence for the importance of chemical pairwise interaction and its relevance to superconductivity. The peak-like structure for MgB_2 [116] is even more pronounced than that for Hg. The largest $\lambda(\mathbf{q})$ calculated on the basis of a 12×12×12 q-mesh is 25.2 which occurs at $\mathbf{q}=(0.0962,0,0)\frac{2\pi}{a}$ close to the Γ point but on the Γ-M line instead of the Γ–A line. Along the Γ-M line the degenerate E_{2g} mode in Γ decomposes into A_1+B_1 modes, while along the Γ–A line the E_{2g} mode changes its character to a E_2 mode and remains degenerate. Our calculations indicate that the A_1 mode contributes most significantly (21.8) to the peak value at this $\mathbf{q}$ point. The eigenvector for this A_1 mode is very similar to that of the E_{2g} mode, because $\mathbf{q}$ is rather close to the Γ point; however, their symmetries are very different. The largest $\lambda(\mathbf{q})$ value on the Γ–A line is 9.8 at $\mathbf{q}=(0,0,0.4167)\frac{2\pi}{a}$ in accordance with earlier results [132]. A similar situation has also been predicted for a hypothetical superconductor $Li_{1-x}BC$ [133]. The same characteristic structure of the phonon line width $\Gamma_{\mathbf{q}\nu}$ as calculated from Eq. (45) for Nb has also been found in a much earlier work [134]. This finding suggests a possible

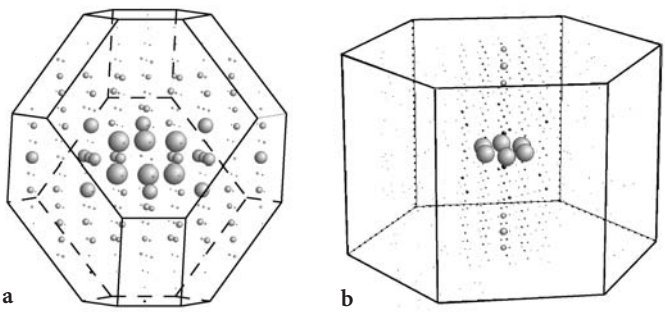

Fig. 13 $\mathbf{q}$ dependence of the electron phonon coupling in a **a** Hg and **b** MgB_2, respectively, together with the corresponding Brillouin zone. The largest spheres in **a** correspond to a $\lambda(\mathbf{q})$ value of 12.3. and in b to a $\lambda(\mathbf{q})$ value of 25.2.

peak-like structure for $\lambda(\mathbf{q})$ unless $N(0)$ and $\omega_{\mathbf{q}\nu}^2$ in Eq. (44) counteract it. It is remarkable that the peak-like structure for Ca [104], which is non-superconducting, is much less pronounced. The detailed origin for it can be analyzed mathematically from Eq. (44) by inspecting the phonon softening which enters through $\omega_{\mathbf{q}\,\nu}$ and $\Gamma_{\mathbf{q}\,\nu}$ and Fermi surface nesting through $N(0)$, factors which are themselves correlated with each other. As described above, a pronounced peak-like structure of e-p coupling is expected from our flat/steep band model for superconductors, which reflects the coexistence of rather different electronic bands around the Fermi level. A general discussion of the peak-like structure in terms of $\lambda_{\mathbf{k}}$ will be left to our future work.

5
Chemical Bonding Variations Caused by e-p Coupling

We introduced a chemical representation ψ in Eq. (25) for the pairwise interaction of conduction electrons. For conventional superconductors, where phonons are the origin of the pairwise constraint, $|\psi\rangle$ for the ground state differs from $|G\rangle$ in Eq. (27) at most by a phase factor $e^{i\theta}$. As this constraint due to phonons is too weak for the normal state in the case of simple superconductors, the $|\psi\rangle$ description for conduction electrons is not efficient enough, so we still use the single particle description $|\mathbf{k}j\rangle$. The pairwise interaction in such simple cases is studied on the basis of bonding indicators commonly used by chemists, with extensions to momentum space and specific electronic states.

A quantity Psib($\Psi_{\mathbf{k}j}$) is introduced to define a bonding property for a single particle state $\Psi_{\mathbf{k}j}$ which can be expanded in terms of a suitable basis set as follows:

$$|\mathbf{k}j\rangle = \sum_{\mathbf{R}L} A_{\mathbf{R}L}^{\mathbf{k}j} |\varphi_{\mathbf{R}L}^{\mathbf{k}j}\rangle \,, \tag{47}$$

where $|\varphi_{\mathbf{R}L}^{\mathbf{k}j}\rangle$ is a basis centered at $\mathbf{R}$, L is a combined index of l and m, and $A_{\mathbf{R}L}^{\mathbf{k}j}$ is the expansion coefficient. Based on Eq. (47), one can define a bonding indicator as Mulliken did for molecules [135], which partitions the electron distribution within a bond. By extending this approach to solids, we obtain a bonding indicator [136]

$$B^{\mathbf{k}j}(\mathbf{R}, \mathbf{R}') = \sum A_{\mathbf{R}L}^{\mathbf{k}j*} \varphi_{\mathbf{R}'L'}^{\mathbf{k}j} S_{\mathbf{R},\mathbf{R}'}^{\mathbf{k}}(L, L') \,, \tag{48}$$

where $S_{\mathbf{R},\mathbf{R}'}^{\mathbf{k}}(L, L')$ is a $\mathbf{k}$-dependent overlap matrix element. An alternative approach to define a bonding indicator is to partition the total energy into pairwise contributions as done by Sutton et al. [137] in the TB bond model. This approach was later implemented into the TB-LMTO package [113] and named *COHP* (*crystal orbital Hamiltonian population*). Applying the same approach to a specific state, we get another bonding indicator [112],

$$B^{\mathbf{k}j}(\mathbf{R}, \mathbf{R}') = \rho_{\mathbf{R},\mathbf{R}'}^{\mathbf{k}j} \langle \varphi_{\mathbf{R}}^{\mathbf{k}} | \mathrm{H} | \varphi_{\mathbf{R}'}^{\mathbf{k}} \rangle \,, \tag{49}$$

where $\rho^{kj}_{R,R'}$ is the density matrix element for state $|\mathbf{k}j\rangle$. $B^{kj}(\mathbf{R},\mathbf{R}')$ in Eq. (49) is a weighted effective hopping integral ($COHP^{kj}_{R,R'}$) between site **R** and **R′** with respect to state $|\mathbf{k}j\rangle$. When considering the occupation factor for state $|\mathbf{k}j\rangle$, the covalent contribution from the selected pairs to the cohesive energy of a solid is obtained. The bonding indicator as defined in Eq. (49) has a conceptual advantage over that in Eq. (48), because it is less basis set dependent. With $B^{kj}(\mathbf{R},\mathbf{R}')$ we can define Psib(Ψ_{kj}) [136]:

$$\mathrm{Psib}(\Psi_{kj}) = \sum_{R<R'} B^{kj}(\mathbf{R},\mathbf{R}')/N\,, \tag{50}$$

where the summation is done over all pairs involved in a state Ψ_{kj}. The condition **R**<**R'** guarantees that every pair is counted only once. *N* is the total number of such pairs, which averages the algebraic sum of the bonding indicators in the numerator of Eq. (50). Because of the symmetry of a solid and the limited range of bond-like interactions as described by $B^{kj}(\mathbf{R},\mathbf{R}')$, the calculation of Psib(Ψ_{kj}) poses no problem. Psib(Ψ_{kj}) can also be applied to the molecular case by simply removing **k** in Eq. (50). It should be mentioned that the pairwise interaction determined by Psib(Ψ_{kj}) is different from that derived from the wave function in Eq. (25), because Ψ_{kj} in Eq. (50) is a solution of Eq. (29), which is a single particle Hamiltonian. However, a quantitative relation has not yet been worked out. Particularly Psib(Ψ_{kj}) can be used to demonstrate the difference between flat band electrons and steep band electrons in the e-p coupling processes and thus provides an explanation for the peak-like structure on chemical reasons.

The actual example MgB_2 may illustrate the approach; see Fig. 8 and Table 1. By means of Eq. (47), the orbital compositions of the Fermi states are quantitatively calculated. Our calculations [112] based on the TB/FP-LMTO method have clearly indicated that Mg has a significant contribution to the steep band (π) states of MgB_2. The covalent interaction between Mg and B along the direction perpendicular to the $B^{2-}_{6/3}$ plane is revealed by using the bonding indicator as in Eq. (49). The substantial covalent bonding contribution of Mg around the Fermi level gives a satisfactory explanation for the rather difficult substitutional chemistry [138] which could not be understood on the basis of earlier work [139] assuming a purely ionic bonding between Mg and B. The e-p coupling between the Mg admixed B-π states and in- as well as out-of-plane phonons is shown to

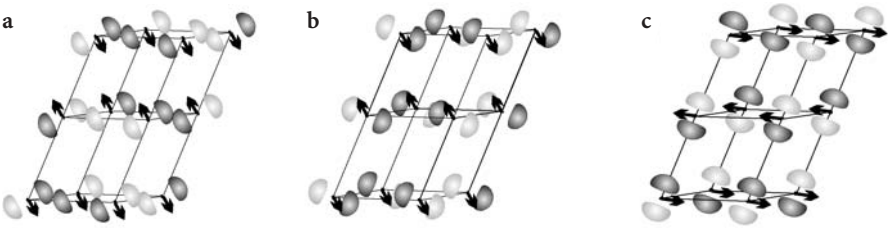

Fig. 14a–c Projection of the orbitals of the: **a** $|Z6\rangle$; **b** $|D6\rangle$; **c** $|F6\rangle$ states of Hg together with the doubled unit cell and the $\mathbf{L}_1$ (a and b) and $\mathbf{L}_3$ (c) phonon patterns represented by *arrows*

be the origin of the small gap, while that between the σ states of mainly B character and the in-plane E_{2g}-like phonons is the origin of the large gap. As can be seen from our results in Fig. 8c, the interesting inter-band hybridization (the third term in Eq. 17) can be mediated through Mg states with d-symmetry, which can enhance T_c in a typical two-band model [31, 32, 140]. As shown in Fig. 8d, the e-p coupling between the E_{2g}-like phonons and the σ states is the strongest among all others and the reason for the very pronounced peak-like structure.

As a second example we have chosen Hg metal. In Fig. 14, the flat band Fermi states $|Z6\rangle$, $|F6\rangle$, $|D6\rangle$ are shown which are coupled to the L_1 and L_3 phonons, respectively, where $|F6\rangle$, $|D6\rangle$ are equivalent states.

Our frozen phonon calculations [136] based on Eqs. (48) and (50) have shown that the variations of Psib($|Z6\rangle$), Psib($|F6\rangle$), Psib($|D6\rangle$) caused by the L_1 phonon (approximately –0.27) are nearly twice as large as those (~–0.14) caused by the L_3 phonon. This result is consistent with that shown in Fig. 14, where the L_1 phonon is close to the peak position, while the L_3 phonon produces a rather small $\lambda(\mathbf{q})$ value. This fact indicates that the variation of chemical pairwise interaction as measured by $\Delta\mathrm{Psib}(\Psi_{kj})$ is tightly connected to the e-p coupling in conventional superconductors. Further knowledge of this relation will help us to understand the superconducting transition close to a structural transition.

6 Summary

In this review a survey on current theories of superconductivity is given. Of course, this survey has to be incomplete but even the discussed theories already reveal the controversial views on the origin of superconductivity. Nevertheless, the pairing of charge carriers has been seen as a trunk of an evolution tree with BCS theory at its bottom. By inspecting the limitations of the BCS theory we have focused on four aspects, namely gap symmetry, pairing mechanisms for electrons/holes, inhomogeneity and properties of the charge carriers. Three basic pairing modes are extracted from the reviewed theories.

In our view, the pairing of electrons/holes is intimately related with chemical bonding. The relation between bond-like interactions in real space and a Cooper pair state is discussed. A signal of relatively strong interactions is the occurrence of flat bands near the Fermi level in the band structure of the normal state. Flat bands besides steep bands at the Fermi level are considered to be a necessary though not sufficient condition for superconductivity to occur.

The conditions for the occurrence of flat bands are discussed, which are based on symmetry reasons, namely local inversion centers for E_{kj}, as well as weak covalent bonding. A peak-like structure of the e-p coupling is expected from our flat/steep band model and has been found in our and others' numerical calculations. We have introduced the functional $\mathrm{Psib}(\Psi_{kj})$ in order to describe quantitatively the bonding property of specific electronic states and as an attempt to analyze the chemical pairwise interactions. The variation of

Psib(Ψ_{kj}) provides an explanation for peak-like structures. The flat/steep band model has been illustrated by inspecting the normal state electronic properties of superconductors from elements to complex compound systems with detailed discussions of Hg and MgB_2. One finds the flat/steep band scenario also in high T_c cuprates. As can be seen from the surveyed theories and a recent experiment [141], it remains unclear whether the oxocuprates have to be understood within an unconventional pairing mechanism or simply as arising from a complex interplay of different mechanisms. Therefore, we focused our discussion on phonon-mediated superconductors.

Acknowledgement We would like to acknowledge A. Bussmann-Holder, O. Gunnarsson, O. Jepsen, R. Micnas and G. Stollhoff for helpful and stimulating discussions.

References

1. Kamerlingh-Onnes H (1911) Akad van Wetenschappen 113:818
2. London F (1938) Phys Rev 54:947
3. (a) Ogg RA Jr (1946) J Chem Phys 14:114; (b) Ogg RA Jr (1946) Phys Rev 69:668; (c) Ogg RA Jr (1946) Phys Rev 70:93
4. (a) Schafroth MR (1955) Phys Rev 100:463; (b) Schafroth MR, Blatt JM, Butler ST (1957) Helv Phys Acta 30:93; (c) Schafroth MR (1958) Phys Rev 130:1244
5. Maxwell E (1950) Phys Rev 78:477
6. Reynolds CA, Serin B, Wright WH, Nesbitt LB (1950) Phys Rev 78:487
7. (a) Fröhlich H (1950) Phys Rev 79:845; (b) Fröhlich H (1952) Proc Roy Soc (London) A215:291
8. (a) Bardeen J (1950) Phys Rev 79:167; (b) (1950) Phys Rev 80:567; (c) (1951) Phys Rev 81:829
9. (a) Cooper LN (1956) Phys Rev 104:1189; (b) Bardeen J, Cooper LN, Schrieffer JR (1957) Phys Rev 106:162; (c) (1957) Phys Rev 108:1175
10. (a) Bednorz JG, Müller KA (1986) Z Phys B 64:189; (b) The current record of Tc is created under pressure for $Ba_2Cu_2Cu_3O_{8-\delta}$; see Gao L, Xue YY, Chen F, Ziong Q, Meng RL, Ramirez D, Chu CW, Eggert JH, Mao HK (1994) Phys Rev B 50:4260
11. (a) Simon A (1997) Angew Chem Int Ed Engl 36:1788; (b) Simon A, Yoshiasa A, Bäcker M, Henn R, Felser C, Kremer RK, Mattausch H (1996) Z Anorg Allg Chem 622:123
12. Meissner W, Ochsenfeld R (1933) Naturwiss 21:787
13. Anderson PW, Schrieffer R (1991) Phys Today June 55
14. The term "exotic" is from Uemura and his coworkers. See, e.g., Brandow B (1988) Phys Rep 296:1 and references therein
15. For a review see, e.g., Lang M, Mueller J (2003) In: Bennemann KH, Ketterson JB (eds) The physics of superconductors, vol 2. Springer, Berlin Heidelberg New York
16. (a) Stewart GR (1984) Rev Mod Phys 56:755; (b) Steglich F (1989) J Phys Chem Sol 50:225; (c) Grewe N, steglich F (1991) In: Gschneidner KA Jr, Eyring L (eds) Handbook on the physics and chemistry of rare earths, vol 14. North-Holland, Amsterdam, p 343; (d) Jourdan M, Huth M, Adrian H (1999) Nature 398:47
17. (a) Eliashberg GM (1960) Zh Eksp Teor Fiz 38:966; (1960) Sov Phys JETP (Engl Transl) 11:696; (b) For a recent review see, e.g., Carbotte JP (1990) Rev Mod Phys 62:1027 and references therein
18. Migdal AB (1958) Zh Eksp Teor Fiz 34:1438; (1958) Sov Phys JETP (Engl Transl) 7:996

19. (a) Osheroff DD, Richardson RC, Lee DM (1972) Phys Rev Lett 28:885; (b) Mahan GD (1990) Many particle physics. Plenum, New York, chap 10
20. For heavy-fermion superconductors see, e.g., (a) Tou H, Kitaoka Y, Asayama K, Geibel C, Schank C, Steglich F (1995) J Phys Soc Japan 64:725; (b) Kohori Y, Matsuda K, Kohara T (1996) J Phys Soc Japan 65:1083; (c) Matsuda K et al. (1997) Phys Rev B 55:15223. For high Tc cuprates, see, e.g., (d) Varma CM (1995) J Phys Chem Sol 56:1685; (e) Scalapino DJ (1995) Phys Repts 250:331; (f) Harlingen DJ van (1995) Rev Mod Phys 67:515; (g) Annett J, Goldenfeld N, Leggett AJ (1996) In: Ginzburg DM (eds) Physical properties of high temperature superconductors, vol 5. World Scientific, Singapore, p 375. For general see, e.g., Brandow B (1988) Phys Rep 296:1 and references therein
21. Randeria M, Duan JM, Shieh L-Y (1990) Phys Rev B 41:327
22. (a) Little WA (1964) Phys Rev A 134:1416; (b) Little WA (1981) Int J Quantum Chem 15:545
23. (a) Ginzburg VL (1964) Zh Eksp Teor Fiz 47:2318 [(1964) Sov Phys JETP 20:1549]; (b) Ginzburg VL (1964) Phys Lett 13:101; (c) Ginzburg VL (1976) Usp Fiz Nauk 118:315 [(1976) Sov Phys Usp 19:174]; (d) Ginzburg VL (1972) Ann Rev Mater Sci 2:663; (e) Ginzburg VL (1987) Int J Mod Phys B 1:651 and references therein
24. Beni G, Pincus P, Kanamori J (1974) Phys Rev B 10:1896
25. Hirsch JE, Scalapino DJ (1985) Phys Rev B 32:5639
26. (a) Suhl H, Matthias BT, Walker LR (1959) Phys Rev Lett 3:552; (b) Moskalenko VA (1959) Fiz Met Metalloved 8:503; (c) Kondo J (1963) Prog Theor Phys 29:1; (d) Geilikman BT, Zaitsev RO, Kresin VZ (1967) Sov Phys Solid State 9:642; (e) Kresin VZ (1973) J Low Temp Phys 11:519; (f) Kresin VZ, Wolf S (1990) Physica C 169:476; (g) Entin-Wohlman O, Imry Y (1988) Physica C 153/155:1323; (h) Chakraverty BK (1993) Phys Rev B 48:4047
27. (a) Bussmann-Holder A, Genzel L, Simon A, Bishop AR (1993) Z Phys B 91:271; (b) Bussmann-Holder A, Genzel L, Simon A, Bishop AR (1993) Z Phys B 92:149
28. Nagamatsu J, Nakagawa N, Muranaka T, Zenitani Y, Akimitsu A (2001) Nature 410:63
29. For a review of experimental evidences of two-gap structure of MgB_2, see Buzea C, Yamashita T (2001) Sci Tech 14:R115
30. (a) Cubitt R, Levett S, Bud'ko SL, Anderson NE, Canfield PC (2003) Phys Rev Lett 90:157002; (b) Souma S et al. (2003) Nature 423:65
31. Lee DH, Ihm J (1987) Solid State Commun 62:811
32. (a) Butler WH, Allen PB (1976) In: Douglass DH (ed) Superconductivity and d- and f-band metals. Plenum Press, New York, p 73; (b) Pinski FJ, Allen PB, Butler WH (1981) Phys Rev B 23:5080; (c) Xu J-H (1988) Solid State Commun 65:135; (d) Bussmann-Holder A, Bishop AR, Simon A (1993) Z Phys B 90:183; (e) Mazin II, Liechtenstein AI, Rodriguez CO, Jepsen O, Andersen OK (1993) Physica C 209:125
33. See, e.g., (a) Mermin D (1979) Rev Mod Phys 51:591; (b) de Gennes PG (1974) In: The physics of liquid crystals. Oxford University Press, chap 1; (c) Coleman S (1985) In: Aspects of symmetry. Selected Erice Lectures, section 1, Cambridge University Press, Cambridge, p113
34. Shirane G, Thomlinson W, Moncton DE (1980) In: Suhl H, Maple MB (eds) Superconductivity in d- and f-band metals. Academic Press, New York, p 381
35. (a) Davidov D, Baberschke K, Mydosh JA, Nieuwenhuys GJ (1977) J Phys F 7:L47; (b) Roth S (1978) Appl Phys 15:1
36. Chu CW, Huang S, Sleight AW (1976) Solid State Commun 18:977
37. McMillan WL (1968) Phys Rev 167:331
38. For a review see, e.g., Kastner MA, Birgeneau RJ, Shirane G, Endoh Y (1998) Rev Mod Phys 70:897
39. (a) Gor'kov LP, Sokol AV (1987) JETP Lett 46:421; (b) Gor'kov LP, Kresin V (2000) J Supercond 13:239; (c) Gor'kov LP (2000) J Supercond 13:765

40. (a) Zaanen J, Gunnarsson (1989) Phys Rev B 40:7391; (b) Poilblanc D, Rice TM (1989) Phys Rev B 39:9749; (c) Schulz HJ (1989) J Phys (France) 50:2833; (d) Machida K (1989) Physica C 158:192; (e) Kato M, Machida K, Nakanishi H, Fujita M (1990) J Phys Soc Jpn 59:1047
41. (a) Cheong S-W, Aeppli G, Mason TE, Mook HA, Hayden SM, Canfield PC, Fisk Z, Clausen KN, Martinez JL (1991) Phys Rev Lett 67:1791; (b) Kremer RK, Hizhnyakov V, Sigmund E, Simon A, Müller KA (1993) Z Phys B Cond Matter 91:169; (c) Tranquada JM, Sternlieb BJ, Axe JD, Nakamura Y, Uchida S (1995) Nature 375:561; (d) Tranquada JM, Axe JD, Ichikawa N, Nakamura Y, Uchida S, Nachumi B (1996) Phys Rev B 54:7489; (e) Bianconi A, Saini NL, Rossetti T, Lanzara A, Perali A, Missori M, Oyanagi H, Yamaguchi H, Nishihara Y, Ha DH (1996) Phys Rev B 54:12018; (f) Wakimoto S, Shirane G, Endoh Y, Hirota K, Ueki S, Yamada K, Birgeneau RJ, Kastner MA, Lee YS, Gehring PM, Lee SH (1999) Phys Rev B 60:R769; (g) Mook HA, Dai P, Dogan F (2002) Phys Rev Lett 88:097004; (h) Ando Y, Segawa K, Komiya S, Lavrov AN (2002) Phys Rev Lett 88:137005
42. (a) Emery VJ, Kivelson SA, Zachar O (1997) Phys Rev B 56:6120; (b) Carlson EW, Orgad D, Kivelson SA, Emery VJ (2000) Phys Rev B 62:3422
43. Castellani C, Di Catro C, Grilli M (1995) Phys Rev Lett 75:4650
44. (a) Jørgensen JD, Dabrowski B, Pei S, Hinks DG, Soderholm L, Morosin B, Schirber JE, Ventunni EL, Ginley DS (1988) Phys Rev B 38:11337; (b) Chaillout C, Cheong S-W, Fisk Z, Lehmann MS, Marezio M, Morosin B, Schirber JE (1989) Physica C 158:183; (c) Kremer RK, Simon A, Sigmund E, Hizhnyakov V (1995) J Magn Magn Mater 140/144:1285; (d) Kremer RK, Sigmund E, Hizhnyakov V, Hentsch F, Simon A, Müller KA, Mehring M (1992) Z Phys B Cond Matter 86:319; (e) Sigmund E, Hizhnyakov V, Kremer RK, Simon A (1994) Z Phys B: Cond Matter 94:17
45. Gor'kov L, Kresin V (2000) J Supercond 13:239 and references therein
46. For a review see: (a) Sachdev S (1999) Quantum phase transitions. Cambridge University Press, Cambridge; (b) Sachdev (2000) Science 288:475 and references therein
47. (a) Landau LD (1956) Zh Eksp Teor Fiz 30:1058 [(1957) Sov Phys JETP 3:920]; (b) Silin VP (1957) Zh Eksp Teor Fiz 33:495 [(1958) Sov Phys JETP 6:389]; (c) Lifshits IM, Azbel' MYa, Kaganov MI (1973) Electron theory of metals. Consultants Bureau, New York
48. (a) Eliashberg GM (1961) Zh Eksp Teor Fiz 41:1241 [(1957) Sov Phys JETP 14:970]; (b) Keldysh LV (1964) Zh Eksp Teor Fiz 47:1515 [(1965) Sov Phys JETP 20:1018]; (c) Rainer D (1986) In: Brewer DC (ed) Progress in low temperature physics, vol X. Elsevier, Amsterdam, p 371
49. (a) Allen PB (1992) Comments Cond Mat Phys 15:327 and references therein; (b) Carbotte JP (1990) Rev Mod Phys 62:1027 and references therein
50. Maksimov EG (2000) Phys Uspekhi 43:965
51. Luttinger JM (1963) J Math Phys 15:609
52. (a) SÛlyom J (1979) Adv Phys 28:201; (b) Voit J (1995) Rep Prog Phys 58:977; (c) Schulz HJ (1991) Int J Mod Phys B 5:57; (d) Maekawa S, Tohyama T (2001) Rep Prog Phys 64:383
53. (a) Anderson PW (1987) Science 235:1196; (b) Anderson PW (1997) The theory of superconductivity in the high-Tc cuprates. Princeton University Press, Princeton, New Jersey
54. Varma CM, Littlewood PB, Schmitt-Rink S, Abrahams E, Ruckenstein AE (1989) Phys Rev Lett 63:1996
55. (a) Nagaosa N, Lee PA (1990) Phys Rev Lett 64:2450; (b) Yoffe LB, Wiegmann PB (1990) Phys Rev Lett 65:653
56. (a) Kalmeyer V, Laughlin RB (1987) Phys Rev Lett 59:2095; (b) Affleck I, Marston JB (1988) Phys Rev B 37:3664

57. Emery VJ, Kivelson SA, Zachar O (1997) Phys Rev B 56:6120
58. Chakravarty S, Laughlin RB, Morr DK, Nayak C (2001) Phys Rev B 63:094503
59. (a) Schrieffer JR, Wen XG, Zhang SC (1989) Phys Rev B 39:11663; (b) Kampf A, Schrieffer JR (1990) Phys Rev B 41:6399; (1990) Phys Rev B 42:7967; (c) Frenkel DM, Hanke W (1990) Phys Rev B 42:6711
60. (a) Kamimura H, Eto M, Matsuno S, Ushio H (1992) Comments Cond Mat Phys 15:303 and references therein; (b) Wood RF (1991) Phys Rev Lett 66:829; (c) Wood RF (1995) In: Salje EKH, Alexandrov AS, Liang WY (eds) Polarons and bipolarons in high-T_c superconductors and related materials. Cambridge University Press, Cambridge; (d) Mott NF (1990) Adv Phys 39:55; (e) Mott NF (1990) Contemp Phys 31:373
61. (a) Millis AJ, Monien H, Pines D (1990) Phys Rev B 42:1671; (b) Pines D (1997) Physica C 282:273 and references therein; (c) Pines D (1997) Z Phys B 103:129; (d) Chubukov AV, Pines D, Schmalian J (2002) cond-mat/0201140; (e) Sadovskii MV (2001) cond-mat/0102111 and references therein
62. (a) Labbe J, Bok J (1987) Europhys Lett 3:1225; (b) Friedel J (1987) J Phys 48:1787; Friedel J (1989) J Phys C 1:7757; (c) Schulz HJ (1987) Europhys Lett 4:609; (d) Newns DM, Tsuei CC, Pattnaik PC, Kane CL (1992) Comments Cond Mat Phys 15:273 and references therein; (e) Markiewicz RS (1997) J Phys Chem solids 58:1179 and references therein; (f) Szotek Z, Gyorffy BL, Temmerman WM, Andersen OK (1998) Phys Rev B 58:522; (h) Andersen OK, Jepsen O, Liechtenstein AI, Mazin II (1994) Phys Rev B 49:4145
63. (a) Alexandrov AS, Ranninger J (1981) Phys Rev B 24:1164; (b) Alexsandrov AS, Mott NF (1994) Rep Prog Phys 57:1197; (c) Alexandrov AS (1995) In: Griffin A, Snoke DW, Stringari S (eds) Bose-Einstein condensation. Cambridge University Press, Cambridge, p. 541; (d) Alexandrov AS (1998) In: Iadonisi G, Schrieffer JR, Chiofalo ML (eds) Models and phenomenology for conventional and high-temperature superconductivity. IOS Press, Amsterdam, p 309; (e) Alexandrov AS (2002) In: Annett JF, Kruchinin S (eds) New trends in superconductivity. Kluwer Academic Publishers, Netherlands, p 71
64. (a) Ranninger J, Robaszkiewicz S (1985) Physica B 135:468; (b) Robaszkiewicz S, Micnas R, Ranninger J (1987) Phys Rev B 36:180; (c) Micnas R, Ranninger J, Robaszkiewicz S (1990) Rev Mod Phys 62:113; (d) Ranninger J (1998) J Phys Chem Solids 59:1759 and references therein; (e) Micnas R, Robaszkiewicz S, Bussmann-Holder A (2002) Phys Rev B 66:104516
65. Norman MR (1993) J Phys Chem Sol 54:1165
66. Anderson PW (2002) arXiv: cond-mat/0201429
67. (a) Marston JB, Affleck I (1989) Phys Rev B 39:11538; (b) Ivanov DA, Lee PA, Wen X-G (2000) Phys Rev Lett 84:3958; (c) Wen X-G, Lee PA (1996) Phys Rev Lett 76:503
68. Halperin BI, Rice TM (1968) Solid State Phys 21:116
69. Zener C (1951) Phys Rev 82:403
70. (a) Hubbard J (1963) Proc R Soc A 276:238; (b) Hubbard J (1964) Proc R Soc A 277:237; (c) Hubbard J (1964) Proc R Soc A281:401; (d) Hubbard J (1965) Proc R Soc A285: 542
71. Schrieffer JR, Wolff PA (1966) Phys Rev B 149:491
72. (a) Bulaevskii LN, Nagaev EL, Khomskii DI (1967) Sov Phys JETP 27:638; (b) Gros C, Joynt R, Rice TM (1987) Phys Rev B 36:381
73. Varma CM, Schmitt-Rink S, Abrahams E (1987) Solid State Commun 62:681
74. (a) Emery VJ (1987) Phys Rev Lett 58:2794; (b) Gaididei YB, Loktev VM (1988) Phys Status Solidi B 147:307
75. (a) Zhang FC, Rice TM (1988) Phys Rev B 37:3759; (b) Zhang FC, Rice TM (1990) Phys Rev B 41:7243
76. Lambrecht WRL, Andersen OK (1986) Phys Rev B 34:2439

77. (a) Belinicher VI, Chernyshev AL, Shubin VA (1997) Phys Rev B 56:3381; (b) Leung PW (2002) Phys Rev B 65:205101; (c) Chernyshev AL, Wood RF, arXiv: cond-mat/0208541
78. (a) Chakraverty BK, Schlenker C (1976) J Phys (Paris) Colloq 37:C4–353; (b) Chakraverty BK (1979) J Phys (Paris) Lett 40:L-99; (c) Lakkis S, Schlenker C, Chakraverty BK, Buder R, Marezio M (1976) Phys Rev B 14:1429; (d) Chakraverty BK, Sienko MJ, Bonnerot J (1978) Phys Rev B 17:3781; (e) Schlenker C, Ahmed S, Buder R, Gourmala M (1979) J Phys C 12:3503
79. (a) Landau L (1933) Phys Z Sowjetunion 3:664; (b) Feynman (1955) Phys Rev 97:66; (c) Holstein T (1959) Ann Phys (N.Y.) 8:343; (d) Toyozawa Y (1961) Prog Theor Phys 26:29; (e) Austin IG, Mott NF (1969) Adv Phys 19:41; (f) Emin D (1973) Adv Phys 22:57; (g) Emin D, Holstein T (1976) Phys Rev Lett 36:323
80. (a) Onoda M, Takahashi T, Nagasawa H (1982) J Phys Soc Jpn 51:3868; (b) Onoda M, Nagasawa H (1983) J Phys Soc Jpn 52:2231; (c) Anderson PW (1973) Mater Res Bull 8:153; (d) Anderson PW (1975) Phys Rev Lett 34:953; (e) Alexandrov AS, Ranninger J (1981) Phys Rev B 23:1796
81. (a) Harris JM, Yan YF, Matl P, Ong NP, Anderson PW, Kimura T, Kitazawa K (1995) Phys Rev Lett 75:1391; (b) Alexandrov AS (1997) Phys Rev Lett 79:4717; (c) Ong NP, Anderson PW (1997) Phys Rev Lett 79:4718
82. (a) Chakraverty BK, Ranninger J, Feinberg D (1998) Phys Rev Lett 81:433; (b) Alexsandrov AS (1999) Phys Rev Lett 82:2620; (c) Chakraverty BK, Ranninger J, Feinberg D (1999) Phys Rev Lett 82:2621; (d) Mello EVL, Ranninger J (1998) Phys Rev B 58:9098; (e) Alexandrov AS (2000) Phys Rev B 61:12315; (f) Bonča J, Katrašnik T, Trugman SA (2000) Phys Rev Lett 84:3153
83. (a) Eagles DM (1969) Phys Rev 186:456; (b) Leggett AJ (1980) In: Pekalski A, Przystawa J (eds) Modern trends in the theory. Springer, NewYork, p 13; (c) Noziéres P, Schmitt-Rink S (1985) J Low Temp Phys 59:195; (d) Drechsler M, Zweger W (1992) Ann Phys (Germany) 1:15; (e) Randeria M, Duan JM, Shieh L-Y (1989) Phys Rev Lett 62:981; (f) de Melo CAR Sá, Randeria M, Engelbrecht JR (1993) Phys Rev Lett 71:3202; (g) Haussmann R (1994) Phys Rev B 49:12975; (h) Pistolesi F, Strinati GC (1994) Phys Rev B 49:6356; (i) Marni M, Pistolesi F, Strinati GC (1998) Eur Phys J B 1:151; (j) Pistolesi F, Noziéres P (2002) Phys Rev B 66:054501
84. Rumer YB (1960) Sov Phys JETP 10:409
85. Anderson PW (1961) Phys Rev 124:41
86. (a) Friedberg R, Lee TD (1989) Phys Rev B 40:6745; (b) Friedberg R, Lee TD (1989) Phys Lett A 138:423; (c) Friedberg R, Lee TD, Ren HC (1991) Phys Lett A 152:417; (d) Friedberg R, Lee TD, Ren HC (1994) Phys Rev B 50:10190
87. (a) Geshkenbein B, Ioffe LB, Larkin AI (1997) Phys Rev B 55:3173; (b) Kulik IO (1988) Int J Mod Phys B 2:851; (c) Ioffe L, Larkin AI, Ovchinnikov YN, Yu L (1989) Int J Mod Phys B 3:2065; (d) Müller KA, Keller H (1997) In: Proc NATO ASI Materials Aspects of High-Tc Superconductivity: 10 years after the discovery, Kluwer; (e) Müller KA (2002) Phil Mag Lett 82:279; (f) Chakraverty BK (1993) Phys Rev B 48:4047
88. (a) Ginzburg VL, Landau LD (1950) Zh Eksper Teor Fiz 20:1064; (b) Gor'kov LP (1959) Zh Eksper Teor Fiz 36:1918: (c) Zh Eksper Teor Fiz 37:833
89. (a) Leggett AJ (1998) J Phys Chem Solids 59:1729; (b) Leggett AJ (1999) Phys Rev Lett 83:392; (c) Leggett AJ (1999) Proc Natl Acad Sci USA 96:8365
90. (a) Matthias BT (1955) Phys Rev 97:74; (b) Matthias BT (1957) In: Gorter CJ (ed) Progress in low temperature physics, vol II. North-Holland, Amsterdam, p 138; (c) Matthias BT (1973) In: Gregory WD, Matthews WN, Edelsack EA (eds) The science and technology of superconductivity, vol 1. Plenum, New York, p 263; (d) Matthias BT (1971) Physica 55:69

91. Hafner J, Hanke W, Bilz H (1977) In: Riste T (ed) Electron-phonon interactions and phase transitions. Plenum Press, New York, p 200
92. (a) Ahn K, Gibson B, Kremer RK, Mattausch H, Stolovits A, Simon A (1999) J Phys Chem B 103:5446; (b) Henn RW, Kremer RK, Simon A (2000) J Supercond 13:471; (c) Henn RW, Bernhard C, Kremer RK, Gulden T, Simon A, Blasius T, Niedermayer C (2000) Phys Rev B 62:14469; (d) Puschnig P, Ambrosch-Draxl C, Henn RW, Simon A (2001) Phys Rev B 64:024519; (e) Ahn K, Grzechnik A, Kremer RK, Simon A, Marshall WG (2003) J Solid State Chem 171:367
93. Simon A (2000) J Supercond 13:691
94. Roberts BW (1976) J Phys Chem Ref Data 5:581
95. For a review, see (a) Testardi LR (1975) Rev Mod Phys 47:637; (b) Weber W (1984) In: Phariseau P, Temmerman W (eds) Electronic structure of complex systems. Nato-ASI Series, Plenum, New York, p 422; (c) Weber W, Mattheiss LF (1982) Phys Rev B 25:2270
96. Deng S, Simon A, Köhler J (1998) Angew Chem Int Ed Engl 37:640
97. (a) Phillips JC, Kleinmann L (1959) Phys Rev 116:287; (b) Harrison WA (1966) In: Pseudopotentials in the theory of metals. Benjamin, New York
98. Batyev ĚG, Pokrovskiĭ VL (1964) Sov Phys JETP 19:181
99. Scalapino DJ (1969) In: Parks RD (eds) Superconductivity, vol 1. Marcel Dekker Inc, New York, p 449
100. (a) Hedin L, Lundqvist S (1969) In: Ehrenreich H, Seitz F, Turnbull D (eds) Solid State Phys 23:1; (b) Anisimov VI, Aryasetiawan F, Liechtenstein AI (1997) J Phys C 9:767
101. (a) Deng S, Simon A, Köhler J (2003) In: International Conference on Dynamic Inhomogenities in Complex Oxides, June 14–20, 2003, Bled, Slovenia, (b) Deng S, Simon A, Köhler J (2004) J Supercond 17:227
102. (a) Kumar N, Sinha KP (1968) Phys Rev 174:482; (b) Ngai KL, Johnson EJ (1972) Phys Rev Lett 29:1607; (c) Ngai KL (1972) Phys Rev Lett 32:215; (d) Kumar N (1974) Phys Rev B 9:4993
103. Jones RO, Gunnarsson O (1989) Rev Mod Phys 61:689
104. Deng S, Simon A, Köhler J (2001) J Phys Chem Solids 62:1441
105. Kohn W, Sham LJ (1965) Phys Rev A 140:1133
106. (a) Kotliar G, Savrasov S (2001) In: Tsvelik AM (eds) New theoretical approaches to strongly correlated systems. Kluwer, New York, p 259; (b) Geoges A, Kotliar G, Krauth W, Rosenberg MJ (1996) Rev Mod Phys 68:13
107. (a) For metals see, e.g., Kohn W, Sham LJ (1965) Phys Rev A 140:1133; (b) For high Tc cuprates, see a conference proceedings of 'Fermiology of HTSC systems', (1993) J Phys Chem Solids 54 (11/12)
108. Luttinger JM (1960) Phys Rev 119:1153
109. Deng S, Simon A, Köhler J (2003) J Solid State Chem 176:412
110. Wannier GH (1937) Phys Rev 32:191
111. (a) Cracknell AP (1973) J Phys C 6:826; (b) (1973) J Phys C 6:841
112. Deng S, Simon A, Köhler J, Bussmann-Holder A (2003) J Supercond 16:919
113. Dronskowski R, Blöchl PE (1993) J Phys Chem 97:8617
114. Hoffmann R (1988) Rev Mod Phys 60:601
115. Krier G, Jepsen O, Burkhardt A, Andersen OK (1999) TB-LMTO-ASA Program Version 4.7, Stuttgart, Germany
116. Deng S, Simon A, Köhler J (2003) J Supercond 16:477
117. Yelland EA et al. (2002) Phys Rev Lett 88:217001
118. (a) Rosner H, An JM, Pickett WE, Drechsler SL (2002), Phys Rev B 66:024521; (b) Mazin II, Kortus J (2002) Phys Rev B 65:180510

119. (a) Hebard AF, Rosseinski MJ, Haddon RC, Murphy DW, Glarum SH, Palstra TTM, Ramirez AP, Kortan AR (1991) Nature 350:600; (b) Haddon RC (1992) Acc Chem Res 25:127
120. (a) Gunnarsson O (1997) Rev Mod Phys 69:575; (b) Lof RW, Veenendaal MA, Koopmans B, Jonkman HT, Sawatzky GA (1992) Phys Rev Lett 68:3924; (c) Erwin SC, Pickett WE (1991) Science 254:842; (d) Capone M, Fabrizio M, Castellani C, Tosatti E (2002) Science 296:2364
121. (a) Gunnarsson O (1997) Rev Mod Phys 69:575; (b) Lof RW, Veenendaal MA, Koopmans B, Jonkman HT, Sawatzky GA (1992) Phys Rev Lett 68:3924; (c) Erwin SC, Pickett WE (1991) Science 254:842; (d) Capone M, Fabrizio M, Castellani C, Tosatti E (2002) Science 296:2364
122. Yang WL, Brouet V, Zhou XJ, Choi HJ, Louie SG, Cohen ML, Kellar SA, Bogdanov PV, Lanzara A, Goldoni A, Parmigiani F, Hussain Z, Shen Z-X (2003) Science 300:303
123. (a) King DM, Shen Z-X, Dessau DS, Marshall DS, Park CH, Spicer WE, Peng JL, Li ZY, Greene RL (1994) Phys Rev Lett 73:3298; (b) Gofron K, Campuzano JC, Ding H, Gu C, Liu R, Dabrowski B, Veal BW, Cramer W, Jennings G (1993) J Phys Chem Solids 54:1193; (c) Liu R, Veal BW, Paulikas AP, Downey JW, Kosti? PJ, Fleshler S, Welp U (1992) Phys Rev B 46:11056
124. (a) Andersen OK, Liechtenstein AI, Jepsen O, Paulsen F (1995) J Phys Chem Solids 56:1573; (b) Pickett WE, Cohen RE (1990) Phys Rev B 42:8764
125. King DM, Shen Z-X, Dessau DS, Wells BO, Spicer WE, Arko AJ, Marshall DS, Dicarlo J, Loeser AG, Park CH, Ratner ER, Peng JL, Li ZY, Greene RL (1993) Phys Rev Lett 70:3159
126. Dessau DS, Shen Z-X, King DM, Marshall DS, Lombardo LW, Dickinson PH, Loeser AG, DiCarlo J, Park C-H, Kapitulnik A, Spicer WE (1993) Phys Rev Lett 71:2781
127. Zhou XJ et al. (2003) Nature 423:398
128. (a) Allen PB (1980) In: Horton GK, Maradudin AA (eds) Dynamical properties of solids, vol 3. North-Holland, Amsterdam, p 95; (b) Allen PB (1972) Phys Rev B 6:2579
129. (a) Savrasov SY (1996) Phys Rev B 54:16470; (b) Savrasov SY, Savrasov DY (1996) Phys Rev B 54:16487
130. Dacorogna MM, Cohen ML, Lam PK (1985) Phys Rev Lett 55:837
131. Allen PB, Dynes RC (1975) Phys Rev B 12:905
132. (a) Kong Y, Dolgov OV, Jepsen O, Andersen OK (2001) Phys Rev B 64:020501(R); (b) Yildirim T, Gülseren O, Lynn JW, Brown CM, Udovic TJ, Huang Q, Rogado N, Regan KA, Hayward MA, Slusky JS, He T, Hass MK, Khalifah P, Inumaru K, Cava RJ (2001) Phys Rev Lett 87:037001-1; (c) Bohnen K-P, Heid R, Renker B (2001) Phys Rev Lett 86:5771
133. An JM, Savrasov SY, Rosner H, Pickett WE (2002) cond-mat/0207542
134. Butler WH, Pinski FJ, Allen PB (1979) Phys Rev B 19:3708
135. Mulliken RS (1955) J Chem Phys 23:1833
136. Deng S, Simon A, Köhler J (2002) J Am Chem Soc 124:10712
137. Sutton AP, Finnis MW, Pettifor DG, Ohta Y (1988) J Phys C 21:35
138. (a) Cava RJ, Zandbergen HW, Inumaru K (2003) Physica C 385:8; (b) Hinks DG, Jorgensen JD, Zheng H, Short S (2002) Physica C 382:166
139. (a) Kortus J, Mazin II, Belashchenko KD, Antropov VP, Boyer LL (2001) Phys Rev Lett 86:4656; (b) Mazin II, Antropov VP (2003) Physica C 385:49
140. Bussmann-Holder A, Bianconi A (2003) Phys Rev B 67:132509
141. Hwang J, Timusk T, Gu GD (2004) Nature 427:714

Struct Bond (2005) 114:143–169
DOI 10.1007/b101019

Unconventional Isotope Effects in Cuprate Superconductors

H. Keller (✉)

Physik-Institut der Universität Zürich, Winterthurerstrasse 190,
CH-8057 Zürich, Switzerland
keller@physik.unizh.ch

Abstract A brief review on unconventional oxygen-isotope ($^{16}O/^{18}O$) effects (OIE) in cuprate high-temperature superconductors (HTS) is presented. First the doping dependence of the OIE on the superconducting transition temperature T_c in various HTS is discussed. For all cuprate HTS families the OIE exponent of T_c (α_O) shows a generic trend: in the underdoped regime α_O is large ($\alpha_O > 0.5$) and becomes small in the optimally doped and overdoped regime. Magnetization, magnetic torque, and muon-spin rotation (μSR) studies of the OIE on the in-plane penetration depth $\lambda_{ab}(0)$ in $La_{2-x}Sr_xCuO_4$ and $Y_{1-x}Pr_xBa_2Cu_3O_{7-\delta}$ indicate a substantial oxygen-mass dependence of $\lambda_{ab}(0)$ which increases with reduced doping. It is remarkable that even in optimally doped $YBa_2Cu_3O_{7-\delta}$ and $La_{2-x}Sr_xCuO_4$ a substantial OIE on $\lambda_{ab}(0)$ is observed, although the OIE on T_c is rather small. The observation of an OIE on the penetration depth indicates that cuprate HTS are non-adiabatic superconductors. The oxygen-isotope shifts of T_c and $\lambda_{ab}(0)$ exhibit a correlation that appears to be generic for various families of HTS. Furthermore, site-selective OIE investigations of $Y_{1-x}Pr_xBa_2Cu_3O_{7-\delta}$ clearly reveal that the planar oxygen atoms mainly contribute to the total OIE on T_c as well as on $\lambda_{ab}(0)$ at all doping levels. These unusual isotope effects strongly suggest that lattice effects play an essential role in the basic physics of cuprate HTS and have to be considered in any realistic theoretical model.

Keywords High-temperature superconductivity · Isotope effect · Electron-phonon interaction · Polarons

List of Abbreviations

HTS High-temperature superconductor
OIE Oxygen-isotope effect

SOIE	Site-selective oxygen-isotope effect
ARPES	Angle resolved photoemission electron spectroscopy
EXAFS	Extended X-ray absorption fine structure spectroscopy
EPR	Electron paramagnetic resonance
BCS	Bardeen-Cooper-Schrieffer theory of superconductivity
μSR	Muon-spin rotation
LEμSR	Low-energy muon-spin rotation
SQUID	Superconducting quantum interference device
FC	Field cooled
NQR	Nuclear quadrupole resonance

1 Introduction

Although the discovery of the cuprate high-temperature superconductors (HTS) [1] in 1986 triggered world-wide an enormous effort to understand these novel materials, there is at present still no convincing microscopic theory describing the mechanism of superconductivity. Due to the high values of the superconducting transition temperature T_c and the early observation of a tiny oxygen-isotope effect (OIE) in optimally doped $YBa_2Cu_3O_{7-\delta}$ [2–4], many theoreticians came to the conclusion that the electron-phonon interaction cannot be responsible for high-temperature superconductivity. As a result, alternative pairing mechanisms of purely electronic origin were proposed. However, the assumption that T_c cannot be higher than 30 K within a phonon-mediated pairing mechanism is not justified [5]. A prominent example is the recent discovery of superconductivity in MgB_2 [6] with a $T_c \approx 39$ K which is accepted to be a purely phonon-mediated superconductor. There is increasing experimental evidence from recent work, such as inelastic neutron scattering (see, e.g., [7, 8]), angle resolved photoemission electron spectroscopy (ARPES) [9], extended X-ray absorption fine structure (EXAFS) studies [10], electron paramagnetic resonance (EPR) [11], isotope effect studies (this work and references therein), and a number of other experiments, that lattice effects play an essential role in the basic physics of HTS and have to be included in reliable theoretical models (see, e.g., [12–21]).

It is well known that the observation of an isotope effect on T_c in conventional superconductors was crucial in the development of the microscopic BCS theory. The isotope shift may be quantified in terms of the relation

$$T_c \propto M^{-\alpha}, \qquad \alpha = -d \ln T_c / d \ln M \,, \tag{1}$$

where M is the isotope mass, and α is the isotope-effect exponent. In the simplest case of weak-coupling BCS theory $T_c \propto M^{-1/2}$ and $\alpha_{\mathrm{BCS}} \simeq 0.5$, in agreement with a number of experiments on conventional metal superconductors. However, there are exceptions of his rule such as Zr and Ru for which $\alpha \simeq 0$.

The conventional phonon-mediated theory is based on the Migdal adiabatic approximation in which the density of states at the Fermi level $N(0)$, the electron-phonon coupling constant λ_{ep}, and the effective supercarrier mass m^* are all

independent of the mass M of the lattice atoms. However, if the interaction between the carriers and the lattice ions is strong enough, the Migdal approximation is no more valid [22]. Therefore, in contrast to ordinary metals, unconventional isotope effects on various quantities, such as the superconducting transition temperature and the magnetic penetration depth are expected for a non-adiabatic superconductor [19,21,22].

In 1990 the University of Zurich group started a project on isotope effects in cuprate HTS which was initiated by K. Alex Müller. Here we review some of our results. They include unconventional isotope effects in HTS on the transition temperature and the in-plane magnetic penetration depth. For a detailed description of our work we refer to Refs. [23–29].

The paper is organized as follows. In the next section the sample preparation and oxygen-isotope exchange procedure used for the isotope-effect studies presented here are described. Some results of the OIE on the transition temperature T_c obtained for different cuprate families and results of the site-selective OIE on T_c in optimally doped $YBa_2Cu_3O_{7-\delta}$ and underdoped $Y_{1-x}Pr_xBa_2Cu_3O_{7-\delta}$ are then presented. Magnetization, magnetic torque, and muon-spin rotation (μSR) studies of the OIE on the in-plane penetration depth $\lambda_{ab}(0)$ in $La_{2-x}Sr_xCuO_4$, optimally doped $YBa_2Cu_3O_{7-\delta}$, and $Y_{1-x}Pr_xBa_2Cu_3O_{7-\delta}$ are then reviewed. Furthermore, results of the site-selective OIE on λ_{ab} in $Y_{0.6}Pr_{0.4}Ba_2Cu_3O_{7-\delta}$ obtained by bulk μSR are reported. We discuss implications of the OIE on λ_{ab} and the empirical relation between the isotope effect on T_c and λ_{ab} observed for different HTS families. The conclusions are in the final section.

2
Sample Preparation and Oxygen-Isotope Exchange

The ideal isotope effect experiment requires a set of samples, which are identical in any respect except to the isotope mass. The difference of any measured physical quantity (not only T_c) can then be attributed to the different mass of a particular element at specific lattice sites in the crystal structure. Since most of the results presented in this review concern oxygen-isotope ($^{16}O/^{18}O$) effect (OIE) studies in cuprate HTS, we only describe here the preparation of oxygen-isotope exchanged samples. For a reliable OIE study the isotope substituted samples to be compared should be of identical quality. This means that both samples should fulfill the following conditions: (i) the samples should be prepared from the same starting material, (ii) the samples should be subject to the same thermal treatment, (iii) the oxygen content of both samples should be exactly identical, (iv) the oxygen distribution within the samples should be the same, (v) in the case of powder samples the grain size distribution should be the same, and (vi) for single-crystal samples the experiments should be performed on the same crystal substituted with ^{16}O and ^{18}O, respectively. Here we shortly describe the procedure to prepare oxygen-substituted $YBa_2Cu_3O_{7-\delta}$ samples using solid reactions (see [30] for details). The experimental setup used for the oxygen-isotope exchange in

$YBa_2Cu_3O_{7-\delta}$ samples is shown schematically in Fig. 1. In order to ensure that the ^{16}O and ^{18}O substituted samples are the subject of the same thermal history, the annealing of the two samples is performed simultaneously in $^{16}O_2$ and $^{18}O_2$ (95% enriched) gas, respectively. In chamber A the isotope exchange (^{18}O) and in chamber B an identical process in normal oxygen (^{16}O) takes place. A liquid nitrogen trap is used to condense (and recycle) the expensive $^{18}O_2$ after the exchange process is finished. The exchange apparatus is equipped with a mass spectrometer (not shown), which allows to view the progress of the isotope exchange.

In order to prepare $Y_{1-x}Pr_xBa_2Cu_3O_{7-\delta}$ samples for the site-selective OIE studies a two-step exchange process is applied [24, 30, 31], which enables simultaneous preparation of three samples: two fully exchanged samples $^{16}O_{pac}$ and $^{18}O_{pac}$ and a site-selective substituted sample $^{18}O_p^{16}O_{ac}$ (or $^{16}O_p^{18}O_{ac}$). Here p, a, and c denote the different oxygen sites in $YBa_2Cu_3O_{7-\delta}$ (p: planar oxygen sites, a: apical oxygen sites, c: chain oxygen sites) as illustrated in Fig. 2. The oxygen substitution procedure is shown schematically in Fig. 3. The exchange process is performed in two steps during one heating run. The three starting samples are all fully exchanged with ^{16}O ($^{16}O_{pac}$). In the first step (500°C, 35 h) ^{16}O is completely substituted by ^{18}O in two of the three samples, while the other sample is tempered under identical conditions in $^{16}O_2$. In the second step (320°C, 200 h) a site-selective oxygen exchange ($^{18}O_p^{16}O_{ac}$) is performed in one of the ^{18}O samples. The other two samples (^{16}O and ^{18}O) are simultaneously tempered in $^{16}O_2$ and $^{18}O_2$ atmosphere, respectively. In order to prepare site-selective substituted $^{16}O_p^{18}O_{ac}$ samples a similar procedure is used [24, 30, 31].

In general, the samples are characterized by X-ray diffraction and SQUID magnetization measurements. The oxygen content of the samples is determined very accurately using a precise volumetric analysis [30, 32]. An example of such an analysis for oxygen-substituted $La_{2-x}Sr_xCuO_y$ samples is shown in Fig. 4. The degree of oxygen exchange and the site-selectivity of the samples can be checked by Raman spectroscopy [24, 31, 33, 34] (see the following section).

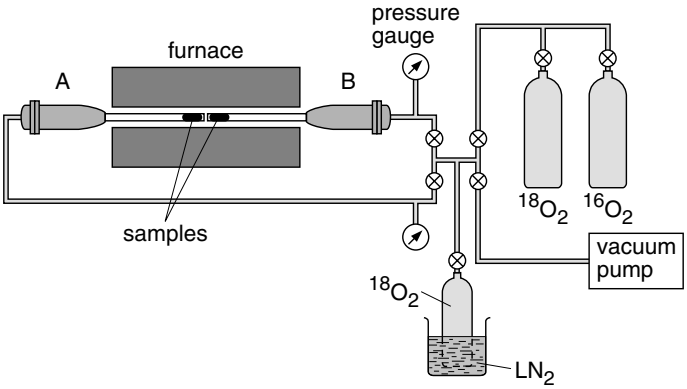

Fig. 1 Experimental setup for the preparation of $^{16}O/^{18}O$ substituted $YBa_2Cu_3O_{7-\delta}$ samples. After [30]

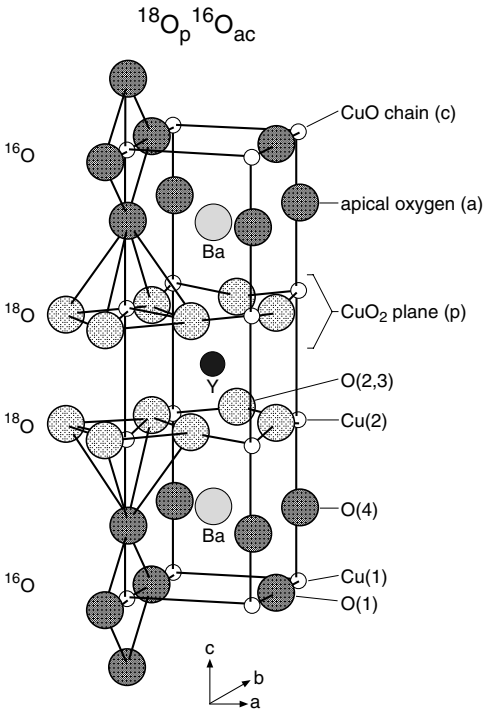

Fig. 2 Crystal structure of $YBa_2Cu_3O_{7-\delta}$ showing the different oxygen sites (p: planar oxygen sites, a: apical oxygen sites, c: chain oxygen sites)

3 Isotope Effect on the Transition Temperature

Since 1987 a number of isotope effect investigations on T_c were performed in most families of cuprate HTS. A comprehensive review of the early work till 1993 is given by Franck [35]. In particular, the oxygen-isotope effect (OIE) on T_c by replacing ^{16}O by ^{18}O was investigated in great detail (see, e.g., [35]). The first OIE experiments were done on optimally doped samples, showing no significant isotope shift [2–4]. However, later experiments revealed a small but finite dependence of T_c on the oxygen-isotope mass M_O [31, 33, 35–37]. It is now well established that the OIE exponent $\alpha_O = -d \ln T_c / d M_O$ as a function of doping shows a trend which appears to be generic for all families of cuprate HTS [24,25,27,33,35,36]: in the underdoped region α_O is large ($\alpha_O \geq \alpha_{BCS} = 0.5$) and becomes small in the optimally doped and overdoped regime. This generic trend is illustrated in Fig. 5 where α_O is plotted vs T_c/T_c^m for various cuprate HTS families (T_c^m is the maximum T_c for a particular family). An interesting case is the single-layer system $La_{2-x}Sr_xCuO_4$. In Fig. 6a the doping dependence of T_c for ^{16}O and ^{18}O samples of $La_{2-x}Sr_xCuO_4$ is shown. It is evident that the T_cs of the ^{18}O samples are lower than those for the ^{16}O samples at all doping levels. The doping dependence of the

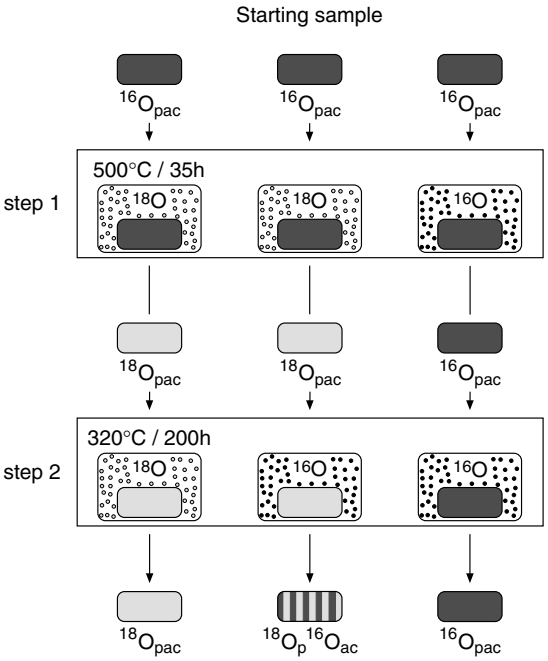

Fig. 3 Schematic diagram of the procedure used for the preparation of fully and site-selective substituted $^{16}O/^{18}O$ $Y_{1-x}Pr_xBa_2Cu_3O_{7-\delta}$ samples. In the first step completely oxygen substituted samples are prepared. The second step is used to prepare the site-selective samples from the completely substituted ones. After [24, 30]

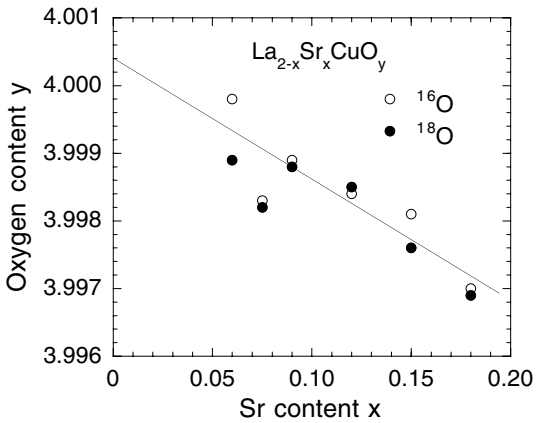

Fig. 4 The oxygen contents of ^{16}O and ^{18}O samples of $La_{2-x}Sr_xCuO_y$ with different Sr content x. The oxygen content y was determined from a very accurate volumetric analysis [32]. Note that y of two samples with equal x are the same within ± 0.0002 per Cu site. After [27]

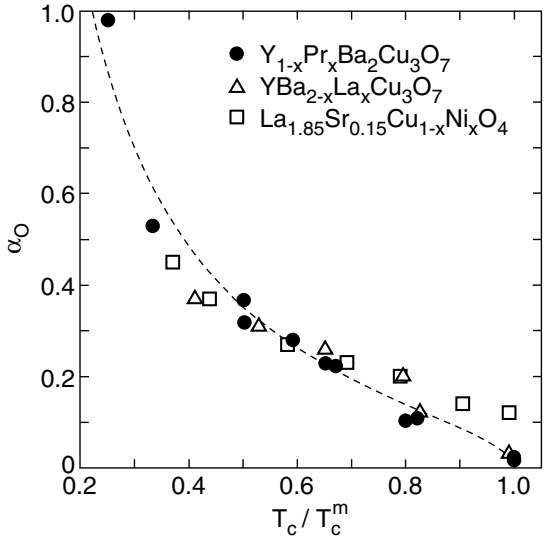

Fig. 5 Isotope-effect exponent α_O vs $\overline{T}_c = T_c/T_c^m$ for various families of cuprate HTS (T_c^m denotes the maximum T_c for a particular family). *Closed circles*: $Y_{1-x}Pr_xBa_2Cu_3O_{7-\delta}$ [34,36, 38] and unpublished data (this work); *open triangles*: $YBa_{2-x}La_xCu_3O_7$ [39]; *open squares*: $La_{1.85}Sr_{0.15}Cu_{1-x}Ni_xO_4$ [40]. The *dashed line* corresponds to $\alpha_O = 0.25\sqrt{(1-\overline{T}_c)/\overline{T}_c}$). After [41]

oxygen-isotope exponent α_O is displayed in Fig. 6b. The exponent α_O increases with decreasing x and becomes very large in the deeply underdoped regime. The large value of α_O at $x \approx 0.125$ may be attributed to a structural instability [42].

It is interesting to note that the copper-isotope (^{63}Cu vs ^{65}Cu) effect exponent α_{Cu} shows a similar trend as α_O [43–46]: both exponents increase monotonically with decreasing doping level x (or T_c). This is illustrated in Fig. 7 where the oxygen and copper isotope effect exponents for $Y_{1-x}Pr_xBa_2Cu_3O_{7-\delta}$ and $Y_{1-x}Pr_xBa_2Cu_4O_8$ are plotted as a function of T_c. Close to optimal doping $\alpha_{Cu} \approx \alpha_O$, whereas in the deeply underdoped regime $\alpha_{Cu} \simeq 0.7\alpha_O$ [44–46]. The substantial oxygen- and copper-isotope effects on T_c in the underdoped regime indicate that lattice vibrations in the CuO_2 planes play a relevant role in cuprate HTS. From this point of view, one would expect that the planar oxygen modes give rise to a larger OIE on T_c than the apical and/or chain oxygen modes. This can be explored by a site-selective oxygen-isotope exchange experiment. Several attempts were made to achieve this goal (see, e.g., [35]). Cardona et al. [47] performed Raman and infrared studies on partially oxygen substituted samples of $YBa_2Cu_3^{18}O_\beta^{16}O_{7-\beta}$ and $TmBa_2Cu_3^{18}O_\beta^{16}O_{7-\beta}$ with $0 \leq \beta \leq 6.1$. No isotope effect on T_c was detected by resistivity measurements if only one out of seven ^{16}O was replaced by ^{18}O. For 85% substitution an isotope shift of $\Delta T_c = 0.3(1)$ K was found in agreement with previous results [35]. These results suggest that the planar oxygen atoms mainly determine the isotope shift of T_c. Nickel et al. [48] reported a negative OIE as-

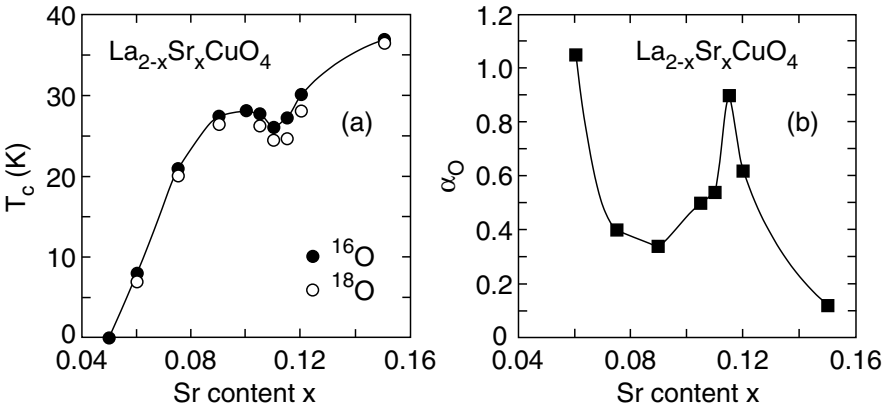

Fig. 6 Dependence of: **a** T_c; **b** oxygen-isotope exponent α_O on the Sr content x for ^{16}O and ^{18}O samples of $La_{2-x}Sr_xCuO_4$. After [25]

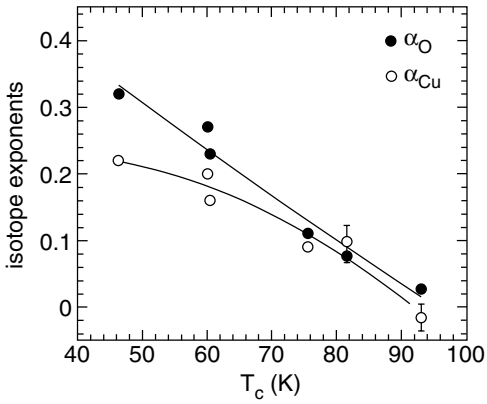

Fig. 7 The oxygen (α_O) and copper (α_{Cu}) isotope exponents as a function of T_c for $Y_{1-x}Pr_xBa_2Cu_3O_{7-\delta}$ and $Y_{1-x}Pr_xBa_2Cu_4O_8$. Data are from [44–46]. After [27]

sociated with oxygen atoms in the CuO_2 planes for highly doped $YBa_2Cu_3O_{7-\delta}$, implying that the apical/chain oxygens make a substantial contribution to the total OIE on T_c. A careful site-selective oxygen-isotope effect (SOIE) experiment was later carried out in optimally doped $YBa_2Cu_3O_{7-\delta}$ by Zech et al. [31]. In contrast to the previous work of Nickel et al. [48], they found that more than 80% of the total (positive) OIE on T_c arises from the oxygen atoms in the CuO_2 planes. Here we briefly describe this experiment. In a fully exchanged ^{18}O sample of $YBa_2Cu_3O_{7-\delta}$ the ^{18}O at the apical (a) and chain (c) sites were replaced by ^{16}O, leaving the ^{18}O in the planes (p) intact, and vice versa. The site-selectivity of the samples was confirmed by Raman spectroscopy as shown in Fig. 8. In Fig. 9 the normalized magnetization curves for all samples investigated are shown in the vicinity of T_c. The fully exchanged samples $\langle^{16}O\rangle^{A,B}$ and $\langle^{18}O\rangle^{A,B}$ of either batch A or B show a total

oxygen-isotope shift of $\Delta T_c = -0.25(5)$ K [$\alpha_O = 0.018(4)$], in agreement with previous reports (see, e.g., [35]). Relative to the ^{16}O oxygenated reference samples, the site-selective samples $\langle {}^{16}O_p^{18}O_{ac}\rangle$ and $\langle {}^{18}O_p^{16}O_{ac}\rangle$ show partial isotope shifts of $\Delta T_c = -0.05(5)$ K and $\Delta T_c = -0.20(5)$ K, arising from the apical/chain (ac) and the planar (p) oxygen sites, respectively. Both site-selective shifts add up to a total shift of $\Delta T_c = -0.25(5)$ K, in agreement with the total ΔT_c for the fully exchanged samples. Note that the two independent experiments A and B yield consistent and complementary results, providing evidence that the planar oxygen atoms mainly ($\geq 80\%$) contribute to the total OIE on T_c. These results were confirmed independently by Zhao et al. [33], who performed SOIE experiments in optimally doped and underdoped samples of $Y_{1-x}Pr_xBa_2Cu_3O_{7-\delta}$. They found that in underdoped $Y_{0.7}Pr_{0.3}Ba_2Cu_3O_{6.97}$ the predominant contribution to the total OIE on T_c also arises mainly from the planar oxygen. Recently, Khasanov et al. [34] studied the SOIE on T_c in underdoped $Y_{0.6}Pr_{0.4}Ba_2Cu_3O_{7-\delta}$. It is evident from Fig. 10 that the OIE on T_c is determined by the planar oxygen atoms (100% within error bar). Figure 11 shows the total and the partial (planar oxygen, apex/chain oxygen) isotope exponent α_O as a function of T_c for $Y_{1-x}Pr_xBa_2Cu_3O_{7-\delta}$.

The isotope shift on T_c was also investigated in the novel superconductor MgB_2 with $T_c \approx 39$ K [49–51]. Whereas the boron-isotope ($^{10}B/^{11}B$) exponent was found to be $\alpha_B \simeq 0.28(2)$ [49–51], only a small magnesium-isotope ($^{24}Mg/^{26}Mg$) effect

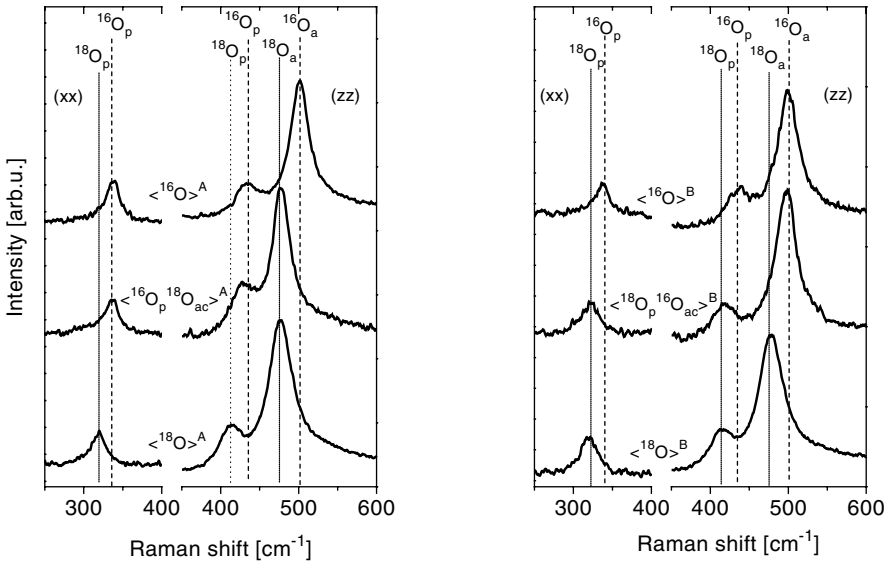

Fig. 8 Room-temperature Raman spectra of the oxygen site-selective substituted $YBa_2Cu_3O_{7-\delta}$ samples: triplet A (*left*), triplet B (*right*). For the (xx) polarization the line corresponds to the out-of phase motion of the planar O(2,3) oxygen (^{16}O: 337 cm^{-1}, ^{18}O: 320 cm^{-1}) and for the (zz) polarization the two lines correspond to the in-phase motion of the planar O(2,3) oxygen (^{16}O: 436 cm^{-1}, ^{18}O: 415 cm^{-1}) and to the stretching mode of the apical oxygen O(4) (^{16}O: 502 cm^{-1}, ^{18}O: 478 cm^{-1}). See also Fig. 2. After [31]

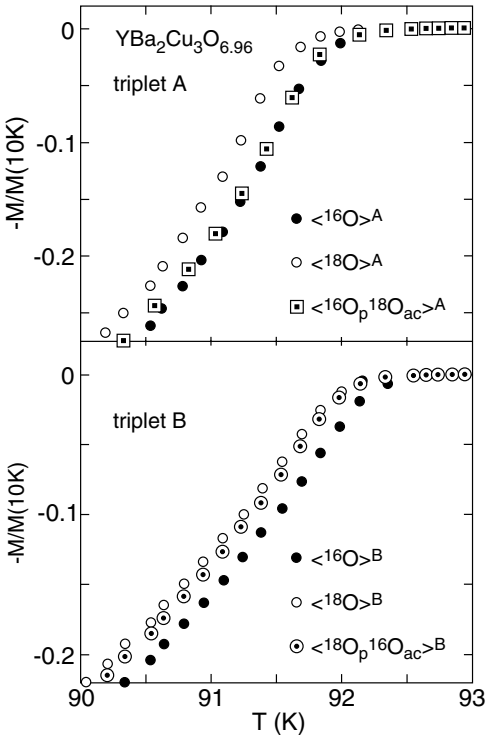

Fig. 9 Magnetization curves near T_c, showing the SOIE in optimally doped $YBa_2Cu_3O_x$ for $x = 6.957(2)$ (triplet A) and $x = 6.963(3)$ (triplet B). It is evident that the planar oxygen mainly contribute to the total OIE on T_c. After [31]

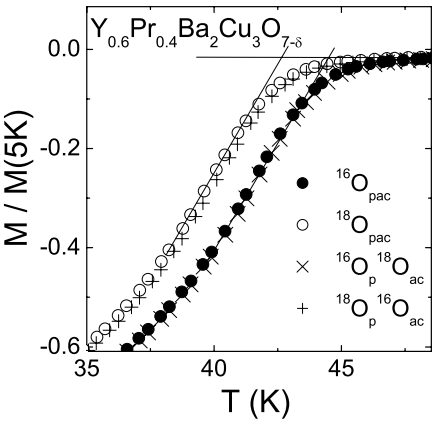

Fig. 10 Section near T_c of the normalized magnetization curves $M(T)/M(T = 5\text{K})$ (1 mT, FC) of the site-selective oxygen substituted $Y_{0.6}Pr_{0.4}Ba_2Cu_3O_{7-\delta}$ samples. After [34]

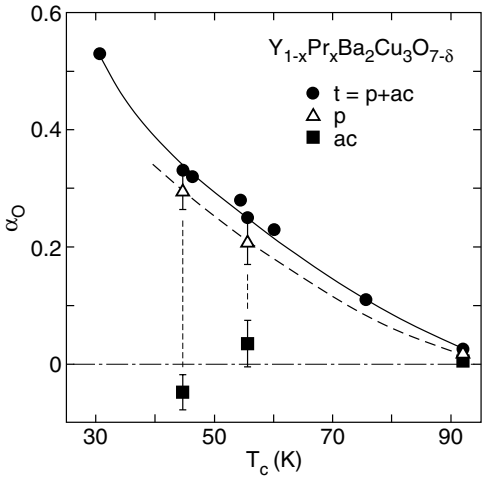

Fig. 11 Total (t) and partial (p, ac) oxygen-isotope exponent α_O as a function of T_c for $Y_{1-x}Pr_xBa_2Cu_3O_{7-\delta}$ (t: all oxygen sites, p: planar oxygen sites, ac: apex and chain oxygen sites). *Solid and dashed lines* are guides to the eye. Data are taken from [31, 33, 34, 36]

with $\alpha_{Mg} \simeq 0.02(1)$ [50] was detected. It is interesting to note that in this layered phonon-mediated superconductor the predominant contribution to the total isotope shift on T_c arises from the B atoms in the planes where superconductivity takes place, similar to the layered cuprate HTS.

4 Oxygen-Isotope Effect on the Magnetic Penetration Depth

The conventional phonon-mediated theory of superconductivity (standard BCS theory) is based on the Migdal adiabatic approximation in which the effective supercarrier mass m^* is independent of the mass M of the lattice atoms. However, if the interaction between the carriers and the lattice is strong enough, the Migdal adiabatic approximation breaks down and m^* depends on M (see, e.g., [22]). A significant experiment to explore a possible coupling of the supercarriers to the lattice is an isotope effect study of the magnetic field penetration depth λ.

For a general Fermi surface the zero-temperature magnetic penetration depth $\lambda_{ii}(0)$ may be written as an integral over the Fermi surface [52]:

$$\frac{1}{\lambda_{ii}(0)^2} = \frac{\mu_0}{2\pi^2 h} \oint dS_F \frac{v_{F_i} v_{F_i}}{|v_F|}, \tag{2}$$

where i denotes the crystallographic axes (a, b, c), and v_{F_i} is the Fermi velocity. For the special cases of spherical or ellipsoidal Fermi surfaces, Eq. (2) leads to the London expression

$$\frac{1}{\lambda_{ii}(0)^2} = \mu_0 e^2 \frac{n_s}{m^*_{ii}}, \tag{3}$$

where n_s is the superconducting carrier density, and m_{ii}^* is the effective mass of the carriers. For a general Fermi surface, it is convenient to *parametrize* experimental data by means of Eq. (3). It should be noted, however, that in this case m_{ii}^* has nothing to do with the band mass, except for spherical or ellipsoidal Fermi surfaces [52]. For HTS, which are superconductors in the clean limit, we may parametrize the in-plane penetration depth λ_{ab} in terms of the relation

$$1/\lambda_{ab}^2(0) \propto n_s/m_{ab}^* \,, \tag{4}$$

where m_{ab}^* is the in-plane effective mass (not band mass) of the charge carriers. According to Eq. (4), this implies that an OIE on λ_{ab} has to be due to a shift in n_s and/or m_{ab}^*:

$$\Delta\lambda_{ab}^{-2}(0)/\lambda_{ab}^{-2}(0) = \Delta n_s/n_s - \Delta m_{ab}^*/m_{ab}^*. \tag{5}$$

Therefore a possible mass dependence of m_{ab}^* can be tested by investigating the isotope effect on λ_{ab}, provided that the contribution of n_s to the total isotope shift is known.

The first observation of a possible OIE on the magnetic penetration depth $\lambda(0)$ in polycrystalline $YBa_2Cu_3O_{6.94}$ by means of magnetization measurements was reported by Zhao and Morris [37]. In a further study Zhao et al. [25,53] extracted the isotope dependence on $\lambda(0)$ in fine-grained samples of $La_{2-x}Sr_xCuO_4$ ($0.06 \leq x \leq 0.15$) from the Meissner fraction $f(0)$. For decoupled grains of average radius $R \leq \lambda$, the isotope dependence of λ can be determined from that of the Meissner fraction f which is given by the Shoenberg formula [54]:

$$f(T) = \frac{3}{2}\left[1 - 3\left(\frac{\lambda(T)}{R}\right)\coth\left(\frac{R}{\lambda(T)}\right) + 3\left(\frac{\lambda(T)}{R}\right)^2\right]. \tag{6}$$

It is evident from Eq. (6) that a change in $\lambda(0)$ due to isotope exchange will lead to a corresponding change in $f(0)$. An example of such a Meissner fraction measurement on fine-grained samples ($R \approx 2-4\,\mu$m) of $La_{2-x}Sr_xCuO_4$ is depicted in Fig. 12. From the measured value $\Delta f(0)/f(0) = -6(1)\%$ for $x = 0.105$ the relative OIE on $\lambda_{ab}^{-2}(0)$ was determined to be $\Delta\lambda_{ab}^{-2}(0)/\lambda_{ab}^{-2}(0) = -9(1)\%$ [53]. It is interesting to note that the OIE on $\lambda_{ab}(0)$ increases substantially, going from optimal doping ($x = 0.15$) to the heavily underdoped ($x = 0.06$) regime [25,53].

In order to obtain more reliable results on the OIE on $\lambda_{ab}(0)$ in layered cuprate HTS the experiments should be performed on high-quality single crystals. However, it is not possible to obtain a complete oxygen-isotope exchange by gas diffusion in single crystals of a large volume ($V \approx 1\times1\times0.3$ mm^3) [55]. Hofer et al. [55] investigated the OIE on T_c and $\lambda_{ab}(0)$ in microcrystals of underdoped $La_{2-x}Sr_xCuO_4$ with a volume of only $V \approx 150\times150\times50\ \mu$m^3 (mass $\approx 10\ \mu$g). In order to measure the magnetization of these microcrystals a highly sensitive magnetic torque sensor with a resolution of $\Delta\tau \simeq 10^{-12}$ Nm was used [56], since commercial SQUID magnetometers do not have the required sensitivity. The superconducting transition of these microcrystals was investigated by cooling the samples in an external magnetic field of 0.1 T at an angle of 45^o with respect

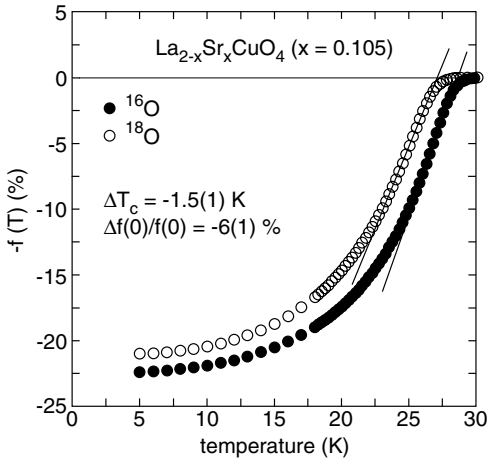

Fig. 12 Temperature dependence of the Meissner effect for oxygen substituted samples of $La_{2-x}Sr_xCuO_4$ ($x = 0.105$). After [53]

to the c-axis. The magnetic torque τ vs temperature obtained for the ^{16}O and ^{18}O microcrystals of $La_{2-x}Sr_xCuO_4$ with $x = 0.080$ and $x = 0.086$ is shown in Fig. 13. It is obvious that T_c is lower for the ^{18}O exchanged microcrystals, and the corresponding isotope shifts of T_c are consistent with previous results obtained for powder samples with similar doping levels [25, 35]. Figure 14 shows $\lambda_{ab}^{-2}(T)$ extracted from the magnetic torque data for the isotope exchanged microcrystals with $x = 0.080$ and 0.086. $\lambda_{ab}^{-2}(0)$ was determined by extrapolating the data to $T = 0$ K using the power law $\lambda_{ab}^{-2}(T)/\lambda_{ab}^{-2}(0) = 1 - (T/T_c)^n$ with $n \approx 5$ (solid lines in Fig. 14). It is evident that both T_c and $\lambda_{ab}^{-2}(0)$ exhibit a substantial OIE. In particular, the relative isotope shift of $\lambda_{ab}^{-2}(0)$ was found to be $\Delta\lambda_{ab}^{-2}(0)/\lambda_{ab}^{-2}(0) = -10(2)\%$ for $x = 0.080$ and -8(1)% for $x = 0.086$, respectively, in agreement with our previous results obtained for fine-grained samples [25, 53].

The muon-spin rotation (μSR) technique is a powerful method to determine the penetration depth in the mixed state of type II superconductors [57]. Khasanov et al. [38] performed a μSR OIE study of λ_{ab} in fine-grained samples of underdoped $Y_{1-x}Pr_xBa_2Cu_3O_{7-\delta}$ ($x = 0.3$ and 0.4). In a powder sample of a layered superconductor λ_{ab} can be extracted from the depolarization rate $\sigma(T) \propto 1/\lambda_{ab}^2(T)$ measured in the mixed state [57]. A sharp increase of $\sigma(T)$ below 10 K was observed which is due to antiferromagnetic ordering of the Cu(2) moments [58]. However, zero-field μSR experiments indicate for both concentrations x no presence of magnetism above 10 K. Therefore, data points below 10 K were excluded in the analysis. The superconducting contribution σ_{sc} was then determined by subtracting the small background contribution measured above T_c. In Fig. 15 the temperature dependence of σ_{sc} for the $Y_{1-x}Pr_xBa_2Cu_3O_{7-\delta}$ samples ($x = 0.3, 0.4$) is depicted. It is evident that for both concentrations x a

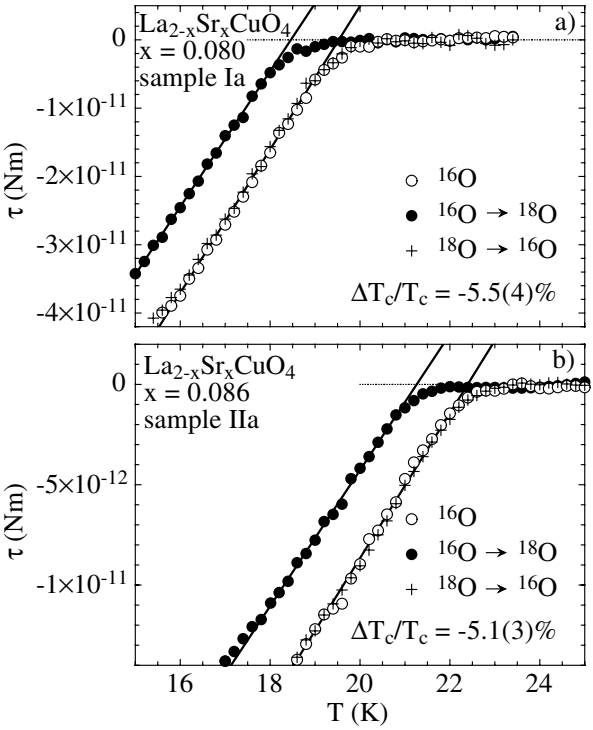

Fig. 13 Magnetic torque τ as a function of temperature for the ^{16}O and ^{18}O microcrystals of $La_{2-x}Sr_xCuO_4$ with: **a** $x = 0.080$; **b** $x = 0.086$. The reproducibility of the oxygen exchange procedure was checked by the backexchange (*crosses*). After [55]

remarkable oxygen isotope shift on T_c as well as on σ_{sc} is observed. The data in Fig. 15 were fitted to the power law $\sigma_{sc}(T)/\sigma_{sc}(0) = 1-(T/T_c)^n$ [57]. The values of $\sigma_{sc}(0)$ obtained from the fits are in agreement with previous results [58]. The exponent n was found to be $n = 2.0(1)$ for $x = 0.3$ and $n = 1.5(1)$ for $x = 0.4$, and within error the same for ^{16}O and ^{18}O. In order to prove that the observed OIE on $\lambda_{ab}(0)$ is intrinsic, the ^{18}O sample with $x = 0.4$ was back exchanged ($^{16}\text{O} \rightarrow {}^{18}\text{O}$). As shown in Fig. 15 the data points of this sample (cross symbols) coincide with those of the ^{16}O sample. From the measured values of $\sigma_{sc}(0)$ the relative isotope shift of $\lambda_{ab}^{-2}(0)$ was found to be $\Delta\lambda_{ab}^{-2}(0)/\lambda_{ab}^{-2}(0) = -5(2)\%$ and -9(2)% for $x = 0.3$ and 0.4, respectively. For the OIE exponent $\beta_O = -d\ln\lambda_{ab}^{-2}(0)/d\ln M_O$, one readily obtains $\beta_O = 0.38(12)$ for $x = 0.3$ and $\beta_O = 0.71(14)$ for $x = 0.4$. This means that in underdoped $Y_{1-x}Pr_xBa_2Cu_3O_{7-\delta}$ the OIE on $\lambda_{ab}^{-2}(0)$ as well as on T_c increases with increasing Pr doping x (decreasing T_c), in excellent agreement with the magnetic torque results on underdoped $La_{2-x}Sr_xCuO_4$ [55].

The most direct way to determine the magnetic field penetration depth λ of a type I or type II superconductor is achieved by a measurement of the magnetic field profile $B(z)$ in the Meissner state inside a superconducting film [59, 60]

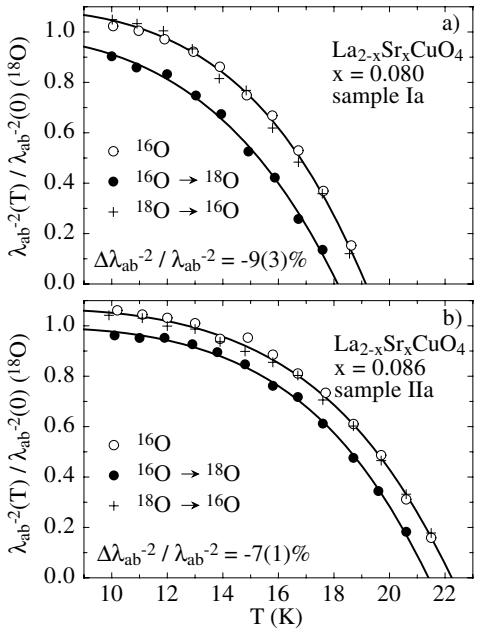

Fig. 14 Normalized in-plane penetration depth $\lambda_{ab}^{-2}(T)/\lambda_{ab}^{-2}(0)(^{18}O)$ for the ^{16}O and ^{18}O microcrystals of $La_{2-x}Sr_xCuO_4$: **a** $x = 0.080$; **b** $x = 0.086$. The reproducibility of the oxygen exchange procedure was checked by the backexchange (*crosses*). After [55]

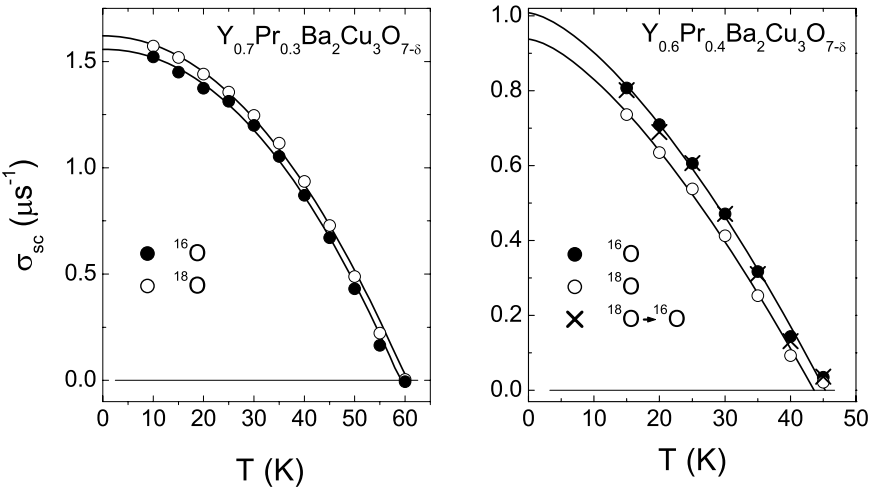

Fig. 15 Temperature dependence of the depolarization rate σ_{sc} in $Y_{1-x}Pr_xBa_2Cu_3O_{7-\delta}$ ($x = 0.3$ and $x = 0.4$), measured in an external magnetic filed of 200 mT (field cooled). The reproducibility of the oxygen exchange procedure was checked by the backexchange (*crosses*). After [38]

using the novel low-energy μSR (LEμSR) technique [61]. In such an experiment spin-polarized low-energy muons are implanted in the film at a known depth z beneath the surface and precess in the local magnetic field $B(z)$ which can be monitored by the muon-spin precession frequency, as in standard μSR. The implantation depth z is controlled by the variation of the energy of the incoming muons. From the measured field profile $B(z)$ the magnetic penetration depth λ can then be extracted in a *straightforward way*. Recently, Khasanov et al. [60] reported the first *direct* observation of the OIE on the in-plane penetration depth λ_{ab} in a nearly optimally doped $YBa_2Cu_3O_{7-\delta}$ thin film using LEμSR. The high-quality c-axis oriented $YBa_2Cu_3O_{7-\delta}$ films were grown in one batch with an area of 2×3 cm^2 and a thickness of 600 nm. A weak external magnetic field of 9.2 mT was applied parallel to the sample surface after the sample was cooled in zero magnetic field from a temperature above T_c to 4 K. In this geometry (the thickness of the sample is negligible in comparison with the width), currents flowing in the ab-planes determine the magnetic field profile along the crystal c-axis inside the film. Spin-polarized muons were implanted at a depth ranging from 20 to 150 nm beneath the surface of the film by varying the energy of the incident muons from 3 to 30 keV. For each implantation energy the average value of the magnetic field $\bar{B}$ and the corresponding average value of the stopping distance $\bar{z}$ were extracted. The value of $\bar{B}$ was determined from the measured μSR time spectrum using a Gaussian relaxation function, and the value of $\bar{z}$ was taken as the first moment of the emulated muon implantation depth profile. Results of this analysis for the ^{16}O and ^{18}O substituted $YBa_2Cu_3O_{7-\delta}$ films are shown in Fig. 16. It is evident that the data points for the ^{18}O film are systematically higher than those for the ^{16}O film, showing that $^{16}\lambda_{ab} < {}^{18}\lambda_{ab}$. The solid lines represent a fit to the $\bar{B}$ data by the function

$$B(z) = B(0)\frac{\cosh[(t-z)/\lambda_{ab}]}{\cosh(t/\lambda_{ab})} \,. \tag{7}$$

This is the form of the field profile $B(z)$ in a superconducting slab of thickness $2t$ in the Meissner state, where $B(0)$ is the field at the surface of the superconductor. The value of z was corrected in order to take into account the surface roughness of the films [59], which was taken as the same (8.0(5) nm) for both samples originating from the same batch. Fits with Eq. (7) to the extracted $^{16}\bar{B}(\bar{z})$ and $^{18}\bar{B}(\bar{z})$ yield $^{16}\lambda_{ab}(4\text{K}) = 151.8(1.1)$ nm and $^{18}\lambda_{ab}(4\text{K}) = 155.8(1.0)$ nm. Taking into account a ^{18}O content of 95%, the relative shift was found to be $\Delta\lambda_{ab}/\lambda_{ab} = ({}^{18}\lambda_{ab} - {}^{16}\lambda_{ab})/{}^{16}\lambda_{ab} = 2.8(1.0)\%$ at 4 K. This value is consistent with earlier estimates of the OIE on λ for optimally doped $YBa_2Cu_3O_{7-\delta}$ [33,37], $La_{1.85}Sr_{0.15}CuO_4$ [62] and $Bi_{1.6}Pb_{0.4}Sr_2Ca_2Cu_3O_{10+\delta}$ [62] obtained *indirectly* from magnetization measurements.

In order to substantiate further the OIE LEμSR results, additional OIE experiments on λ_{ab} based on measurements of the Meissner fraction f in fine $YBa_2Cu_3O_{7-\delta}$ powder were performed [60]. The powder samples were ground and then passed through a 10-μm sieve. The oxygen exchange was analogous to the one used for the thin film samples [60]. The ^{18}O content in the powder

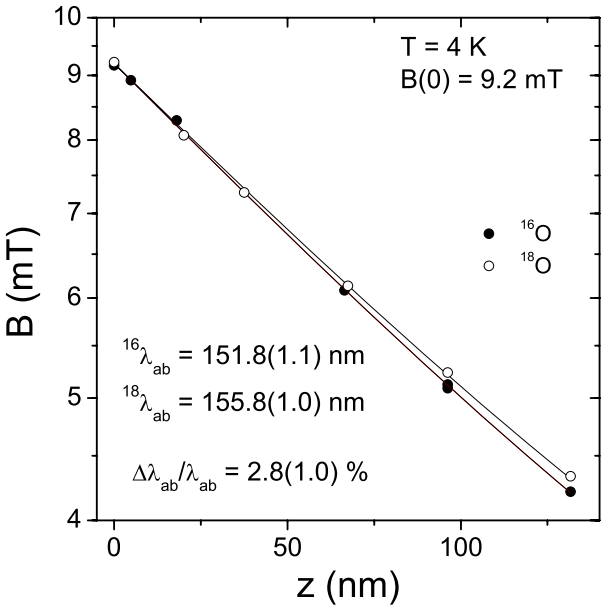

Fig. 16 Magnetic field penetration profiles $B(z)$ on a logarithmic scale for a ^{16}O substituted (*closed symbols*) and a ^{18}O substituted (*open symbols*) $YBa_2Cu_3O_{7-\delta}$ film measured in the Meissner state at 4 K and an external field of 9.2 mT, applied parallel to the surface of the film. The data are shown for implantation energies 3, 6, 10, 16, 22, and 29 keV starting from the surface of the sample. *Solid curves* are best fits by Eq. (7). Error bars are smaller than the size of symbols. After [60]

samples was determined to be 89(2)%. The value of the Meissner fraction f was extracted from 1 mT FC SQUID magnetization measurements. Figure 17 shows the temperature dependence of λ_{ab}^{-2} for the ^{16}O/^{18}O substituted $YBa_2Cu_3O_{7-\delta}$ fine powder samples, determined from f using the Shoenberg formula (Eq. 6) [60]. Taking into account a ^{18}O content of 89%, the relative oxygen-isotope shift at 4 K was estimated to be $\Delta\lambda_{ab}/\lambda_{ab} = 3.0(1.1)\%$. This value is in a good agreement with the LEμSR data (see Fig. 16 and Table 1). In order to demonstrate the intrinsic character of the isotope effect, a back exchange experiment was performed. For this purpose the ^{16}O sample was annealed in $^{18}O_2$ gas ($^{16}O \rightarrow {}^{18}O$) and the ^{18}O sample in $^{16}O_2$ gas ($^{18}O \rightarrow {}^{16}O$). The results of the back exchange experiments are shown in Fig. 17 (cross symbols).

In order to explore which phonon modes are relevant for the OIE on λ_{ab}, Khasanov et al. [34] performed a detailed study of the site-selective OIE (SOIE) in underdoped $Y_{0.6}Pr_{0.4}Ba_2Cu_3O_{7-\delta}$ powder samples by means of bulk μSR. The site selectively substituted ^{18}O (^{16}O) samples were prepared, following the procedure as described above. Again the site-selectivity of the oxygen exchange was checked by Raman spectroscopy (Raman spectra for $YBa_2Cu_3O_{7-\delta}$ are displayed in Fig. 8). The magnetization curves of the site-selective substituted ^{18}O (^{16}O)

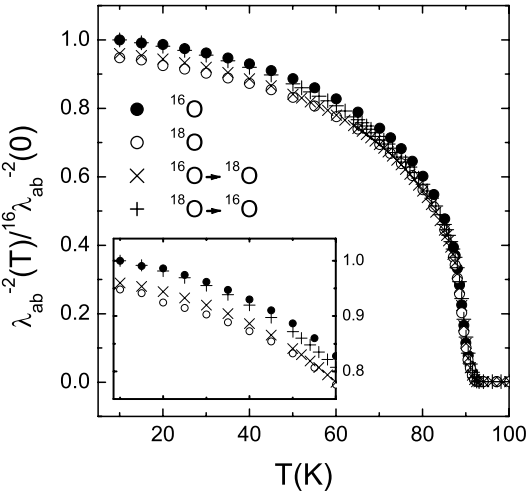

Fig. 17 Temperature dependence of λ_{ab}^{-2} normalized by $^{16}\lambda_{ab}^{-2}(0)$ for ^{16}O and ^{18}O substituted $YBa_2Cu_3O_{7-\delta}$ fine powder samples as obtained from low-field SQUID magnetization measurements. The *inset* shows the low-temperature region between 10 K and 60 K. The reproducibility of the oxygen exchange procedure was checked by the backexchange (*crosses*). After [60]

samples of $Y_{0.6}Pr_{0.4}Ba_2Cu_3O_{7-\delta}$ are shown in Fig. 10. Figure 18 shows the temperature dependence of the superconducting part of the μSR depolarization rate σ_{sc} ($\sigma_{sc} \propto \lambda_{ab}^{-2}$) for the $Y_{0.6}Pr_{0.4}Ba_2Cu_3O_{7-\delta}$ site-selective samples. A substantial oxygen isotope shift of T_c as well as of σ_{sc} is present. More importantly, the data

Table 1 Summary of the main OIE results for $La_{2-x}Sr_xCuO_4$ and $Y_{1-x}Pr_xBa_2Cu_3O_{7-\delta}$ obtained using various experimental techniques and types of samples (FP: fine powder, P: powder, SC: single crystal, TF: thin film). A complete list of OIE results for $La_{2-x}Sr_xCuO_4$ obtained from magnetization data is given in [25]

Sample	Method (sample type)	T_c (^{16}O) (K)	$\Delta T_c/T_c$ (%)	$\Delta\lambda_{ab}/\lambda_{ab}$ (%)	$\Delta m_{ab}^*/m_{ab}^*$ (%)	Ref.
$La_{1.85}Sr_{0.15}CuO_4$	SQUID (FP)	37.0(1)	-1.4(4)	2.8(3)	5.6(5)	[53]
$La_{1.895}Sr_{0.105}CuO_4$		27.8(1)	-5.4(4)	4.4(5)	9(1)	
$La_{1.914}Sr_{0.086}CuO_4$	Torque (SC)	22.40(5)	-4.8(2)	4.0(5)	8(1)	[55]
$La_{1.920}Sr_{0.080}CuO_4$		19.52(5)	-5.7(3)	5(1)	10(2)	
$La_{1.85}Sr_{0.15}CuO_4$	μSR (P)	37.63(2)	-1.0(1)	2.2(6)	4.4(1.1)	[29]
$YBa_2Cu_3O_{7-\delta}$	LEμSR (TF)	89.3(1)	-0.22(16)	2.8(1.0)	5.5(2.0)	[60]
$YBa_2Cu_3O_{7-\delta}$	SQUID (FP)	91.66(3)	-0.26(5)	3.0(1.1)	6.0(2.2)	[60]
$YBa_2Cu_3O_{7-\delta}$		91.71(3)	-0.28(5)	2.4(1.0)	4.8(2.0)	
$YBa_2Cu_3O_{7-\delta}$	μSR (P)	91.45(5)	-0.3(1)	2.6(5)	6(1)	[29]
$Y_{0.8}Pr_{0.2}Ba_2Cu_3O_{7-\delta}$		73.6(1)	-1.3(3)	2.4(7)	4.8(1.7)	[29]
$Y_{0.7}Pr_{0.3}Ba_2Cu_3O_{7-\delta}$		60.6(1)	-2.8(5)	2.5(1.0)	5(2)	[38]
$Y_{0.6}Pr_{0.4}Ba_2Cu_3O_{7-\delta}$		45.3(1)	-4.6(6)	4.5(1.0)	9(2)	[38]
$Y_{0.6}Pr_{0.4}Ba_2Cu_3O_{7-\delta}$		44.6(1)	-3.7(4)	3.1(5)	6(1)	[34]
$Y_{0.6}Pr_{0.4}Ba_2Cu_3O_{7-\delta}$		44.6(1)	-3.3(4)	3.3(4)	6.6(9)	[34]

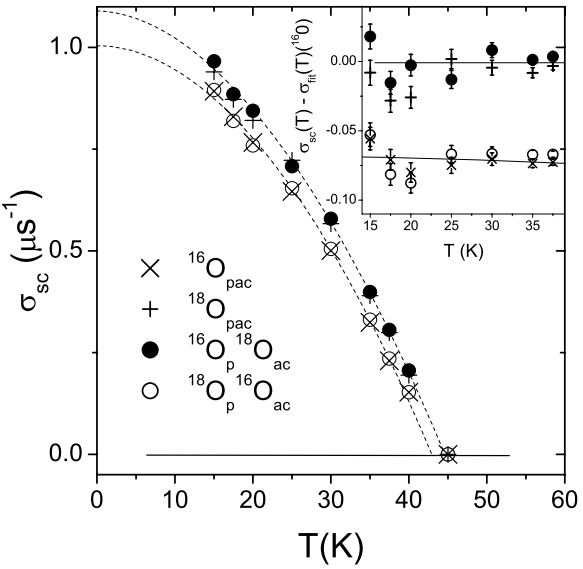

Fig. 18 Temperature dependence of the depolarization rate σ_{sc} in site-selective $Y_{0.6}Pr_{0.4}Ba_2Cu_3O_{7-\delta}$ samples (200 mT, FC). Data points below 10 K are not shown (see text and [34] for an explanation). The *solid lines* correspond to fits to the power law $\sigma_{sc}(T)/\sigma_{sc}(0) = 1 - (T/T_c)^n$ for the $^{16}O_{pac}$ and $^{18}O_{pac}$ samples. The *inset* shows the data after subtracting the fitted curve for the $^{16}O_{pac}$ sample. After [34]

points of the site-selective $^{16}O_p{}^{18}O_{ac}$($^{18}O_p{}^{16}O_{ac}$) samples coincide with those of the $^{16}O_{pac}$($^{18}O_{pac}$) samples. In order to present these results in a clearer way, the power law curve $\sigma_{sc}(T)/\sigma_{sc}(0) = 1-(T/T_c)^n$, fitting the temperature dependence of σ_{sc} for the $^{16}O_{pac}$ sample, was subtracted from the experimental data (see inset in Fig. 18). It is evident that the experimental points for the two pairs of samples mentioned above coincide within error bars, indicating that the *planar oxygen sites* (CuO_2 planes) *mainly contribute* (100% within error bar) to the total OIE on T_c and λ_{ab}. The corresponding oxygen-isotope shifts were found to be $\Delta T_c/T_c = -3.7(4)\%$ and $\Delta\lambda_{ab}^{-2}(0)/\lambda_{ab}^{-2}(0) = -6.2(1.0)\%$.

Recently, the boron-isotope ($^{10}B/^{11}B$) effect on the magnetic penetration depth λ was also investigated in the novel phonon-mediated superconductor MgB_2 by means of bulk μSR [51]. No boron isotope effect on $\lambda(0)$ was found within experimental error [51], $\Delta\lambda(0)/\lambda(0) = 0.8(8)\%$, in contrast to the substantial OIE on $\lambda_{ab}(0)$ observed in cuprate HTS at all doping levels.

5 Discussion of the Results

The main OIE results for T_c and λ_{ab} presented in this review are summarized in Table 1. The corresponding results for the site-selective OIE obtained for

$Y_{1-x}Pr_xBa_2Cu_3O_{7-\delta}$ are listed in Table 2. The present findings unambiguously show that there is an OIE on T_c and $\lambda_{ab}(0)$ at all doping levels which appears to be generic for cuprate HTS. Furthermore, the results obtained for the site-selective substituted $Y_{0.6}Pr_{0.4}Ba_2Cu_3O_{7-\delta}$ (see Table 2) clearly indicate that the oxygen site within the CuO_2 planes mainly contributes to the total OIE on T_c and $\lambda_{ab}(0)$. Since for fixed Pr concentration the lattice parameters remain essentially unaffected by the isotope substitution [63,64], these results unambiguously demonstrate the existence of a coupling of the charge carriers to phonon modes involving movements of the oxygen atoms in the CuO_2 plane. Bussmann-Holder et al. [12, 65] considerd a two-band model which includes in addition to in-plane Cu $d_{x^2-y^2}$ and O $p_{x,y}$ bands also out-of-plane orbitals (e.g. Cu $d_{3z^2-r^2}$ and O p_z states). With doping strain-induced plane buckling/octahedra tilting occurs which dynamically produces hybridization between e.g. $d_{x^2-y^2}$ and p_z and $d_{3z^2-r^2}$ and $p_{x,y}$ electronic states. The doping-induced buckling/tilting gives rise to strong electron-phonon processes. In this model all oxygen sites (plane, apex, and chain) in the crystal structure of $Y_{1-x}Pr_xBa_2Cu_3O_{7-\delta}$ (see Fig. 2) should in principle contribute to the total OIE on T_c and $\lambda_{ab}(0)$, but the dominant contribution arises from the planar oxygen atoms as shown by the experiments. Here the fundamental questions arise. Is the observation of an OIE on the zero-temperature penetration depth (superfluid density) a direct signature of strong lattice effects? And what is the relevance of this finding for the pairing mechanism? In order to answer adequately these questions, more experimental – and in particular more theoretical – work is needed. In the following we only discuss a few points related to these questions.

Under the assumption that we can *parametrize* experimental data of $\lambda_{ab}(0)$ in terms of Eq. (4), it follows from Eq. (5) that the isotope shift of λ_{ab} is due to an isotope shift of n_s and/or m^*_{ab}. It was demonstrated by a number of independent experiments that for $La_{2-x}Sr_xCuO_4$ [25,27,53,55] and $Y_{1-x}Pr_xBa_2Cu_3O_{7-\delta}$ [33,34,38] the change of n_s during the oxygen exchange procedure is negligibly small. For instance, the results for $La_{2-x}Sr_xCuO_4$ shown in Fig. 4 clearly show

Table 2 Summary of SOIE results for $Y_{1-x}Pr_xBa_2Cu_3O_{7-\delta}$ obtained by using various experimental techniques and types of samples (FP: fine powder, P: powder)

Sample	Sample type	Method	T_c (^{16}O) (K)	$\Delta T_c/T_c$ (%)	$\Delta\lambda_{ab}/\lambda_{ab}$ (%)	Ref.
$YBa_2Cu_3O_{7-\delta}$	$^{16}O_p^{18}O_{ac}$	SQUID (FP)	92.3 (1)	-0.05(5)	-	[31]
	$^{18}O_p^{16}O_{ac}$			-0.22(5)	-	
	$^{18}O_{pac}$			-0.27(5)	-	
$YBa_2Cu_3O_{7-\delta}$	$^{18}O_p^{16}O_{ac}$	SQUID (FP)	92.9(1)	-0.27(5)	2.0	[33]
	$^{18}O_{pac}$			-0.32(5)	3.5	
$Y_{0.7}Pr_{0.3}Ba_2Cu_3O_{7-\delta}$	$^{18}O_p^{16}O_{ac}$	SQUID (FP)	55.2(2)	-2.64(9)	2.4	[33]
	$^{18}O_{pac}$			-3.08(9)	3.5	
$Y_{0.6}Pr_{0.4}Ba_2Cu_3O_{7-\delta}$	$^{16}O_p^{18}O_{ac}$	μSR (P)	44.6(1)	0.09(36)	0.9(5)	[34]
	$^{18}O_p^{16}O_{ac}$			-3.3(4)	3.3(5)	
	$^{18}O_{pac}$			-3.7(4)	3.1(5)	

that the difference in hole densities of the ^{16}O and ^{18}O samples is negligible, so that the observed large isotope effects are intrinsic. Moreover, recent nuclear quadrupole resonance (NQR) studies of ^{16}O and ^{18}O substituted optimally doped $YBa_2Cu_3O_{7-\delta}$ powder samples revealed that the relative change of the hole density $\Delta n/n$ caused by the oxygen exchange must be less than 10^{-3} [60]. The absence of an observable OIE on n_s implies that the change of $\lambda_{ab}(0)$ is mainly due to a change on m^*_{ab}. From Eqs. (4) and (5) it follows that

$$\Delta m^*_{ab}/m^*_{ab} \simeq -\Delta\lambda^{-2}_{ab}(0)/\lambda^{-2}_{ab}(0) = 2\Delta\lambda_{ab}(0)/\lambda_{ab}(0). \tag{8}$$

This implies that in HTS m^*_{ab} depends on the oxygen mass M_O with $\Delta m^*_{ab}/m^*_{ab} \simeq 5 - 10\%$, depending on doping level (see Table 1). Note that such an isotope effect on m^*_{ab} is *not expected* for a conventional weak-coupling phonon-mediated BCS superconductor. In fact in HTS the charge carriers are very likely coupled to optical phonons, as revealed for instance by inelastic neutron scattering [7,8], ARPES [9, 15], EXAFS [10], and EPR [11] studies. Strong interaction between the charge carriers and the lattice ions leads to a *break down* of the adiabatic Migdal approximation [22], and consequently the effective supercarrier mass m^* depends on the mass of the lattice atoms. To our knowledge there are just a few theoretical models [19,21,22,66,67] which predict an OIE on the magnetic penetration depth λ (or effective carrier mass m^*). Recently, Bussmann-Holder et al. [19] have shown that the OIE on $\lambda_{ab}(0)$ can be understood in terms of polaronic effects on the single-particle energies within the framework of a two-band model of superconductivity. The predicted oxygen-isotope shifts $\Delta\lambda_{ab}(0)/\lambda_{ab}(0)$ are in good agreement with the experimental results. Lanzara et al. [9] used ARPES to probe the electron dynamics (velocity and scattering rate) in different families of cuprate HTS. They observed in all families an abrupt characteristic change of the electron velocity at 50 - 80 meV, commonly referred to as *kink* (change of the slope of the dispersion $E(k)$), which they ascribe to coupling of the electrons to phonons associated with the movement of the oxygen atoms. Recently, the OIE on the electron dispersion anomaly (*kink*) was also investigated in $Bi_2Sr_2CaCu_2O_{8+\delta}$ by ARPES [68]. As a result, the ^{16}O and ^{18}O dispersions $E(k)$ show that the *kink* separates the low-energy regime, where the spectra show negligible OIE, from the high-energy regime, where the spectra exhibit an appreciable OIE. This suggests that phonons contribute significantly to the electron self energy. According to Eq. (2), the in-plane penetration depth $\lambda_{ab}(0)$ is related to the Fermi velocity v_F. Therefore, it is very likely that the unconventional OIE on $\lambda_{ab}(0)$ and the anomalous OIE on the electron dynamics (*kink* structure) are interconnected and have the same physical origin. Simply speaking, in both experiments the effective carrier mass m^* is modified upon oxygen isotope substitution ($^{16}O \rightarrow {}^{18}O$) which causes a change in the magnetic penetration depth $\lambda(0)$ and in the electron velocity $v = \partial E/\partial k$, respectively. However, a thorough theoretical interpretation of these OIE results is still missing.

Khasanov et al. [34] reported an empirical linear relation between the OIE exponents $\alpha_O = -d\ln T_c/d\ln M_O$ and $\beta_O = -d\ln\lambda^{-2}_{ab}(0)/d\ln M_O$ for underdoped $La_{2-x}Sr_xCuO_4$ and $Y_{1-x}Pr_xBa_2Cu_3O_{7-\delta}$. In Fig. 19 we plot $\Delta\lambda_{ab}(0)/\lambda_{ab}(0) \propto \beta_O$

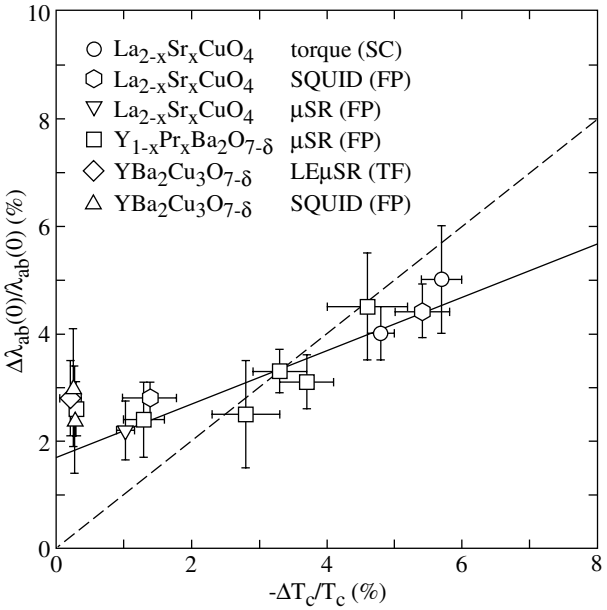

Fig. 19 Plot of the OIE shift $\Delta\lambda_{ab}(0)/\lambda_{ab}(0)$ vs the OIE shift $-\Delta T_c/T_c$ for $La_{2-x}Sr_xCuO_4$ and $Y_{1-x}Pr_xBa_2Cu_3O_{7-\delta}$ using different experimental techniques and types of samples. The data are taken from Table 1. The *dashed line* corresponds to $\Delta\lambda_{ab}(0)/\lambda_{ab}(0) = |\Delta T_c/T_c|$. The *solid line* indicates the flow to 2D-OSI criticality and provides with Eq. (9) an estimate for the oxygen isotope effect on d_s, namely $\Delta d_s/d_s = 3.3(4)\%$

vs $-\Delta T_c/T_c \propto \alpha_O$ for $Y_{1-x}Pr_xBa_2Cu_3O_{7-\delta}$ and $La_{2-x}Sr_xCuO_4$ for the data listed in Table 1. It is obvious from Fig. 19 that there is a correlation between the OIE on T_c and $\lambda_{ab}(0)$ which appears to be universal for cuprate HTS. Different experimental techniques (SQUID magnetization, magnetic torque, bulk μSR, LEμSR) and different types of samples (single crystals, powders, thin films) yield within error bars consistent results, indicating that the observed *isotope effects are intrinsic* and not a measurement artifact of the particular experimental method or sample used. As indicated by the dashed line, at low doping level $\Delta\lambda_{ab}(0)/\lambda_{ab}(0) \approx |\Delta T_c/T_c|$, whereas close to optimal doping $\Delta\lambda_{ab}(0)/\lambda_{ab}(0)$ is almost constant and considerably larger than $|\Delta T_c/T_c|$ ($\Delta\lambda_{ab}(0)/\lambda_{ab}(0) \approx 10|\Delta T_c/T_c|$). This generic behavior is qualitatively consistent with the empirical Uemura relation T_c vs $\sigma(0) \propto \lambda_{ab}^{-2}(0)$ [69, 70] and with the "parabolic ansatz" proposed in [41] in a *differential way*. According to the Uemura relation [69, 70], in the underdoped regime the simple relation $T_c \simeq C/\lambda_{ab}^2(0)$ holds, where C is a "universal" constant for all cuprate families. From this relation one readily obtains the relation $\Delta\lambda_{ab}(0)/\lambda_{ab}(0) = 1/2|\Delta T_c/T_c|$, which differs by a factor of 2 from the experimental OIE results (dashed line in Fig. 19). However, the physical meaning of this factor 2 is still unclear.

In a different approach it was shown [71–74] that the empirical relation between the oxygen-isotope shift of $\lambda_{ab}(0)$ and T_c naturally follows from the doping driven 3D-2D crossover and the 2D quantum superconductor to insulator (2D-QSI) transition in the highly underdoped limit. Close to the 2D-QSI transition the following relation holds [73,74]:

$$\Delta\lambda_{ab}(0)/\lambda_{ab}(0) = (\Delta d_s/d_s - \Delta T_c/T_c)/2\,, \tag{9}$$

where $\Delta d_s/d_s$ is the oxygen-isotope shift of the thickness of the superconducting sheets d_s of the sample. The solid line in Fig. 19 represents a best fit of Eq. (9) to the data with $\Delta d_s/d_s = 3.3(4)\%$. Since the lattice parameters are not modified by oxygen substitution [63,64], the observation of an isotope shift of d_s implies local lattice distortions involving oxygen which are coupled to the superfluid [73,74]. It was shown [72] that in anisotropic superconductors, falling into the 3D-XY universality class at finite temperature and into the 2D-XY-QSI universality class at zero temperature, the isotope effects on transition temperature, specific heat, and magnetic penetration depth are related by universal relations. They imply a dominant role of fluctuations so that pair formation and pair condensation do not occur simultaneously. Therefore, the isotope effects do not provide direct information on the underlying pairing mechanism and must be attributed to a shift of the phase diagram upon isotope substitution caused by the electron-phonon interaction [72]. Until now it was assumed that the 2D-QSI transition at low doping ($x_c \approx 0.06$) is a pure transition from an insulating to a superconducting phase. However, very recently Shengelaya et al. [75] observed hole-rich metallic domains in lightly doped $La_{2-x}Sr_xCuO_4$ ($0.01 \leq x \leq 0.06$) well below the critical doping x_c by means of electron paramagnetic resonance (EPR). This implies that the phase below x_c is a complex phase, and not simply an insulating phase. Furthermore, a finite size scaling analysis of the in-plane penetration depth data of $Y_{1-x}Pr_xBa_2Cu_3O_{7-\delta}$ provides clear evidence for a finite size effect on λ_{ab}, revealing the existence of superconducting domains with spatial nanoscale extent and its significant change upon oxygen-isotope exchange [73,76]. The OIE on the length L_c of the superconducting domains along the c-axis was found to be $\Delta L_c/L_c \approx 14\%$ for $x = 0$, 0.2, and 0.3 [73,76]. This again uncovers the existence and relevance of the coupling between the superfluid, lattice distortions, and anharmonic phonons which involve the oxygen lattice degrees of freedom.

6 Conclusions

In conclusion the unconventional isotope effects presented here clearly demonstrate that lattice effects play an important role in the physics of cuprates. The fact that a substantial OIE on λ_{ab} is observed, even in optimally doped cuprates, strongly suggests that cuprate HTS are non-adiabatic superconductors. This is in contrast to the novel high-temperature superconductor MgB_2 for which within experimental error no boron ($^{10}B/^{11}B$) isotope effect on the magnetic penetration

depth was detected [51]. The site-selective OIE studies of T_c and λ_{ab} indicate that the phonon modes involving the movements of oxygen within the superconducting CuO_2 planes are essential for the occurrence of superconductivity in cuprate HTS. This is in agreement with inelastic neutron scattering [7, 8], ARPES [9, 15], EXAFS [10], and EPR [11] results, indicating a strong interaction between charge carriers and Cu-O bond-stretching-type of phonons. In particular, EPR investigations [11] revealed that the local Q_4/Q_5 tilting modes of the CuO_6 octahedra are coupled to the Q_2 Jahn-Teller modes considered to be relevant for the (bi)polaron formation and the occurrence of superconductivity in cuprate HTS [77]. The generic relation between the OIE on T_c and λ_{ab} shows that, in contrast to conventional phonon-mediated superconductors, λ_{ab} (superfluid density) is a crucial parameter for understanding the role of phonons in cuprates. Since fluctuations play a dominant role in underdoped HTS close to the 2D QSI transition, the pair formation very likely occurs at a higher temperature T_p than pair condensation which takes place at T_c [72]. In this case the observed isotope effects do not give information on the microscopic pairing mechanism, but are associated with a shift of the phase diagram upon isotope substitution induced by the electron-phonon interaction [72]. However, it still remains an open question whether phonons are *directly* or *indirectly* involved in the pairing. It is interesting to note that in colossal magnetoresistance (CMR) manganites similar peculiar OIE on various quantities (e.g., ferromagnetic transition temperature, charge-ordering temperature) were observed [78]. This suggests that in both classes of perovskites, HTS and CMR manganites, lattice vibrations are essential. The present results raise serious doubts that models, neglecting lattice degrees of freedom, as proposed for instance in [79], are potential candidates to explain superconductivity in cuprate HTS.

Acknowledgements I would like to thank M. Angst, A. Bussmann-Holder, K. Conder, D. Di Castro, D.G. Eshchenko, J. Hofer, E. Kaldis, J. Karpinski, S.M. Kazakov, R. Khasanov, K. Kishio, B.I. Kochelaev, S. Kohout, E. Liarokapis, M. Mali, E. Morenzoni, K.A. Müller, N. Nagaosa, J. Roos, T. Sasagawa, I.M. Savić, Z.-X. Shen, T. Schneider, A. Shengelaya, H. Takagi, M. Willemin, D. Zech, and G.M. Zhao for their collaborations and discussions. This work was supported by the Swiss National Science Foundation and by the NCCR program *Materials with Novel Electronic Properties (MANEP)* sponsored by the Swiss National Science Foundation.

References

1. Bednorz JG, Müller KA (1986) Z Phys B 64:189
2. Batlogg B, Cava RJ, Jayaraman A, van Dover RB, Kourouklis GA, Sunshine S, Murphy DW, Rupp LW, Chen HS, White A, Short KT, Mujsce AM, Rietman EA (1987) Phys Rev Lett 58:2333
3. Bourne LC, Crommie MF, Zettl A, zur Loye HC, Keller SW, Leary KL, Stacy AM, Chang KJ, Cohen ML, Morris DE (1987) Phys Rev Lett 58:2337
4. Morris DE, Kuroda RM, Markelz AG, Nickel JH, Wei JYT (1988) Phys Rev B 37:5936
5. Carbotte JP (1990) Rev Mod Phys 62:1027

6. Nagamatsu J, Nakagawa N, Muranaka T, Zenitani Y, Akimitsu J (2001) Nature (London) 410:63
7. McQueeney RJ, Petrov Y, Egami T, Yethiraj M, Shirane G, Endoh Y (1999) Phys Rev Lett 82:628
8. Chung JH, Egami T, McQueeney RJ, Yethiraj M, Arai M, Yokoo T, Petrov Y, Mook HA, Endoh Y, Tajima S, Frost C, Dogan F (2003) Phys Rev B 67:014517
9. Lanzara A, Bogdanov PV, Zhou XJ, Kellar SA, Feng DL, Lu ED, Yoshida T, Eisaki H, Fujimori A, Kishio K, Shimoyama JI, Noda T, Uchida S, Hussain Z, Shen ZX (2001) Nature (London) 412:510
10. Bianconi A, Saini NL, Lanzara A, Missori M, Rosetti T, Oyanagi H, Yamaguchi H, Oka K, Ito T (1996) Phys Rev Lett 76:3412
11. Shengelaya A, Keller H, Müller KA, Kochelaev BI, Conder K (2001) Phys Rev B 63:144513-1
12. Bussmann-Holder A, Müller KA, Micnas R, Büttner H, Simon A, Bishop AR, Egami T (2001) J Phys Condens Matter 13:L169
13. Mihailović D, Kabanov VV (2001) Phys Rev B 63:054505
14. Bussmann-Holder A, Micnas R (2002) J Supercond 15:321
15. Shen ZX, Lanzara A, Ishihara S, Nagaosa N (2002) Phil Mag B 82:1349
16. Eschrig M, Norman MR (2003) Phys Rev B 67:144503
17. Tachiki M, Machida M, Egami T (2003) Phys Rev B 67:174506
18. Schachinger E, Tu JJ, Carbotte JP (2003) Phys Rev B 67:214508
19. Bussmann-Holder A, Micnas M, Bishop AR (2004) Phil Mag 21:1257
20. Kulić ML (2004) cond-mat/0404287
21. Bussmann-Holder A (2004) (this volume)
22. Alexandrov AS, Mott NF (1994) Int J Mod Phys 8:2075
23. Müller KA (1990) Z Phys B 80:193
24. Zech D, Conder K, Keller H, Kaldis E, Liarokapis E, Poulakis N, Müller KA (1995) In: Mihailović D, Ruani G, Kaldis E, Müller KA (eds) Anharmonic properties of high-T_c cuprates. World Scientific, Singapore, p 18
25. Zhao GM, Conder K, Keller H, Müller KA (1998) J Phys Condens Matter 10:9055
26. Müller KA (2000) Physica C 341–348:11
27. Zhao GM, Keller H, Conder K (2001) J Phys Condens Matter 13:R569
28. Keller H (2003) Physica B 326:283
29. Khasanov R, Shengelaya A, Morenzoni E, Conder K, Savić IM, Keller H (2004) J Phys Condens Matter 16:S4439
30. Conder K (2001) Mater Sci Eng R32:41
31. Zech D, Keller H, Conder K, Kaldis E, Liarokapis E, Poulakis N, Müller KA (1994) Nature (London) 371:681
32. Conder K, Rusiecki S, Kaldis E (1989) Mater Res Bull 24:581
33. Zhao GM, Ager JW III, Morris DE (1996) Phys Rev B 54:14982
34. Khasanov R, Shengelaya A, Morenzoni E, Angst M, Conder K, Savić IM, Lampakis D, Liarokapis E, Tatsi A, Keller H (2003) Phys Rev B 68:220506(R)
35. Franck JP (1994) In: Ginsberg DM (ed) Physical properties of high temperature superconductors IV. World Scientific, Singapore, p 189
36. Franck JP, Jung J, Mohamed AK (1991) Phys Rev B 44:5318
37. Zhao GM, Morris DE (1995) Phys Rev B 51:16487
38. Khasanov R, Shengelaya A, Conder K, Morenzoni E, Savić IM, Keller H (2003) J Phys Condens Matter 15:L17
39. Bornemann HJ, Morris DE (1991) Phys Rev B 44:5532
40. Babushkina N, Inyushkin A, Ozhogin V, Taldenkov A, Kobrin I, Vorob'eva T, Molchanova L, Damyanets L, Uvarova T, Kuzakov A (1991) Physica C 185/189:901
41. Schneider T, Keller H (1992) Phys Rev Lett 69:3374
42. Pickett WE, Cohen RE, Krakauer H (1991) Phys Rev Lett 67:228

43. Franck JP, Harker S, Brewer JH (1993) Phys Rev Lett 71:283
44. Zhao GM, Kirtikar V, Singh KK, Sinha APB, Morris DE, Inyushkin AV (1996) Phys Rev B 54:14956
45. Morris DE, Sinha APB, Kirtikar V, Inyushkin AV (1998) Physica C 298:203
46. Williams GVM, Pringle DJ, Tallon JL (2000) Phys Rev B 61:R9257
47. Cardona M, Liu R, Thomsen C, Kress W, Schönherr E, Bauer M, Genzel L, König W (1988) Solid State Commun 67:789
48. Nickel JH, Morris DE, Ager JW (1993) Phys Rev Lett 70:81
49. Bud'ko SL, Lapertot G, Petrovic C, Cunningham CE, Anderson N, Canfield PC (2001) Phys Rev Lett 86:1877
50. Hinks DG, Claus H, Jorgensen JD (2001) Nature (London) 411:457
51. Di Castro D, Angst M, Eshchenko DG, Khasanov R, Roos J, Savić IM, Shengelaya A, Bud'ko SL, Canfield PC, Conder K, Kazakov SM, Ribeiro RA, Keller H (2004) Phys Rev B70:014519-1
52. Chandrasekhar BS, Einzel D (1993) Ann Physik 2:535
53. Zhao GM, Hunt MB, Keller H, Müller KA (1997) Nature (London) 385:236
54. Shoenberg D (1940) Proc R Soc A 175:49
55. Hofer J, Conder K, Sasagawa T, Zhao GM, Willemin M, Keller H, Kishio K (2000) Phys Rev Lett 84:4192
56. Willemin M, Rossel C, Brugger J, Despont M, Rothuizen H, Vettiger P, Hofer J, Keller H (1998) Appl Phys 83:1163
57. Zimmermann P, Keller H, Lee SL, Savić IM, Warden M, Zech D, Cubitt R, Forgan EM, Kaldis E, Karpinski J, Krüger C (1995) Phys Rev B 52:541
58. Seaman CL, Neumeier JJ, Maple MB, Le LP, Luke GM, Sternlieb BJ, Uemura YJ, Brewer JH, Kadono R, Kiefl RF, Kreitzman SR, Riseman TM (1990) Phys Rev B 42:6801
59. Jackson TJ, Riseman TM, Forgan EM, Glückler H, Prokscha T, Morenzoni E, Pleines M, Niedermayer C, Schatz G, Luetkens H, Litterst J (2000) Phys Rev Lett 84:4958
60. Khasanov R, Eshchenko DG, Luetkens H, Morenzoni E, Prokscha T, Suter A, Garifianov N, Mali M, Roos J, Conder K, Keller H (2004) Phys Rev Lett 92:057602-1
61. Morenzoni E, Kottmann F, Maden D, Matthias B, Meyberg M, Prokscha T, Wutzke T, Zimmermann U (1994) Phys Rev Lett 72:2793
62. Zhao GM, Kirtikar V, Morris DE (2001) Phys Rev B 63:220506-1
63. Conder K, Zech D, Krüger C, Kaldis E, Keller H, Hewat AW, Jilek E (1994) In: Sigmund E, Müller KA (eds) Phase separation in cuprate superconductors. Springer, Berlin Heidelberg New York, p 210
64. Raffa F, Ohno T, Mali M, Roos J, Brinkmann D, Conder K, Eremin M (1998) Phys Rev Lett 81:5912
65. Bussmann-Holder A, Bishop AR, Büttner H, Egami T, Micnas R, Müller KA (2001) J Phys Condens Matter 13:L545
66. Scalapino DJ, Scalettar RT, Bickers NE (1987) In: Wolf SE, Kresin VZ (eds) Proceedings of the international conference on novel mechanisms of superconductivity. Plenum Press, New York, p 475
67. Grimaldi C, Cappelluti E, Pietronero L (1998) Europhys Lett 42:667
68. Gweon GH, Sasagawa T, Zhou SY, Graf J, Takagi H, Lee DH, Lanzara A (2004) Nature 430:187
69. Uemura YJ, Luke GM, Sternlieb BJ, Brewer JH, Carolan JF, Hardy WN, Kadono R, Kempton JR, Kiefl RF, Kreitzman SR, Mulhern P, Riseman TM, Williams DL, Yang BX, Uchida S, Takagi H, Gopalakrishnan J, Sleight AW, Subramanian AM, Chien CL, Cieplak MZ, Gang Xiao, Lee VY, Statt BW, Stronach CE, Kossler WJ, Yu XH (1989) Phys Rev Lett 62:2317
70. Uemura YJ, Le LP, Luke GM, Sternlieb BJ, Wu WD, Brewer JH, Riseman TM, Seaman CL, Maple MB, Ishikawa M, Hinks DG, Jorgensen JD, Saito G, Yamochi H (1991) Phys Rev Lett 66:2665

71. Schneider T, Keller H (2001) Phys Rev Lett 86:4899
72. Schneider T (2003) Phys Rev B 67:134514
73. Keller H, Schneider T (2004) cond-mat/0401505
74. Schneider T, Keller H (2004) New Journal of Physics 6:144
75. Shengelaya A, Bruun M, Kochelaev BI, Safina A, Conder K, Müller KA (2004) Phys Rev Lett 93:017001
76. Schneider T, Khasanov R, Conder K, Keller H (2003) J Phys Condens Matter 15:L763
77. Müller KA (1999) J Supercond 12:3
78. Zhao GM, Keller H, Greene RL, Müller KA (1999) In: Kaplan TA, Mahanti SD (eds) Physics of manganites. Kluwer Academic/Plenum Publishers, New York, p 221
79. Anderson PW, Lee PA, Randeria M, Rice TM, Trivedi N, Zhang FC (2004) J Phys Condens Matter 16:R755

Struct Bond (2005) 114: 171–204
DOI 10.1007/b101020

Neutron Scattering Investigations of Charge Inhomogeneities and the Pseudogap State in High-Temperature Superconductors

Albert Furrer (✉)

Laboratory for Neutron Scattering, ETH Zürich & PSI Villigen, 5232 Villigen PSI, Switzerland
albert.furrer@psi.ch

Abstract Neutron spectroscopy applied to the study of rare-earth based high-temperature superconducting materials provides detailed information on the local charge distribution in the copper-oxide planes. It is found that the observed crystal-field spectra separate into different local components whose spectral weights distinctly depend on the doping level, i.e., there is clear evidence for cluster formation; thus the onset of superconductivity has to result from percolation. Furthermore, the linewidths of crystal-field transitions provide direct information concerning the temperature at which an energy gap opens due to the pairing

of the charge carriers. Over a wide doping range, from the underdoped to the overdoped region, the opening of the gap is observed at a characteristic temperature T* above the superconducting transition temperature T_c. The pseudogap temperature T* exhibits large shifts upon pressure application and oxygen (and partially copper) isotope substitution, which suggests that phonons or lattice fluctuations involving the oxygen (and partially copper) ions are important for the pairing mechanism. The temperature dependence of the relaxation data is consistent with a gap function of predominantly d-wave symmetry; moreover, it supports the unusual behaviour of the gap function in the pseudogap region, i.e., a breakup of the Fermi surface into disconnected arcs in the temperature range $T_c<T<T^*$.

Keywords High-temperature superconductors · Charge inhomogeneity · Pseudogap · Crystal-field interaction · Inelastic neutron scattering

List of Abbreviations and Symbols

AF	Antiferromagnet, antiferromagnetic
ARPES	Angle-Resolved Photo-Emission Spectroscopy
CF	Crystal Field
INS	Inelastic Neutron Scattering
NMR	Nuclear Magnetic Resonance
NQR	Nuclear Quadrupole Resonance
R	Rare Earth
SC	Superconductivity, superconductor
SG	Spin Glass
T_c	Superconducting transition temperature
T_N	Néel temperature
T*	Pseudogap temperature
XANES	X-ray Absorption Near-Edge Spectroscopy

1 Introduction

The discovery of high-temperature superconductivity in the perovskites La_2CuO_4 [1] and $YBa_2Cu_3O_7$ [2] has given rise to a huge amount of materials research. In particular, there has been a myriad of publications reporting on the change of the superconducting properties upon both ion substitution at various sites in these compounds and application of external fields. The latter include magnetic fields, pressure and irradiation (e.g., by light ions and by fast neutrons, resulting in structural disorder). The most important substitutions include changes of the oxygen stoichiometry (e.g., by oxygen reduction), oxygen and copper isotope substitution, partial exchange of Y^{3+} by Ca^{2+} and La^{3+} by Sr^{2+} (or Ba^{2+}) in $YBa_2Cu_3O_x$ and La_2CuO_4, respectively, and partial exchange of copper ions by other transition metal ions. Surprisingly, it has been realized that the superconducting transition temperature T_c is essentially unchanged upon replacing the Y^{3+} and La^{3+} ions by paramagnetic rare-earth (R^{3+}) ions. This surprising observation is in contrast to conventional superconductors, for which paramagnetic ions usually have a large detrimental effect on supercon-

ductivity. It is therefore important to achieve a detailed understanding of the low-energy electronic properties which define the magnetic ground state of the R ions. In particular, information on the crystal-field (CF) interaction at the R site is highly desirable, for the following reasons:

1. For many high-T_c compounds superconductivity and long-range three-dimensional magnetic ordering of the R ion sublattice coexist at low temperatures (with the exception of R=Ce and R=Pr which have a drastic detrimental effect on superconductivity). An understanding of both the nature of the magnetic ordering and its apparent lack of influence on T_c requires a detailed knowledge of the CF states of the R ions.
2. In most high-T_c compounds the R ions are situated close to the superconducting copper-oxide planes where the superconducting carriers are located, thus the CF interaction at the R sites constitutes an ideal probe of the local symmetry as well as the local charge distribution of the superconducting CuO_2 planes and thereby monitors directly changes of the carrier concentration induced by ion substitutions and external fields. This property results from the short-range nature of the leading terms in the CF potential.
3. The intrinsic linewidths of CF transitions are found to vary with temperature which is essentially a reflection of the density-of-states associated with the charge carriers at the Fermi energy. Linewidth studies can therefore reveal information about the opening as well as the symmetry of the energy gap.

The methods of choice for studying the CF interaction are spectroscopic techniques which provide direct information on the CF energy levels. For the high-T_c compounds most results have been obtained by inelastic neutron scattering and to a lesser extent by Raman scattering. Both techniques have their merits and should be considered as complementary methods. Raman scattering, on the one hand, can be applied to very small samples of the order of 10 μm^3; it provides highly resolved spectra so that small line shifts and splittings can be detected [3], and it covers a large energy range so that intermultiplet transitions can easily be observed [4]. Neutron scattering, on the other hand, is not restricted to particular points in reciprocal space, i.e., interactions between the R ions can be observed through the wavevector dependence [5], the intensities of CF transitions can easily be interpreted on the basis of the wavefunctions of the CF states, and data can be taken over a wide temperature range which is of importance when studying linewidths of CF transitions.

In the present work we summarize the basic principles and provide representative examples of CF excitations observed by neutron spectroscopy in high-T_c superconducting materials. The next section introduces the Hamiltonian of the CF interaction as well as the corresponding neutron cross-section and describes the linewidths of the CF transitions both in the normal and in the superconducting state. In some examples we shortly demonstrate how to arrive at a unique set of CF parameters and thereby to a detailed understanding of the electronic ground state of the R ions. The following two sections deal with aspects 1 and 2 mentioned above, respectively, and we believe that they are

most crucial for our current understanding of the phenomenon of high-T_c superconductivity. High-temperature superconductors are basically different from classical superconducting compounds in the sense that superconductivity is usually realized through doping. The undoped system is antiferromagnetic (AF) and insulating (Fig. 1). At small doping, the Néel temperature T_N decreases rapidly and vanishes. The system enters then a spin-glass (SG) phase. Upon further doping superconductivity (SC) appears below a critical temperature T_c, with $(T_c)_{max}$ at a doping level of approximately 0.2 holes/CuO_2, but the system behaves like a strange metal. The homogeneous parent compound is structurally distorted by the doping elements, thus the question arises whether the doping process results in an extended electronic structure or whether the injected charge carriers are locally trapped. In the latter case the system becomes electronically inhomogeneous, and the superconducting state is reached by a percolation process [6]. Such inhomogeneities have actually been observed by a variety of local techniques [7] and most prominently by neutron CF spectroscopy. Of similar importance is the relaxation behaviour of CF excitations. The lifetime of CF states is finite because of the interaction with the charge carriers, thus the temperature dependence of the intrinsic linewidth of CF excitations reflects the density-of-states at the Fermi energy similar to nuclear magnetic resonance (NMR) and nuclear quadrupole resonance (NQR) experiments and thereby reveals information on the opening of the energy gap. There is ample evidence that the energy gap opens at $T^*>T_c$ in a large doping range [8–10]. CF spectroscopy has the advantage to probe the static susceptibility in zero magnetic field (NMR needs a static external field) as well as at THz frequencies (NMR and NQR work at MHz frequencies). The latter point is crucial for the understanding of the data, since it yields new information not available by NMR or NQR. The analysis of the relaxation data provides information on the nature of the gap function as discussed later. Some final conclusions and an outlook are summarized in the final section.

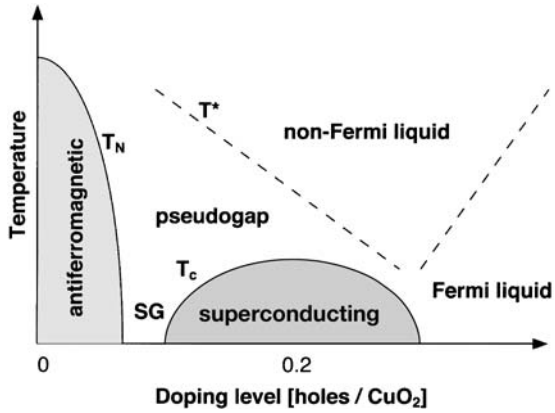

Fig. 1 Generic phase diagram of high-T_c superconductors vs doping

2
The Crystal-Field Interaction

2.1
The Crystal-Field Hamiltonian

The electrostatic and spin-orbit interactions lift the degeneracy of the unfilled $4f^n$ configuration of the R ions and give rise to the J-multiplets (Fig. 2). The degeneracy of the J-multiplets of magnetic ions embedded in a crystal lattice is partly removed by the crystal-field potential V_{CF} which, in a simple point-charge picture, arises from the electric charges $Z_i|e|$ of the surrounding ions located at the positions $\mathbf{R}_i$:

$$V_{CF}(\mathbf{r}) = \sum_i \frac{Z_i e^2}{|\mathbf{r} - \mathbf{R}_i|}. \tag{1}$$

V_{CF} has to remain invariant under the operations of the point group which characterizes the symmetry at the R site, and can be expressed by spherical harmonics, which are the basis vectors of the representations of the related rotation group. Using the tensor operator method and due to the fact that for 4f-shells terms up to 6*th* order are relevant, the related Hamiltonian can be constructed in a very simple way:

$$H_{CF} = \sum_{n=1}^{6} \sum_{m=0}^{n} A_n^m (Y_n^m + Y_n^{-m}). \tag{2}$$

Y_n^m are tensor operators of rank n and A_n^m are complex CF parameters. The number of non-zero CF parameters depends on the point symmetry at the

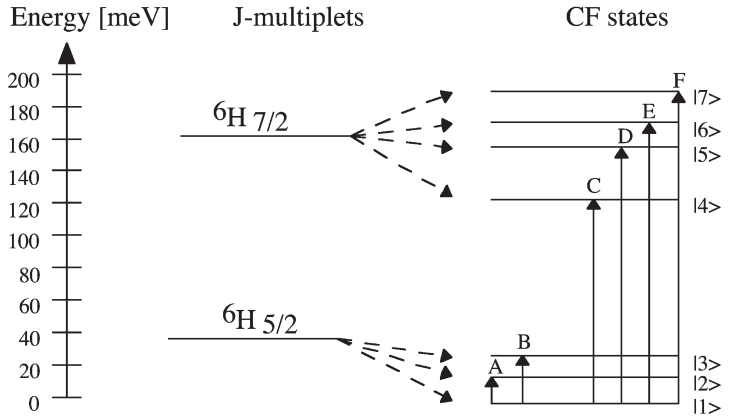

Fig. 2 Energy-level scheme of Sm^{3+} ions in $SmBa_2Cu_3O_7$ for the lowest two J-multiplets as derived from neutron spectroscopy [18]. The *arrows* denote the observed CF transitions. The figure is taken from [9]

R site. For instance, for tetragonal and orthorhombic symmetry there are five and nine independent CF parameters, respectively. The wave functions Γ_i and energy levels E_i are obtained by diagonalization of the CF Hamiltonian (Eq. 2). As explicit CF calculations are not needed in the present context, we refer to some recent review articles addressing the CF interaction in high-T_c superconductors for further details [8–10].

In principle, V_{CF} defined by Eq. (1) is a long-range potential, however, in high-T_c compounds V_{CF} is dominated by the higher-order CF parameters ($n \geq 4$) in Eq. (2) which have a short-range nature; thus V_{CF} essentially reflects the local symmetry and charge distribution in the CuO_2 planes as stated in 2 in the previous section.

2.2 Neutron Cross-Section

The CF interaction (Eq. 2) gives rise to discrete energy levels E_i which can be spectroscopically determined by the inelastic neutron scattering (INS) technique. In the experiment the sample is irradiated by a monochromatic neutron beam, and the scattered neutrons are analysed according to the energy transfer

$$\pm\hbar\omega = \frac{\hbar^2}{2\,m}\left(k_0^2 - k_1^2\right), \tag{3}$$

where m denotes the neutron mass, and k_o and k_1 are the wave numbers of the incoming and scattered neutrons, respectively. The corresponding momentum transfer is given by

$$\hbar\mathbf{Q} = \hbar(\mathbf{k}_0 - \mathbf{k}_1), \tag{4}$$

where **Q** is the scattering vector. In these experiments both energy gain and energy loss processes can be measured, i.e., the R^{3+} ion is either de-excited from a higher to a lower state, and the neutron gains the corresponding energy, or vice versa. Therefore one expects the measured energy spectrum to exhibit resonance peaks which can be attributed to transitions between different CF levels. In the analysis of these peaks a unique identification of the observed transitions is only possible by considering the relative intensities of the various transitions. For a system of N noninteracting ions the thermal neutron cross-section for the CF transition $|\Gamma_i\rangle \rightarrow |\Gamma_j\rangle$ is given in the dipole approximation by [11]

$$\frac{d^2\sigma}{d\Omega d\omega} = \frac{N}{Z}\left(\frac{\gamma e^2}{m_e c^2}\right)^2 \frac{k_1}{k_0} \exp\{-2W\} F^2(Q) \cdot \exp\left\{-\frac{E_i}{k_B T}\right\} M_{ij}^2 \cdot \delta\{E_i - E_j \pm \hbar\omega\}, \tag{5}$$

where exp{–2W} is the Debye-Waller factor, F(Q) the magnetic form factor, and

$$M_{ij} = \langle \Gamma_i | J_\perp | \Gamma_j \rangle \tag{6}$$

is the transition matrix element with $J_\perp$ being the component of the total angular momentum operator perpendicular to the scattering vector **Q**. The remaining symbols in Eq. (5) have their usual meaning. The matrix elements M_{ij} (Eq. 6) are most crucial for a proper identification of the observed CF transitions.

2.3 Linewidth of Crystal-Field Excitations

The δ-function in the neutron cross-section for CF transitions (Eq. 5) only applies for non-interacting rare-earth ions. However, the CF states are subject to interactions with phonons, spin fluctuations, and charge carriers, which limit the lifetime of the excitation; thus the observed CF transitions exhibit line broadening. The δ-function in Eq. (5) has therefore to be replaced by a Lorentzian. The interaction with the charge carriers is by far the dominating relaxation mechanism in metallic rare-earth compounds. The corresponding linewidth $\Gamma_n(T)$ increases almost linearly with temperature according to the well-known Korringa law [12]

$$\Gamma_n(T) = 4\pi(g-1)^2 J(J+1)\,[N(E_F)\cdot j_{ex}]^2 \cdot T\,, \tag{7}$$

where g denotes the Landé factor, $N(E_F)$ the density-of-states of the charge carriers at the Fermi energy E_F, and j_{ex} the exchange integral between the charge carriers and the 4f electrons of the rare-earth ions. The inclusion of CF effects slightly modifies the low-temperature limit of Eq. (7) according to the theory of Becker, Fulde and Keller [13]:

$$\Gamma_n^{ij}(T) = 2j_{ex}^2\left[M_{ij}^2 \coth\left(\frac{\hbar\omega_{ij}}{2k_BT}\right)\chi''(\hbar\omega_{ij}) + \sum_{i\neq k} M_{ik}^2 \frac{\chi''(\hbar\omega_{ik})}{\left(\exp\left\{\frac{\hbar\omega_{ik}}{k_BT}\right\}-1\right)} + \sum M_{kj}^2 \frac{\chi''(\hbar\omega_{kj})}{\left(\exp\left\{\frac{\hbar\omega_{kj}}{k_BT}\right\}-1\right)}\right], \tag{8}$$

where $\hbar\omega_{ij}=E_i-E_j$, and $\chi''(\hbar\omega)$ is the imaginary part of the susceptibility summed over the Brillouin zone. In the normal state and for a non-interacting Fermi liquid we have [8]

$$\chi''(\hbar\omega_{ij}) = \pi N^2(E_F)\,\hbar\omega_{ij}\,. \tag{9}$$

In superconducting compounds, however, the pairing of the charge carriers creates an energy gap Δ below the superconducting transition temperature T_c (or a pseudogap below a characteristic temperature T*); thus CF excitations

with energy $\hbar\omega<2\Delta$ do not have enough energy to span the gap, and consequently there is no interaction with the charge carriers. For an isotropic gap, the intrinsic linewidth in the superconducting state is then given by

$$\Gamma_s(T) = \Gamma_n(T) \cdot \exp\left\{-\frac{\Delta}{k_B T}\right\}. \tag{10}$$

This means that $\Gamma_s(T \ll T_c < T^*) \approx 0$, and line broadening sets in just below T_c (or T^*) where the superconducting gap (or the pseudogap) opens. The exponential temperature dependence of $\Gamma_s(T)$ was nicely demonstrated in the first neutron spectroscopic study on the classical superconductor $La_{1-x}Tb_xAl_2$ [14].

Recently, Lovesey and Staub [15] put forward the idea that the relaxation rate of CF transitions in high-T_c compounds is dominated by phonon interactions. In their model calculations for $Ho_{0.1}Y_{0.9}Ba_2Cu_3O_7$ they use a truncated CF level scheme, i.e., they neglect all but three out of the seventeen CF states which leads to an unreasonably good agreement with the experimental data. However, as demonstrated by Boothroyd [16], the inclusion of the complete set of CF levels produces a drastically different temperature dependence of the linewidth. Moreover, phonon relaxation exhibits a continuous temperature behaviour of the linewidth and cannot reproduce the step-like features observed in several high-T_c copper-oxide compounds. In conclusion, although phonon damping is present, it is certainly not the dominating relaxation mechanism of CF transitions in high-T_c cuprates.

2.4 Examples

2.4.1 Crystal-Field Transitions Within the Ground-State J-Multiplet

A considerable effort has been involved to study the CF interaction in the $RBa_2Cu_3O_x$ systems for which the symmetry at the R site is orthorhombic for $x>6.4$ and tetragonal for $x\leq 6.4$. As an example we present the results of a CF study performed for $ErBa_2Cu_3O_7$. The CF interaction splits the 16-fold degenerate ground-state J-multiplet $^4I_{15/2}$ of the Er^{3+} ions into eight Kramers doublets. All seven transitions out of the CF ground-state $|0\rangle$ and in addition some excited-state CF transitions were measured by neutron spectroscopy [17]. Figure 3 shows the energy spectra observed at low temperature (T=10 K) which exhibit three inelastic lines A, B, C in a low-energy window ($\Delta E<11$ meV) and four inelastic lines D, E, F, G in a high-energy window ($65<\Delta E<85$ meV). This spectral information (i.e., seven energies and seven intensities) was sufficient to arrive at an unambiguous description of the CF interaction in terms of nine independent CF parameters [17] as illustrated by the very good agreement between the observed and calculated energy spectrum displayed in Fig. 3.

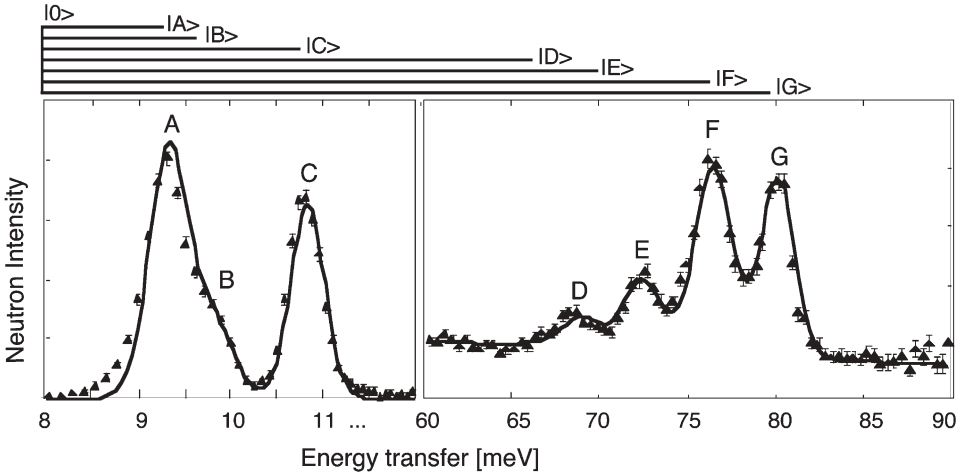

Fig. 3 Energy spectra of neutrons scattered from $ErBa_2Cu_3O_{6.98}$ at T=10 K [17]. The *lines* represent the calculated spectra. The *arrows* on top of the figure denote the observed ground-state CF transitions. The figure is taken from [9]

2.4.2 Intermultiplet Crystal-Field Transitions

Often the CF splittings observed in the ground-state J-multiplet are not sufficient to determine unambiguously the CF parameters. This is the case, e.g., for $SmBa_2Cu_3O_7$, since there are only three doublets within the ground-state J-multiplet $^6H_{5/2}$ associated with Sm^{3+}, which does not allow to determine the nine non-vanishing CF parameters. In principle, the number of observables can be

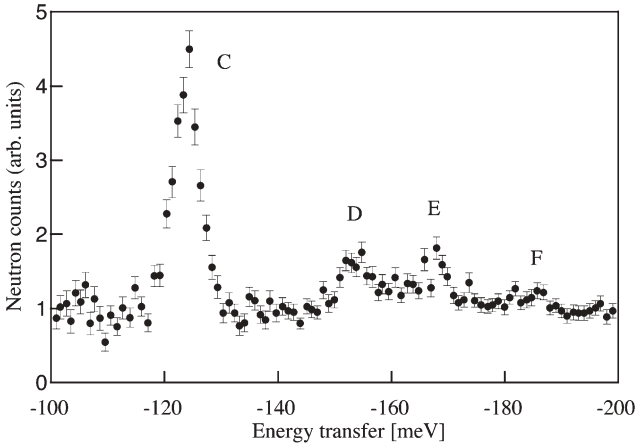

Fig. 4 Energy spectrum of neutrons scattered from $SmBa_2Cu_3O_7$ at T=10 K [18]. The figure is taken from [9]

increased by measurements of intermultiplet transitions (Fig. 2). Such experiments have become possible due to the copious flux of epithermal neutrons produced at spallation neutron sources.

The energy spectrum displayed in Fig. 4 shows CF ground-state transitions to the four doublet states within the first-excited J-multiplet $^6H_{7/2}$ of the Sm^{3+} ions in $SmBa_2Cu_3O_7$. The corresponding energy level scheme is shown in Fig. 2. This information, together with the observed CF transitions within the ground state has allowed a precise determination of the CF parameters [18].

3 Doping Effects and Charge Inhomogeneities

3.1 Hole-Doped (p-Type) Superconductors

3.1.1 Oxygen Reduction in $ErBa_2Cu_3O_x$ (6<x<7)

One of the most interesting aspects of the superconductivity in the $RBa_2Cu_3O_x$ compounds is the relation between T_c and the oxygen stoichiometry (see Fig. 1). Annealed systems show the well-known two-plateau structure of T_c (Fig. 5a). Charge transfer from the CuO chains to the CuO_2 planes certainly plays a crucial role in the oxygen-vacancy induced suppression of superconductivity in $YBa_2Cu_3O_x$, and this should manifest itself in the oxygen stoichiometry dependence of the observed CF energy spectra in $ErBa_2Cu_3O_x$ (Fig. 6) [17]. When going from x=6 to x=7, the transitions B, D, E shift slightly to lower energies and the transitions A,F,G move up to higher energies, whereas the energy of the transition C remains unchanged. It could be shown that the observed shifts of the CF transitions are due to both structural changes and charge transfer

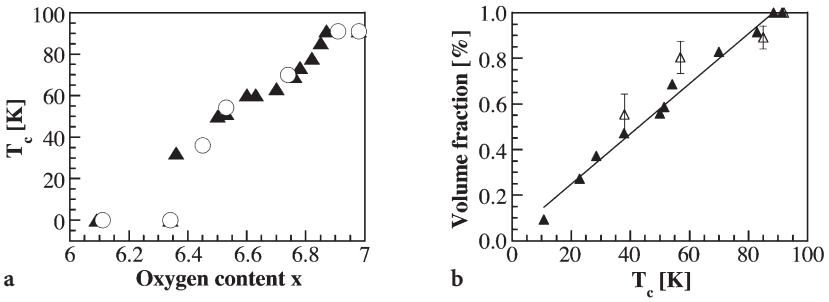

Fig. 5 **a** Superconducting transition temperature T_c vs oxygen content x for $ErBa_2Cu_3O_7$ [17]. **b** Superconducting volume fraction (Meissner fraction) vs T_c determined for $ErBa_2Cu_3O_x$. The *full and open triangles* refer to SQUID magnetometry results [21] and to the analysis of the CF spectra [17], respectively. The figure is taken from [9]

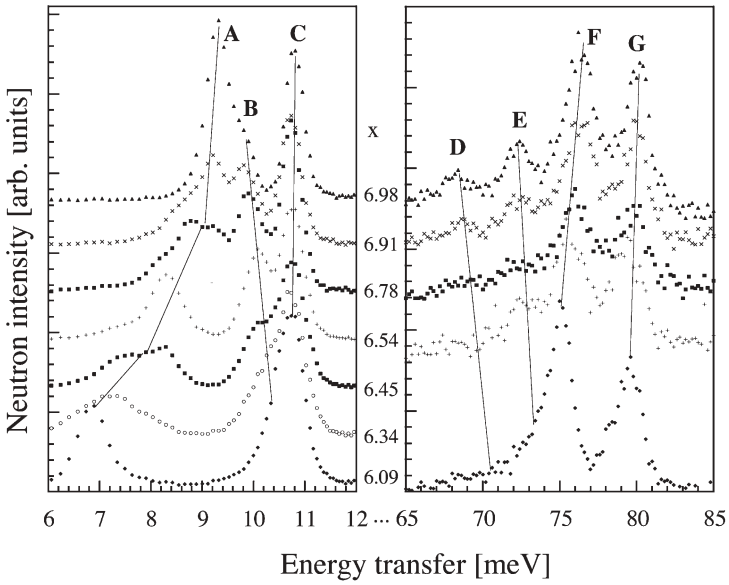

Fig. 6 Energy spectra of neutrons scattered from $ErBa_2Cu_3O_7$ at T=10 K [17]. The *lines* indicate the x-dependence of the observed CF transitions. The figure is taken from [9]

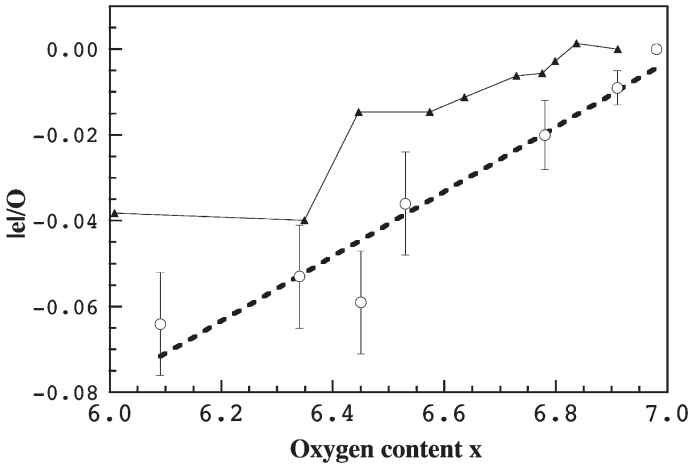

Fig. 7 Charge transfer vs oxygen content x derived from CF spectroscopic experiments on $ErBa_2Cu_3O_x$ [17] (*circles*), in comparison with the results obtained for $YBa_2Cu_3O_x$ from bond valence sum considerations [22] (*triangles*). The *line* is a guide to the eye

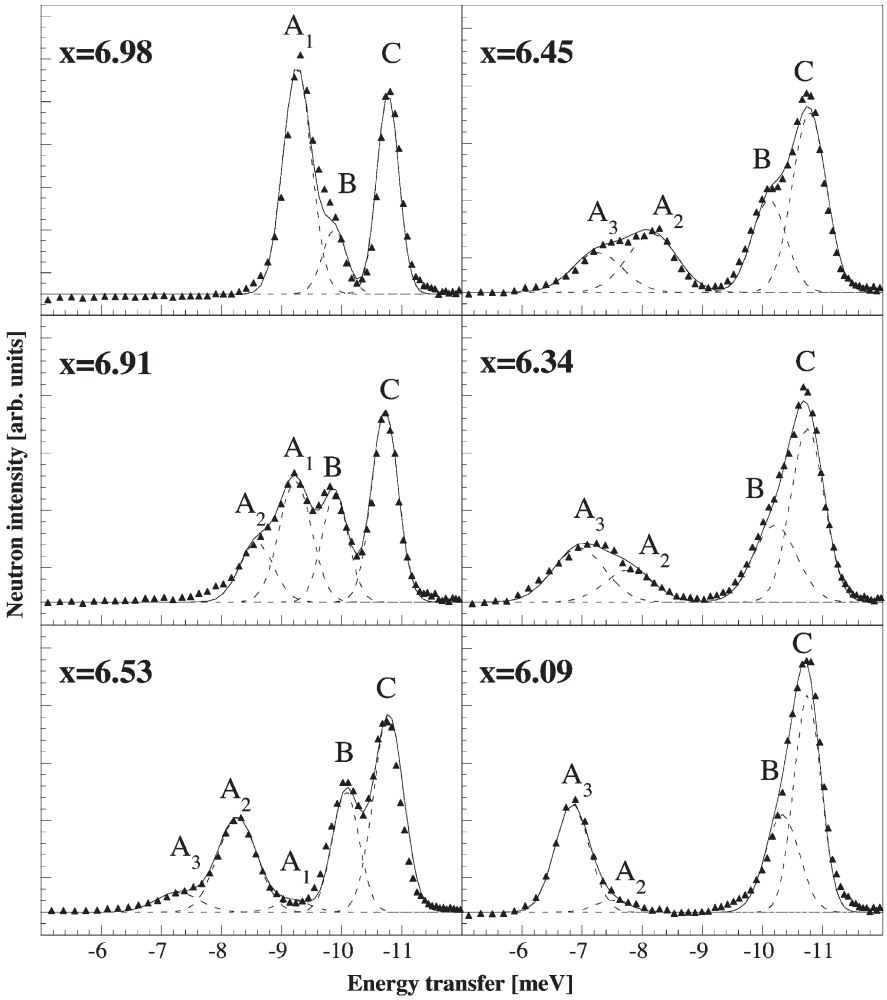

Fig. 8 Energy spectra of neutrons scattered from $ErBa_2Cu_3O_x$ at T=10 K [19]. The *full lines* are the result of a least-squares fitting procedure. The *broken lines* indicate the subdivision into individual CF transitions

effects [17, 19]. In particular, it was found that a charge of 0.07 |e|/O is transferred into the planes when going from x=6 to x=7, which means that about 28% of the created holes go into the planes (see Fig. 7). Similar conclusions have been obtained for the related compound $HoBa_2Cu_3O_x$ [20]. These results show an almost linear dependence of the charge transferred as a function of x. This is in agreement with the results of neutron diffraction experiments on $ErBa_2Cu_3O_x$ which give evidence for a linear decrease of the c axis upon hole doping [21], but in contrast to the conclusions of bond valence sum arguments derived in similar experiments on $YBa_2Cu_3O_x$ where the two-plateau structure

of T_c has been suggested to be due to the non-linearity of the hole transfer into the planes [22].

Upon increased resolution conditions (Fig. 8) we observe that the lowest CF transition A in $ErBa_2Cu_3O_x$ is actually built up of three different components A_1, A_2, and A_3, whose main characteristics can be summarised as follows:

1. Intensities: the individual components A_i have maximum weight close to x=7.0, x=6.5, and x=6.0, respectively (Fig. 9a–c). With the CF interaction being a local probe, there is no doubt that these substructures originate from

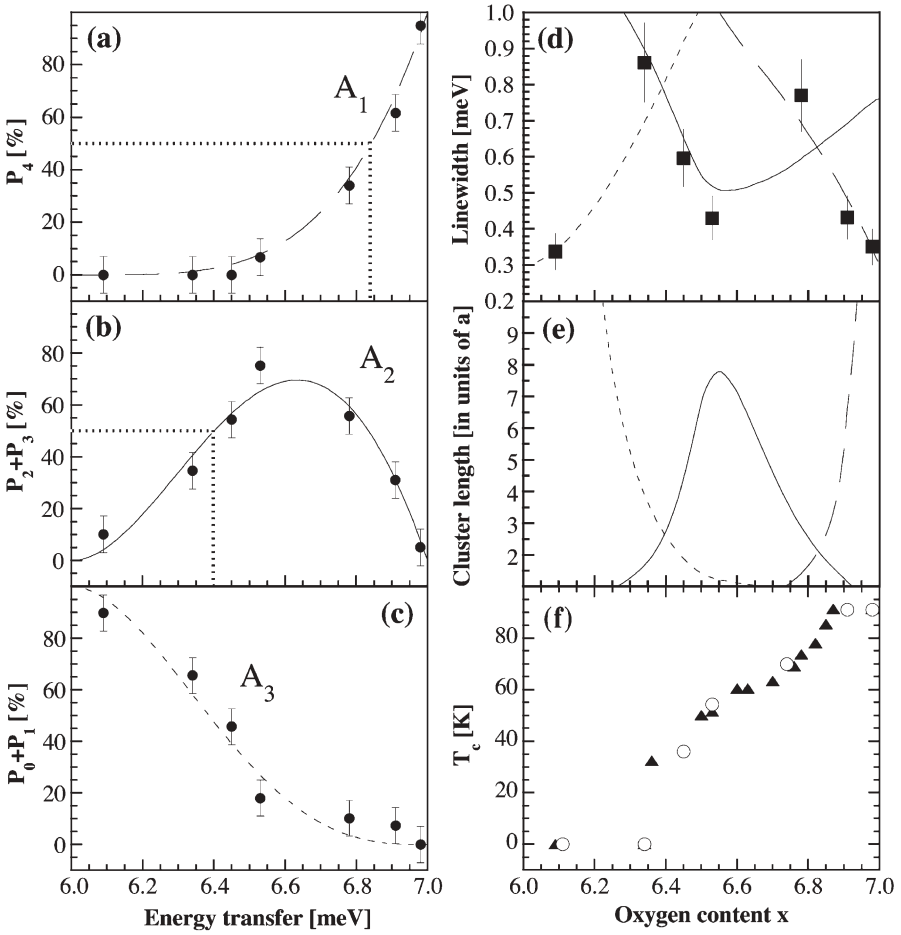

Fig. 9 **a–c** Proportions of the lowest-lying CF transitions A_i of $ErBa_2Cu_3O_x$ as a function of the oxygen content x [19]. The *full, dashed and broken lines* refer to the geometrical probability functions P_k defined by Eq. (11). The *dotted lines* mark the critical concentration for bond percolation. **d** Intrinsic linewidths of the CF transitions A_i at T=10 K [32]. **e** Mean cluster length vs oxygen content x determined by a Monte-Carlo simulation [32]. **f** Superconducting transition temperature T_c vs oxygen content x for $ErBa_2Cu_3O_x$ [17]

different local environments of the Er^{3+} ions which obviously coexist in the compound $ErBa_2Cu_3O_x$.

2. Energies: whereas all the CF transitions are independent of energy for oxygen content $x \geq 6.5$ within experimental error, they shift slightly when going from $x \approx 6.5$ to $x \approx 6.0$ (see Fig. 8). This may be due to the structural discontinuities at the orthorhombic to tetragonal phase transition at $x \approx 6.4$.
3. Linewidth: as visualized in Fig. 9d, the intrinsic linewidths of the transitions A_i are much smaller for oxygen contents where these transitions individually reach their maximum weight, namely for $x \approx 6.0$, 6.5, and 7.0.

All these facts and their interpretation provide clear experimental evidence for cluster formation. It is tempting to identify the three clusters associated with the transitions A_1, A_2, and A_3 by two local regions of metallic ($T_c \approx 90$ K, $T_c \approx 60$ K) and a local region of semiconducting character, respectively [19]. Figure 9a–c shows the fractional proportions of the three cluster types which exhibit a continuous behaviour vs the oxygen content x, consistent with the earlier conclusion that the transfer of holes into the CuO_2 planes is linearly related to the oxygenation process [17]. Furthermore, the continuous increase of the metallic states A_1 and A_2 can explain the increase of the superconducting volume fraction as observed by magnetic susceptibility measurements [21] when the oxygen content is raised from x=6 to x=7 (Fig. 5b). It should be mentioned that these results have been nicely confirmed by μSR [23] and inelastic neutron scattering [24] experiments showing the coexistence of superconductivity and antiferromagnetism at low doping. Also photoemission experiments [25] indicate the existence of a strong electronic inhomogeneity in the underdoped regime of $Bi_2Sr_2CaCu_2O_8$.

Our current understanding of the superconducting properties of $ErBa_2Cu_3O_x$ (and more generally all the $RBa_2Cu_3O_x$ compounds) involves a percolation mechanism of electric conductivity as discussed in both theoretical [6] and experimental [26] work. For x=6 the system is a perfect semiconductor. When adding oxygen ions into the chains, holes are continuously transferred into the CuO_2 planes. By this mechanism the number of local regions with metallic character (associated with the CF transition A_2) rises, which can partially combine to form larger regions. For some critical concentration a percolative network is built up, and the system undergoes a transition from the semiconducting to the conducting state (with $T_c \approx 60$ K). Upon further increasing the hole concentration a second (different) type of metallic clusters (associated with the CF transition A_1) is formed which start to attach to each other and induce a transition into another conducting state (with $T_c \approx 90$ K) at the percolation limit.

For a two-dimensional square structure the critical concentration for bond percolation is $p_c = 50\%$ [27]. From the fractional proportions of A_2 and A_1 displayed in Fig. 9a–c we can then immediately determine the critical oxygen concentrations for the transitions from the semiconducting to the $T_c \approx 60$ K-superconducting state and to the $T_c \approx 90$ K-superconducting state to be $x_2 = 6.40$ and $x_1 = 6.84$, respectively, which is in excellent agreement with the observed

two-plateau structure of T_c (see Fig. 9a,b,f). For three-dimensional structures, on the other hand, the critical concentration for bond percolation is 20%(face-centred cubic)$<p_C<$30%(simple cubic) [27], resulting in $6.21<x_2<6.31$ and $6.64<x_1<6.73$, which is inconsistent with the observed two-plateau structure of T_c. This reinforces the well known fact that the superconductivity in the perovskite-type compounds has indeed a two-dimensional character. A similar percolation model based on oxygen ordering effects in the CuO chains and the presence of oxygen-poor regions acting as superconducting grain boundaries gives a critical value $x_1=6.74$ [28, 29].

Combined statistical and geometrical considerations may be useful to understand the x-dependent profiles of the fractional proportions of the three cluster types visualized in Fig. 9a–c. A local symmetry model [30] was developed which defines specific probabilities $P_k(y)$ to have, for a given oxygen content x=6+y, k of the four oxygen chain sites (0,1/2,0), (1,1/2,0), (0,1/2,1) and (1,1/2,1) nearest to the R^{3+} ion occupied (see Fig. 10):

$$P_k(y) = \binom{4}{k} y^k (1-y)^{4-k}, \qquad (0 \le k \le 4)\,. \tag{11}$$

The fractional proportion of the cluster type A_1 exhibits the behaviour predicted by the probability function $P_4(y)$ (i.e., all the oxygen chain sites being occupied). Similarly, the fractional proportions of the cluster types A_2 and A_3 follow the sum of the probability functions $P_3(y)+P_2(y)$ (i.e., one or two empty oxygen chain sites) and $P_1(y)+P_0(y)$ (i.e., one or none oxygen chain site being occupied), respectively. The above probability functions are shown in Fig. 9a–c by lines which excellently reproduce the experimental data.

The x-dependent linewidth of the CF transitions allows one to estimate the size of the clusters, since a line broadening is due to structural inhomogeneities and gradients in the charge distribution which occur predominantly at the

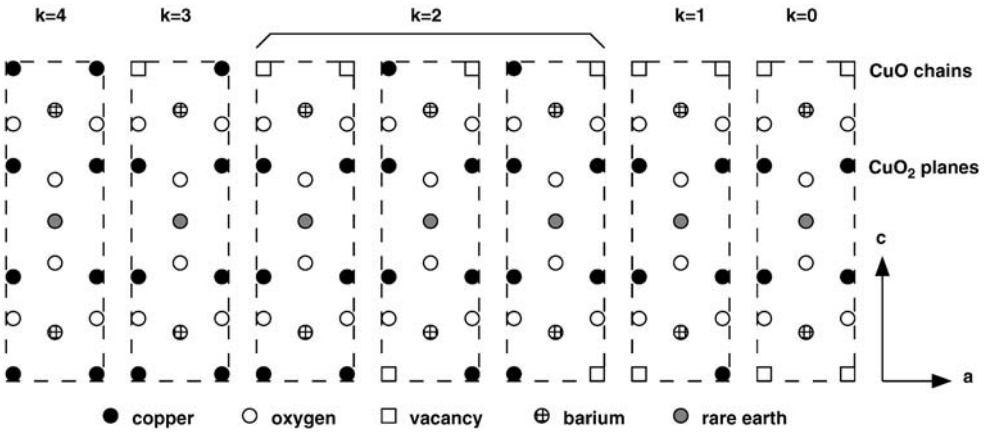

Fig. 10 Schematic visualisation of the different chain-oxygen configurations in $RBa_2Cu_3O_x$

border lines between different cluster types. For a cluster of mean length L (in units of the lattice parameter a) in the (a,b)-plane the fraction of unit cells at the border of the cluster and inside the cluster is $4(L-1)/L^2$ and $\{(L-2)/L\}^2$, respectively. In a first approximation the total linewidth is then given by [31]

$$\Gamma = \frac{1}{L}\sqrt{(L-2)^2\,\Gamma_0^2 + 4(L-1)\left[\left(\frac{\Delta E}{2}\right)^2 + \Gamma_0^2\right]}, \tag{12}$$

where Γ_0 is the intrinsic linewidth for infinite cluster size (i.e., for x=6 and x=7 exactly realized), and ΔE corresponds to the energetic separation of the CF transitions A_i for two coexisting cluster types. More specifically, from Fig. 8 we derive $\Delta E = E(A_1)-E(A_2) \approx 1.0$ meV and $\Delta E = E(A_2)-E(A_3) \approx 1.5$ meV at high and low oxygen concentrations x, respectively, and $0.3 \leq \Gamma_0 \leq 0.4$ meV.

The lines of Fig. 9d are the results of Monte-Carlo simulations of the doping mechanism [32]. These simulations start from the ortho-II structure at x=6.5 with some degree of disorder and show that the sizes of the clusters at percolation (Fig. 9e) are of the order of L=2–3 (7–10 Å), which is of the order of the superconducting coherence length in these materials. These numbers compare favourably with theoretical estimates by Hizhnyakov and Sigmund [6].

Evidence for the strongly inhomogeneous distribution of holes in the CuO_2 planes also results from other techniques such as magnetic susceptibility [26], NMR [33], electron paramagnetic resonance [34], Mössbauer [35], Raman [36], or even neutron diffraction [21] experiments. Various theoretical models have also predicted that under doping these systems become highly unstable and tend to phase separate into hole-rich and hole-poor regions [6, 37, 38].

3.1.2 External Pressure

Another important property of the $RBa_2Cu_3O_x$ compounds is the strong dependence of the critical temperature upon external pressure. As shown in Fig. 11a $\partial T_c(x)/\partial p$ increases by an order of magnitude around x=6.7 [39]. Is this anomaly due to an enhanced charge transfer into the planes upon pressure $\partial n(x)/\partial p$ around x=6.7? In order to answer this question both neutron diffraction and CF experiments were performed for $ErBa_2Cu_3O_x$ under hydrostatic pressure for several oxygen contents as visualized for x=6.54 in Fig. 11b. From the derived CF parameters it was found that the charge transfer into the planes under pressure, $\partial n(x)/\partial p$, is independent of the oxygen content x and equals 0.12 |e|/O/10 kbar [40]. This result indicates that the large value of $\partial T_c(x)/\partial p$ measured for $x \approx 6.7$ is not due to an anomalously high charge transfer process. Let us rewrite

$$\frac{\partial T_c}{\partial p}(x) = \frac{\partial T_c}{\partial n}\frac{\partial n}{\partial p}(x) = \frac{\partial T_c}{\partial x}\frac{\partial x}{\partial n}\frac{\partial n}{\partial p}(x)\,. \tag{13}$$

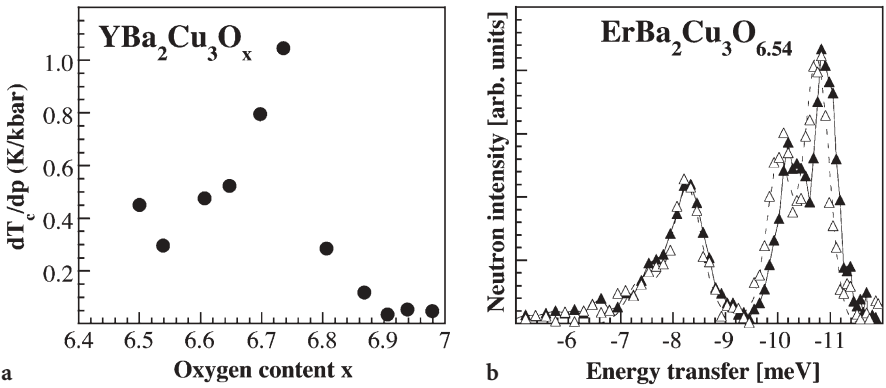

Fig. 11 **a** Pressure dependence of T_c vs oxygen content x observed for $YBa_2Cu_3O_x$ [39]. **b** Pressure dependence of the CF spectra of $ErBa_2Cu_3O_{6.54}$ at T=10 K [40]

From the above-mentioned result, $\partial n(x)/\partial p$=constant, as well as from the linear charge-transfer process upon oxygen doping derived above, $\partial n/\partial x$=constant, we obtain

$$\frac{\partial T_c}{\partial p}(x) \propto \frac{\partial T_c}{\partial x}(x)\,. \tag{14}$$

In other words, Eq. (14) clearly tells us that the same mechanism is responsible for the large enhancement of both $\partial T_c/\partial x$ and $\partial T_c/\partial p$ in the vicinity of x≈6.7, i.e., the proximity of the percolation limit plays an important role and has to be considered.

3.2 Electron-Doped (n-Type) Superconductors

The R_2CuO_4 (R=La, Pr, Nd) family is extremely interesting, since these compounds can either become p- or n-type conductors upon doping. Doping La_2CuO_4 with divalent ions such as Ba^{2+} or Sr^{2+} oxidizes the CuO_2 planes leaving holes as carriers. In contrast, doping Nd_2CuO_4 and Pr_2CuO_4 with tetravalent ions such as Ce^{4+} or Th^{4+} reduces the CuO_2 planes, giving rise to electrons as carriers. It should be noticed that both p- and n-type compounds are found to crystallize in a tetragonal structure.

In order to detect the effect of doping into the CuO_2 planes in n-type superconductors, INS experiments were carried out to study of the lowest ground-state singlet-doublet CF excitation $|\Gamma_4\rangle \rightarrow |\Gamma_5\rangle$ of Pr^{3+}in $Pr_{2-x}Ce_xCuO_4$ [41]. This compound is superconducting in a narrow doping range (0.11<x<0.18) with maximum T_c=25 K. As for the $RBa_2Cu_3O_x$ compounds (see above), the observed energy spectra are found to separate into different stable states whose spectral weights distinctly depend on the doping level (see Fig. 12). For the undoped

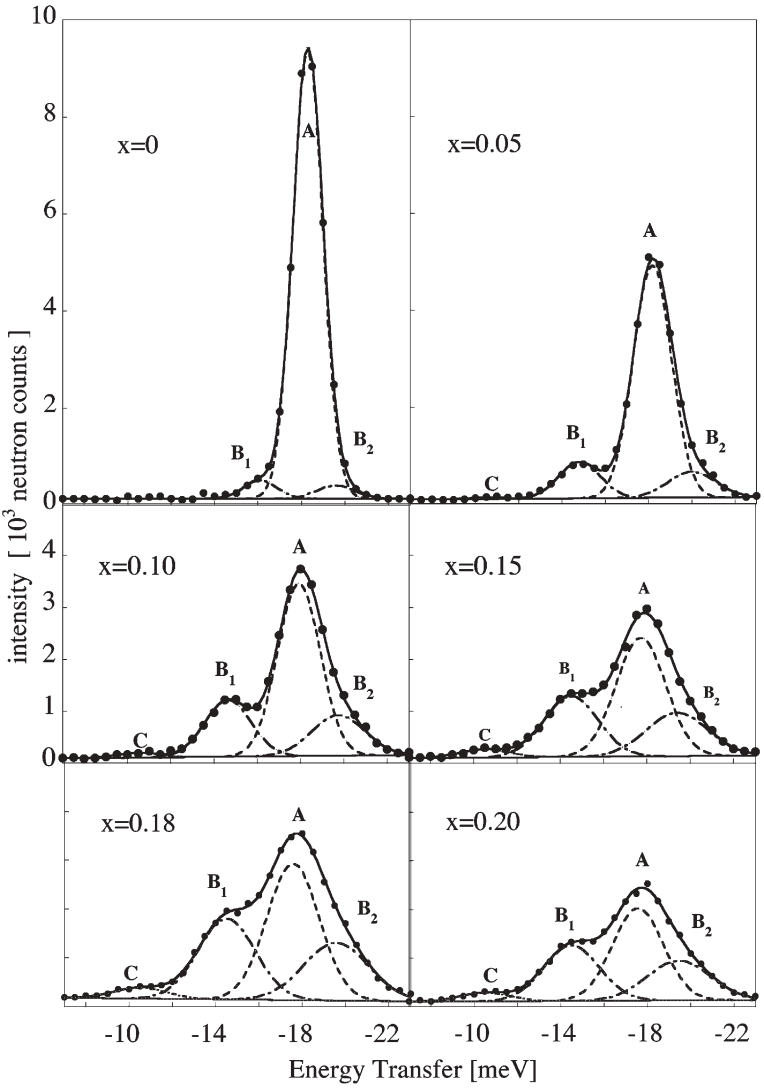

Fig. 12 Energy spectra of neutrons scattered from $Pr_{2-x}Ce_xCuO_4$ at T=10 K [41]. The *lines* are as in Fig. 8. The figure is taken from [9]

compound an intense CF transition is observed at 18 meV (A) with some minor shoulders on both the low- and high-energy side (B_1 and B_2, respectively). With increasing doping, the transition A loses intensity, whereas the B_1 and B_2 transitions gain intensity. At higher doping, there is a fourth line emerging, marked with C.

One explanation for these observations could be a line broadening due to antiferromagnetic correlations between the Pr^{3+} ions. However, this effect should

be most pronounced in the low-doping regime, in contrast to the observations. Moreover, these correlations have been shown to result in a dispersion of the CF transitions in a range between 18.2 meV and 19.2 meV [42, 43]. This cannot influence the observed spectra, because the bandwidth of the dispersion (≈1 meV) corresponds to the instrumental resolution. Hence, even for x=0, the lines B_1 and B_2 cannot be explained by such an effect. Therefore, with the CF interaction being a local probe, there is no doubt that these lines originate from different local environments of the Pr^{3+} ion. Furthermore, because the intensity ratios of the B_1 and B_2 transitions are constant for all Ce contents, one has to assume that these transitions are caused by the same local environment and therefore represent a splitting of the Γ_5 doublet into two singlet states. Although diffraction techniques confirmed the tetragonal symmetry in the entire doping range, the splitting of the Γ_5 doublet clearly shows that the local structure has a lower symmetry.

The CF spectra of Fig. 12 provide clear experimental evidence for cluster formation. The clusters associated with the transitions A, B(=B_1+B_2), and C can be identified by local regions of undoped, intermediately doped and highly doped character, respectively. Upon doping with Ce^{4+} ions and reducing oxygen, electrons are continuously transferred into the CuO_2 planes. By this mechanism the number of local electron-rich regions (associated with the transitions B and C) rises, which can partially combine to form larger regions. Finally, it could be shown [41] that for a critical volume fraction of 50% a two-dimensional percolative network is built up [27], and the system undergoes a transition from the insulating to the metallic state. The change of the relative intensities of the transitions A, B and C could be well reproduced [41] by assuming a similar statistical model as the one presented above for $ErBa_2Cu_3O_x$ (see Eq. 11). Different local environments of the R ions in these systems have also been inferred from Raman scattering [3, 44].

4
Relaxation Effects and the Pseudogap

4.1
General Remarks

Superconductivity is the result of two distinct quantum phenomena, pairing of the charge carriers at a characteristic temperature T* and long-range phase coherence at the superconducting transition temperature T_c. In conventional superconductors these two phenomena occur simultaneously, i.e., $T^*=T_c$. In contrast, for high-temperature superconductors we have $T^*>T_c$ over a large doping range, thus the so-called pseudogap region ($T_c<T<T^*$) is clearly the most challenging part of the phase diagram (see Fig. 1). The experimental discovery of the pseudogap region gave rise to an impressive number of models for the mechanism of high-temperature superconductivity [45]. Consequently,

experiments which produce changes of the pseudogap temperature T* are of crucial importance to discriminate between the different pairing scenarios developed for the cuprate superconductors. In the past, measurements of the isotope effect were essential to establish the BCS model of classical superconductors. Likewise, experiments searching for isotope effects on the pseudogap temperature T* may be of crucial importance to discriminate between the different pairing scenarios developed for the cuprate superconductors. X-ray absorption near-edge spectroscopy (XANES) experiments [46] revealed a huge oxygen isotope effect associated with the onset of local lattice fluctuations in underdoped $La_{1.94}Sr_{0.06}CuO_4$, whose characteristic temperature T* increases from 110 to 170 K upon replacing ^{16}O by ^{18}O. A large oxygen isotope effect as well as a large copper isotope effect on the pseudogap was also observed by neutron crystal-field spectroscopy for slightly underdoped $HoBa_2Cu_4O_8$ with $\Delta T^* \approx 50$ K [47] and $\Delta T^* \approx 25$ K [48], respectively. The same technique applied to underdoped, optimally doped and overdoped $La_{1.96-x}Sr_xHo_{0.04}CuO_4$ (Ho@LSCO) with x=0.10, 0.15 and 0.20 yielded oxygen isotope shifts $\Delta T^* \approx 20$, 10 and 5 K, respectively [49, 50]. Surprisingly, NMR and NQR experiments resulted in an absence or a very small oxygen isotope shift ΔT^* in $YBa_2Cu_4O_8$ [51, 52] which was attributed to the slow time scale of the order of $\tau \approx 10^{-8}$ s [46, 47, 53]. The large oxygen (and copper) isotope shifts ΔT^* observed by XANES and neutron spectroscopy experiments (which are fast techniques with a time scale of $\tau \leq 10^{-13}$ s) were quantitatively accounted for by models based on dynamical charge ordering [53], phonon-induced stripe formation [54], and bipolaron formation associated with Jahn-Teller-like oxygen vibrations [55].

Similarly to isotope substitution, the application of pressure affects the lattice degrees of freedom, thus it could be used as an independent tool to confirm the experimental and theoretical findings described above. Unfortunately, there are only few pressure-dependent experiments on the pseudogap temperature T* in the literature, and the results are contradicting. NQR experiments for $YBa_2Cu_4O_8$ [56] as well as resistivity measurements for quenched and Ca-doped $YBa_2Cu_3O_7$ compounds [57] show a (continuous) decrease of T* with increasing pressure, whereas from the analysis of resistivity measurements for optimally doped $Hg_{0.82}Re_{0.12}Ba_2Ca_2Cu_3O_{8+\delta}$ a linear increase of T* with pressure is reported [58]. Recently, neutron spectroscopy experiments under hydrostatic pressure were performed for the optimally doped compound $Ho@La_{2-x}Sr_xCuO_4$ [50]. It was found that the pseudogap temperature decreases from $T^* \approx 60$ K at ambient pressure to $T^* \approx 55$ K for p=0.8 GPa, i.e., $\Delta T^* \approx -5$ K. This is in qualitative agreement with the previously observed oxygen isotope shift $\Delta T^* \approx +10$ K [49, 50], thereby supporting the pairing scenarios which are based upon electron-phonon induced effects [53–55].

In the following sections we summarize the results of neutron spectroscopic investigations of the oxygen and copper isotope effect on the relaxation rate of CF excitations in both $HoBa_2Cu_4O_8$ and $Ho@La_{2-x}Sr_xCuO_4$ (i.e., exchange of both ^{16}O vs ^{18}O and ^{63}Cu vs ^{65}Cu, respectively) as well as the effect of hydrostatic pressure for the latter compound.

4.2 Oxygen Isotope Effect in $HoBa_2Cu_4O_8$

The $HoBa_2Cu_4O_8$ compound is excellently suited for studying oxygen isotope effects, because it is highly stoichiometric and the stoichiometry does not change upon both $^{16}O \rightarrow ^{18}O$ and $^{18}O \rightarrow ^{16}O$ substitution. The critical temperatures T_c of the ^{16}O and ^{18}O compounds were determined by magnetometry to be (79.0±0.1) K and (78.5±0.1) K, respectively. The observed oxygen isotope shift $\Delta T_c \approx (-0.5 \pm 0.2)$ K can be described by the isotope coefficient α defined by the relation $T_c \propto M^{-\alpha}$, where M is the mass of the oxygen ion. For $HoBa_2Cu_4O_8$ we deduce $\alpha = 0.05 \pm 0.02$, in agreement with literature data on the isostructural compound $YBa_2Cu_4O_8$ [51, 52].

Figure 13 shows energy spectra for $HoBa_2Cu_4{}^{18}O_8$. There are two strong ground-state CF transitions at $\hbar\omega_1 = 0.6$ meV and $\hbar\omega_2 = 1.3$ meV, i.e., $\hbar\omega_i \ll 2\Delta_{max}$

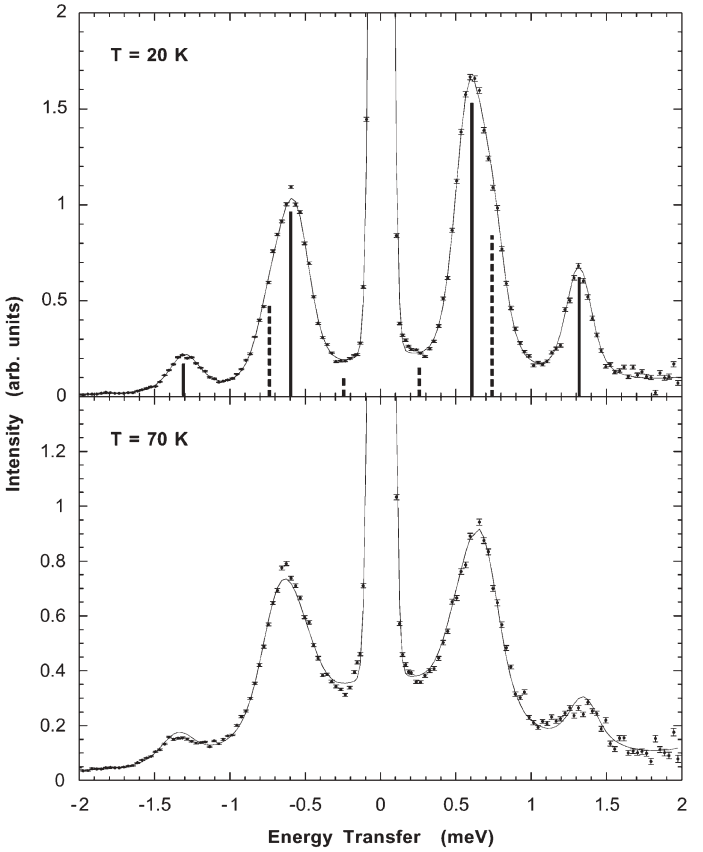

Fig. 13 Energy spectra of neutrons scattered from $HoBa_2Cu_4{}^{18}O_8$ [47]. The *solid lines* are fits to the data. The *solid and dashed vertical bars* indicate the energy and intensity of the ground-state and excited-state CF transitions, respectively. The figure is taken from [47]

(≈66 meV [59]). With increasing temperature the CF transitions exhibit line broadening. In addition, excited CF states become increasingly populated giving rise to excited CF transitions. The energy spectra were fitted according to the neutron cross-section for CF transitions as defined by Eq. (5). The final spectra were obtained by convoluting the instrumental resolution function with the CF intrinsic Lorentzian function, whose linewidth is given in the normal state by the Korringa law (Eqs. 8 and 9). The only free parameters in the fitting procedure were an overall scale factor for the intensities and a temperature-dependent linewidth $\Gamma(T) \propto [N(E_F) j_{ex}]^2$. The results of the fitting procedure are shown by solid lines in Fig. 13.

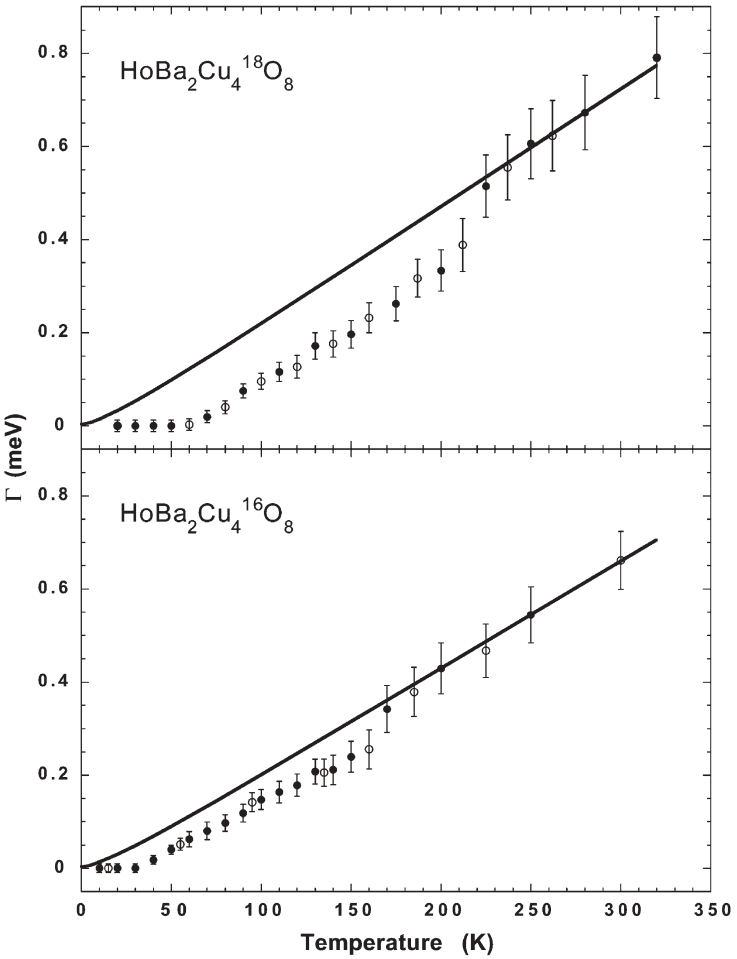

Fig. 14 Temperature dependence of the intrinsic linewidth Γ (HWHM) corresponding to the $\Gamma_3 \rightarrow \Gamma_4$ ground-state CF transition in $HoBa_2Cu_4{}^{16}O_8$ and $HoBa_2Cu_4{}^{18}O_8$ [47]. The *lines* denote the linewidth in the normal state calculated from the Korringa law

Figure 14 (upper panel) shows the temperature dependence of the intrinsic linewidth Γ (HWHM) corresponding to the CF transition from the ground state to the first excited state at $\hbar\omega_1$=0.6 meV for the ^{18}O compound. The linewidth is zero below 60 K, then it increases almost linearly up to 210 K. The linewidth is step-like enhanced between 210 and 220 K. Above 220 K it increases again linearly as expected for the normal state. We therefore identify the temperature where the step-like enhancement occurs with the temperature where the pseudogap opens, i.e., we set T*≈220 K. The lower panel of Fig. 14 shows the temperature dependence of the intrinsic linewidth derived for the same CF transition in the ^{16}O compound. We recognise that the relaxation behaviour of the ^{16}O sample has a similar shape as for the isotope substituted ^{18}O compound, but the step-like enhancement of the linewidth occurs at much lower temperatures between 160 and 170 K, i.e., T*≈170 K. These relaxation data give therefore evidence for a large isotope shift ΔT*≈50 K which, in analogy to the isotope effect on T_c, gives rise to a huge isotope coefficient α^*(O)≈-2.2±0.6 [47].

4.3 Copper Isotope Effect in $HoBa_2Cu_4O_8$

Investigations of a copper isotope effect on the pseudogap temperature T* are likewise of great interest. The critical temperatures of the ^{63}Cu and ^{65}Cu compounds were measured by magnetometry to be (79.0±0.1) K and (78.6±0.1) K, respectively, giving a copper isotope shift ΔT_c=(–0.4±0.2) K which is in agreement with literature data on the isostructural compound $YBa_2Cu_4O_8$ [60]. Figure 15 displays the temperature dependence of the intrinsic linewidth (HWHM) corresponding to the lowest CF ground-state transition at $\hbar\omega_1$=0.6 meV. For the ^{63}Cu compound (left panel) the linewidth is zero at the lowest temperatures, then

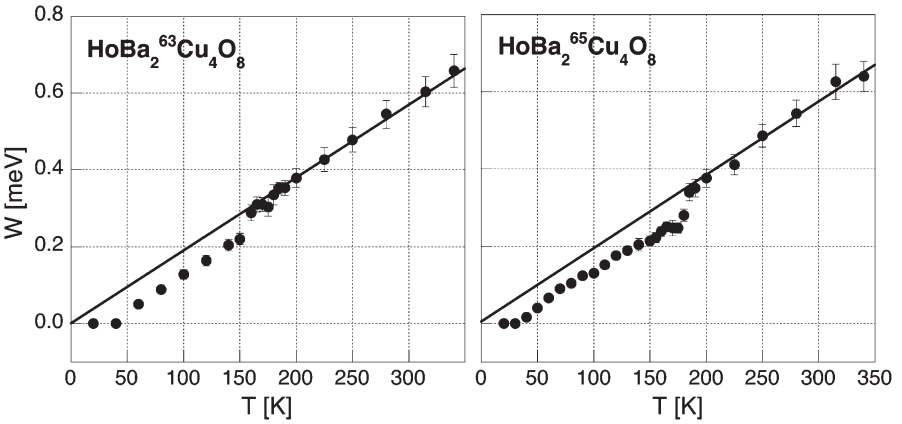

Fig. 15 Temperature dependence of the intrinsic linewidth W (HWHM) corresponding to the $\Gamma_3 \rightarrow \Gamma_4$ ground-state CF transition in $HoBa_2{}^{63}Cu_4O_8$ and $HoBa_2{}^{65}Cu_4O_8$ [48]. The *lines* denote the linewidth in the normal state calculated from the Korringa law

it increases monotonically up to 150 K. A notable enhancement occurs between 150 and 160 K. Above 160 K the linewidth increases almost linearly with temperature as predicted by the Korringa law. We therefore identify the temperature where the enhancement occurs with the temperature where the pseudogap opens, i.e., we set $T^* \approx 160$ K. The linewidth observed for the ^{65}Cu compound (right panel) exhibits a similar relaxation behaviour, but the enhancement occurs at higher temperatures between 180 and 185 K, i.e., we set $T^* \approx 185$ K. These experiments give evidence therefore for a large copper isotope effect $\Delta T^* \approx 25$ K, with a corresponding isotope coefficient $\alpha^*(Cu) \approx -4.9 \pm 3.2$ [48]. This is roughly twice as large as the corresponding oxygen isotope coefficient. The relevant mechanism giving rise to a copper isotope effect on T^* has to be associated with a local copper phonon mode which could be either a copper-oxygen bond stretching mode or an umbrella-type motion [61] involving in-plane or out-of-plane displacements of the copper ions, respectively. The latter mode is absent in the single-layer high-T_c compound $La_{2-x}Sr_xCuO_4$ because of the inversion symmetry at the Cu site, thus a study of the copper isotope effect in this compound could definitely discriminate between the possible copper modes as shown in the following sections.

4.4 Oxygen and Copper Isotope Effects in Ho@$La_{2-x}Sr_xCuO_4$

The effect of oxygen and copper isotope substitution was investigated for optimally doped $La_{1.81}Sr_{0.15}Ho_{0.04}CuO_4$ ($T_c \approx 32$ K) [49], which exhibits a strong ground-state CF transition at $\hbar\omega = 0.185$ meV, i.e., $\hbar\omega \ll 2\Delta_{max}$ (≈ 16 meV [62]). Further CF transitions are expected to appear above 10 meV and to be at least an order of magnitude less intense, which means that the observed low-energy CF spectrum will not be contaminated by excited-state transitions for temperatures up to 100 K. Figure 16 shows the temperature dependence of the intrinsic linewidth W (FWHM) for the four isotope substituted samples. For the ^{16}O compound (panel a) the linewidth is rather small below 30 K, then it increases monotonically up to 60 K. Above 60 K the linewidth increases linearly as expected for the normal state, i.e., we set $T^*(^{16}O) \approx 60$ K. The temperature evolution of the intrinsic linewidth determined for the ^{18}O compound (panel b) has a similar shape as for the ^{16}O compound; however, the crossover into the normal state occurs at a higher temperature, i.e., we set $T^*(^{18}O) \approx 70$ K. Our data therefore give evidence for a large oxygen isotope shift of the pseudogap temperature T^* at optimum doping, namely $\Delta T^*(O) \approx 10$ K, which is equivalent to an oxygen isotope coefficient $\alpha^*(O) \approx -1.3$.

For the ^{63}Cu compound (panel c) as well as for the ^{65}Cu compound (panel d) the relaxation behaviour is similar to the ^{16}O compound, and there is practically no difference between the ^{63}Cu and ^{65}Cu data, i.e., we have $T^*(^{63}Cu) \approx T^*(^{65}Cu) \approx 60$ K. This means that there is no copper isotope effect on T^*, i.e., $\Delta T^*(Cu) \approx 0$. This is in contrast to the case of $HoBa_2Cu_4O_8$ for which a large value of $\Delta T^*(Cu) \approx 25$ K was reported [48]. This large copper isotope shift was associated with a local copper mode, although the experiment did not provide direct

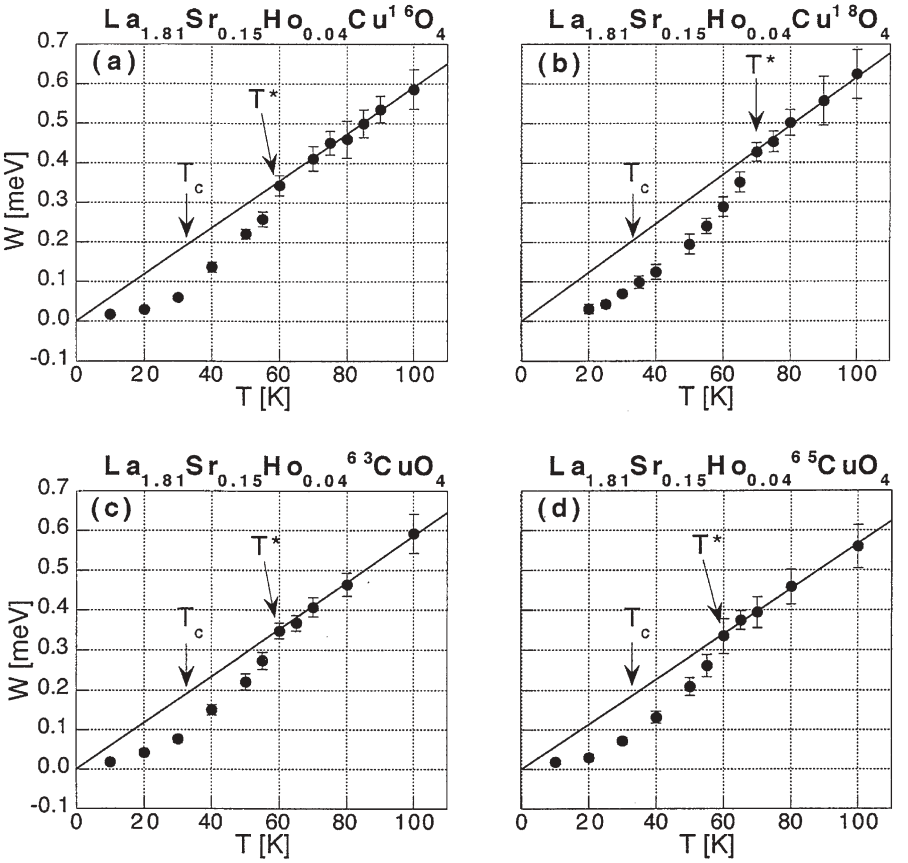

Fig. 16a–d Temperature and isotope dependence of the intrinsic linewidth W (FWHM) corresponding to the lowest ground-state CF transition in $La_{1.81}Sr_{0.15}Ho_{0.04}CuO_4$ [49]. The *lines* denote the linewidth in the normal state calculated from the Korringa law. The figure is taken from [68]

information about the specific type of lattice mode involved. By comparing $\Delta T^*(Cu)$ for both $HoBa_2Cu_4O_8$ and $La_{1.81}Sr_{0.15}Ho_{0.04}CuO_4$, it is now possible to assign the copper mode to the umbrella-type mode [61], which is present in the former but not in the latter.

4.5 Pressure Effect in $Ho@La_{2-x}Sr_xCuO_4$

The polycrystalline $La_{1.81}Sr_{0.15}Ho_{0.04}Cu^{16}O_4$ sample investigated under hydrostatic pressure was the same as that used for the experiments at ambient pressure, see previous section. The superconducting transition temperature was determined by a.c. magnetic susceptibility measurements to be T_c=32.5±0.3 K at ambient pressure and T_c=35.2±0.3 K at p=1.0 GPa, i.e., the pressure-induced enhancement of

T_c is in good agreement with literature data [63, 64]. In order to apply hydrostatic pressure in the INS experiments, the sample was enclosed in an axially symmetric pressure cell made of hardened aluminium [65]. The total accessible sample volume in the pressure cell amounted to about 1.6 cm^3. At low temperatures (T<20 K) the strong ground-state crystal-field transition occurs at an energy transfer $\hbar\omega$=0.191±0.003 meV [50] which is slightly higher than the energy transfer $\hbar\omega$=0.185±0.002 meV determined at ambient pressure (see previous section).

Figure 17 shows the temperature dependence of the intrinsic linewidth W (FWHM) measured at p=0.8 GPa. The derived linewidth is rather small below 30 K, then it increases monotonically up to 55 K. Above 55 K the linewidth increases linearly as expected from the Korringa law for the normal state which is indicated as a full line taken from the data at ambient pressure (see Fig. 16). We therefore set T*(p=0.8 GPa)≈55 K. The temperature evolution of the linewidth at ambient pressure (see Fig. 16a) has a similar shape, however, the crossover into the normal-state behaviour occurs at T*(p=0)≈60 K. The pressure-induced shift is therefore ΔT*≈–5 K, i.e., we have dT*/dp≈–6 K/GPa, in reasonable agreement with dT*/dp≈–10 K/GPa determined for slightly underdoped $YBa_2Cu_4O_8$ [56].

Because of intensity problems (intensity loss due to the pressure cell) it was not possible to perform an unambiguous analysis of the energy spectra taken at T≥70 K, thus the Korringa line could not be determined from the data taken at p=0.8 GPa over a sufficiently wide temperature range. Instead, it was assumed that the slope of the Korringa line which according to Eqs. (7) to (9) is essentially proportional to the square of the density-of-states at the Fermi level, $[N(E_F)]^2$, remains unaltered upon hydrostatic pressure application. Of course, this assumption has to be supported by strong (experimental) arguments. First, the Hall coefficient (which is a measure of the charge density) of $La_{2-x}Sr_xCuO_4$

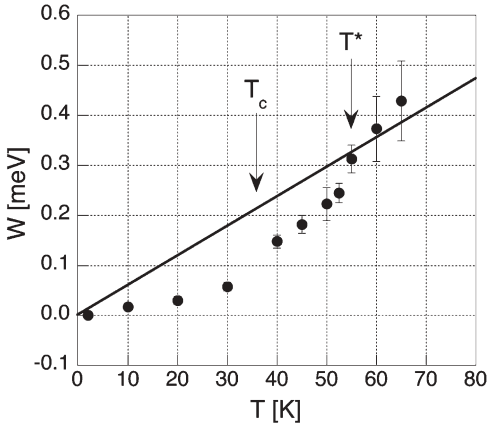

Fig. 17 Temperature dependence of the intrinsic linewidth W (FWHM) corresponding to the lowest ground-state CF transition in $La_{1.81}Sr_{0.15}Ho_{0.04}Cu^{16}O_4$ for p=0.8 GPa [50]. The *line* denotes the linewidth in the normal state calculated from the Korringa law

(0.08≤x≤0.24) does not change with pressure up to p=1.5 GPa [63]. Second, use can be made of the fact that the crystal-field potential is an ideal probe of the local structure and charge distribution in the CuO_2 planes and thereby monitors directly the corresponding changes induced by doping and pressure. We find that the observed pressure-induced shift of the crystal-field transition from $\hbar\omega$=0.185 meV (p=0) to $\hbar\omega$=0.191 meV (p=0.8 GPa) can be explained by structural effects alone. More specifically, extrapolating the crystal-field parameters of Ho^{3+} in $La_{2-x}Sr_xCuO_4$ from p=0 to p=0.8 GPa on the basis of the pressure-induced structural changes determined by neutron diffraction [66] yields a pressure-induced upward shift of the crystal-field transition by 0.006 meV, in excellent agreement with the observations.

The opposite effects of isotope substitution and pressure on the pseudogap temperature T* in optimally doped $La_{1.81}Sr_{0.15}Ho_{0.04}Cu^{16}O_4$, namely $\Delta T^*(^{16}O\rightarrow ^{18}O)\approx+10$ K [49] and $\Delta T^*(0\rightarrow 0.8$ GPa$)\approx-5$ K [50], respectively, can be explained qualitatively by using a simple model based on the concept of bipolaron formation by the Jahn-Teller effect. As a matter of fact, Jahn-Teller polarons were the theoretical basis for the discovery of high-temperature superconductivity by Bednorz and Müller [1]. In this model the polaronic bandwidth W is expressed in terms of an exponential renormalization factor [55]:

$$W = Wb \exp\left\{-\frac{E_{JT}}{\hbar\omega}\right\}, \tag{15}$$

where W_b is the bare bandwidth, E_{JT} the Jahn-Teller energy, and $\hbar\omega$ the energy of the active Jahn-Teller mode(s). Obviously the bandwidth W can be modified by isotope substitution and pressure which both affect $\hbar\omega$ in a specific manner. Since $\hbar\omega$ is inversely proportional to the square root of the oxygen mass, the substitution of ^{16}O by ^{18}O reduces $\hbar\omega$ by typically 5% which according to Eq. (15) results in a band narrowing; thus T* is expected to increase as experimentally observed [49]. On the other hand, the application of hydrostatic pressure results in an enhancement of $\hbar\omega$ by $\partial(\hbar\omega)/\hbar\omega=\gamma\Delta V/V$, where $\gamma\approx2$ is the Grüneisen parameter and $\Delta V/V$ the pressure-induced volume change. For p=0.8 GPa we estimate a 1–2% increase of $\hbar\omega$, which according to Eq. (15) widens the polaronic band and therefore lowers the pseudogap temperature T* as experimentally observed [50]. The above considerations also explain the experimental fact that $|\Delta T^*|$ is smaller for the case of pressure application (p=0.8 GPa) than for the case of oxygen isotope substitution.

5
Nature of the Gap Function

Ever since the discovery of high-T_c superconductivity there has been a debate concerning the symmetry of the gap function. Partially conflicting results were reported from techniques probing either the surface or the bulk [67]. Neutron

crystal-field spectroscopy experiments are inherently bulk-sensitive, thus an analysis of the relaxation data available for optimally doped $La_{1.81}Sr_{0.15}Ho_{0.04}CuO_4$ [49] and slightly underdoped $HoBa_2Cu_4O_8$ [47] was performed in terms of different gap functions [68]. Since the characteristic temperatures T_c and T^* are very different for these compounds, it is convenient to express the relaxation data in reduced units, i.e., the temperature T in units of T^* and the linewidth W(T) in units of $W(T^*)$ as visualised in Fig. 18.

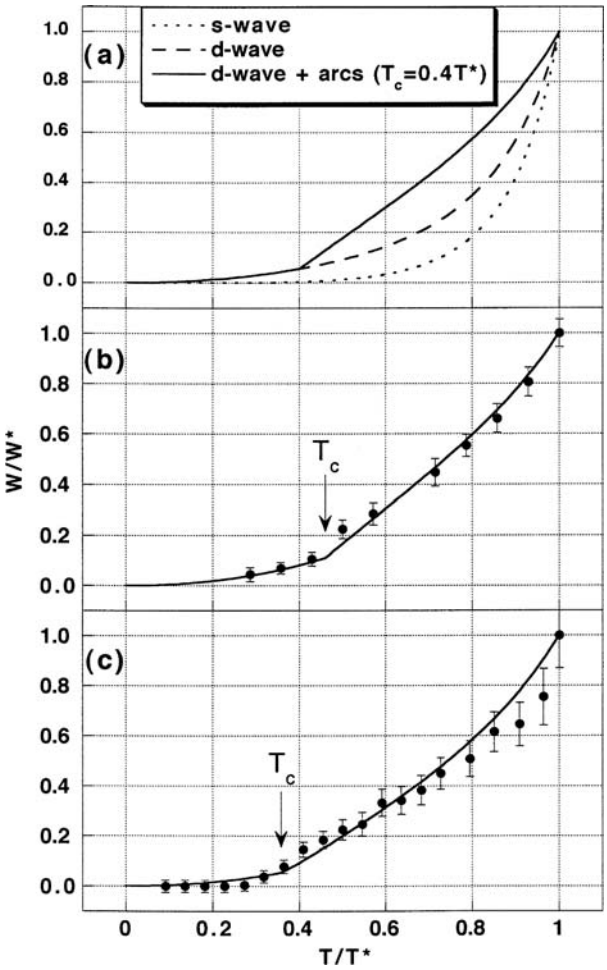

Fig. 18a–c Temperature dependence of the linewidth of low-energy crystal-field transitions in high-temperature superconductors in reduced units: **a** model calculations for different types of gap functions (see text); **b** relaxation data derived for $La_{1.81}Sr_{0.15}Ho_{0.04}Cu^{18}O_4$ [49]; **c** relaxation data derived for $HoBa_2Cu_4{}^{18}O_8$ [47]. The lines in b and c denote least-squares fits on the basis of a d-wave gap function including the occurrence of gapless arcs of the Fermi surface in the pseudogap region ($T_c \ll T^*$) as described in the text. The figure is taken from [68]

The model calculations were based on the procedure described by Mesot et al. [59]. The temperature dependence of the gap amplitude was described by the expression $\Delta(T)=\Delta(0)\cdot[1-(T/T^*)^4]$ [69], and the maximum gap amplitude was set to $\Delta_{max}/k_B=2T^*$ which is a realistic value for the compounds under consideration. Figure 18a shows calculations for an s-wave and a d-wave (x^2-y^2) gap function. It can readily be seen that none of these models is able to explain the observed linewidth behaviour displayed in Fig. 18b,c. In particular, the anomalous behaviour around T_c cannot be reproduced. This is due to the neglect of the temperature dependence of the gap function in the pseudogap region as predicted theoretically [70, 71] and observed by angle-resolved photoemission spectroscopy (ARPES) measurements in underdoped $Bi_2Sr_2CaCu_2O_{8+x}$ [72]. More specifically, the gradual development of gapless arcs of the Fermi surface between T_c and T^* opens additional relaxation channels in crystal-field linewidth studies in the pseudogap region. Indeed, the model calculations including the presence of gapless arcs produce relevant modifications of the linewidth above T_c as visualised in Fig. 18a.

A least-squares fitting procedure to the relaxation data displayed in Fig. 18b,c was performed on the basis of a d-wave gap function including the gapless arc features of the Fermi surface at $T_c<T<T^*$. Since the latter effect was only observed at a few selected temperatures [72], a linear evolution of the gapless arcs with temperature was assumed. The only fitting parameter was the amplitude Δ_{max} of the d-wave gap function. The temperature evolution of the linewidths resulting from the least-squares fitting procedure is in reasonable agreement with the experimental data as shown in Fig. 18b,c, corresponding to gap amplitudes $\Delta_{max}=(1.5\pm0.3)\cdot T^*$ and $\Delta_{max}=(1.7\pm0.2)\cdot T^*$, respectively. It should be noticed that a similarly good agreement can be obtained by using a mixed (s+d)-wave gap function, with s- and d-wave components of the order of 25% and 75%, respectively. Nevertheless, the gap function has undoubtedly predominant d-wave character.

6
Conclusions and Outlook

We have shown that neutron spectroscopy is a powerful tool to determine unambiguously the CF potential in rare-earth based high-T_c superconducting materials. This provides detailed information on the electronic ground state of the R ions which is important to understand the observed coexistence between superconductivity and long-range magnetic ordering of the R ion sublattice at low temperatures. Moreover, the inhomogeneous decay of the antiferromagnetic state of the parent compound as well as the inhomogeneous evolution of the superconducting state upon doping can be directly and quantitatively monitored, resulting in the onset of bulk superconductivity by a percolation mechanism. For underdoped systems, the origin of the inhomogeneities is believed to lie in the small hole density which gives rise to a strong enhancement of

phase fluctuations. A direct consequence of the phase fluctuations is the appearance of transitions or crossovers associated with the superconducting gap and the pseudogap which may merge in the overdoped regime. These effects were observed through studying the temperature dependence of the linewidth of CF splittings, and the doping dependence of the pseudogap temperature T* was quantitatively established [73] and found to be in good agreement with the results obtained by ARPES experiments [74]. From the analysis of the temperature dependence of the relaxation data there is strong evidence that the novel electronic properties in terms of gapless arcs of the Fermi surface, experimentally observed for underdoped $Bi_2Sr_2CaCu_2O_{8+\delta}$ [72] in the pseudogap region, are also present in the Y- and La-based high-temperature superconductors, thereby being presumably a generic feature of all copper-oxide perovskites. Finally, the pseudogap temperature T* is found to exhibit large shifts upon oxygen (and in bilayer systems also copper) isotope substitution as well as pressure application. The observed isotope- and pressure-induced shifts of T* can qualitatively be accounted for by considering a Jahn-Teller polaron-like mechanism [55]. The importance of phonons or lattice fluctuations for the pairing mechanism in high-temperature superconducting materials was reinforced by the observation of strong electron-phonon coupling effects in recent ARPES experiments performed for $La_{2-x}Sr_xCuO_4$, $Bi_2Sr_2CaCu_2O_{8+\delta}$, and Pb-doped $Bi_2Sr_2CuO_{6+\delta}$ [75].

As mentioned above, experimental studies of the electronic structure and the Fermi surface of high-T_c superconductors in the normal state provide key information on the pseudogap issue. ARPES experiments are clearly the most direct technique, but so far they have only been performed successfully for $Bi_2Sr_2CaCu_2O_{8+\delta}$ because of instrumental reasons. In order to achieve sufficient energy resolution (of the order of 5 meV), photons with energies of the order of 20 eV had to be used [69, 72, 74]. Such low-energy photons do not penetrate into the bulk; thus essentially they probe the surface. This implies perfect conditions for the sample surface which so far could only be achieved for $Bi_2Sr_2CaCu_2O_{8+\delta}$ and not for the widely studied $La_{2-x}Sr_xCuO_4$ and $YBa_2Cu_3O_x$ compounds. In order to make ARPES experiments a truly bulk-sensitive probe (and thereby to make it applicable to other high-T_c compounds due to the release of the stringent requirements concerning the sample surface), higher photon energies (of the order of 100 eV) should be used which, however, have detrimental consequences concerning the energy resolution (which can only be improved at the expense of intensity). Nevertheless, this problem will be overcome by novel ARPES instruments which are presently being installed at third-generation synchrotron sources; thus we may soon expect more detailed information about the evolution and the nature of the pseudogap in a wide variety of high-T_c compounds.

The situation concerning the pseudogap in the electron-doped high-T_c compounds is not clear at present. Only very recently information about the pseudogap was reported on the basis of optical spectroscopy [76] and tunnelling [77] experiments. Both techniques probe only the surface, thus bulk techniques are needed to establish a reliable phase diagram of electron-doped high-T_c super-

conductors as well as to find out whether it is generically similar or different as compared to the hole-doped high-T_c compounds. Neutron crystal-field relaxation experiments are inherently bulk-sensitive and therefore ideally suited to explore the pseudogap issue in the electron-doped high-T_c systems. Compounds with the highest T_c are of the type $R_{2-x}Ce_xCuO_{4+\delta}$ (R=Pr, Nd, Sm). Superconductivity is observed in a narrow doping range $0.11<x<0.18$ [77] with maximum T_c=24 K for x=0.15. The lowest-lying CEF excitations for R=Pr and R=Nd have energies of the order of 20 meV [41–43], whose linewidths cannot be measured with sufficient precision with today's neutron spectrometers. Compounds with heavy rare-earth elements usually have smaller CF energies. Unfortunately, electron-doped high-T_c compounds of type $R_{2-x}Ce_xCuO_{4+\delta}$ cannot be synthesized for heavy rare earths, but they can be doped into this structure [78] up to a concentration of about 10%. Recently, we have been able to observe an intense CF transition at $\hbar\omega\approx1.7$ meV for $Pr_{1.85}Ce_{0.15}CuO_{4+\delta}$ doped with 10% Ho; however, the transition showed the existence of side lines which did not allow a reliable determination of the linewidth [79]. These side lines are due to Ho-Ho dimer splittings whose scattering can be considerably reduced for lower Ho concentrations; thus investigations of a sample with a lower Ho content will certainly shed light on the pseudogap issue in electron-doped high-T_c-compounds.

Acknowledgements Financial support by the Swiss National Science Foundation through the projects No. 20-58903.99 and 20-66948.01 as well as the NCCR MaNEP project is gratefully acknowledged. The author is grateful to P. Allenspach, K. Conder, P.S. Häfliger, W. Henggeler, S. Janssen, J. Mesot, A. Podlesnyak, D. Rubio Temprano, U. Staub (PSI, Villigen, Switzerland), J. Karpinski, S. M. Kazakov (ETH, Zurich, Switzerland), H. Mutka (ILL, Grenoble, France), P. Vorderwisch (HMI, Berlin, Germany), R. Osborn, A.D. Taylor (ISIS, Didcot, U.K.), A. Sokolov, and V. Trounov (PNPI, Gatchina, Russia) for their participation in the experimental work as well as for numerous stimulating discussions and in particular to K.A. Müller (Univ. of Zurich, Switzerland) for invaluable and sagacious advice at various project states.

References

1. Bednorz JG, Müller KA (1986) Z Phys B Condensed Matter 64:189
2. Wu MK, Ashburn JR, Torng CJ, Hor PH, Meng RL, Gao L, Huang ZJ, Wang YQ, Chu CW (1987) Phys Rev Lett 58:908
3. Jandl S, Dufour P, Strach T, Ruf T, Cardona M, Nekvasil V, Chen C, Wanklyn BM, Piñol S (1996) Phys Rev B 53:8632
4. Strach T, Ruf T, Cardona M, Lin CT, Jandl S, Nekvasil V, Zhigunov DI, Barilo SN, Shiryaev SV (1996) Phys Rev B 54:4276
5. Henggeler W, Chattopadhyay T, Roessli B, Vorderwisch P, Thalmeier P, Zhigunov DI, Barilo SN, Furrer A (1997) Phys Rev B 55:1269
6. Hizhnyakov V, Sigmund E (1988) Physica C 156:655
7. Sigmund E, Müller KA (eds) (1994) Phase separation in cuprate superconductors. Springer, Berlin Heidelberg New York
8. Mesot J, Furrer A (1997) J Supercond 10:623

9. Mesot J, Furrer A (1998) The crystal field as a local probe in rare-earth based copper-oxide superconductors. In: Furrer A (ed) Neutron scattering in layered copper-oxide superconductors. Kluwer, Dordrecht, p 335
10. Mesot J, Rubio Temprano D, Furrer A (2002) Neutron crystal-field spectroscopy in rare-earth based high-temperature superconductors. In: Trends in applied spectroscopy, vol 4. Research Trends, Trivandrum, p 75
11. Trammell GT (1953) Phys Rev 92:1387
12. Korringa J (1950) Physica (Utrecht) 16:601
13. Becker KW, Fulde P, Keller J (1977) Z Phys B Condensed Matter 28:9
14. Feile R, Loewenhaupt M, Kjems JK, Hoenig HE (1987) Phys Rev Lett 47:610
15. Lovesey SW, Staub U (2000) Phys Rev B 61:9130
16. Boothroyd AT (2001) Phys Rev B 64:066501
17. Mesot J, Allenspach P, Staub U, Furrer U, Mutka H, Osborn R, Taylor A (1993) Phys Rev B 47:6027
18. Guillaume M, Henggeler W, Furrer A, Eccleston RS, Trounov V (1995) Phys Rev Lett 74:3423
19. Mesot J, Allenspach P, Staub U, Furrer A, Mutka H (1993) Phys Rev Lett 70:865
20. Staub U, Mesot J, Guillaume M, Allenspach P, Furrer A, Mutka H, Bowden Z, Taylor A (1994) Phys Rev B 50:4068
21. Radaelli PG, Segre CU, Hinks DG, Jorgensen JD (1992) Phys Rev B 45:4923
22. Cava RJ, Hewat AW, Hewat EA, Batlogg B, Marezio M, Rabe KM, Krajewski JJ, Peck WF Jr, Rupp LW Jr (1990) Physica C 165:419
23. Niedermayer C, Bernhard C, Blasius T, Golnik A, Moodenbaugh A, Budnick JI (1998) Phys Rev Lett 80:3843
24. Sidis Y, Ulrich C, Bourges P, Bernhard C, Niedermayer C, Regnault LP, Andersen NH, Keimer B (2001) Phys Rev Lett 86:4100
25. Pan SH, O'Neal JP, Badzey RL, Chamon C, Ding H, Engelbrecht JR, Wang Z, Eisaki H, Uchida S, Gupta AK, Ng KW, Hudson EW, Lang KM, Davis JC (2001) Nature 413:282
26. Kremer AK, Sigmund E, Hizhnyakov V, Hentsch F, Simon A, Müller KA, Mehring M (1992) Z Phys B Condensed Matter 86:319
27. Kirkpatrick S (1973) Rev Mod Phys 45:574
28. Kubo Y, Igarashi H (1989) Phys Rev B 39:725
29. Osofsky MS, Cohn JL, Skelto EF, Miller MM, Soulen JRJ, Wolf SA, Vanderah TA (1992) Phys Rev B 45:4917
30. Allenspach P, Furrer A, Rupp B (1990) Charge distribution in the CuO_2 planes of $ErBa_2Cu_3O_x$ ($6<x<7$) determined by neutron crystal-field spectroscopy. In: Aksenov VL, Bogolubov NN, Plakida NM (eds) Progress in high-temperature superconductivity, vol 21. World Scientific, Singapore, p 318
31. Furrer A, Mesot J, Allenspach P, Staub U, Fauth F, Guillaume M (1994) Neutron spectroscopy in $RBa_2Cu_3O_x$ (R=rare earth, $6<x<7$) compounds: charge transfer, phase separation, spin fluctuations. In: Sigmund E, Müller KA (eds) Phase separation in cuprate superconductors. Springer, Berlin Heidelberg New York, p 101
32. Furrer A, Allenspach P, Fauth F, Guillaume M, Henggeler W, Mesot J, Rosenkranz S (1994) Physica C 235/240:261
33. Hammel PC, Reyes AP, Fisk Z, Takigawa M, Thompson JD, Heffner KH, Cheong SW (1990) Phys Rev B 42:6781
34. Wübbeler G, Schirmer OF (1990) Phys Stat Sol (b) 174:K21
35. Hodges JA, Bonville P, Imbert P, Jéhanno G, Debray P (1991) Physica C 184:270
36. Poulakis N, Palles D, Liarokapis E, Conder K, Kaldis E (1996) Phys Rev B 53:R534
37. Emery VJ, Kivelson SA, Lin HQ (1990) Phys Rev Lett 64:475

38. Grilli M, Raimondi R, Castellani C, Di Castro C, Kotliar G (1991) Phys Rev Lett 67:259
39. Bucher B, Karpinski J, Kaldis E, Wachter P (1990) J Less-Common Metals 164/165:20
40. Mesot J, Allenspach P, Staub U, Furrer A, Blank H, Mutka H, Vettier C, Kaldis E, Karpinski J, Rusiecki S (1990) J Less-Common Metals 164/165:59
41. Henggeler W, Cuntze G, Mesot J, Klauda M, Saemann-Ischenko G, Furrer A (1995) Europhys Lett 29:233
42. Sumarlin IW, Lynn JW, Chattopadhyay T, Barilo SN, Zhigunov DI (1994) Physica C 219:195
43. Henggeler W, Chattopadhyay T, Roessli B, Vorderwisch P, Thalmeier P, Zhigunov DI, Barilo SN, Furrer A (1997) Phys Rev B 55:1269
44. Strach T, Ruf T, Cardona M, Jandl S, Nekvasil V (1997) Physica B 234/236:810
45. Batlogg B, Varma C (2000) Phys World 13(2):33
46. Lanzara A, Zhao GM, Saini NL, Bianconi A, Conder K, Keller H, Müller KA (1999) J Phys Condens Matter 11:L541
47. Rubio Temprano D, Mesot J, Janssen S, Conder K, Furrer A, Mutka H, Müller KA (2000) Phys Rev Lett 84:1990
48. Rubio Temprano D, Mesot J, Janssen S, Conder K, Furrer A, Sokolov A, Trounov V, Kazakov SM, Karpinski J, Müller KA (2001) Eur Phys J B 19:5
49. Rubio Temprano D, Conder K, Furrer A, Mutka H, Trounov V, Müller KA (2002) Phys Rev B 66:184506
50. Furrer A, Conder K, Häfliger PS, Podlesnyak A (2004) Physica C 408/410:773
51. Williams GVM, Tallon JL, Quilty JW, Trodahl HJ, Flower NE (1998) Phys Rev Lett 80:377
52. Raffa F, Ohno T, Mali M, Roos J, Brinkmann D, Conder K, Eremin M (1998) Phys Rev Lett 81:5912
53. Andergassen S, Caprara S, Di Castro C, Grilli M (2001) Phys Rev Lett 87:056401
54. Bussmann-Holder A (2000) J Supercond 13:773
55. Gor'kov LP (2000) J Supercond 13:765
56. Machi T, Kosuge M, Koshizuka N, Yasuoka H (1996) NQR study in $YBa_2Cu_4O_8$ under high pressure. In: Nakayima S, Murakami M (eds) Advances in superconductivity IX. Springer, Berlin Heidelberg New York, p 111
57. Shen LJ, Lam CC, Anand V, Li SH, Jin X (2000) Physica C 341/348:929
58. De Mello EVL, Orlando MTD, González JL, Caixeiro ES, Baggio-Saitovich E (2002) Phys Rev B 66:092504
59. Mesot J, Böttger G, Mutka H, Furrer A (1998) Europhys Lett 44:498
60. Williams GVM, Pringle DJ, Tallon JL (2000) Phys Rev B 61:R9257
61. Röhler J (2000) Physica C 341/348:2151
62. Sato T, Yokoya T, Naitoh Y, Takahashi T, Yamada K, Endoh Y (1998) Phys Rev Lett 83: 2254
63. Murayama C, Iye Y, Enomoto T, Môri N, Yamada N, Matsumoto T, Kubo Y, Shimakawa Y, Manako T (1991) Physica C 183:277
64. Yamada N, Ido M (1992) Physica C 203:240
65. Strässle T, Divis M, Rusz J, Janssen S, Juranyi F, Sadikov R, Furrer A (2003) J Phys Condens Matter 15:3257
66. Takahashi H, Shaked H, Hunter BA, Radaelli PG, Hitterman RL, Hinks DG, Jorgensen JD (1994) Phys Rev B 50:3221
67. Müller KA, Keller H (1997) 's' and 'd' wave symmetry components in high-temperature cuprate superconductors. In: Kaldis E (ed) High-temperature superconductivity: ten years after the discovery. Kluwer, Dordrecht, p 7
68. Furrer A, Rubio Temprano D, Mesot J, Conder K, Müller KA (2002) J Supercond 15:361

69. Ding H, Yokoya T, Campuzano JC, Takahashi T, Randeria M, Norman MR, Mochiku T, Kadowaki K, Giapintzakis J (1996) Nature 382:51
70. Wen XG, Lee PA (1996) Phys Rev Lett 76:503
71. Engelbrecht JR, Nazarenko A, Randeria M, Dagotto E (1998) Phys Rev B 57:13406
72. Norman MR, Ding H, Randeria M, Campuzano JC, Yokoya T, Takeuchi T, Takahashi T, Mochiku T, Kadowaki K, Guptasarma P, Hinks DG (1998) Nature 392:157
73. Rubio D, Mesot J, Conder K, Janssen S, Mutka H, Furrer A (2000) J Supercond 13:727
74. Campuzano JC, Ding H, Norman MR, Fretwell HM, Randeria M, Kaminski A, Mesot J, Takeuchi T, Sato T, Yokoya T, Takahashi T, Mochicku T, Kadowaki K, Guptasarma P, Hinks DG, Konstantinovic Z, Li ZZ, Raffy H (1999) Phys Rev Lett 83:3709
75. Lanzara A, Bogdanov PV, Zhou XJ, Kellar SA, Feng DL, Lu ED, Yoshida T, Elsaki H, Fujimori A, Kishio K, Shimoyama JI, Noda T, Uchida S, Hussain Z, Shen ZX (2001) Nature 412:510
76. Onose Y, Taguchi Y, Ishizaka K, Tokura Y (2002) Phys Rev Lett 87:217001
77. Alff L, Krockenberger Y, Welter B, Schonecke B, Gross R, Manske D, Naito M (2003) Nature 422:698
78. Martins GB, Rao D, Valdivia JA, Pires MA, Barberis GE, Rettori C, Venegas PA, Oseroff S, Fisk Z (1995) Phys Rev B 51:11909
79. Häfliger PS, Podlesnyak A, Conder K, Pomjakushina E, Furrer A (2004) Is there a pseudogap in electron-doped high-temperature superconductors? In: Schefer J, Castellazzi D, Braun-Shea M (eds) (2004) PSI – Scientific Report 2003, vol III. PSI, Villigen, p 28

Struct Bond (2005) 114: 205–266
DOI 10.1007/b101021

Nanoscale Properties of Superconducting Cuprates Probed by the Electron Paramagnetic Resonance

B. I. Kochelaev[1] (✉) · G. B. Teitel'baum[2]

[1] Kazan State University, 420008 Kazan, Russia
boris.kochelaev@ksu.ru
[2] E. Zavoisky Institute for Technical Physics of the Russian Academy of Sciences, 420029 Kazan, Russia
grteit@dionis.kfti.kcn.ru

Abstract The basic principles of EPR in the high-Tc materials are presented with the accent on the novel features of these compounds in comparison with the conventional metallic systems. An overview is given on the various results obtained in the past years with the emphasis on the analysis of the local properties. Among the issues discussed in the details are the unusual normal state properties, the magnetic fluctuations, the phonon effects, stripe phase and the nanoscale phase separation resulting from the interplay of the lattice distortions with the strong electron correlations. The special attention is focused on their relevance to the origin of the high-temperature superconductivity. The main conclusions followed from EPR experiments in the cuprates are discussed. Some recent developments are addressed and compared to theoretical models.

Keywords Superconductivity · Magnetic resonance · Cuprates · Phase separation · Localized states

List of Abbreviations

AF	Antiferromagnetic
ARPES	Angle Resolved Photoemission Spectroscopy
BCS	Bardeen-Cooper-Schrieffer
BPP	Bloembergen-Purcell-Pound
CEF	Crystal Electric Field
DM	Dzyaloshinskii-Moria
EPR	Electron Paramagnetic Resonance
G	Gauss
g	g-factor
GHz	Gigaherz
HTSC	High Temperature Superconductor
HTT	High Temperature Tetragonal
INS	Inelastic Neutron Scattering
K	Kelvin
LSCO	Lanthanum-Strontium Copper Oxide
LTO	Low Temperature Orthorhombic
LTT	Low Temperature Tetragonal
μ_B	Bohr Magneton
NMR	Nuclear Magnetic Resonance
Oe	Oersted
PCF	Paramagnetic Chain Fragment
RE	Rare Earth
RKKI	Ruderman-Kittel-Kasuya-Iosida
SC	Superconducting
T	Tesla
YBCO	Yttrium-Barium Copper Oxide

1 Introduction

1.1 The EPR of Conventional Superconductors (Historical Remarks)

The magnetic resonance as a method of study of superconducting materials played an important role already at a very early stage of investigations of a conventional superconductivity. In particular, the nuclear magnetic resonance (NMR) was used by Hebel and Slichter [1] to observe a sharp enhancement of the nuclear spin relaxation rate just below the critical temperature T_c of the superconducting transition. It was one of the key experiments supporting the BCS theory of superconductivity. It was realized that the nuclear spin relaxation to conduction electrons becomes more effective due to the coherent factors caused by the Cooper pairing and it is additionally enhanced by the high density of electron states appearing at the edge of the superconducting energy gap near the Fermi surface. At the same time an evident and attractive idea to observe the spin resonance of superconducting electrons could not be very helpful because of obvious reasons: a small intensity of the resonance signal and its large linewidth. In the normal state this intensity is proportional to a rather small Pauli spin susceptibility and it is greatly reduced in the superconducting state because of the singlet electron pairing. The linewidth of the resonance signal is determined usually by the spin-orbit scattering of conduction electrons by impurities and other defects of the crystal lattice, which give a large contribution even at their small concentration.

Electron paramagnetic resonance (EPR) has been shown to be an effective method to study the conventional superconductors with paramagnetic impurities. These materials attracted a considerable interest since the paramagnetic impurities are responsible for an effective pair breaking mechanism in the conventional superconductors and because of the problem of a coexistence of superconductivity and magnetism. The first EPR signal in the superconductor was observed in the intermetallic compound La_3In using the Gd^{3+} ion as a probe [2] and then it was investigated in details in other similar compounds [3, 4] (see the review [5]). In accordance with expectations these experimental results could be interpreted in a similar way to the NMR findings, since the main interaction of Gd^{3+} impurity in metal at small concentrations is the isotropic exchange coupling to the conduction electrons. Nevertheless the EPR measurements on Er^{3+} ions in lanthanum quickly gave completely different results [6]. Instead of broadening, the EPR line appreciably and abruptly reduced just after transition to the superconducting state. One could conclude that the EPR measurements can give information which could not be obtained by the NMR method. It was found later that the broadening mechanism in this case was different from expected one being determined by the anisotropic interactions between the Er^{3+} ions, and the EPR line was narrowed because of a sufficient modification of the RKKI exchange interaction between the para-

magnetic impurities via conduction electrons upon a transition to the superconducting state [7, 8]. This experiment also gave an impulse to understanding that the superconducting state stimulates a collective motion of total magnetic moments of the paramagnetic impurities and the conduction electrons (the bottleneck regime) [9]. This topic was investigated later in great detail [10]. It is important to point out that the EPR linewidth in the deep bottlenecked regime in metals with paramagnetic impurities is usually determined by the relaxation rate of conduction electrons to the lattice, while the coupling between the paramagnetic probe and the conduction electrons is hidden. It gives an effective method to study spin kinetics of conduction electrons (see the review of Barnes [11]).

1.2 EPR Silence of the Bulk High-T_c Superconductors

The discovery of the high-T_c superconductivity by Bednorz and Müller [12] created a great interest to the EPR study of doped layered cuprates and their parent compounds. The main reason for that was a widely accepted opinion that the basic superconducting events occur in CuO_2 planes. The ion Cu^{2+} in this plane of the parent compounds has an electronic configuration d^9 with a singlet orbital $d(x^2-y^2)$ as a ground state. This type of ion is used as a probe in many dielectric crystals and gives a very good EPR signal [13, 14]. Moreover, the search for high-T_c superconductivity by Bednorz and Müller was guided by the Jahn-Teller polaron model, associated with the Cu^{2+} ion in the oxygen octahedron. Additional interest in the EPR measurements was stimulated by the NMR findings that there is no enhancement of the nuclear spin relaxation rate in the high-T_c superconductors at the phase transition to the superconducting state. At the same time a weak isotope effect and other experiments created widespread belief that the mechanism of the Cooper pairing in cuprate is not related to the electron-phonon interaction as in the conventional superconductors (see, for example, the book [15]). In particular, great attention was paid to the role of the antiferromagnetic spin fluctuation in the CuO_2 plane caused by the huge isotropic exchange interactions between the Cu ions. It was also quite natural to study the spin dynamics in this plane by the EPR method. However, any attempt to observe the bulk EPR response of the Cu spin-system was giving a negative result. The nature of the EPR silence of superconducting cuprates and their parent compounds was a subject of intensive theoretical and experimental investigations (see the review [16]). In particular, Chakravarty and Orbach proposed that the EPR line in the undoped La_2CuO_4 is severely broadened below room temperature by the anisotropic Dzyaloshinskii-Moriya (DM) interactions [17]. They argued that the EPR could be observed at elevated temperatures, since the linewidth should be greatly narrowed by the fast spin fluctuations. Simon et al. [18] have extended the search of the EPR signal in $La_2CuO_{4+\delta}$ ($0 \leq \delta \leq 0.12$) up to 1150 K and no EPR signal had been observed. The nature of the EPR silence will be discussed later in connection with a strong electron-phonon coupling.

2
Basic Properties of High-T_c Compounds and the Types of EPR Spin-Probes

2.1
Specifics of Electronic and Structural Properties

In this section we give a brief overview of structural and basic electronic information on three typical HTSC which we will mostly discuss later (for the extended reviews see [19–23], for the earlier summaries of magnetic resonance studies see [24, 25] (NMR) and [26] (EPR)). In $La_{2-x}Sr_xCuO_4$ (LSCO) all the ranges of doping, from the antiferromagnetic (AF) phase to the metallic one, passing through a spin-glass regime, can be obtained by replacing Sr^{2+} for La^{3+}. The superconducting (SC) phase has an optimally doped state, with the highest T_c, and underdoped and overdoped regimes. Below the certain temperature dependent on Sr content phase transition from a high temperature tetragonal (HTT) to a low temperature orthorombic (LTO) structure takes place (see the phase diagram in Fig. 1). $YBa_2Cu_3O_y$ (YBCO 123) has a phase diagram similar

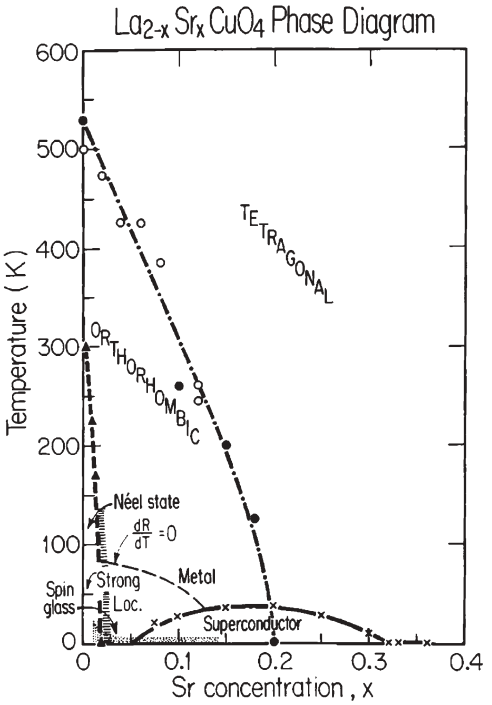

Fig. 1 Phase diagram for $La_{2-x}Sr_xCuO_4$ summarizing structural, magnetic, and transport properties [32]. The *narrow dashed line* (dR/dT=0) separates the region of metallic linear resistance from that of logarithmically increasing resistance. The conductance in the Neel state is strongly localized

to LSCO but an evolution from the AF phase to the optimally doped system, obtained by changing the oxygen content, is not as easy to control and the overdoped regime can hardly be reached. Finally $YBa_2Cu_4O_8$ (YBCO 124) is characterized by its thermal stability and precise stoichiometry. It is important that HTSC are strongly second type and a magnetic field penetrates the bulk in the form of Abrikosov vortices [27].

The typical structure of HTSC consists of the alternating stacks of electronically active metallic CuO_2 layers and insulating layers playing the role of charge reservoirs. Some structures are characterized by complex sequences in which one can recognize a given number n of CuO_2 layers. A possible classification is based on the number n which also seems to control other properties. For instance T_c increases with n until n=3 and then it decreases.

$La_{2-x}Sr_xCuO_4$ is a single-layer (n=1) compound, with a one-to-one intercalation of a La_2O_2 block layer and a CuO_2 sheet (Fig. 2). The amount of Sr corresponds to the carrier concentration, namely the number of holes per CuO_2 unit. In La_2CuO_4 the Cu^{2+} spin moments are antiferromagnetically (AF) ordered below the Neel temperature T_N~315 K. T_N is strongly reduced by Sr doping, and for x=0.02 the long-range magnetic order disappears at any temperature. The conductivity increases as the copper ions become mixed valent while the holes frustrate the AF ordering. In the Sr concentration range between the AF and SC phases one has a spin glass state (see the phase diagram in Fig. 1). Due to a cooperative Jahn-Teller structural transition the original CuO_6 octahedra are elongated along the c-axis and the Cu hole is localized on the $d(x^2–y^2)$ orbital. Bonding (filled) and antibonding (half-filled) orbitals are formed with the O($2p$) electrons. Correlation effects and on-site repulsion induce the AF insulating state for La_2CuO_4, with a magnetic Cu^{2+} ion. The hole injected by charge

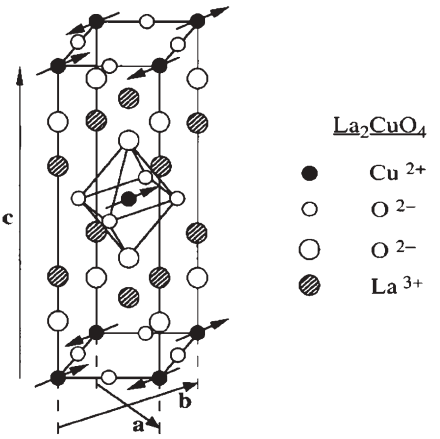

Fig. 2 Crystal and magnetic structure of La_2CuO_4. The *small arrows* indicate the arrangement of Cu spins in the Neel state. The *elongated octahedron* of oxygen ions is drawn for the Cu at the body centre. The rotation of this octahedron gives rise to the orthorhombic phase in which a and b are no longer equal

doping occupies a state which is a linear combination of oxygen 2*p* orbitals with copper 3*d* orbitals.

One of the generic features of these compounds is phase separation on a microscopic scales which exists in a certain doping range [28–30]. The interaction of the doped holes and the AF background together with the considerable lattice distortions are thought to be the important elements for the microscopic mechanism of HTSC.

YBCO 123 has an oxygen-deficient perovskite structure with two crystallographically and chemically different copper sites, corresponding to the CuO_2 planes (n=2) and CuO_3 chains (Fig. 3). In analogy with LSCO, YBCO123 undergoes a phase transition from a HTT to a LTT structure, which in this case is controlled by the oxygen content. The magnetic and electrical properties of $YBa_2Cu_3O_{7-\delta}$ as a function of oxygen content $y=7-\delta$ result from the chemical difference of the copper atoms and from the particular features of the structures. For $\delta>0.65$ one has the AF parent compound, equivalent to La_2CuO_4, with T_N dropping fast with decreasing δ. Superconductivity appears for $\delta<0.65$, with a plateau with $T_c\sim60$ K for $0.25<\delta<0.5$, while T_c is about 92 K for $\delta<0.1$ (this step-like phase diagram may be interpreted in terms of oxygen ordering and cation valence related to the oxygen coordination [31]). In terms of the number of holes in the CuO_2 plane, the phase diagram is similar to that of LSCO [32] (Fig. 1).

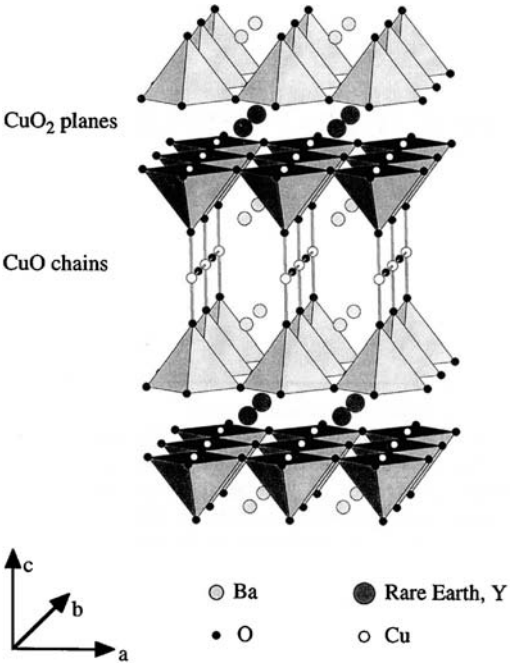

Fig. 3 Crystal structure of YBCO 123 with the indication of CuO_2 planes and oxygen chains. The planar Cu sites are located in the centres of CuO_5 pyramids

The structure of YBCO 124 is very similar to the one of YBCO 123, shown in Fig. 3, with the difference that the single linear CuO_3 chains are replaced by double chains. This double-chain structure causes a particular stability of the system and no structural phase transitions are observed at high temperatures. Also the oxygen content does not change up to 1100 K and YBCO 124 has no magnetic counterpart as YBCO 123. T_c ranges from 75 K to about 81 K depending on the sample preparation.

2.2 Possible EPR Spin Probes

2.2.1 Spin Impurities Weakly Interacting with CuO_2 Plane

The EPR is the powerful method for the investigation of the local properties of high T_c materials. On the background of the bulk EPR silence, discussed above, it enables one to obtain the important information about the symmetry, internal fields and the electron density in the vicinity of sites where the special spin probe is inserted. It helps to study the imperfections of structure and the different substitution effects. One should mention that, since the sensitivity of the EPR is six orders of magnitude higher than that of NMR, it is most suitable for the elucidation of subtle phenomena taking place in the key structural fragments of the superconducting compounds – CuO_2 planes.

Similar to the conventional superconductors the high-T_c superconducting materials and their parent compounds can be investigated by the EPR method using as a probe the paramagnetic impurities. Analysing the EPR data one has to bear in mind that it is highly dependent on the type of the spin probe we are dealing with. One has to distinguish different types of these probes depending on the strength of their coupling to the strongly correlated spin-system of the CuO_2 plane.

The weak coupling limit is often realized when the spin probe substitutes the rare earth site in the structure. The most popular spin probes of this sort are Gd^{3+} ions diluted in high-T_c compounds. Gd^{3+} ions (S^{Gd}=7/2, L=0) interact weakly with the surrounding electrons with spin $\boldsymbol{S}^i$. For any hole doping level the Gd^{3+} ESR is well described by the simplified Hamiltonian

$$H = g^{Gd}\mu_B \vec{S}^{Gd}\vec{H} + D\{(S_z^{Gd})^2 - \frac{1}{3} S^{Gd}(S^{Gd}+1)\} + \sum_\alpha J_\alpha S_\alpha^{Gd} S_\alpha^i . \quad (1)$$

The corresponding spectrum consists of seven lines, corresponding to the fine structure split in the crystalline electric filed of the tetragonal symmetry. Usually the EPR data are consistent with an isotropic g-factor of $g^{Gd}\approx$1.99 which is independent of hole doping and of temperature. The typical value of the fine splitting constant D~1–3 kOe.

The influence of spins S^i on the Gd spin probe may be considered in terms of internal ("hyperfine") magnetic field $H=JS_i/g^{Gd}\mu_B$. For the rare earth site in

case of LSCO compound such a field is induced by two contributions: by the four adjacent Cu spins and by the Cu atom beneath La site along the c-axis. The typical value of this field is ~1 kOe. For the YBCO compound the internal field in the RE position is induced by eight adjacent Cu spins (from the neighbouring CuO_2 planes) and depends on the orientation of the corresponding magnetic structures. The typical value of the internal field is several kOe.

In the case of a weak coupling the EPR measurements are generally similar to the NMR information apart from an important difference regarding time scale: the EPR frequency is three orders higher than the NMR frequency. The last factor also ensures the high sensitivity of EPR: it is six orders of magnitude higher than that of NMR.

2.2.2 Spin Impurities Strongly Interacting with CuO_2 Plane

The strong coupling of the EPR spin probe takes place when this probe is inserted in the CuO_2 plane. Usually such a spin probe substitutes the Cu ion. Its interaction with the neighbouring Cu ions is very strong (depending on the value of the local Cu moments the effective magnetic fields are of order 100 kOe and even more). Moreover this interaction is highly sensitive to the AF fluctuations in the CuO_2 plane and the corresponding form-factor is enhanced at the AF wave vector $\mathbf{Q}_{AF}=(\pi/a;\pi/a)$, where a is the lattice constant. The typical example of such a spin probe is Mn^{2+} doped in the CuO_2 plane. Note, that for the case of the strong coupling the EPR information is sufficiently different from that provided by NMR giving an opportunity to study the coupling of the CuO_2 magnetization to other degrees of freedom.

2.2.3 Intrinsic EPR Centres

It is very interesting that in such strongly correlated systems as cuprates the nature provides us with the intrinsic spin probes. We mean here the appearance of the localized spin states with the Kramers symmetry, which give rise to the EPR signal (of course we do not consider here the cases of simple imperfections of a structure and different admixtures). In this case the main interest is connected more with the topological nature of such states, rather than with usage of them as a simple spin probe. The examples of such intrinsic EPR centres are:

1. Magnetic moments created upon nonmagnetic zinc doping of the HTSC, when the Zn ion due to the strong correlations induces the local magnetic moment at the adjacent Cu sites.
2. Local moments in the CuO_2 planes induced by the Sr doping of LSCO.
3. Localized magnetic moments appearing at the ends of the strongly correlated chains in YBCO 123 compounds.

3
Basic Equations for the EPR of Strongly Correlated Systems

3.1
EPR of Undoped CuO_2 Planes

To give a general idea for the spin relaxation description we consider at first the basic equations for the EPR of a strongly correlated Cu spin system in the CuO_2 plane, although this signal was never observed (the EPR silence was mentioned above). The Hamiltonian of the Cu spin-system can be written in the following form:

$$H_{Cu} = \mu_B \sum_i \mathbf{H}\mathbf{g}_\sigma \boldsymbol{\sigma}_i + \frac{J_0}{2} \sum_{\langle ij \rangle} \boldsymbol{\sigma}_i \boldsymbol{\sigma}_j + H_{int} \,. \tag{2}$$

The first term is the Zeeman energy of the Cu ions with the gyromagnetic tensor $\mathbf{g}_\sigma$ in an external magnetic field $\mathbf{H}$, $\boldsymbol{\sigma}_i$ is the spin operator (do not confuse with the Pauli operator, which differs by a factor of 2), μ_B is the Bohr magneton. The second contribution is the very strong isotropic exchange coupling (with a constant J_0=1580 K) between the Cu ions, a symbol $\langle ij \rangle$ means the sum over the nearest Cu ions in the plane. H_{int} represents all interactions of the Cu ions, which do not conserve their total spin $\boldsymbol{\sigma}_0 = \sum_i \boldsymbol{\sigma}_i$: anisotropic spin-spin and hyperfine interactions, spin-lattice coupling and others. Because of the very strong isotropic exchange coupling between the Cu ions one should expect a single EPR line. A standard way to describe the EPR signal of such a system is the formalism developed by Anderson and Weiss [33] and Kubo and Tomita [34]. If the z-axis is directed along the external magnetic field, the transverse spin relaxation rate $\Gamma_{\sigma L}$ to the other degrees of freedom ("lattice") can be written in the form

$$\Gamma_{\sigma L}(\omega) = \frac{1}{2} \int_{-\infty}^{+\infty} d(t - t') \exp\left[i\omega(t - t')\right] K_{\sigma L}(t - t') \tag{3}$$

with the correlation function $K_{sL}(t–t')$ for the Cartesian spin components of the total spin $\sigma_0^{\mp} = \sigma_0^x \mp i\sigma_0^y$

$$K_{\sigma L}(t - t') = - \frac{\langle [\sigma_0^-, H_{int}]_t \, [\sigma_0^+, H_{int}]_{t'} \rangle}{\hbar^2 \langle \sigma_0^- \, \sigma_0^+ \rangle} \,. \tag{4}$$

Here $[\ldots]_t \exp(iH_0t)=[\ldots] \exp(-iH_0t)$ is the Heisenberg representation with the Hamiltonian $H_0=H_{Cu}–H_{int}$; the anisotropy of g_σ-factor is neglected and the Cu Larmor frequency $\omega_\sigma=g_\sigma\mu_B H/\hbar$. The symbol $\langle \ldots \rangle$ means here an averaging with a statistical operator: $\langle A \rangle = \mathrm{Sp}\rho_0 A$ with $\rho_0=\exp(-H_0/k_BT)/\mathrm{Spexp}(-H_0/k_BT)$. In the case of the Lorenz shape of the EPR line, what should be expected for the strongly correlated systems $\Gamma_{\sigma L}(\omega_\sigma)$ defines a half-width at the half-height of the resonant line: $\Delta H=\hbar\Gamma_{\sigma L}(\omega_\sigma)/g_\sigma\mu_B$. The multi-spin correlation function $K_\sigma(t)$

can be calculated by the moments method or using a decoupling procedure. In the first case it is useful to notice that at $t=t'$ Eq. (4) corresponds to the second moment $K_\sigma(0)=M_2$ of the EPR line. For the strongly correlated system $K_{\sigma L}(t)$ decays very fast describing in the paramagnetic phase strong local spin fluctuations caused by the exchange interactions. An assumption of a Gaussian distribution of fluctuations reduces the task of the EPR linewidth to calculations of the two parameters M_2 and an exchange frequency ω_{ex}:

$$K_{\sigma L}(t-t') = M_2 \exp\left[-\pi\omega_{ex}^2 (t-t')^2/4\right]$$
$$\omega_{ex}^2 = \frac{2}{\pi M_2}\frac{\partial^2}{\partial t \partial t'} K_{\sigma L}(t-t')\Big|_{t=t'} . \tag{5}$$

In principle both values M_2 and ω_{ex} are temperature dependent. In the high-temperature limit the linewidth can be found by standard calculations of the second and fourth moments of the EPR line. An example of the decoupling method for $K_{\sigma L}(t)$ will be given in the next section.

3.2 EPR of a Weakly Coupled Paramagnetic Impurity

Now we consider the EPR response of a single paramagnetic impurity weakly coupled to the strongly correlated spin-system of the CuO_2 plane. It can be represented by the Hamiltonian

$$H_{imp} = g_s \mu_B \mathbf{H}\mathbf{S} + J_{s\sigma} \sum_i \mathbf{S}\boldsymbol{\sigma}_i + H_{str} + H_{sL} \tag{6}$$

The first term is the Zeeman energy of the impurity with the gyromagnetic factor g_s in an external magnetic field **H**, **S** is the spin operator. The second contribution is the isotropic exchange coupling (with a constant $J_{s\sigma}$) of the impurity to the nearest Cu ions. H_{str} represents the fine and hyperfine structure of the spin energy levels, H_{sL} is the coupling of the impurity to the lattice, in particular to phonons. In the case of an unresolved EPR spectra the transverse spin relaxation rate will be determined by Eqs. (3) and (4) with a substitution $\sigma \to S$, where the role of H_{int} will play the all last three interactions in Eq. (6). It will be useful for the following discussion to consider in some details the contribution to the relaxation rate from the coupling of the impurity to the Cu spin-system. In this case the four-spins correlation function of the type (Eq. 4) $K_{s\sigma}(t)$ can be decoupled in a product of the pair spin correlation functions for the impurity and the Cu ions. Using then the fluctuation-dissipation theorem and a high temperature approximation $k_B T \gg \hbar\omega$, the relaxation rate $\Gamma_{s\sigma}$ can be reduced to the expression [35]

$$\Gamma_{s\sigma}(\omega) = \left(\frac{J_{s\sigma}}{\hbar}\right)^2 \frac{k_B T}{N} \sum_{\mathbf{q}} F_{\mathbf{q}}^2 \,\mathrm{Im}\left[\frac{\chi_\sigma^{\parallel}(\mathbf{q}, \omega-\omega_s)}{\omega-\omega_s} + \frac{\chi_\sigma^{\perp}(\mathbf{q},\omega)}{\omega}\right]. \tag{7}$$

Here $\chi_\sigma^{\parallel(\perp)}(\mathbf{q}, \omega)$ is the longitudinal (transverse) dynamical spin susceptibility of the Cu spin system, N is the number of Cu ions in the CuO_2 plane, $\mathbf{q}$ is the two-dimensional wave vector, ω_s is the impurity resonance frequency. One can easily recognize a sufficient similarity of Eq. (7) to the well known nuclear spin relaxation rate $1/T_1$ in cuprates. The main difference is an appearance of the constant $J_{s\sigma}$ instead of the hyperfine coupling constant A. The form factor $F_\mathbf{q}$ accounts for the positions of the magnetic moments in the lattice. It plays the crucial role in filtering of magnetic fluctuations driving the spin relaxation responsible for the EPR line width of the spin probe.

One should mention again that the relaxation rate $\Gamma_{s\sigma}$ taken at $\omega=\omega_s$ determines the homogeneous contribution to the EPR linewidth, which may be written as $\Gamma_{s\sigma}/\gamma_s$ with γ_s being the probe gyromagnetic ratio $\gamma_s=g_s\mu_B/\hbar$.

The main condition of a weakness of the impurity coupling to the Cu spin-system is the relation

$$\Gamma_{s\sigma} \ll \Gamma_{\sigma L}\,, \tag{8}$$

where $\Gamma_{\sigma L}$ is the relaxation rate of the Cu magnetization to the lattice, which can be represented by phonons, spin fluctuations with $\mathbf{q}\neq 0$, and so on. In this case the g-factor of the impurity experiences the Knight shift, given by

$$\frac{\Delta g_s}{g_s} = \lambda\chi_\sigma^0\,, \qquad \lambda = \frac{zJ_{s\sigma}}{g_s g_\sigma (\mu_B)^2}\,. \tag{9}$$

Here χ_σ^0 is the bare static Cu spin susceptibility of the plane per the Cu ion, z is a number of the nearest to the impurity Cu ions. As a typical weakly coupled paramagnetic impurity is used the Gd^{3+} ion, with the dominant relaxation channels dependent on the magnetic lattice structure.

Let us consider first the YBCO compounds, where Gd^{3+} impurity substitutes Y positions. In this case $F_\mathbf{q}$ is determined by the eight neighboring Cu moments from two adjacent CuO_2 planes. Neglecting the dipolar interaction, one has

$$F_\mathbf{q} = 8\cos\left(\frac{q_x a}{2}\right)\cos\left(\frac{q_y a}{2}\right)\cos\left(\frac{q_z c}{2}\right) \tag{10}$$

For the wave vectors in the vicinity of $(\pi/a, \pi/a)$ the form-factor tends to zero, making the Gd linewidth insensitive to AF fluctuations (we neglect the difference of the lattice constants in a CuO_2 plane, c being the interplane spacing). The dominant contribution in this case originates from the vicinity of $\mathbf{q}=0$, that is from the homogeneous susceptibility.

For Gd^{3+} substituting the La ion in LSCO compounds the situation is more complicated. Four adjacent Cu ions give the form factor which is one half of that for YBCO, but there exists also an important additional contribution from the Cu site beneath the rare earth site along the c-axis. The coupling of this Cu mo-

ment with a spin probe proceeds via the apical oxygen of the CuO_6 octahedron. Due to significant contribution of the dipolar field term it is difficult to obtain transparent explicit expression for the form-factor [25]. All that we need for further analysis is that $F_{\mathbf{q}}$ has maxima at $\mathbf{q}$=0 and at the border of the Brillouine zone. Therefore in addition to the influence of the homogeneous fluctuations with $\mathbf{q}$=0 there exists an important relaxation channel governed by the AF fluctuations with the wave vectors in the vicinity of $(\pi/a,\pi/a)$.

If the spin probe, for example Mn ion, substitutes the Cu ion, the corresponding form-factor is given by

$$F_{\mathbf{q}} = 2(\cos q_x a + \cos q_y a) \tag{11}$$

but in this case the relaxation picture cannot be described solely by Eq. (7), since the condition of weak coupling Eq. (8) is violated due to extremely strong coupling of Mn ion to the Cu spin-system in the CuO_2 plane.

3.3 EPR of a Strongly Coupled Paramagnetic Impurity

In contrast to the Eq. (8) case a collective motion of magnetic moments of the impurities and Cu ions can appear, creating the so-called bottleneck regime. A more precise a relaxation dominated bottleneck condition is the following (see Fig. 4):

$$\Gamma_{s\sigma} + \Gamma_{\sigma s} \gg \left|\Gamma_{\sigma L} - \Gamma_{sL} + i(\omega_s - \omega_\sigma)\right| . \tag{12}$$

Between the relaxation rates from the impurities to the Cu spins and back exists a 'detailed balance' relationship:

$$\chi_s^0 \Gamma_{s\sigma} g_\sigma^2 = \chi_\sigma^0 \Gamma_{\sigma s} g_s^2 . \tag{13}$$

Here χ_s^0 is the bare susceptibility of paramagnetic impurities with a concentration c related to the number of the Cu ions:

$$\chi_s^0 = cN(g_s \mu_B)^2 \frac{S(S+1)}{3k_B T} . \tag{14}$$

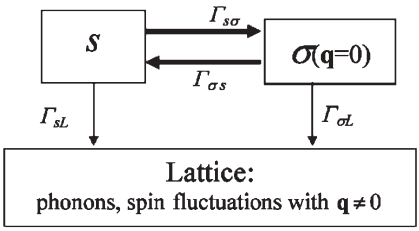

Fig. 4 A block-scheme of the relaxation rates between the magnetic moments of probes (S) and Cu ions in the CuO_2 plane (σ) and the lattice

In the bottleneck regime the effective relaxation rate is controlled mainly by the relaxation rates of the impurities and Cu ions to the lattice weighted by the corresponding static spin susceptibilities:

$$\Gamma_{eff} = \frac{\chi_s^0 \Gamma_{sL} + \chi_\sigma^0 \Gamma_{\sigma L}}{\chi_s + \chi_\sigma} + \frac{\langle (\Delta\omega)^2 \rangle}{\Gamma_{s\sigma}} . \tag{15}$$

The last term takes into account a partial opening of the bottleneck, $\langle (\Delta\omega)^2 \rangle$ is the mean square of the local fields distribution at the impurity sites, $\chi_{s(\sigma)}$ is the renormalized spin susceptibility of the impurities (Cu ions),

$$\chi_{s(\sigma)} = \chi_{s(\sigma)}^0 \frac{1 + \lambda \chi_{s(\sigma)}^0}{1 - \lambda^2 \chi_s^0 \chi_\sigma^0} \tag{16}$$

The effective g-factor and intensity of the collective EPR signal are

$$g_{eff} = \frac{g_s \chi_s + g_\sigma \chi_\sigma}{\chi_s + \chi_\sigma} , \quad I_{eff} \propto \chi_s + \chi_\sigma . \tag{17}$$

It is worth pointing out that in a deep bottleneck regime the strong coupling between two subsystems $\Gamma_{s\sigma}$ disappears from the effective relaxation rate (Eq. 15), since the last term can be neglected. This is a consequence of a commutation of the total spin of the two subsystems with the isotropic exchange coupling between them.

Usually the paramagnetic probe is chosen in such a way that its spin-lattice relaxation Γ_{sL} can be neglected in Eq. (15) and, also, $\chi_s \gg \chi_\sigma$. Then in the deep bottleneck regime the EPR linewidth is controlled mainly by the sufficiently reduced relaxation rate of the Cu magnetic moment to the lattice $\Gamma_{eff} \approx (\chi_\sigma / \chi_s) \Gamma_{\sigma L}$, while the EPR intensity is defined by the paramagnetic probe susceptibility $I_{eff} \propto \chi_s$. It gives an opportunity to measure $\Gamma_{\sigma L}$, although the EPR signal of Cu ions is not observable. A clear proof of the bottleneck regime in LSCO was given in [35] using the Mn^{2+} probe (see below). This method was used to study the nature of the Cu magnetic moment relaxation and the mentioned above the EPR silence problem.

4
Superconducting vs Normal Properties of Cuprates

4.1
EPR of Gd^{3+} in LSCO

The properties of the high T_c materials are in a close connection with the behaviour of the magnetic fluctuations [22, 27]. The latter determine the magnetic susceptibility and manifest themselves in such parameters of EPR from the

different spin probes, as position, width and intensity of the signal. The behaviour of a susceptibility and hence of a resonance line is highly sensitive to the density of holes in the CuO_2 planes. Depending on doping, the charge carriers in such strongly correlated electron systems reveal both the itinerant and the localized properties. In the underdoped systems a pseudogap [36] which opens at the temperatures considerably above T_c reduces the susceptibility upon cooling, whereas for the overdoped systems the susceptibility exhibits the metallic like behaviour. The search of the correlation between the properties of the normal and superconducting states still remains one of the most important problems for the HTSC field.

In this section we address the results of EPR investigations [37] of the magnetic fluctuations and their link to the electron and superconducting properties of the LSCO ceramics doped by small amount of gadolinium, which served as a spin probe. The observation that the Gd^{3+} ions show linear with temperature Korringa-like behavior of their spin relaxation [38, 39] shows that, although being quite away from copper-oxide planes, they still probe some density of states at these key elements of structure, which are responsible for superconductivity. Similar behaviour of the Gd^{3+} EPR signal was already revealed in YBCO at the very beginning of the EPR study of HTSC [98, 99]; see below.

The EPR measurements of the powder samples of the $La_{1.99-x}Sr_xGd_{0.01}CuO_4$ for different values of Sr doping x ranging from 0.08 up to 0.35 were performed using a standard X-band spectrometer in a wide temperature range [37]. The additional characterization of the samples under investigation included X-ray, resistivity, a.c. susceptibility measurements. The EPR response measured at a frequency of 9.3 GHz. was observed for all studied samples. A typical EPR spectrum is shown in Fig. 5. Its overall width is about 7 kG and the most resolved components are centred between 2 and 3 kG.

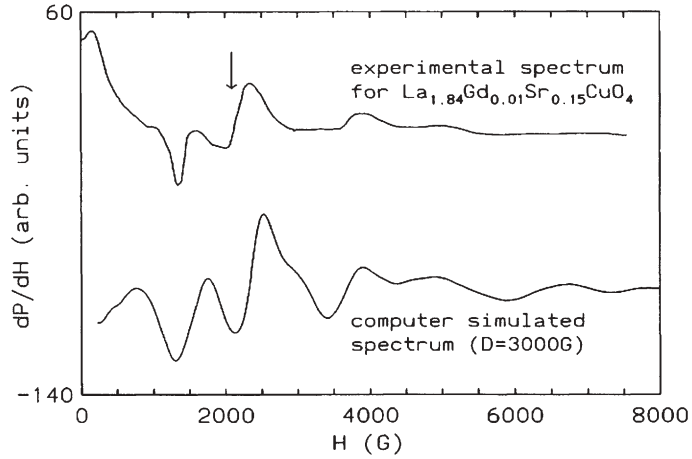

Fig. 5 Experimental and computer simulated Gd^{3+} EPR line for the $La_{1.99-x}Sr_xGd_{0.01}CuO_4$ compound [37]

The width of every component of the spectrum was both a function of temperature and of strontium content. As a consequence of partial overlapping of the components of the spectrum with the temperature it was possible to follow the peak-to-peak linewidth ΔH over the entire temperature range for the only component marked at Fig. 5. Typical plots of ΔH vs T for $La_{1.99-x}Sr_xGd_{0.01}CuO_4$ samples with different Sr content are presented in Fig. 6. For all samples studied there is a certain interval where ΔH obeys the linear law (the corresponding linear fits to the Korringa-like law $\Delta H=(1/\gamma)(a+bT)$ are shown in Fig. 6; $\gamma=g\mu_B/\hbar$ is the electron gyromagnetic ratio).

At the same time it was found that for the underdoped samples $x\leq 0.15$ the linewidths deviate from the straight line at low temperatures, while for the over-

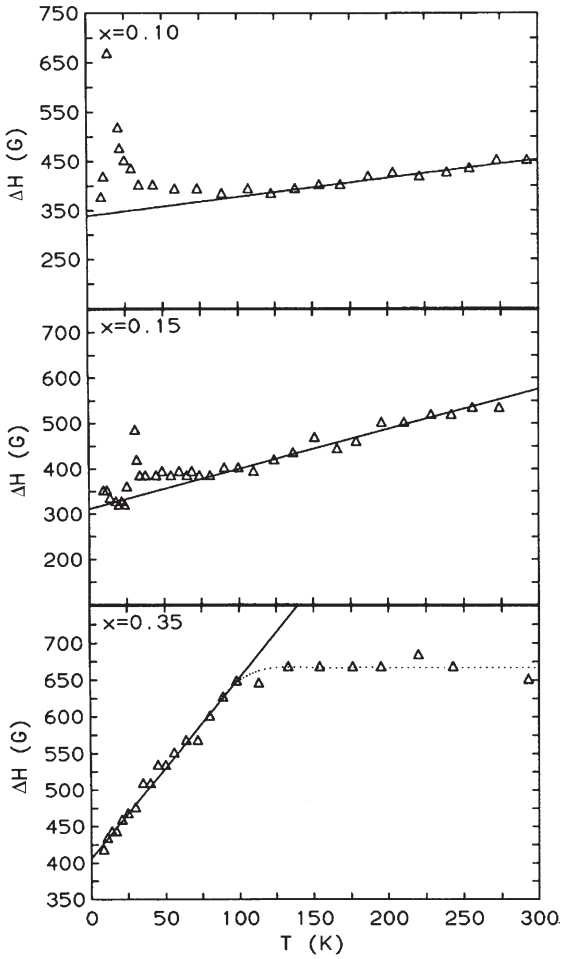

Fig. 6 The temperature dependence of the Gd^{3+} EPR linewidth for the $La_{1.99-x}Sr_xGd_{0.01}CuO_4$ for different Sr content x [37]

doped samples, in contrast, the observed ΔH saturates in a high-temperature limit [37]. (The x dependent broadening of ΔH for the lower temperatures, which is attributed to the influence of the magnetic fluctuations of the Cu moments will be discussed further later).

The observed EPR signal is due to the resonance of Gd^{3+} ions and its structure corresponds to the fine structure splitting of their ground state in the crystalline electric field (CEF) of a lattice. The typical shape of the resonance line indicates that the fine splitting is comparable with the Zeeman energy. Therefore for the reliable evaluation of the spectra one has to make the appropriate simulation of the Gd^{3+} EPR powder spectrum. As a result it was possible to reproduce the positions of the lines and their relative intensities, taking the fine structure constant D=0.28 cm^{-1} (±10%). Note that this value is larger than 0.14 cm^{-1}, estimated for the YBCO compound [40, 41]. The linear Korringa law $\Delta H=(1/\gamma)(a+bT)$ was used in the simulations with the parameter b being proportional to the integral intensity of a corresponding component (the simulation revealed that saturation of $\Delta H(T)$ at high temperature for the compound with the Sr content x=0.35, which is visible in Fig. 6, being just a spurious effect of interference of the neighbouring components of spectra).

To analyse the high temperature part of their experimental data the authors of [37] used the approach of Barnes [11], who obtained the following expression for the Korringa slope parameter b for every component of a fine-splitted spectrum of a spin-probe:

$$b = 4\pi M^2 k_B \left[N(E_F) J_{sf}\right]^2 \tag{18}$$

with $M^2=S(S+1)-S_z(S_z+1)$. Here M is the matrix element which connects a state $|S_z\rangle$ of a Gd^{3+} local moment with $|S_z-1\rangle$ state, $N(E_F)$ is the density of states at the Fermi level, J_{sf} is the exchange integral between local spins and conduction electrons (from the comparison of the EPR and heat capacity data it follows that J_{sf}~2.5 meV [39]). The factor M^2, determining the probability of a corresponding transition, describes the Barnes-Plefka [11] enhancement of the relaxation with respect to the standard Korringa rate in the absence of a fine structure. Such an enhancement occurs in exchange-coupled crystal field split systems where the g factors of localized and itinerant electrons are approximately equal but the relaxation of conduction electrons towards the "lattice" is strong enough to inhibit bottleneck effects. To obtain Eq. (18) from Eq. (7) one has to assume that at high enough temperatures the main contribution to the integration over q originates from the homogeneous transversal fluctuations with the form factor $F_{\mathbf{q}}$ fixed at $\mathbf{q}$=0. Then using the approximation of noninteracting quasiparticles, which makes it possible to get [42]

$$\frac{1}{N}\sum_{\mathbf{q}} \mathrm{Im}\left[\chi_{\sigma}^{\perp}(\mathbf{q},\omega)\right] = \pi N^2(E_F)\,\hbar\omega\,, \tag{19}$$

one comes to Eq. (18) with $J_{sf}=2J_{s\sigma}$ in accordance with the $F_{\mathbf{q}=\mathbf{0}}$ determined above for Gd^{3+} in the LSCO compound.

4.2
Experimental Relationship Between T_c and the Normal Density of States

On the basis of the above consideration it was possible to investigate the behaviour of the normal density $N(E_F)$ of charge carriers in the metal oxide. The observed change of the slope b of the $\Delta H(T)$ curves upon variation of the strontium concentration x means that the density of states at the Fermi level is also a function of x, since according to Eq. (18) $N(E_F)$ is proportional to the square root of b (Fig. 7). All data except the points near x=0.12 can be very well fitted by nearly square root law $b^{1/2}=2.89(x-0.006)^{0.49}$ over the entire range of Sr concentration.

One of the crucial important problems for the HTSC field still remains the search of the correlation between the parameters which determine their normal and superconducting states [43, 44]. In this respect it was very interesting to study the correspondence of the density of states at the Fermi level $N(E_F)$ both to the concentration of carriers n and the critical temperature T_c. The critical temperatures of the whole set of studied $La_{1.99-x}Sr_xGd_{0.01}CuO_4$ [37] obeyed the well-known [45] dome shape dependence on Sr content (see Fig. 42). In order to find out how the critical temperature scales with the density of states, the logarithm of T_c for the powder samples studied by EPR was plotted vs the inverse square root of the slope b. As can be seen from Fig. 8, all experimental points (except the two ones corresponding to x=0.25 and 0.28) are located near the straight line, and therefore it is possible to conclude that for underdoped samples of the investigated compound a universal empirical relationship, which connects T_c with $N(E_F)$, holds on

$$d[\ln(T_c)]/d[1/N(E_F)] = const\,. \tag{20}$$

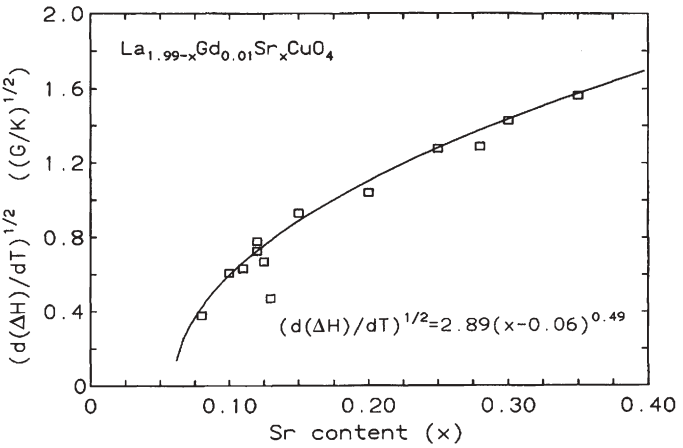

Fig. 7 Square root of the Korringa slope $b=d(\Delta H)/dt$ as a function of the Sr content in the samples [37]. The *solid line* represents a best fit

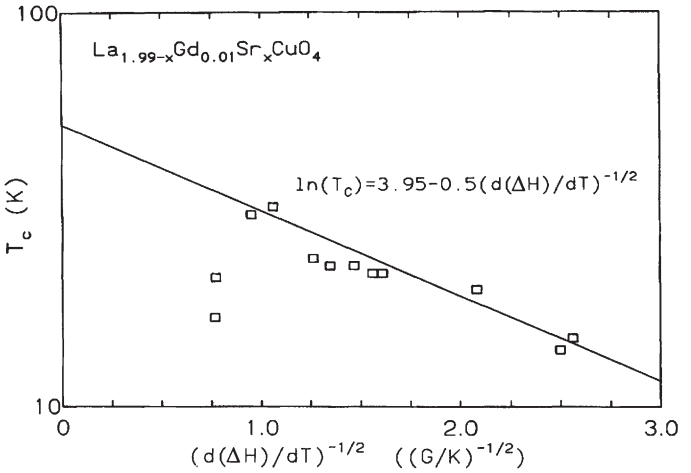

Fig. 8 The dependence of T_c on the inverse square root of the Korringa slope $b=d(\Delta H)/dt$ [37]

The integration of this simple relation leads one to the following expression for the critical temperature:

$$T_c = \alpha \exp(-1/\beta b^{1/2}) \tag{21}$$

where α and β are the fitting parameters, which were estimated as 51.9 and 0.5 correspondingly. Comparing this result with the well known BCS-like expression for the critical temperature $T_c=\Omega\exp(-1/\lambda)$ (here $\lambda=VN(E_F)$ is the effective coupling constant, V is the pairing potential, and Ω is the characteristic frequency), one can estimate from the experimental data plotted in Fig. 8 the effective coupling constant λ. For the underdoped samples it increases with x from approximately 0.8 to 2, thus giving the evidence that for the compound under investigation one deals with the rather strong coupling. However, the subsequent decrease of λ observed for the overdoped samples gives reasons to believe, that either the coupling constant becomes a nonlinear function of $N(E_F)$, due to the change of the strength of interaction itself, or there appears another type of interaction which reduces λ in the overdoped region. Note that, in this respect, there exists an observation that the charge carriers character changes from the O(2p) holes to the Cu(3d) type in the overdoped region [46].

All these features give an evidence that the superconducting transition is a result of a nontrivial interplay between the different degrees of freedom of electron, phonon and spin nature.

The similar EPR measurements were also performed [47] for the series of $La_{2-x}Ba_xCuO_4$ compounds doped by Gd ions. The dependence of the high temperature Korringa slopes vs x was similar to that discussed above (except in the vicinity of 1/8 doping) whereas the low temperature upturns of the linewidths were much more pronounced.

One should also mention here the EPR measurements of Er^{3+} added to the over-doped $La_{2-x}Sr_xCuO_4$ [48] where it was found that satisfactory fitting of the temperature dependence of the relaxation rate of Er^{3+} requires a nonzero Korringa term which increases with the level of Sr doping.

4.3 Interplay Between Magnetic Properties and Superconductivity in YBCO

The important results were obtained with help of high field EPR of Gd ions, doped in YBCO, which was investigated at frequencies up to 235 GHz [49]. In these experiments it was possible to study the shift of the resonance frequency which is proportional to the magnetic susceptibility at the Gd site. It was found that the observed Knight shift of EPR frequency and the spin relaxation rate are proportional to the nuclear Knight shift of ^{89}Y and its nuclear relaxation rate, observed in [50] for a whole temperature range. The data obtained for the EPR shift being substituted in the expression for the relaxation rate enable one to obtain the reasonable estimation of relaxation rate for YBCO without usage of density of states obtained by other methods.

The longitudinal Gd shift for all oxygen content y is in excellent agreement with ^{89}Y Knight shift data [50] at temperatures above 80 K where data for both set of experiments are available (Fig. 9). The decrease of shift (susceptibility) upon cooling starting at temperatures higher than T_c corresponds to the pseudogap opening, typical for the underdoped compounds. It was found [51], that the effective coupling of Gd spins with the CuO_2 electronic states is by one order of magnitude stronger than that for the Y nuclear spins. This is especially advantageous at low temperatures when the long NMR spin relaxation rates and small shifts make precise ^{89}Y shift measurements difficult or impossible. Note, that Gd

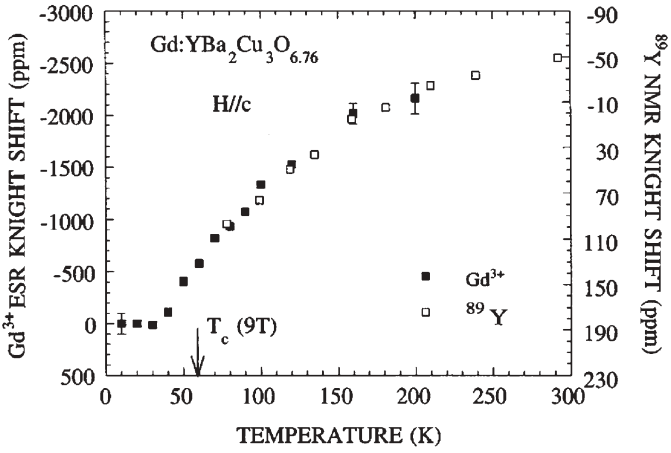

Fig. 9 Comparison of Gd^{3+} EPR and ^{89}Y NMR Knight shifts of $YBa_2Cu_3O_y$ [50]. ESR: y=6.76. NMR: y=6.75. The best fit yields a "hyperfine" coupling constant ratio $^{Gd}A/^{89}A$=10.5

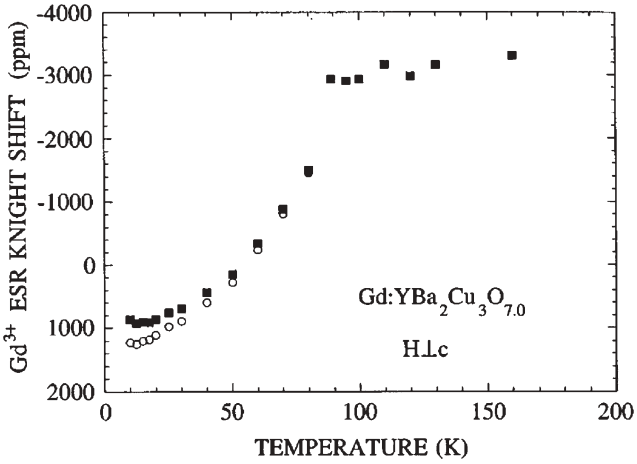

Fig. 10 Gd^{3+} EPR Knight shift proportional to the conduction electron spin susceptibility, $\chi(T)$ of $YBa_2Cu_3O_{7.0}$ (*squares*) [50]. The *open circles* show Gd shift corrected for diamagnetic shifts

ESR data [51] are the most precise determination of $\chi(T)$ in $YBa_2Cu_3O_{7.0}$ below T_c to date. It was shown (see Fig. 10) that below T_c it initially falls faster than the Yoshida function, expected for the isotropic *s*-wave superconductor, and is not as flat below $T_c/2$. Together with the later observation of the linear T dependence [51] this gives in an opinion of authors an additional evidence in favour of *d*-wave singlet pairing (note, however, that there still exists a certain controversy between the data on the pairing symmetry obtained by different methods; see later).

For $\boldsymbol{H}\perp\boldsymbol{c}$ the resonance for the superconducting state of underdoped samples has an anomalous shape at low temperatures: it consists of a narrow peak (Fig. 11 displays the shift of the narrow component) and a tail towards higher fields. The anomaly is evident at the intermediate concentrations, y=6.53 and 6.76 below 40 K, where for $\boldsymbol{H}\perp\boldsymbol{c}$ the line is split into two components. One line appears near the resonance field of the y=6.76 compound with $\boldsymbol{H}\perp\boldsymbol{c}$ while the resonance field for the other is lower by 7.5 mT. A most important observation is that this splitting was unchanged upon variation of frequency from 245 GHz (8.8 T) to 296 GHz (10.6 T) at 22 K and was also observed at 158 GHz. The authors [50] suggest that this anomaly may be caused by a small magnetic moment on the Cu planes which orders magnetically below 40 K, but further experiments are needed to verify this hypothesis which may be in a close relevance to the phase separation issue (see later).

Thus Gd^{3+} EPR appeared to be a powerful technique for exploring the microscopic local properties of high-T_c oxides. It is complementary to ^{89}Y NMR in that it is more suitable for the superconducting state. The observed anomalous splitting of the line for $\boldsymbol{H}\perp\boldsymbol{c}$ indicates that new ideas are required to understand the local field at the Y site at low temperatures. In addition to such traditional

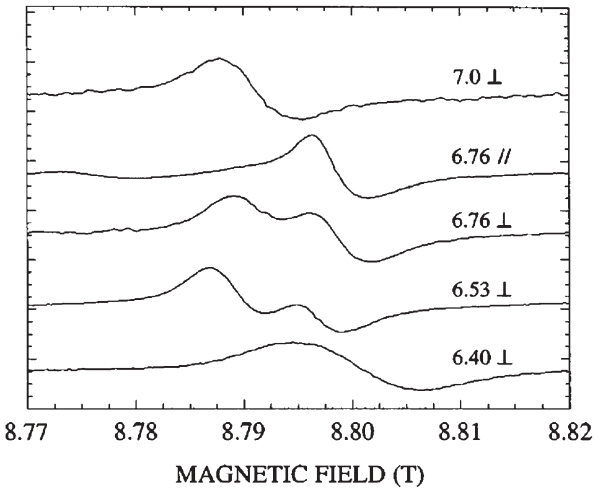

Fig. 11 Gd^{3+} EPR spectra of $YBa_2Cu_3O_y$ at 245 GHz and 20 K for various values of y [50]. Note the line splitting for $\boldsymbol{H}\perp\boldsymbol{c}$ and y=6.76 and 6.53

methods as specific heat, susceptibility or photoelectron spectroscopy (see for example review [36] and the reference therein) the EPR measurements of the spin probes offer the opportunity to study the variation of $N(E_F)$ via the observation of the temperature dependence of their spin relaxation rate and of the Knight shift.

5
Electron Spin-Lattice Relaxation

5.1
Bottleneck Regime in Cuprates

The first direct observation of the coherent motion of the transverse magnetic moment of the CuO_2 plane together with the total transverse magnetic moment of impurities was performed in the case of the Mn^{2+} ions substituting the Cu^{2+} ions in $La_{2-x}Sr_xCuO_4$ [35]. This magnetic probe was chosen for the following reasons. An electron configuration of the Mn^{2+} ion is $3d^5$ with a ground state L=0 and S=5/2. In this case a modulation of the spin-orbit interaction by the lattice vibrations is frozen, resulting in a small spin-lattice relaxation rate Γ_{sL}. At the same time the exchange coupling between the Mn and Cu ions $J_{s\sigma}$ is of the same nature as for the Cu-Cu coupling J_0 and expected to be not too much smaller. If one takes the Mn-Cu exchange constant $J_{s\sigma}$=500 K, one can roughly estimate an expected relaxation rate from Mn to the Cu spin-system, having in mind that it is isomorphic to the nuclear spin relaxation rate; see Eq. (7). The ratio of electron and nuclear relaxation rates is approximately equal to

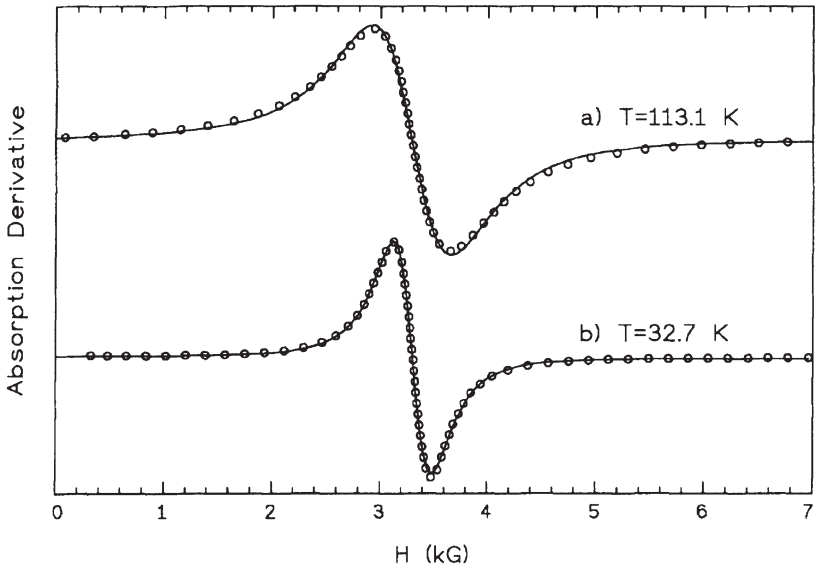

Fig. 12 A typical fit of powder spectrum of Mn^{2+} EPR in $La_{1.8}Sr_{0.2}Cu_{0.98}Mn_{0.02}O_{4+\delta}$ (*circles*) on the assumption of Lorentzian line shape (*solid line*) [35]

$\Gamma_{s\sigma}T_1 \approx (J_{s\sigma}/A)^2$. Therefore the desired estimation can be made using an experimental value of the ^{63}Cu nuclear relaxation rate. If we take the hyperfine coupling constant A=100 kOe and $1/T_1$=2700 s^{-1} (which is doping and temperature-independent at high temperatures [52]), we obtain $\Gamma_{s\sigma} \approx 10^{13}\ s^{-1}$. This value is sufficiently larger than the resonance frequency and therefore the EPR signal of the Mn ion should not be observed. Nevertheless an intensive single EPR line with a Lorenz shape was detected in the samples with Mn concentrations y=0.01, 0.02, 0.03, 0.06 and for Sr doping level x=0, 0.1, 0.2, 0.3 [35] (see Fig. 12). The measurements were performed using a standard Varian E-line spectrometer at the frequency 9.3 GHz in the temperature range $T_c < T \leq 300$ K. Figure 13 displays the temperature dependence of the EPR linewidth in $La_{1.8}Sr_{0.2}CuO_4$ with different Mn concentrations. With decreasing temperature the linewidth decreases, passes through a minimum at T_{min} and increases on further cooling.

An existence of the EPR signal indicates that the conditions for the bottleneck regime (Eq. 12) as well as $\chi_\sigma \ll \chi_s$ are satisfied, making it possible to observe the collective EPR response with a reduced linewidth. Besides the enormous value of $\Gamma_{s\sigma}$ and the smallness of Γ_{sL}, these conditions for a bottleneck regime are also provided by the small difference of the Mn and Cu g-factors $(g_s - g_\sigma)/g_s \approx 0.1$. One can conclude that a deep bottleneck regime is realized at temperatures $T > T_{min}$. In this temperature range the linewidth is inversely proportional to the Mn concentration in accord with the discussion of the first term in Eq. (15). Therefore the linewidth is determined in this region by the relaxation rate $\Gamma_{\sigma L}$ of the Cu magnetic moment to the lattice. However, at low temperatures $T < T_{min}$ the Mn

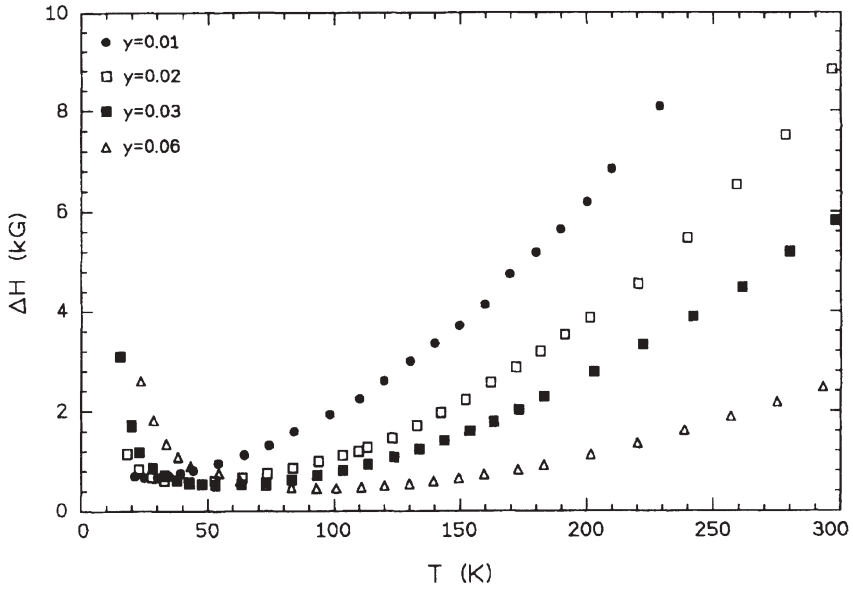

Fig. 13 Temperature dependence of Mn^{2+} EPR linewidth in $La_{1.8}Sr_{0.2}Cu_{1-y}Mn_yO_{4+\delta}$ with y=0.01, 0.02, 0.03, and 0.06 [35]

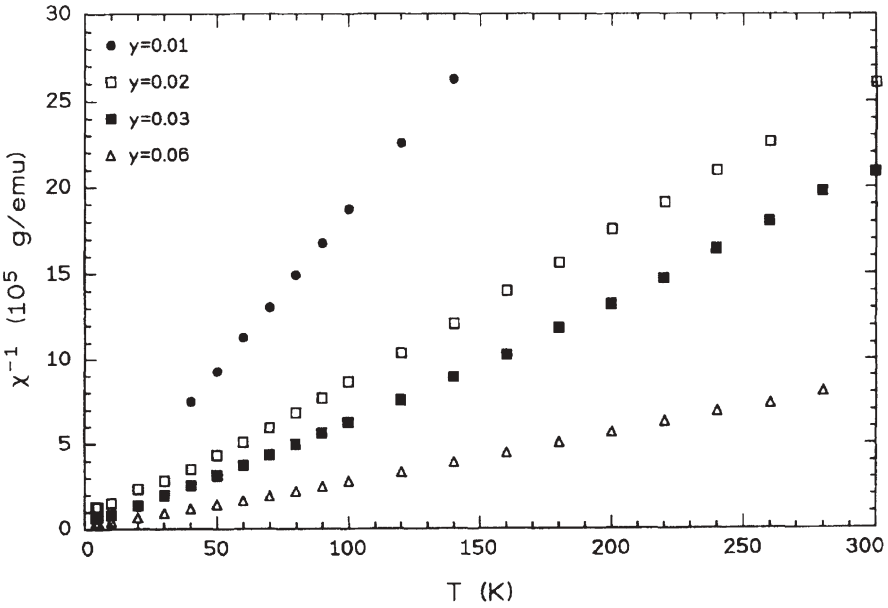

Fig. 14 Temperature dependence of the total reciprocal magnetic susceptibility for $La_{1.8}Sr_{0.2}Cu_{1-y}Mn_yO_{4+\delta}$ with y=0.01, 0.02, 0.03, and 0.06 [35]. The measurements were performed at constant field H_0=3.3 kG

concentration dependence of the linewidth is changed becoming proportional to y instead of the inverse proportionality, what can indicate a partial opening of the bottleneck. This conclusion can be made on the basis of a well known behaviour of the nuclear relaxation rate at low temperatures for the Sr doped samples: $1/T_1 \rightarrow 0$ with decreasing temperature to zero. The same behaviour should be expected for Γ_{so}, which can break the condition at Eq. (9) at low enough temperatures. It means that the second term in Eq. (12) for the Γ_{eff} becomes important at $T<T_{min}$. Since the EPR linewidth at these temperatures becomes roughly proportional to the Mn concentration, the authors of [35] made a proposal that the mean square of the local fields distribution $\langle(\Delta\omega)^2\rangle$ is likely to be due to the Mn-Mn interactions.

Measurements of the static magnetic susceptibility of the same samples confirm an expectation that the main contribution comes from the Mn impurities. The temperature dependence of the reciprocal magnetic susceptibility of $La_{1.8}Sr_{0.2}CuO_4$ with Mn concentrations y=0.01, 0.02, 0.03, 0.06 is shown in Fig. 14. One can see that the spin susceptibility is proportional to the Mn concentration, and only at low temperatures there is a slight deviation from the Curie-Weiss behaviour. The EPR intensity agrees very well with these measurements as it expected for a bottleneck regime.

5.2 Electron Spin Relaxation Caused by the Lattice Motion

5.2.1 Transverse Spin-Lattice Relaxation in the CuO_2 Plane

The key experiments, which threw light on the nature of the electron spin-lattice relaxation in the CuO_2 plane, were performed by Shengelaya et al. [53, 106]. They used an advantage of the bottleneck regime in $La_{2-x}Sr_xCuO_4$ activated by 2% (y=0.02) Mn^{2+} ions to look for a possible oxygen isotope effect of the Cu spin dynamics. They observed a large effect on the EPR linewidth in the underdoped samples, see Fig. 15. The isotope effect decreases with Sr doping and practically disappears in the overdoped region. The temperature dependence of the linewidth for the both isotopes displayed in Fig. 16 is very similar to the observed one earlier; compare Fig. 13. One can see that the isotope effect disappears at high temperatures.

The isotope effect indicates an important role of the lattice motion in the relaxation of the Cu magnetization. The authors proposed that an interaction between the Cu^{2+} ion and the lattice vibrations in general is the same as in insulators, i.e. due to the modulation of the crystal electric field by the lattice distortions and the spin-orbit coupling of the Cu ions. This mechanism is typical for a dielectric crystal and gives usually a rather slow spin-lattice relaxation, since the Kramers doublet is not sensitive to the electric field because of its time reversal symmetry properties. Nonvanishing matrix elements of the spin-lattice coupling usually appear due only to the external magnetic field, which

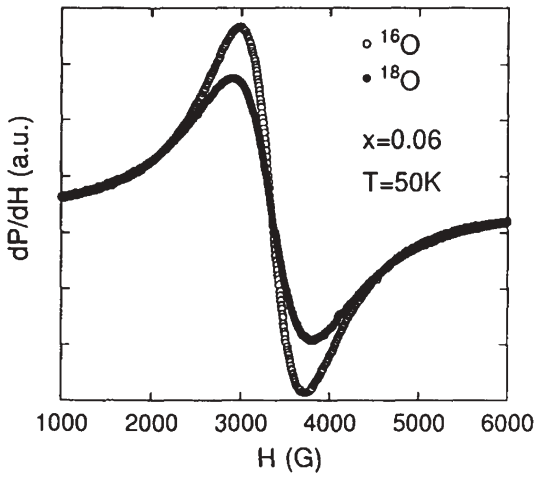

Fig. 15 EPR signal of ^{16}O and ^{18}O samples of $La_{1.94}Sr_{0.06}Cu_{1.98}Mn_{0.02}O_4$ measured at T=50 K under identical experimental conditions [106]

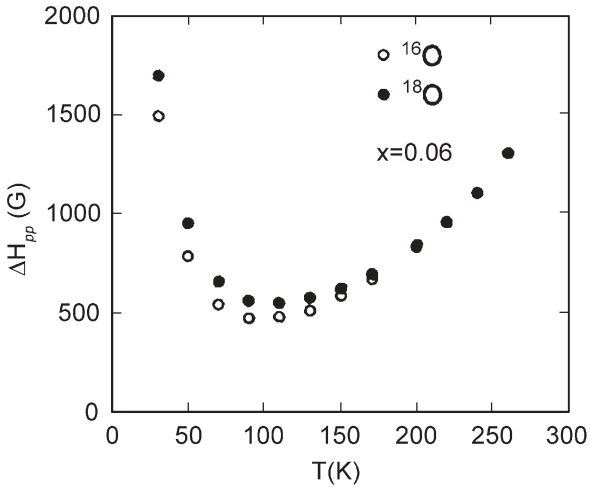

Fig. 16 Temperature dependence of the peak-to-peak EPR line-width H_{pp} for ^{16}O and ^{18}O samples of $La_{1.94}Sr_{0.06}Cu_{1.98}Mn_{0.02}O_4$ [53]

gives an additional very small factor ($g\mu_B H/\Delta_0$) where Δ_0 is the crystal field splitting between the ground and the excited orbital states. In the case of the CuO_2 plane the eigenstates of the Cu spin-system are defined mainly by the very large isotropic Cu-Cu exchange interactions instead of the Zeeman interaction. Roughly speaking, the role of the magnetic field splitting will play the Cu-Cu exchange coupling J_0~1500 K. It should greatly enhance the spin-lattice relaxation rate [54]. Moreover, there is an additional reason for such enhancement

related to a strong anharmonicity of the involved normal modes of the oxygen octahedron. It turns out that the spin-lattice interaction in the Cu orbital ground state $d(x^2-y^2)$ involves only the Q_4 and Q_5 modes related to the tilts of the octahedron z axis and pure rotations of the octahedra shown in Fig. 36. These modes are strongly anharmonic being responsible for a structural phase transition from a high-temperature tetragonal (HTT) to a low-temperature orthorhombic and tetragonal (LTO, LTT) phase. As a result, besides vibrations near the minima of a potential energy $V(Q_4,Q_5)$, there is quantum tunnelling between the minima. The latter leads to a more sufficient modulation of the crystal field at the Cu ion causing a more effective spin-lattice relaxation. Since the tunnelling frequency between the minima depends exponentially on the oxygen mass, it gives a large isotope effect of the Cu electron spin-lattice relaxation rate $\Gamma_{\sigma L}$. For typical values of parameters this mechanism gave an estimation $\Gamma_{\sigma L} \sim 2 \cdot 10^{11}$ s^{-1} at T=200 K for the doping level x=0.1. At higher temperatures the relaxation rate increases almost linearly with temperature. This value is too large for observing the EPR signal from Cu ions without Mn probes at the usual frequencies. This can explain the EPR silence in the superconducting cuprates and their parent compounds. The described model is in a good agreement with experimental results on the temperature dependence of the EPR linewidth and the isotope effect [53].

5.2.2 Spin-Lattice Relaxation of the Rare Earth Impurities

It has already been shown that the Gd^{3+}-ion with L=0 is the most common via EPR probes of rare-earth ions to study the superconducting cuprates. As for other rare-earth ions having $L \neq 0$, the spin-lattice relaxation time is usually very short due to the spin-phonon interaction, and their linewidths are too broad to detect the signal. Nevertheless, Abdulsabirov et al. and Kan et al. have observed the Er^{3+}-signal in Er-doped $YBa_2Cu_3O_y$ [55, 56] and $La_{2-x}Sr_xCuO_4$ [48] below the critical temperature. It gives an additional opportunity to obtain information about electron-phonon interactions in these materials. As reported by Kan et al. [48] the linewidth can be fitted by the sum of following terms:

$$\Delta H = \Delta H_0 + bT + c\Delta^3/[\exp(\Delta/T) - 1] \quad (22)$$

The first term is the residual linewidth which is closely connected with the molecular field at the Er site. The second corresponds to the Korringa relaxation mechanism where the Er^{3+} local moments couple to the host conduction carriers through an exchange interaction. The third corresponds to the relaxation due to the Orbach-Aminov process mediated by the two-phonons via the excited energy level of Er^{3+} [57, 58]. The parameter b depends on the exchange interaction with carriers and the density of states at the Fermi level, Δ is the energy separation between the ground and first excited electronic states of Er^{3+} ion and the parameter c depends on the strength of the orbit-lattice coupling.

A detailed study of the temperature dependence of the Er-EPR linewidth in YBCO and LSCO was performed by Shimizu et al. [59, 60] for various levels of the hole doping. They find that the temperature dependence of the relaxation rate can be very well fitted by Eq. (22). The results for $YBa_2Cu_3O_{6.43}$:Er are displayed in Fig. 17. The authors came to the conclusion that the orbital energy splitting Δ decreases monotonously with increasing hole doping level. In particular, the authors report for $Er_{0.01}Y_{0.99}Ba_2Cu_3O_y$ that this decrease is from 140 K at y=6.1 of the oxygen content to 110 K at y=6.93. However, an additional investigation of this issue by Ivanshin et al. [61] revealed a different approach to the dependence of Δ on the hole doping level. They found that for the non-superconducting samples with y=6.0, 6.12 the temperature dependence of the linewidth could be fitted without the Korringa contribution, but with two Orbach-Aminov terms with different energy separations Δ_1=80 K and Δ_2=120 K. The contributions of these two terms are consistent with Δ^3 factor in Eq. (22). At the same time, in the case of a superconducting sample with y=6.46 the temperature dependent contribution can be entirely attributed to the Orbach-Aminov process with the single value Δ=125 K (see Fig. 18) and for y=6.85 with Δ=108 K. These values of Δ are quite consistent with theoretical predictions by Eremin et al. [56] for three lowest energy levels of Er^{3+} in YBCO: Δ=92, 107, 125 (the other excited levels are sufficiently higher) and with measurements by the inelastic neutron scattering (INS) in $ErBa_2Cu_3O_y$ [62]. However,

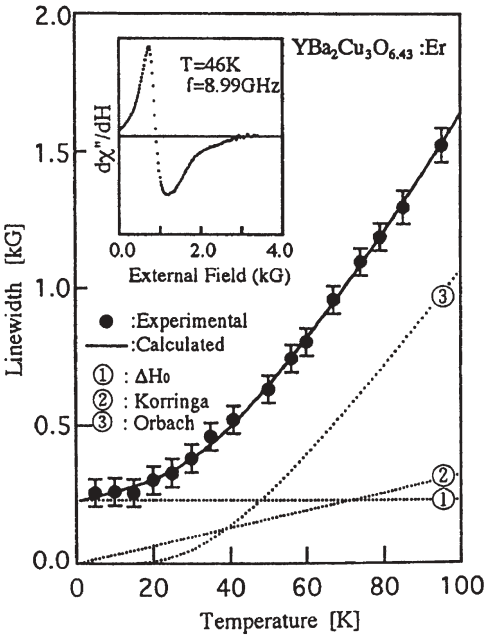

Fig. 17 Temperature dependence of Er^{3+}-linewidth [59]. *Dotted lines* indicate the linewidths responsible for three terms in Eq. (22). *Solid line* is the sum of the terms

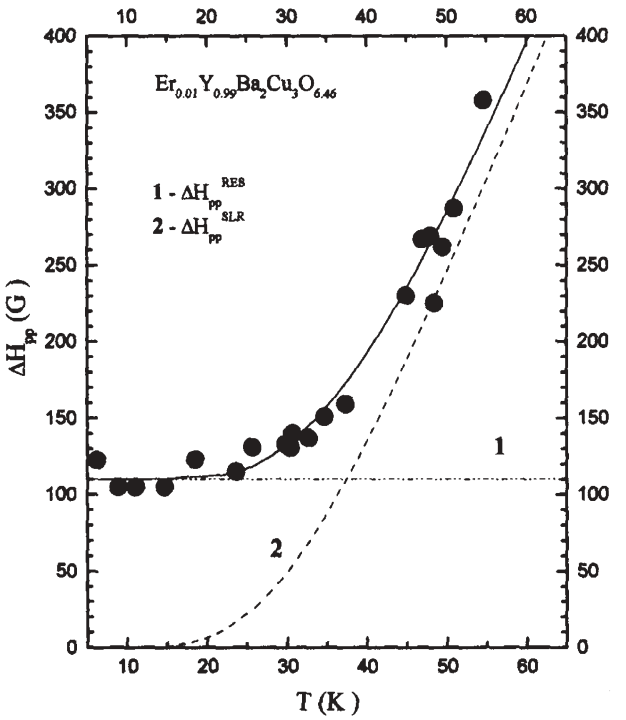

Fig. 18 Temperature dependence of the Er^{3+}-EPR linewidth in $Y_{099}Er_{001}Ba_2Cu_3O_{6.46}$ [61]. *Dashed lines* are contributions from the residual ESR linewidth (1) and the Orbach-Aminov process (2); *solid line* is a sum of both contributions

the reason why the contributions of these excited states so strongly depend on the oxygen content is unclear. The authors speculate that this behaviour is related to the phase separation into the hole-rich and hole-poor regions of the samples.

Another type of information was revealed from the EPR linewidth of the 1% Yb^{3+} impurity in YBCO [63]. The ground state of this ion is the Kramers doublet. It was found that the temperature dependent contribution can be rather well described in terms of the two-phonon Raman process. Since the corresponding spin relaxation rate is $\Gamma_{sL}=CT^9f(\theta_D/T)$ [14] with a known universal function $f(z)$, it gives an opportunity to estimate the Debye temperature θ_D, a convenient characteristic of the phonon spectra. Measurements of θ_D as a function of the hole doping level can be related to the superconducting properties of cuprates. As a rule, the value of θ_D is extracted either from elastic constants or specific heat measurements. The experimental data, which were obtained for YBCO compounds using these methods, are very controversial. So, the value of θ_D measured from ultrasonic sound velocities in the work of Ledbetter [64] is much lower than that derived from the specific heat studies [65]. Moreover, as was shown in [66], θ_D in YBCO depends strongly on temperature. The EPR results for θ_D together with T_c

Table 1 Critical and Debye temperatures vs oxygencontent y

y	6.85	6.67	6.45	6.0
T_c (K)	85	65	40	–
θ_D (K)	450	370	280	250

as a function of the oxygen content are presented in Table 1. The critical temperature T_c of the studied samples was determined from the temperature dependence of microwave absorption in a low magnetic field. It was found that the measured values of θ_D and T_c are consistent with a relation between them in the frame of the BCS theory for the conventional superconductivity in the strong coupling limit. A value of the electron-phonon coupling constant λ was estimated as $4<\lambda<10$ using the extended McMillan's equation [67].

It is worth to mention that recently there was observed the EPR signal from Dy^{3+}, Tb^{3+}, and Nd^{3+} rare earth impurities in YBCO compound [68].

5.3 Electron Longitudinal Relaxation Rate

Information on the spin-lattice relaxation rate obtained from the measurements of the EPR linewidth is related to the kinetics of the transversal to the external magnetic field magnetization. In the strongly correlated systems the transversal and the longitudinal relaxation times are usually equal: $T_2=T_1$. However, it is not necessarily always the case. Then one can expect $T_2<T_1$, and measurements of T_1 can give an additional independent information. It was effectively used for dielectric crystals [13, 14]. However, only little was known about the electron T_1 values in superconducting cuprates. The reason is rather clear: it is very difficult to measure relaxation times as short as 10^{-8} to 10^{-10} s at typical EPR linewidths 0.1–1 kOe. In such a case, to achieve saturation factor $s=(g\mu_B H_1/\hbar)^2 T_1 T_2 \sim 1$ by the standard EPR saturation method (H_1 is an alternating magnetic field), it is necessary to use microwave power more than 1 kW. This is quite unrealistic because of huge heating of the sample.

The first measurements of T_1 in HTSC materials was performed by Atsarkin et al. [69, 70] using a special technique. The method used in their work can be considered as a modified version of the modulation technique suggested by Herve and Pescia as early as 1960 [71]. A sample under study was prepared as fine powder embedded in paraffin or epoxy. It was placed into a specially designed microwave cavity with its walls transparent to alternating magnetic field in the MHz range. Microwave power at the resonance frequency 9.3 GHz, before entering the cavity, was subjected to a deep amplitude modulation at the modulation frequency $\Omega/2\pi \sim 10^6$ Hz. As a result, the EPR saturation factor s is modulated as well, and the oscillating component of the longitudinal spin magnetization $M_z(t)$ arises:

$$M_z(t) = U \cos \Omega t + \mathrm{V} \sin \Omega t \tag{23}$$

Here U and V are, respectively, the in-phase and out-of-phase parts of $M_z(t)$ relative to the modulation wave form. The oscillating magnetization, Eq. (23), induces the in-phase (u) and out-of-phase (v) parts of the a.c. voltage in a pickup coil wound on the cavity and having its axis parallel to the external magnetic field. Then this signal is amplified, lock-in detected, accumulated, and processed. One can show that under conditions of $s \ll 1$ and $T_2 \ll T_1$ the following equation holds:

$$\frac{v}{u} = \Omega T_1 , \tag{24}$$

which enables one to determine readily the value T_1. The method can also work at $T_2 \sim T_1$, though in such a case Eq. (24) must be replaced by a more complicated equation.

The first measurements by this method of T_1 for Gd^{3+} in $GdBa_2Cu_3O_y$ with y=6.84, 6.78, 6.49 and 6.40 were rather interesting. In particular, the value of the relaxation rate T_1^{-1} falls within the range 10^8–10^9 s^{-1}, which is much less then the transversal relaxation rate T_2^{-1} estimated from the EPR linewidth. The temperature dependence of T_1^{-1} was found to be in a good agreement with the nuclear relaxation rate behaviour of ^{89}Y and ^{17}O.

Detailed investigations of the longitudinal spin-lattice relaxation for the impurity Gd^{3+} in $Y_{0.99}Gd_{0.01}Ba_2Cu_4O_8$ revealed a nearly cubic power temperature dependence of the relaxation rate $T_1^{-1} \sim T^3$ at T<60 K [72]; see Fig. 19. This is

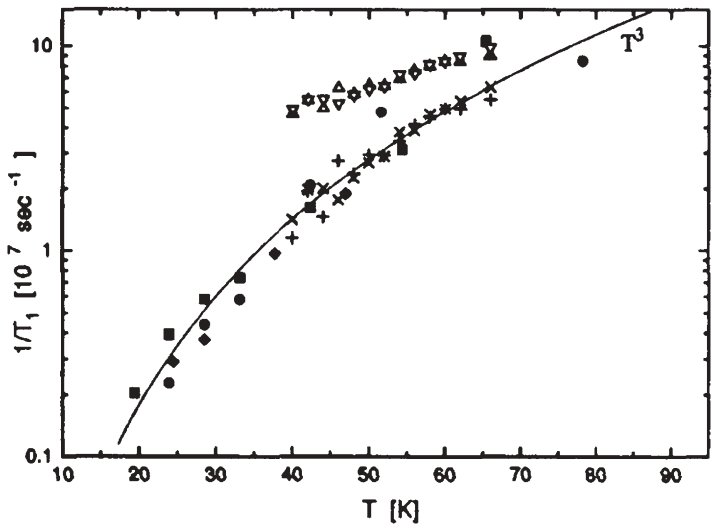

Fig. 19 Temperature dependence of the Gd^{3+} spin-lattice relaxation rate in $Y_{0.99}Gd_{0.01}Ba_2Cu_4O_8$ [72]. Data obtained by the modulation technique (*filled symbols*): B_0=0.18T (*squares, circles*), B_0=0.4T (*diamonds*). Data obtained from the EPR line width: ±1/2 transition (+), 1/2→3/2 transition (x). The *solid curve* represents T^3 function

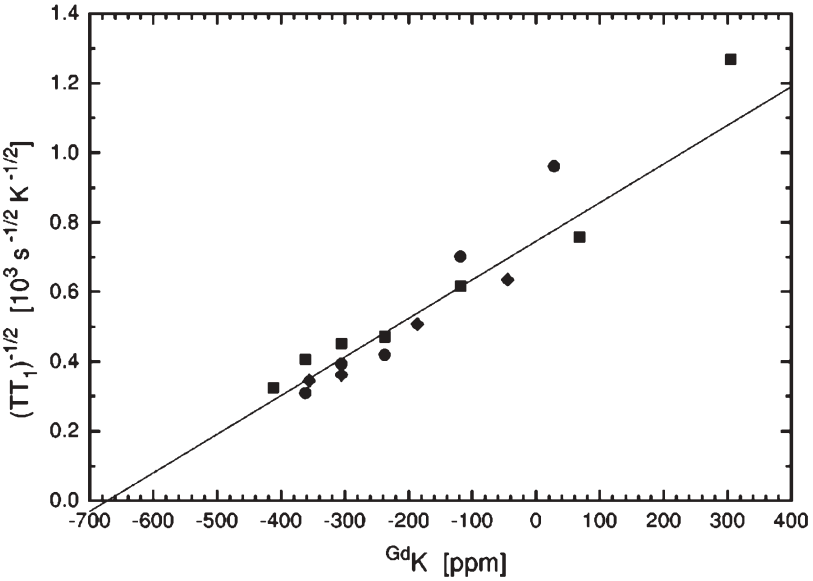

Fig. 20 Square root of the normalized Gd^{3+} spin-lattice relaxation rate as a function of the EPR Knight shift in $Y_{0.99}Gd_{0.01}Ba_2Cu_4O_8$ [72]. The *symbols* are the same as in Fig. 19

consistent with the high-filed EPR measurements of the Knight shift data [51] and in opinion of authors [72] with the predictions based on the *d*-wave superconducting pairing [73] (see, however, the discussion below). It was also found that $(T\,T_1^{-1})^{-1/2}$ is proportional to the Knight shift ^{G}K (Fig. 20) suggesting the validity of the Korringa relation for the Y sites that are not sensitive to the antiferromagnetic correlations.

6
Fingerprints of the Strong Electron Correlations

6.1
Localized Moments in the CuO_2 Plane

It is well established that additional holes in the CuO_2 plane go to the oxygen *p*-orbitals because of the very strong Coulomb repulsion on the lowest Cu *d*-orbitals. Created by doped holes in the CuO_2 plane carriers have a complicated electronic structure because of the *p-d* hybridization and spin correlations. It is unlikely that these carriers can give the EPR signal because of the expected very small intensity and large linewidth. However, in the case of localization the hole can create a paramagnetic centre, which is able to give the EPR response.

This type of EPR signal was observed in single-crystalline samples of $La_{2-x}Sr_xCuO_4$ with $0<x<0.2$ at *X*-band frequency 9.1 GHz in the temperature range

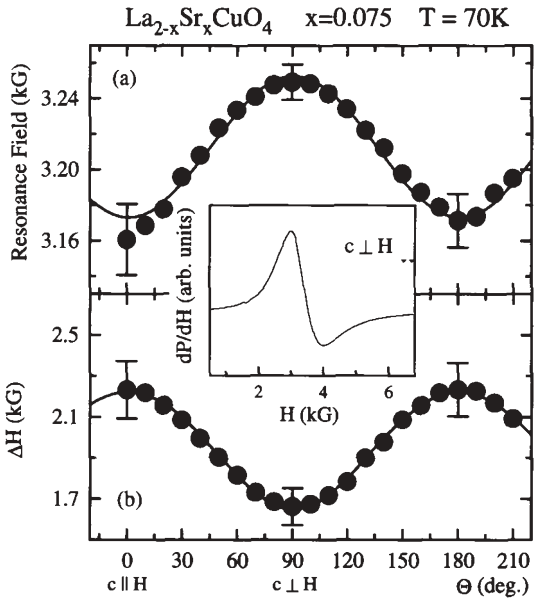

Fig. 21a, b Angular dependence of: **a** the resonance field; **b** the linewidth ΔH for $La_{2-x}Sr_x$-CuO_4 by rotating the c axis with respect to the magnetic field [75]. An axial symmetric behaviour is indicated by the *solid lines*. The *inset* shows the EPR spectrum with a Lorentzian line shape for the crystal orientation $\boldsymbol{c \perp H}$

$20<T<300$ K [74, 75]. A broad but well defined single EPR line has been detected, which is represented by Fig. 21 for the sample x=0.075. The line shape shown in the inset indicates a typical metallic behaviour. The angular dependence of the resonance field (Fig. 21a) and the linewidth (Fig. 21b) with respect to the crystal c-axis is typical for a paramagnetic centre with spin S=1/2 with anisotropic g-factor with uniaxial symmetry. For a centre with S >1/2 with unresolved fine structure one expects a minimum in the angular dependence of the linewidth near θ=60° which clearly is not observed and strictly can be excluded. An estimation of the EPR intensity for the sample with x=0.075 has shown that 1% of the doped holes are included in the formation of paramagnetic centres. Probably these centres exist in the regions of the samples with a poor concentration of Sr. All the features of the observed EPR signal were explained on the basis of a three-spin polaron model suggested by Emery and Reiter [76]. This polaron is built up by the doped electron holes on the oxygen ion and two adjacent Cu ions. Properties of this polaron depend on interference between its local motion near the Sr impurity and the Jahn-Teller effect. The concentration of the polarons depends, of course, on the Sr doping level. At high enough local concentrations the holes can be delocalized giving no EPR signal. It is consistent with a very low intensity of the EPR signal for the relatively large concentrations x=0.16 and 0.2.

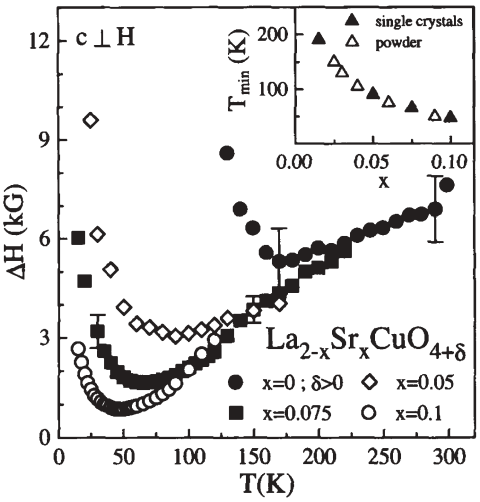

Fig. 22 Temperature dependence of the linewidth ΔH in [75]. The *inset* shows the temperatures T_{min} of the linewidth minima vs x. The results of measurements with ceramic samples are also included for comparison

As can be seen from Fig. 22, a signal was also observed in nominally pure $La_2CuO_{4+\delta}$. The antiferromagnetic phase transition in this material was found to be close to 150 K, indicating substantial excess of oxygen δ. To reduce δ the undoped (x=0) material has been annealed in argon atmosphere at 1200 K. Then the EPR signal vanishes completely in accord with previous findings [16, 18]. Similar EPR signals induced by the fast quenching of $La_2CuO_{4+\delta}$ were observed in [101].

A theoretical study of other types of clusters in the CuO_2 plane which could give the EPR response was carried out by Eremin and Sigmund [77].

6.2 Localized Moments in the Cu-O Chain

It seems that among a large number of the EPR investigations of the $YBa_2Cu_3O_y$ ceramics only a few can relate an observed signal to a bulk effect connected with the oxygen doping because of the difficulties in the interpretations of results. When the high-quality single crystals became available, one could make more definite conclusions [78–81]. As an example we consider the EPR study of almost 30 high-quality single crystals from three different laboratories (Shubnikov-Institute for Crystallography in Moscow, Institut für Physik der Universität Frankfurt/Main, and Institut für Physikalische Hochtechnologie, Jena) [81]. Well-defined but weak EPR signals were observed in crystals with oxygen concentrations $6.7<y<6.9$ and for temperatures $80<T<200$ K. A typical example of an experimentally observed spectrum is shown in Fig. 23 for

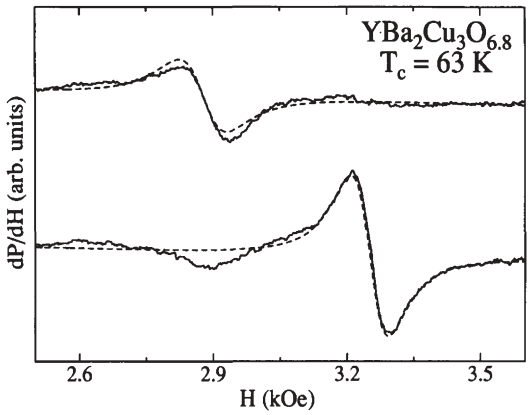

Fig. 23 Absorption derivative dP/dH vs magnetic field H in $YBa_2Cu_3O_{6.8}$ at two different crystal orientations at 105 K [81]. The fits with Lorentzian line shapes are indicated by *dashed lines*

$YBa_2Cu_3O_{6.8}$ (T_c=63 K) at 105 K. A summary of the angle-dependent measurements for this sample is presented in Fig. 24.

The highest probability for creating of paramagnetic centres by the oxygen doping can be expected for the Cu-O chains. At the oxygen content y=6 all the Cu(1) ions have a d^{10} configuration which is not paramagnetic. With increasing doping (y>6) a neutral oxygen atom accepts two electrons from neighbouring Cu^{1+} ions, yielding a Cu^{2+}-O^{2-}-Cu^{2+} configuration. Superexchange interactions will couple the two Cu^{2+} ions to a spin singlet in the ground state. This fragment is practically unobservable because of a huge exchange integral, which should be expected of the same order as in the CuO_2 plane, J~1500 K. Each new oxygen

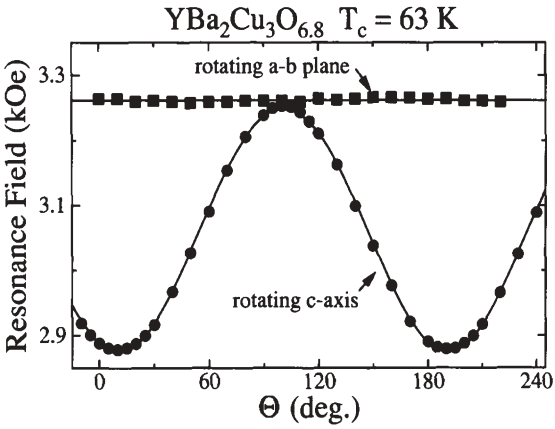

Fig. 24 Angular dependence of the resonance field H_{res} in $YBa_2Cu_3O_{6.8}$ for rotations around two different crystallographic orientations [81]. The results of fits are indicated by *solid lines*

atom joining to this shortest fragment of a chain can take now only one electron from the nearest Cu(1) ion to form Cu^{2+}. In other words, fragments of a chain with n oxygen atoms have $2n$ holes (relatively to the closed configurations p^6 and d^{10}) still having a spin singlet in the ground state, giving no EPR signal. The appearance of paramagnetic chain fragments (PCF) with an odd number of holes can be expected in the region of oxygen doping where the orthorhombic phase II (ortho II) transforms into ortho I. It is worth mentioning that the creation of PCFs is closely related to the transfer of holes into the CuO_2 planes. According to theoretical calculations of Uimin et al. [82] within an improved lattice-gas model, a sufficient probability to meet such PCFs is found for oxygen concentrations $6.6<y<6.9$. This is exactly the concentration region where EPR signals were observed in the samples studied. Figure 25 shows the phase diagram T_c vs y and the observed intensities of the EPR absorption for crystals with different oxygen concentrations at a constant temperature (T=105 K). The right scale shows the number of PCF (n_{pcf}) estimated from the EPR intensity. These results are compared to the mentioned calculations [82] of the number PCF as a function of the doping level (inset in Fig. 25). The maximum of the EPR absorption is located close to y=6.8 on the borderline between the ortho-II and ortho-I phases, exactly where it was predicted by the theory. The absolute numbers of PCF differ by a factor of 2–3, which is not astonishing considering the experimental uncertainties and the simplified model assumptions.

The PCF with the even number of holes mentioned above can give the EPR signal in the excited states. A detailed theoretical and experimental investigations of a particular type of a such PCF giving the EPR signal in the excited state at the "half" field with g-factor g=4.2 were performed by Eremin et al. [83].

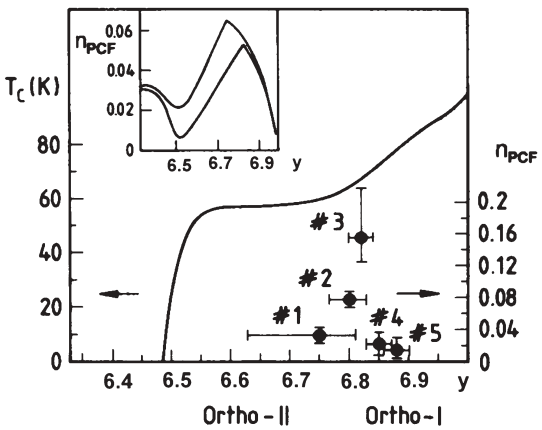

Fig. 25 Oxygen concentration dependence of the fraction of paramagnetic chain fragments n_{PCF} as calculated from the integrated intensity of the EPR signal in $YBa_2Cu_3O_y$ (*full symbols*, right scale) [81]. The concentration dependence of the superconducting phase transition temperature T_c is also shown (*solid line*, left scale). The *inset* shows the concentration dependence of n_{PCF} for two different "sample preparation" temperatures as calculated in [82]

The shortest "even" fragment Cu-O-Cu was also considered by Likodimos et al. [84] in order to interpret their EPR results on PrBCO system, however they used rather unrealistic parameters.

6.3 The EPR from Nonmagnetic Impurities (Zn)

Among the great number of high-T_c materials studies, most have been focused on peculiarities that are absent in conventional "low temperature" superconductivity. From that point of view a study of the substitution of Cu ion with ions of other elements [86, 87] gives curious information. Very impressive is the fact, first reported in [88, 89], that in lanthanum compounds doping with only 2.5 at.% of Zn or Ga is enough to completely suppress the superconductivity. Since Zn and Ga have a closed-shell $3d^{10}$ configuration, this strong effect on the superconductivity is striking. In terms of conventional superconductivity, the role of such nonmagnetic impurities should be minor, and therefore this substitution somehow affects the characteristic nature of high-T_c superconductivity. Zn doping in the La-Sr-Cu-O compound is a problem of special interest. Since the ionic radii of Zn^{2+} (0.75 Å) and Cu^{2+} (0.73 Å) are almost equal, it is expected that zinc occupies copper sites in the CuO_2 planes. Since the preferable valence state for both Zn and Cu ions is 2+, Zn doping does not change the formal charge balance and hence the concentration of carriers should not be affected. The main difference between these ions is that Zn^{2+} has a closed shell $3d^{10}$ nonmagnetic configuration, whereas Cu^{2+} has a S= 1/2 magnetic moment. As a result, the substitution of a copper ion by a zinc ion leads to elimination of one spin from the spin lattice. Thus this could be regarded as a way to probe the spin correlations in high-T_c superconductors. The La-Sr-Cu-O compound is the most convenient system for this purpose, because the important role of the CuO_2 planes can be investigated without the complications induced by CuO chains or other structure fragments.

Among the various reasons for the suppression of the superconductivity transition with Zn doping, one may consider the following: (i) due to the spin sublattice defects spin correlations which may be responsible for superconductivity are destroyed; (ii) localized magnetic moments (magnetic impurities) are created by Zn doping in spite of the fact that Zn^{2+} ions are nonmagnetic. These moments can suppress superconductivity, (note that (i) and (ii) could prove to be combined.).

The discussion of both versions needs experimental data on the magnetic properties. In particular to support version (ii), experimental proof of the appearance of localized moments is needed. Therefore the main aim of work [90] was to search for localized magnetic moments and to determine their nature, or to rule out version (ii) altogether. In order to do this, the $La_{2-x}Sr_xCu_{1-y}Zn_yO_4$ system was investigated by measurements of EPR, which is a very sensitive detector of the formation of localized moments. The resistivity and magnetic susceptibility were also measured. The analysis of all these experimental data

enabled the authors of [91] to outline the mechanism of localized moments formation by doping with nonmagnetic ions.

The X-band EPR spectra obtained [90, 91] in the temperature range of 6–360 K for every studied sample of the series $La_{2-x}Sr_xCu_{1-y}Zn_yO_4$ (x=0, 0.2; y=0, 0.01, 0.03), including quenched and annealed, oriented and nonoriented samples, differ to greater or lesser degrees from each other. The only common feature of all spectra was a signal with an isotropic g-factor: g~2.1 and linewidth ΔH~350 G (see, for example, the top spectra in Fig. 26a,b). The only parameter of this line which depends on temperature (inversely proportional) is the integral intensity. The careful analysis of this signal together with the low temperature susceptibility gives evidence that it is due to the 0.6% admixture of spurious paramagnetic phase.

The orientation procedure (in strong magnetic field with the following fixation by paraffin) leads to the appearance of new anisotropic signal in the EPR-spectra of Zn-doped La-Sr-Cu-O samples, which depends on the angle between the orientation axis of the sample and the applied magnetic field. At high enough temperatures it masks the background signal mentioned above, but at lower temperatures they are well separated (Fig. 26). Since this new signal arises due to Zn doping, it is of paramount importance to evaluate the effective magnetic moment per zinc ion from its integral intensity. The values of the moments, which were obtained by comparison (at room temperature) with the signal of the standard sample, are equal to 1.6 μ_B (y=0.01) and 1.5 μ_B

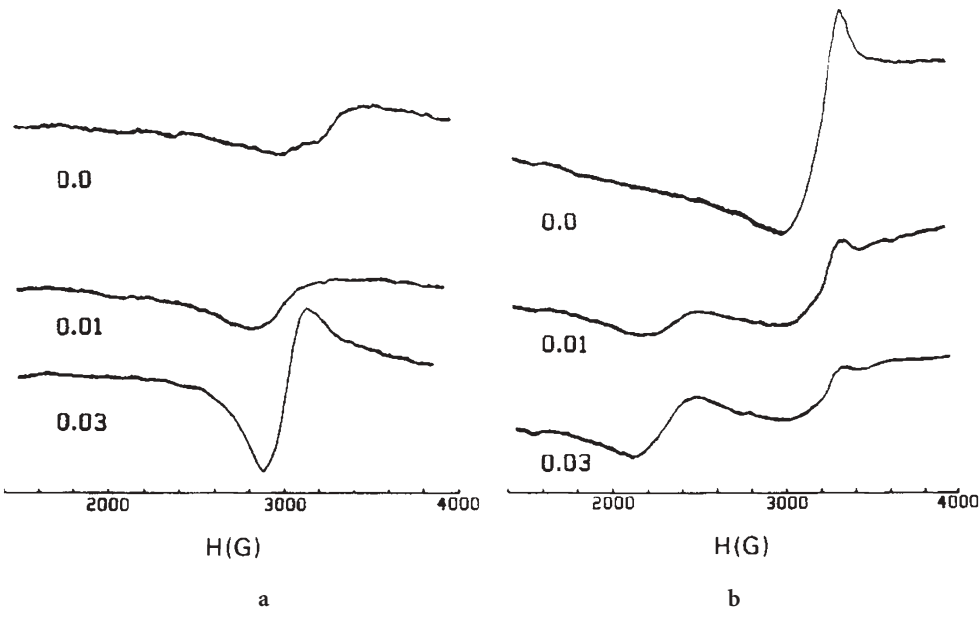

Fig. 26a, b EPR-spectra (first derivatives) of $La_{1.8}Sr_{0.2}Cu_{1-y}Zn_yO_4$ oriented samples [91] at: **a** 300 K; **b** 40 K

(y=0.03) per zinc ion. This result is very close to the effective magnetic moment of the Cu^{2+} ion, which is equal to 1.7 μ_B. Therefore, outwardly the situation seems to be as follows: each zinc ion added to the La-Sr-Cu-O system creates one paramagnetic moment with a value close to that of the Cu^{2+} ion.

From the experimental values of g-factor, for two samples with different Zn concentrations, one can evaluate the anisotropy spin-orbital corrections to the free electron g-factor value to be 0.025–0.038, which seems to be quite realistic for Cu^{2+}. Note that EPR data overall allow one to conclude that doping of the La-Sr-Cu-O system with Zn leads to the formation of a complex connected with the Zn ion, having a localized magnetic moment at the copper ion.

The possibility of localized moment formation directly on the Zn^{2+} ion seems to be far less probable because of the spherical symmetry of its $3d^{10}$ shell. Localization of magnetic moments on oxygen ions is also excluded due to the small magnitude of spin-orbital interaction, which is unable to produce the necessary g-shift from the free electron value.

The temperature dependences of the resonance line parameters observed in [90, 91] are quite typical for a system whose magnetic moments begin to correlate and tend to form some kind of order or spin glass state at low temperatures.

The authors of [90, 91] suggested that a mechanism of localized magnetic moments creation by doping with nonmagnetic ions is connected with the unusual symmetry of the spin correlations in the CuO_2 plane. (Speaking about the spin correlations in the cuprates one has to bear in mind that up to the large extent they are due to lattice forces emerging at hole doping. In fact, already at the very early stage of HTSC investigations it was found [28] that a local hole on a d^9 Cu-site distorts surrounding lattice so that the distortions on different sites interact with each other. The elastic energy minimizes itself by bringing occupied Cu sites together, inducing their strong exchange interaction and spin correlations.) According to it the elimination of a Cu spin from the spin lattice gives rise to the perturbation of the whole sequence of the exchange spin couplings between neighbouring spins, which either terminates on another Zn hole or extends to the infinity. The energy cost to create such a sequence increases with distance, either logarithmically or linearly, where the latter case corresponds to confinement [92]. Therefore to minimize the energy connected with such a perturbation this sequence of the exchange couplings must be torn forming a free localized moment with the Kramers symmetry near each of the Zn ions.

Now let us touch upon the problem of superconductivity suppression. The obvious explanation is that the suppression of T_c is caused by pair-breaking due to localized magnetic moments [93], created by substitution of Cu with Zn. The formation of these moments could be due to the string character of the physical states in an electron spin liquid.

The EPR finding [90, 91] that Zn substitution induces the creation of localized magnetic moments, which are localized on Cu ions, was confirmed in a lot of various further investigations (see [94] for the review). For example we men-

tion here the interesting studies of ^{89}Y NMR [95], Gd^{3+} EPR [96] as well as the EPR on the intrinsic Zn induced localized moments in YBCO [97].

7
Study of Phase Separation by Means of EPR

7.1
Heterogeneity of YBCO

7.1.1
Local Probe at the Y-Position

From the very beginning the high-T_c materials were heterogeneous, being prepared in a polycrystalline form [12]. Rather soon, however, it was realized that the studied samples display non-homogeneous properties at a sufficiently lower scale than the granular size. This tendency to a nanoscale phase separation was found in mono-crystals too. Among the first evidence of this phenomenon were the EPR measurements of the YBCO superconductors activated by the rare earth ions Gd^{3+} and Eu^{2+} [98, 99].

The Gd^{3+} ion substitutes the Y-ion in $Y_{1-x}Gd_xBa_2Cu_3O_{7-\delta}$ in any proportion: $0 \le x \le 1$. It was found that the EPR spectra for $x=0.01$ and $x=1$ show a Korringa-like spin relaxation behaviour similar to the usual metal in samples with different degrees of the oxygen deficiency. For the samples with $\delta=0.15$, it is not surprising because the temperature dependence of a resistivity above T_c has a metallic character, but for the samples with $\delta=0.5$ this result was unexpected, because the corresponding temperature dependence showed the "semiconducting" behaviour. To make consistent on the one hand the different behaviour of the resistivity for the samples with $\delta=0.15$ and $\delta=0.5$ and on the other hand the metallic character of EPR for the both samples, the authors proposed that the samples under study are heterogeneous and consist of the metallic and dielectric regions.One may think that for the sample with $\delta=0.15$, there is percolation, while for $\delta=0.5$ there is not.

Another unequivocal conclusion was derived from the analysis of the EPR lineshape for the samples of $GdBa_2Cu_3O_{7-\delta}$. In this case the single-line spectrum was observed for both samples with $\delta=0.15$ and $\delta=0.5$. The lineshape of the Gd^{3+} EPR signal showed a noticeable deviation from a Lorentzian, especially for the $GdBa_2Cu_3O_{6.85}$ sample; see Fig. 27. According to the previous idea it was natural to suppose that the observed EPR signal consists of two signals with nearly equal g-factors ($g=1.99$) but with different linewidths. The best simulation of the observed EPR spectra for any temperatures was obtained by the superposition of the two Lorentz lines with the following linewidth values. For the first line ascribed to the metal regions, the linewidth linearly depends on the temperature with the $\Delta H=a+bT$ law, where $a=580$ Oe and $b=0.9$ Oe/K. For the second one ascribed to the dielectric regions, the linewidth does not depend on

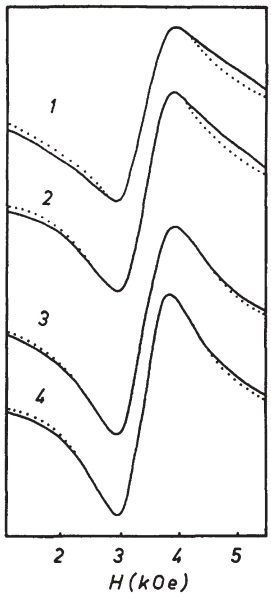

Fig. 27 EPR signal for $GdBa_2Cu_3O_{7-\delta}$ [99]. (1) δ=0.15 at T=300 K; (2) δ=0.15 at T=100 K; (3) δ=0.5 at T=300 K; (4) δ=0.5 at T=100 K. The *solid line* is the experimental line. *Dotted line* is the Lorentzian line

the temperature and is equal to 1000 Oe. The pronounced nonlinearity of the observed temperature dependence of ΔH in the normal state (Fig. 28) proves to be the result of interference of these two signals.

A combined analysis of the EPR intensities and of a relative contribution of the dispersion signal to the EPR line has shown that for the $GdBa_2Cu_3O_{6.5}$ sample the fractions of the dielectric and metallic regions are equal, while in the

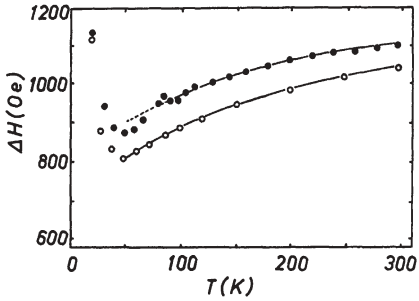

Fig. 28 Linewidth as a function of the temperature for two $GdBa_2Cu_3O_{7-\delta}$ samples [99]. The *filled circles* correspond to δ=0.15; the *open circles* to δ=0.5. *Solid lines* are the resulting linewidths of simulated spectra obtained as a sum of two Lorentz lines with ΔH=(580+0.9T) Oe and ΔH=1000 Oe taken in proportion 3:7 for the sample with δ=0.15 and 1:1 for the sample with δ=0.5

$GdBa_2Cu_3O_{6.85}$ sample the metallic fraction was estimated as 75%. Moreover, it was concluded that, metallic regions form a net in which no less than 10% of the metal volume has characteristic dimensions considerably smaller than the skin depth.

7.1.2 Local Probe at the Ba-Position

The ground state of the Eu^{2+} ion is $^8S_{7/2}$. It is similar to Gd^{3+} ion, although the europium ion has a smaller charge, and it substitutes the Ba^{2+} ions. In the $YBa_{1.5}Eu_{0.5}Cu_3O_{7-\delta}$ samples, the strong EPR signal was observed with a g-value close to g=2 (see Fig. 29). A comparison of the observed lineshape with the Lorentzian allows to conclude that the EPR signal for Eu^{2+} ions consists of two lines. The first one has $\Delta H=a+bT$ with a=300 Oe and b=1 Oe/K, and the second has the linewidth value of the order 1000 Oe independent of temperature. As a result of a large difference in these two linewidths at the temperatures studied, the measured linewidth (Fig. 30) is determined by a narrow line only. Having in mind the same origin of these two signals as for the $GdBa_2Cu_3O_{7-\delta}$ samples, it is clear that the measured linewidth belongs entirely to the metallic fraction of the samples. This is the reason for linear temperature dependence and for the coincidence of the linewidth value for both samples. The lineshape analysis similar to that for gadolinium samples shows that for the

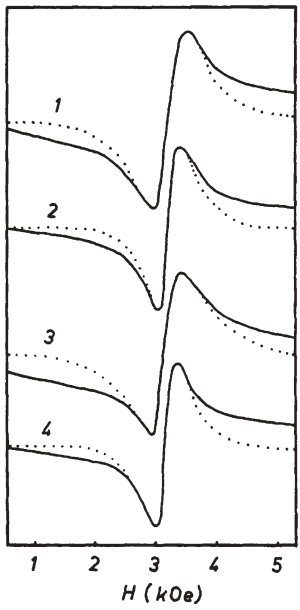

Fig. 29 EPR signal for $YBa_{1.5}Eu_{0.5}Cu_3O_{7-\delta}$ [99]. (1) δ=0.2, T=300 K; (2) δ=0.2, T=100 K; (3) δ=0.5, T=300 K; (4) δ=0.5, T=100 K. *Dotted line* is the Lorentzian

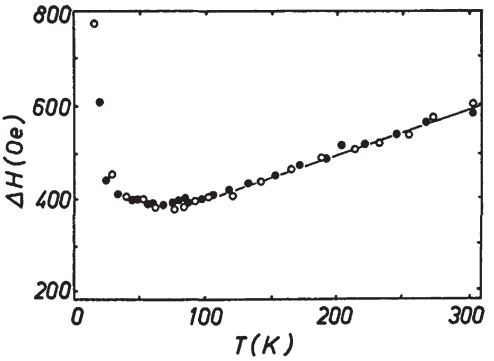

Fig. 30 Linewidth as a function of the temperature for two $YBa_{1.5}Eu_{0.5}Cu_3O_{7-\delta}$ samples [99]. The *filled circles* correspond to δ= 0.2; the *open circles* to δ=0.5. The *solid line* corresponds to ΔH=(300+T) Oe

$YBa_{1.5}Eu_{0.5}Cu_3O_{7-\delta}$ samples with a small oxygen deficiency, the fraction of dielectric phase is slightly more that 20% and, for the sample with large oxygen deficiency, it is equal to 50%.

7.2 Heterogeneity of LSCO

The generic phase diagram in hole-doped cuprates is by now well established. At a critical concentration of doping x_{c1}~0.06, superconductivity sets in at T=0, and ends at a higher doping level x_{c2}~0.25. Both are the critical endpoints of the superconducting phase-transition line [103]. At the former, a transition from an insulating to the superconducting state has been assumed until very recently [103]. However, using finite-size scaling for the susceptibility of a series of concentrations $x<x_{c1}$, the following was inferred: The material consists of antiferromagnetic (AF) domains of variable size, separated by metallic domain walls [104]. More recently Ando corroborated this early finding by measuring the in-plane resistivity anisotropy in untwinned single crystals of LSCO and YBCO in the lightly doped region, interpreting their results in terms of metallic stripes present [105].

The EPR study of the very underdoped sample $La_{2-x}Sr_xCu_{0.98}Mn_{0.02}O_4$ with x=0.03 in a bottleneck regime revealed an evidence of the electronic phase separation [106]. Besides the broad EPR line described previously, there was detected at low temperatures an *additional* narrow EPR line at the same resonant magnetic field; see Fig. 31. In principle, this situation is similar to that discussed in the preceding sections on the basis of the EPR study of YBCO using Gd^{3+} and Eu^{2+} ions as a probe. However, there is an important difference, since these ions are weekly coupled to the CuO_2 plane and their EPR signal give an information on their own relaxation rate toward the Cu spin system. In contrast, in the case of the Mn ions the EPR signal gives the information on the Cu relaxation rate

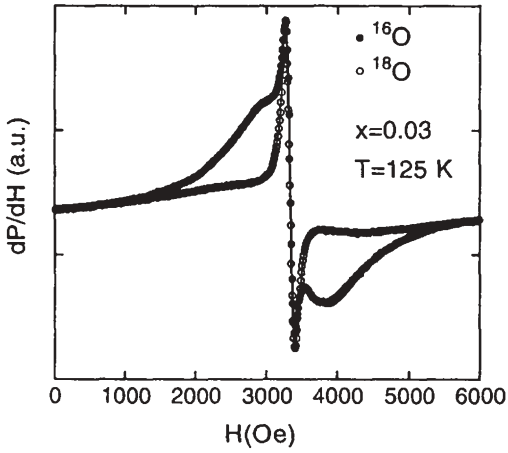

Fig. 31 EPR signal of ^{16}O and ^{18}O samples of $La_{1.97}Sr_{0.03}Cu_{0.98}Mn_{0.02}O_4$ measured at T=125 K under identical experimental conditions [106]. The *solid lines* represent the best fits using a sum of two Lorentzian components with different linewidths: a narrow and a broad one

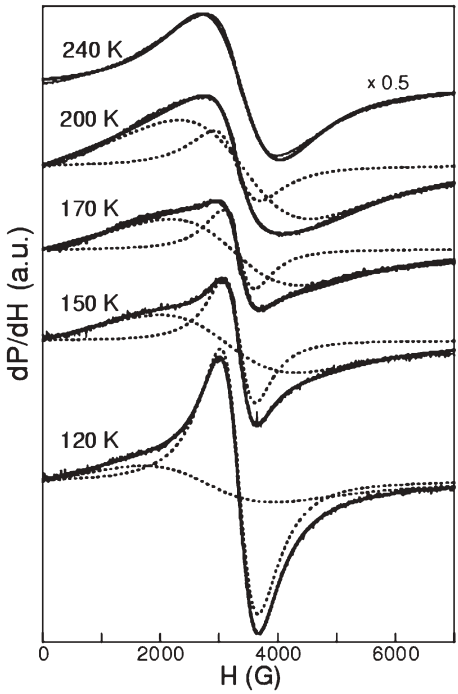

Fig. 32 An evolution of the EPR spectra of $La_{1.97}Sr_{0.03}Cu_{0.98}Mn_{0.02}O_4$ with decreasing temperature [107]. The *dotted lines* show contributions of the broad and narrow EPR signals

to the lattice because of the bottleneck regime, as it was explained in detail earlier. It is important, in particular, that this relaxation rate and its isotope effect are very sensitive to the hole concentration. Recently a detailed investigation of the additional EPR line was performed for doping concentrations $0.01 \leq x \leq 0.06$ [107]. A development of the EPR spectra with cooling of the sample is shown in Fig. 32. Important information was obtained from the temperature dependence of the EPR *intensity* (Fig. 33). One can see that the two components observed for samples follow a completely different temperature dependence. The intensity of the broad component has a broad maximum and strongly decreases with decreasing temperature. This was explained by taking into account

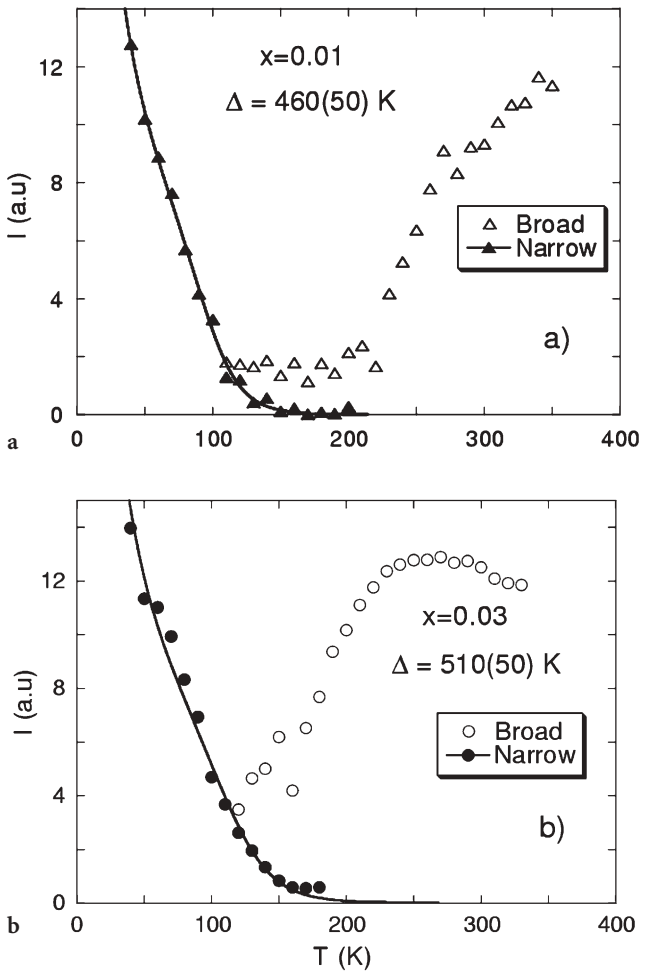

Fig. 33a, b Temperature dependence of the narrow and broad EPR signal intensity in $La_{2-x}Sr_xCu_{0.98}Mn_{0.02}O_4$ with different Sr doping: **a** x=0.01; **b** x=0.03 [107]. The *solid lines* represent fits using the model described in the text

the AF order present in samples with very low Sr concentration. It is expected that upon approaching the AF ordering temperature, a strong shift of the resonance frequency and an increase of the relaxation rate of the Cu spin system will occur. This will break the bottleneck regime of the Mn^{2+} ions, and as a consequence the EPR signal becomes unobservable. In contrast to the broad line, the narrow signal appears at low temperatures and its intensity increases with decreasing temperature. This indicates that the narrow signal is due to the regions where the AF order is suppressed. It is known that the AF order is destroyed by the doped holes, and above x=0.06 AF fluctuations are much less pronounced. Therefore, it was natural to relate the narrow line to regions with locally high carrier concentration and high mobility. This assumption is strongly supported by the absence of an oxygen isotope effect on the linewidth of the narrow line as well. The linewidth of the broad component and its temperature dependence are strongly doping-dependent, whereas the linewidth of the narrow component is very similar for samples with different Sr doping (Fig. 34). Another important indication was obtained from the temperature dependence of the EPR intensity. Since the narrow line was related to hole-rich regions, an exponential increase of its intensity at low temperatures indicates an energy gap for the existence of these regions.

The authors came to a conclusion that this phase separation is assisted by the electron-phonon coupling [28, 108]. More precisely, the latter induces via exchange by phonons the anisotropic interactions between the elementary excitations (polarons) created by the holes. This interaction reduces to the usual elastic forces, if one neglects the retardation effects and optical modes [109]. The attraction between the polarons may result in a bipolaron formation when they approach close enough to each other. The bipolaron formation can be

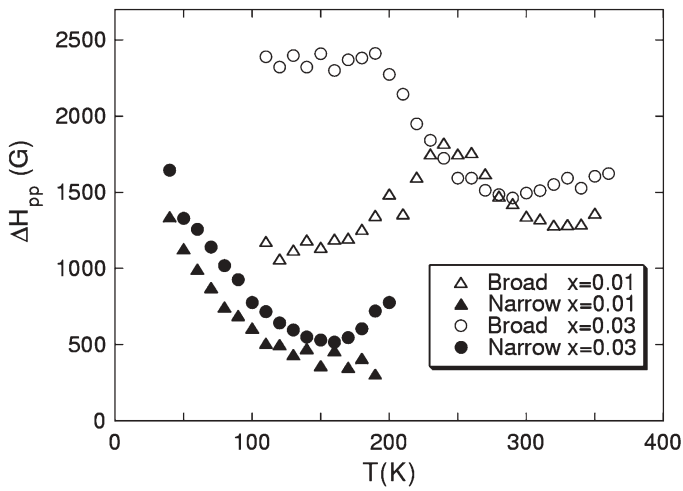

Fig. 34 Temperature dependence of the peak-to peak linewidth ΔH_{pp} for the narrow and broad EPR lines [107]

a starting point for creating of hole-rich regions by an attraction additional polarons. So, the bipolaron formation energy Δ can be considered as an energy gap for a formation of hole-rich regions.

To apply the described above model for an interpretation of the EPR results one has to keep in mind that the spin dynamics of the coupled Mn-Cu system experiences a strong bottleneck regime. In this case, as discussed previously, the EPR intensity is proportional to the sum of spin susceptibilities (Eq. 17). The latter results in a Curie-Weiss temperature dependence of the EPR intensity, since the spin susceptibility of Mn is sufficiently larger than the spin susceptibility of the strongly correlated Cu spin-system. It means that the EPR intensity of the narrow line is proportional to a volume of the sample occupied by the hole-rich regions as the Mn^{2+} ions randomly distributed in the sample. To propose that the volume in question in the underdoped samples is proportional to the number of coupled polarons, the EPR intensity from the hole-rich regions will be proportional to the product of the Curie-Weiss susceptibility of the bottlenecked Mn-Cu system $C/(T-\theta)$ and the number of the bipolarons N_{bi}

$$I_{narrow} \propto \frac{C}{T-\theta} N_{bi} \tag{25}$$

The latter can be estimated in a way used by Mihailovic and Kabanov [110]. If the density of state is determined by $N(E) \sim E^{\alpha}$, the number of the bipolarons is

$$N_{bi} = \left(\sqrt{z^2 + x} - z \right)^2, \qquad z = KT^{\alpha+1} \exp\left(-\frac{\Delta}{K_B T} \right). \tag{26}$$

Here x is the level of the hole doping, and K is the temperature independent parameter. The experimental points for the narrow line intensity of the samples x=0.03 were fitted for the two-dimensional system with α=0 and the Curie temperature θ=–8 K, which was found from the measurements of the static susceptibility. The parameter K and C were kept the same for all samples and the only free parameter was the energy gap Δ. The result of fitting is given in Fig. 33a,b. One can see that the energy gap is almost independent of the doping level. It is important to mention that a particular mechanism of the bipolaron formation is not involved to obtain the formula for the temperature dependence of the EPR intensity for the narrow line. Nevertheless the energy of the bipolaron formation Δ was estimated for a particular case of the elastic interactions between the three-spin polarons mentioned above and for the Zhang-Rice singlets on the basis of the extended Hubbard model [108]. Both estimates gave reasonable values consistent with experimental results.

It is interesting to compare these EPR results with other experiments performed in lightly doped LSCO. Recently Ando et al. [105] measured the in-plane anisotropy of the resistivity ρ_b/ρ_a in single crystals of LSCO with x=0.02–0.04. They found that at high temperatures the anisotropy is small, which is consistent with the weak orthorhombicity present. However, ρ_b/ρ_a grows rapidly with

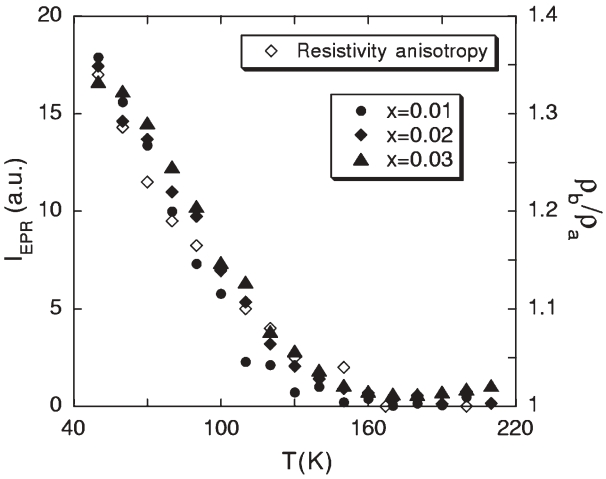

Fig. 35 Temperature dependence of the narrow EPR line intensity in $La_{2-x}Sr_xCu_{0.98}Mn_{0.02}O_4$ [107] and of the resistivity anisotropic ratio in $La_{1.97}Sr_{0.03}CuO_4$ obtained in [105]

decreasing temperature below 150 K. This provides macroscopic evidence that electrons self-organize into an anisotropic state because there is no other external source to cause the in-plane anisotropy in LSCO. It is remarkable that the temperature dependence of ρ_b/ρ_a is very similar to the behaviour of the narrow EPR line intensity; see Fig. 35. It means that the *microscopic* EPR measurements [106, 107] and the *macroscopic* resistivity measurements by Ando et al. [105] provide evidence of the same phenomenon: the formation of hole-rich metallic stripes in lightly doped LSCO well below x_{c1}=0.06. This conclusion is also supported by a recent angle-resolved photoemission (ARPES) study of LSCO that clearly demonstrated that metallic quasiparticles exist near the nodal direction below x=0.06 [111].

The EPR measurements do not detect the phase separation above x_{c1}=0.06. The question arises whether it reflects reality, or a limitation of the EPR method. The main difference of the EPR signals from the hole-rich and hole-poor regions is the spin relaxation rate of the Cu spin system, which results in different EPR linewidths. One would expect these local differences of the relaxation rate to be averaged out by the spin diffusion. The spin diffusion in the CuO_2 plane is expected to be very fast because of the huge exchange integral between the Cu ions. A rough estimate shows that during the Larmor period a local spin temperature can be transported over 100 Cu-Cu distances. It means that all the different nanoscale regions should relax to the lattice with a single relaxation rate, and they could not be distinguished with EPR. However, the AF order which appears below T_N in the hole-poor regions in lightly doped LSCO freezes the process of spin diffusion, and it gives an opportunity to observe different EPR lines from the two types of regions. With increasing doping magnetic order gets suppressed, spin diffusion becomes faster, extended, and one

can no longer distinguish different regions with EPR. This does not mean that the phase separation in hole-rich and hole-poor regions does not exist at $x>0.06$, but most probable that the spin diffusion averages out the EPR response from these regions. The interesting exception here is the situation when the spin fluctuations are pinned and effectively frozen due to the buckling of CuO_2 planes in the vicinity of the structural phase transitions or due to the commensurability effects near $x\sim1/8$ doping (see next paragraph for the details).

7.3 Stripe Fluctuations in LTT and LTO Phases of LSCO

7.3.1 Nonsuperconducting Compounds

The observation of stripe order of charges and spins in $La_{1.62-x}Nd_{0.4}Sr_xCuO_4$ by neutron and hard X-ray diffraction techniques [112–114] has renewed the interest in the problem of the relationship between magnetism and hole doping in high-T_c superconductors [28], which appeared to be closely related with their structural properties. AF correlated spin domains in the CuO_2 planes, separated by quasi-one-dimensional charge walls statically order in the so-called low temperature tetragonal (LTT) phase of this compound. A transition from the usual low temperature orthorhombic (LTO) phase to the LTT phase can be induced by doping of $La_{2-x}Sr_xCuO_4$ by other rare earths (RE) with smaller ionic radii [115, 116]. The low temperature (LT) structural transition results in a change of the direction of tilting of the CuO_6 octahedra from [110] to [100] direction in the notation of the high temperature tetragonal unit cell (see Fig. 36). The absolute value of tilt Φ remains almost constant. These octahedra tilts cause the different buckling of CuO_2 planes. It is argued that the orientation of tilts along [100] direction provides pinning of stripe correlations [112] with the pattern shown in Fig. 37. In the particular case of Nd doping the LT transition occurs at $T_{LT}\sim70$ K. The onset of the static spin order in $La_{1.62-x}Nd_{0.4}Sr_xCuO_4$ crystals decreases from ~50 K for $x=0.12$ down to ~15 K for $x=0.20$ [113]. Based on d.c. magnetization measurements it has been concluded that in this region of Sr doping static spin order coexists with bulk superconductivity [113, 117].

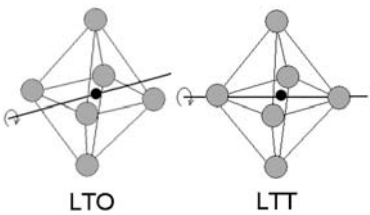

Fig. 36 The CuO_6 octahedral tilts specific for the LTO and LTT phases

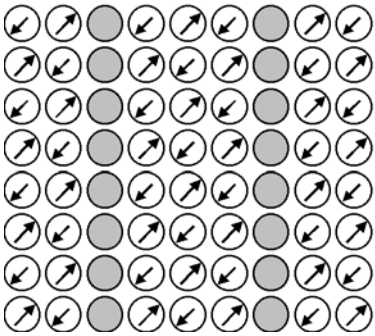

Fig. 37 The possible stripe structure corresponding to the AF domains separated by the charged domain walls [112]. The *circles* represent the copper ions whereas the *arrows* indicate the magnetic moment's orientation. The *shadowed circles* correspond to the nonmagnetic sites with the distributed hole density

Further susceptibility measurements on polycrystalline samples have also been interpreted as an evidence for such a coexistence [118].

The Cu spin dynamics in such systems was studied by means of ESR of Gd in the LTT phase of Eu doped $La_{2-x}Sr_xCuO_4$ for samples of different Sr and Eu concentrations x and y [119, 120]. The role of Eu was to induce the transition to the LTT phase due to the mismatch in ionic radii while hole concentration was changed independently by Sr doping ($0.05<x<0.20$). Substitution by Eu (instead of Nd used in [112–114]) was chosen because Eu^{3+} in its ground state possesses only with Van Vleck paramagnetism and the influence on susceptibility and ESR of thermally excited magnetic states lying 400 K above the ground state is much weaker in comparison to magnetic Nd^{3+} ions and can be correctly subtracted [121]. Moreover, in the case of Eu substitution there is no influence of permanent magnetic moments on the magnetism of the CuO_2 planes.

In order to tune independently the hole content and the tilt angle Φ the authors of [120] used polycrystalline samples of $La_{1.99-x-y}Gd_{0.01}Eu_ySr_xCuO_4$ with the different Eu and Sr contents, y and x respectively. X-ray diffraction measurements show that the RE doped samples are in the LTT structural phase below T_{LT}~130 K. According to the earlier studies [121–123] the tilt angle Φ increases with increasing y and decreasing x, respectively. Remarkably, if Φ exceeds a certain critical value Φ_c the specific heat and susceptibility data suggest that the samples are not bulk superconductors.

ESR of Gd impurities has been measured at a frequency of 9.3 GHz. (For details of analysis of the Gd spectra see [8, 12, 13]). The width ΔH of a central component of the spectrum as a function of temperature is shown in Figs. 38 and 39 for different representative compositions. (The contribution to the linewidth due to population of the excited magnetic states of Eu^{3+} has been subtracted from the experimental data [119, 120]). A generic feature of all Sr doped samples is a linear temperature dependence of ΔH at high temperatures. At low T, i.e., *within* the LTT phase, the $\Delta H(T)$ dependence exhibits an upturn which

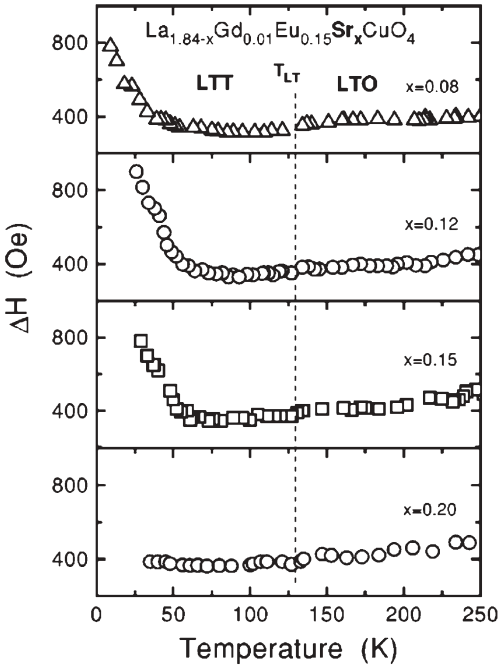

Fig. 38 The linewidth $\Delta H(T)$ of a central component of the Gd^{3+} ESR spectrum for the samples with a fixed Eu content y=0.15 and various Sr concentrations [120]

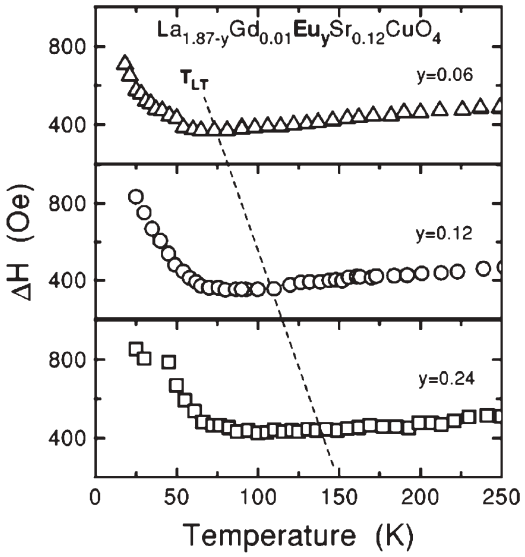

Fig. 39 The linewidth $\Delta H(T)$ of the central component of the Gd^{3+} ESR spectrum for the samples with a fixed Sr content x=0.12 and various Eu concentrations [120]

depends on the composition of dopants x and y. As it was found in [119] the temperature dependence of the Gd^{3+} ESR linewidth in $La_{2-x-y}Eu_ySr_xCuO_4$ is determined by the coupling between Gd and Cu spins and is thus sensitive to the frequency of the spin fluctuations of Cu ω_{sf}. Qualitatively it is inversely proportional to the measured linewidths and for some compositions of dopants the fluctuations of copper spins in the CuO_2 planes begin to slow rapidly below a certain characteristic temperature T_{TLT}. (The detailed analysis of $\Delta H(T)$ behaviour will be presented in the next section).

The main trends of the spin dynamics in the LTT phase of $La_{2-x-y}Eu_ySr_xCuO_4$ are seen in Fig. 40 where the inverse fluctuation frequency ω_{sf} is plotted at different temperatures as a function of the Sr and Eu concentrations. Slowing of the Cu spin dynamics is maximum for Sr contents x=0.12 and is more pronounced for the higher Eu concentrations y>0.12. Sr doping above x=0.15 leads to a considerable weakening of the temperature dependence of the fluctuation frequency in the LTT phase.

Note, that the increase of $1/\omega_{sf}$ in spite of an increasing number of charge carriers in the underdoped region is in clear contrast to the suppression of the magnetic correlations known for the LTO phase of $La_{2-x}Sr_xCuO_4$. The observed behaviour may be due to the development and ordering at low temperatures of a periodical charge and spin modulations (stripes) in the CuO_2 planes similar

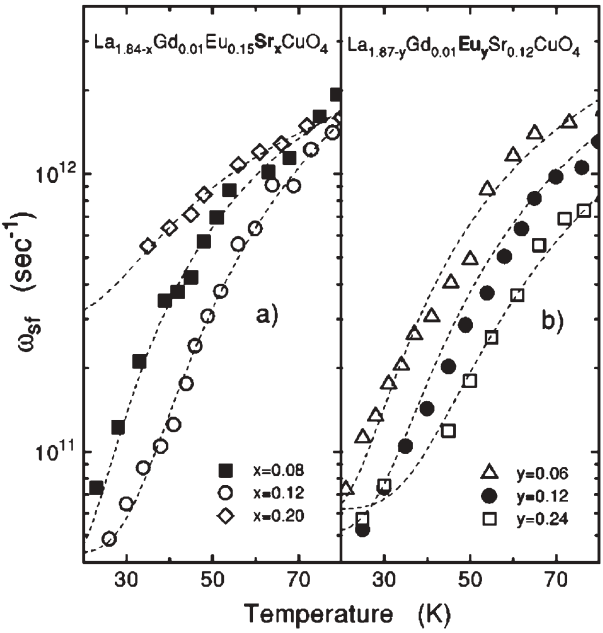

Fig. 40a, b The decay frequency ω_{sf} evaluated from the $\Delta H(T)$ dependences shown in Figs. 38 and 39. *Dashed curves* are results of the fitting using a phenomenological function $\omega_{sf}=A+B\exp(-C/T)$ [120]

to that found in Nd doped $La_{2-x}Sr_xCuO_4$ [112–114]. For x=0.12 it develops already below 50 K. However in the ESR measurements of the respective Eu doped samples no signatures for static magnetic bulk order was found down to 25 K although the decrease of ω_{sf} in the LTT phase for about two orders of magnitude evidences for a strong tendency of the system to order magnetically. Indeed, the establishment of at least a local magnetic order below T_0~25–27 K has been observed in a polycrystalline $La_{1.68}Eu_{0.2}Sr_{0.12}CuO_4$ sample by means of muon spin relaxation (μSR) [124]. This is in a contradiction to the much higher value of T_0 obtained in a neutron diffraction experiment by Tranquada et al. [112, 113] due to the different energy scales of the two types of experiments. For a smaller Sr content of x=0.10 the magnetic order is not seen in ESR down to the lowest temperature of the measurement 8 K [120]. In terms of the stripe model low ordering temperatures could be a result of the increasing imperfection of the stripe pattern when deviating from the 1/8 Sr content.

The disappearance of the specific features of the low temperature spin dynamics in the LTT phase for Sr concentrations x=0.17–0.20 corresponds well with the appearance of a strong superconducting a.c. signal for the samples with these stoichiometries. As was mentioned above, at these and higher Sr concentrations buckling of the CuO_6 octahedra decreases below a critical value and the samples exhibit fully developed bulk superconductivity in the LTT phase. The authors [119, 120] came to conclusion that the Gd EPR data show a narrow crossover region for *both* the superconducting as well as for the anomalous magnetic properties of the LTT structural phase of $La_{2-x}Sr_xCuO_4$ which is determined by critical buckling of the CuO_6 octahedra.

7.3.2 Superconducting Compounds

The interest to the microscopic phase separation in the superconducting LSCO has received a new impetus after the recent neutron scattering experiments [46, 125] in the LTO phase of $La_{2-x}Sr_xCuO_4$ which revealed the presence of incommensurate AF order very similar to that observed in the LTT compound $La_{1.6-x}Nd_{0.4}Sr_xCuO_4$ for a wide doping region around x=0.12. However, on a larger time scale magnetic fluctuations in $La_{2-x}Sr_xCuO_4$ are dynamical, especially for the superconducting state, and their relevance to the stripe structure is a matter of debate. In particular, the dynamical nature of the microscopic phase separation hinders the investigation of its properties by means of low frequency local methods such as conventional NMR.

Therefore it was of great importance to investigate the phase diagram and the magnetic fluctuations properties of superconducting $La_{2-x}Sr_xCuO_4$ and related compounds shifting the measurements to larger frequencies. This section is devoted to analysis of the Gd^{3+} EPR measurements [126, 127] which are focused mainly on the analysis of the temperature and doping dependence of the low frequency magnetic fluctuations for the superconducting $La_{2-x}Sr_xCuO_4$ with hole doping covering the entire superconducting region of the phase diagram.

The temperature behaviour of the multiline Gd^{3+} ESR spectrum for $T>Tc$ is qualitatively very similar to that for the Eu doped compounds described in the previous section: a linear dependence of ΔH on temperature which is followed by the rapid growth of the linewidth at low T (the typical temperature dependence of the ΔH for the most intense central component is shown in Fig. 41). However, after cooling below 40 K the behaviour of superconducting and nonsuperconducting (Eu doped) samples becomes different: the linewidth of superconducting LSCO exhibits the downturn starting at a temperature T_m, dependent on x, whereas for other samples which are not bulk superconductors ΔH continues to grow upon further lowering temperature (see Fig. 41).

Such behaviour may be explained by taking into account the fact that, in addition to the important but temperature independent residual inhomogeneous broadening, the linewidth is given by different homogeneous broadening terms linked to the magnetic fluctuations in the CuO_2 planes via Eq. (7): (i) the Korringa relaxation due to the interaction of Gd^{3+} spins with the charge carriers, which was discussed in much detail above (it corresponds to the $\mathbf{q}=0$ contribution in Eq. 7); (ii) the critical contribution caused by the interaction of Gd with AF correlated copper spins (this term originates from the $\mathbf{Q}_{AF}=(\pi/a;\pi/a)$ contribution to Eq. (7) taken at $\omega=\omega_s$) gives rise to the homogeneous broadening of the Gd ESR line.

To derive the expression for last contribution one has to assume that the integrand in Eq. (7) is peaked at $\mathbf{q}=\mathbf{Q}_{AF}=(\pi/a;\pi/a)$ (see, e.g. [128]) with the corresponding susceptibility

$$\chi_\sigma^{\parallel(\perp)}(\mathbf{Q}_{AF}, \omega) = \chi_\sigma^{\parallel(\perp)}(\mathbf{Q}_{AF})/(1 - i\omega\tau), \tag{27}$$

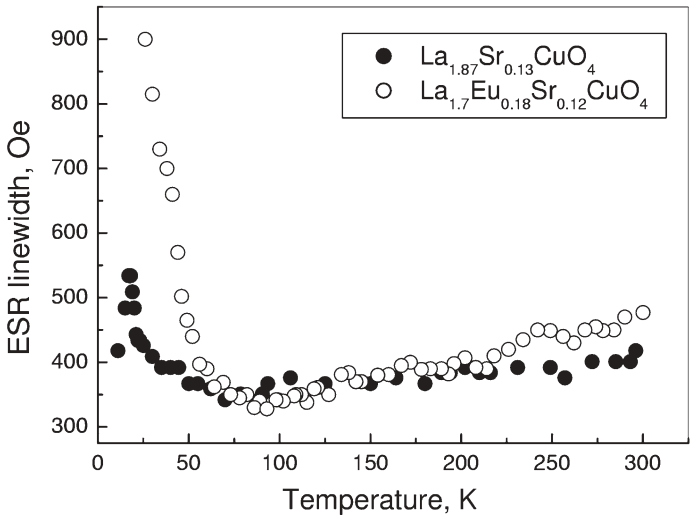

Fig. 41 The ESR linewidth temperature dependence for LTO superconducting LSCO and LTT nonsuperconducting LESCO [127]

where $\tau=\tau_\infty exp(E_a/kT)$ is the AF fluctuations life-time ($\sim 1/\omega_{sf}$), τ_∞ is its value at the infinite temperature and E_a the activation energy, proportional to the spin stiffness ρ_s ($E_a=2\pi\ \rho_s$) [129]. Then rewriting the static susceptibility in terms of spin correlators and introducing the internal field at Gd site, H_{Gd}, (see above for the definitions) after averaging over the random orientation of the local Cu moments with respect to the external magnetic field it is possible to obtain

$$\Delta H = \frac{1}{3}(\gamma H_{\mathrm{Gd}})^2 M^2 \left[\tau + \frac{2\tau}{1+(\omega_s\tau)^2}\right] \tag{28}$$

with M^2 being Barnes-Plefka factor [11] introduced similar to Eq. (18).

This term describes the standard Bloembergen-Purcell-Pound (BPP) behaviour: the broadening of the EPR line upon cooling with the downturn at a certain freezing temperature T_m corresponding to $\omega_s\tau=1$.

It was observed in [126, 127] that, depending on the Sr content, the linewidth behaviour transforms from the BPP-like (with the maximum at T_m) to the pure Korringa (linear) temperature dependence. Based on the observation that the relative weight of the BPP-contribution compared with the Korringa one decreases with increasing Sr doping, it was concluded [126, 127] that at low x the Gd spin probes the almost magnetically correlated state and at the high x – the almost nonmagnetic metal. The corresponding phase diagram is shown in Fig. 42.

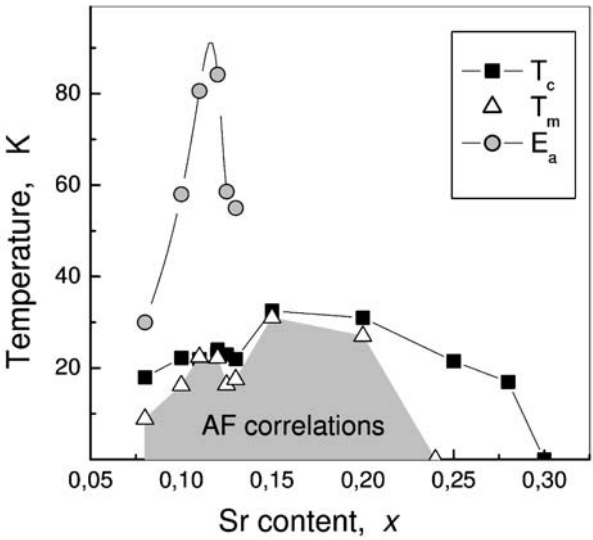

Fig. 42 The phase diagram of the magnetic fluctuations of superconducting $La_{2-x}Sr_xCuO_4$ [127]. The *triangles* correspond to the magnetic transition temperature $T_m(x)$, *squares* to the superconducting transition temperature $T_c(x)$ and the *circles* to the magnetic fluctuations activation energy $E_a(x)$

The different temperature dependencies of the linewidth for superconducting and nonsuperconducting samples may be explained assuming that for the superconducting samples the linewidth below T_c is governed by fluctuating fields which are transversal to the magnetic responsible for the Zeeman splitting of the Gd spin states (the second term in Eq. 28). Since these fluctuations are induced by Cu moments lying in the CuO_2 planes, it means that Gd ions are subjected to the constant magnetic field normal to these planes. This may indicate that the magnetic flux lines penetrating in the layered superconducting sample tend to orient normally to the basal planes where the circulating superconducting currents flow. (The difference of the T_m and T_c values observed for the samples with small x enabled the authors [127] to conclude that the possible distortion of ESR lineshape owing to the non-resonant microwave absorption as the main reason for the apparent narrowing of the ESR line below T_c seems to be improbable).

Since the measurements [126, 127] were carried out at nonzero external field it is very important to consider the flux lattice effects. At typical ESR fields of ~0.3T, which are oriented normal to the CuO_2 layers, the period of lattice is 860 Å, whereas the vortex cores sizes for $La_{2-x}Sr_xCuO_4$ is 20 Å. As the upper critical field equals to 62 T, it is clear that in the case of ESR the vortex cores occupy only 0.5% of the CuO_2 planes. According to [130, 131] the Cu spins in the vortex cores may be AF ordered. Therefore the phase diagram in Fig. 42 indicates that not only the spins in the normal vortex cores are AF correlated, but the AF correlations are spread over the distances of the order of magnetic correlation length which at low doping reaches 600–700 Å [131].

Numerical simulations of the temperature dependencies of the Gd ESR linewidths for the compounds with different Sr content make it possible to estimate the values of the parameters in the expression for the linewidth: the maximal internal field H_{Gd} is about 200 Oe; $\tau_\infty = 0.3 \times 10^{-12}$ s and the corresponding activation energies E_a which are shown in Fig. 42. One of the key moments of [127] was the comparative Gd EPR analysis of the magnetic fluctuations for the different metalloxides, such as $La_{2-x}Sr_xCuO_4$ (LSCO) [37], $La_{2-x}Ba_xCuO_4$ (LBCO) [47], $(La\text{-}Eu)_{2-x}Sr_xCuO_4$ (LESCO) [120], $(La\text{-}Nd)_{2-x}Sr_xCuO_4$ (LNSCO) [129]. Note that for LBCO the measurements were restricted by the doping region in the vicinity of the well known T_c dip, whereas the last two series discussed in the previous part corresponded to the nonsuperconducting LTT phase. (Since the influence of the Nd magnetic moments for the LNSCO compound hinders the ESR measurements the activation energy for this compound was estimated from the measurements of the nuclear spin relaxation on Cu and La nuclei [129]).

It is established [127] that for all LSCO-based compounds the activation energy of magnetic fluctuations is enhanced near the 1/8 doping. This indicates the important role of the commensurability and gives evidence of the *plane* character of the inhomogeneous spin and charge distributions. The maximal activation energies are 80 K for $La_{2-x}Sr_xCuO_4$, 144 K for $La_{2-x}Ba_xCuO_4$, 160 K for $(La\text{-}Eu)_{2-x}Sr_xCuO_4$ and 143 K for $(La\text{-}Nd)_{2-x}Sr_xCuO_4$. Note that the signatures

of the bulk superconductivity [127] for $La_{2-x}Ba_xCuO_4$ and $(La\text{-}Eu)_{2-x}Sr_xCuO_4$ become visible upon the suppression of the activation energy down to 80–85 K. It is possible to conclude that these values of the activation energy are probably the critical ones for the realization of the bulk superconducting state. Fluctuations with the higher activation energies are effectively pinned and suppress superconductivity.

The observed phase separation in the superconducting LSCO was accompanied by the slowing down of magnetic fluctuations, which gradually freeze upon cooling [132]. Note that the features of the phase separation in the superconducting LSCO were observed also in the $^{63,65}Cu$ and ^{139}La NMR [126, 127, 133, 134]. According to the measurements of high field NMR in the compounds with the enhanced spin stiffness the effective magnetic moment of copper in the superconducting LSCO is ~0.09 μ_B.

Thus the Gd EPR studies in LSCO compounds enabled the authors [126, 127] to conclude that: (i) the inherent feature of their superconducting state is the dynamical nanoscale phase separation [28]; (ii) in the vicinity of 1/8 doping this separation may be realized in a form of dynamic stripes; (iii) it is possible to determine the critical spin-stiffness which separates the compounds with the bulk superconducting phase from the nonsuperconducting one.

8 Concluding Remarks

EPR experiments have offered microscopic tools to study the magnetic, electronic and lattice properties of HTSC and have played an essential role in solving some relevant issues. At the same time those experiments have put important constraints on any theory for the mechanism of high-temperature superconductivity.

The information gained from the EPR measurements depends on the interaction of the spin probe with the key element of the high-T_c materials – CuO_2 planes. In the case of a week coupling the EPR measurements give generally similar to the NMR information besides an important difference – much higher sensitivity and frequency. Note that for the strong coupling the EPR information is sufficiently different from that provided by NMR giving an opportunity to study the coupling of the CuO_2 magnetization to other degrees of freedom.

EPR experiments have elucidated the evolution of the electronic properties and of the spin dynamics when the parent insulating antiferromagnets are driven towards the metallic and superconducting state by doping, yielding evidence of the localization of the holes with possible phase separation in charged domain walls or stripes.

The local character of the method made it a powerful tool for study of the generic phase separation in cuprates, which contributed a lot to the evolution of this idea from the initial stage up to elucidation of the stripe phase picture. EPR appeared to be an effective method to study the low frequency fluctuations

at the cases of full NMR wipeout, which often takes place at low doping regime, at the start of phase separation.

The EPR experiments have revealed an essential role of the strong coupling of electrons to the local static and dynamic lattice distortions in the properties of high-T_c superconductors. This method has a large potential for elucidation of this important problem.

Due to its extreme sensitivity the EPR is effective tool for study of substitution effects, for example with its help it was established by doping with isovalent non-magnetic impurities the local magnetic moments are created induced in the CuO_2 plane.

The investigations discussed in a present review cannot be considered as a full account on EPR studies of high-T_c superconductors. The selection of the material reflects only the part of activity in this interesting field and probably has an impact of our own taste. In addition to some results of the past which appeared to be connected with the important steps in understanding of HTSC properties we touched the hot issues of interplay between the localized and itinerant properties in strongly correlated electron systems.

Some of the presented results, such as the determination of the superconducting wave function symmetry, are connected with the problem which still remains the matter of debates. The EPR evidences of the *d*-symmetry (together with similar conclusions obtained from NMR, ARPES and other measurements) disagree with the *s*-symmetry deduced from the muon spin rotation, tunnelling and other experiments. An attempt to build a bridge between these two ways of thinking belongs to K.A. Müller, who proposed that the electron wave function in the superconducting state has a supersymmetry being a superposition of contributions with *s*- and *d*-symmetries with the relative weight depending on the distance from the surface [135]. Near the surface the *d*- contribution is dominating, whereas in the depth of material the situation is opposite. Accordingly the experiments dealing with the vicinity of the surface layer reveal the *d*-superconductivity, whereas the experiments sensing the bulk reveal the *s*-superconductivity. It seems that this issue should be closely related, also, to the heterogeneity of cuprates due to their generic phase separation and the mixed state in experiments with high magnetic fields. In particular, the mentioned EPR evidence [51] in favour of the *d*-symmetry does not contradict to the supersymmetry idea since the measurements were performed at the magnetic field of the order 10 T. At this field the vortex lattice is very dense and practically the whole volume between the vortices is near the "surface" – a normal state of the cores. Similar arguments can be given in the case of the phase separation. We think that the EPR method is capable of shedding additional light on this crucial problem.

Acknowledgements The authors are very grateful to K.A. Müller, A. Shengelaya and Yu.I. Talanov for reading of a draft version of the manuscript and for the valuable remarks and suggestions. The work of B.I.K was supported by the Grant of the President of the Russian Federation for the leading scientific schools N 1708.2003.2, and by the Grants BRHE REC-007 and INTAS 01-0654, that of G.B.T. by Department of Physics of the RAS through the Contract N 020703-996 and by RFBR through the Grant N 04-02-17137.

References

1. Hebel LC, Slichter CP (1959) Phys Rev 113:1504
2. Al'tshuler TS, Garifullin IA, Kharakhashyan EG (1972) Fiz Tv Tela 14:263
3. Rettory R, Davidov D, Chaikin P, Orbach R (1973) Phys Rev Lett 30:437
4. Davidov D, Rettory R, Kim HM (1974) Phys Rev B 9:147
5. Babershke K (1976) Z Phys B 24:53
6. Alekseevsky NE, Garifullin IA, Kochelaev BI, Kharakhashyan EG (1973) Pis'ma ZhETF 18:323; (1977) Zh Eksp Teor Fiz 72:1523
7. Kochelaev BI, Tagirov LR, Khusainov MG (1979) Zh Eksp Teor Fiz 76:578; (1979) Sov Phys JETP 49:291
8. Kochelaev BI, Tagirov LR (1984) Solid State Commun 53:961; (1984) Zh Eksp Teor Fiz 89:1358
9. Kosov AA, Kochelaev BI (1978) Zh Eksp Teor Fiz 74:148
10. Tagirov LR, Trutnev KF (1984) Zh Eksp Teor Fiz 86:1092; (1987) J Phys F Metal Phys 17:695
11. Barnes SE (1981) Adv Phys 30:801
12. Bednorz JG, Müller KA (1986) Z Phys B 64:188
13. Al'tshuler SA, Kozyrev BM (1972) Electron paramagnetic resonance of transition elements compounds, 2nd edn. Nauka, Moscow
14. Abragam A, Bleaney B (1970) Electron paramagnetic resonance of transition ions. Clarendon Press, Oxford
15. Anderson PW (1988) The theory of high Tc superconductivity. Princeton University Press
16. Punnoose A, Singh RJ (1995) Int J Mod Phys B 10:1123
17. Chakravarty S, Orbach R (1991) Phys Rev Lett 64:224
18. Simon P, Bassat JM, Oseroff SB, Fisk Z, Cheong SW, Wattiaux A, Schulz S (1993) Phys Rev B 48:4216
19. Batlogg B, Chu CW, Chu WK, Gubser DU, Müller KA (ed) (1996) Proc 10th Anniversary of HTS Workshop on Physics, Materials and Applications. World Scientific, Singapore
20. Chu CW (1997) In: Lerner RG, Trigg GL (eds) Superconductivity: high temperature (Encyclopedia of applied physics 20). VCH, New York
21. Cyrot M, Pavuna D (1992) Introduction to superconductivity and high T_c materials. World Scientific, Singapore
22. Kastner MA, Birgeneau RJ, Shirane G, Endoh Y (1998) Rev Mod Phys 70:897
23. Norman MR, Pepin C (2003) Rep Progr Phys 66:1547
24. Berthier C, Julien MH, Horvatic M, Berthier Y (1996) J Phys I 6:2205
25. Rigamonti A, Borsa F, Caretta P (1998) Rep Progr Phys 61:1367
26. Elschner B, Loidl A (1998) Handbook on the physics and chemistry of rare earths: special issue on high-$T_c$superconductors. Elsevier Science BV, Amsterdam
27. Tinkham M (1996) Introduction to superconductivity. McGraw-Hill, New York
28. Gorkov LP, Sokol AV (1987) JETP Lett 46:420
29. Emery VJ, Kivelson SA (1993) Phys C 209:597
30. Mihailovic D, Müller KA (1997) In: Liarokapis E, Kaldis E (eds) Materials aspects of high T_c superconductivity: 10 years after the discovery. Dordrecht, Kluwer
31. Castellani C, Di Castro C, Grilli M (1997) Z Phys B 103:137
32. Keimer B et al. (1992) Phys Rev B 46:14034
33. Anderson PW, Weiss PR (1953) Rev Mod Phys 25:269
34. Kubo R, Tomita KJ (1953) J Phys Soc Jpn 9:888
35. Kochelaev BI, Kan L, Elschner B, Elschner S (1994) Phys Rev B 49:13106
36. Timusk T, Statt B (1999) Rep Prog Phys 62:61

37. Kataev VE, Greznev YuS, Teitel'baum GB, Breuer M, Knauf N (1993) Phys Rev B 48:13042
38. Kataev VE, Kukovitskii EF, Talanov Y, Teitel'baum GB (1988) JETP Lett 48:476
39. Kataev VE, Greznev YuS, Kukovitskii EF, Teitel'baum GB, Breuer M, Knauf N (1992) JETP Lett 56:385
40. Causa MT, Fainstein C, Nieva G, Sánchez R, Steren LB, Tovar M, Zysler R, Vier DC, Schultz S, Oseroff SB, Fisk Z, Smith JL (1988) Phys Rev B 38:257
41. Shaltiel D, Barnes SE, Bill H, Francois M, Hagemann H, Jegondaz J, Lovy D, Monod P, Peter M, Revcolevschi A, Sadowski W, Walker E (1989) Physica C 161:13
42. Slichter CP (1989) Principles of magnetic resonance, 3rd edn. Springer, Berlin Heidelberg New York
43. Pickett WE, Krakauer H, Cohen RE, Singh DJ (1992) Science 255:46
44. Anderson PW (1992) Science 256:1526
45. Takagi H, Ido T, Ishibashi S, Uota M, Uchida S, Tokura Y (1989) Phys Rev B 40:2254
46. Yamada K, Lee C-H, Kurahashi K, Wada J, Wakimoto S, Ueki S, Kimura H, Endoh Y, Hosoya S, Shirane G, Birgeneau RJ, Greven M, Kastner MA, Kim YJ (1998) Phys Rev B 57:6165
47. Rameev BZ, Kukovitskii EF, Kataev VE, Teitel'baum GB (1995) Physica C 246:309
48. Kan L, Elschner S, Elschner B (1991) Solid State Commun 79:61
49. Janossy A, Brunel L-C, Cooper JR (1996) Phys Rev B 54:10186
50. Alloul H, Ohno T, Mendels P (1989) Phys Rev Lett 63:1700
51. Jánossy A, Fehér T, Oszlányi G, Williams GVM (1997) Phys Rev Lett 79:2726
52. Imai Y, Slichter CP, Yoshimura K, Kosuge K (1993) Phys Rev Lett 72:726
53. Shengelaya A, Keller H, Müller KA, Kochelaev BI, Conder K (2001) Phys Rev B 63:144513
54. Kochelaev BI (1999) J Supercond 12:53
55. Abdulsabirov RY, Zhdanov RS, Izygson YS, Korableva SL, Kurkin IN, Sedov LL, Yasonov IV (1989) Supercond Phys Chem Tech 2:52
56. Eremin MV, Kurkin IN, Rodionova MP, Salikhov IK, Sedov LL, Tagirov LR (1991) Supercond Phys Chem Tech 4:716
57. Finn CB, Orbach R, Wolf WP (1961) Proc Phys Soc 77:261
58. Aminov LK (1962) Zh Eksp Teor Fiz 42:783
59. Shimizu H, Fujiwara K, Hatada K (1997) Physica C 282/287:1349; (1998) Physica C 299:169
60. Shimizu H, Fujiwara K, Hatada K (1997) Physica C 288:190
61. Ivanshin VA, Gafurov MR, Kurkin IN, Kurzin SR, Shengelaya A, Keller H, Gutmann M (1998) Physica C 307:61
62. Mesot J, Allenspach P, Staub U, Furrer A, Mutka H, Osborn R, Taylor A (1993) Phys Rev B 47:6027
63. Aminov LK, Ivanshin VA, Kurkin IN, Gafurov MR, Salikhov IK, Keller H, Gutmann M (2001) Physica C 349:30
64. Ledbetter H (1992) J Mater Sci 7:2905
65. Inderhees SE, Salamon MB, Friedmann TA, Ginsberg DM (1987) Phys Rev B 36:2401
66. Junod A, Eckert D, Graf T, Kaldis E, Karpinski J, Rusiecki S, Sanchez D, Triscone G, Muller J (1990) Physica C 168:47
67. McMillan (1968) Phys Rev 167:331
68. Gafurov MR, Ivanshin VA, Kurkin IN, Rodionova MP, Keller H, Gutmann M, Staub U (2003) J Magn Res 161:210
69. Atsarkin VA, Demidov VV, Vasneva GA (1995) Phys Rev 52:1290
70. Atsarkin VA, Vasneva GA, Demidov VV (1995) Zh Eksp Teor Fiz 108:927 [(1995) JETP 81:509]
71. Herve J, Pescia CR (1960) Hebd Seances Acad Sci 251:665

72. Atsarkin VA, Demidov VV, Vasneva GA, Feher T, Janossy A, Dabrowski B (2000) Phys Rev 61:R14944
73. Bulut N, Scalapino DJ (1992) Phys Rev Lett 68:706
74. Sichelschmidt J, Elschner B, Loidl A (1997) Physica B 230:841
75. Kochelaev BI, Sichelschmidt J, Elschner B, Lemor W, Loidl A (1997) Phys Rev Lett 79:4274
76. Emery VJ, Reiter G (1988) Phys Rev B 38:4547
77. Eremin MV, Sigmund E (1994) Solid State Commun 90:765
78. Kochelaev BI, Tagirov LR, Garifullin IA, Garifyanov NN, Khaliullin GG, Alekseevskii NE, Mitin AV, Nizhankovskii VI, Khlybov EP (1990) Exp Tech Phys 38:359
79. Garifullin IA, Garifyanov NN, Alekseevskii NE (1991) Physica C 179:9
80. Sichelschmidt J, Elschner B, Loidl A, Fischer P (1994) Z Phys B 93:407
81. Sichelschmidt J, Elschner B, Loidl A, Kochelaev BI (1995) Phys Rev B 51:9199
82. Uimin G, Rossat-Mignod (1992) Physica C 199:251; Uimin G, Stepanov V (1993) Ann Phys (Germany) 2:284; Uimin G (1994) Phys Rev B 50:9531
83. Eremin MV, Eremina RM, Gafurov MR, Ivanshin VA, Kurkin IN, Kurzin SP, Keller H, Gutmann M (2000) J Exp Theor Phys 90:363
84. Likodimos V, Guskos N, Palios G, Koufoudakis A, Typek J, Bojanowski B, Wabia M (1995) Phys Rev B 52:7682
85. Shaltiel D, Bill H, Fischer P, Francois M, Hagemann H, Pete M, Sekhar Ravi Y, Sadowski W, Scheel HJ, Triscone G, Walker E, Yvon K (1989) Physica C 158:424
86. Tarascon JM, Greene LH, Barboux P, McKinnon WR, Hull GW, Orlando TP, Delin KA, Foner S, McNiff EJ (1987) Phys Rev B 36:8393
87. Maeno Y, Fujita T (1987) In: Wolf SA, Kresin VZ (eds) Novel superconductivity. Plenum Press, New York; (1988) Physica C 153:1105
88. Gang Xiao, Chieplak MZ, Gavrin A, Streitz FH, Bakhshai A, Chien CL (1988) Phys Rev Lett 60:1446
89. Hilscher G, Pillmazr N, Eibler R, Bauer E, Remschnig K, Rogl P (1988) Z Phys B 72:461
90. Kataev VE, Kukovitskii EF, Teitel'baum GB, Finkel'stein AM (1990) Pis'ma ZhETF 51:115
91. Finkel'stein AM, Kataev VE, Kukovitskii EF, Teitel'baum GB (1990) Physica C 168:370
92. Polyakov AM (1977) Nucl Phys B 120:429
93. Abrikosov AA, Gor'kov LP (1960) Zh Eksp Teor Fiz 39:1781
94. Sachdev S, Vojta M (2000) cond-mat/0009202
95. Alloul H, Mendels P, Casalta H, Marucco JF, Arabski J (1991) Phys Rev Lett 67:3140
96. Janossy A, Cooper JR, Brunel LC, Carrington A (1994) Phys Rev B 50:3442
97. Zagoulaev S, Monod P, Jegoudez J (1995) Phys Rev B 52:10474
98. Kochelaev BI, Alekseevskii NE, Garifullin IA, Garifyanov NN, Mitin AV, Nizhankovskii VI, Tagirov LR, Khaliullin GG, Khlybov EP (1988) Proceedings of the 24th AMPERE Congress, Poznan
99. Alekseevskii NE, Mitin AV, Nizhankovskii VI, Garifullin IA, Garifyanov NN, Khaliullin GG, Khlybov EP, Kochelaev BI, Tagirov LR (1989) J Low Temp Phys 77:87
100. Baranov PG, Badalyan AG (1994) In: Sigmund E, Müller KA (eds) Phase separation in cuprate superconductors. Springer, Berlin Heidelberg New York, p 118; Baranov PG, Badalyan AG, Ilyin IV (1995) Fiz Tv Tela 37:3296
101. Shirmer OF, Wübbeler G, Wahlbrink Th (1994) In: Sigmund E, Müller KA (eds) Phase separation in cuprate superconductors. Springer, Berlin Heidelberg New York, p 131
102. Tallon JF et al. (1995) Phys Rev B 51:12911
103. Schneider T (2003) In: Bennemann KH, Ketterson JB (eds) The physics of conventional and unconventional superconductors. Springer, Berlin Heidelberg New York
104. Cho JH, Chou FC, Johnston DC (1993) Phys Rev Lett 70:222
105. Ando Y, Segawa K, Komiya S, Lavrov AN (2002) Phys Rev Lett 88:137005

106. Shengelaya A, Keller H, Müller KA, Kochelaev BI, Conder K (2000) J Supercond 13:955
107. Shengelaya A, Bruun M, Kochelaev BI, Safina A, Conder K, Müller KA (2003) cond-mat/0310152; (2004) Phys Rev Lett 93:017001
108. Kochelaev BI, Safina AM, Shengelaya A, Keller H, Müller KA, Conder K (2003) Mod Phys Lett B 17:415
109. Aminov LK, Kochelaev BI (1962) Zh Eksp Teor Fiz 42:1303
110. Mihailovic D, Kabanov VV (2001) Phys Rev B 63:54505
111. Yoshida T et al. (2003) Phys Rev Lett 91:027001
112. Tranquada JM, Sternlieb BJ, Axe JD, Nakamura Y, Uchida S (1995) Nature 375:561; Tranquada JM, Axe JD, Ichikawa N, Nakamura Y, Uchida S, Nachumi B (1996) Phys Rev B 54:7489
113. Tranquada JM, Axe JD, Ichikawa N, Moodenbaugh AR, Nakamura Y, Uchida S (1997) Phys Rev Lett 78:338
114. Zimmermann MV, Vigliante A, Niemöller T, Ichikawa N, Frello T, Madsen J, Wochner P, Uchida S, Andersen NH, Tranquada JM, Gibbs D, Schneider JR (1998) Europhys Let 41:629
115. Büchner B, Braden M, Cramm M, Schlabitz W, Hoffels O, Braunisch W, Müller R, Heger G, Wohlleben D (1991) Physica C 185:903
116. Crawford MK, Harlow RL, McCarron EM, Farneth WE, Axe JD, Chou H, Huang Q (1991) Phys Rev B 44:7749
117. Ostenson JE, Bud'ko S, Breitwisch M, Finnemore DK, Ichikawa N, Uchida S (1997) Phys Rev B 56:2820
118. Moodenbaugh AR, Lewis LH, Soman S (1997) Physica C 290:98
119. Kataev V, Rameev B, Büchner B, Hücker M, Borowski R (1997) Phys Rev B 55:R3394
120. Kataev V, Rameev B, Validov A, Büchner B, Hücker M, Borowski R (1998) Phys Rev B 58:R11876
121. Büchner B, Breuer M, Cramm M, Freimuth A, Micklitz H, Schlabitz W, Kampf AP (1994) J Low Temp Phys 95:285
122. Cramm M, Büchner B, Fiack A, Holland-Moritz E, Müller R, Schlabitz W, Braden M, Hohlwein D (1994) Physica C 235:855
123. Büchner B, Breuer M, Freimuth A, Kampf AP (1994) Phys Rev Lett 73:1841
124. Wagener W, Klauss H-H, Hillberg M, de Melo MAC, Kopmann W, Birke M, Litterst FJ, Büchner B, Micklitz H (1998) J Magn Magn Mater 177:545
125. Suzuki T, Goto T, Chiba K, Shinoda T, Fukase T, Kimura H, Yamada K, Ohashi M, Yamaguchi Y (1998) Phys Rev B 57:R3229
126. Kuhns P, Reyes AP, Moulton W, Kukovitskii EF, Vavilova EL, Teitel'baum GB (2002) Proceedings of the Physical Phenomena in High Magnetic Fields-IV. Santa Fe, NM, World Scientific, p 297
127. Teitel'baum GB, Kataev VE, EL Kuhns P, Reyes AP, Moulton W (2003) JETP Lett 72:726
128. Zha Y, Barzykin V, Pines D (1996) Phys Rev B 54:7561
129. Teitel'baum GB, Abu-Shiekah IM, Bakharev O, Brom HB, Zaanen J (2001) Phys Rev B 63:020507(R)
130. Arovas DP, Berlinsky AJ, Kallin C, Zhang SC (1997) Phys Rev Lett 79:2871
131. Lake B, Aeppli G, Clausen KN, McMorrow DF, Lefmann K, Hussey NE, Mangkorntong N, Nohara M, Takagi H, Mason TE, Schröder A (2001) Science 291:832
132. Julien M-H, Campana A, Rigamonti A, Carretta P, Borsa F, Kuhns P, Reyes AP, Moulton WG, Horvatic M, Berthier C, Vietkin A, Revcolevschi A (2001) Phys Rev B 63:144508
133. Ohsugi S, Kitaoka Y, Yamanaka H, Ishida K, Asayama K (1994) J Phys Soc Jpn 63:2057
134. Goto T, Chiba K, Mori M, Suzuki T, Seki K, Fukase T (1997) J Phys Soc Jpn 66:2870
135. Müller KA (2002) Phil Mag Lett 82:270

Struct Bond (2005) 114: 267–285
DOI 10.1007/b101022

Electron-Phonon Coupling in High-T_C Superconductors

T. Egami (✉)

Oak Ridge National Laboratory, Oak Ridge, TN37831, USA and
Departments of Materials Science and Engineering and Physics and Astronomy,
University of Tennessee, Knoxville TN 37996, USA

Abstract For a long time the majority opinion on the role of phonons in the mechanism of high-temperature superconductivity has been that it is either irrelevant or even harmful, in spite of a large amount of experimental observations on the lattice effects. However, recent more direct experimental evidence of strong electron-phonon coupling and isotope effects suggest that we should not dismiss its role so easily. We argue that the electron-phonon coupling in strongly correlated electron systems is unconventional and substantially different from that in simple metals. In the cuprates certain phonons induce strong inter-site charge transfer, which can be spin dependent. This could lead to a strong spin-charge-phonon coupling, and to formation of the vibronic state in the presence of nano-scale phase separation. It is most likely that the unconventional electron-phonon coupling is the critical element of the mechanism of superconductivity in the cuprates.

Keywords Lattice effect · Phonons · Electron-phonon coupling · Mechanism of superconductivity

1 Introduction

At the time of discovery of high-temperature superconductivity (HTSC) in 1986 [1], it was already obvious that the standard BCS theory cannot explain this novel phenomenon. Soon the near absence of the isotope effect was reported [2], and nearly everybody rushed to the conclusion that the HTSC mechanism involves something other than phonons, most probably spin excitations, and could be quite exotic. The observations of the apparent *d*-symmetry of the superconducting order parameter fueled this conjecture, and since then it has been widely believed that the HTSC is a purely electronic phenomenon to be explained fully by an electronic model, such as the *t-J* Hamiltonian [3]. Phonons were labeled irrelevant, and were forgotten.

On the other hand a large amount of literature suggests that the local lattice structure reflects the onset of HTSC in various ways, as reviewed in the article by Bianconi in this volume [4]. While the majority view has been that they are merely the collateral effects of strong coupling, recent observations present a more direct evidence of strong electron-phonon (*e-p*) coupling. For instance the photoemission results show that electron dispersion has a "kink" around 70 meV or so below the Fermi level [5], indicating that electrons are strongly renormalized by some excitations. Lanzara et al. [6] presented strong evidence that these excitations are oxygen phonons, by demonstrating that the position of the kink in energy is largely independent of the superconducting gap size and the superconductive critical temperature, T_C, and roughly corresponds to that of the zone-edge longitudinal-optical (LO) phonons, which are suspected to interact strongly with electrons [7, 8]. More recently they have shown that the kink position shifts with the isotopic mass of oxygen, convincingly proving the phononic origin of the kink, and furthermore demonstrated that the isotope substitution results in strong renormalization of the electron bandwidth, thus the electron effective mass [9]. The last explains the isotope effect on the effective mass determined by the penetration depth measurement [10, 11].

The argument against the relevance of phonons for HTSC is usually based upon the following observations:

1. There is no evidence of strong *e-p* coupling in the normal state transport properties.
2. The isotope effect is weak when T_C is high.
3. The phonon mechanism usually prefers the *s*-wave superconductivity, while there is preponderance of evidence for the *d*-wave superconductivity.
4. The phonon mechanism is attractive and competes against the magnetic mechanism, which is repulsive.
5. The value of T_C is too high for the BCS mechanism.

However, none of them are strong arguments, as discussed by Allen [12]. The transport properties are dominated by highly mobile nodal quasiparticles with

relatively weak *e-p* coupling, and even for them photoemission has shown the evidence of the e-p coupling. The isotope effect is absent in a number of superconductors [2], and that itself does not imply non-phonon mechanism. Phonons can produce *d*-wave superconductivity, either in the antiferromagnetic background [13] or when the coupling is sufficiently anisotropic [14], and when they do they do not compete against the magnetic mechanism. While the critical temperature is limited to 30 K for the BCS mechanism within the framework of the McMillan theory [15], which is based upon the electronic state of Nb, in some strong coupling approximation, for instance in the Allen-Dynes theory, it can be higher [16].

The crucial point is that the usual arguments against the phonon mechanism are based upon the knowledge of the conventional *e-p* coupling for a nearly free electron systems, while the *e-p* coupling in the cuprates can be very different from that of the simple metals because of their strong ionicity, covalency and electron correlation. In this article we argue that the *e-p* coupling in the cuprates is quite different from the conventional one, and could be *unconventional*. The departure from the regular behavior originates from the strong coupling of certain phonon modes to charge and spin through phonon-induced inter-site charge transfer that can be spin polarized. While the BCS mechanism is based upon the coupling of long-wave, zone-center acoustic phonons to nearly-free electrons, the active phonons in the cuprates are short-wave optical phonons middle of the zone or near the zone-edge.

2
Electron-Phonon Coupling in Ferroelectric Oxides

Before discussing the *e-p* coupling in the cuprate it is instructive to review the *e-p* coupling in ferroelectric oxides, such as $BaTiO_3$. The classical picture of ferroelectricity is based upon the ionic model. Displacements of positive ions against negative ions produce internal electric fields (Lorentz field), which induce polarization. If the feedback is positive, that is, the induced polarization is larger than the originally assumed one, spontaneous ferroelectric polarization is produced [17]. In reality, however, the ionic polarization calculated from the ionic valences and the ionic displacements, which can be determined accurately by X-ray diffraction, is smaller than the measured one, often by as much as a factor of two [18]. This discrepancy originates from an electronic effect of the covalent bond. Ionic displacements change the strength of the covalent bond, and results in charge transfer, which produces electronic polarization.

For instance, in $BaTiO_3$ the nominal valences are Ba^{2+}, Ti^{4+}, and O^{2-}. However, the Ti-O bond is strongly covalent, while the Ba-O bond is more ionic. Nominally the *d*-orbital of Ti is empty, d^0, but in $BaTiO_3$ a Ti *d*-orbital overlaps with a *p*-orbital of oxygen, and forms a *p-d* hybridized orbital. If a Ti^{4+} ion is displaced to the right toward an O^{2-} ion (Fig. 1), it produces an electric dipole

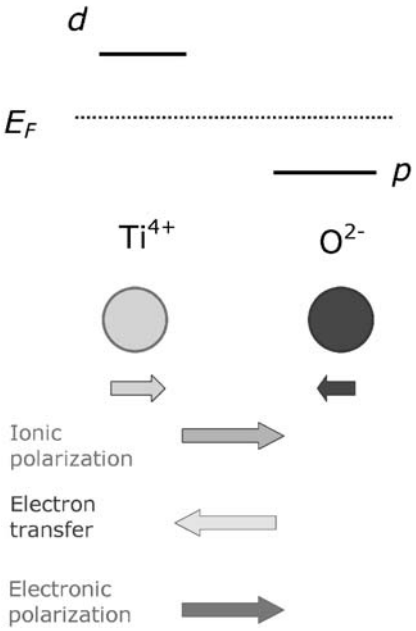

Fig. 1 Electronic levels in titanates and charge transfer due to ionic displacement resulting in electronic polarization

pointing to the right. At the same time the p-d hybridization is increased, so that the bonding orbital assumes more Ti character. This is equivalent to partially moving electronic charge (ΔZ) from O^{2-} to Ti^{4+} over the distance between O and Ti, a, and produces an electronic polarization, $\Delta Z a$. Thus the total polarization is equal to

$$P = Zu + \Delta Z a \tag{1}$$

where Z is the ionic charge and u is the ionic displacement. We may re-write Eq. (1) in terms of the dynamic Born effective charge, Z^*, as

$$P = Z^* u, \qquad Z^* = Z + \Delta Z \frac{a}{u} \tag{2}$$

Since $a/u \gg 1$, Z^* can be much larger than Z. For instance the Born effective charge of Ti can be larger than +8. An elegant method to calculate the electronic polarization from the first-principles in terms of the Berry phase was recently developed by R. Resta and D. Vanderbilt [19–21], raising the level of understanding of this phenomenon to an unprecedented height.

3 Electron-Phonon Coupling in the Cuprates

3.1 Model Calculation

The undoped cuprates, such as La_2CuO_4, are charge-transfer (CT) insulators in the Zaanen-Zawazky-Allen classification [22]. The nominal valence of Cu is +2, with d^9 configuration. The Cu orbital involved in the Cu-O bond is the x^2-y^2 orbital, which hybridizes with the oxygen *p*-orbital to form bonding and anti-bonding σ-orbitals. The highest level, the anti-bonding σ-orbital, is half-filled. Since the *d*-level of Cu has a large on-site Coulomb repulsion energy, *U*, of about 8 eV, the σ-orbital splits into the filled lower Hubbard band mainly of the oxygen *p*-character and the empty upper Hubbard band mainly of the Cu *d*-character. Thus the insulating gap is a CT gap. If a Cu ion is displaced toward an O ion (Fig. 2) the *p*-*d* hybridization increases, and electron is transferred from the *p*-orbital to the *d*-orbital, just as in the case of the Ti-O bond. However, in the hole doped cuprates the situation is greatly different. Doped holes occupy the top of the lower Hubbard band, thus mainly the oxygen *p*-orbitals. When the Cu-O bond is compressed, holes, rather than electrons, move from oxygen to copper, creating the current, thus the electronic polarization, of the opposite sign compared to the undoped case (Fig. 2).

A model calculation mode on the one-dimensional two-band Hubbard model with Su-Schrieffer-Heeger (SSH) *e*-*p* coupling to the LO phonon illustrates this point quite well [7, 23]. The Hamiltonian of the system is

$$H = \sum_{i,j,\sigma} \left(t_{ij} + \frac{\alpha}{a}(u_i - u_j) \right) (c^+_{i,\sigma} c_{j,\sigma} + c^+_{j,\sigma} c_{i,\sigma}) + \sum_i [\varepsilon_i n_i + U n_{i\uparrow} n_{i\downarrow}] \tag{3}$$

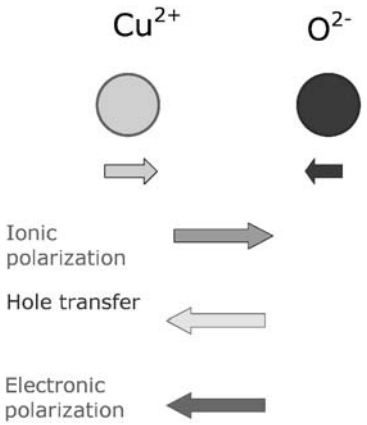

Fig. 2 Charge transfer in doped cuprates. Displacements of Cu and O transfers holes from O to Cu, resulting in polarization opposite to the ionic polarization

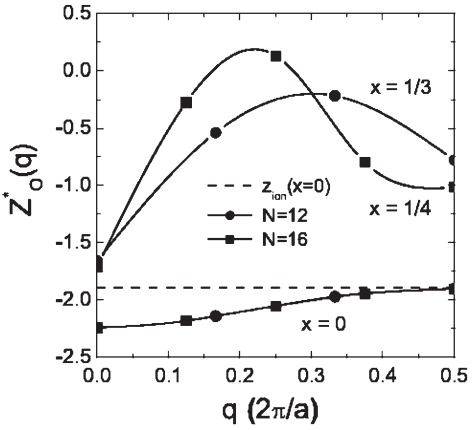

Fig. 3 The q dependence of the effective charge of oxygen in the 1-d Hubbard model due to the LO phonon monde, calculated for the ring of N=12 sites with doping level x=0, 1/3 and for N=16 with x=0, 1/4. The *dashed line* indicates the ionic value (static charge) [23]

where u_i is the displacement of the i-th ion and $n_i=c_i^+c_i$. The effective charge was calculated based upon the bond current induced by the phonon [23], and is strongly dependent on q, the phonon wavevector (Fig. 3). Note that at q=0 the effective charge is close to the ionic value, but is greatly changed toward the middle of the zone. Note that the electronic polarization is anti-parallel to the ionic polarization, and thus nearly cancels the ionic charge, or even reverses the sign. The maximum of the electronic polarization depends upon the doping level, but roughly corresponds to the value of $2k_F$ for each doping. Thus this phenomenon is a part of the Kohn anomaly, renormalized by the many-body effects.

3.2 Optical Conductivity and Spin-Phonon Coupling

Since the SSH coupling modifies the hopping integral, t, the effect of the phonon is not limited to the electronic structure near the Fermi level. As shown in Fig. 4 in terms of the optical conductivity, $\sigma(\omega)$, the entire portion of the electronic band is affected by the strain caused by the phonon. It has been observed that the violation of the optical sum rule extends to high energy ranges, and was used to argue the electronic origin of the pairing [24–26]. The result shown in Fig. 4 indicates that this observation does not exclude the phononic mechanism.

The modification of t by the LO phonon implies that the magnetic interaction will also be affected, since in the t-J model, $J=t^2/U$ [3]. Actually, the model calculations showed that the actual effect of the phonons on spins is quite extensive. Figure 5 shows the change in the total spin structure function, $S(q)$, due to the LO phonons at the zone boundary, q=0.5 (π) [23]. If we resolve for

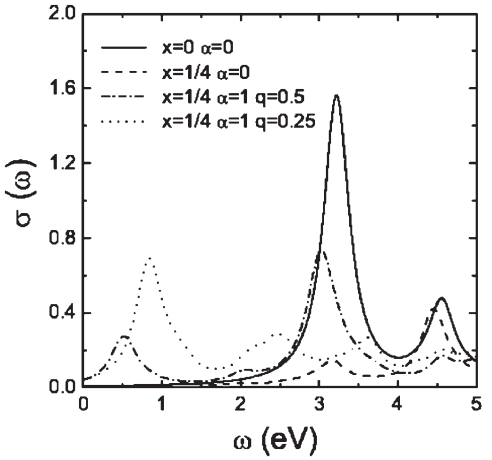

Fig. 4 Optical conductivity for the N=16 ring, with x=0, 1/4, and without phonon (α=0, a=1), with α=1 and q=0.5 (breathing) phonon mode, and with α=1 and q=0.25 phonon mode

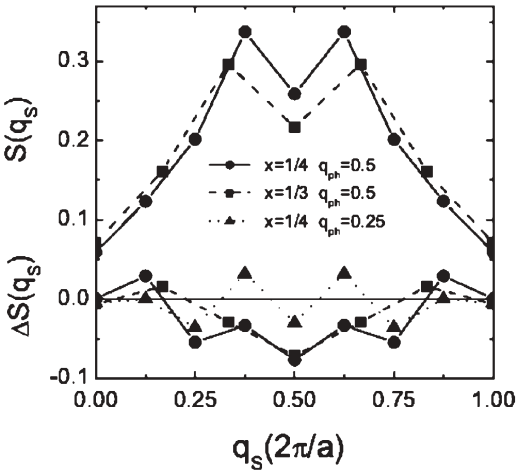

Fig. 5 Total spin correlation structure factor, $S(q)$, for the charge density x=1/4 and 1/3 (*above*), and the change in $S(q)$ due to the LO phonon at q=0.5 (π) (*below*) [15]. Note that the effect is small at the zone-center, while it becomes more pronounced toward the zone-boundary. It also shows that the q=0.25 phonon mode has almost no effect on the spin

energy in terms of $S(q, \omega)$, as shown in Fig. 6, the effect of the LO phonon on the spin dynamics is significant [23]. It is seen that the q=0.5 (π) phonon produces strong softening of spin excitation at an incommensurate q value that must be related to the spin/charge stripe formation. This is because the phonon-induced charge transfer is spin-dependent because of the local exchange field. Thus we may call the *e-p* interaction in the cuprates *unconventional*.

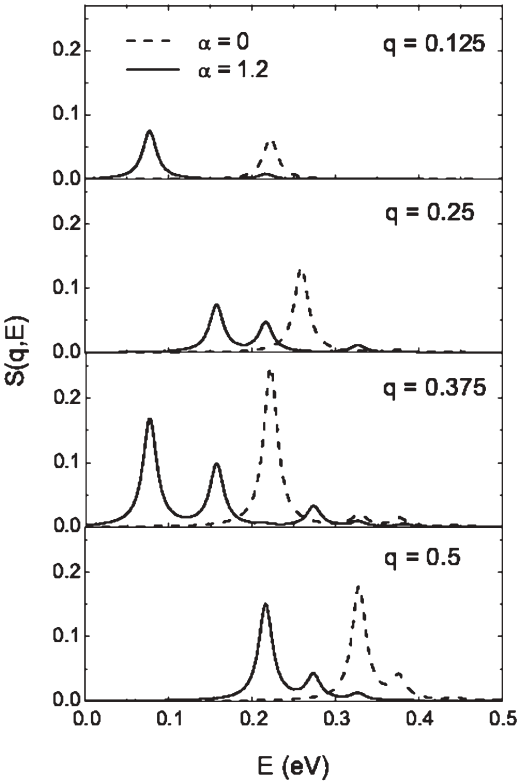

Fig. 6 The dynamic spin structure factor, $S(q, \omega)$, with (α=1.2) and without (α=0) the LO phonon at q=0.5 (π), at several values of q

3.3 LO Phonon Softening

In the ferroelectric oxides the effect of strongly increased Born effective charge is to harden the LO phonons and soften the TO phonons, leading to the ferroelectric transition through the soft TO mode [27]. In the case of an insulator, the zone-center ($\boldsymbol{q}$=0) modes are related by

$$\left(\frac{\omega_{LO}}{\omega_{TO}}\right)^2 = \frac{\varepsilon_0}{\varepsilon_\infty} \tag{4}$$

where ε_0 and ε_∞ are the dielectric constants below and above the phonon frequency, which is the well-known Lyddane-Sachs-Teller (LST) relationship. In ferroelectric solids ε_0 diverges at T_C, accompanied by softening of the TO mode at $\boldsymbol{q}$=0 through Eq. (4). In the cuprates, ω_{LO}=ω_{TO} at $\boldsymbol{q}$=0 because of metallic screening. However, since the charge density is relatively low, at $\boldsymbol{q}$>0 screening is not expected to be complete, and the short-range dipolar interactions are

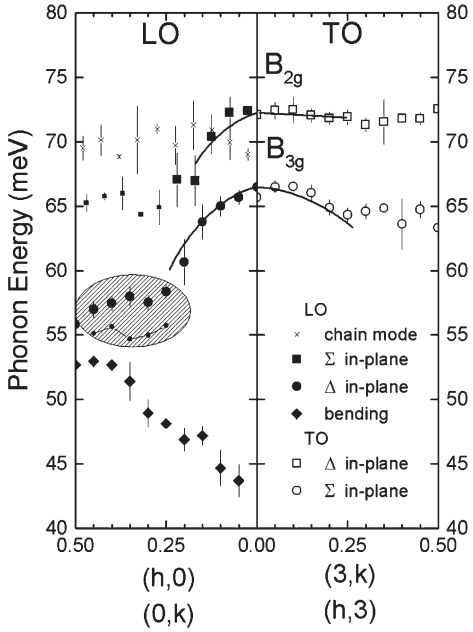

Fig. 7 Dispersion of the Cu-O bond-stretching modes. The LO modes (*left*) soften toward the zone-boundary, while the TO modes (*right*) remain mostly dispersionless. Small signs describe weak phonon peaks due to other modes, such as the apical oxygen modes [32]

expected to be present. Indeed the early studies by Pintschovius and Reichardt [28, 29] showed that while most phonon modes remain little changed by doping, the in-plane Cu-O bond-stretching LO mode softens strongly near the zone-boundary. More recent studies [30–32] confirmed this softening, and revealed further anomalies such as the strong in-plane anisotropy and unusual temperature dependence (Fig. 7).

If we try to explain the LO mode softening using the lattice dynamic models, one has to introduce an attractive force between oxygen ions only in one direction [30], which is highly counter-intuitive. The recent report that the LO phonon softening is much weaker in heavily doped $La_{1.7}Sr_{0.3}CuO_4$ [33] strongly supports our view that the softening is an electronic effect. While the LDA calculations [34] and the non-local density theory [35] explain this softening to some extent, the physics of this softening deserves careful study. Early on Tachiki and Takahashi [36, 37] proposed a phenomenological approach to explain the LO phonon softening in terms the dielectric function:

$$\omega_{LO}^2(\boldsymbol{q}) = \omega_{TO}^2(\boldsymbol{q}) + \frac{\varepsilon_0 - \varepsilon_\infty}{\varepsilon(\boldsymbol{q}) - \varepsilon_\infty}(\omega_{LO}^2 - \omega_{TO}^2) \tag{5}$$

where $\varepsilon(\boldsymbol{q})$ is the dielectric function at $\boldsymbol{q}$, and ω_{LO} and ω_{TO} are the LO and TO frequencies in the unscreened insulator in which optical phonons are assumed

to be dispersionless. Therefore $\omega_{LO}(\boldsymbol{q}) < \omega_{TO}(\boldsymbol{q})$ means a negative dielectric constant, a situation known as overscreening. Tachiki and Takahashi argued that such an overscreening may originate from the anti-resonant vibronic state, and enhance the *e-p* coupling. As pointed out by Ginzburg [38], $\varepsilon > 1$ for regular screening so that $1/\varepsilon < 1$; however, when $\varepsilon < 0$, $|1/\varepsilon|$ can be greater than 1, and thus can amplify the coulomb interaction. Tachiki and Takahashi argued that this effect can lead to high values of T_C. The argument above shows that the overscreening can result from the phonon-induced charge transfer to reduce Z^* which results in the LO phonon softening [7, 8], without invoking anti-resonance with charge dynamics.

Based upon this *e-p* coupling mechanism the linearized Eliashberg equation for strong coupling superconductivity was solved numerically [14]. The dielectric function was phenomenologically determined from the experimentally determined phonon dispersion using Eq. (5), and the electronic dispersion was modeled to fit the results of the photoemission experiments. It was found that if we assume the depth of the extended saddle point in the electronic dispersion to be 30 meV, a transition temperature, T_C, well over 100 K can be achieved for *d*-wave superconductivity. While the magnitude of T_C depends upon the details and cannot be taken too seriously, this calculation demonstrates that strong *d*-wave superconductivity can result from the coupling of the zone-edge LO phonons to Cu-O charge transfer. The anisotropic *s*-wave solution is also attainable, and whether the *d*-wave or the anisotropic *s*-wave solution becomes the ground state depends upon details of the parameters. Thus, while the phononic mechanism does not necessarily give the *d*-wave solution, it can be fully compatible with it. This calculation phenomenologically assumed very strong enhancement of the *e-p* coupling by the vibronic effect. In the following we discuss how this vibronic nature arises due to the structural and chemical complexity of the system.

4
Spatial Inhomogeneity and Pseudo-Gap

4.1
Spatial Inhomogeneity

Even though the *e-p* coupling is strong and unconventional, that alone does not appear to be sufficient to explain the HTSC, since the value of the *e-p* coupling constant, λ, obtained from the ARPES is of the order of 1–2, and is not large enough to explain the HTSC. In addition, if the value of λ is too large, polarons will form, increasing the effective mass and decreasing T_C. That is a part of the reason why many do not believe in the phonon mechanism. However, the effective mass of overlapping extended polarons may be not so large [39], and more importantly this conclusion was obtained based upon the strong coupling theory, which still assumed the Migdal theorem. If the coupling is non-adia-

batic, this conclusion may not be warranted. It is possible that a new state that allow non-linear, non-adiabatic interaction will be formed with the mid-range values of λ in certain circumstances.

A possible candidate for such a situation is the structural and electronic inhomogeneity that appears to be present in the HTSC cuprates. The possibility of electronic inhomogeneity has long been suspected [40], and there is ample evidence of local structural distortion that suggests spatial inhomogeneity [41]. However, they have largely been dismissed as collateral byproduct of strong coupling, and were never given proper recognition, until the spectacular results of the STM/STS studies by J.C. (Seamus) Davis and his group [42, 43] surprised many people who never believed in inhomogeneity. They have shown that at low temperatures the *a*-*b* plane of Bi-cuprates, such as $Bi_2Sr_2CaCu_2O_8$ (BSCCO-2212), has two kinds of nano-scale regions, one with a well-defined superconductive gap with sharp quasi-particle (QP) peaks at the edge of the gap, and the other with a wider, but less clearly defined gap (pseudo-gap, PG) with no QP peaks (PG matter). The size of the nano-regions is of the order of 30–40 Å. As the level of hole doping is reduced the PG matter gains in volume (area) at the expense of QP. At low doping the PG matter develops checker-board-like charge density waves (CDW) with the periodicity of about 4.5*a*, where *a* is the Cu-Cu distance in the plane. Interestingly, the nodal particles along (π, π) are present in both regions in about the same state, and do not see this inhomogeneity. While both QP and PG matter are made of states around the $(\pi, 0)$ points, the sharp QP peaks develop only in the metal-like QP regions, and the PG matter appears insulating.

This observation by STM/STS is still controversial [44]. It is not yet clear whether this inhomogeneity exists in the bulk as well as the surface where the STM/STS observation was made, and whether it is required for HTSC or is merely an interesting by-product. It is difficult to imagine, however, that the surface has created such inhomogeneity. It is more natural to assume that in systems with strong disorder, such as BSCCO-2212, the surface simply pins dynamic inhomogeneity. Also internal lattice distortions have been observed in all compounds including $YBa_2Cu_4O_8$, which is totally stoichiometric without the element of disorder [45].

In addition, the LO phonon dispersion discussed above suggests inhomogeneity. As shown in Fig. 7, the Cu-O bond-stretching LO phonon branch is strongly softened toward the zone-boundary, while in the undoped cuprate it shows slight hardening. Then it may appear reasonable to assume that the amount of softening is proportional to the doped charge density. However, for $La_{2-x}Sr_xCuO_4$ it was shown that the amount of softening is the same for all the superconductive phase, and disappears in the insulating phase [46]. In $YBa_2Cu_3O_{6+x}$ it is also constant as shown in Fig. 8, but the intensity of the softened branch changes with x [47]. This observation can be understood only in terms of microscopic phase segregation into the phase with softening and without softening. It is, however, unlikely that these phases represent fully doped and undoped phases, since the Coulomb energy penalty for such stark elec-

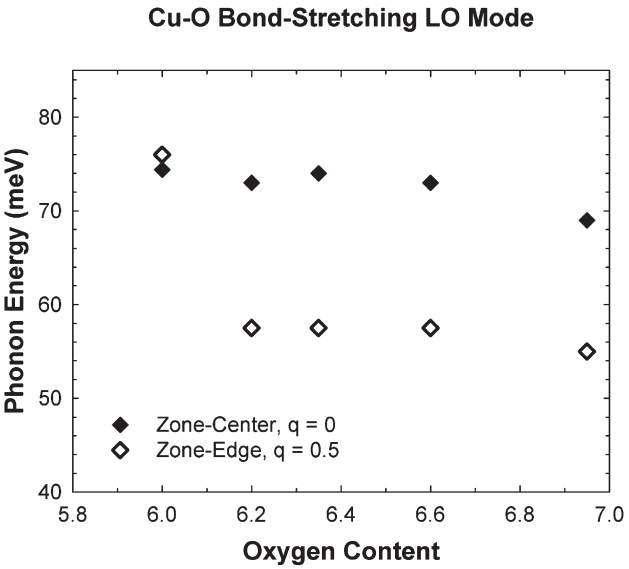

Fig. 8 Cu-O bond-stretching LO mode in $YBa_2Cu_3O_x$ at the zone center (q=0) and zone-edge (q=0.5) [47]. The amount of softening is independent of the charge density, x

tronic phase segregation must be huge. It is more likely that both phases have about the same charge density, but in the phase without softening charges are localized into CDW or stripes, and the phonon branch splits into the one which looks like in the undoped phase and the other one localized around the charge stripes, the edge mode [48]. Thus even in YBCO which has relatively little disorder in the optimally doped phase and shows no sign of phase separation so far, microscopic phase segregation appears to be present. This is why we believe that inhomogeneity is an intrinsic feature of the HTSC cuprates [49].

4.2 Pseudo-Gap

Another point that should be discussed here is the nature of the pseudo-gap (PG). The presence of PG was first suggested by the NMR experiments, but then various probes confirmed its presence [49, 50]. The temperature below which PG is observed is called the pseudo-gap temperature, T_{PG}, and generally it wraps around T_C in the phase diagram, and extrapolates to zero at the doped hole density x=x_{max} where T_C goes to zero as well (Fig. 9) [50]. In this case formation of the PG is required for HTSC. However, this view was recently challenged by Tallon and Loram [51] who advocates that T_{PG} extrapolates to the center of the T_C dome at x_0 (Fig. 9). We will then call the first kind T_{PG1}, and the second kind T_{PG2}, which is slightly lower than T_{PG1}. Theoretical interpretations also go in two ways. T_{PG1} is generally interpreted as the pairing temperature

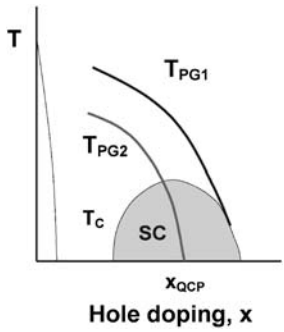

Fig. 9 Two kinds of pseudo-gap temperature

[52]. In this interpretation, local pairs exist below T_{PG1}, but they are incoherent down to T_C where the long-range SC coherence is achieved through the Josephson junction between the paired regions. At the same time it is the temperature below which local distortions are observed. Thus it is likely that it is the temperature where the structural inhomogeneity sets in and the QP and PG matter become separated. On the other hand T_{PG2} is regarded as an independent phase transition temperature near which there are strong fluctuations that couple holes into pairs [53].

Let us examine the second kind first. T_{PG2} extrapolates to zero at x_0, but this concentration is also close to the metal-insulator transition (MIT) revealed by applying high magnetic field [54]. Thus x_0 must be a quantum critical point (QCP), and it has been argued that the closing of PG and fluctuations associated with the QCP constitute the pairing mechanism [53]. One possibility is that the nature of the QCP is magnetic, and increased spin fluctuations around it contribute to pairing [55]. While the long-range antiferromagnetic (AFM) order disappears at a very small value of x (~0.02), dynamic AFM correlations remain up to high values of x, as the spin excitation spectra measured by inelastic neutron scattering indicate. The strength of AFM correlations can be assessed by integrating the spin scattering intensity of inelastic neutron scattering (magnetic susceptibility). Such an attempt by Bourges [56] made for YBCO shows that the magnetic intensity integrated up to 50 meV decreases linearly with x, and extrapolates to zero just beyond the optimum concentration, close to x_0. Thus the characterization of x_0 as the spin QCP appears to be reasonable. However, an important point to note is that the result by Bourges suggests that *the spin fluctuations themselves diminish to zero at* x_0. This means that the transition at x_0 occurs not because of the loss of magnetic correlation due to dilution, but because of the disappearance of local spin polarization, perhaps due to transformation to a Pauli paramagnet, a regular spin degenerated metal. In this scenario the presence of a QCP does not help at all for pairing, since it is not accompanied by strong spin fluctuation as the data by Bourges indicates.

Another significant change that occurs at x_0 is that the entropy of superconductive transition is constant above, close to the BCS value, and starts to

decrease below x_0 with decreasing x. Loram *et al.* interpreted this observation as the evidence of pair formation above T_C, i.e. PG phenomenon, below x_0 [57]. However, an alternative interpretation is that the SC state becomes *inhomogeneous* below x_0. In this scenario SC and AFM compete, and as soon as AFM correlation becomes significant the SC state does not cover the whole volume.

Now it should be noted that the signature of local distortion is observed at T_{PG1}, not at T_{PG2} [58]. This is very significant, since it implies that the inhomogeneity of the SC state and the structural inhomogeneity are two different phenomena. While AFM competes against SC, local distortion does not, and it appears that the local distortion and electronic phase separation are *required* for SC to occur, as we noted earlier.

5
Vibronic Mechanism of Superconductivity

Why, then, is phase separation necessary for HTSC? Superconductivity is the macroscopic quantum coherence phenomenon, and the notion that it requires inhomogeneity does not appear to make any sense. An answer to this question was suggested first by J. C. Phillips [49, 59, 60] and more recently by A. Bianconi [4, 61]. The idea is that inhomogeneity results in charge confinement that produces gaps in electron dispersion and a high density of states (DOS) at the Fermi level (shape resonance). Phillips further speculated that the resultant superconductivity is highly inhomogeneous, and has filamental character [59], which seems to be true for underdoped samples. While this idea certainly has great merit, its weakness is that the coincidence of the high DOS with the Fermi level requires a highly regular structure of a specific dimension. If the dimension is wrong it causes anti-resonance, with the Fermi level at the minimum of the DOS.

While the argument above assumes a conventional *e-p* coupling with Fermi liquid, it is possible to extend the argument even further by considering a non-adiabatic *e-p* coupling. The result of confinement is not only to reduce the bandwidth, increasing the density of states (DOS), but also to reduce the group velocity of electrons. If the group velocity is sufficiently reduced to make it comparable to the sound velocity the Migdal theorem is no longer valid, and we have to consider a resonant, non-adiabatic vibronic coupling [14, 62]. If an electron is free and its Fermi velocity far exceeds the sound velocity the usual perturbative approach can describe the *e-p* coupling. When their velocities are comparable the vertex correction becomes significant, and this will greatly enhance the *e-p* coupling, although a reliable theory of such a coupling is not yet available. In this case strong coupling does not lead to structural instability since the vibronic frequency is finite, unless electrons become totally localized to a polaronic (stripe) state. In addition to the unconventional nature of the *e-p* coupling in the cuprates, formation of the vibronic state due to structural inhomogeneity that confines charge appears to be the second critical component of the HTSC phenomenon.

6
Other Issues with Lattice and Spin

6.1
Stability of Stripes

Another aspect of the lattice effect worth mentioning here is the lattice effect on the stability of spin/charge stripes. As shown in Fig. 10 as λ is increased T_C goes down because of polaron formation. Polarons have a large mass, and thus reduces the Bose condensation temperature. Thus destabilizing polarons would help superconductivity. In the cuprates it is likely that the polaron-polaron interaction leads to formation of stripes, so that the question of polaron stability directly means the stability of stripes. Both the elastic interaction and the kinetic energy prefer the stripe formation, while the Coulomb energy opposes it. The two-dimensional nature of the cuprates is critical in tilting the balance toward the stripe formation. The stability condition of the stripes, however, can be discussed in much the same way as that for polarons. The ionic size effect is prominent for the polarons in the colossal magnetoresistive (CMR) manganites [63] as well as in the stripe formation [64]. For the manganites this size effect was initially explained in terms of the bandwidth control by the ionic size that leads to the bending of the Mn-O-Mn bond [65]. However, a careful examination showed that the amount of band-narrowing is too small to account for the effect [66, 67]. We proposed a more plausible scenario in terms of the renormalization of the elastic energy by the long-range stress field which changes the effective coupling constant by a factor of two [64, 68]. Buckling of the CuO_2 plane stabilizes stripes that compete against superconductivity and reduces T_C, as observed by experiment [69, 70].

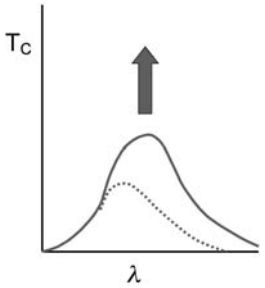

Fig. 10 The value of T_C vs electron-phonon coupling parameter, λ, when the CuO_2 plane is buckled and polarons (stripes) are stable (*dashed line*) and when it is flat (*solid line*). A vibronic mechanism will push it up further

6.2 Role of the Spin

The discussion above converged to the speculation that the local AFM order competes against superconductivity. This idea is diametrically opposed to the conventional thinking of the majority. While the majority can always be wrong, could we ignore preponderance of evidence on the significance of the spins that led the majority to conclude that they play the dominant role in the mechanism? The cuprates are very complex systems with a number of competing degrees of freedom. It is only reasonable to assume that this complexity is not unrelated to the remarkable HTSC phenomenon in this family of compounds [49]. Then, rather than to try to attribute the mechanism to a single degree of freedom, why not consider the synergetic effect of all degrees of freedom? The question should not be whether "spin or lattice", but how spin and lattice can work together to create this phenomenon.

The first hint in that direction is that our calculations show an unexpectedly strong dynamic spin-charge-phonon coupling. Aside from the role of this coupling for the formation of the stripe phase, the important consequence is that the phonons bring down the energy scale of spin excitations as well as charge excitations to the level of the phonon energy. Thus phonons are dynamically dressed by spin as well as by charge. This may justify calling this *e-p* interaction "unconventional". Note that this effect of LO phonons cannot be correctly described by the *t-J* Hamiltonian, since in the *t-J* model the effect of the oxygen phonon on the Cu-Cu exchange is integrated over the phonon $\boldsymbol{q}$ vector, while the *t-J* model and the RVB theory is effective in describing the zone-boundary mode producing Cu-Cu dimers in the local singlet state [71].

This spin-charge-phonon coupling brings about an interesting possibility of a synergetic effect of spin, charge and lattice in pair formation. The regular spin fluctuation mechanism based upon the AFM correlations has a disadvantage that if the spin correlation is strong the carrier mobility is low, while if the spin correlation is weak the spin excitation energy is low. The spin-phonon coupling mechanism pegs the excitation frequency to the phonon frequency, so that the coupling strength will not be weakened when the spin correlation becomes weak [72]. Furthermore the recent observation on the dispersion of spin excitation [73, 74] may be related to the resonance of spin excitations with the phonons. The dispersion of spin excitations shown in [73] has a node around 60 meV, very close to the zone-boundary LO phonon energy. It is possible that the resonance above the phonon energy and anti-resonance below created the rotation of the incommensurate pattern as observed.

7 Concluding Remarks

The majority opinion today on the role of phonons in the mechanism of high-temperature superconductivity is still strongly negative. However, this bias is largely based upon the assumption of the conventional *e-p* coupling mechanism, while the *e-p* coupling in the cuprates can be unconventional, due to strong covalency, ionicity and electron correlation. Our recent calculation shows that the Cu-O bond-stretching phonons are strongly coupled both charge and spin, through the phonon-induced spin-polarized charge transfer between Cu ions through oxygen. Such an unconventional *e-p* coupling can produce effects not included in the BCS theory. In addition spatial inhomogeneity appears to be an indispensable ingredient of the HTSC phenomenon, even though it is difficult to comprehend why inhomogeneity helps, rather than hurts, superconductivity. A distinct possibility to resolve this conundrum is the vibronic, non-adiabatic resonance of phonon, charge and spin. The phonon mechanism is not "conventional" after all in the strongly correlated electron systems such as the cuprates, and could even be a significant part of the mechanism of high temperature superconductivity.

Acknowledgments The author acknowledges K.A. Müller, J.B. Goodenough, L. Gor'kov, J.C. Phillips, P.W. Anderson, A. Bussmann-Holder, N. Nagaosa, M. Khomoto, Z.-X, Shen, A. Lanzara, D. Mihailovic, E. Weger, J.J. Tu, E.W. Plummer, A.R. Bishop, M. Tachiki, R.J. McQueeney, M. Yethiraj, H.A. Mook, P. Dai, M. Arai, C. Frost, S. Tajima, Y. Endoh, for valuable insights, discussions and comments. This work was supported by the National Science Foundation through DMR01-02565.

References

1. Bednorz JG, Müller KA (1986) Z Phys B 64:189
2. Frank JP (1993) In: Ginsberg D (ed) Physical properties of high temperature superconductors III. World Scientific, Singapore, p 189
3. For example: Anderson PW (1997) The theory of superconductivity in the high-T_C cuprates. Princeton University Press, Princeton
4. Bianconi A (this volume)
5. Bogdanov PV et al. (2000) Phys Rev Lett 85:2581
6. Gweon GH, Sasagawa T, Zhou SY, Graf J, Takagi H, Lee DH, Lanzara A (2004) Nature 430:187
7. Ishihara S, Egami T, Tachiki M (1997) Phys Rev B 55:3163
8. Petrov Y, Egami T (1998) Phys Rev B 58:9485
9. Lanzara A (unpublished)
10. Zhao G-M, Hunt MB, Keller H, Müller KA (1997) Nature 385:236
11. Khasanov R, Shengelaya A, Conder K, Morenzoni E, Savic IM, Keller H (2003) J Phys Cond Mat 15:L17
12. Allen PB (2001) Nature 412:494
13. Pao C-H, Schüttler H-B (1995) J Supercond 8:633

14. Tachiki M, Machida M, Egami T (2003) Phys Rev B 67:174506
15. McMillan WL (1968) Phys Rev 167:331
16. Allen PB, Dynes RC (1975) Phys Rev B 12:905
17. Slater JC (1950) Phys Rev 78:748
18. Hippel AR von (1970) J Phys Soc Japan 28 [Suppl 1]
19. Resta R (1992) Ferroelectrics 136:51
20. King-Smith RD, Vanderbilt D (1993) Phys Rev B 47:1651
21. Resta R (1994) Rev Mod Phys 66:899
22. Zaanen J, Sawatzky GA, Allen JW (1985) Phys Rev Lett 55:418
23. Piekarz P, Egami T (unpublished)
24. Basov DN, Singley EJ, Dordevic SV (2002) Phys Rev B 65:054516
25. Molegraaf HJA, Presura C, Marel D van der, Kes PH, Li M (2002) Science 295:2239
26. Santander-Syro AF, Lobo RPSM, Bontemps N, Konstantinovic Z, Li ZZ, Raffy H (2003) Eur Phys Lett 62:568
27. Cowley RA (1962) Phys Rev Lett 9:159
28. Pintschovius L, Pyka N, Reichardt W, Rumiantsev AY, Mitrofanov NL, Ivanov AS, Collin G, Bourges P (1991) Physica C 185/189:156
29. Pintchovius L, Reichardt W (1994) In: Ginsberg D (ed) Physical properties of high temperature superconductors IV. World Scientific, Singapore, p 295
30. McQueeney RJ, Petrov Y, Egami T, Yethiraj M, Shirane G, Endoh Y (1999) Phys Rev Lett 82:628
31. Egami T, Chung J-H, McQueeney RJ, Yethiraj M, Mook HA, Frost C, Petrov Y, Dogan F, Inamura Y, Arai M, Tajima S, Endoh Y (2002) Physica B 62:316
32. Chung J-H, Egami T, McQueeney RJ, Yethiraj M, Arai M, Yokoo T, Petrov Y, Mook HA, Endoh Y, Tajima S, Frost C, Dogan F (2003). Phys Rev B 67:014517
33. Mizuki T, Endoh Y (private communication)
34. Krakauer H, Pickett WE, Cohen RE (1993) Phys Rev B 47:1002
35. Falter C, Hoffmann GA (2000) Phys Rev B 61:14537; (2001) Phys Rev B 64:054516
36. Tachiki M, Takahashi (1988) Phys Rev B 38:218
37. Tachiki M, Takahashi (1989) Phys Rev B 39:293
38. Ginzburg VL, Kizhnits DA (1976) High temperature superconductivity. Consultants Bureau, New York
39. Ranninger J (1992) In: Bar-Yam T, Egami T, Mustre-de Leon J, Bishop AR (eds) Lattice effects in high-TC superconductors. World Scientific, Singapore, p 389
40. Gorkov LP, Sokol AV (1987) JETP Lett 46:420
41. Egami T, Billinge SJL (1996) In: Ginsberg D (ed) Physical properties of high temperature superconductors V. World Scientific, Singapore, p 265
42. Pan SH, O'Neal JP, Badzey RL, Chamon C, Ding H, Engelbrecht JR, Wang Z, Eisaki H, Uchida S, Gupta AK, Ng K-W, Hudson EW, Lang KM, Davis JC (2001) Nature 413:282
43. Lang KM, Madhavan V, Hoffman JE, Hudson EW, Eisaki H, Uchida S, Davis JC (2002) Nature 415:412
44. For example: Bobroff J et al. (2002) Phys Rev Lett 89:157002; Loram JW, Tallon JL, Liang WY (2004) Phys Rev B 69:060502
45. Sendyka TR, Dmowski W, Egami T, Seiji N, Yamauchi H, Tanaka S (1995) Phys Rev B 51:6747
46. McQueeney RJ, Sarrao JL, Pagliuso PG, Stephens PW, Osborn R (2001) Phys Rev Lett 87:77001
47. Egami T (2001) AIP Conf Proc 554:38
48. Martin I, Kaneshita E, Bishop AR, McQueeney RJ, Yu ZG (2004) Phys Rev B 70:224514
49. Phillips JC, Saxena A, Bishop AR (2003) Rep Prog Phys 66:2111

50. Timusk T, Statt B (1999) Rep Prog Phys 62:61
51. Tallon JL, Loram JW (2001) Physica C 349:53
52. For example: Kotliar G, Liu J (1989) Phys Rev B 38:5142
53. For example: Castellani C, Di Castro C, Grilli M (1997) Z Phys 130:137
54. Boebinger G et al. (1996) Phys Rev Lett 77:5417
55. For example: Sachdev S (2003) Rev Mod Phys 75:913
56. Bourges P (2000) In: Furrer A (ed) Neutron scattering in novel materials. World Scientific, Singapore, p 252; cond-mat/0009373
57. Loram JW, Luo J, Cooper JR, Liang WY, Tallon JL (2001) J Phys Chem Solids 62:59
58. For example: Saini NL et al. (2003) Eur Phys J B, 36:75
59. Phillips JC (1990) Phys Rev B 41:8968
60. Phillips JC (2002) Phys Rev Lett 88:216401
61. For example: Bianconi A (2000) Int J Mod Phys B 14:3289
62. Goodenough JB, Zhou J (1990) Phys Rev B 42:4276
63. Hwang HY et al. (1995) Phys Rev Lett 75:914
64. Egami T, Louca D (2002) Phys Rev B 65:094422
65. Ramirez AP (1997) J Phys Cond Matter 9:8171
66. Radaelli PG et al. (1997) Phys Rev B 56:8265
67. Fernandez-Baca JA et al. (1998) Phys Rev Lett 80:4012
68. Louca D, Egami T (1999) Phys Rev B 59:6193
69. Büchner B, Breuer M, Freimuth A, Kampf AP (1994) Phys Rev Lett 73:1841
70. Chmaissem O, Jorgensen JD, Short S, Knizhnik A, Eckstein, Shaked H (1999) Nature 397:45
71. Shen Z-X, Lanzara A, Ishihara S, Nagaosa N (2002) Phil Mag B 82:1349
72. Jarborg T (2002) Phys Lett A 295:154
73. Hayden SM, Mook HA, Dai PC, Perring TG, Dogan F (2004) Nature 429:531
74. Tranquada JM, Woo H, Perring TG, Goka H, Gu GD, Xu G, Fujita M, Yamada K (2004) Nature 429:534

Struct Bond (2005) 114: 287–330
DOI 10.1007/b101023

Nanoscale Lattice Fluctuations in Cuprates and Manganites

Antonio Bianconi (✉) · Naurang L. Saini

Dipartimento di Fisica, Università di Roma "La Sapienza", P. le A. ldo Moro 2, 00185 Roma, Italy

Abstract Local lattice displacements giving a nanoscale inhomogeneous pattern due to mesoscopic phase separation in the correlated transition metal perovskites play a distinct role for high T_c superconductivity (HTcS) in the copper oxides and for colossal magneto resistance (CMR) in manganese oxides. Experimentally the local structure physics of these correlated oxides owes a lot to the extended X-ray absorption fine structure (EXAFS) using polarized synchrotron radiation sources, a local and fast experimental probe that has revealed several key structural aspects. Here we have briefly reviewed some of our studies

on the local displacements in the electronically active Cu-O lattice in the copper oxide superconductors and the Mn-O lattice of the manganese oxide CMR and charge ordered systems, exploiting the EXAFS technique. In the copper oxides the determination of polaronic distortions by polarized Cu-K-edge EXAFS has revealed superlattice of distorted stripes intercalated with undistorted stripes with the chemical potential tuned near a shape resonance for the interband scattering in a system with two electronic components that can amplify the critical temperature. On the other hand, the Mn K-edge EXAFS has been applied to underline the importance of the local Mn-O displacements to characterize various phases in the perovskite manganese oxides.

Keywords Lattice distortions · Nanoscale heterogeneitics · Cuprates · Manganites

1 Introduction

Advances in the materials growth techniques and development of new experimental tools have generated a wealth of information with significant implications on the complex phases of the condensed matter, with the highly correlated transition metal oxides revealing exotic quantum phenomena [1–6]. In the case of the highly correlated oxides the mere knowledge of the long-range crystallographic structure does not help to explain their basic properties, such as the high T_c superconductivity (HTcS) in the copper oxides (cuprates), colossal magneto resistance (CMR) in the manganese oxides (manganites) [7–11] and the fascinating metal-insulator transition in the other related oxides [4]. Indeed, the basic characteristics of these doped oxides appear to depend strongly on the nanoscale and local atomic structure that has been revealed by a series of experiments sensitive to the local structure and the nanoscale electronic structure [12–17].

Let us take the example of cuprates, which are layered materials with CuO_2 planes separated by the insulating rocksalt oxide layers. The importance of the CuO_2 planes has created a major interest to study electronic and structural behaviour of these basic structural elements since the discovery of the superconductivity in these materials. In fact, thanks to the experimental and theoretical efforts of more than a decade and half, the research in the high T_c cuprates has entered in a new phase where it is becoming recognized that the electronic ground state of these oxides is more complex than considered at the beginning. As a matter of fact, the material evolves from an insulator to a superconductor by introducing holes into the parent antiferromagnetic insulator. Indeed it is hard to understand the normal and the superconducting state properties of these materials by considering simply the spin and charge degrees of freedom in a doped 2D anti-ferromagnetic CuO_2 lattice. The expected intrinsic electronic properties (charge and spin dynamics) of a homogeneous low density 2D correlated electron fluid in a doped Mott insulator [18] have not succeeded in explaining the complex experimental features of the metallic phase of high T_c superconductors. There is now a growing consensus that the anom-

alous electron-lattice interactions, the fundamental basis for the superconductivity in metals, in a correlated electron fluid are a key ingredient for the normal and the superconducting state of these oxides [12, 13]. Recent experiments on the electronic structure have indicated a possible energy scale related to the Cu-O displacements [19] that appears to be having a direct influence on a possible electron-phonon interaction in these materials [20–23]. In addition, the isotope effect experiments [24–28] cannot be ignored, which creates a further plateform to treat these materials with proper consideration of the electron-lattice interactions. It should be emphasized that the electronic pairing correlations in the cuprate superconductors are of short range character, resulting the short coherence length; therefore the local structure rather than the average one could have a key importance in these materials.

The characterization and quantification of the local lattice distortions in these materials has shed light on the tendency toward phase separation [2, 29] at the metal to insulator transition and/or at critical charge densities where the Fermi surface changes its topology, known as electronic topological transitions (ETT) [30]. In these systems the phase separation occurs at mesoscopic or nanoscale length scales, giving the striped phases [13] that can compete or coexist with the superconductivity. Incidentally, in addition to the short range nature of the superconducting correlations, the self-organized textures of electrons and molecules, related with the interplay of the charge, spin and lattice excitations, appear over a short length scale. The later is also true for the other transition metal oxides as the CMR manganites, nickelates and other related systems [4, 12, 13], and therefore the study of the local atomic displacements is needed for the understanding of the physics of these transition metal oxides.

The main experimental probes, used to determine the local displacements in the transition metal oxides, are the pair distribution function (PDF) analysis of neutron and x-ray diffraction, extended x-ray absorption fine structure (EXAFS) and ion channelling [31–38]. The PDF is based on real space (Fourier transform) analysis of diffraction patterns measured up to high wave vector, involving diffuse peaks due to atomic displacements, in addition to the main diffraction peaks, and hence is a probe of the local structure, providing information on the distribution of the atomic distances [39]. On the other hand, the ion channelling exploits any change in the channelling yield of ions through various crystallographic planes due to atomic displacements, providing information on the local structure in a very short time scale ($\sim 10^{-15}$ s) [40]. The most direct method to probe local structure is EXAFS, which is a site selective method, providing information on the local atomic distribution around a selected absorbing site through scattering of the photoelectron exited from the X-ray absorbing atom with near neighbours [41, 42]. Although these techniques have their own limitations to determine quantitative atomic displacements, there is good agreement on the local lattice displacements determined by these techniques in the complex transition metal oxides [31–38].

The contribution of EXAFS has been vital due to availability of high brilliance and polarized X-ray synchrotron radiation sources. In combination to

the recent technical advances and available high brilliance polarized X-ray synchrotron radiation sources, the EXAFS spectroscopy has allowed us to determine directional and quantitative atomic displacements, offering a unique approach to pin point short-range atomic displacements and their dynamics, being a fast (~10^{-15} s) and local (~5–6 Å) probe [41, 42].

Here we have briefly reviewed some of the important results on the local structure of the cuprate superconductors. We have focused on the problems of intrinsic local charge and structural inhomogeneities and superconductivity in the copper oxides. We also report some results on the manganites, that appear to show self-organization and texturing at a short length scale to point out similarities and differences between the two classes of materials. We have limited the presentation to the studies of the local structure by EXAFS, and referred the related work, wherever required in the text. The following section is dedicated to the basic concepts on the EXAFS as a probe of local and instantaneous atomic displacements, involving also the salient features of the data analysis and the experimental approach used with relevant justifications. Here we have restricted the focus on the experimental results on the local structure around the transition metal site (Cu in the cuprates and Mn for the manganites) obtained by the EXAFS studies made at the K-edge of the respective elements, i.e., Cu K-edge and Mn K-edge EXAFS. We have described characteristic local displacements around the Cu, measured on various copper oxide superconductors using polarized Cu K-edge EXAFS. This is followed by the results providing further insight to the local displacements within the CuO_2 plane, revealing asymmetry of the square plane, which seems to have direct implication on the fundamental electronic structure and the pairing interaction in the cuprate superconductors. The following section is dedicated to the local displacements with variable Cu-O bonds, underlying importance of the strain fields in the superconductivity and the self-organized texturing in these metal oxides. We have also provided some results on the effect of external disorder (i.e., the substitutional disorder) on the local Cu-O displacements in these materials. The last part of the results is to describe the characteristic local displacements, measured by Mn K-edge EXAFS on the charge ordered and CMR manganites, with the $La_{1-x}Ca_xMnO_3$ as a model system. This has been followed by a brief summary with relevant conclusions drawn on the basis of the local structure with respect to the electronic properties.

2
Basics of the EXAFS as a Probe of Local and Instantaneous Displacements

Before getting through the experimental results, we would like to recall briefly the basic aspects of the X-ray absorption technique, focusing on the EXAFS. The X-ray absorption coefficient μ(E) is generally given by the product of the matrix element times the joint density of states for the electronic transitions from the initial to final states. It can be solved in the real space for electronic

transitions from an initial localized core level to a final state, described as an outgoing spherical wave which interferes with the waves backscattered from the neighbouring atoms [41–46], i.e.,

$$\mu(E) = \mu_0(E)\,[1 + \sum_{n\geq 2} \chi_n(E)] \tag{1}$$

where $\mu_0(E)$ is the so-called atomic absorption coefficient for the selected atomic core level and $\chi_n(E)$ represents the contribution arising from all multiple scattering pathways beginning and ending at the central absorbing atom and involving (n–1) neighbouring atoms.

The modulation function $\chi(E)$ can be extracted from the experimentally recorded absorption coefficient and is given as

$$\chi(E) = \sum_{n\geq 2} \chi_n(E) = \frac{\mu(E) - \mu_0(E)}{\mu_0(E)} \tag{2}$$

The shortest scattering pathway is the one which involving the first shell with only the single scattering term $\chi_2(E)$ being relevant. This term can be isolated from the $\chi_n(E)$ by the Fourier filtering because multiple scattering pathways for the first shell, that contribute to $\chi_n(E)$ with $n\geq 3$ as well as all contributions from further shells, at longer scattering path lengths.

The single scattering EXAFS signal $\chi_2(k)$ for the first shell can be written as

$$\chi_2(k) = \frac{S_0^2\, e^{-2R_i/\lambda}}{kR_i^2} A_i(k) \cdot e^{-2k^2\sigma_i^2} \sin[2kR_i + \delta_i(k)] \tag{3}$$

where R_i is the radial distance for the first shell and $\delta_i(k)$, the phase function determined by both the photoabsorber and the nearest neighbour backscatterer. The S_0^2 is an amplitude correction factor due to the photoelectron correlation and is also called the passive electron reduction factor, $A_i(k)$ is the scattering power, λ is the photoelectron mean-free path and the σ_i^2 is the correlated Debye Waller factor of the photoabsorber-backscatterer pairs. The scattering power is given by $A_i(k)=N_i^* F_i(k)$, where N_i^* is the average coordination number and $F_i(k)$ is the backscattering amplitude of the neighbouring atoms, and hence Eq. (3) takes the following form:

$$\chi_2(k) = \sum_i N_i^* \frac{S_0^2\, e^{-2R_i/\lambda}}{kR_i^2} F_i(k) \cdot e^{-2k^2\sigma_i^2} \sin[2kR_i + \delta_i(k)] \tag{4}$$

Here the photoelectron wave vector (k) is given by

$$k = \frac{p}{\hbar} = \frac{\sqrt{2m(E - E_0)}}{\hbar} \tag{5}$$

E is the incident photon energy while E_0 is zero of the ejected photoelectron energy.

For the oriented single crystal samples the EXAFS signal has a dependence on the angle between the preferred sample direction and the X-ray polarization vector. The EXAFS equation for the polarized K-edge EXAFS can be generalized as

$$\chi_2(k) = \sum_i 3N_i \cos^2(\theta_i) \frac{S_0^2 \, e^{-2R_i/\lambda}}{kR_i^2} F_i(k) \, e^{-2k^2\sigma_i^2} \sin[2kR_i + \delta_i(k)] \quad (6)$$

where N_i is the equivalent number of neighbouring atoms at a distance R_i sitting at the angle (θ_i) with respect to the direction of the electric field of the polarized X-ray beam [28]. Therefore, with the polarized light and single crystal samples, the EXAFS could be exploited to obtain information on directional local structure. In fact, the approach of the polarized EXAFS is very useful to study the local structure of complex systems such as the high T_c cuprates and the CMR manganites.

To extract the structural parameters from an EXAFS signal, the shift of the photoelectron energy origin E_0 and the phase shifts should be known. These parameters can be either fixed or allowed to vary when an experimental EXAFS is parameterised. For the complex systems such as the high T_c cuprates and the CMR manganites, the K-edge EXAFS probes a cluster of about 5–8 Å around the central absorbing atom. Therefore, the Cu-K-edge EXAFS is an ideal probe to investigate microscopic changes in the local lattice structure of the CuO_2 planes in high T_c compounds.

While the CMR manganites has higher disorder, the cuprates have very small disorder and it is generally hard to determine these small atomic displacements using the conventional EXAFS on powder samples due to the fact that there are large correlations between various parameters (amplitude parameters and the phase parameters) to be determined [41]. For this purpose a well-defined approach to decrease the number of parameters is to be used. Polarized EXAFS has a clear edge over the EXAFS from powder samples due to the fact that it permits to determine the small and directional displacements precisely in the complex systems. In addition, it should be mentioned that the polarized EXAFS for the nearest neighbour (1st order correlation function) is very strong and unique technique that permits a quantification of local and small atomic displacements.

Here we focus on the local distortions in the electronically active Cu-O network in the cuprates and Mn-O networks in the manganites, restricting to the first oxygen coordination shell (i.e. in-plane Cu-O bond distances and the Mn-O distances respectively in the two families). In the **E∥ab** Cu K-edge EXAFS on the cuprates, the signal due to the Cu-O bond distances is well separated from the longer bond contributions and can be easily extracted and analysed separately. The extracted EXAFS signals due to the Cu-O bond distances represent only single backscattering of the photoelectron emitted at the Cu site by its nearest neighbour in-plane oxygen atoms and probe the correlation function of the Cu and oxygen pairs. The approach is to avoid any multiple scattering signals that generally make the data analysis complex. We have used the standard procedures to draw the pair distribution function (PDF) of local Cu-O

bond-lengths from analysis of the EXAFS oscillations only due to the Cu-O distances. In this procedure the EXAFS signal due to the Cu-O is simulated by the least squares fit with an input model containing a distribution of several distances (where the N_{tot} is fixed to the nominal value and σ^2_{CuO} for each distance is given by the Einstein model for a correlated Cu-O distribution) respecting the number of allowed fit parameters to be less than ($2\Delta R\Delta k/\pi$) [41]. The only variable parameter is the relative probability of different distances with a constraint of N_{tot} to be fixed. Same results were obtained while two distances model was used to fit the Cu-O EXAFS (with fit parameters are the two distances (R) their relative probabilities and the associated two σ^2_{CuO}) for deriving the PDF. The feasibility of these methods has been shown earlier for the case of cuprates [34–38, 47, 48] and other complex systems [50, 51]. Similar approach has been used to determine the PDF of Mn-O bonds for the case of manganites.

Here we should mention that the all the measurements presented here are performed in the fluorescence yield (FY) mode using multi-element Ge x-ray detectors array [52, 53]. The emphasis was given to measure the spectra with a high signal to noise ratio and up to a high momentum transfer and purposefully we measured several scans to accumulate the total fluorescence counts to be ~3 million to limit the relative errors to be less than 0.1% above the absorption threshold. The EXAFS signals were corrected for the X-ray fluorescence self-absorption before the analysis [54–56]. For further details on the experiments and data analysis we refer our earlier publications [34–38, 47, 48, 57, 58].

3
Local Structure of the High T_c Cuprates by Cu K-edge EXAFS

3.1
Characteristic Local Cu-O Displacements in the Cuprates

By exploiting the polarized EXAFS on various cuprate superconductors, we have revealed the characteristic Cu-O local displacements in these oxides. Here we will start the discussion with presentation of these experimental data, suggesting that the local Cu-O distortions in these oxides resemble with the Q_2 type of the phonon mode [59].

Figure 1 shows an example of the pair distribution function (PDF) of the Cu-O bonds in the $La_{1-x}Sr_xCuO_4$ (x=0.15) determined by the in-plane and the out-of-plane polarized EXAFS, probing respectively the Cu-O(planar) and Cu-O(apical) bond lengths. The PDF indicates that a part of the Cu-O lattice sites is distorted with Q_2-type symmetry associated with the Jahn-Teller (JT) distortions in the cuprates. The Q_2-type distortion is pictorially represented as the inset of Fig. 1.

These local lattice distortions detected by the EXAFS are found to be similar in different families of cuprate superconductors [34–38, 47, 48, 57, 58]. We have compared the distribution of the Cu-O bonds (lower panel of Fig. 1) in

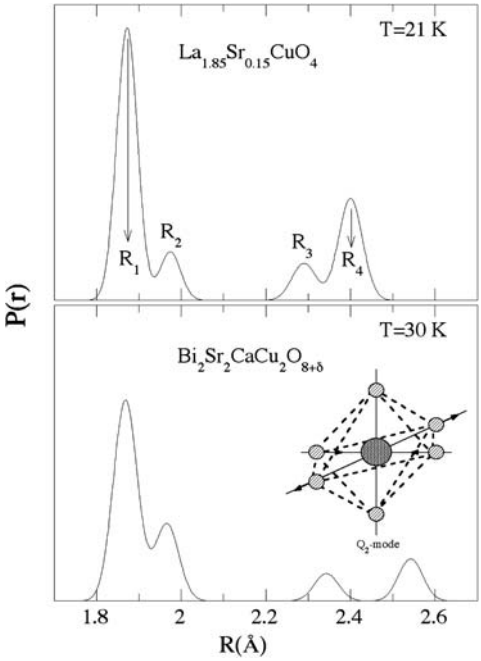

Fig. 1 Pair distribution function (PDF) of Cu-O bonds in the $La_{1.85}Sr_{0.15}CuO_4$ (*upper*) and $Bi_2Sr_2CaCu_2O_{8+\delta}$ (*lower*) systems measured by the in-plane and the out-of-plane polarized EXAFS, probing respectively the Cu-O(planar) and Cu-O(apical) bond lengths. The *inset* to the lower panel shows a pictorial view of the Q_2 mode of the Jahn-Teller distortions. The *circles with shadow* represent the metallic ion and the *circles with diagonal bars* represent the oxygens. In the Q_2 mode two oxygen atoms moved away and two get closer

the $La_{2-x}Sr_xCuO_4$ (LSCO) system (CuO_6 octahedra) with the one in the $Bi_2Sr_2CaCu_2O_{8+\delta}$ (Bi2212) system (CuO_5 pyramids). There are two well separated Cu-O(planar) distances ($\Delta R \sim 0.08$ Å) for the CuO_4 square planes in both systems. It is worth mentioning that the two in-plane distances are within the range of the average Cu-O(planar) distances in the crystallographic structures of all synthesized cuprate superconductors [60, 61]. The short Cu-O(planar) bond lengths are approximately similar to the one observed in the average crystallographic structure; however, the longer anomalous Cu-O(planar) bonds, R_2=1.96 Å seem to be associated with a tilting of the CuO_4 square planes in the (110) direction, resulting in two oxygen atoms per CuO_4 square plane getting displaced along the c-axis (two long bonds R_2 and two short bonds R_1) with a rhombic distortion (Q_2-type) as in the low temperature tetragonal (LTT) like structure [62].

The presence of two Cu-O(apical) distances, R_3 and R_4, separated by $\Delta R \sim 0.14 \pm 0.02$ and 0.18 ± 0.02 Å for the LSCO and Bi2212 systems respectively, is a consequence of the distortions in the CuO_4 square plane where the short Cu-O(apical) bonds R_3 are the anomalous ones, associated with the distorted CuO_6

(CuO_5) octahedra (pyramids) since in a rhombic distortion the in-plane elongation is accompanied by the out-of-plane bond shortening, as indeed the case for the cuprates [59]. The amplitude of the Cu-O displacements, determined by the elongation of the Cu-O bonds, suggests that the distortions in the cuprates are in an intermediate electron-lattice coupling regime.

It should be mentioned that the rhombic distortions with in-plane elongation are observable only below a characteristic temperature T* where it is possible to detect the anomalous long Cu-O(planar) bonds, larger than the amplitude of the thermal fluctuations. On the other hand, the Cu-O(planar) PDF shows a single peak above this temperature with a width determined by the thermal fluctuations. This is illustrated in Fig. 2 where we have shown the Cu-O(planar) PDF for the LSCO system at T>T* and T<T* [37, 47].

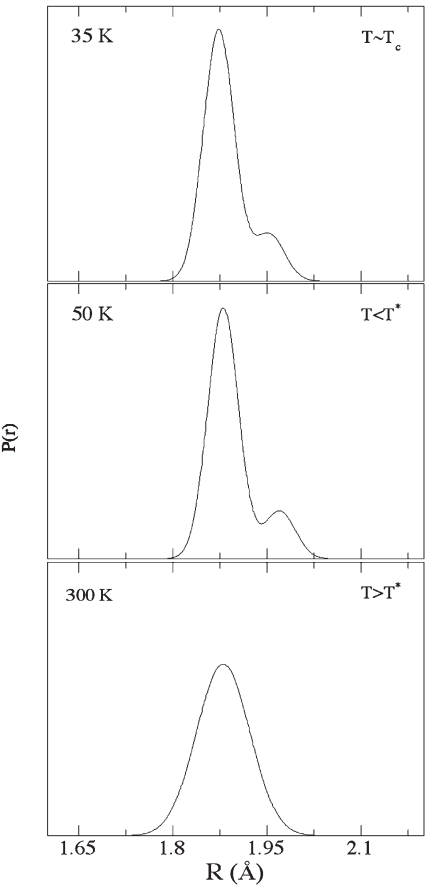

Fig. 2 The Cu-O(planar) PDF at T<T* (50 K and 35 K) and at T>T* (300 K) in the LSCO system [37]. The Q_2-type of distortions are observable below a temperature T* where we could detect the anomalous long Cu-O(planar) bonds, larger than the amplitude of the thermal fluctuations

As shown above, the rhombic Cu-O local displacements appear to be characteristic to the high T_c cuprates, revealed by a the fast technique such as EXAFS; however, the dynamics of these could vary in different families and at different doping, implying different T* for different families, that could be different if measured by other probes depending on the time scales of the techniques used.

3.2 Asymmetry of the in Plane Cu-O Displacements

Having discussed the nature of the local Cu-O displacements, characteristic to the cuprate superconductors, we would now restrict our focus on the in-plane Cu-O displacements. Exploiting the polarization dependence of the EXAFS signal we have found that the local Cu-O displacements in the two orthogonal Cu-O bond directions (denoted as a_t and b_t) are different [63]. For this work, the $Bi_2Sr_2CaCu_2O_{8+\delta}$ (Bi2212) has been taken as a model system, also due to the fact that this system has been widely studied to explore intrinsic inhomogeneities and their implication on the fundamental electronic structure, being suitable for a wide range of experimental techniques. Figure 3 shows the Fourier transform (FT) of the EXAFS signals measured on the Bi2212 system with polarization vector of the synchrotron light falling parallel to the two orthogonal in-plane Cu-O bonds. Just to recap, the peaks in the FT are due to the backscattering of the emitted photoelectrons from the neighbouring atoms and hence the FT provides a global atomic distribution around the absorbing site (around Cu in the present case). The peaks do not represent the real atomic distances and the position should be corrected for the photoelectron backscattering phase shifts to find the quantitative value to the atomic positions with respect to the Cu atom. There are evident differences in the FT along the two polarizations with major differences around the Cu-Sr/Ca peak. The Cu-O peak in the $E \| b_t$

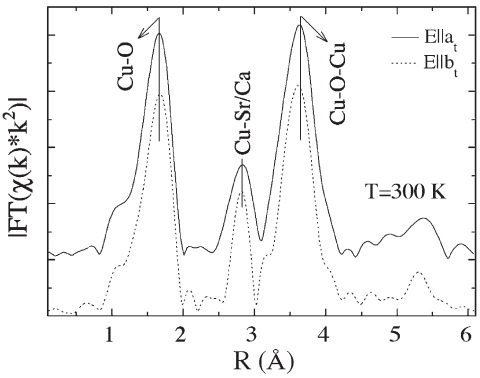

Fig. 3 Magnitude of the Fourier transform $|FT(k^2\chi)|$ of the EXAFS spectra measured in the two orthogonal Cu-O-Cu bond directions (denoted by $\mathbf{E}\|\mathbf{a}_t$ and $\mathbf{E}\|\mathbf{b}_t$). The k range is 3–19 $Å^{-1}$ and no correction has been made for the phase shifts due to photoelectron backscattering

appears to be shifted towards higher R while the Cu-O-Cu peak shows a shift towards lower R-value. On the other hand, the Cu-Sr/Ca peak shows a large increase and gets sharp in the E‖b_t geometry. The anisotropy in the distribution of Sr/Ca atoms suggests a large re-distribution of the Cu-Sr/Ca bonds and complex distortions of the lattice. Although the absolute differences may be difficult to extract due to complex interference effects of different backscatterings of the photoelectrons, the evident differences are large enough to state that the atomic distribution is anisotropic with respect to the two Cu-O-Cu directions.

The anisotropy along the two orthogonal Cu-O bond directions within the CuO_2 plane was quantified by the modelling of the EXAFS spectra due to the Cu-O bonds using the similar approach as discussed in the previous sections [34–38, 47, 48, 57, 58, 63]. Figure 4 shows the PDF of the CuO_2 plane along the two orthogonal Cu-O bond directions. The resulting distribution lies in the range of 1.8–2.05 Å, independent of the polarization direction. The PDF obtained in the a_t direction at 300 K is compared (lower panel) with the PDF obtained by the analysis of the EXAFS spectra measured in the same direction at low temperature (30 K). The bond distribution well reproduces the results at low temperature (see, for example, the previous section); however, due to larger distance

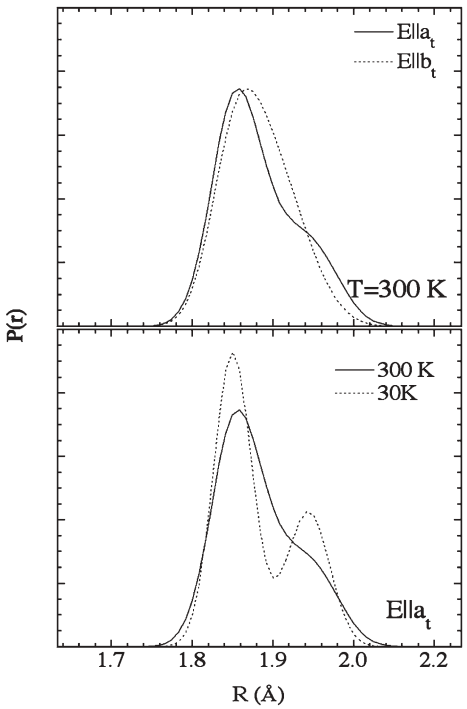

Fig. 4 Cu-O pair distribution along the two orthogonal Cu-O-Cu directions (*upper*). The distribution in the **E‖a**$_t$ (*solid line*) at 300 K is compared with that of at 30 K in the same direction (*lower*)

broadening at higher temperature the PDF at 300 K show an asymmetric distribution of the Cu-O bonds instead of a clear two peak function at 30 K. The large distribution of the Cu-O distances along the two orthogonal directions within the CuO_2 plane evidently shows distorted nature of the square plane.

The PDF along the two Cu-O-Cu bond directions are different. While the Cu-O distribution along the E‖b_t is a single peak function (however broad) centred around the average bond length (~1.9 Å), the distribution along the E‖a_t appears with more like a two peak function (appearing at ~1.88 Å and ~1.98 Å). The PDF evolves in a clear two-peak function at low temperature (lower panel of Fig. 3 comparing the PDF along $\mathbf{a}_t$ direction at 30 K and 300 K). The outcome of the present experiment, shown as PDF at 300 K, not only indicates anisotropy of the Cu-O distribution in the CuO_2 square plane but also provides an evidence for a preferential tilting of the CuO_2 plane giving higher probability of longer and shorter bonds arranged in one of the two Cu-O-Cu directions. This observation is consistent with the electronic anisotropy of the Γ-M and Γ-M1 directions at the Fermi surface of the Bi2212 system [64, 65]. The present experiment adds further information and suggests preferential tilting of the CuO_2 planes with higher probability of shorter and longer Cu-O bonds in the $\mathbf{a}_t$ direction. Recently anomalous phonon dispersion has been interpreted as a dynamic unit cell doubling in the CuO_2 plane along the direction of Cu-O-Cu bonds giving a short range charge ordering [33, 66–68]. The present experiment can account the dynamic unit cell doubling in the CuO_2 plane along the direction of the Cu-O-Cu bonds as argued on the basis of the anomalous phonon dispersion [63, 69]. In summary, we have shown microscopic anisotropy of atomic distribution along the two orthogonal Cu-O-Cu bonds of the CuO_2 square plane. The pair distribution of the Cu-O bonds along the two orthogonal directions shows significant differences, with preferential elongation and shortening of a part of the Cu-O bonds. We believe that the preferential tilting of the CuO_2 plane, giving anisotropy to the Cu-O bond distribution, is responsible for the evident asymmetry to the Fermi surface of the same system where $(\pi, 0)$ and $(0, \pi)$ points are different. Also this anisotropy results a strong redistribution of the Cu-O orbitals [69] with inhomogeneous charge distribution in the CuO_2 plane.

3.3 Lattice Displacements with Variable Cu-O Bonds

Structurally the high T_c cuprates are heterogeneous materials made of alternated layers of metallic body centred cubic (bcc) CuO_2 layers and insulating rock-salt face centred cubic (fcc) A-O (M= Ba, Sr, La) layers [70–72]. The expected degree of bond length matching between the two intergrowth layers is expressed in terms of the Goldschmidt tolerance factor [70–72] $t = \dfrac{r_{A^{3+}} + r_{O^{2-}}}{\sqrt{2}\,(r_{A^{3+}} + r_{O^{2-}})}$ where $r_{A^{3+}}$, $r_{Cu^{2+}}$ and $r_{O^{2-}}$ are the room temperature ionic radii. The tolerance factor in hole doped cuprates is less than 1 indicating that the lattice mismatch between the

two sub-lattices is such that the CuO_2 sheets are under compression and rock-salt (A-O) layers under tension. The importance of the lattice mismatch (or chemical pressure) on the superconducting transition temperature was noted by several experiments [60, 61, 73–75] showing that T_c is not simply controlled by a single variable: the doping [76].

In order to measure the actual lattice strain in the CuO_2 sublattice we have exploited Cu K-edge EXAFS to obtain the direct measure of the average in plane lattice compressive strain due to mismatch called the micro-strain $\varepsilon = \frac{d_0 - \langle R_{Cu-O} \rangle}{d_0}$, where $\langle R_{Cu-O} \rangle$ is the measured average inplane Cu-O bond-length [77] and d_0 is the Cu-O equilibrium distance, 1.97 Å, that is the Cu^{+2}-O^{-2} bond length measured by EXAFS for a free Cu ion in water. This value is close to that of an unstrained CuO_2 plane ~1.985 (±0.005) Å in undoped $Sr_2CuO_2Cl_2$ [78] considering the correction due to effect of hole doping on the Cu-O bonds (~0.16 doped holes per Cu site). The micro-strain is related to the expected tolerance factor as shown in panel (a) of Fig. 5 however it is a direct measure of the strain field and therefore it has allowed to detect that the superconducting critical temperature at fixed hole doping is a function of the

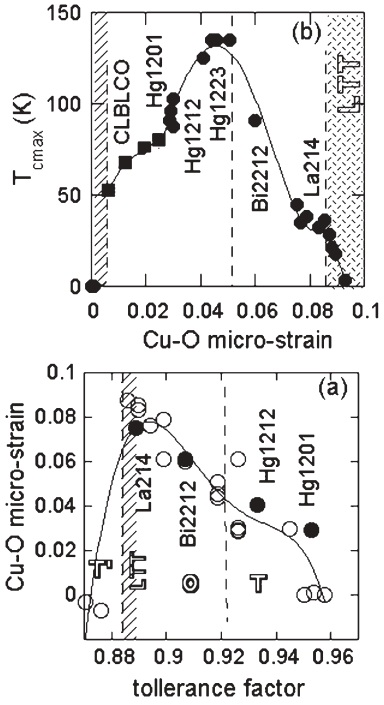

Fig. 5 **a** The measured micro-strain of the Cu-O bond as a function of the expected tolerance factor. **b** The maximum superconducting critical temperature at optimum doping (0.16 holes per Cu site) for many different systems as a function of the Cu micro-strain [77]

strain field as shown in panel (b) of Fig. 5. This shows that the maximum critical temperature at about 135 K occurs for a optimum micro-strain of about 5%. For a micro-strain larger than 8.5% the strain field localizes the doped holes and the insulating striped phase suppresses the superconducting phase in the low temperature tetragonal (LTT) phase.

The $La_2CuO_{4.1}$ (LCO), and $Bi_2Sr_2CaCu_2O_{8+\delta}$ (Bi2212) and $HgBa_2CuO_{4+\delta}$ (Hg1201) (and $HgBa_2CaCu_2O_{6+\delta}$ (Hg1212)) systems are used as representative for the La-based ($[(La_2O_{2+\delta})CuO_2]$), Bi-based ($[Bi_2O_{2+\delta}(Sr_2O_2Ca)Cu_2O_4]$) and Hg-based ($[HgO_\delta(Ba_2O_2)CuO_2]$ (and $[HgO_\delta(Ba_2O_2Ca)Cu_2O_4]$)) superconducting families containing respectively the La-O, Sr-O and Ba-O as rock-salt layers that sustain different chemical pressure on the CuO_2 planes, where the dopants are interstitial oxygen ions in the block layers.

Figure 6a shows the Cu-O pair distribution function (PDF) in the LCO, Bi2212, Hg1201 and Hg1212 systems determined by the EXAFS analysis in the normal state, at a high temperature (T=200 K). The mean Cu-O bond-lengths (vertical bars) show a clear evolution with the change in the chemical pressure on the CuO_2 plane and increases from La-based to Hg-based systems. This is expected due to different mismatch between the rock-salt layers (respectively La-O, Sr-O and Ba-O for the La-based, Bi-based and Hg-based systems) and the CuO_2 lattice, sustaining different chemical pressure on the CuO_2 plane.

To enlighten further the local Cu-O displacements, we have determined the PDF at different temperatures. Figure 6b shows the distribution at three different temperatures for the LCO, Bi2212 and Hg1201 samples. Interestingly the Cu-O bonds distribution for a micro-strain larger than 5% turns asymmetric

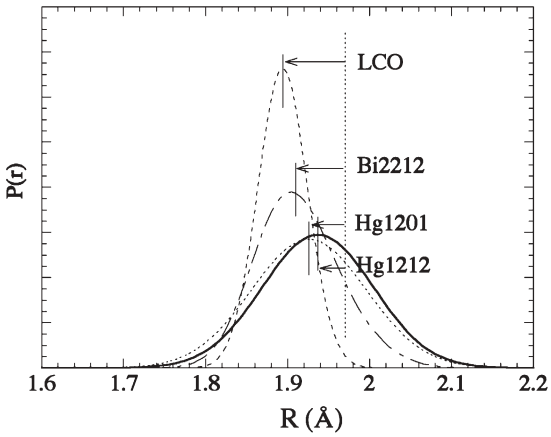

Fig. 6 **a** Cu-O pair distribution function (PDF) for different systems measured at 200 K. The *solid vertical bars* refer to the mean Cu-O distance in the respective systems, while the *dotted vertical bar* represents the Cu-O distance with no chemical pressure (see the text). **b** Cu-O pair distribution function (PDF) above T* (*solid line*) is compared with the PDF below T* (*dashed line*) and below T_c (*dotted line*) for the $La_2CuO_{4.1}$ (*upper*), Bi2212 (*middle*) and Hg1201 (*lower*)

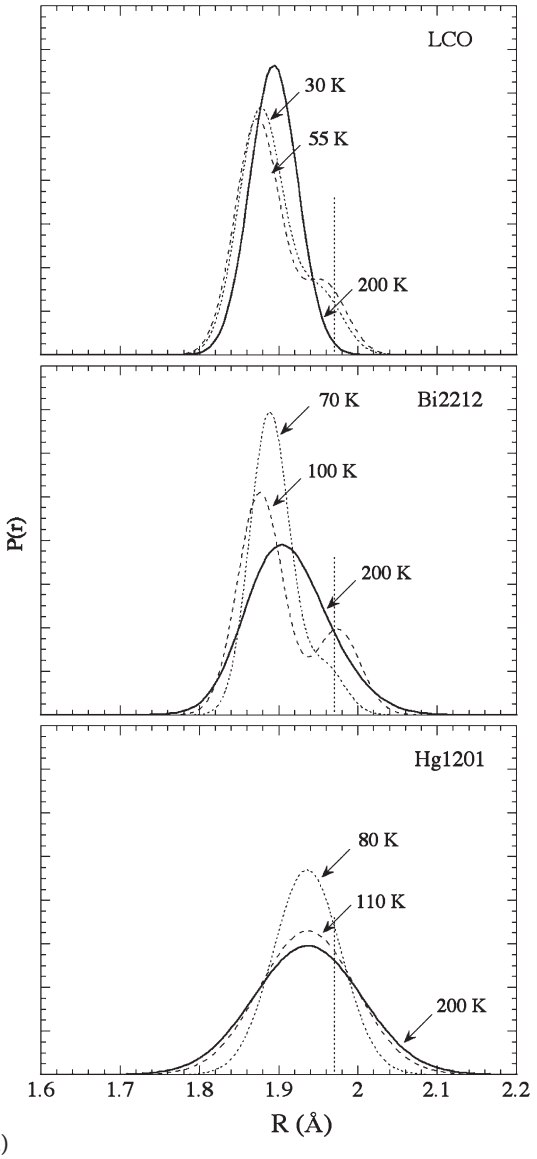

Fig. 6 (continued)

with two peak function below the T* as in the case of LCO (T*~190 K) and the Bi2212 (T*~140 K) systems while for a micro-strain lower than 5% it remains symmetric as for the Hg1201 in the whole temperature range (within the experimental uncertainties). In addition, the pair distribution function reveals a significant change across the superconducting transition temperature T_c (T_c~40 K, 87 K and 94 K respectively for the LCO, Bi2212 and Hg1201 systems respectively).

Here we could briefly summarize this section. We have shown how the local Cu-O displacements evolve with the chemical pressure in the cuprate superconductors while the charge density in the CuO_2 plane is kept fixed (at the optimum doping level with $\delta \sim 0.16$). The temperature dependence of the Cu-O bond distribution shows unusual behavior, turning to a two peak function below the characteristic temperature T*, the temperature which depends on the Cu-O bond lengths. In addition, there is a small change in the distribution function at the superconducting transition temperature, showing a reduced probability of the longer bonds in the two-peak function, revealing importance of electron-lattice interaction in the pairing mechanism. On the basis of the present findings, we can conclude that the chemical pressure on the electronically active CuO_2 plane, that appears to control the electron-lattice interaction is a key parameter to understand the phase diagram in high T_c superconductors.

3.4
Effect of Substitutional Disorder on the Cu-O Displacements

In the previous section we have shown that, while the character of local Cu-O displacements in the cuprates remain similar (rhombic distortions) below the characteristic temperature T* (different for different systems), these distortions vary from system to system and they also depend on the chemical pressure on the CuO_2 plane. Here we would present some results pointing the influence of the substitutional disorder on the Cu-O displacements. We take the La-based cuprates as the model, with the $La_2CuO_{4.1}$ (LCO), $La_{1.85}Sr_{0.15}CuO_4$ (LSCO) and $La_{1.48}Nd_{0.4}Sr_{0.12}CuO_4$ (LNSC) systems representing respectively the oxygen doped, Sr doped and Nd doped systems with increasing substitutional disorder. We find that this disorder in the CuO_2 plane results a significant change in the T* and the associated local Cu-O displacements.

While the Cu-O displacements in the LCO and the LSCO systems are represented in the previous sections, Fig. 7 shows the Cu-O distribution in the LNSC system at two temperatures across the T*, along with the difference between the two distributions [79]. The Cu-O PDF for the LSCO at a temperature $T<T^*$ [37] is also shown for a ready reference to compare the differences between the two systems. The Cu-O distribution in the LNSC displays an asymmetric peak, either at a temperature lower than the T* or above it. There is a small redistribution of Cu-O bonds across the T* that could be seen in the difference. In the anomalous phase at ($T<T^*$) there is an elongation of a part of the Cu-O bonds. This elongation of the Cu-O bonds is similar to the one observed in the LSCO system and associated with appearance of the rhombic distortion of the CuO_2 plane resulting longer Cu-O bonds. However, while the bond distribution gets two-peak function at low temperature, from a single peak function above the T* in the LSCO system [37], it remains asymmetric in the LNSC, with a probability weight transfer across the

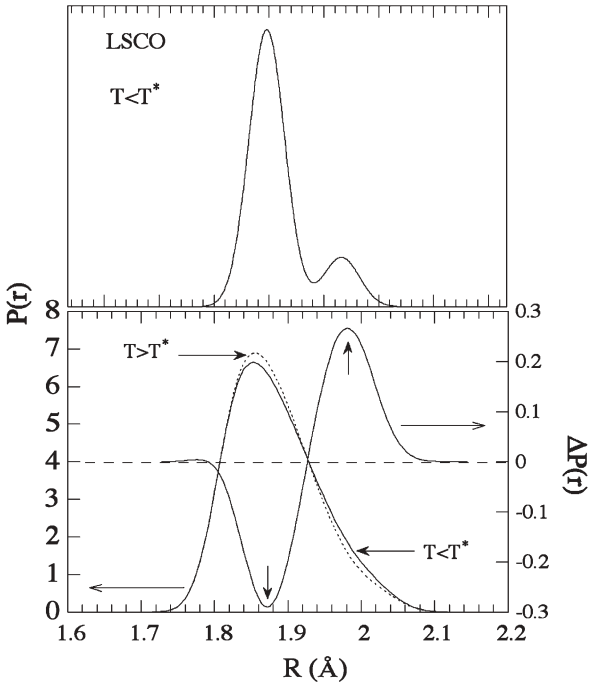

Fig. 7 Cu-O pair distribution for the $La_{1.48}Nd_{0.4}Sr_{0.12}CuO_4$ system for T<T* (*solid line*) and T>T* (*dotted line*) [79] is shown with the difference of the distribution across the T* (*lower*). The Cu-O PDF for the $La_{1.85}Sr_{0.15}CuO_4$ at T<T* is shown [37] for comparison

T* [79]. This further indicates that stripe ordering in the cuprates below the T* is associated with the dynamic local Cu-O displacements rather than a static disorder. The superconductivity survives with stripe ordering associated to a large contribution of dynamic local lattice displacements as the case of LSCO, while it gets anomalously suppressed with charge stripe ordering associated with less dynamic character of local lattice displacements.

It has been reported that the magnetic order plays important role in the superconductivity of the cuprates while the stripe ordering could co-exist with the superconductivity [80]. Indeed the superconductivity gets suppressed when the magnetic order appears [80]. Our finding suggests that the superconductivity disappears when the local Cu-O displacements, associated with the charge stripe ordering, get less dynamic. Commenting the present results with respect to the earlier results on the magnetic order it could be stated that the local Cu-O displacements are less dynamic in presence of magnetic ordering. Therefore the two results compliment each other. Thus the local Cu-O displacements are more static in the absence of superconductivity, while magnetic ordering is present (as shown by other experiments [80]); on the other hand the dynamic contribution gets increased while the system is superconducting with suppressed magnetic order.

4
Instantaneous Local Displacements in Cuprates by Cu K-Edge XANES

4.1
Characteristic Response of Temperature Dependent Local Displacements in the Cuprates

As discussed above, the X-ray absorption spectroscopy is a tool to study instantaneous local lattice distortions, with EXAFS, characterized by the single scattering process [41] probing the first order pair correlation function while the XANES, characterized by the multiple scattering process, determining higher order of the local distribution function [41, 81, 82]. Here we would like to show capabilities of the XANES spectroscopy to measure local and instantaneous displacements in the cuprates, supporting the results obtained by the EXAFS. We have selected few examples of the temperature dependent Cu K-edge XANES results revealing a particular change in the local lattice displacements across the characteristic temperature T* sited above. In fact, the XANES spectra, measuring instantaneous local geometry, show an abrupt change in the temperature dependent spectral weight at this temperature T*. The experimental XANES spectra are interpreted using full-multiple scattering (MS) calculations, reproducing the experimental results [81–83]. The particular temperature dependence of the local displacements has been discussed with several relevant examples.

Figure 8 shows representative Cu K-edge XANES spectra measured on the La-based cuprate system ($La_{1.48}Sr_{0.12}Nd_{0.4}CuO_4$) in the in-plane (**E**∥**ab**) and out-of-plane (**E**∥**c**) polarization geometries [84]. The XANES spectra show the peaks which are denoted by standard notations [85] in the polarized XANES spectra. The main absorption features are denoted by B_1 and B_2 in the **E**∥**ab** spectrum and A_1 and A_2 in the **E**∥**c** spectrum. The unpolarized spectrum is shown in the lower panel (Fig. 8). The unpolarized spectrum contains information on the local and instantaneous displacements in the overall cluster around the central atom. In fact in complex systems, such as the high T_c cuprates, the displacements are anisotropic with doping and temperature and hence the unpolarized spectrum is a useful tool to obtain important information on the local and anisotropic geometrical displacements around the selected site (i.e. the Cu). In the lower panel (Fig. 8), we have shown a difference between a spectrum measured at a temperature (80 K) larger than the T* (~60 K) and a spectrum at a low temperature (20 K).

Absorption features in the polarized Cu K-edge XANES spectrum are due to multiple scattering of the photoelectron emitted at the Cu site in the direction of the electric field, and their physical origin is revealed by the MS calculations for the La_2CuO_4 [85]. The calculated spectrum is also displayed in Fig. 8**.** The details on the calculations could be found in our earlier publications [84–86] for the La_2CuO_4 system, showing a very good agreement for the experimental features in respect to their energy positions and relative intensity. From the

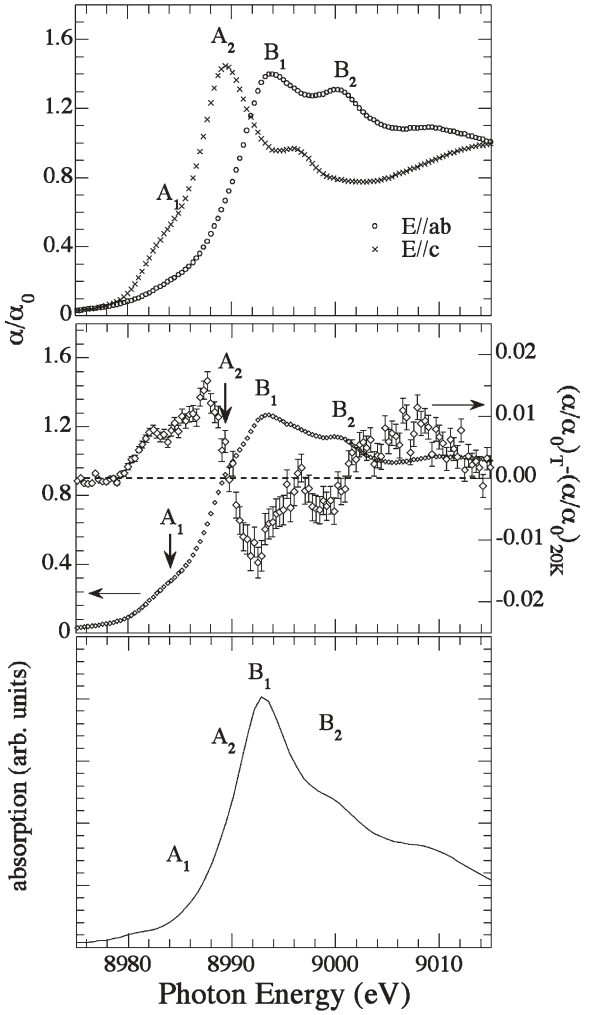

Fig. 8 Polarized Cu K-edge XANES of the $La_{1.48}Sr_{0.12}Nd_{0.4}CuO_4$ single crystal measured with the E‖ab and E‖c at 20 K (*upper*). Different absorption features have been identified by second derivative of the absorption spectra and denoted as A_1 and A_2 in the E‖c spectrum and by B_1 and B_2 in the E‖ab spectrum. An unpolarized spectrum measured at 20 K on the same system has been shown (*middle*) along with a difference spectrum between a spectrum measured above the charge stripe ordering. A calculated XANES spectrum for the La_2CuO_4 (without including the Nd and Sr in the cluster) is also shown (*lower panel*) to identify nature of different peaks. The absorption peaks are well reproduced in the calculated spectrum [84]

calculated spectrum it is easy to find the origin of different features observed in the experimental spectrum. The features A_1 and A_2 are determined by multiple scattering of the ejected photoelectron off apical oxygen and La, Nd and Sr atoms (sitting at 45° from the CuO_2 plane) while the peak B_1 corresponds to multiple scattering off the in-plane oxygen and Cu in the CuO_2 plane. The peak B_2 includes multiple scattering contributions similar to the main peak B_1 and also contributed by multi channel effects [85].

It could be seen that there is a high-energy spectral weight transfer resulting the positive and negative difference with a maximum difference of ~2% of the normalized absorption (Fig. 8). On cooling the sample, the spectral weight around the peak A_1 (A_2) is decreased with an increase around the peak B_1 (B_2). We have plotted temperature dependence of the XANES peak intensity ratio $R=(b_1-a_1)/(b_1+a_1)$ in Fig. 9. Here the b_1 and a_1 represents intensities of the peaks B_1 and A_1 probing high energy spectral weight transfer (from the core excitations $Cu1s\rightarrow\varepsilon p_z$ (peak A_1) to the $Cu1s\rightarrow\varepsilon p_{xy}$ (peak B_1). The ratio R shows clear increase below the T* (~60 K).

We have studied several model systems and found that the R, determined by the unpolarized Cu K-edge XANES, shows an abrupt change across the T*. Another example is given in Fig. 10, revealing temperature dependent R, with an abrupt change at ~60 K, for the $La_{1.875}Ba_{0.125}CuO_4$ system. This further confirms that the ratio R could be taken as a good indicator of the T* in the cuprates, where the local and instantaneous displacements show an abrupt change.

To explore the nature of these local displacements around the Cu atom across the T*, we have made multiple scattering calculations and calculated Cu K-edge XANES spectra for different distortions [84]. For this purpose we have taken a simple approach by taking the $HgBa_2CuO_{4+\delta}$ (Hg1201) system as a model for the calculations having the Cu-O plane to be crystallographically flat due to a small mismatch between the CuO_2 planes and the rock-salt oxide layer.

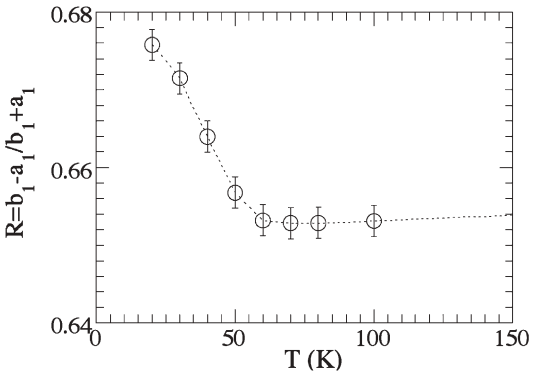

Fig. 9 Temperature evolution of the peak intensity ratio $R=(b_1-a_1)/(a_1+b_1)$ for the $La_{1.48}Sr_{0.12}Nd_{0.4}CuO_4$. The ratio shows a clear change across a characteristic temperature T* (~60 K)

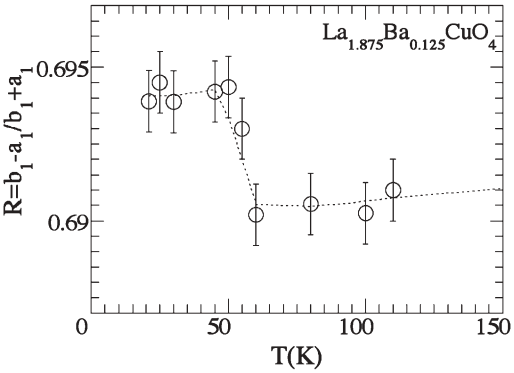

Fig. 10 Temperature evolution of the peak intensity ratio $R=(b_1-a_1)/(a_1+b_1)$ for the $La_{1.875}Ba_{0.125}CuO_4$. As for the $La_{1.48}Sr_{0.12}Nd_{0.4}CuO_4$, the ratio shows a clear change across the T*

In addition the simple structural unit cell with tetragonal crystal structure (a~3.8755 Å; c~9.4952 Å) [87] provides the added advantage to simulate different local lattice distortions and investigate the evolution of the XANES spectrum with different geometrical displacements.

Figure 11 shows Cu K-edge XANES measured at room temperature on a powder sample of Hg1201 superconductor, along with a calculated spectrum using the multiple scattering theory. The real-space multiple scattering of the photoelectron excited from the Cu 1 s states to the cluster of atoms within a radius of ~7 Å from the central Cu. The features observed in the experimental spectrum could be satisfactorily reproduced not only with respect to the relative intensities, but also in energy separations.

The calculations were extended to a distorted CuO_2 plane considering a particular rhombic distortion revealed by the EXAFS (see above). Evolution of the absorption differences with increasing weight of the distorted sites (Q_2-type rhombic distortion), are shown in Fig. 11. It is clear from the calculated absorption differences that the Q_2-type of rhombic distortion introduces the spectral weight transfer, as observed in the experimental spectra below the T*. Thus the results of the calculations are consistent with the experimental findings, suggesting that the observed weight transfer is due to an octahedral distortion where one of the Cu-O-Cu direction gets elongated (see above), observable only when the amplitude of the lattice fluctuations become larger than the amplitude of thermal fluctuations.

Coming back to Figs. 9 and 10, showing anomalous change in the ratio $R=(b_1-a_1)/(b_1+a_1)$, we can state that the Q_2 type of rhombic distortions of the CuO_2 plane could be considered a suitable response function to determine the T*. It is worth noting that, even if the change across the T* is different, with different magnitude, the change is clear. The differences of R in different systems are due to different strain on the CuO_2 plane (see above) because of different substitutional disorder (rock-salt blocks are different).

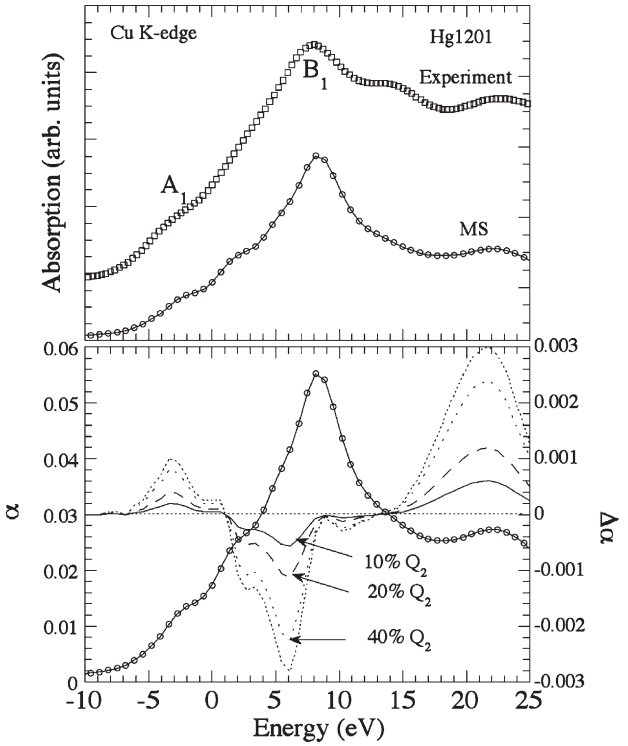

Fig. 11 Calculated absorption spectrum for the Hg1201 is compared with an experimental Cu K-edge XANES measured on the same system (*upper*). The calculated absorption is plotted along with absorption differences with respect to the calculated spectra considering variable quantity of distorted sites (Q_2-type of rhombic distortion). The rhombic distortion is at the origin of spectral weight transfer between the peaks A_1 and B_1 [84]

In Fig. 12 we have plotted T* (defined by the abrupt local geometrical change as reflected by the anomalous increase of the XANES peak intensity ratio R) as a function of the hole concentration in the La-based cuprate superconductors. This temperature has been compared with the one obtained by the wipeout fraction of Cu NQR [88, 89]. The T*, obtained by the two techniques, agree quite well in the underdoped regime within the experimental uncertainties.

In summary, we have shown that XANES spectroscopy is an important tool to study instantaneous local geometry in the complex systems such as the cuprate superconductors. Temperature dependent Cu K-edge XANES on some model systems have revealed an abrupt high-energy spectral weight transfer across the characteristic temperature T* due to change in the instantaneous local geometry around the Cu, showing a particular evolution of temperature dependent XANES peak intensities with an order parameter like behaviour. Exploiting multiple scattering calculations of different distortions we have demonstrated that the abrupt change in the spectral weight transfer, reflected

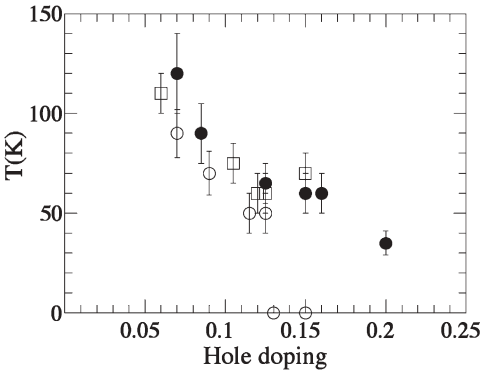

Fig. 12 Doping dependence of the T* determined from the change of the XANES peak intensity ratio R (*squares*) plotted with the one obtained by wipeout fraction of Cu NQR (*circles*). The *open circle* corresponds to the data for the $La_{2-x}Sr_xCuO_4$ [88] while the *closed circles* represent the one obtained for $La_{1.6-x}Sr_xNd_{0.4}CuO_4$ system [89]

by the XANES peak intensities, is due to the appearance of the Q_2-type of Jahn-Teller distortions below the T*, consistent with the EXAFS results presented here (see earlier sections). It should be mentioned that the XANES has been widely used as a local probe and the anomalous temperature dependence appears to be commonly observed by other authors [90, 91]; however, we have quantified the temperature dependence using the new approach to exploit the spectral weight transfer and simulate these changes using the multiple scattering calculations.

4.2 Large Isotope Effect on the T* and the Local Displacements in the Cuprates

Above we have shown how the capabilities of the XANES spectroscopy could be exploited to study the local displacements in the inhomogeneous cuprates. Here we have further exploited the approach to study the effect of the oxygen isotope mass in the local structure and the characteristic temperature T* using the Cu K-edge XANES spectroscopy [25]. We have taken the $La_{1.94}Sr_{0.06}CuO_4$ system where the largest oxygen isotope effects on both superconducting transition temperature and the effective supercarrier mass have been observed [92]. Obviously XANES is an ideal tool due to the fact that it probes the statistical distribution of the conformations of the cluster of atoms around the Cu via electron scattering, and is a very sensitive to distortions of the local structure of oxygens around the photoabsorbing atom and probes instantaneous lattice conformations.

Figure 13 shows the normalized Cu K-edge X-ray absorption near edge spectra for the ^{16}O and ^{18}O samples at 200 K. We denote the well-resolved peak features by A_1, A_2, B_1 and B_2. These features, which extend from about 8 eV to

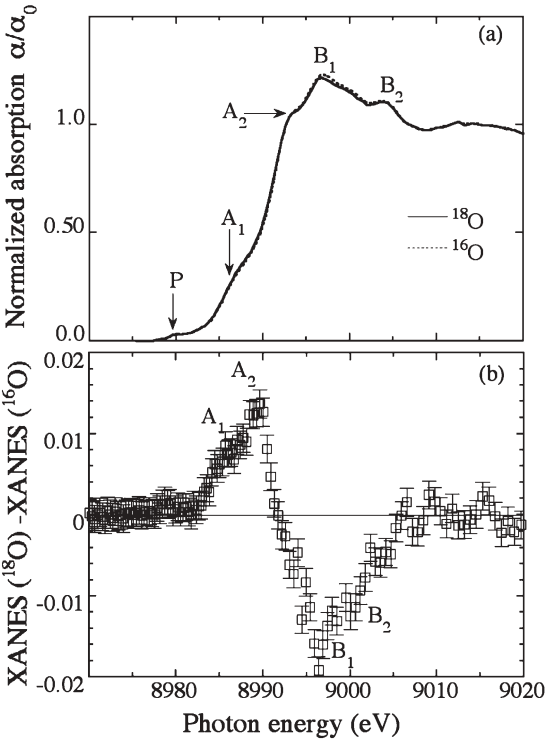

Fig. 13 Cu K-edge XANES spectra of $La_{1.94}Sr_{0.06}CuO_4$ with ^{16}O and ^{18}O isotopes (*panel a*) measured at 200 K. The difference between the two is shown in the *lower panel* (*panel b*). The $^{16}O \rightarrow ^{18}O$ isotope effect on the Cu site structure induces a decrease of the peak B_1 with an increase of peak A_1 [25]

40 eV above the threshold, have been identified as multiple scattering resonances, as discussed in the previous section. The effect of isotope substitution on the distribution of local Cu site conformations can be directly seen in Fig. 13, where we report the difference between the spectra of the two isotopes at 200 K. There is a large variation of the XANES spectrum due to isotope substitution, of the order of 2% of the normalised absorption. This is a direct measure of the effect of isotope mass on the distribution of Cu site structural conformations spanned during the dynamic lattice displacements. We observe an energy shift of peaks A_1 (and A_2), and an intensity decrease of peak B_1 (and B_2) in the ^{18}O spectrum. These changes are clearly related with the effect of changing the oxygen mass on the lattice displacements involving the rhombic distortion of the Cu-O square planes (see above).

Using the similar approach discussed in the previous section, we have plotted temperature dependence of R in Fig. 14. The temperature dependence of R (Fig. 14) shows that the crossover temperature T* increases by about 60 K upon replacing ^{16}O (~110±10 K) with ^{18}O (~170±10 K) for the ^{18}O sample. This re-

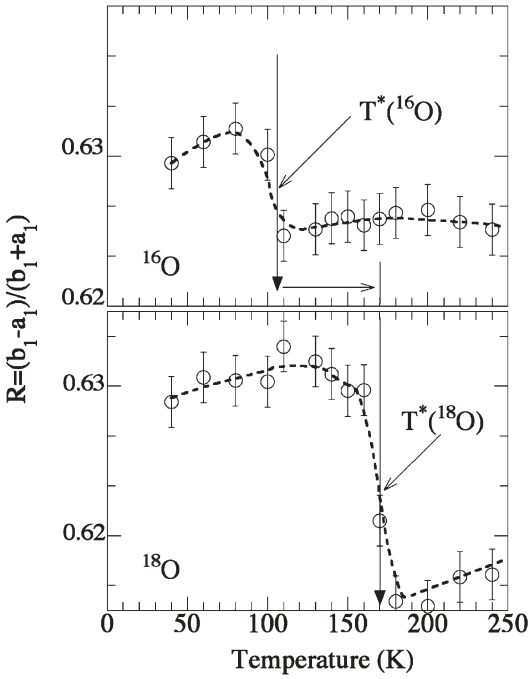

Fig. 14 Temperature evolution of the XANES intensity ratio $R=(b_1-a_1)/(b_1+a_1)$ where $b_1(a_1)$ is the intensity of XANES peak $B_1(A_1)$ for the ^{16}O (*upper*) and ^{18}O (*lower*) substituted samples. The T* is estimated to be ~110 (±10)K for the ^{16}O sample, and ~170 (±10)K for the ^{18}O sample giving a large oxygen isotope shift of ~60 K [25]

sult indicates that the isotope substitution leads to a large change in the local geometry, with a giant effect on the T*. Later, a large isotope effect on the T* was revealed by neutron scattering measurements on a different system [27]. It is worth mentioning that some of the theoretical models for the cuprates are able to reproduce such a large isotope effect on the T* [21, 93, 94].

T* is associated with the temperature below which the coexisting charge carriers in distorted and undistorted Cu sites could be well distinguished within the time scale of the X-ray absorption technique as revealed by atomic pair distribution of CuO_2 plane (see above). When the temperature is lowered, with the fixed time scale of the XANES, measuring change in higher order pair distribution, we observe an anomalous change in the local structure across the temperature T* due to a sudden change in the statistical distribution of the Cu-site due to a transition in an ordered phase. Obviously, T* could be different if measured by other techniques depending on the time scale. It is worth mentioning that the difference below T* (see, e.g. Fig. 14) is much smaller than that above it. This may be due to the fact that the average local structure deviation in the ordered phase due to isotope substitution is less than that in the disordered phase.

5
Temperature Dependent Correlated Debye Waller Factors Measured by Cu K-Edge EXAFS

5.1
A Brief Recall to the Diffraction and EXAFS Debye-Waller Factors

As discussed earlier, the effect of temperature on the EXAFS signal is taken care of by the exponential term $\exp(-k^2\sigma_i^2)$ were σ_i is the Debye-Waller factor (DWF) of the absorber-scatterer pair. It should be mentioned that σ_i appearing in the EXAFS equation is not the same as that determined by the diffraction experiments. While the diffraction DWF takes into account the mean-square deviation (MSD) of a given atom from its average site in the crystal, EXAFS Debye-Waller factor measures the broadening of the distance between two atomic sites, i.e. represents the distance broadening between the absorber and the scatterer. In other words, the EXAFS Debye-Waller factor is a measure of the mean square relative displacements (MSRD), determined by the correlated movement of the absorber and the scatterer, and also referred as the correlated Debye Waller factor.

In terms of atomic correlations, the EXAFS Debye-Waller factor σ_{AB} for an atomic pair containing the absorber (A) and the backscatterer (B) can be defined as [34–37]:

$$\sigma_{AB}^2 = \sigma_A^2 + \sigma_B^2 - 2\rho\sigma_A\sigma_B$$

where σ_A and σ_B are the atomic Debye-Waller factors and ρ is the correlation coefficient for a relative displacements of the two atoms. Therefore the two extreme cases for the EXAFS Debye-Waller factor, σ_{AB} are, $\rho=0$, an uncorrelated pair distribution, giving

$$\sigma_{AB\,(\rho=0)}^2 = \sigma_A^2 + \sigma_B^2$$

and

$$\sigma_{AB\,(\rho=1)}^2 = (\sigma_A - \sigma_B)^2$$

The $\rho=0$ and $\rho=1$ cases are the limiting situation for the EXAFS Debye-Waller factors of a pair of atoms.

Let us take an experimental example of the in-pane Cu-O displacements in the $La_{2-x}Sr_xCuO_4$ system to enlighten the differences in the MSD and the MSRD, measured respectively by diffraction and the EXAFS. Figure 15 shows the Debye Waller factors of Cu and O as a function of temperature for a single crystal of LSCO (x=0.13), measured by high resolution neutron diffraction [95]. The expected EXAFS Cu-O Debye-Waller factors for the fully uncorrelated $\rho=0$, and fully correlated $\rho=1$, distribution have been derived using the diffraction data.

The figure suggests that the expected DWF in the EXAFS measurements should be the one with $\rho=1$. However, this is valid only for a crystallographi-

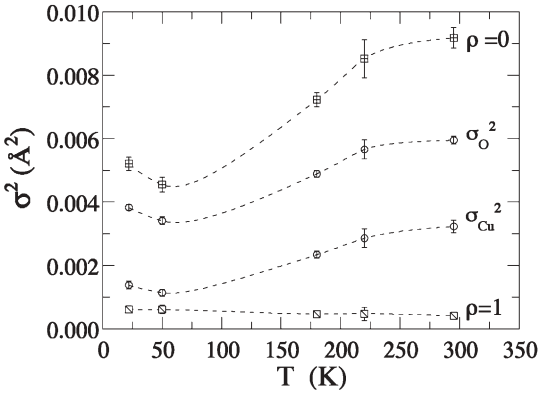

Fig. 15 The diffraction Debye Waller factors σ^2_{Cu} and σ^2_O for Cu and oxygen [104] are plotted. The expected Debye Waller factor for the pair, σ^2_{CuO} for a correlated distribution (ρ=1) and uncorrelated distribution (ρ=0) are shown (*squares*). Theoretically the temperature dependence of the MSRD for the Cu-O pair could be given by correlated Einstein model (*solid line*) [37]

cally ordered structure and, in the presence of any disorder (static or dynamic), the DWF measured by the EXAFS is different with the correlation coefficient being different from unity. Indeed, if static structural distortions are present, the EXAFS Debye-Waller factor σ_{AB} could be presented as a superposition of a temperature independent (static σ^2_+) and temperature dependent (dynamic σ^2_d) terms, i.e.,

$$\sigma^2_{AB} = \sigma^2_+ + \sigma^2_d$$

The temperature-dependent part σ^2_d could be given by the simple correlated Einstein model as [34]

$$\sigma^2_d = \frac{\hbar}{2\omega m_r} \frac{1 + e^{-\hbar\omega/k_B t}}{1 - e^{-\hbar\omega/k_B t}}$$

where ω is the bond vibration frequency, m_r is the reduced mass of the pair, and $\Theta_E = \hbar\omega/k_B$ is the Einstein temperature. Thus the total $\sigma^2_{AB}(T)$ in this approximation depends on ω and T with a constant σ^2_+.

Considering all the above facts, it is clear that the EXAFS Debye-Waller factor provides important information on the local atomic displacements. The next subsections provide some examples of the use of the MSRD as tool to study the local Cu-O displacements in the cuprate superconductors. Before we proceed to discuss some examples, it is worth mentioning that the Cu-O MSRDs have been determined by the Cu K-edge EXAFS measurements. We have used conventional procedure for the Cu-O EXAFS analysis considering a single distance for the Cu-O coordination shell, where the effective DWF includes the distortion effects, accounting static and dynamic displacements. This approach is

adopted to make a direct comparison of the temperature dependent distortions in the CuO_2 plane. Except the radial distance R and the σ^2 all other parameters were kept constant (i.e., two parameter fit) in the conventional least squares paradigm [34–37]. The starting parameters were taken from diffraction experiments [87, 95–97] on the systems studied.

5.2 Temperature Dependent Cu-O Displacements from Underdoped to Overdoped Regime of the Cuprates

One of the interesting properties of copper oxide superconductors is the electronic crossover from underdoped to overdoped phase, with abnormal transport properties [1–4]. While the underdoped regime is characterized by a complex state of matter, in which low temperature orders, related with various electronic degrees of freedom appear, the overdoped regime seems to behave like normal metal. Here we take example of doping dependent local Cu-O displacements in CuO_2 plane to show that the electronic crossover from the underdoped to the overdoped regime is related with the local structure. The $La_{2-x}Sr_xCuO_4$ (LSCO) copper oxide has been taken as model system the present study and the temperature dependent local Cu-O displacements (dynamic and static) are determined by the correlated DWF of the Cu-O bonds.

Figure 16 shows temperature dependence of the Cu-O DWF, revealing some evident differences between the underdoped and overdoped samples. While the underdoped and optimally doped systems show anomalous temperature dependence, we do not see any evident temperature dependent anomaly for the overdoped case. Indeed, we can define two anomalous temperatures in the underdoped regime, a temperature T_s where an increase of σ^2 appears, followed by the transition temperature T_c, where the σ^2 shows a small decrease. The increase at T_s is evident in the underdoped systems ($Sr_{0.105}$ and $Sr_{0.13}$) and optimally doped system ($Sr_{0.15}$); however, the overdoped system ($Sr_{0.2}$) shows a negligible change. On the other hand, the drop in σ^2 at the T_c is better seen only for the slightly underdoped and the optimally doped systems.

Here it is worth recalling that the $La_{1.48}Sr_{0.12}Nd_{0.4}CuO_4$ (LNSC) system reveals similar anomalous upturn in σ^2 below the charge stripe ordering temperature (see, e.g. Fig. 17) [79]. This is consistent with the charge heterogeneities in the LNSC system shown by several experiments [80]. In fact, appearance of any charge density wave like instability is accompanied by an anomalous change in the DWF, known for several density wave systems [98]. Considering these experimental facts, we think that the anomalous upturn in the σ^2 (Fig. 17) is due to the instability related to the charge heterogeneities and the temperature T*, discussed in earlier sections. Ion-channelling measurements [31] have revealed similar temperature dependent anomalies in the excess displacements (a parameter analogous to the DWF measuring dynamic and static distortions). Neutron PDF studies also show similar local lattice response [32], extending a further support. Below the T_s, the Cu-O bond distribution becomes larger

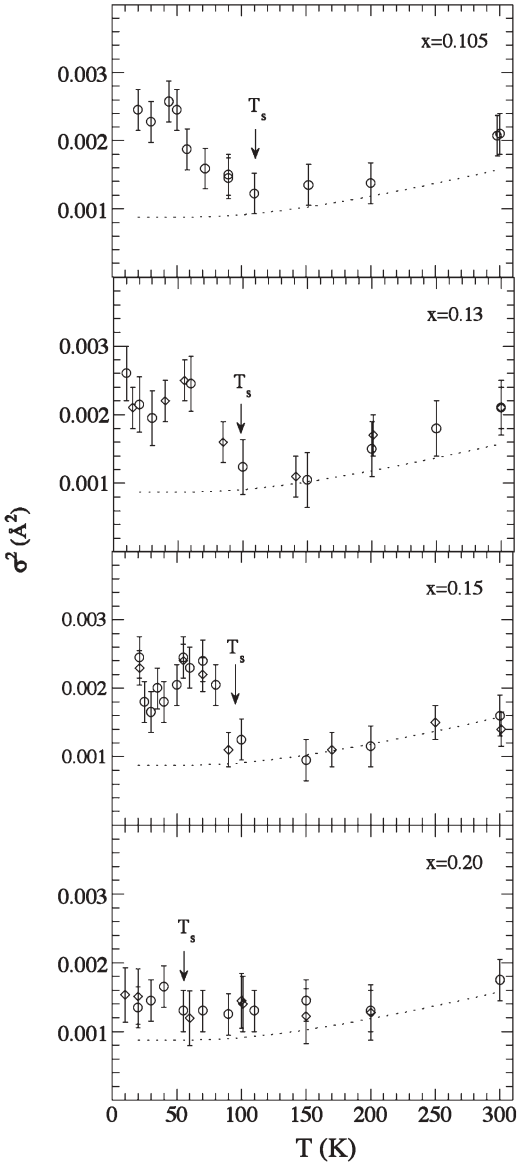

Fig. 16 Temperature dependence of the correlated Debye-Waller factors (*symbols*) of the Cu-O pairs (σ^2) for the underdoped $La_{1.895}Sr_{0.105}CuO_4$ (*upper*) and $La_{1.87}Sr_{0.13}CuO_4$ (*upper middle*), optimally doped $La_{1.85}Sr_{0.15}CuO_4$ (*lower middle*) and an overdoped $La_{1.8}Sr_{0.2}CuO_4$ (*lower*) samples, determined by polarized Cu K-edge EXAFS. The expected temperature dependence of the Debye-Waller factor for a fully correlated motion of Cu and O is shown by *dotted lines*. *Different symbols* in the plots correspond to different data sets. The underdoped and optimally doped samples reveal a clear upturn (with variable amplitude) in the DWF around 100 K, while the upturn is less evident in the overdoped case and seems to appear at lower temperature. Approximate values of T_s are indicated

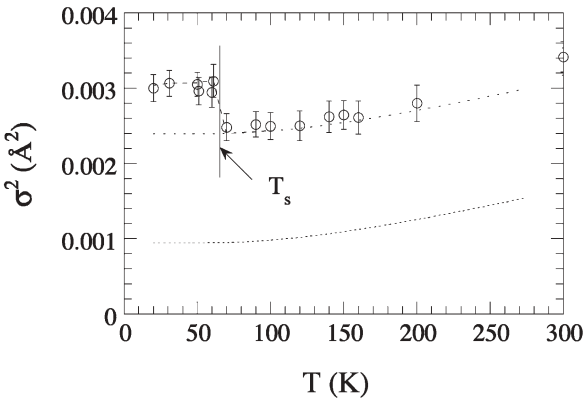

Fig. 17 Temperature dependence of the correlated Debye-Waller factors (*symbols*) of the Cu-O pairs (σ^2). The expected temperature dependence of the Debye-Waller factor for a fully correlated motion of Cu and O, calculated by Einstein model, is shown by *lower dotted line*, a constant value of 0.00145 (σ_+^2) is added to guide the temperature dependence of the experimental Debye-Waller factor (*upper dotted line*)

than that due to the thermal fluctuations and the spatial heterogeneous structure could be well distinguished [34–37] as discussed in earlier sections.

The amplitude of the upturn provides a measure to the barrier height in the multi-well potential and it seems that the barrier height decreases with increasing doping and the system gets more homogeneous in the overdoping regime, in which the spatial heterogeneity could not be distinctly identified within the experimental resolution. It should be noted that within the experimental data points (Fig. 16) we can hardly see a change in the T_s; however, it seems that the anomalous upturn in the σ^2 appears to decrease with increasing the doping.

It should be noted that the LNSC system reveals a sharp change in σ^2 at the anomalous temperature (~60 K), while the upturn for the $Sr_{0.105}$ system is gradual with $\sigma_+^2=0$, unlike the LNSC system. In fact, there is a significant contribution of temperature independent part ($\sigma_+^2\neq0$) for the LNSC system, presumably due to Nd substitution in place of La, resulting larger substitutional disorder and chemical pressure on the Cu-O plane [77]. On the other hand, the gradual change in the $Sr_{0.105}$ system indicates that there may not be a clear transition at the upturn temperature (~110 K) and it appears as an onset of the stripe-like inhomogeneity related with dynamic local Cu-O displacements, with short-range order. Indeed, the upturn temperature could also be recognized as the temperature below which the Q_2-like displacements (denoted by T*, see above) become thermally stable with formation of polaron liquid of filamentary segments [21, 99]. The stabilization of Cu-O displacements at the anomalous temperature could be followed by formation of stripe clusters and stripe segments (as the strings) [100], before getting the stripe order at a lower temperature.

To conclude the discussion, we have shown the correlated DWF as an order parameter of instantaneous Cu-O displacements in the $La_{2-x}Sr_xCuO_4$ superconductor. The local Cu-O displacements show anomalous change at a temperature T_s, with variable amplitude as a function of doping. The amplitude of the anomaly decreases with the increasing doping. The present results seem to be consistent with a local structural crossover from underdoping to overdoping. In addition, the σ^2 shows an anomaly at the T_c, revealing a close relation between the superconductivity and the local Cu-O displacements. We will discuss this point in the next section.

5.3 Critical Role of the Cu-O Displacements in the Cuprate Superconductors

Here we show an example of local lattice distortions in different materials with increasing chemical pressure on the CuO_2 layers, measured using correlated Debye-Waller factors as an order parameter. The results provide experimental evidence in favour of critical role of local lattice fluctuations in the high T_c superconductivity in the cuprates.

Figure 18 shows temperature dependence of the σ^2 for the LCO, Bi2212 and Hg1201 systems representing three different families of the cuprates. As discussed in the previous section, we can easily define at least two temperatures (T_s and T_c) where the σ^2 shows anomalies within the temperature region measured here. There is an anomalous increase below the temperature T_s followed by a decrease around the superconducting transition temperature T_c. The increase at T_s appears in the LCO and Bi2212 systems; however, the Hg1201 system does not show any evident up turn. On the other hand, the drop of the σ^2 at the superconducting transition temperature T_c appears common to all the systems (however, less evident in the LCO system). The Hg1201 system manifests a large drop in the σ^2 around the superconducting transition temperature. Interestingly, the absolute values of the σ^2 are similar (within the experimental uncertainties) at the superconducting transition temperature, however, quite different above the T_s.

Here we should mention that, apart from the static and dynamic distortions of the CuO_2 lattice, the distance broadening contains contribution from thermal vibration. The contribution of the thermal vibration could be described by the Einstein model which is generally used to describe the thermal vibrations of atoms in a crystal lattice. However, in the present case the thermal contribution to the σ^2 should be similar (for a pair of Cu and O atoms) for all the systems and hardly affects the following discussion.

Let us discuss the anomalous increase of the σ^2 at a temperature T_s. We have discussed the anomalous upturn in the σ^2 in the earlier section, assigning it to an instability related with charge heterogeneity in the CuO_2 plane. Therefore the anomalous increase in the σ^2 for the LCO (T_s~190 K) and Bi2212 (T_s~140 K) systems correspond to appearance of charge heterogeneity in the CuO_2 plane. X-ray diffraction measurements on the LCO system has clearly demonstrated

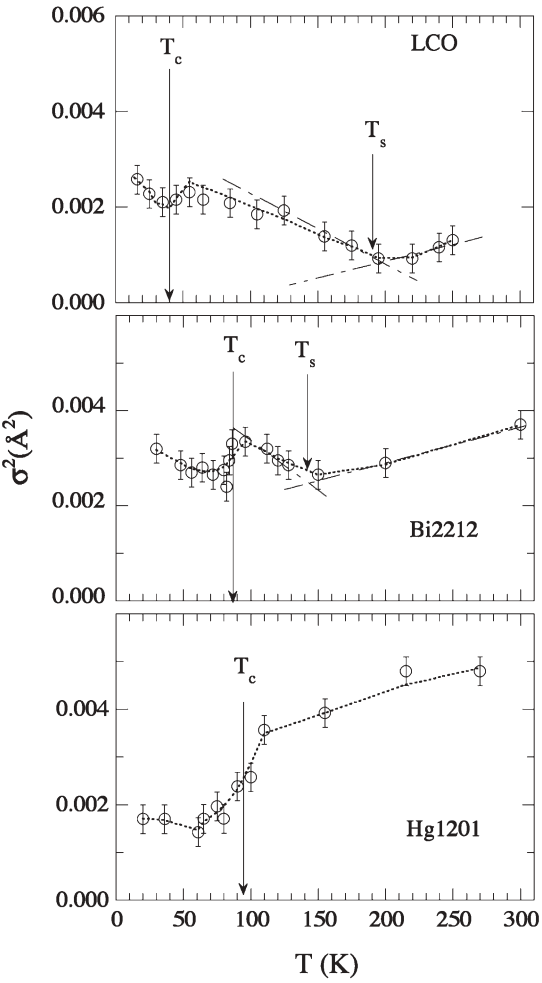

Fig. 18 Temperature dependence of the Cu-O(planar) Debye-Waller factor σ^2 determined by EXAFS; $La_2CuO_{4.1}$ (*upper*), Bi2212 (*middle*) and Hg1201 (*lower*). The *dashed line* is a guide to the eyes. The resulting Debye-Waller factor σ^2 shows abnormal temperature dependence with an increase below a temperature T_s followed by a decrease around the superconducting transition temperature T_c. The *error bars* represent the average estimated noise level

onset of charge ordering to be ~190 K [101] which is consistent with the observation of the upturn in the σ^2 in this system.

One of the important features revealed here is an anomalous drop of the σ^2 around the superconducting transition temperature T_c. This is a clear indication that the appearance of the superconducting state is accompanied by the decrease of the instantaneous local lattice distortions and hence a direct evidence of the role of electron lattice interactions in the superconducting pairing. The drop at the T_c is different for different systems and found to be

maximum for the Hg-based compound where the block-layers are Ba-O giving smaller mismatch than the case of Bi2212 (Sr-O) and LCO (La-O). Below T_c the σ^2 shows a small increase, however, within the experimental uncertainties. The anomalous decrease at the superconducting transition temperature provides a direct evidence for an important role of critical lattice fluctuations in the superconducting state. At the superconducting transition the drop of the σ^2 at T_c could be due to transfer of electron lattice interaction energy in the pairing mechanism (the superconductivity is a coherent phenomena and the decrease might be related to decrease of incoherent distortions in the striped phase). It should be noted that the two anomalies are correlated; while the upturn at the T_s increases, the drop at the T_c decreases.

Summarizing, we have determined local Cu-O displacements in the cuprates using temperature dependence of the correlated Debye-Waller factors in different families. The results show that the anomalous displacements depend on the chemical pressure on the CuO_2 plane. The temperature dependence of the Cu-O DWF shows unusual behaviour with a drop at the superconducting transition temperature and upturn at the temperature T_s, providing direct evidence for an intimate relationship between the high T_c superconductivity, charge heterogeneities and the local Cu-O displacements.

6
Local Mn-O Displacements in the CMR and Charge Ordered Manganites

While the scientific debate on the local displacements and their role in the superconductivity of the cuprates continues due to the fact that the amplitude of these distortions is quite small, it is getting generally recognized that the fundamental properties of the manganites, hosting colossal magneto-resistance (CMR) and the charge ordered textures, strongly depend on the local displacements [49, 102–104]. Several experiments have revealed that polarons in these materials are associated with Jahn-Teller (JT) distortions. The JT distortions in the doped manganites are found to be of Q_3-type [59]. Here we have exploited the EXAFS technique to reveal quantitative measurement of the JT distortions of the MnO_6 octahedra. Again, the quantitative measurement of the distortions could be possible by high k-resolution EXAFS measurements. The added advantage of fluorescence detection was to get the partial absorption cross-section only due to the Mn, avoiding the residual contribution of the absorption due to other atomic species. Here an example of the $La_{1-x}Ca_xMnO_3$ system [102, 105] is presented, showing the colossal magneto-resistance (CMR) (x=0.25) and charge ordering (x=0.5). The sample with x=0.25 shows the CMR regime above the metal-to-insulator transition at T_{cm}~240 K.

We have used similar approach as of cuprates to determine the local displacements, and extracted local Mn-O bond-lengths distribution from the analysis of the EXAFS oscillations due to the Mn-O distances. The PDF of the Mn-O bonds at a temperature below (20 K) and above (300 K) the CMR tran-

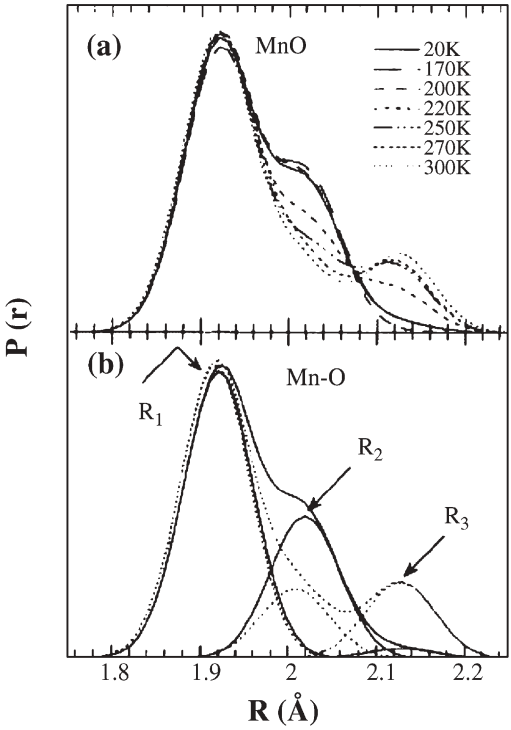

Fig. 19 Temperature dependence of the Mn-O pair distribution function (PDF) for the $La_{0.75}Ca_{0.25}MnO_3$ system. The PDF at low temperature (20 K) at higher temperature (300 K) are shown with their components [49]

sition in the x=0.25 system are shown in Fig. 19. The PDF appear as asymmetric distribution of Mn-O bonds, peaked around R_1~1.92±0.01 Å, R_2~2.01±0.01 Å and R_3~2.13±0.01 Å depending on the temperature. The distribution is a two peak function with R_1~1.92±0.01 Å and R_2~2.01±0.01 Å at low temperature while it gets a three peak function in the CMR phase. In the metallic region ($T<T_{cm}$) the two distances, R_1 and R_2, have probability of nearly four and two bonds, respectively [49]. The probability associated with the R_1 remains nearly constant with temperature, while the probability of the R_2 gets a value ~1 bond at $T>T_{cm}$ with a crossover temperature 200 $K<T_{cm}$ where the long bond R_3 appears with a probability of 1.

We should recall that the undoped $LaMnO_3$ compound is known to show a spontaneous distortion of the MnO_6 octahedra due to the Jahn-Teller effect associated with the Mn^{3+} sites. Increasing the concentration of the Ca^{2+} ions, an insulator-to-metal transition is observed with a collapse of the difference between the crystallographic lattice parameters. However, the local structure in the metallic phase with 25% doping of the Ca^{2+} is expected to diverge from the average crystallographic structure because of local and instantaneous distortions. At low

temperature, the short distance R_1 in the PDF is close to the average crystallographic distance, considering indetermination given by the thermal broadening extracted from diffraction data [102]. The separation between local bond distances, R_1 and R_2, ΔR_p~0.09 Å, provides the amplitude of the instantaneous local Mn-O distortions due to the dynamic deformations associated with polarons. The polaronic lattice distortions are slightly larger than the indetermination of the Mn-O bond lengths due to the thermal vibrations, ΔR_t~0.04 Å, giving a ratio $\Delta R_p/\Delta R_t$~2, indicating the presence of polarons in the intermediate coupling regime (IJTP) as in the metallic phase of high T_c superconductors (see above). In fact, the local structure of MnO_6 octahedra contains four in-plane bonds of ~1.92±0.01 Å and two out-of-plane bonds of ~2.01±0.01 Å, showing a small Jahn-Teller distortion (Fig. 9). The ratio N_2/N_1~2/4 of the probability distributions of the two Mn-O bonds (R_2 and R_1) in the metallic phase is consistent with a nearly homogeneous spatial distribution of dynamically axial elongated polaronic MnO_6 octahedra due to overlapping intermediate JT polarons.

On the other hand, at $T>T_{cm}$ (in the insulating phase), the system shows the presence of more elongated MnO_6 octahedra with a longer bonds (R_3) such that ΔR_p=0.21 and the ratio $\Delta R_p/\Delta R_t$~5 indicating that the associated polarons are in the strong coupling regime. The probability of one very long R_3 bond per Mn site indicates that the small JT polarons spans about 50% of the Mn sites. Therefore we find that in the insulating phase the two distorted sites A and B, shown in Fig. 20, coexist and each one spans about 50% of the Mn sites. This indicates

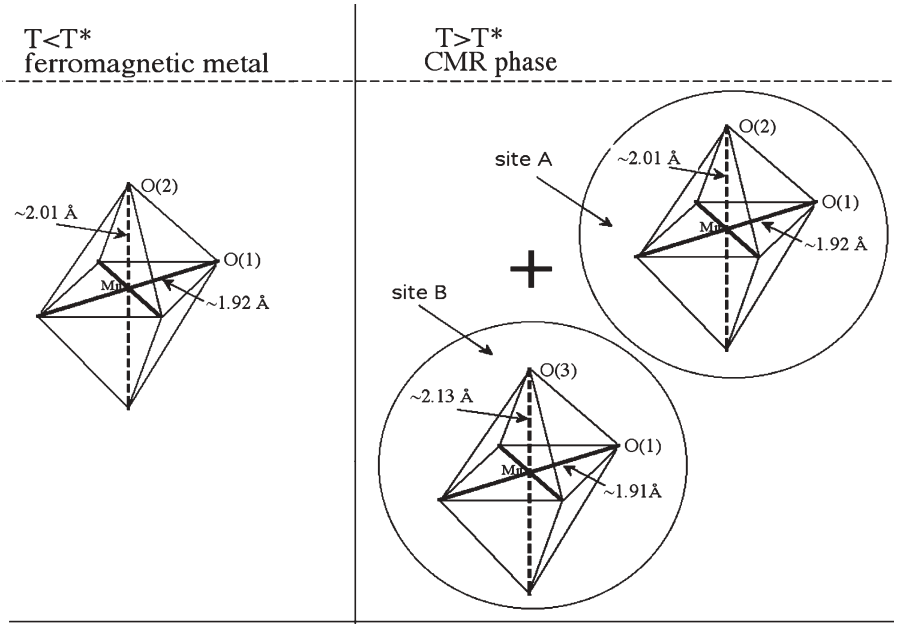

Fig. 20 A cartoon of the possible MnO_6 octahedral local distortions in the metallic phase at $T<T^*$ (T_{cm}) (20 K) and the insulating phase at $T>T^*$ (T_{cm}) (300 K)

that the CMR transition is not only accompanied by the appearance of polarons with large amplitude but also shows a concomitant decrease in the spatial extent of the polaronic charges [49].

Figure 21 shows the Mn-O bond distribution for the charge ordered $La_{1-x}Ca_xMnO_3$ (x=0.50), which could be compared to prove that different phases of the system could be characterized by different MnO_6 octahedral distortions. While at high temperature the system $La_{0.5}Ca_{0.5}MnO_3$ shows distorted MnO_6 octahedra with two different distances (evident from a broad Mn-O distribution), at low temperature the octahedra are largely distorted with four different distances (two peak function) [105]. From temperature dependent study, we find that: i) there are large MnO_6 octahedral distortions in the commensurate charge ordered state at low temperature; ii) the distortions are greatly reduced in the charge disordered phase at high temperature. From the measured Mn-O distribution on the $La_{0.5}Ca_{0.5}MnO_3$, we could characterize the different octahedral distortions in the charge ordered and disordered phases. At high temperature

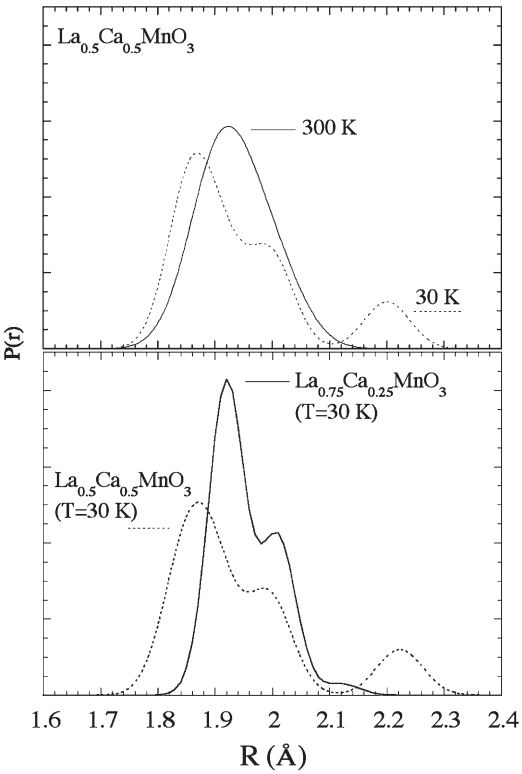

Fig. 21 The Mn-O pair distribution function (PDF) for the $La_{0.5}Ca_{0.5}MnO_3$ system in the charge ordered insulating phase at 30 K (*dotted line*) and charge disordered phase at 300 K (*solid line*). The Mn-O PDF in the metallic phase of the $La_{0.75}Ca_{0.25}MnO_3$ is compared with the insulating phase of the $La_{0.5}Ca_{0.5}MnO_3$ at 30 K (*lower panel*)

there are only two Mn-O distances, 1.88±0.01 Å with probability of bonds ~4, and long bonds, ~2.01±0.01 Å with a probability ~2. On the other hand, at low temperature there are longer Mn-O bonds (2.20±0.01 Å). Indeed the Mn-O distribution at low temperature suggests that the MnO_6 octahedra have Q_3-type of JT distortions, coexisting with Q_2-type of JT distortions. Instead the PDF at high temperature reveals presence of quasi Q_2-type of distortion [105]. Figure 10 provides a good example of the metallic and insulating phases of the manganites (see, e.g., lower panel) to be characterized by their local atomic displacements.

In summary, we have characterized different MnO_6 octahedral distortions in the charge ordered and colossal magnetoresistive $La_{1-x}Ca_xMnO_3$ system as a function of temperature. In the charge ordered $La_{0.5}Ca_{0.5}MnO_3$ system the small local JT distortions persist even at high temperature while the system is in the charge disordered state, indicating short-range charge correlations in the macroscopically disordered phase [107–110]. Similar study on the CMR $La_{0.25}Ca_{0.75}MnO_3$ system reveals large local distortions in the insulating phase with smaller distortions persisting even in the metallic state at low temperature. The results underline short range ordered correlations to be important for the understanding of the CMR in these manganese oxides. We have also shown that the JT distortions and their spatial distribution play an important role to characterize the metal-insulator transition in the CMR phase [49].

7
Superconducting Shape Resonance of the Interband Pairing Term in a Superlattice of Quantum Stripes

A direct compelling experimental evidence of the spatial self organization of the local lattice in the CuO_2 plane of Bi2212 has been obtained by resonant X-ray diffraction [111] (Fig. 22). Using tunable synchrotron radiation X-ray energy it has been possible to tune the photon wavelength around the Cu K-edge and to use the anomalous diffraction to isolate the superstructure reflections due only to the CuO_2 sublattice. The results of the experiment on the superstructure of Bi2212 have shown that the Cu-O local lattice distortions and the Cu dimpling out of plane show a large anharmonic modulation with a periodicity of the order of 4.7 lattice units of the orthorhombic lattice, i.e., of the order of 2.4 nanometers in the diagonal direction of the CuO_2 lattice in agreement with EXAFS data [48] and previous standard X-ray diffraction works [112, 113]. The effect of this modulation on the electronic structure of the CuO_2 plane is relevant since the hopping integrals t and t′ should be modulated [114, 115] with the same spatial period. The additional periodicity induces the splitting of the single 2D band in several sub-bands [48] and the single 2D Fermi surface of the antibonding Cu $3d_{x^2-y^2}$ O $2p_{x,y}$ band split into several finite Fermi surface arcs. The presence of finite Fermi surface arcs has been identified in the normal phase of Bi2212 [64, 65, 116, 117]. The presence of sub-bands crossing the Fermi level

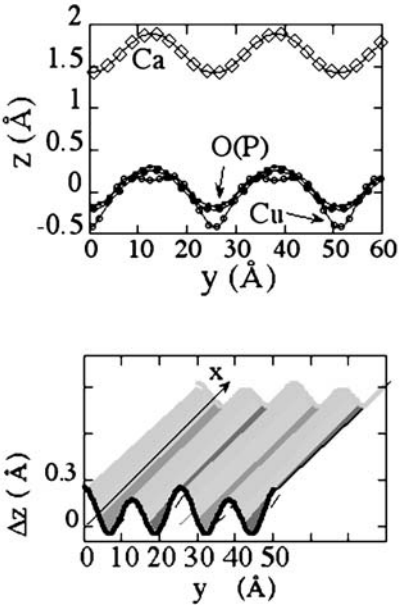

Fig. 22 The modulation of the position of the Cu ions in the diagonal direction of the planar CuO_2 lattice, i.e. in the b direction of the orthorhombic lattice of Bi2212 measure by anomalous X-ray diffraction tuning the wavelength of the incident photon beam around the Cu K-edge absorption edge [111]

due to the lattice modulation has shown that the description of the superconducting phase of cuprates requires a multiband scenario [118–122].

The multiband scenario, theoretically predicted since 1959, is not realized in standard materials because of mixing between bands due to the short mean free path for interband impurity scattering of single electrons, but becomes possible for the sub-bands of a periodic heterostructure. Moreover it can be easily shown [120–122] that when the chemical potential is tuned to a particular Van Hove singularity where the Fermi surface of one of the sub-bands shows an electronic topological transition (ETT) [30] with the variation of its dimensionality from 1D to 2D (or 2D to 3D) the exchange like integral giving the non diagonal term in the pairing shows a "shape resonance" [123] that gives a large amplification of the critical temperature.

The superconducting shape resonance in a heterostructure made of two intercalated sublattices has been now clearly observed in diborides where T_c is amplified by tuning the chemical potential in a energy window around a quantum critical point where one of the sub-bands of the boron multilayer changes its dimensionality from 2D to 3D [124–127].

8 Conclusion

In conclusion we have shown that the intrinsic physics of cuprates is driven by a nanoscale phase separation near quantum critical points for electronic topological transitions with formation of mesoscopic lattice modulations where the chemical potential and lattice inhomogeneity are self organized. It seem to us that the experiments show the formation of an interesting lattice modulation at the level of the wavelength of the electrons at the Fermi level such that the interband pairing between the sub-bands show a fascinating quantum resonance that can make stable the superconducting condensate at high temperature.

References

1. Bar-Yam Y, Egami T, Mustre de Leon J, Bishop AR (eds) (1992) Lattice effects in high T_c superconductors. World Scientific, Singapore
2. Müller KA, Benedek G (eds) (1993) Phase separation in cuprate superconductors. World Scientific, Singapore
3. Mihailovic D, Ruani G, Kaldis E, Müller KA (eds) (1995) Anharmonic properties of high Tc cuprates. World Scientific, Singapore; Kaldis E, Liarokapis E, Müller KA (eds) (1996) High T_c superconductivity 1996: ten years after the discovery. NATO ASI Series 343. Kluwer
4. Imada M, Fujimori A, Tokura Y (1998) Rev Mod Phys 70:1039 and references therein
5. Oyanagi H, Bianconi A (eds) (2001) Physics of local lattice distortions. AIP Conference Proceedings, vol 554. American Institute of Physics, Melville, New York
6. Sachdev S (ed) (1999) Quantum phase transitions. Cambridge University Press, Cambridge; Sachdev S (2003) Rev Mod Phys 75:913; Sachdev S (2003) Science 288:475
7. See, e.g., a review by Rao CNR, Arulraj A, Cheetham AK, Raveau B (2000) J Phys Cond Matter 12:R83; Rao CNR, Cheetham AK (1997) Science 276:911
8. Tokura Y (ed) (2000) Colossal magnetoresistive oxides. Gordon and Beach Science, New York and references therein
9. Dagotto E, Hotta T, Moreo A (2001) Phys Rep 344:1; Moreo A, Yunoki S, Dagotto E (1999) Science 283:2034
10. Millis AJ (1998) Nature 392:147
11. Edwards DM (2002) Adv Phys 51:1259 and references therein
12. Bishop AR, Shenoy SR, Sridhar S (eds) (2002) Intrinsic multiscale structure and dynamics. World Scientific, Singapore
13. Bianconi A, Saini NL (eds) (2000) Stripes and related phenomena. Kluwer/Plenum, New York
14. McElroy K, Simmonds RW, Hoffman JE, Lee D-H, Orenstein J, Eisaki H, Uchida S, Davis JC (2003) Nature 422:592
15. Matsuda A, Fujii T, Watanabe T (2003) Physica C 388/389:207
16. Vershinin M, Misra S, Ono S, Abe Y, Ando Y, Yazdani A (2004) Science 303:1995 and references therein; Misra S, Oh S, Hornbaker DJ, DiLuccio T, Eckstein JN, Yazdani A (2002) Phys Rev Lett 89:0870021
17. Haase J, Slichter CP (2003) J Supercond 16:473; Haase J, Sushkov OP, Horsch P, Williams GVM (2004) Phys Rev B 69:094504

18. Anderson PW (1997) The theory of superconductivity in the high-T_c cuprates. Princeton University Press, Princeton
19. Lanzara A, Bogdanov PV, Zhou XJ, Kellar SA, Feng DL, Lu ED, Yoshida T, Eisaki H, Fujimori A, Kishio K, Shimoyama J-I, Noda T, Uchida S, Hussain Z, Shen Z-X (2001) Nature 412:510 ; Zhou XJ, Yoshida T, Lanzara A, Bogdanov PV, Kellar SA, Shen KM, Yang WL, Ronning F, Sasagawa T, Kakeshita T, Noda T, Eisaki H, Uchida S, Lin CT, Zhou F, Xiong JW, Ti WX, Zhao ZX, Fujimori A, Hussain Z, Shen Z-X (2003) Nature 423:398
20. Shen Z-X, Lanzara A, Ishihara S, Nagaosa N (2002) Philos Mag B 82:1349; Ishihara S, Nagaosa N (2004) Phys Rev B 69:144520
21. Bussmann-Holder A, Müller KA, Micnas R, Büttner H, Simon A, Bishop AR, Egami T (2001) J Phys Condens Matter 13:L169; Bussmann-Holder A, Bishop AR, Büttner H, Egami T, Micnas R, Müller KA (2001) J Phys Condens Matter 13:L545
22. Bishop A, Mihailovic D, Mustre de Leon J (2003) J Phys Condens Matter 15:L169–L175
23. Rösch O, Gunnarsson O (2004) Phys Rev Lett 92:1464031 and references therein
24. Zech D, Keller H, Conder K, Kaldis E, Liarokapis E, Poulakis N, Müller KA (1994) Nature (London) 371:681; Zhao G-M, Hunt MB, Keller H, Müller KA (1997) Nature (London) 385:236
25. Lanzara A, Zhao G-M, Saini NL, Bianconi A, Conder K, Keller H, Müller KA (1999) J Phys Condens Matter 11:L541
26. Müller KA, Zhao G-M, Conder K, Keller H (1998) J Phys Condens Matter 10:L291
27. Rubio Temprano D, Mesot J, Janssen S, Conder K, Furrer A, Mutka H, Müller KA (2000) Phys Rev Lett 84:1990; Hofer J, Conder K, Sasagawa T, Zhao G-M, Willemin M, Keller H, Kishio K (2000) Phys Rev Lett 84:4192
28. Gweon G-H, Sasagawa T, Zhou SY, Graf J, Takagi H, Lee D-H, Lanzara A (2004) Nature 430:187
29. Sigmund E, Müller KA (ed) (1994) Phase separation in cuprate superconductors. Springer, Berlin Heidelberg New York
30. Lifshitz IM (1960) Soviet Physics JEPT 11:1130–1135
31. Sharma RP, Ogale SB, Zhang ZH, Liu JR, Wu WK, Veal B, Paulikas A, Zhang H, Venkatesan T (2000) Nature 404:736; Sharma RP (2002) (unpublished)
32. Bozin ES, Kwei GH, Takagi H, Billinge SJL (2000) Phys Rev Lett 84:5856 and references therein
33. McQueeney RJ, Petrov Y, Egami T, Yethiraj M, Shirane G, Endoh Y (1999) Phys Rev Lett 82:628; McQueeney RJ, Sarrao JL, Pagliuso PG, Stephens PW, Osborn R (2001) Phys Rev Lett 87:077001
34. Saini NL, Bianconi A, Oyanagi H (2001) J Phys Soc Jpn 70:2092; Saini NL, Oyanagi H, Ito T, Scagnoli V, Filippi M, Agrestini S, Campi G, Oka K, Bianconi A (2003) Eur Phys J B 36:75; Saini NL, Oyanagi H, Scagnoli V, Ito T, Oka K, Bianconi A (2003) J Phys Soc Jpn 72:829; Saini NL, Oyanagi H, Scagnoli V, Ito T, Oka K, Bianconi A (2003) Europhys Lett 63:125
35. Bianconi A, Saini NL, Lanzara A, Missori M, Rossetti T, Oyanagi H, Yamaguchi H, Oka K, Ito T (1996) Phys Rev Lett 76:3412
36. Saini NL, Lanzara A, Oyanagi H, Yamaguchi H, Oka K, Ito T, Bianconi A (1997) Phys Rev B 55:12759
37. Saini NL, Lanzara A, Bianconi A, Oyanagi H, Yamaguchi H, Oka K, Ito T (1996) Physica C268:121
38. Saini NL, Lanzara A, Bianconi A (1997) In: Johnson RL, Schmidt-Böcking H, Sonntag BF (eds) X-Ray and inner-shell processes. AIP Conference Proceedings 389. Woodbury, New York, p 565

39. Billinge SJL, Thorpe MF (eds) (1998) Local structure from diffraction. Plenum, New York
40. Gemmell DS (1974) Rev Mod Phys 46:129
41. Bianconi A, Incoccia L, Stipcich S (eds) (1983) EXAFS and near edge structure. Springer, Berlin Heidelberg New York
42. Prinz R, Koningsberger D (eds) (1988) X Ray absorption: principle, applications techniques of EXAFS, SEXAFS and XANES. Wiley, New York
43. Bianconi A, Garcia J, Marcelli A, Benfatto M, Natoli CR, Davoli I (1985) J Physique (Paris) 46(C9):101
44. Benfatto M, Natoli CR, Bianconi A, Garcia J, Marcelli A, Fanfoni M, Davoli I (1986) Phys Rev B 34:5774
45. Bianconi A (1988) In: Prinz R, Koningsberger D (eds) X Ray absorption: principle, applications techniques of EXAFS, SEXAFS and XANES. Wiley, New York
46. Bianconi A, Garcia J, Benfatto M (1988) In: Mandelkow E (ed) Topics in current chemistry 145. Springer, Berlin Heidelberg New York, p 29
47. Saini NL, Lanzara A, Oyanagi H, Yamaguchi H, Oka K, Ito T, Bianconi A (1997) Phys Rev B 55:12759
48. Bianconi A, Saini NL, Rossetti T, Lanzara A, Perali A, Missori M, Oyanagi H, Yamaguchi H, Nishihara Y, Ha DH (1996) Phys Rev B 54:12018
49. Lanzara A, Saini NL, Brunelli M, Natali F, Bianconi A, Radaelli PG, Cheong S-W (1998) Phys Rev Lett 81:878
50. Stern EA, Ma Y, Hanske-Petitpierre O, Bouldin CE (1992) Phys Rev B 46:687
51. Babanov YA, Shvetsov VR (1986) J Phys (Paris) 47:C8–37; J Non Cryst Solid 79:1
52. Oyanagi H, Shioda R, Kuwahara Y, Haga K (1995) J Synchrotron Rad 2:99; Oyanagi H (1998) J Synchrotron Rad 5:48
53. Oyanagi H, Fonne C, Gutknecht D, Dressler P, Henck R, Lampert M-O, Ogawa S, Kasai K, Mohamed SB (2003) Nuclear Inst Meth Phys Res A 513:340
54. Tröger L, Arvanitis D, Baberschke K, Michaelis H, Grimm U, Zschech E (1992) Phys Rev B 46:3283
55. Goulon J, Goulon-Ginet C, Cortes R, Dubois JM (1982) J Phys 43:539
56. Pfalzer P, Urbach J-P, Klemm M, Horn S, DenBoer ML, Frenkel AI, Kirkland JP (1999) Phys Rev B 60:9335
57. Lanzara A, Saini NL, Bianconi A, Hazemann JL, Soldo Y, Chou FC, Johnston DC (1997) Phys RevB 55:9120
58. Saini NL, Lanzara A, Bianconi A, Oyanagi H (1998) Phys Rev B 58:11768
59. See, e.g., Müller KA (2000) In: Bianconi A, Saini NL (eds) Stripes and related phenomena. Kluwer/Plenum, New York
60. Ihara H (1994) Bull Electrotech Lab 58:64
61. Izumi F, Takayama-Muromachi E (1995) In: Shi D (ed) High temperature superconducting materials and engineering. Pergamon, p 81
62. Axe JD, Moudden AH, Hohlwein D, Cox DE, Mohanty KM, Moodenbaugh AR, Xu Y (1989) Phys Rev Lett 62:2751
63. Saini NL, Lanzara A, Bianconi A, Oyanagi H (2000) Eur Phys J B 18:257
64. Saini NL, Avila J, Bianconi A, Lanzara A, Asensio MC, Tajima S, Gu GD, Koshizuka N (1997) Phys Rev Lett 79:3467; (1999) Phys Rev Lett 82:2619; (2000) Physica C 341/348: 2071
65. Saini NL, Avila J, Asensio MC, Tajima S, Gu GD, Koshizuka N, Lanzara A, Bianconi A (1998) Phys Rev B 57:R11101
66. Chung J-H, Egami T, McQueeney RJ, Yethiraj M, Arai M, Yokoo T, Petrov Y, Mook HA, Endoh Y, Tajima S, Frost C, Dogan F (2003) Phys Rev B 67:014517

67. Pintschovius L, Reichardt W, Kläser M, Wolf T, Löhneysen H van (2002) Phys Rev Lett 89:037001; Pintschovius L, Braden M (1999) Phys Rev B 60:R15039
68. Fukuda T, Mizuki J, Ikeuchi K, Fujita M, Yamada K, Baron AQR, Tsutsui S, Tanaka Y, Endoh Y Cond-Mat/0306190
69. Saini NL, Oyanagi H, Molle M, Garg KB, Kim C, Bianconi A (2004) J Phys Chem Sol 65:1439
70. Rao CNR, Ganguli AK (1995) Chem Soc Rev 24:1
71. Edwards PP, Peakok GB, Hodges JP, Asab A, Gameson I (1996) In: Kaldis E, Liarokapis E, Müller KA (eds) High T_c superconductivity: ten years after the discovery. NATO ASI, vol 343. Dordrecht, Kluwer, p 135
72. Goodenough JB (1990) Supercond Sci Technol 3:26; Goodenough JB, Marthiram A (1990) J Solid State Chem 88:115; Zhu YT, Manthiram A (1994) Phys Rev B 49:6293
73. Attfield JP, Kharlanov AL, McAllister JA (1998) Nature 394:157; Locquet JP, Perret J, Fompeyrine J, Mächler E, Seo JW, Van Tendelloo G (1998) Nature 394:453
74. Sato H, Tsukada A, Naito M, Matsuda A (2000) Phys Rev B 61:12447
75. Marezio M, Licci F (1997) Physica C 282:53
76. Batlogg B, Varma CM (2000) Phys World 13(2)
77. Bianconi A, Bianconi G, Caprara S, Di Castro D, Oyanagi H, Saini NL (2000) J Phys Cond Mat 12:10655; Agrestini S, Saini NL, Bianconi G, Bianconi A (2003) J Phys A Math Gen 36:9133 and references therein
78. Miller LL, Wang XL, Wang SX, Stassis C, Johnston DC, Faber J Jr, Loong C-K (1990) Phys Rev B 41:1921
79. Saini NL, Oyanagi H, Lanzara A, Di Castro D, Agrestini S, Bianconi A, Nakamura F, Fujita T (2001) Phys Rev B 64:132510–1
80. Ichikawa N, Uchida S, Tranquada JM, Niemöller T, Gehring PM, Lee S-H, Schneider JR (2000) Phys Rev Lett 85:1738 and references therin
81. Benfatto M, Natoli CR, Bianconi A, Garcia J, Marcelli A, Fanfoni M, Davoli I (1986) Phys Rev B 34:5774
82. Durham PJ (1988) In: Prinz R, Koningsberger D (eds) X-Ray absorption: principles, applications, techniques of EXAFS, SEXAFS, XANES. Wiley, New York
83. Wu ZY, Benfatto M, Natoli CR (1992) Phys Rev B45:531; Wu ZY, Benfatto M, Natoli CR (1993) Solid State Commun 87:475
84. Saini NL, Oyanagi H, Wu Z, Bianconi A (2002) Supercond Sci Technol 15:439–445
85. Li C, Pompa M, Congiu Castellano A, Della Longa S, Bianconi A (1991) Physica C175: 369; Bianconi A, Li C, Della Longa S, Pompa M (1992) Phys Rev B 45:4989
86. Wu Z, Saini NL, Bianconi A (2001) Phys Rev B 64:092507
87. Wagner JL, Radaelli PG, Hinks DG, Jorgensen JD, Mitchell JF, Dabrowsky B, Knapp GS, Beno MA (1993) Physica C 210:447; Radaelli PG, Wagner JL, Hunter BA, Beno MA, Knapp GS, Jorgensen JD, Hinks DG (1993) Physica C 216:348
88. Hunt AW, Singer PM, Thruber KR, Imai T (1999) Phys Rev Lett 82:4300
89. Singer PM, Hunt AW, Cederström AF, Imai T (1999) Phys Rev B 60:15345
90. Röhler J, Larisch A, Schafer R (1991) Physica C 191:57; Röhler J (1994) In: Kaldis E (ed) Materials and crystallographic aspects of HTc-superconductivity. Kluwer, Netherlands, p 353
91. Oyanagi H, Oka K, Unoki H, Nishihara Y, Murata K, Yamaguchi H, Matsushita T, Tokumoto M, Kimura Y (1989) J Phys Soc Jpn 58:2896; Oyanagi H, Kimura H, Terashima T, Bando Y (1995) J Phys Soc Jpn 64:2563
92. Zhao G-M, Conder K, Keller H, Müller KA (1998) J Phys Condens Matter 10:9055
93. Mustre de Leon J, De Coss R, Bishop AR, Trugman SA (1999) Phys Rev B 59:8359
94. Andergassen S, Caprara S, Di Castro C, Grilli M (2001) Phys Rev Lett 87:056401

95. Braden M, Schweiss P, Heger G, Reichardt W, Fisk Z, Gamayunov K, Tanaka I, Kojima H (1994) Physica C 223:396
96. Radaelli PG, Hinks DG, Mitchell AW, Hunter BA, Wagner JL, Dabrowsky B, Vandervoort KG, Viswanathan HK, Jorgensen JD (1994) Phys Rev B 49:4163
97. Yamamoto A, Onoda M, Takayama-Muromachi E, Izumi F, Ishigaki T, Asano H (1990) Phys Rev B 42:4228; Beskrovnyi AI, Dlouhà M, Jiràk Z, Vratislav S, Pollert E (1990) Physica C 166:79; Beskrovnyi AI, Dlouhà M, Jiràk Z, Vratislav S (1990) Physica C 171:19
98. Grüner G (1994) Density waves in solids. Frontiers in physics, vol 89. Addison-Wesley, USA
99. Bishop A, Mihailovic D, Mustre de Leon J (2003) J Phys: Condens Matter 15:L169–L175
100. Kusmartsev FV (2002) Europhys Lett 57:557; (2001) Europhys Lett 54:786
101. Bianconi A, Di Castro D, Bianconi G, Pifferi A, Saini NL, Chou FC, Johnston DC, Colapietro M (2000) Physica C 341/348:1719
102. Radaelli PG et al. (1996) Phy Rev Lett 75:4488; Radaelli PG et al. (1996) Phys Rev B 54: 8992
103. Tokura Y, Nagaosa N (2000) Science 288:462
104. Ahn KH, Lookman T, Bishop AR (2004) Nature 428:401
105. Schiffer P, Ramirez AP, Bao W, Cheong S-W (1995) Phys Rev Lett 75:3336; Chen CH, Cheong SW (1996) Phys Rev Lett 76:4042
106. Agrestini S, Saini NL, Lanzara A, Natali F, Bianconi A (2000) Int J Mod Phys B 14: 2852–2857
107. Kim KH, Uehara M, Cheong S-W (2000) Phys Rev B 62:R11945
108. Kiryukhin V, Koo TY, Ishibashi H, Hill JP, Cheong S-W (2001) Phys Rev B 67:064421 (2003) and references therein; Phys Rev B 63:144406
109. Radaelli PG, Iannone G, Marezio M, Hwang HY, Cheong S-W, Jorgensen JD, Argyriou DN (1997) Phys Rev B 56:8265–8276
110. Zhang J, Dai P, Fernandez-Baca JA, Plummer EW, Tomioka Y, Tokura Y (2000) Phys Rev Lett 86:3823
111. Bianconi A, Lusignoli M, Saini NL, Bordet P, Kvick Å, Radaelli PG (1996) Phys Rev B 54:4310
112. Bianconi A (1993) In: Muller KA, Benedek G (eds) Phase separation in cuprate superconductors. World Scientific, Singapore, pp 125–138 and Final Discussion of the meeting in June 1992, p 350
113. Bianconi A, Missori M, Saini NL, Oyanagi H, Yamaguchi H, Oyanagi H, Yamaguchi H, Nishiara Y, Ha DH, Della Longa S (1995) In: Mihailovic D, Ruani G, Kaldis E, Müller KA (eds) Anharmonic properties of high T_c cuprates. World Scientific, Singapore, pp 127–138; Proceedings of the Workshop held in Bled, 1–6 September 1994
114. Bianconi A (2000) Int J Mod Phys B 14:3289
115. Saini NL, Bianconi A (2000) Int J Mod Phys B 14:3649
116. Bianconi A, Saini NL, Lanzara A, Avila J, Asensio MC, Tajima S, Gu GD, Koshizuka N (1999) Physica C 317/304, 318
117. Bianconi A, Saini NL, Valletta A, Lanzara A, Avila J, Asensio MC, Tajima S, Gu GD, Koshizuka N (1998) J Phys Chem Solids 59:1884
118. Bianconi A, Missori M, Saini NL, Oyanagi H, Yamaguchi H, Ha DH, Nishiara Y (1995) J Superconductivity 8:545
119. Perali A. Bianconi A, Lanzara A, Saini NL (1996) Solid State Commun 100:181
120. Bianconi A, Valletta A, Perali A, Saini NL (1997) Solid State Commun 102:369
121. Valletta A, Bianconi A, Perali A, Saini NL (1997) Z Phy B 104:707
122. Bianconi A, Valletta A, Perali A, Saini NL (1998) Physica C Superconductivity 296: 269

123. Bianconi A (2002) Ugo Fano and shape resonances. In: Bianconi A, Marcelli A, Saini NL (eds) X-rays and inner shell processes. AIP conference Proceedings. AIP, Melville, New York
124. Bianconi A, Di Castro D, Agrestini S, Campi G, Saini NL, Saccone A, De Negri S, Giovannini M (2001) J Phys Condens Matter 13:7383
125. Bianconi A, Di Castro D, Agrestini S, Zangari G, Saini NL, Saccone A, De Negri S, Giovannini M, Profeta G, Continenza A, Satta G, Massidda S, Cassetta A, Pifferi A, Colapietro M (2002) Phys Rev B 65:174515
126. Bussmann-Holder A, Bianconi A (2003) Phys Rev B 67:132509
127. Bianconi A, Agrestini S, Bussmann-Holder A (2004) J Superconductivity 17:205

Struct Bond (2005) 114: 331–364
DOI 10.1007/b101024

Dynamic Inhomogeneity, Pairing and Superconductivity in Cuprates

Dragan Mihailovic (✉) · Viktor V. Kabanov

Jozef Stefan Institute and Dept. of Mathematics and Physics, Jamova 39, 1000 Ljubljana, Slovenia
Dragan.mihailovic@ijs.si

Abstract In cuprates there is a significant body of evidence for the existence of electronically driven dynamic inhomogeneity which might arise from the existence of polarons, bipolarons or other charged objects such as stripes, whose presence may be an essential ingredient for high-temperature superconductivity. In this review we examine the experimental evidence for such objects, defining the length, time and energy scales of the relevant elementary excitations. The dynamics of the objects below and above T_c are examined in detail with femtosecond spectroscopy and compared with magnetic and other measurements. The dynamically inhomogeneous state is described theoretically by considering an interaction between electrons, spins and the lattice. By symmetry, only electrons in degenerate states can couple to the lattice and spins to give an *anisotropic*, *d*-wave symmetry interaction. The proposed interaction acts on a mesoscopic length-scale, taking into account the interplay

of Coulomb repulsion between particles and anisotropic elastic strain, and leads to the formation of bipolaron pairs and stripes. The predicted symmetry breaking associated with pairing and stripe formation are observed in numerous experiments. The phenomenology associated with the co-existence of pairs and clusters (stripes) is found to apply to many different experiments ranging from femtosecond dynamics to transport measurements. Excitations of the system are described quite well in terms of a two-level system, although we find that a complete description may require a more complicated energy landscape due to presence of mesoscopic objects such as stripes or clusters. The formation of the superconducting state can be understood quantitatively to be the result of the establishment of phase coherence percolation across pairs and stripes

Keywords Superconductivity · Inhomogeneity · Femtosecond spectroscopy · Jahn-Teller effect · Local pairing · Stripes

1 Introduction

Inhomogeneity appears to play an important role in determining the fundamental physics of many oxides, including superconducting cuprates, complex manganites and relaxor ferroelectrics. Even though the origins of the observed inhomogeneity are not yet entirely understood, it is believed to be related to nano-scale charge and spin ordering, driven by interactions between the doped charge carriers and their interaction with the lattice. Competition between interactions, particularly Coulomb and lattice deformations on different length-scales may lead to meso-scale ordering of charges and spins, reflected by phonon anomalies at finite wavevectors, phase separation, nano-scale pattern formation and incommensurate spin nanostructures.

Signatures of inhomogeneity have been found by very different experiments [1], probing on various time- and length-scales – in real space or in *k*-space – often leading to seemingly different and inconsistent interpretations. Many techniques typically give information which involves either spatial or temporal averaging (or most often both) and thus reveal different aspects of the problem from their respective viewpoints. Many such experiments which probe average lattice or electronic properties fail to observe inhomogeneities and some of these apparent discrepancies are not yet clearly understood. For example, local probe techniques which freeze the motion of ions on short timescales (e.g. XAFS [2] or neutron PDF studies [3]) which are eminently suitable for detection of these meso-scale patterns and deviations of lattice structure from the average, appear to be inconsistent with slower techniques such as NMR [4], or standard diffraction techniques which also appear to show no evidence of static inhomogeneity. For example, recent resonant X-ray scattering experiments have not shown any evidence of charge ordering or inhomogeneity. The resolution in these experiments, however, is limited by the X-ray wavelength of λ=2.2 nm, and the features on a length-scale of the coherence length ξ_s~1–2 nm

might be missed [5]. A different problem occurs with optical experiments, such as femtosecond pump-probe experiments, which have spatial resolution which is limited by the wavelength of light (typically 800 nm).

Yet, a multi-component response, as a sign of an inhomogeneous state has been consistently observed in time-resolved and many other experiments, such as ESR [6], NMR [7], magnetic susceptibility [8], as well as optical conductivity [9] and ARPES [10] (peak-dip-hump structure).

One possible way to resolve these discrepancies is to assume that inhomogeneity dynamics occurs on a timescale which is relatively fast. Although this cannot explain the static surface inhomogeneity observed in scanning tunnelling microscope measurements [11], which show both a superconducting gap and pseudogap structure on the surface, these static features might be due to surface pinning on defects or impurities.

Thus, the experimental challenge of the last decade has been to invent and perfect new techniques for the investigation of bulk dynamic inhomogeneities on time-scales sufficiently short to give information on the dynamics of the relevant excitations giving new insight into the microscopic origins of the dominant interactions leading to the observed dynamic complexity.

The experimental observations of inhomogeneity have also posed fundamental challenges for theories attempting to describe the multi-component inhomogeneous ground state in a consistent and unified manner – and leads to a description of superconductivity. The interplay of different phases with different symmetry, interacting on a mesoscopic scale is thought to be particularly interesting, and will be explored in some detail.

The review is divided into four parts. First we briefly summarise some of the evidence and arguments for the existence of lattice inhomogeneity and the inhomogeneity of the electronic structure. In the second part, we concentrate on a series of time-resolved optical experiments, which give a great deal of information on charge carrier dynamics on fast timescales, revealing ubiquitous presence of multi-component pair recombination dynamics associated with the presence of a dynamic spatially inhomogeneous electronic structure. The distinguishing feature of time-resolved experiments is that they can distinguish between different excitations even when these have the same energy scale, i.e. situations where spectroscopies such as ARPES, Raman, infrared, STS etc. – which cannot intrinsically distinguish between homogeneous and inhomogeneous lineshapes – fail. The important and generic results of time-resolved experiments on cuprates are analysed theoretically using a phenomenological level using effectively two-level systems, which leads to a two-component description of the ground state. The inhomogeneity is inferred to be mesoscopic or microscopic rather than macroscopic.

In the third section, our theoretical understanding of the electronic ground state and pairing is developed. The line of reasoning which we use is motivated by the original ideas of G. Bednorz and Muller KA on Jahn-Teller polarons, which lead to the discovery of high-temperature superconductivity in $La_{2-x}Ba_XCuO_4$ [12]. A model Hamiltonian is proposed to describe the symme-

try-allowed interactions which are consistent not only with the time-resolved experiments, but also numerous others, such as NMR, bulk susceptibility, Raman and ARPES etc. Some of the important and very specific manifestations of the proposed model interaction are discussed, particularly related to spatial symmetry breaking, in agreement with observations of such phenomena in the superconducting cuprates.

Finally in the last section we consider how the proposed picture can lead to superconductivity and describe the phase diagram arising from the inhomogeneous-state description. In each section, the issues are separately justified with the interpretations as concise as possible, and limited to the issues in hand. We also include criticisms and open issues wherever these are thought to be important.

2
Evidence for Inhomogeneity: Length, Time and Energy Scales

At present there is no single technique which can reliably give accurate spatially-resolved, real-time picture of the nano-scale lattice dynamics, electronic or spin structure, and these have to be deduced by combining the results of different techniques. For example, local probe techniques such as XAFS and neutron scattering with pair-distribution function (PDF) analysis, give information on near-instantaneous positions of atoms in relation to their nearest neighbours, but their accuracy is limited by the limited range of wavevectors k which can be measured, and have pitfalls in modelling the data, leading to ambiguity in atomic displacements which are deduced [2]. NMR has an even shorter range, and has a relatively slow timescale of the order of 10^{-7} s, averaging out any dynamics which might be occurring on faster timescales. STM is limited to the surface, and is a quasi-static probe of the inhomogeneity in the density of surface states, but has nevertheless received a great deal of attention lately.

In the time-domain, optical time-resolved techniques can accurately measure electronic relaxation times and pair recombination processes in the bulk on timescales from femtoseconds to microseconds, but since the spatial resolution is limited, the existence of spatial inhomogeneity is deduced on the basis of the observation of multi-component relaxation processes and modelling of the electronic structure.

2.1
Length-Scales: Real Space

Direct measurements of a dynamical inhomogeneities in bulk are not yet within the realm of experimental possibility, so information on length-scales needs to be pieced together from different techniques. Scanning-tunnelling microscopy (STM) experiments of DeLozanne et al. [11] on the surface of $YBa_2Cu_3O_{7-\delta}$ and more recently by the Berkeley groups on $Bi_2Sr_2CaCu_2O_8$ [11] show the local

density of electronic states at different points on the surface to be very inhomogeneous, with a characteristic length-scale of the order of l_0~1–2 nm. The surface inhomogeneity clearly shows the lattice symmetry properties, e.g. tetragonal *d*-wave-like symmetry surrounding single defects for example [11]. Certainly BiSCO and YBCO superconductors appear to be inhomogeneous on the surface, yet the two materials differ significantly in the details. YBCO shows quite clear stripe-like features along the crystallographic *b* axis – which appear to be connected with its Cu-O chain structure – while BiSCO shows features with typically fourfold symmetry. Unfortunately the exposed surfaces observed by STM are *not* CuO_2 layers in either case, but intermediate layers in the charge reservoirs (Bi-O layers or Cu-O chains respectively). Whether these inhomogeneities are also present in the bulk cannot be deduced from STM experiments, but the observed length scale is clearly in the range of l_0~1–2 nm, with some additional hints of the existence of larger objects, resembling charge or spin density wave segments, observed by Howald et al. [11].

A structural length scale can also be deduced from diffuse diffraction measurements. For example, Kimura et al [13] deduced a structural coherence length of 1.7 nm in underdoped $La_{1.9}Sr_{0.1}CuO_4$ at 315 K (i.e. near the pseudogap temperature). The structural coherence length is deduced from the *k*-linewidth of the diffuse central peak (Δk=0.06 Å^{-1}). Well below T_c (at T=13.5 K) the structural coherence length is extended to l_s>10 nm (the linewidth is resolution limited). Unfortunately there are presently no detailed studies of structural inhomogeneities in LSCO over a large range of temperatures, but recent studies on superconducting $YBa_2Cu_3O_{6+x}$ have revealed the existence of c-axis order as well as in-plane inhomogeneity on a similar length-scale of 1–2 nm above T_c. Islam et al. [14] find diffuse peaks in neutron scattering which originate from mutually coupled, primarily longitudinal displacements along the *a* axis of the CuO_2, CuO chain and apical O or Ba atoms. The characteristic *T*-dependence of these peaks shows them to be related to the pseudogap *T**. A similar temperature dependence is also displayed by atomic displacements observed in ion-channelling experiments [15].

The structural coherence length scale appears to be linked with the length scales deduced from spin-ordering [16], which also shows similar temperature dependence.

We can also obtain an intrinsic structural coherence length scale from the QP lifetimes measured by femtosecond spectroscopy. The QP recombination time τ_R is related to the anharmonic lifetime τ_{anh} of high-frequency phonons involved in the QP recombination process, whose lifetime in turn is limited by the escape time of their decay products, namely acoustic phonons. Thus τ_R is essentially determined by the acoustic phonons' mean free path, which in determined by the length-scale of structural inhomogeneities. So the structural length scale $l_0=v_s\tau_R$ where v_s is the sound velocity. From the data on τ_R for YBCO and other cuprates, near T_c, we obtain – rather remarkably – a characteristic length of $l_0\approx$2 nm. l_0 decreases slowly above T_c but increases more rapidly below T_c. The length scale determined from the re-

combination time will be discussed in more detail later in the section on QP dynamics.

The fact that the superconducting coherence length in hole-doped cuprates ξ_s~1–2 nm is very similar to the inhomogeneity length scale l_0 at temperatures near the superconducting T_c is probably not a coincidence, and has important implications for superconductivity, and particularly supporting the existence of percolative superconductivity.

2.2 *k*-Space–Derived Length Scale

Inelastic neutron scattering experiments on phonons in hole-doped $YBa_2Cu_3O_{7-\delta}$ [17], $La_{2-x}Sr_xCuO_4$ [18] and inelastic X-ray scattering in electron-doped $Nd_{1.86}Ce_{0.14}CuO_{4+\delta}$ [19] all show a strong phonon anomaly starting close to the middle of the Brillouin zone (BZ). The data show a high-frequency optical phonon mode near 85 meV, which is well-defined at the zone centre, but becomes strongly damped and virtually disappears in the middle of the BZ. A mode then re-appears at near 70 meV towards the edge of the BZ in the $(\varphi, 0)$ direction (corresponding to the Γ–M direction in LSCO). The wavevector of the centre of the anomaly k_0 corresponds rather closely to the length-scale l_0 of real-space textures in STM images as discussed in the previous section. The two can be related by $k_0 \sim \pi/l_0$, where π/k_0=2–3 unit cells (0.8–1.2 nm) in LSCO [18]. The anomaly appears over a relatively range of wavevectors Δk corresponding to the range of spatial distortion with a range of Δl_0.

The fact that Δk spans approximately half the BZ, implies that there is no long range order associated with these anomalies, which would also imply the existence of clear new peaks in diffraction experiments. Long range ordered charge stripes would appear over a much narrower range of k than the nanoscale objects seen by STM, and their existence can also be excluded by the STM, INS data discussed above, as well as resonant X-ray scattering [5] and many other diffraction techniques. Moreover commensurate or incommensurate *static* stripes should give rise to a clearly observable zone folding, but this is not observed in X-ray diffraction (XRD) or Raman scattering, supporting the view that the inhomogeneous structure is dynamic. We conclude that the INS and inelastic X ray scattering experiments speak for the existence of dynamic bulk inhomogeneities which have a similar length-scale l_0 as the ones observed on the surface by STM.

It should be mentioned that such anomalies in k-space have also been observed in other non-superconducting materials such as La_2NiO_4. The details (e.g. temperature-dependence, characteristic range Δk, and general texture of the nanoscale structure) are different however. Indeed a concise experimental comparison with superconducting cuprates still needs to be performed. The existence of phonon anomalies in La_2NiO_4 and La_2MnO_4 implies the existence of charge inhomogeneity and also charge ordering, but does not necessarily imply superconductivity as well. The view of the present authors is that the

occurrence of superconductivity depends on whether the inhomogeneity is associated with pairs, single polarons or a charge-ordered (CDW) state. As we shall see later, the evidence for spin singlets [20, 48] and absence of a Curie susceptibility in the cuprates overwhelmingly supports the view that the inhomogeneity is associated with singlet pair formation.

2.3 Time-Scales: Dynamic Probes

Possibly the first experiments which unambiguously showed the presence of an inhomogeneous *electronic* structure of bulk materials on a picosecond timescale were non-equilibrium Raman experiments with picosecond laser pulses, which clearly showed the presence of localized states in metallic, optimally doped YBCO [21] . The activation energies for hopping of photoexcited carriers was found to be close to the "pseudogap energy" scale E_p in YBCO, with E_a=34 ~210 meV, depending on doping. The experiments also showed clearly that the hopping process was coupled to the lattice [22]. Subsequent more detailed and systematic time-resolved pump-probe experiments (to be explained in more detail in the following section) showed the presence of multiple intrinsic relaxation times, which appeared to confirm the co-existence of localised and itinerant states [23, 24] with vastly different timescales. The pair recombination dynamics appears on a timescale of 10^{-13} s, while localised states appear to have a distribution of lifetimes which extend to hundreds of microseconds [24, 25].

XAFS and neutron PDF experiments probe the local structure on timescales of the order of 10^{-15} to 10^{-12} s. In the case of XAFS, the motion of excitations whose energy scales are less than ~500 meV is effectively "frozen". This energy scale is a few tens of meV in the case of neutron PDF. Significantly, XAFS structure snapshots are on a timescale, which is faster than both the pair recombination time and lattice motion. This means that it can be used to "freeze" the structure of lattice distortions associated with local pairs, which occur on an energy scale of the pseudogap (<100 meV); hence the techniques have been very important in pointing out the presence of inhomogeneities in cuprates and other oxides [26]. The interpretation of these structures in terms of long-range ordered stripes has proved controversial [2], although there appears to be an emerging consensus that significant deviations from an average structure exist on timescales 10^{-10} to 10^{-14} s.

Another clear indication of the relevant timescale comes from the linewidths of anomalous phonon spectra observed in INS around k_0, which are of the order of ΔE~4–5 meV [18]. The implied lifetime of the excitations is $\tau=h/\pi c\Delta E$ ~300 fs. This is comparable with the superconducting pair recombination lifetime of τ_R~300–1000 fs as measured directly by femtosecond optical techniques using time-resolved pump-probe excited state absorption [23]. A similar lifetime is obtained by THz radiation pump-probe [27] experiments which directly measure the condensate recovery as a function of time after excitation by 70 femtosecond optical pulses. The connection between the appearance of charge-

related inhomogeneity in INS and pair recombination measured by optical time-resolved techniques is clearly implied.

2.4 Energy Scale of the Relevant Interactions

The energy scale of the anomalies in INS and ARPES is ~50–100 meV, and is the same as the magnitude of the pseudogap E_p in the equivalent doping range, as determined by single particle tunnelling [28], femtosecond timescale pump-probe recombination experiments [23, 29, 30], non-equilibrium Raman experiments [22], and other techniques which measure the *charge* excitation spectrum. As an example, in Fig. 1, we compare the "pseudogap" magnitude determined by QP recombination [23] and tunnelling [28] with the anomaly observed in neutron data [17] (shaded area). The excitation has the same energy scale, virtually the same lifetime and a similar temperature dependence, confirming that the "object" observed in INS and time-resolved experiments is one and the same. The energy scale of inhomogeneity thus appears to be defined by the charge-excitation "pseudogap" E_p. From the observation that *charge* excitations in YBaCuO typically show a higher energy gap than *spin* excitations [20], it would appear that spin inhomogeneity and ordering follows the formation charge inhomogeneities, which seemingly occur first.

Another energy scale in cuprates is defined by the superconducting T_c, but at present we are not aware of any evidence of a link between the appearance

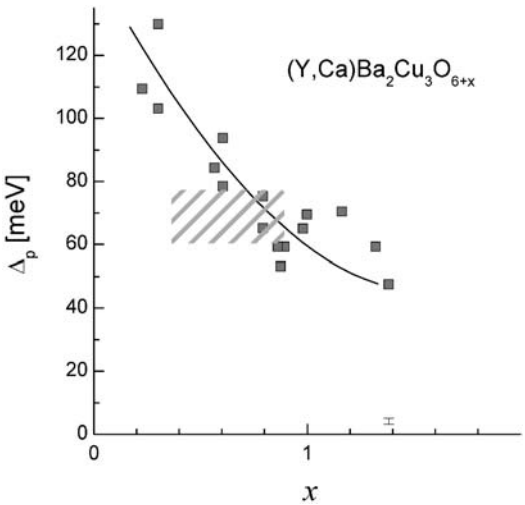

Fig. 1 The magnitude of the pseudogap from time-resolved QP recombination experiments compared to the energy scale of the anomalies observed in neutron data in YBCO (*shaded region*) [18], connecting lattice anomalies with QP recombination dynamics

of inhomogeneities and the onset of superconductivity at T_c. Thus inhomogeneity appears to be intimately related primarily to the "pseudogap" behaviour in cuprates, while superconductivity itself is associated with the Γpoint of the Brillouin zone, i.e. the zero-momentum state.

3 Time Resolved Experiments Probing the Dynamics of the Inhomogeneous State

The measurement of the time-resolved optical response in general gives detailed information on low-energy excited state lifetimes, more specifically on quasiparticle recombination and related inhomogeneity dynamics. Generally, the pump-probe technique involves a measurement of the change of reflectivity (or transmittance, for the case of a thin film) of the superconductor as a function of time after a short "pump" laser pulse excitation. Although the energy of laser photons used to excite the superconductor is large compared to the gap, the photoexcited charge carriers quickly relax from 1.5 eV to low energies by electron-electron and electron-phonon scattering. This process is known to proceed on a timescale of~10–100 fs. A gap in the low-energy excitation spectrum (such as occurs in a superconductor or semiconductor or charge-density-wave system), may lead to a bottleneck situation where QPs accumulate at the bottom of the band (see Fig. 2). These photoexcited quasi-

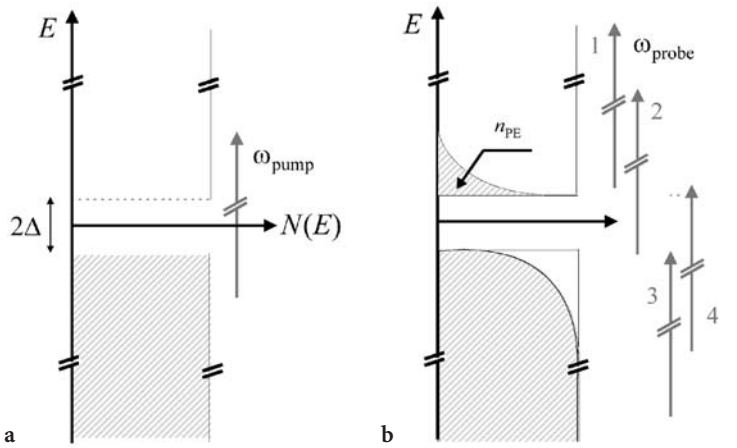

Fig. 2 A schematic diagram of the photoexcitation and subsequent relaxation processes in cuprates: **a** pump**; b** probe laser pulses; these are separated by a variable time delay. All possible probe processes are shown in **b**. Whether the change is a photoinduced absorption or bleaching depends on *which* optical processes (1 to 4) are dominant. If by coincidence all probe transition probabilities are equal, there is no photoinduced signal (see paper by Dvorsek et al. in [30])

particles are detected by the probe photons using a suitably delayed laser pulse by what is effectively an excited state absorption of photoexcited quasiparticles (as shown in Fig. 2) [29, 30]. The measurement of the amplitude of the changes in probe pulse reflectivity (or transmittance) as a function of time directly measures the recombination dynamics. The temperature dependence of the excited state absorption in pump-probe measurements can be used to determine the temperature dependence of the gap, its magnitude, as well as – to some extent – its symmetry on pairing timescales.

Following initial pioneering experiments of time-resolved reflectivity on cuprates [31], the technique has been shown to give excellent reproducibility from sample to sample, and data from different groups have been in close agreement. (The variances which have been reported so far have been related to the low-temperature lifetime (well below T_c) which appears to be strongly dependent on the heating caused by the pump laser pulses, and possibly also sample quality [32]).

3.1
Experimental Observations of Multi-Component Relaxation

The typical time-resolved reflectivity response for YBCO is shown in Fig. 3. The response at short times (from 0.1 to 5 ps) is qualitatively similar in all HTS materials. At short times after photoexcitation a fast response is observed with τ_1=0.3~1 ps (depending on material), which is almost T-independent, followed at longer times (but still on the picosecond timescale) by a somewhat slower decay. This second decay appears only *below* T_c, and its lifetime is T-dependent, showing clear signs of divergence as T_c is approached from below. (The divergence of τ_S is an unambiguous indication that it represents recombination across a superconducting gap which is temperature dependent near T_c, since $\tau_S \propto 1/\Delta_s(T)$, and $\Delta_s(T) \to 0$ as $T \to T_c$.).

In addition to the response on the 0.1–3-ps timescale, a ubiquitous long-lived response is observed which has been attributed to localised states [24]. This will be discussed later.

The two fast responses may have the same or opposite sign in different materials, which is a consequence of the different optical processes of the probe pulse [29] (shown in Fig. 2). In YBCO [23], LaSCO, NdCeCuO [33] and HgBaCaCuO [29] they typically have the same sign for 800 nm probe wavelength (YBCO and Hg-1223 are also shown in Fig. 3), while in Tl-based and Bi-based cuprates they have opposite signs [34]. Remarkably, the temperature dependence of the amplitude (i.e. magnitude of photoinduced reflectivity or absorption) of the two responses appears to be quite universal in the cuprates (Fig. 4). A careful analysis of the amplitude of the two signals gives two distinct temperature dependences. The superconducting state response τ_s, always disappears abruptly at T_c, while the other faster response τ_p, disappears asymptotically at much higher temperature T^*. The component with the fast response, whose relaxation time is τ_p, can be unequivocally associated with the "pseudo-

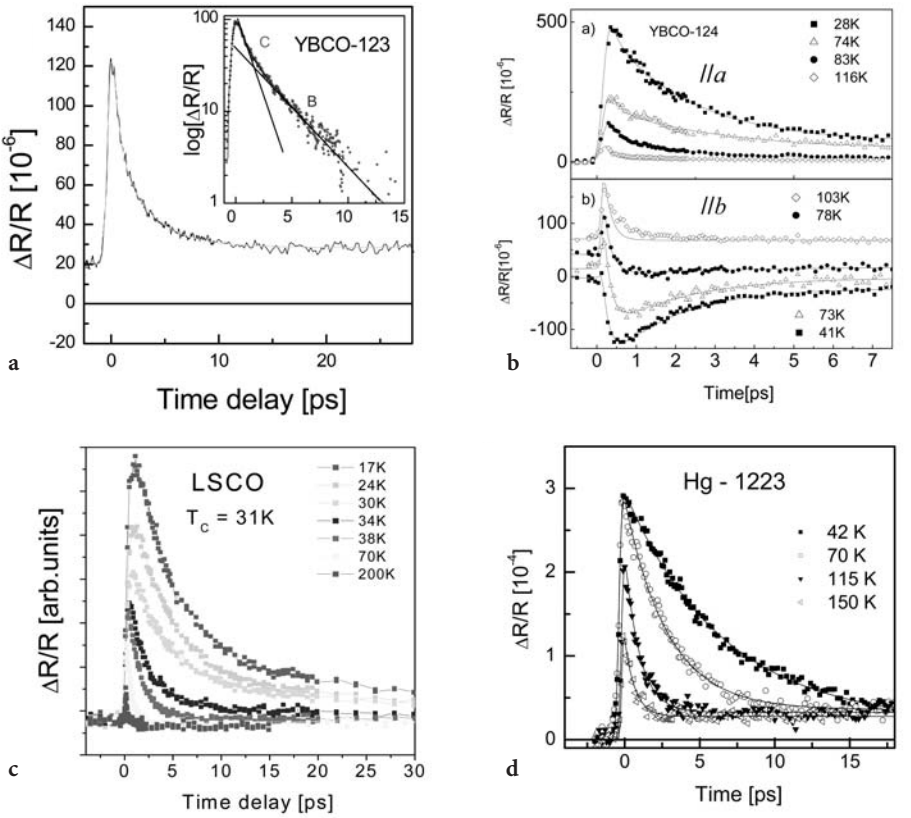

Fig. 3 **a** Typical time-resolved optical response in YBCO. The logarithmic scale (*insert*) emphasises the existence of two fast recombination components below T_c. One component disappears above T_c. The time-decay behaviour is very similar in other cuprates such as **b** $YBa_2Cu_4O_8$, where the two components have different sign, depending on probe polarisation, **c** in $La_{2-x}Sr_xCuO_4$ and **d** Hg-1223 [30]

gap", while the slower response with a lifetime τ_s is associated with the appearance of a superconducting gap.

In the Hg-cuprate and LSCO, where the two signals have the same sign and the lifetimes $\tau_s \approx \tau_p$ the deconvolution of the two signals is more ambiguous. Nevertheless a comparison with YBCO, LSCO, Tl and Bi-based superconductors shows quite convincingly that the universal two-component dynamics on the picosecond timescale and two-component temperature-dependence is observed in all cuprates investigated so far. This universal multi-component response is clear indication of the ubiquitous presence of inhomogeneity in cuprates.

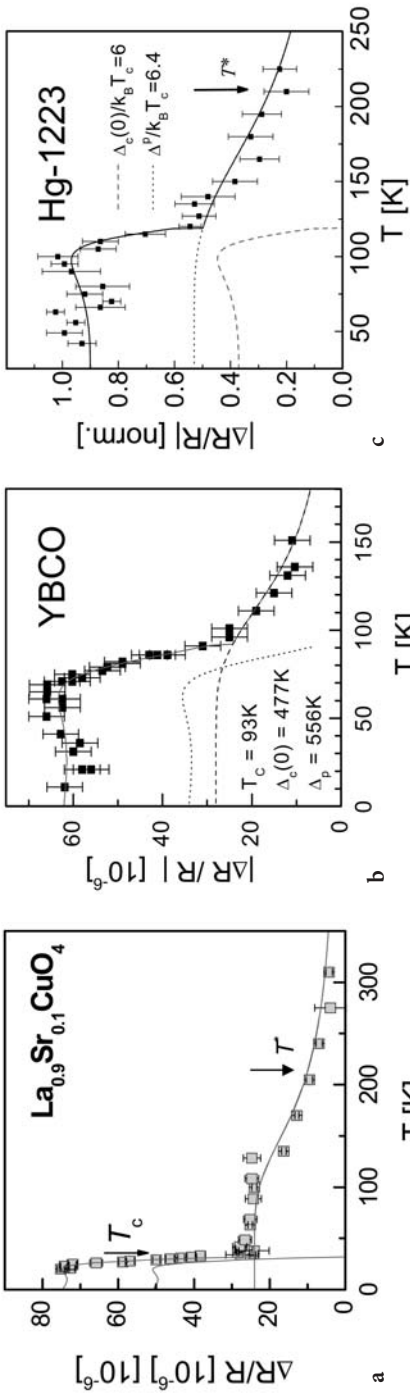

Fig. 4a–c The temperature dependence of the photoinduced signal amplitude in: **a** LaSrCuO; **b** YBCO; **c** Hg-1223. Two distinct responses are observed. One disappears at T_c, while the other is associated with the pseudogap T^* and asymptotically falls above that temperature. This remarkable behaviour is universal in the cuprates [23, 24, 30]

3.2
Modelling in Terms of Two-Level Systems

The description of quasiparticle recombination across a superconducting gap for classical superconductors was first considered by Rothwarf and Taylor [35], who postulated a set of differential equations, describing QP recombination via the emission (and re-absorption) of phonons. In classical superconductors the QP recombination lifetime is typically $\tau_R \sim 10^{-9}$ s. In HTS materials, the gap is quite large and is comparable to high-energy phonon frequencies, $\Delta \sim \hbar\omega_p$, and the recombination timescale is in the picosecond range [29].

The recombination dynamics in HTS was considered in detail theoretically by Kabanov et al. [29]. In addition to the calculation of the lifetime (which follows the approach by Rothwarf and Taylor [35]), they also calculate and verify the temperature-dependence of the QP population under bottleneck (i.e. near steady-state) conditions. Using an effectively two-level system description, expressions for the temperature-dependence of the QP population – and hence of the T-dependence of the transient optical response – were derived.

Two cases are considered: (i) a T-independent gap (applicable to the formation of local bipolarons for example, which can be described by a two-level system) and (ii) a T-dependent superconducting gap (e.g. a BCS-like $\Delta(T)$) (shown schematically in Fig. 5). The T-dependence of the QP density for the two cases is given by two expressions:

$$n_{\mathrm{QP}}(\mathrm{T}, \Delta_p) \propto \frac{1}{\Delta_0} \{1 + \frac{2\nu}{\mathrm{N}(0)\hbar\Omega} e^{-\Delta_0/k_B T}\}^{-1}, \quad \text{for } \Delta_p = \text{constant} \tag{1}$$

and

$$n_{\mathrm{QP}}(\mathrm{T}, \Delta_{BCS}) \propto \frac{1}{\Delta(T)+k_B T/2} \left\{1 + \frac{2\nu}{\mathrm{N}(0)\hbar\Omega} \sqrt{\frac{2k_B T}{\pi\Delta(T)}} e^{-\Delta_0/k_B T}\right\}^{-1}, \tag{2}$$

for a BCS-like $\Delta(T)$, where N(0) is the density of states, ν is the number of phonons emitted, Ω is the phonon frequency [29].

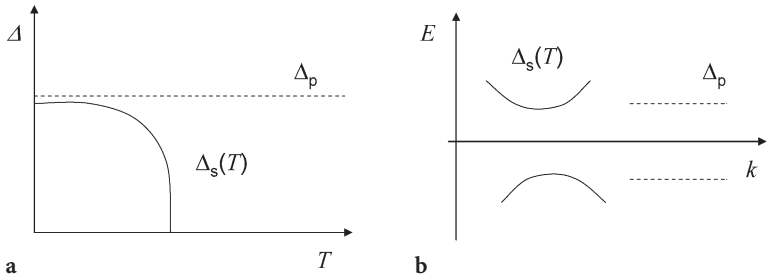

Fig. 5a, b A schematic drawing of the temperature dependence of the two gaps inferred from time-resolved QP recombination experiments on YBCO. The pseudogap Δ_p signifies the bipolaron binding energy, while the $\Delta_s(T)$ is the temperature-dependent collective gap associated with the superconducting state

In case the gap Δ is temperature *independent*, the response is predicted to fall off asymptotically at high temperatures. In the case where Δ is *T*-dependent, and closes at T_c, the signal must also fall to zero at T_c. Both *s*-wave and *d*-wave gap cases have been calculated.

Comparison of the theory with experimental data of both the *T*-dependence of the non-equilibrium QP density (Fig. 4) and lifetime (Fig. 6) gives remarkable agreement for each component separately. The pseudogap relaxation dynamics is modelled with a *T*-independent gap (Eq. 1), while the superconducting gap is modelled using a BCS-like gap $\Delta_s(T)$ (Eq. 2).

A fit to the data in Fig. 4 universally shows that the two components in the time-resolved response imply a *simultaneous* presence of a superconducting gap $\Delta_s(T)$ and a *T*-independent gap Δ_p. The latter is interpreted as the bipolaron (pair) binding energy, i.e. the energy scale associated with the appearance of inhomogeneity.

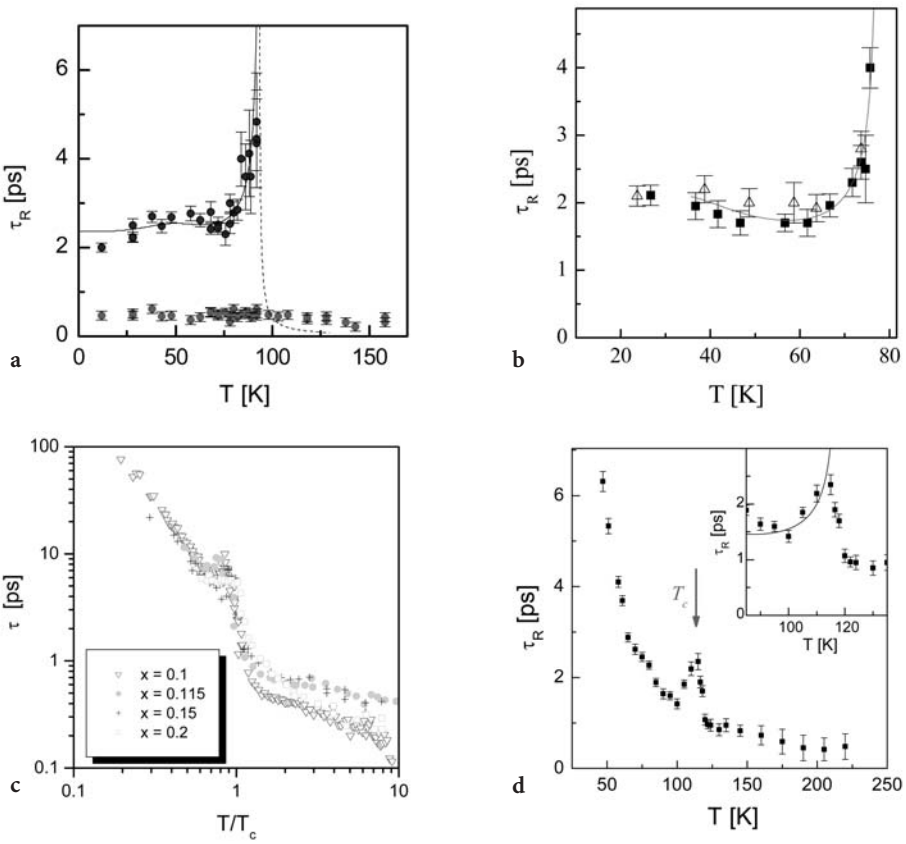

Fig. 6a–d The QP lifetime as a function of temperature in: **a** YBCO; **b** YBCO-124; **c** LaSrCuO; **d** Hg-1223 [30]. Similar behaviour was also observed in Tl-1223, $Nd_{2-x}Ce_xCuO_4$ [33] and other cuprates

This experimentally observed two-component dynamics is highly unusual and cannot be easily understood. For example, it cannot be described as a cascade of processes in a homogeneous medium. This is best seen from the data on $YBa_2Cu_3O_{7-\delta}$: the magnitudes of the two gaps Δ_p and $\Delta_s(T=0)$ are approximately equal in magnitude near optimal doping (Fig. 7), which clearly rules out a relaxation cascade processes. The only way to describe the situation is to assume that the system is *inhomogeneous*, with the two different relaxation processes occurring in different areas (on the nanoscale), or different regions in *k*-space (with no cross-relaxation on the pairing timescale).

Remarkably, an excellent fit to the *T*-dependence of the optical response is obtained when an *s*-wave gap is used in Eqs. (1) and (2), for either component. On the other hand, Kabanov et al. have shown that all attempts to fit the data with a substantially anisotropic gap or a simple *d*-wave gap, particularly for $\Delta_s(T)$ fail [29]. Both the *T*-dependence and the intensity dependence are distinctly s-like. This discrepancy between the predicted behaviour for a simple *d*-wave gap and the time-resolved data has proved to be very robust. Experiments from different groups have given similar data, none of which could be fit with a *d*-wave gap.

There are two possible ways to understand the apparent discrepancy. Either the model of Kabanov et al. [29] is inappropriate, or our understanding of the gap structure on the femtosecond timescale is incomplete and the electronic structure of the cuprates based on simple *s* and *d*-wave gaps needs to be re-examined.

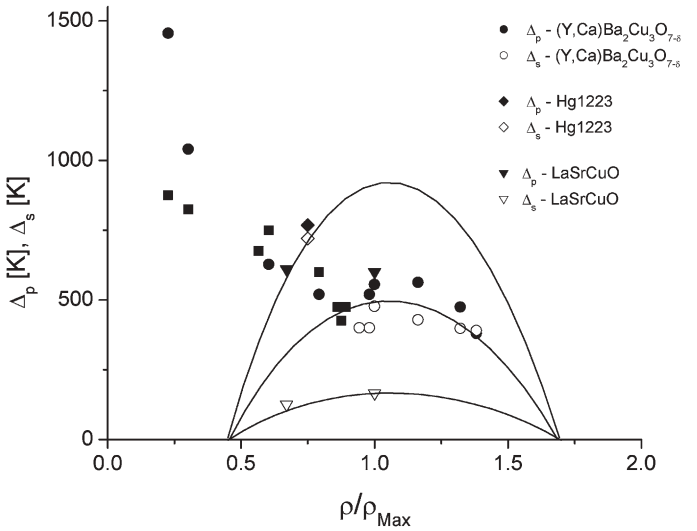

Fig. 7 The magnitude of the pseudogap Δ_p and superconducting gap $\Delta_s(T)$ as a function of doping in $YBa_2Cu_3O_{7-\delta}$ and $Y_{1-x}Ca_xBa_2Cu_3O_{7-\delta}$, $La_{2-x}Sr_xCuO_4$. and Hg-1223. The remarkable feature of the data is that the energy gaps associated with pair recombination above T_c are similar in magnitude, whereas the superconducting gaps are quite different, corresponding to the very different T_cs of the three materials

Fortunately, testing Kabanov's model has proved to be straightforward, because there exist a number of other materials with a gap in the low-energy spectrum, particularly charge-density wave (CDW) materials. Thus a number of quasi-1D and quasi-2D compounds were measured ($K_{0.3}MoO_3$, 1T-TiS_2 and 2H-$TaSe_2$ respectively) with time-resolved spectroscopy [36]. All showed excellent agreement with Kabanov's model, particularly the temperature (in)dependence of the gap(s) and relaxation time.

Moreover, systematic time-resolved studies as a function of doping in LaSCO and YBCO, as well as Hg-1223 and YBCO-124 have shown the *values* of the pseudogap Δ_p and superconducting gap Δ_s to be very close to those measured by single-particle tunnelling or ARPES, and also follow the same systematic dependence on doping. (Fig. 7). The gap ratios $2\Delta/kT_c$ are systematically found to be in the range 8–10, for the materials measured so far, in agreement with numerous other techniques. We conclude that the gap structure on the pairing timescale cannot be described by a simple *d*-wave picture.

Kabanov et al. [29] also calculated the *T*-dependence of the QP recombination lifetime in cuprates. The predicted lifetime is also dependent on the magnitude of the gap Δ. In case Δ is temperature-dependent, then the lifetime shows a divergence of τ_s as $\Delta \to 0$, as T_c is approached from below:

$$\tau = \tau_{anh} \frac{\hbar^2 \omega_p^2}{12kT\Delta(T)} \tag{3a}$$

where τ_{anh} is the phonon anharmonic lifetime, ω_p is the characteristic frequency of the emitted phonon and *k* is Boltzmann's constant. The lifetime at intermediate temperatures (at $T=T_c/2$) was estimated on the basis of experimentally observed anharmonic phonon lifetimes in YBCO [37], and was found to be of the order of 0.8 ps, in remarkable agreement with the observed optical transient lifetime of τ=1 ps [29], considering all parameters were independently experimentally determined. More importantly, the predicted divergence has also been observed in many cuprates [29], below T_c (such as in Fig. 6).

The appearance of the divergent QP lifetime τ_s near T_c is clearly consistent with the *T*-dependence of the QP density $n(T)$ and $\Delta_s(T)$ deduced from analysis of the *T*-dependence of the amplitude of the time-resolved signal below T_c (Fig. 4). In addition to the divergence at T_c arising from $\Delta(T) \to 0$ as $T \to T_c$, the lifetime is expected to diverge at low *T*, as is indeed observed in many cuprates [29, 32, 34].

Another rather surprising fact is that, when we use the value of the gap measured by pump-probe spectroscopy ($2\Delta_0$=900 K) at optimum doping [29], the gap ratio $2\Delta_0/kT_c$=10 gives the recombination lifetime near T_c as

$$\tau = \tau_{anh} \frac{\hbar^2 \omega_p^2}{2.4\Delta_0^2} \tag{3b}$$

Considering that $\hbar\omega_p \approx \Delta_0$, then the recombination lifetime is approximately equal to the zero-temperature anharmonic lifetime of the emitted phonon, $\tau \approx \tau_{anh}$.

The underlying physics of the recombination process was first discussed by Rothwarf and Taylor [35], where they considered the kinetics of the QP recombination in terms of the emission and re-absorption of phonons. As two QPs recombine, the energy is released to a phonon (there are no other excitations to carry off the energy), which has to have an energy $\hbar\omega_q > 2\Delta$; otherwise the recombination cannot take place (Fig. 8). (In high-T_c cuprate superconductors where the gap is large, we are limited to optical phonons.) These optical phonons can also be efficiently re-absorbed in a pair-breaking process, thus creating a bottleneck in the QP relaxation process. The only way that the energy can be released is if the emitted optical phonon decays anharmonically to lower-energy phonons which carry off the energy in a way that it cannot be re-absorbed.

This process can be easily understood in the bipolaron pairing picture. Suppose two QPs recombine to form a bipolaron of size l_0. In this process, an optical phonon is emitted, but it remains in the Rothwarf-and-Taylor (RT) loop until the anharmonic decay products (i.e. acoustic phonons) leave the bipolaron volume. At that point, the pairs can no longer be excited. The most obvious consequence is that the lifetime is determined by the time that the acoustic phonons leave the bipolaron volume, which, to first approximation, can be given by $\tau_R = l_0 / v_s$, where v_s is the sound velocity (see Fig. 9). (This process can also be treated more rigorously, taking into account the escape kinetics of acoustic phonons in addition to the two RT equations [38], but the underlying physics is the same.) The same picture holds for stripes, except that the l_0 describes the characteristic size of the stripe or cluster.

From the analysis presented above we see that we can determine the characteristic size of bipolarons or clusters from the measured QP lifetime τ_R by using the relation $l_0 = v_s \tau_R$. In Fig. 10 we have plotted l_0 for $La_{2-x}Sr_xCuO_4$, Hg-1223 and $Nd_{2-x}Ce_xCuO_4$ as a function of normalised temperature, normalised to the

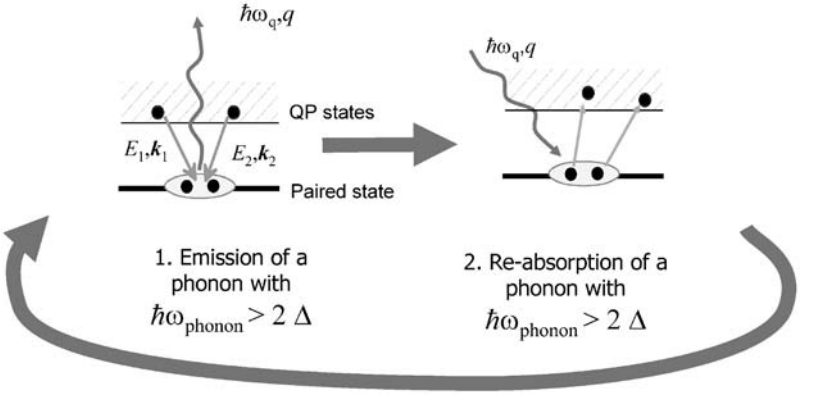

Fig. 8 Recombination of two QPs proceeds with the emission of an optical phonon with energy $\hbar\omega_q > 2\Delta$. The re-absorption of the phonon breaks a pair. The repetition of this sequence leads to a Rothwarf-Taylor bottleneck [35]

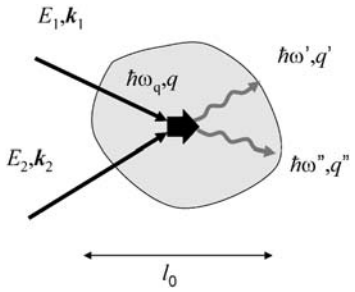

Fig. 9 Real-space representation of QP recombination showing the decay of emitted optical phonon into two acoustic phonons. When the acoustic phonons escape the bipolaron volume, they can no longer be re-absorbed to break pairs

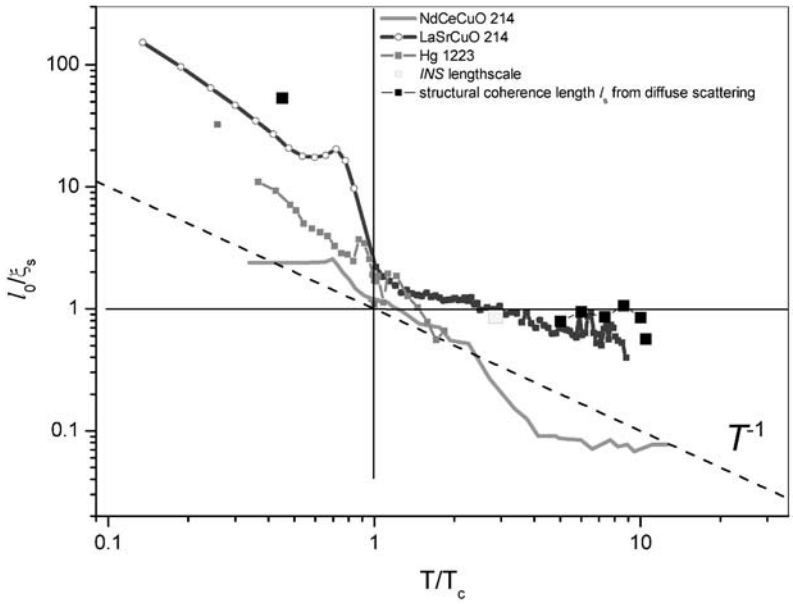

Fig. 10 Normalized length scale l_0 vs T/T_c determined from the phonon escape time τ_R in LSCO, Hg-1223 and NdCeCuO from [33]

superconducting coherence length ξ_s. Remarkably, in spite of the fact that *p*-type and *n*-type materials have very different coherence lengths, $l_0/\xi_s \approx 1$ near T_c. Moreover, the data exhibits approximate scaling behaviour $l_0=\xi_s T^{-\nu}$ which might be expected for a quantum critical point (QCP) at $T=0$, where the critical exponent of $\nu \approx 1$ is found typically in random systems, such as glasses. The fact that the observed behaviour is seen in all the cuprates (including *p*- and *n*-type materials) is a good indication that the underlying physics is quite universal.

3.3
k-Space Description of QP Recombination Dynamics and Gap Anisotropy

Time-resolved experiments seem to suggest that there are very few – or no – QP states at low energy. On the other hand, there are many experiments which *do* show a *d*-wave-like gap in the density of states, so we need to consider the possibility that the picture of the low-energy electronic structure at short times can be different than in the steady state. In other words, we need to take into account the short timescale of the experiments, and more specifically the *k*-dependence of the recombination processes involved in QP recombination on fast timescales.

First, let us consider the sequence of events after short laser pulse excitation. The initial excitation of electron-hole pairs by the laser pulse and the subsequent relaxation to states near the Fermi energy of these carriers takes place within a few tens of femtoseconds [39]. This process is reasonably well understood, and has been studied in normal metals, superconductors and semiconductors in some detail. Before reaching low energies, the carriers have undergone a cascade of scattering events, rapidly losing memory of their initial momentum, and occupying all available momentum states approximately equally (see Fig. 11).

As already discussed in a real space picture (Fig. 9), the next step in the energy relaxation process is the recombination of QPs to the ground state via the emission of one or more phonons [29]. If a phonon exists, whose energy is greater than the twice the gap, $\hbar\omega_q > 2\Delta$, then all the energy released in the QP recombination can be carried off in a first-order process by a single phonon. Such a process involves the recombination of two QPs with momenta $\boldsymbol{k}_1$ and $\boldsymbol{k}_2$, and energy E_1 and E_2, to a pair state with momentum $\boldsymbol{k}_{pair}$ at E_F, and the emission of a phonon with momentum $\boldsymbol{q}$ of energy $\hbar\omega_q$.

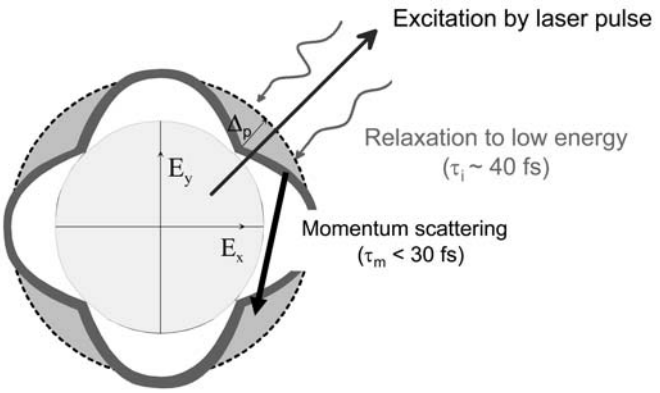

Fig. 11 Schematic diagram showing the initial relaxation of hot electrons excited by the pump laser pulses. The relaxation proceeds via carrier-carrier scattering and via phonon emission, whereby the particles encounter of the order of 50 scattering events before reaching the gap, losing memory of their initial momentum. Once they have reached the gap, they occupy all momentum states approximately equally

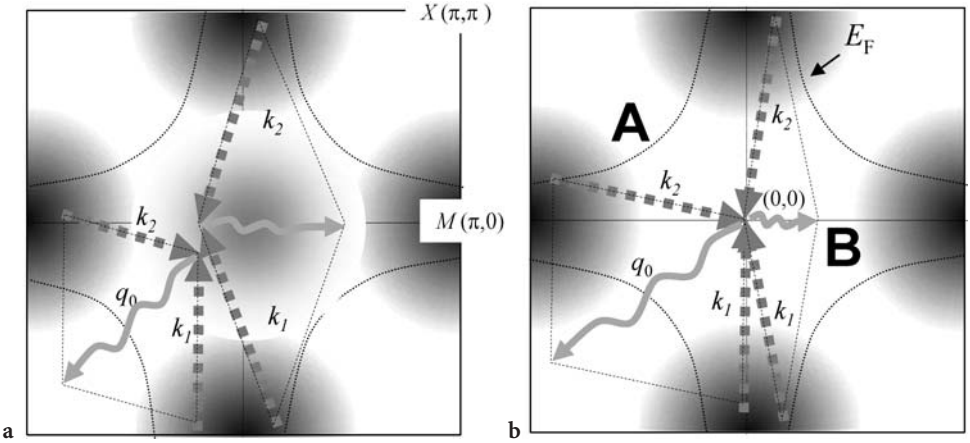

Fig. 12a, b Recombination processes involving two QPs with k_1 and k_2 respectively (*dashed arrows*) and an emitted phonon (*wavy line*) for: **a** $T>T_c$ where the final state momentum is not necessarily zero; **b** the condensate $T<T_c$ where the pair momentum is strictly zero (in the absence of current). The electronic structure is based on ARPES, whereby the *shaded areas* at the M point represent a large spectral density at an energy Δ below E_F

E and ***k*** conservation restrictions are quite different in the pseudogap state and in the superconducting state, because the final (pair) state momenta are different in the two cases (see Fig. 12a, b):

1. In the pseudogap state (Fig. 12a), with $T^* > T > T_c$, pre-formed pairs may be mobile, and the final pair state momentum is determined by their centre-of-mass kinetic energy, so there are no strict kinematic restrictions on the final state pair momentum, such as in the superconducting state. In describing the recombination process we can therefore simply consider energy conservation pertaining to a two-level system of QPs in the excited states and bound pairs in the ground state, separated by a gap Δ_p, [29].
2. Pairs in the superconducting condensate (Fig. 12b), for $T<T_c$ are usually considered to have zero net momentum $k_{condensate}=0$, so $\boldsymbol{k}_1+\boldsymbol{k}_2-\boldsymbol{q}=0$, and the gap Δ_s separating QP states and the condensate pairs is T-dependent.

To obtain a better understanding of the recombination kinematics in this case, we have plotted the relevant processes in *k*-space (Fig. 12). To make the picture as realistic as possible, we discuss the recombination using an electronic structure based on the generic features observed in recent ARPES measurements on $La_{2-x}Sr_xCuO_4$ [40]. The spectral intensity A(k,ω) at 10 K obtained from the raw ARPES data on LaSrCO is shown schematically in Fig. 12. Shades of grey represent the value of A(k,ω) at a binding energy Δ(k) corresponding to the peak in A(k,ω). These peaks – which are interpreted as a sign of the presence of QP states relevant in the recombination process – occur at an energy $E=E_F-E_\Delta$. E_Δ is doping-dependent and is shown plotted on the energy-vs-doping diagram in Fig. 7 as a function of doping *x*. The dashed arrows in Fig. 12b represent the two

types of QP recombination processes involving $k_{pair}=0$ pairs in the condensate as the final state, which satisfy momentum and energy conservation, $\boldsymbol{k}_1+\boldsymbol{k}_2-\boldsymbol{q}_R=0$ and $E_1+E_2-\hbar\omega=0$ respectively. It is easy to see that the emitted phonons (wavy lines) can have only certain values of momenta q_R (shown shaded in Fig. 12). At the same time they must have an energy $\hbar\omega_q>2E_\Delta$ (60–80 meV), which in cuprates is limited to high-frequency optical modes involving predominantly O motion.

The conclusion from these analyses is that Kabanov's model for QP recombination is perfectly valid provided momentum selection rules and realistic anisotropy of the band structure is taken into account. The pseudogap response clearly implies that the short-timescale picture with the main QP density at the M points can be described well by Kabanov's model. The superconducting state response on the other hand has stricter selection rules with the requirement that $\boldsymbol{q}_{pairs}=0$, but again provided the real DOS is taken into account, Kabanov's model still describes the picture very well, of course considering each component separately.

In addition to the two-component ultrafast response on the picosecond timescale discussed above, in all cuprates there is also a ubiquitous much slower response, with a timescale which is longer than 1 ns, which appears to be glass-like without a clearly defined lifetime [24, 25]. This is present in CDW systems as well [24], and is attributed to localised intra-gap states. It has been suggested that the origin of these processes may be related – at least in cuprates – to relaxation of nodal quasiparticles [41]. However, its appearance in many CDW systems such as $K_{0.3}MoO_3$ suggests that this model of d-wave nodal relaxation is probably not applicable, and that clearly this very slow relaxation component is not an exclusive feature of the *d*-wave state. Because these states are probably not very important for the mechanism of superconductivity, nor are they likely to *drive* the formation of an inhomogeneous state, we shall not discuss them further here.

3.4
Origin of the Two-Component Femtosecond Response

In summarising the time-resolved experiments, we infer two unusual features which are ubiquitous in the cuprates:

- The QP gap structure on the femtosecond timescale shows large gap behaviour, with negligible density of states at low energy, and dynamics which is similar to (more isotropically gapped) CDW systems.
- The recombination dynamics shows a two-component response on the 0.2–5 picosecond timescale, corresponding to recombination across a *T*-dependent SC gap Δ_s and a *T*-independent "pseudogap" Δ_p respectively, where the magnitudes of the two gaps are doping-dependent (Fig. 7).

The observation of two relaxation times at short timescales, one associated with the pseudogap Δ_p, and the other with a T-dependent superconducting (or collective) gap by time-resolved spectroscopy in *all* cuprates so far (Fig. 7), implies that the response is intrinsic and a universal at the fundamental level. The observation of a clear two-component response in $La_{2-x}Sr_xCuO_4$ at all doping levels excludes the possibility that the two responses come from spatially separate parts in the crystal, such as charge-reservoir layers and CuO_2 planes respectively. Thus the two-component response can be attributed to the CuO_2 planes, and implies a two-component ground state, which – considering the resolution of the optical time-resolved experiments – can only exist on a mesoscopic or microscopic length scale.

An interesting feature of the systematic study shown in Fig. 7 is the fact that the pseudogap Δ_p measured on the femtosecond timescale appears to be of similar magnitude in LSCO, YBCO and Hg-1223, in spite of the fact that T_c differs by nearly a factor of 4. The temperature-dependent gap $\Delta_s(0)$, on the other hand, is closely related to T_c, giving a nearly constant *gap ratio* at optimum doping $2\Delta_s^{opt}(0)/kT_c$=9.4 (LSCO), 10.1 (YBCO) and 12 (Hg-1223). We have recently shown that the relation between two gaps can be determined by the percolative threshold for phase coherence at finite temperature [57], or more concisely, given the characteristic energy scale Δ_p for the formation of pairs, then T_c (and whence $\Delta_s(0)$) is determined by the geometrical size of the pairs or objects filling the plane *and* their number, which depends on temperature, as we shall see later.

4
Model Description of the Dynamically Inhomogeneous State

Very soon after the discovery of superconductivity in cuprates, the possible existence of electronic inhomogeneity was recognized by Gorkov and Sokol [42], while the possibility of spin stripes was discussed by Zannen and Gunnarson [43], Emery and Kivelson [44] and others. However, it has taken quite some time to show experimentally that these inhomogeneities may be relevant to understanding the normal state and superconductivity [1] and obtain specific details which are necessary for a concise model to be proposed.

Here we approach the problem of the cuprates from the viewpoint that bosonic pairs are just a special kind of doping-induced impurity state. For specific reasons the materials prefer to form pairs rather than single polarons: competition between highly anisotropic elastic strain and Coulomb repulsion V_C leads (at low doping) to the formation of nanoscale pairs in preference over single polarons.

The doped holes do not have sufficient binding energy E_B to form bound states at high temperatures $kT>E_B$ and behave as a Fermion gas. For $kT^*<E_B$, a new structural phase starts to nucleate surrounding doped holes (i.e. polarons of well-defined lattice symmetry), leading to the coexistence of pairs and larger objects such as stripes, particularly as doping increases. In a more usual system

exhibiting a structural phase transition, the length of these objects grows, showing critical behaviour, as the structural phase transition temperature T_s is approached. However, in the cuprates, it appears that the doped holes which precipitate in the formation of a new phase also prevent long-range structural ordering, favouring the formation of a superconducting state instead. The small energy difference between pairs and clusters (stripes) leads to their co-existence in the pseudogap state below T^*.

In this section we shall concentrate on a microscopic description of the inhomogeneous state, starting with an examination of the symmetry of the interaction from inelastic neutron scattering experiments. We then describe an effective symmetry-invariant Hamiltonian and discuss its consequences for the appearance of an inhomogeneous state, and how this can lead to pre-formed pairs, stripes and superconductivity.

4.1 Symmetry of the Interactions and Some Consequences

The key to determining the symmetry of the interaction Hamiltonian for the system comes from the idea that the finite size coherence length ξ_s defines the extent of the pair, which in turn means that the interaction between particles composing a pair is not at k=0, but at finite $k=\pi/\xi_s$. Thus, any lattice or structural effect associated with the formation of pairs of size ξ_s should result in a visible phonon anomaly in k-space at a wavevector corresponding to $k_0=\pi/\xi_s$. Examination of the k-dependence of the phonon dispersion spectrum, measured by INS [17, 18], or IXS [19] appears to support this notion strongly. Anomalies at long wavelengths ($k\rightarrow 0$) are not evident (or small). Rather, the largest anomalies appear at large k (towards the zone boundary) in hole-doped cuprates [17, 18] and slightly smaller k in electron-doped cuprates [19]. The point in k-space where an anomaly occurs also uniquely identifies the symmetry of the interaction which causes it. More precisely, the observation of a phonon anomaly at a particular point in k-space can be used to define the interaction between phonons, electrons (or holes) and spins, which is symmetry-invariant under the operations of the appropriate symmetry group of k at that point in the Brillouin zone. The phonon dispersion anomalies for $La_{2-x}Sr_xCuO_4$ are in the (ξ,0,0), or $\Gamma\rightarrow$M direction [18]. The group of k in this direction has C_{2v} symmetry [45]. Hence an interaction which causes an anomaly at this point in k-space will lead to a distortion of the lattice whose symmetry is reduced from tetragonal symmetry (D_{4h}) within a volume of size $l=\pi/k_0$ [45]. The interaction at k_0 thus creates mesoscopic areas (or objects), whose symmetry is reduced (ultimately C_{2v} – once larger objects corresponding to a new phase are formed), while the undistorted surroundings have a higher symmetry (D_{4h}). Note that the symmetry of small objects whose diameter is of the order of a unit cell cannot be easily defined, and strictly speaking, the proper symmetry group can be used only when larger, meso-scale objects are formed (by analogy to the symmetry transformation taking place at a structural phase transition).

Knowing the symmetry of the interaction enables one to write a Hamiltonian H_{MJT} with the correct symmetry properties [45], which acts on a length scale defined by l_0. This effective interaction acts on a scale given by the length-scale of the inhomogeneities, and can be written in either real space or k-space. The real-space formulation is given as [45, 46]

$$\begin{aligned} H_{\mathrm{JT}} = \sum_{\mathrm{n,l,s}} & (\sigma_{0,\mathrm{l}}\{n_{\mathrm{x}}^2 + n_{\mathrm{y}}^2\} g_0(\mathbf{n})\}(b_{1+\mathrm{n}}^{\dagger} + b_{1+\mathrm{n}}) \\ & + \sigma_{3,\mathrm{l}}\{(n_{\mathrm{x}}^2 + n_{\mathrm{y}}^2)\} g_3(\mathbf{n})\}(b_{1+\mathrm{n}}^{\dagger} + b_{1+\mathrm{n}}) \\ & + \sigma_{1,\mathrm{l}}\{n_{\mathrm{x}} n_{\mathrm{y}} g_1(\mathbf{n})\}(b_{1+\mathrm{n}}^{\dagger} + b_{1+\mathrm{n}}) \\ & + \sigma_{2,\mathrm{l}} S_{z,\mathrm{l}}\{(n_{\mathrm{x}}^2 + n_{\mathrm{y}}^2)\, g_2(\mathbf{n})\}(b_{1+\mathrm{n}}^{\dagger} + b_{1+\mathrm{n}})\,. \end{aligned} \tag{4}$$

where b and $b\dagger$ represent phonon operators and S_z is the z component of the local spin. σ_{i} are the Pauli matrices representing the degenerate electronic states. The first term describes the coupling between electrons in non-degenerate states and is isotropic. The next two terms describe coupling between electrons in degenerate electronic states and the lattice of x^2–y^2 and xy symmetry respectively, while the last term described the coupling of the z-component of spin S_z to the electronic states. (All other couplings are forbidden to first order). The coupling functions $g_i(\mathbf{n})$ are given by

$$g_i(\mathbf{n}) = g_i \frac{\exp[-(a/l)\sqrt{n_{\mathrm{x}}^2 + n_{\mathrm{y}}^2}]}{n_{\mathrm{x}}^2 + n_{\mathrm{y}}^2} \tag{5}$$

where $\mathbf{n}=(n_x,n_y)$ with $n_x,n_y \geq 1$, and g_i are the coupling constants. The function $g_i(\mathbf{n})$ describes the spatial dependence of the effective interaction, as shown in Fig. 13. It is an effective interaction which takes into account the isotropic Coulomb repulsion $V_{\mathrm{c}}(\mathrm{r})$ and the attraction due to an anisotropic lattice strain, conforming to the crystal symmetry properties. A similar interaction can be written in k-space [46], except that $\mathrm{g}(\boldsymbol{k})$ then describes the effective interaction with a peak at $k_0=2\pi/l$. The electron-lattice interaction described by the first term in Eq. (4) is isotropic. In principle all phonons which have the appropriate τ_1 symmetry can couple to the electronic states. The second and third terms describe an interaction with anisotropic d-like deformations of xy and x^2–y^2 symmetry respectively, and the last term describes the spin interactions with the out-of-plane component $\mathrm{S_z}$. (In-plane components are not allowed by symmetry.) One of the main conclusions from this analysis [45, 46] is that non-degenerate electronic levels coupling to phonons and spins can only give rise to a symmetric (s-wave) deformation, while coupling to *doubly degenerate* electronic states (of E_{g} symmetry in the high symmetry group) can give rise also to an anisotropic d-wave like interaction in addition to the symmetric one. Because the interaction is between electrons in degenerate states and phonons and spins, the latter may be viewed as a finite-k or *mesoscopic* Jahn-Teller effect

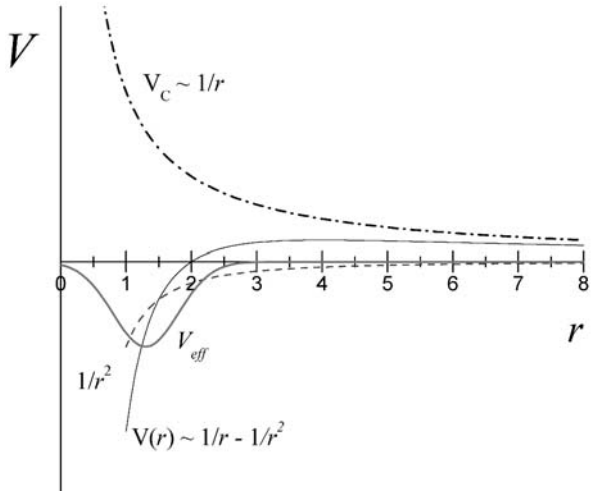

Fig. 13 The two most relevant potentials acting on particles in the cuprates are Coulomb ($1/r$) and strain (of the form $1/r^2$ in the continuum limit). The total potential has a shallow maximum, which gives rise to a rich energy landscape of stripes, checkerboards and bipolaron pairs. At short distances, Coulomb repulsion overcomes strain preventing on-site double occupancy. V_{eff} describes an effective potential used to describe the short-range Jahn-Teller pairing interaction at finite k [45–47]

(to distinguish it from the more standard single-ion JT effect, or cooperative JT effect – which leads to long range order).

An important feature of the effective interaction at (Eq. 4) is not only that it is highly anisotropic, but also that it peaks at finite k (or at finite range l_0). We have justified this on the basis of experimental observations, but we can also justify it theoretically if we consider the two most relevant fundamental interactions acting on doped holes, namely (highly anisotropic) elastic strain and an (isotropic) Coulomb repulsion. The total V is clearly highly anisotropic, and has a minimum at a distance l, depending on the difference between V_c and V_s. The interaction at Eq. (5) is a simplification of the more general form in Fig. 13. The anisotropy arises simply as a consequence of orbital symmetry of the constituent atoms (primarily Cu d-orbitals and O p-orbitals) and the crystal symmetry.

The state which H_{JT} (Eq. 4) implies is dynamically inhomogeneous [46], where distorted and undistorted regions coexist (Fig. 14) with a inhomogeneity on a scale defined by k_0 or ξ_s, but have different symmetry and different energies. In real space, the interaction H_{JT} describes polaron-like objects of size $l_0 \approx \pi/k_0$, whose symmetry is reduced compared to the bulk of the crystal.

A very important question for superconductivity is how doped holes might order within such a model. Taking into account that the particles are charged and including the repulsive Coulomb interaction in its general form, we have shown that Eq. (4) can be reduced to a lattice gas model [47]. Taking only the x^2–y^2 term in Eq. (4), the interaction becomes

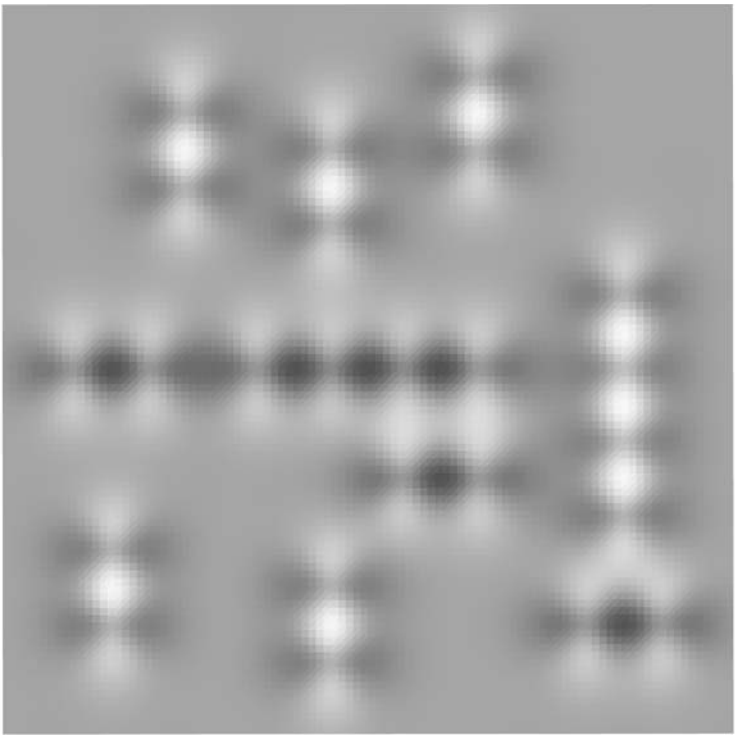

Fig. 14a, b Real-space picture of a dynamically inhomogeneous state, depicting the CuO_2 plane of the cuprates. The *shade of grey* represents the sign of the effective interaction for the case of x^2–y^2 symmetry (second term in the Hamiltonian (Eq. 4)) Pairs and stripes are shown

$$H = [\sum_{i,j} -V_l(i-j)\, S_i^z\, S_j^z + V_C\,(i-j)\, Q_i Q_j] \tag{6}$$

where S_i^z is an operator describing the anisotropic lattice interaction (Eq. 4), whose value is $S_i^z=1$ for the state ($n_{i,1}=1$,$n_{i,2}=0$), $S_i^z=-1$ for ($n_{i,1}=0$,$n_{i,2}=1$) and $S_i^z=0$ for ($n_{i,1}=0$,$n_{i,2}=0$). $Q_i=(S_i^z)^2$. Here $n_{i,\alpha}$ are the occupation numbers of twofold degenerate states $\alpha=1,2$ at site i. The Coulomb interaction is formulated as $V_C(\mathbf{m})=e^2/\varepsilon_0 a(m_x^2+m_y^2)^{1/2}$, where e is the electric charge, a is the lattice constant and ε_0 is the dielectric constant and $\mathbf{m}=(m_x,m_y)$ is a vector. The attractive lattice interaction is written as

$$V_l(\mathbf{s}) = (1/\omega) \sum_m (m_x^2 - m_y^2)\, \{(s_x + m_x)^2 - (s_y + m_y)^2\}\, g(\mathbf{m})\, g(\mathbf{s}+\mathbf{m}) \tag{7}$$

The interaction at Eq. (7) now describes the ordering of JT polarons on a lattice in an x-y plane in the presence of competing Coulomb interaction V_C and short range anisotropic attraction, where $g(\mathbf{m})$ has been defined in Eq. (5) and $\mathbf{s}=(s_x,s_y)$ is a vector. The short-range attraction is generated by the interaction

of electrons with optical phonons, whose range is determined by the dispersion of optical phonons.

In principle, the objects created by the interaction can be single polarons, bipolarons, stripes, etc., the stability of which is determined primarily by the balance between elastic energy V_l and Coulomb repulsion V_C on the mesoscopic scale. Monte-Carlo studies have shown [47] that the mode Eq. (5) can lead to the formation of both pairs and mesoscopic objects such as stripes and clusters, depending only on the ratio of parameters V_C/V_l and the doping level. Both xy- and x^2–y^2-symmetry stripes are allowed by symmetry, corresponding to "diagonal" stripes or stripes parallel to the bond axes respectively. Indeed, STM measurements strongly suggest that these exist, but may have different energies [11]. However, for the majority of experiments, the energy difference separating the distorted and undistorted regions can be associated with the pseudogap Δ_p, and the state can be very effectively described in terms of a two-level system [6, 8, 45, 46, 48] of spin singlets (S=0) in the ground state, and unpaired (S=1/2) spins in the excited state. The existence of *pairs* would imply the existence of spin singlets (S=0) in the ground state, and unpaired (S=1/2) spins in the excited state. Conversely, the presence of single isolated polarons would give rise to a substantial Curie susceptibility due to unpaired localised spins. Moreover the spin susceptibility at any give T increases with doping. Hence – as already discussed – the existence of single polarons in the ground state is apparently ruled out by magnetic measurements, while static susceptibility measurements [8, 20, 48], and NMR Knight shift data [20] (Fig. 15), support the proposed model description of spin singlets in the ground state and S=1/2

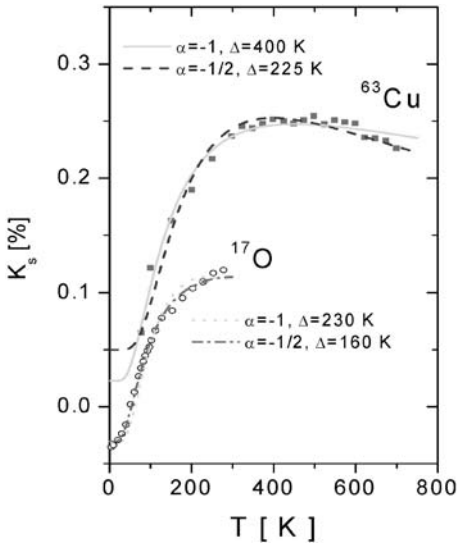

Fig. 15 The NMR knight shift as a function of temperature follows the behaviour expected for a two-level system of bipolarons (S=0) and excited state (S=1/2) Fermions [20]

Fermions in the excited state. The magnetic response is thus quantitatively consistent with the existence of pre-formed Jahn-Teller *bi*polaron pairs in the ground state [8, 45, 46, 49]. Note that the same two-level system has also been used to fit the temperature-dependence of the femtosecond-timescale time-resolved experiments.

4.2
Evidence of the Symmetry-Breaking Interaction: Loss of Inversion Symmetry

The distorted objects have reduced symmetry, so we expect to observe manifestations of symmetry breaking as pairing distortions start to occur. Evidence for local inversion symmetry breaking below the pseudogap temperature is plentiful both in Raman [50, 51] and infrared spectroscopy [52]. For example, the T-dependence of broken-symmetry Raman modes rather convincingly follow two-level-system behaviour [50] (see Fig. 16). There is also a large amount of evidence for the existence of a spontaneous polarization in cuprates over a wide range of doping [53],with the observation of phenomena such as pyroelectricity and piezoelectricity [54], which imply the existence of on a non-centrosymmetric structure, such as C_{2v} symmetry. Note that this inversion symmetry-breaking is a specific prediction of the model at Eq. (4), and to our knowledge, there is no other theoretical model currently available which predicts these symmetry breaking phenomena in the cuprates.

4.3
Stripes and Pairs: Overcrowded State

At high doping density, the distorted regions might aggregate to form longer stripes or clusters, with the same symmetry properties defined by H_{JT} (henceforth we generically use the term stripe to signify any aggregated object larger than a pair). A comprehensive discussion of superconductivity involves the formation of a phase-coherent state within such a system of co-existing pairs, "stripes" and – at finite temperature – Fermions in the excited state. The T-dependence of the length-scale l_0 measured by QP recombination experiments (Fig. 10) is an indication that stripes and clusters form at low temperatures.

However, it is not immediately obvious whether stripes should have significantly lower energy than single bipolarons. To be relevant, the energy difference between bipolarons and stripes should be at least on a scale of kT_c, giving a more complicated energy level structure, e.g. a three-level system. One answer to the question as to whether there is an additional energy scale *for different types of stripes or clusters* comes from experiments.

One indication that the state has more than one component has come from time-resolved experiments on the femtosecond timescale, where very early, there was evidence for the co-existence of metallic and localised states [1, 21, 22].

A careful fit to the magnetic susceptibility data [8] also shows that a two-level description originally proposed by Alexandrov, Kabanov and Mott [56] is

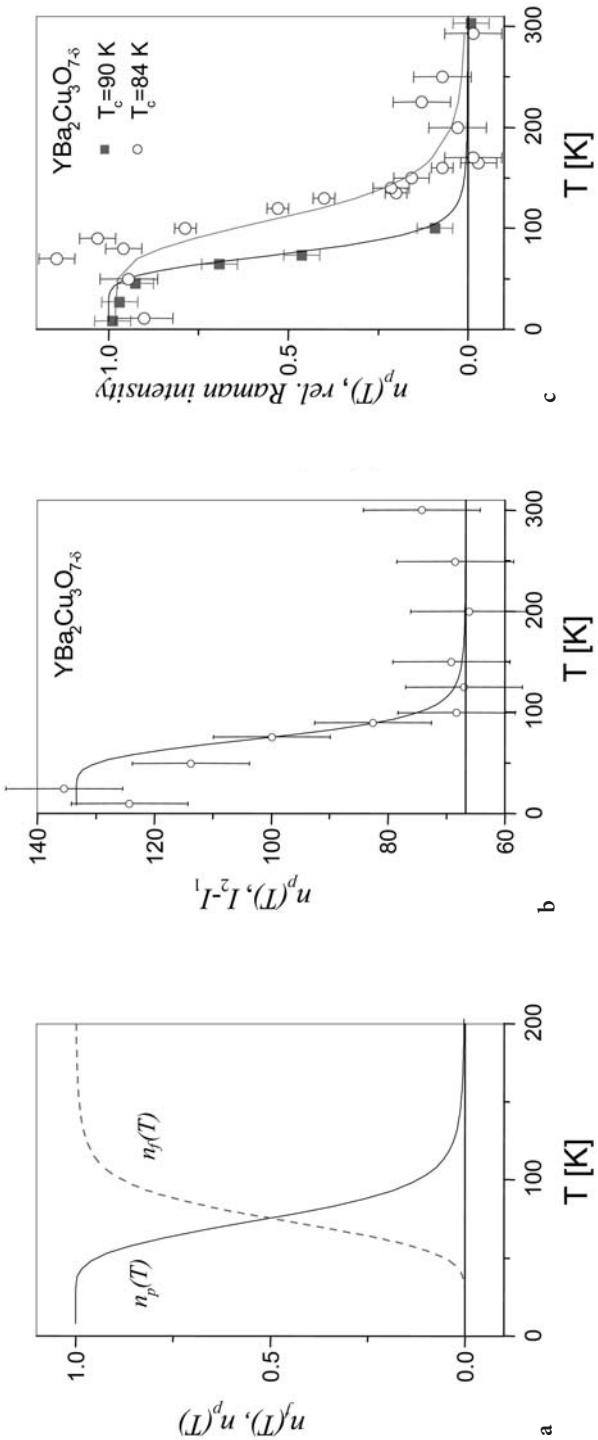

Fig. 16 The temperature-dependence of the ground state and excited state population in a two-level system with a gap Δ for YBCO. **b** The T-dependence of the anomalous phonon intensity measured by INS [18]. **c** The temperature-dependence of Raman scattering intensity for modes forbidden in the centro-symmetric high-temperature structure. The broken-symmetry modes can be assigned to infrared modes, which become Raman-active when inversion symmetry is broken by the formation of pairs or stripes. The two samples correspond to the optimally doped YBCO (T_c=90 K) and underdoped YBCO (T_c=84 K) [46]

not completely sufficient. A more accurate fit to the susceptibility data can be obtained when a temperature-independent Pauli-like contribution is included, yet only one energy scale (Δ_p) is used to fit the whole data set, suggesting that the excitation energies for bipolarons and stripes are indistinguishable, or very close in energy. Note that when stripes are included [8] overall there are two Fermionic contributions to the susceptibility in the mixed state of pairs and stripes. (i) At high temperatures (above T^*), we have a Fermi gas, where the susceptibility is nearly T-independent, and there are neither bipolarons nor stripes present. (ii) At low temperatures, both bipolarons and stripes are present, the latter with a Pauli-like contribution to the susceptibility. This temperature-independent susceptibility can then be understood to come from metallic stripes [8]. (A similar conclusion regarding metallicity of the stripes was derived on the basis of theoretical arguments by Mihailovic and Kabanov [45].) Yet further indication for the existence of stripes or clusters with energy states within the pair-gap energy scale is the slow and glass-like dynamics of the intra-gap state relaxation [24] and recent ESR data show the existence of two components even in lightly doped $La_{2-x}Sr_xCuO_4$ ($0.01<x<0.06$) [55].

We can conclude that there appear to be strong experimental and theoretical arguments for the co-existence of bipolarons and larger objects, such as stripes in cuprates not only at optimum doping and in the underdoped state, but also in the overdoped state. Clearly pairs must exist in the ground state, otherwise at very low temperatures, the cuprates would not be superconducting.

5 Superconductivity

There are two fundamentally different types of dynamics which need to be considered in the discussion of superconductivity in an inhomogeneous system:

1. In the first case, the inhomogeneity is simply thermally fluctuating according to the relevant statistics defined by the energy scale of the bound state Δ_p in relation to kT. In other words, charge-rich inhomogeneities (polarons or bipolarons) may form, disappear, and reform in different spatial locations, driven by thermal fluctuations. The inhomogeneities are still static in the sense that the objects have *no centre-of-mass motion,* i.e. their kinetic energy is small compared to their binding energy. Nevertheless their presence fluctuates on a fast timescale $\tau \sim \hbar/\Delta_p$ (of the order of 10^{-14} s).
2. The other possibility is that the dynamic inhomogeneity is associated with the centre of mass *motion* of bosons (bipolarons).

For some models of superconductivity (Bose-Einstein condensation for example) it is essential that the pairs are mobile [56] (case 2). For other models (such as percolative superconductivity [57]) motion of pairs is not essential. It is thus important to determine experimentally which of the two cases applies to the cuprates.

A common objection to superconductivity models based on Bose condensation of bipolarons in the cuprates is based on "overcrowding". In order to ensure that the interparticle distance is greater than the effective bipolaron radius r_0, the latter has to be smaller than the coherence length ξ_s, i.e. $r_0 \ll \xi_s$. In the cuprates this might be satisfied only in the dilute (strongly underdoped) case, while in the optimally doped and overdoped cuprates the model is probably not applicable.

An alternative scenario proposed by the present authors [57] considers bipolarons where the kinetic energy of the pairs plays no part, whereby a macroscopic superconducting state is formed by phase coherence percolation by Josephson coupling (i.e. pair tunnelling) between deformed regions, *including* coupling across metallic stripes. A schematic picture of a phase coherence percolation is shown in Fig. 17. It was shown [57] that if each doped carrier created a distortion of size πl_0^2 (or $\pi\xi_s^2$, since $l_0 \approx \xi_s$ at T_c) in the CuO_2 plane of a cuprate superconductor, then at the percolation threshold, the doped carrier density corresponds to the onset of the superconducting state. The percolation threshold for 2D is at 1/2 area fraction in a bond-percolation model (which is a good approximation to the case in hand). In $La_{2-x}Sr_xCuO_4$, this corresponds to x=0.06 at T=0.

Doping beyond this point leads to filling beyond 1/2 effective 2D volume fraction, there are more stripes and fewer pairs, whence the percolation threshold between pairs is reached at lower temperature, in effect lowering T_c from it would be if space were not filled with stripes. In this picture, stripes are detrimental to high T_cs. Higher T_c appear to be limited by the topological necessity that overlapping pairs form (Fermionic) stripes at higher doping.

The superconducting gap $\Delta_s(T)$ appears as result of long-range order arising from Josephson coupling across stripes and pairs, leading to the characteristic mean-field like temperature dependence of $\Delta_s(T)$ clearly observed for QP re-

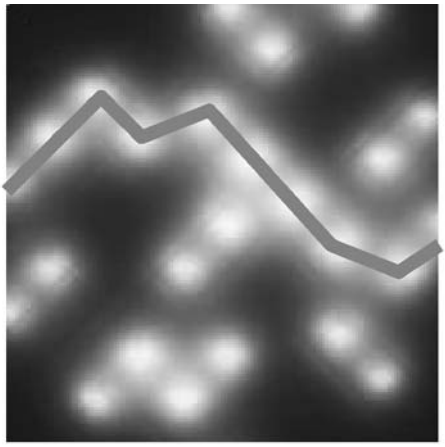

Fig. 17 Macroscopic phase coherence by Josephson percolation across pairs and stripes. The *white areas* depict charge density. The *line* indicates a phase-coherent percolation path

combination in the femtosecond spectroscopy experiments. Hence the simultaneous presence of Δ_p and $\Delta_s(T)$ in the time-resolved optical data can be understood. In this model, the ratio of T_c to Δ_p is dependent on the effective geometrical size of the pair (which is in turn related to the coherence length), as discussed previously in this review and in [57]. It should be mentioned here that if pairs can tunnel between inhomogeneities [57], it is not particularly important whether the inhomogeneities are dynamic or static, provided the inhomogeneities exist on a timescale which is longer than the pair tunnelling time.

6 Conclusions

In this review we have presented an overview of the dynamical state of cuprate superconductors based on experimental observations on short timescales. The observed behaviour appears to be quite universal, defining the underlying physical mechanisms which lead to the appearance of superconductivity in these materials. We have also described a theoretical model to account for the dynamically inhomogeneous state, which quantitatively and self-consistently describes many of the general features of the observed dynamics on the femtosecond timescale as well as experiments on slower timescales, such as NMR [20] and magnetic susceptibility [8]. The model also predicts very specific symmetry breaking phenomena observed in Raman [50, 51], infrared spectroscopy [52] and a class of ferroelectric phenomena [53, 54] which are also observed in cuprate superconductors. Moreover, transport properties, particularly resistivity, have also been quantitatively described by model [58].

The emerging picture is one in which the inhomogeneity is coincident with singlet pairing, while the formation of a superconducting state at T_c is governed by Josephson coupling between inhomogeneous regions [57].

We conclude by noting that formally, we have divided the description of superconductivity into three parts: (i) a microscopic model for formation of bipolaron pairs and stripes as the dominant form of inhomogeneity, considering primarily the competition of highly anisotropic elastic attraction and Coulomb repulsion $V(\mathbf{r})$ between particles, concisely taking the appropriate symmetry considerations into account, (ii) a set of two-level systems describing the pseudogap behaviour of pairs and stripes, and (iii) the formation of superconducting state in an inhomogeneous medium via phase coherence percolation.

More experiments and modelling are necessary in order to clarify the details of mesoscopic ordering of carriers into stripes [59]. Although one should expect that a detailed examination of new experiments will reveal additional complexity, it seems that the proposed finite-wavevector Jahn-Teller model can describe the salient features very successfully.

It is remarkable that the two main concepts, namely Jahn-Teller polarons and perculation, which we have discussed here, also approved in the original paper by Bednorz and Müller in 1986 [12].

Acknowledgments I would like to thank K.A. Muller, A.R. Bishop, J. Demsar, T. Mertelj, S. Billinge, T. Egami, D. Pavuna and I. Bozovic for helpful comments and discussions.

References

1. For an early review see: Mihailovic D, Müller KA (1997) In: Kaldis E, Liarokapis E, Müller KA (eds) High T_c superconductivity 1996: ten years after the discovery. NATO ASI, Ser E, vol 343. Kluwer, p 243. For a more recent overview see, for example, Bishop AR et al. (2003) J Phys C Cond Matt 15:L169
2. See for example: Bianconi A et al. (1996) Phys Rev Lett 76:3412; Acosta-Alejandro M et al. (2002) J Superconductivity 15:355 and references therein
3. Bozin et al. (2000) Physica C 341:1793; Bozin et al. (2000) Phys Rev Lett 84:5856
4. Bobroff J et al. (2002) Phys Rev Lett 89:157002; (2003) Phys Rev Lett 91:189702
5. Abbamonte P et al. (2001) Science 297:581
6. Shengelaya A et al. (2001) Phys Rev B 63:144513; Kochelaev BI (1997) Phys Rev Lett 79: 4274
7. Teplov MA et al. (1999) J Superconductivity 12:113
8. Müller KA et al. (1998) J Phys Condens Matter 10:L291
9. Calvani P et al. (2004) J Supercond 17:127; Lucarelli A et al. (2003) Phys Rev Lett 90:37002
10. See for example: Damascelli A et al. (2003) Rev Mod Phys 75:473
11. Derro DJ et al. (2002) Phys Rev Lett 88:97002; Pan SH et al. (2001) Nature 413:282; Howald C et al. (2003) Phys Rev B 67:014533; McElroy et al. (2003) Nature 422:592; Verchinin M et al. (2004) Science (to appear)
12. Bednorz G, Müller KA (1986) Z Phys B 64:189
13. Kimura H et al. (2000) J Phys Soc Jpn 69:851
14. Islam Z et al. (2002) Phys Rev B 66:092501
15. Sharma RP (2000) Nature 404:736
16. Arai M et al. (2000) Int J Mod Phys B 14:3312
17. Petrov Y et al. cond-mat/003413
18. McQueeney RJ et al. (1999) Phys Rev Lett 82:628
19. d'Astuto M et al. (2002) Phys Rev Lett 88:167002–1
20. Mihailovic D et al. (1999) Phys Rev B 60:R6995
21. Mihailovic D et al. (1995) In: Mihailovic D, Ruani G, Kaldis E, Muller KA (eds) Anharmonic properties of high-Tc cuprates. World Scientific, Singapore, p 148
22. Mertelj T et al. (1997) Phys Rev B 55:6061
23. Demsar J et al. (1999) Phys Rev Lett 82:4918
24. Kabanov VV et al. (1999) Phys Rev B 61:1477
25. Thomas TN et al. (1996) Phys Rev B 53:12436
26. Egami T, Billinge SJL (1996) In: Ginsberg DM (ed) Physical properties of high-temperature superconductors. World Scientific, Singapore, p 265; Bozin ES et al. (2000) Phys Rev Lett 84:5856; Tranquada MJ et al. (1995) Nature 375:561
27. Averitt RD et al. (2001) Physical Rev B 6314:0502
28. See for example: Deutscher G (1999) Nature 397:410 or Renner et al. (1998) Phys Rev Lett 80:149; (1998) Phys Rev Lett 80:3606
29. Kabanov VV et al. (1999) Phys Rev B 59:1497
30. Demsar J et al. (2001) Phys Rev B 63:054519; Dvorsek D et al. (2002) Phys Rev B 66:020510; Stevens CJ et al. (1997) 78:2212
31. Kazeroonian AS et al. (1991) Sol Stat Comm 78:95; Brorson SD et al. (1990) Sol Stat Comm 74:1305; Reitze DH et al. (1992) Phys Rev B 46:14309; Han SG et al. (1990) Phys Rev Lett

65:2708; Chwalek JM et al. (1990) Appl Phys Lett 57:1696; Albrecht W (1993) Appl Phys A 57:203
32. Segre GP et al. (2002) Phys Rev Lett 88:137001; Demsar J et al. (2003) Phys Rev Lett 91:16701
33. Lu Y et al. (1993) Appl Phys Lett 63:979
34. Easley GL et al. (1990) Phys Rev Lett 65:3445; Smith DC et al. (2000) Physica C 341:2219; (2000) Physica C 341:2221; Gay P et al. (1999) J Low Temp Phys 117:1025
35. Rothwarf A, Taylor BN (1967) Phys Rev Lett 19:27
36. Demsar J et al. (1999) Phys Rev Lett 83:800; Mihailovic D et al. (2001) J Phys Chem Sol 62:113; Demsar J et al. (2002) Phys Rev B 66:041101
37. Mihailovic D et al. (1991) Phys Rev B 44:237
38. Mihailovic D, Kabanov VV (to be published)
39. Allen PB (1987) Phys Rev Lett 59:1460; Brorson SD et al. (1987) Phys Rev Lett 59:1962; Dobryakov AL et al. (2001) JETP 92:267
40. Ino A et al. (2002) Phys Rev B 65:094504
41. Feenstra BJ et al. (1997) Phys Rev Lett 79:4890
42. Gorkov LP, Sokol AB (1987) Pis'ma ZhETF 46:333; (1987) JETP Lett 46:420
43. Zaanen J, Gunnarson O (1989) Phys Rev B 40:7391
44. Emery VJ, Kivelson SA, Tranquada M (1999) Proc Natl Acad Sci 96:8814 and references therein
45. Mihailovic D, Kabanov VV (2001) Phys Rev B 63:054505; Kabanov VV, Mihailovic D (2000) J Superc 13:959
46. Kabanov VV, Mihailovic D (2002) Phys Rev B 65:212508
47. Mertelj T, Kabanov VV, Mihailovic D (2005) Phys Rev Lett (in print)
48. Alexandrov AS, Kabanov VV, Mott NF (1996) Phys Rev Lett 77:4786
49. Bishop AR et al. (2003) J Phys C Condens Matter 15:L169
50. Misochko OV et al. (1999) Phys Rev B 59:11495
51. Sugai S et al. (2003) Phys Rev B 68:184504
52. Reedyk M, Timusk T (1992) Phys Rev Lett 69:2705; Homes et al. (1995) Can J Phys 73:663
53. Mihailovic D, Heeger AJ (1990) Solid State Comm 75:319; Mihailovic D, Poberaj I, Mertelj A (1993) Phys Rev B 48:16634
54. Butler DP et al. (1999) J Appl Phys 85:1075; (1998) J Appl Phys 84:1680 etc.; Mihailovic D et al. (1993) Physica C 185/189:781
55. Schengelaya A, Bruun M, Kochelaev BI, Safina A, Conder K, Müller KA (2004) Phys Rev Lett (to be published)
56. Alexandrov AS, Mott NF (1994) High temperature superconductors and other superfluids. Taylor and Francis
57. Mihailovic D, Kabanov VV, Müller KA (2002) Europhys Lett 57:254
58. Mihailovic D, Kabanov VV (2004) J Superconductivity 17:21
59. Ahn KH et al. (2004) Nature 428:401; Bishop AR et al. (2003) Europhysics Lett 63:289 and references therein

Struct Bond (2005) 114: 365–384
DOI 10.1007/b105675

Evidences for Polaron Formation in Cuprates

Annette Bussmann-Holder[1] (✉) · Hugo Keller[2] · K. Alex Müller[2]

[1] Max-Planck-Institute for Solid State Research, Heisenbergstrasse 1, 70569 Stuttgart, Germany
a.bussmann-holder@fkf.mpg.de
[2] Physik-Institut der Universität Zürich, Winterthurerstrasse 190, 8057 Zürich, Switzerland

This article is dedicated to Prof. Arndt Simon on the occasion of his 65th birthday.

Abstract It is widely believed that the essential physics of high temperature superconducting copper oxides are governed by the properties of their antiferromagnetic parent compounds. Since these are Mott-Hubbard insulators being dominated by strong electronic correlations, continuations of this physics to the doped superconducting regime have been considered to be sufficient to describe the hole pairing mechanism. However, such a rather simplistic and naïve scenario cannot account for the complexity of the phase diagram and most importantly neglects the crucial effects stemming from the underlying lattice. It is shown here, that extensions of the Hubbard model (with the limiting case of the t-J model) including polaronic lattice effects yield a reasonable physical picture to describe the antiferromagnetic properties as well as the exotic isotope effects observed in the doped compounds. It is concluded that the most important lattice effects stem from a coupling of the electronic degrees of freedom to a JT Q_2-type lattice distortion.

Keywords High temperature superconductivity · Polaron effects · t-J and JT models

1 Introduction

The discovery of high-temperature superconductivity in copper oxides [1] was guided by the knowledge that the copper ion is one of the strongest Jahn-Teller (JT) ions known so far [2]. In the JT effect the orbital degeneracy of electronic states is lifted by the coupling to the lattice which undergoes a lattice distortion. The coupling and the symmetry of the lattice distortion strongly depend on the symmetry of the orbitally degenerate states and careful group theoretical analysis has to be done in order to find the appropriate phonon mode as well as the related displacement pattern [3]. The occurrence of superconductivity in such a system would be rather novel as compared to conventional BCS type superconductors since the JT coupling is local and – as a consequence – the pair coherence length should also not extend over numerous lattice constants but be local as well. Superconducting copper oxides, however, turned out to be full of unexpected surprises which substantially complicated such intriguing scenarios as the JT mechanism. In contrast to conventional band structure theory, these half-filled band systems are not metals but doped antiferromagnetic insulators. Their phase diagram covers a variety of exotic states as, e.g., the pseudogap state, the strange metal behavior, a conventional Fermi liquid, a possible coexistence of superconductivity with antiferromagnetic fluctuations, quantum criticality. The antiferromagnetic insulating state of the undoped or lightly doped systems has rapidly been attributed to a strong Coulomb repulsion at the copper ion sites which inhibits that holes occupy the copper d electronic states [4, 5]. The energy scale involved in this process is the largest and has consequently been taken as the one which mediates the hole pairing mechanism. The motivation for these considerations has various origins: i) the magnitude of the superconducting transition temperatures is exceedingly high ruling out a conventional BCS mechanism; ii) in the underdoped to optimally doped systems conventional Fermi liquid theory seems to break down; iii) the phonon energies are obviously much smaller than the onsite Coulomb repulsions [6]; iv) the vanishing isotope effect on T_c at optimum doping and the pronounced isotope effect on the penetration depth seem to rule out BCS type pairing [7, 8]; v) the extremely short coherence length of the pairing state provides evidence that *local* energy scales are relevant, as, e.g., provided by the onsite Hubbard U.

In contrast to the above points which support a pairing mechanism due to strong correlations only, there is a huge amount of experimental evidences which highlight the important role played by the lattice. One of the first direct findings is the isotope effect on T_c, which approaches and even exceeds the BCS value in the underdoped regime and exhibits its largest values at the boundary to the antiferromagnetic state [7, 8]. The London penetration depth λ_L shows an unexpected isotope effect [8] which is absent in conventional BCS theory. The onset of phonon softening and hardening at the superconducting transition has been observed by various techniques [9] together with lattice anom-

alies occurring in the superconducting regime only [10]. Local lattice anomalies have been observed by EXAFS [4], evidencing that the regular lattice coexists dynamically with a locally distorted one. EPR [11], STM [12], NMR [13] and other probes have shown that the superconducting compounds are highly inhomogeneous. Two components have been observed in various other experiments as photo-induced relaxation effects [3], infrared response [14], ARPES [15], EPR [16]. The onset temperature T* for the pseudogap regime has been shown to be strongly isotope dependent with a reversed sign and one of the largest isotope effects ever observed [17]. Various experiments have provided substantial evidence that the superconducting order parameter is not of purely d-wave symmetry but that a coexisting s-wave component is present [18–20]. From the above facts it must be concluded that a t-J model alone is insufficient to capture the complex physics of high T_c cuprates [21].

The chapter is organized in the following way. In the first section we review the essential physics of the single band t-J model. Extensions to more bands are not included even though there are numerous examples of it in the literature. The end of the section summarizes criticisms to this model based on experimental and theoretical facts. In the following section natural extensions of the t-J model are proposed, and their consequences for HTSC are discussed consecutively. The results of our model are finally summarized and compared to experimental data followed by conclusions.

2
The t-J Model and Its Extensions

Soon after the discovery of HTSC it was mostly agreed that the essential physics of the copper oxides can be attributed to the only common element in all these structurally very diverse compounds, i.e., to the copper oxygen planes. It has been emphasized in a variety of work that the chains in YBCO or the apical oxygen ions also contribute in a hidden way via, e.g., charge transfer, to superconductivity, the majority, however, concentrated on the planes. Here the most obvious energy scale is given by the large Hubbard U at the copper ion lattice site giving rise to the introduction of the t-J model [21–23]. The simplest model in this respect is a one band model where doped hole states, which dominantly occupy the oxygen ion p-states, hybridize with the central copper ion d states to form a state where the copper ion hole together with the doped hole shared by the surrounding four oxygen ions can be represented by a single strongly hybridized effective band [21]. Extensions to three band models or more complex multiband models have subsequently been introduced, but the transparency and the use of very few parameters of the single band model have made this the most fashionable one within models that concentrate on strong correlations only. This is the reason why we show its derivation here in detail, but also note that it is unlikely that such a simplistic view is able to capture the physics of the complex HTSC compounds.

2.1 The Standard Case

The essential physics of the single band t-J model are displayed in Fig. 1 where the electronic states of a copper oxygen plaquette are shown [21]. The Hamiltonian adequate for such a plaquette reads

$$H = \sum_{i,\sigma} \varepsilon_d d^+_{i,\sigma} d_{i,\sigma} + \sum_{i,\sigma} \varepsilon_p p^+_{i,\sigma} p_{i,\sigma} + U \sum_i d^+_{i\uparrow} d_{i\uparrow} d^+_{i\downarrow} d_{i\downarrow} \\ + \sum_{i,\sigma} \sum_{l\in\{i\}} V_{il} d^+_{i,\sigma} p_{l,\sigma} + H.c. \tag{1}$$

where $d^+_{i,\sigma}, p_{i,\sigma}$ creates a hole at site i with spin σ in the copper $d_{x^2-y^2}$, oxygen p_x, p_y states, respectively. U is the on-site Coulomb repulsion at the copper site and V measures the overlap between the copper and oxygen ion wave functions. The phase of the wave functions is taken into account by the convention $V_{il}=t_0$ for $l=i-\frac{1}{2}\hat{x}$, $l=i-\frac{1}{2}\hat{y}$ and $V_{il}=-t_0$ for $l=i+\frac{1}{2}\hat{x}$, $l=i+\frac{1}{2}\hat{y}$ with t_0 being the amplitude of the hybridization, and the Cu-Cu distance is the unit length scale. For simplicity $\varepsilon_d=0$, $\varepsilon_p>0$ and $t_o \ll U$, ε_p, $U-\varepsilon_p$. In the undoped state all copper states are occupied by a single hole as long as $t_0=0$. For finite t_0 the Hamiltonian Eq. (1) can be mapped onto the $S=1/2$ Heisenberg Hamiltonian

$$H_s = J \sum_{\langle ij \rangle} \vec{S}_i \vec{S}_j \tag{2}$$

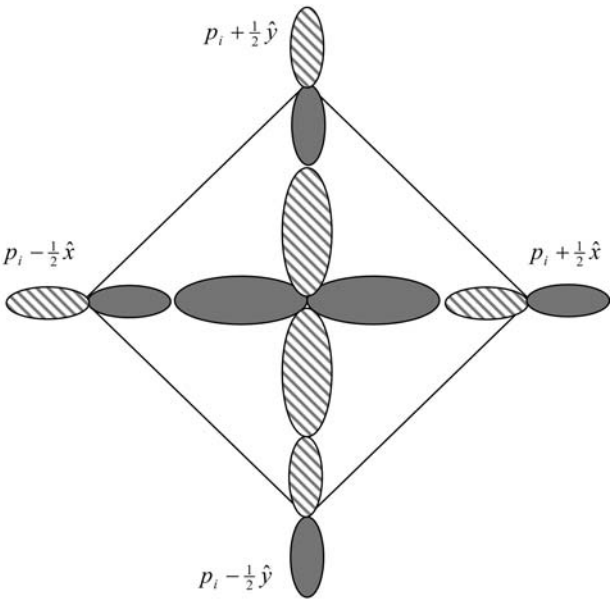

Fig. 1 Schematic diagram of the hybridization of the oxygen hole and the Cu hole; the *dashed and full areas* represent the sign of the wave function

with $\langle ij \rangle$ being nearest neighbor copper ions,

$$J = \frac{4t_0^4}{\varepsilon_p^2 U} + \frac{4t_0^4}{2\varepsilon_p^3} \tag{3}$$

and $\vec{S}_i$ the spin –1/2 operators of the copper holes.

In general, the doping induced additional holes can either occupy Cu d-states if $\varepsilon_p > U$ or oxygen p-states if $\varepsilon_p < U$. In the former case the reduction to a single band model is straightforward, whereas in the latter case this is not obvious. It was, however, shown in [21] that a reduction to a single band is possible by assuming that the energy of the doped hole is, to zeroth order in t_0, ε_p. An energy gain may be obtained by hybridizing the oxygen hole state with the copper hole state through antiferromagnetic superexchange. The four oxygen hole states can then form symmetric and antisymmetric combinations with respect to the central copper ion, and combine to either triplet or singlet states. Obviously, the lowest energy state in such a scenario is the symmetric singlet state Ψ^- [21] where the hole is shared by the four oxygen ions and has antiparallel spin alignment with respect to the central copper ion spin (see Fig. 2 where a projection of this state is shown). The large energy difference to the corresponding triplet state Ψ^+ has been taken as justification to work in the subspace of the Ψ^--state only. The hopping of this state from site i to j is then accompanied by the simultaneous hopping of the copper hole from j to i (Fig. 2).

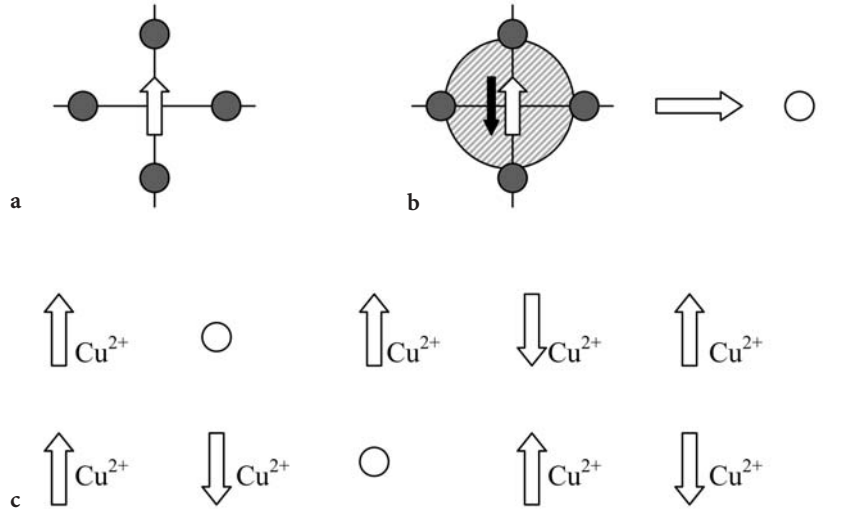

Fig. 2a–c Schematic representation of the reduction to the single band model and Eq. (6): **a** Cu-O_4 plaquette without hole; **b** Cu-O_4 plaquette with hole corresponding to the Ψ^- singlet state being shared by all neighboring oxygen ions; this state is equivalent to the empty hole state at the copper site represented by *open circles* when the reduction to the single d-band is made; **c** 1D d-representation of the single band model showing the motion of Ψ^-through the lattice (Eq. 6)

The kinetic energy of this motion is given by an effective hopping Hamiltonian:

$$H_t = \sum_{i \neq j, \sigma} t_{ij} (\Psi_j^- d_{i,\sigma})^+ \Psi_i^- d_{j,\sigma} \tag{4}$$

where Ψ^- is equivalent to the Heitler-London model of the hydrogen molecule. The effective hopping integral t_{ij} is derived within second order perturbation theory. Basically two different hopping processes can be distinguished: one involves the spin exchange between the copper and oxygen holes, the other is the effective O hole hopping. The conclusion of the analysis is that the nearest neighbor hopping integral is the largest one, whereas the next nearest neighbor oxygen-oxygen hole hopping is one order of magnitude smaller. All higher order processes are much smaller and are consequently neglected. The finding that the second nearest neighbor transfer integral is an order of magnitude smaller than the nearest neighbor one is taken as evidence that this can also be neglected to continue then in the subspace of a single band only (see Fig. 2). This assumption is based on the argument that the creation of a Cu d hole at site *i* is equivalent to the simultaneous destruction of the Ψ_i^- state at the same site. In contrast, the Ψ_i^- requires that no hole is in the *d* state at site *i*. After projecting out the empty states Eq. (4) reduces to

$$H_t = \sum_{i \neq j, \sigma} t_{ij} (1 - n_{i,-\sigma})\, d_{i,\sigma}^+ d_{j,\sigma} (1 - n_{j,-\sigma}) \tag{5}$$

Since the singlet state does not interact magnetically with all other d-holes, the final effective Hamiltonian is given by

$$H = \sum_{i \neq j, \sigma} t_{ij} (1 - n_{i,-\sigma})\, d_{i,\sigma}^+ d_{j,\sigma} (1 - n_{j,-\sigma}) + J \sum_{\langle ij \rangle} \vec{S}_i \vec{S}_j \tag{6}$$

where both contributions to Eq. (6) contain Cu holes, only. Equation (6) is thus the final single band Hamiltonian, which is derived from a two band model in the limit of large onsite U.

Even though a variety of physical aspects of this model seem to have very intriguing properties, it remains rather unlikely that applications of this model to the doped cuprates are possible. Despite, it has to be pointed out that for the undoped compounds the Hamiltonian in Eq. (2) is valid. It is not only the neglect of lattice degrees of freedom, which makes possible applications to HTSC unfavorable, but also a variety of approximations which have been introduced there. The first point to mention is the doping independence of *U* [24]. If this quantity remains in the strong coupling limit, antiferromagnetism would survive at any doping level. It is argued, of course, that antiferromagnetic fluctuations persist with increasing doping and mediate the hole pairing; however, it has been established experimentally, that *U* [24] substantially decreases with doping such that the overdoped systems display conventional Fermi liquid behavior. The neglect of the triplet state within the above approach presents another serious problem, since the singlet only state becomes unstable in this

case [25]. In addition, a major problem stems from the neglect of other than nearest neighbor hopping integrals. This neglect means that the hopping to the nearest neighbor is accompanied by either a spin flip or by the formation of a triplet state, which has been ruled out from the beginning for energy considerations. However, if one assumes that this is true, a spin flip of the doped hole must take place which is energetically nearly as costly as the triplet formation. Thus it appears that just the second nearest neighbor hopping integral is the crucial one to overcome the above problems. The estimates, that this is an order of magnitude smaller than the nearest neighbor one, are not in agreement with band structure calculations [26] which empirically show that T_c increases with the ratio of t_2/t_1within a given cuprate family (here t_1, t_2 are nearest and second nearest neighbor transfer integrals). The single band t-J model also ignores that mainly all HTSC compounds are *not* tetragonal, but are orthorhombically distorted. Here it is frequently argued that the orthorhombic distortion is small, but, in contrast, superconductivity is suppressed in LSCO upon the transition to the low-temperature tetragonal phase [27]. The mapping of the two-band model onto a single band one faces another problem since the large U at the copper site inhibits additional holes to occupy Cu d-states. Also here band structure calculations have shown [26] that eventually copper s states have to be included which would require to extend the model to a multi band one. Furthermore the unique properties of O^{2-} have to be taken into account since the oxygen ion $2p^6$ state is unstable as a free ion whereas the simply ionized state $2p^5$ is stable [28]. This phenomenology requires that doped holes occupy the oxygen p orbitals to lower the O^{2-} site energy. Consequently the limit $t_o \ll U, \varepsilon_p, U-\varepsilon_p$ is not necessarily realized any more and the Heisenberg Hamiltonian loses its meaning, especially if U is reduced by doping. As already mentioned above, the most important neglect of the model, is to rule out lattice effects from the very beginning. Lattice effects are known to modify the exchange interaction in a decisive way. In addition, the oxygen ions on the considered plaquette become inequivalent for a variety of lattice modes. The analysis in terms of symmetric and antisymmetric states is getting more complicated and energy arguments vary substantially as compared to those proposed in [21, 23]. Isotope effects, as reported experimentally, are completely absent and phase segregation or inhomogeneity are excluded. In addition, it remains questionable that the above outlined experimental facts can be included by perturbative approaches within the t-J model.

In the following section we introduce natural extensions of the t-J model and show that lattice effects and more than nearest neighbor hopping terms are needed in order to explain a variety of isotope effects. We do not explicitly address the pairing mechanism, i.e., we do not rule out that strong correlations contribute to it, but we show that major effects stemming from the lattice do not necessarily compete with a t-J scenario but cooperate to yield high T_cs.

2.2 Coupling to the Lattice

The importance of lattice effects within the t-J model has been addressed in a variety of previous work since substantial modulations in the hopping integral as well as the onsite and Coulomb energies may be a consequence [4, 29, 30]. These – in turn – modify the Zhang-Rice singlet state binding energy which has been estimated to be of the order of 5 eV. In this context, coupling to specific planar phonon modes has been investigated as, e.g., the half-breathing longitudinal mode [10], the buckling mode [31], the full breathing mode [30, 32]. These studies are motivated by experimental findings of a substantial softening of the half-breathing mode in the superconducting regime, whereas the buckling mode and the full breathing mode do not exhibit such pronounced anomalies.

Here we start from a different aspect since we do not consider a specific phonon mode, but consider in general the possible nature of the electron-phonon coupling within the t-J model. The coupling of electronic degrees of freedom to the lattice degrees of freedom is known to have subtle consequences to both, lattice and electrons. However, only few scenarios exist which have profound consequences for the ground state properties of the coupled system:

1. Electron-phonon coupling may cause the formation of a charge density wave instability [33].
2. A superconducting state may result in the sense of the BCS mechanism.
3. A Peierls instability can occur [34].
4. A combined charge-spin-density-wave instability could set in [35].
5. Polaron formation may take place [36].

One can systematically rule out various consequences from the above choices:

1. A structural instability is expected.
2. Superconductivity is accompanied by a doping independent isotope effect, and an isotope effect on the penetration depth does not exist.
3. A Peierls instability is, like 1, accompanied by a structural phase transition.
4. A combined charge-spin density wave instability competes with superconductivity.
5. Polaron formation is neither in contrast to superconductivity nor does it lead to structural transformations as long as it remains dynamic and local.

Consequently, we concentrate in the following on polaronic effects within the extended t-J model, which are manifold, but, for brevity, we discuss only the most important ones within the context of isotope effects, which occur in the hopping integrals. All other consequences have been addressed in this volume in one of the previous sections [37] and are not repeated here for brevity. The Hamiltonian, which we consider, describes a three band model which is a minimal model to describe the physics of the Cu-O planes, namely [38]

$$H = H_0 + H_{ch-L} + H_{sp-L} + H_L$$

$$H_0 = \sum_{i,\sigma} E_d\, d^+_{i,\sigma}\, d_{i,\sigma} + \sum_{i,\sigma} E_{ch}\, c^+_{i,\sigma}\, c_{i,\sigma} + U \sum_i d^+_{i\uparrow}\, d_{i\uparrow}\, d^+_{i\downarrow}\, d_{i\downarrow}$$
$$+ \sum_{i,\sigma} \sum_{l\in\{i\}} V_{il}\, d^+_{i,\sigma}\, c_{l,\sigma} + H.c.$$

$$H_{ch-L} = \sum_{i,j,\vec{r}=\vec{x},\vec{y}} [\gamma u_{ij,r}\, c^+_{i,\sigma}\, c_{j,\sigma} + h.c.] \tag{7}$$

$$H_{sp-L} = \sum_{i,j,\vec{r}=\vec{x},\vec{y}} [\gamma u_{ij,r}\, c^+_{i,\sigma}\, c_{j,\sigma} + h.c.]$$

$$H_L = \sum_{i,\vec{r}=\vec{x},\vec{y}} \left[\frac{p^2_{i,r}}{2M} + \frac{M}{2}\, \omega^2 u^2_{i,r} \right]$$

where c^+, c, d^+, d are electron (hole) creation and annihilation operators in the charge (ch) and spin (sp) channels at sites i, j with band energies E_{ch}, E_d. $V_{il}=\pm t_0$ is the hybridization matrix between copper and oxygen states where the sign refers to the phase of the wave functions, and U is the onsite Coulomb repulsion at the copper site. While H_0 transforms to the t-J model in the limit $t_0 \ll U$, E_{ch}, $U–E_{ch}$, the Hamiltonians H_{ch-L} and H_{sp-L} are a consequence of charge-, spin- lattice coupling proportional to γ, where $u_{i,j}$ are the oxygen ion displacements along $\vec{r}=\vec{x}, \vec{y}$, the unit vectors along the axis directions, and p, ω are the momentum and frequency of the oscillator i with mass M. Both band energies, the doped hole band and the spin related one, have the same momentum k dependent dispersion, however with different k-space weight, since both are assumed to be mostly relevant to the CuO_2 planes, namely

$$E_k = -2t_1(\cos k_x a + \cos k_y b) + 4t_2 \cos k_x a \cos k_y b - \mu\,, \tag{8}$$

with $a \neq b$ being the in-plane lattice constants and t_1, t_2 are nearest and next nearest neighbor hopping integrals, respectively, and μ is the chemical potential which controls the number of particles, and has been shown to scale linearly with doping [39]. Phonon degrees of freedom appearing in the Hamiltonian in Eq. (7), can be eliminated by standard techniques [36]. The most important terms which appear in the transformed system are a spin charge interaction term proportional to $V_{sp-ch} n_{ch} n_{sp}$ [40] together with a renormalization of the band energies:

$$\tilde{E}_{sp,\,ch} = -2t_1 \exp\left[-\gamma^2 \coth \frac{\hbar\omega}{2kT} \right] (\cos k_x a + \cos k_y b) \tag{9}$$
$$+ 4t_2 \exp\left[-\gamma^2 \coth \frac{\hbar\omega}{2kT} \right] \cos k_x a \cos k_y b - \Delta^* - \mu\,,$$

where Δ^* is the energy shift induced by the displacement u_i of the nearest neighbor oxygen ions surrounding the copper ion. The most important term, however, is the polaronic band narrowing proportional to γ.

The model we are now dealing with is a coupled spin-charge phonon system with strong phonon mediated *interband* interactions between the spin and the charge channel [40]. Superconductivity may arise here from either attractive interactions in the spin channel, mostly mediated by antiferromagnetic fluctuations, or from electron-lattice interactions within the charge channel, or, finally, from a combined cooperative effect between both subsystems. Details of how to map the resulting Hamiltonian onto an effective two-band BCS type Hamiltonian have been given in a previous section [37] and are not repeated here. We assume in the following that within our two-band model attractive pairing interactions stem from the spin channel whereas those in the charge channel are too weak to induce superconductivity here. The interband interactions between both components are the important terms which induce superconductivity also in this channel.

3
Isotope Effects

3.1
Gap and Order Parameter Symmetry

Superconducting properties of the coupled charge-spin-lattice system are studied within an effective two-band Bogoliubov quasiparticle approach. The resulting scenario is a two gap superconducting state, analogous to MgB_2 [41], with the distinction that the order parameters are of different symmetries. In addition, and opposite to MgB_2, in cuprates mostly a time-averaged gap is observed caused by fast fluctuations [42]. Experimental evidences for coexisting gaps have been proposed by various techniques, where especially Andreev reflection measurements support this scenario [18]. However, from other techniques substantial evidence has also been obtained that the order parameter in cuprates is not of pure d-wave symmetry but has an admixture of an s-wave order parameter [14, 19, 20]. The superconducting gaps $E_{g,s}$ (s-wave gap), $E_{g,d}$ (d-wave gap) have been calculated as a function of doping for various coupling constants γ and fixed ratio of t_2/t_1=–0.3 as suggested by band structure calculations for YBCO [26]. Figure 3 shows the individual gaps as a function of doping for various coupling constants. The ratio of the individual gaps with respect to the average one, namely $E_g = \sqrt{E_{g,s}^2 + E_{g,d}^2}$, is nearly doping and coupling independent and exhibits values which are very close to those of [18].

Figure 4 shows the average gap $E_g = \sqrt{E_{g,s}^2 + E_{g,d}^2}$ as a function of the corresponding T_c where experimental data points for $Y_{1-x}Ca_xBa_2Cu_3O_{7-\delta}$ [18] have been added for direct comparison.

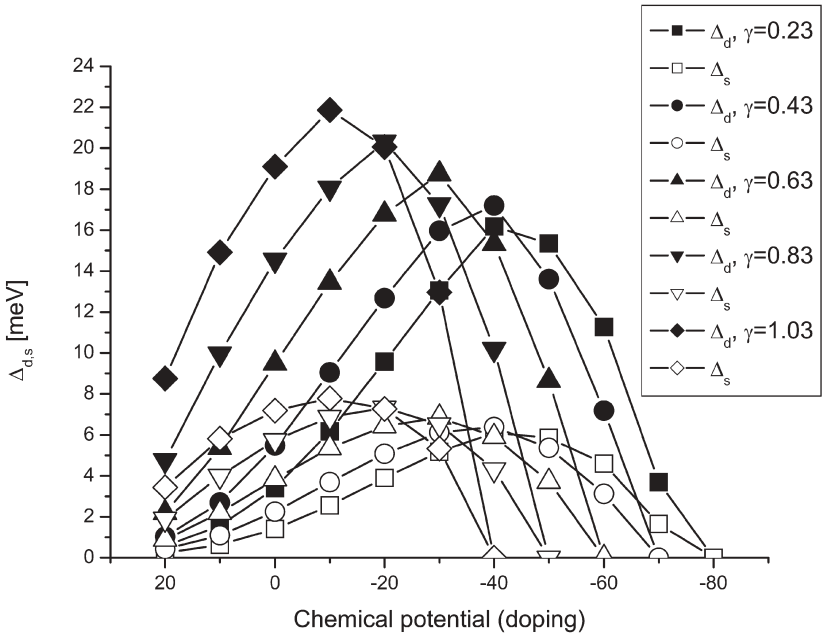

Fig. 3 The superconducting gaps (d-wave; *full symbols*, s-wave: *open symbols*) as functions of doping for various values of the polaronic coupling γ as indicated in the figure

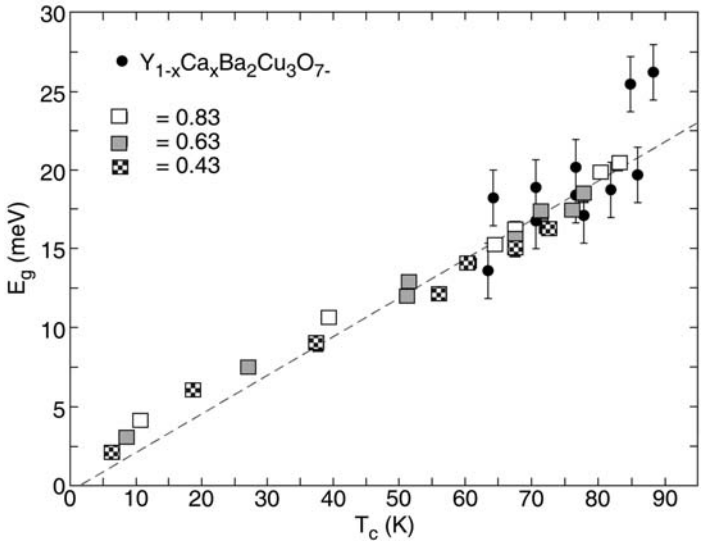

Fig. 4 The average superconducting energy gap $E_g=\sqrt{E_{g,d}^2 + E_{g,s}^2}$ as a function of the superconducting transition temperature T_c. *Squares* are calculated values with γ=0.43, 0.63, 083 (*checkerboard, grey, white*), respectively, whereas *full circles* are experimental data points for $Y_{1-x}Ca_xBa_2Cu_3O_{7-\delta}$ taken from [18]

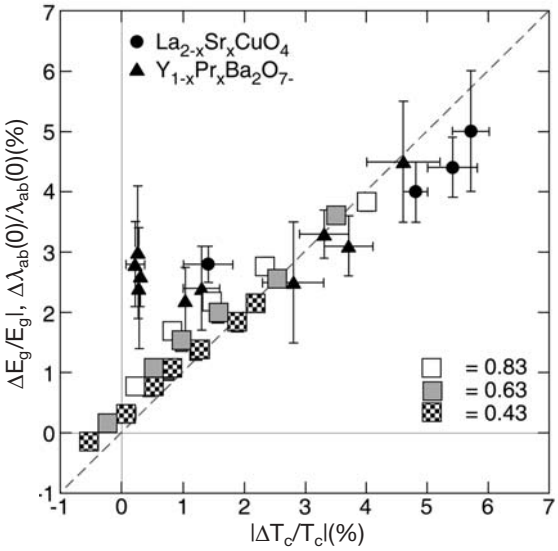

Fig. 5 Relative isotope shift of the average gap $\sqrt{E_{g,d}^2 + E_{g,s}^2}$ ($|\Delta E_g/E_g|$) as a function of the relative isotope shift of the superconducting transition temperature T_c ($|\Delta T_c/T_c|$). Both gaps, the s-wave gap $E_{g,s}$ and the d-wave gap $E_{g,d}$ show nearly the same isotope shift. *Squares* are calculated values with γ=0.43, 0.63, 083, respectively. The *dashed line* is a guide to the eye. *Full triangles and circles* refer to experimental oxygen-isotope effect data of the zero-temperature in-plane magnetic penetration depth $\lambda_{ab}(0)$ and T_c taken from [38]. The ratio of t_2/t_1=0.3 in all calculations and the corresponding figures

Furthermore, we have calculated the oxygen-isotope ($^{16}O/^{18}O$) effects on E_g and T_c for various values of γ and the same parameters as in Fig. 3. As shown in Fig. 5, the relative isotope shifts $|\Delta E_g/E_g| = |(^{18}E_g - ^{16}E_g)/^{16}E_g|$ and $|\Delta T_c/T_c| = |(^{18}T_c - ^{16}T_c)/^{16}T_c|$ are found to be equal (dashed line). This striking finding is in excellent agreement with experimental data [8] of the oxygen-isotope effect on the zero-temperature in-plane magnetic penetration depth $\lambda_{ab}(0)$ and T_c also included in Fig. 5 for direct comparison. However, the saturation effects observed in $\Delta\lambda_{ab}(0)/\lambda_{ab}(0)$ at optimum doping are not found for $|\Delta E_g/E_g|$ and appear only if t_1/t_2 is strongly enhanced as compared to the present value. The close resemblance between $|\Delta E_g/E_g|$ and $\Delta\lambda_{ab}(0)/\lambda_{ab}(0)$ in Fig. 5 is not accidental since in both quantities the leading term for the isotope effect stems from the band energies. Interestingly, a similar linear relation has recently been reported for the band energy isotope effect as a function of the gap values [43].

3.2 Isotope Effects on T_c

Within the above described two-band scenario, isotope effects on T_c can only arise from the band narrowing effect proportional to γ. From Eq. (9) it is seen

that the nearest neighbor as well as the second nearest neighbor transfer integrals are affected by it in an analogous way. However, as will be shown below, their effect is markedly different for the isotope effect on T_c. In Fig. 6 we show the total isotope exponent as a function of the chemical potential for both hopping integrals (t_1, t_2) and various polaronic couplings γ.

Even though we do not consider the case γ=0 in Fig. 6 it is obvious there that for small values γ of the isotope effect nearly vanishes whereas with increasing γ the experimentally observed trends appear. In order to clarify the symmetry of the coupling lattice distortion which causes these isotope effects, the following analysis has been performed: i) first only t_1 is renormalized by γ whereas t_2 is bare; ii) only t_2 is renormalized and t_1 remains unrenormalized. The results are shown in Fig. 7. Clearly, the isotope effect due to t_1 only deviates strongly from experimental observations in the underdoped regime where it approaches zero. On the other hand t_2 follows the total isotope effect correctly. This result admits to draw conclusions about the lattice distortion which governs the isotope dependence of the gaps, T_c and $\lambda_{ab}(0)$. The half-breathing mode (Fig. 8, left panel), which shows anomalous softening [10], is dominated by t_1, and obviously carries the wrong isotope dependence.

Since the same symmetry considerations also apply to the perpendicular direction of the half breathing mode, the full breathing mode can be excluded as well. Recently much attention has also been paid to the coupling to the B_{1g} buckling mode [31] (Fig. 8, middle panel). However, this mode is also domi-

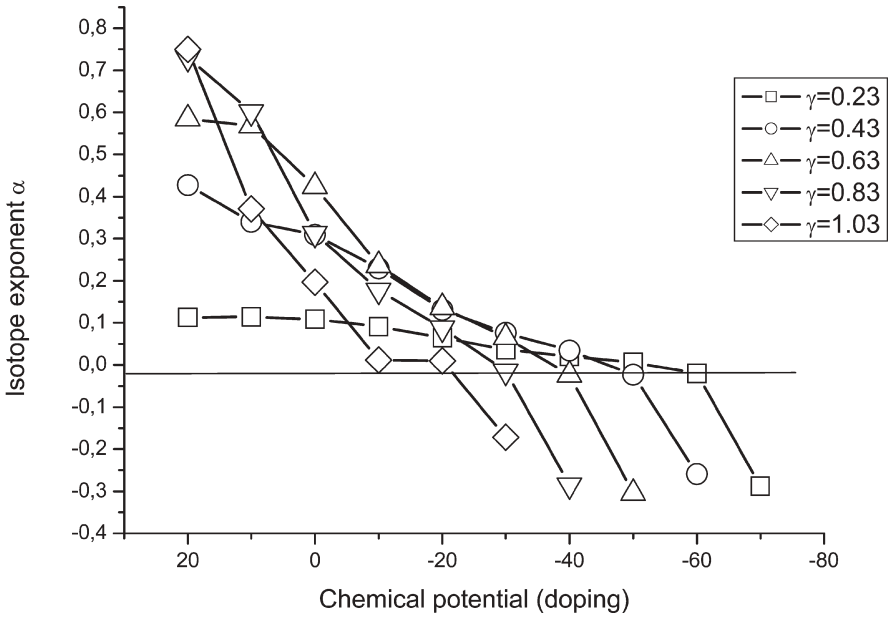

Fig. 6 The isotope exponent α as a function of doping for different polaronic coupling strengths γ as indicated in the figure

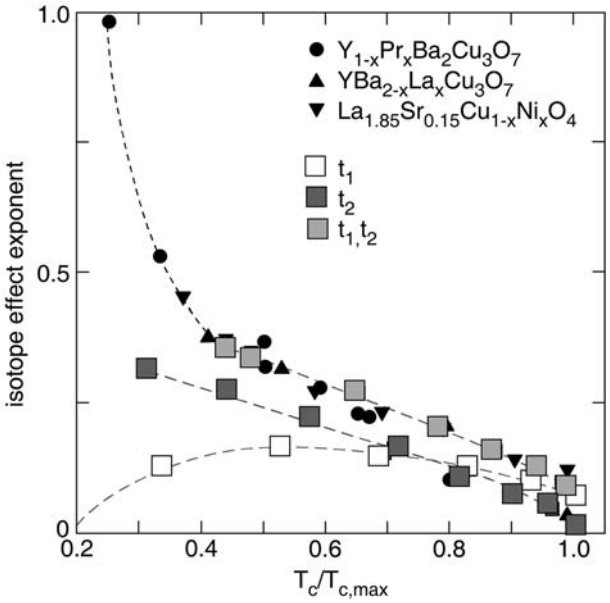

Fig. 7 Calculated isotope effect exponent α as a function of $T_c/T_{c,max}$ for γ=0.83 ($T_{c,max}$ is the maximum T_c for a given family of HTSC). The *grey squares* are calculated by renormalizing both hopping elements t_1, t_2 through the polaronic coupling proportional to γ^2. The *white squares* are calculated by renormalizing t_1 only, whereas for the *dark squares* t_2 is renormalized, t_1 remains bare. The *black symbols* are experimental data points for various HTSC taken from [8]. The *dashed lines* are a guide to the eye

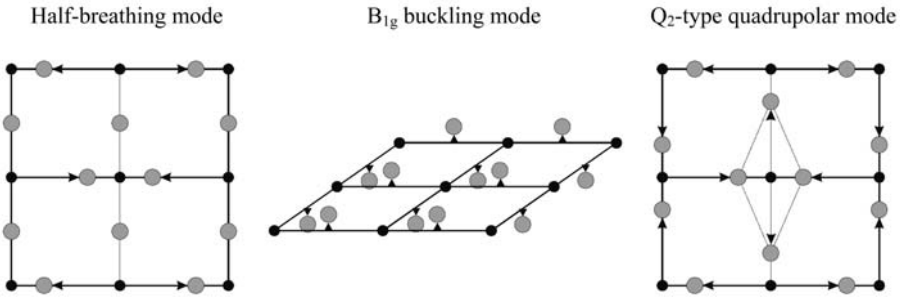

Fig. 8 The relevant lattice modes which renormalize the hopping integrals t_1, t_2 (*from left to right*: half-breathing mode, B_{1g} buckling mode, Q_2-type quadrupolar type mode). The *arrows* indicate the ionic displacements, the *small black circles* refer to the Cu ions with their corresponding spin, while the *large grey circles* stand for the oxygen ions

nated by nearest neighbor transfer only and does not involve the hopping to next nearest neighbors. The crucial role of t_2 can consequently only be taken into account by considering the quadrupolar (pseudo JT) Q_2-type mode as the origin of the observed effects (Fig. 8, right panel). Our explanation is consistent with the interpretation of EPR data [11], but also with data for perovskite type manganites [44], where the dominant role of the JT formation has been demonstrated by isotope experiments.

3.3 Isotope Effects on the Penetration Depth

Evidence for an isotope effect on the penetration depth has been obtained in a variety of experiments, but only very recently has it been measured directly for the first time [8]. Theoretically, the previous experimental studies have been addressed in various works. Polaron and bipolaron formation has been discussed to be at its origin [45, 46]; nonadiabatic effects caused by JT polaron formation have been considered as well [45, 47]. A doping driven crossover from 3D to 2D has been shown to yield scaling relations where the isotope effect on T_c correlates with the one on λ_L [48]. In [45] it is assumed that two contributions to the isotope effect exist – one stemming from the conventional BCS electron-phonon coupling, and the other being related to nonadiabaticity caused by dynamic charge transfer due to polaron formation. In accordance with the new penetration depth data, it is predicted that the isotope effects on T_c and λ_L have opposite signs and are related to each other [45, 48]. However, the relation between both is not linear in [45] but depends on the number of normal state carriers, i.e. varies within the different cuprate families. A linear relation is observed in [48] in the limit that the system is close to a quantum critical point in the underdoped regime.

In the following a similar analysis analogous to [45, 46] is performed, where, however, a decomposition of the isotope exponents is not used, but rather the consequences of polaronic coupling in our two-component scenario are investigated. Results from previous calculations have already given the correct trend, but the important second nearest neighbor hopping term has been neglected there [49]. The penetration depth λ_L is anisotropic as a consequence of the two-channel superconductivity and is obtained from the superfluid stiffness ρ_s via the relation

$$\lambda_L^{-2} = \mu_0 e^2 n_s / m^* \propto \rho_s \tag{10}$$

where m^* is the effective mass, n_s the superconducting carrier density and μ_0 the vacuum permeability. The superfluid stiffness is calculated within linear response theory through the relation between the current and the induced transverse gauge field [37]:

$$\rho_s^{\alpha} = \frac{1}{2V} \sum_k \left\{ \left(\frac{\partial \tilde{E}_k}{\partial k_\alpha} \right)^2 \frac{\partial f(E_k)}{\partial E_k} + \frac{1}{2} \frac{\partial^2 \tilde{E}_k}{\partial k_\alpha^2} \left[1 - \frac{\tilde{E}_k}{E_k} \tanh \frac{E_k}{2kT} \right] \right\} \tag{11}$$

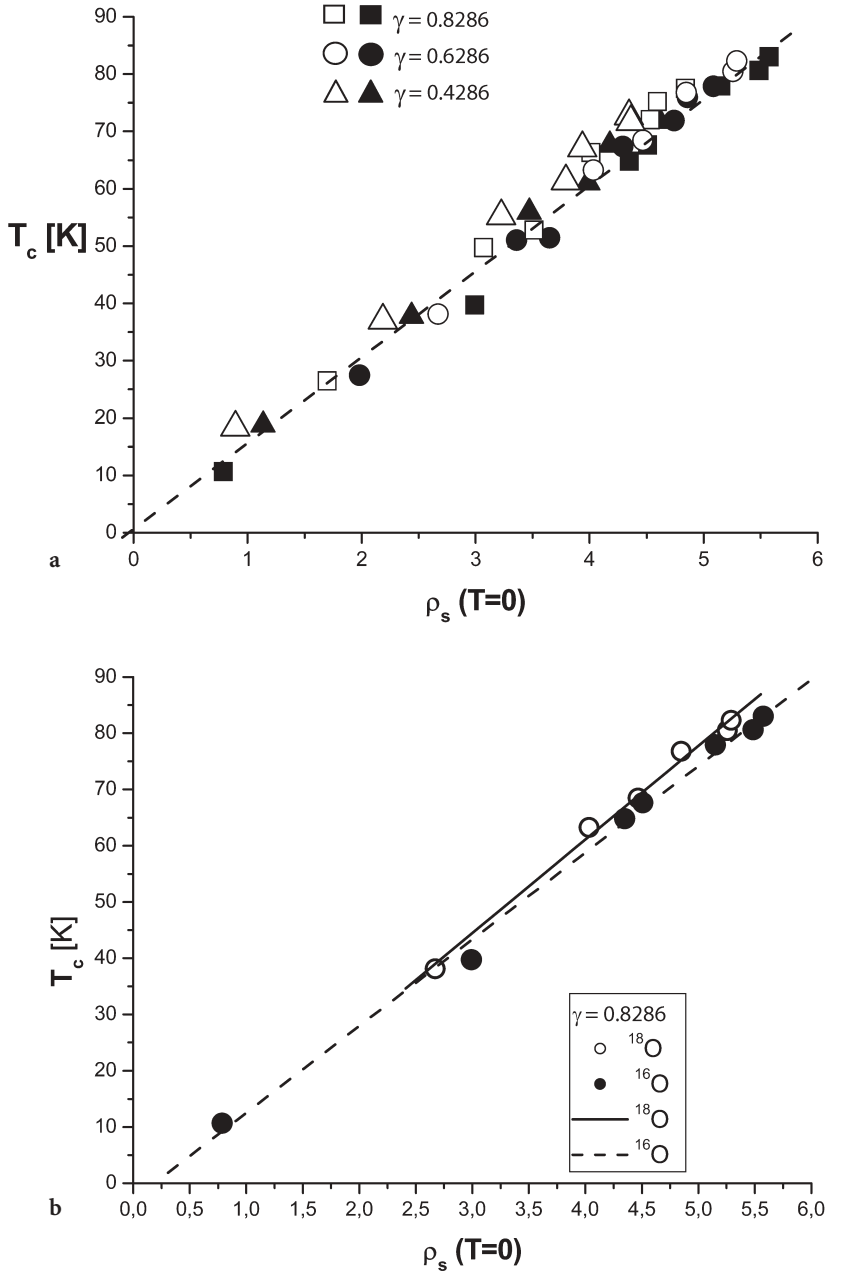

Fig. 9 **a** T_c as a function of the superfluid stiffness ρ_s for various values of γ as indicated in the figure; *full symbols* refer to ^{16}O, *open symbols* to ^{18}O. **b** T_c as a function of the superfluid stiffness ρ_s for γ=0.8286 only, in order to amplify the isotope effect on ρ_s more clearly

with $E = \sqrt{\tilde{E}^2 + \bar{\Delta}^2}$ and $\alpha = x, y, z, f(E_{k_\alpha})$ is the Fermi function. In Eq. (11) an isotope effect on λ_L may arise either from an isotope effect on m^* or from one on the carrier density. Experimentally this question cannot be uniquely clarified [8]. However, back exchange experiments have clearly evidenced that the carrier density is not changed upon isotopic substitution. One could conclude from this fact that m^* is affected by the isotopic substitution whereas the carrier density remains the same. However, the enhanced mass and volume of ^{18}O as compared to ^{16}O can have an effect on the carrier density since this is coupled to the lattice through polaron formation. The results are shown in Fig. 9 a,b, where T_c is given as function of ρ_s for different values of γ. Here open symbols refer to ^{18}O whereas full symbols show the results for ^{16}O. In Fig. 9b data for ^{16}O and ^{18}O are shown for γ=0.8286 only in order to show the isotope effect on ρ_s more clearly. Besides observing a clear isotope effect on ρ_s, there is a linear relation between T_c and ρ_s reproducing the Uemura plot [50]. It is important to note that the equality in Eq. (10) is a consequence of approximating the Fermi surface by a sphere, i.e. using a parabolic band dispersion. In the present approach this does not hold any more since explicitly the second nearest neighbor hopping integral is included, which has been shown to be the most important quantity in obtaining the correct isotope effect on T_c and on λ_L. We can thus safely conclude that the observed isotope effect is a consequence of the effective carrier density. Since $\rho_s \propto 1/\lambda_L^2$ the resulting isotope effect on λ_L is obtained and shown in Fig. 10. The calculated

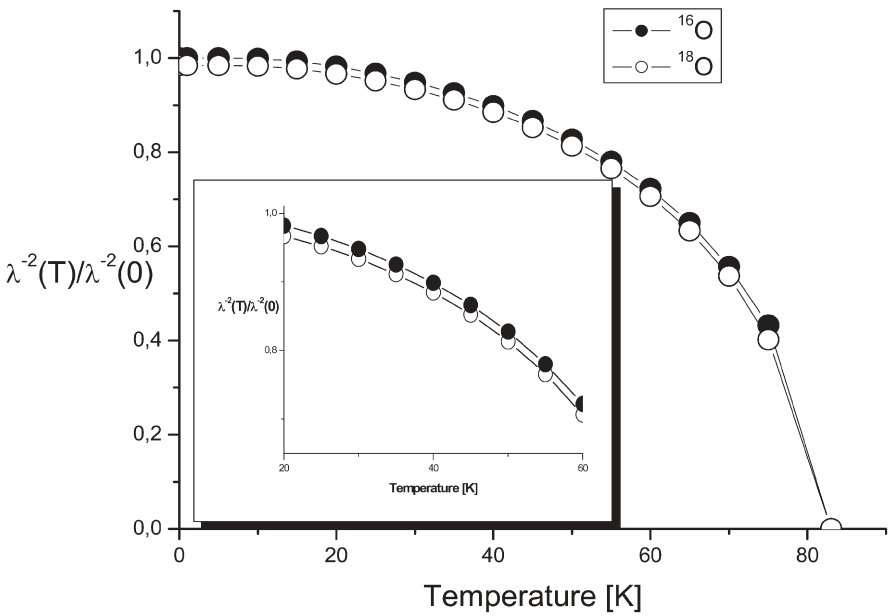

Fig. 10 The normalized penetration depth as a function of temperature; *full circles* refer to ^{16}O, *open circles* to ^{18}O. *The inset* shows the same on an enlarged and limited scale in order to make the isotope effect more clear

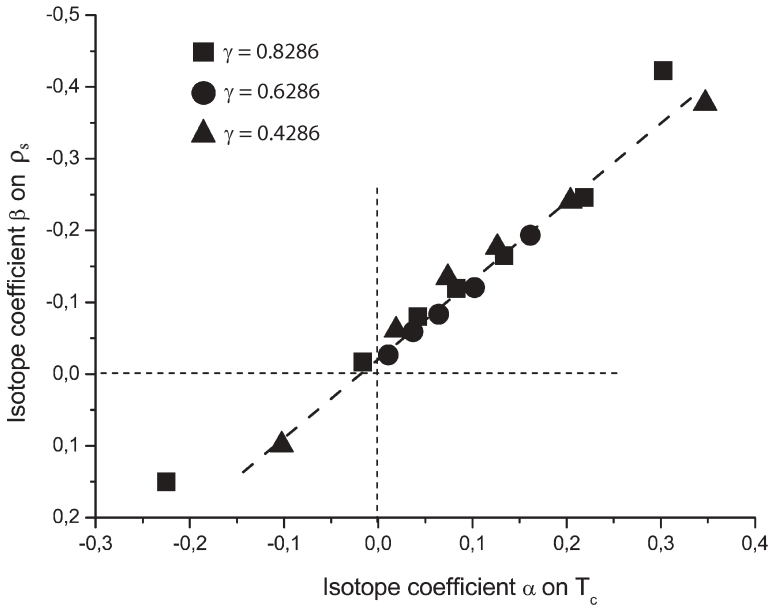

Fig. 11 The isotope coefficient β on ρ_s in relation to the isotope coefficient α on T_c for various values of γ as indicated in the figure

temperature dependence of $\lambda^{-2}(T)/\lambda^{-2}(0)$ shows systematic depressions for the ^{18}O system as compared to the ^{16}O compound in agreement with the experimental data [8].

An interesting correlation of the isotope exponent β on λ_L and α on T_c is obtained by comparing them for various couplings to each other. This is shown in Fig. 11. Obviously there is a linear relation between both and a sign reversal of β as compared to α. This finding explains our recent results of a linear correlation between the isotope effect on the superconducting gap and the one on the penetration depth [8]. The sign reversal of β with respect to α has also been predicted in [45, 48]; however, the linear relation obtained here has only been obtained in [48] in the limit of the quantum critical end point in the underdoped regime. In accordance with [45] the isotope effect on the penetration depth may be due to an isotope effect on the carrier density.

4 Conclusions

In this short contribution we have shown that natural extensions of the three band Hubbard model which incorporate the coupling to the lattice, are an *essential* ingredient for any model for high T_c cuprates in order to understand the observed unconventional isotope effects. The most important findings are that

the isotope effects are a consequence of polaron formation where the second nearest neighbor transfer integral t_2 causes the isotope effects. This observation suggests that the important lattice mode in this respect is a pseudo JT Q_2-type mode as also suggested by chemical consideration [51, 52] and rules out that half-, full-breathing and buckling modes are the origin of unconventional isotope effects within our approach. We are thus dealing with a combined t-J – JT model, which is complementary to the scenario of coexistence of preformed pairs and itinerant electrons (see [3, 37]). The polaron formation is spatially limited to regions around the doped holes and always remains dynamic. In this way a coexistence of the regular lattice with the distorted one takes place which is strongly reminiscent of mesoscopic phase segregation. The two components of our model do not compete with each other but cooperate, and in this way high T_cs are possible.

Acknowledgement It is a pleasure to acknowledge many useful and fruitful discussions with R. Micnas, A. Simon, A. R. Bishop, and V. Z. Kresin and the other authors of this book.

References

1. Bednorz JG, Müller KA (1986) Z Phys Cond Mat 64:189
2. Müller KA (1966) In: Blinc R (ed) Magnetic resonance and relaxation. North Holland, pp 192–208
3. Mihailovic D, Kabanov VV (2005) (this volume)
4. Bianconi A (2005) (this volume)
5. Anderson PW (1987) Science 235:1196
6. Varma CM, Schmitt-Rink S, Abrahams E (1987) Solid State Comm 62:681
7. Franck JP (1994) In: Ginsberg DM (ed) Physical properties of high temperature superconductors IV. World Scientific, Singapore, pp 189–293
8. Keller H (2005) (this volume)
9. Genzel L, Wittlin A, Bauer M, Cardona M, Schönherr E, Simon A (1989) Phys Rev B 40:2170
10. Egami T (2005) (this volume)
11. Kochelaev BI (2005) (this volume)
12. Pan SH et al. (2001) Nature 413:282–285
13. Haase J, Slichter CP (2003) J Supercond 16:473–475
14. Dumm M, Komiya S, Ando Y, Basov DN (2003) Phys Rev Lett 91:077004
15. Lanzara A et al. (2001) Nature 412:510
16. Shengelaya A et al. (2004) Phys Rev Lett 93:017001
17. Furrer A (2005) (this volume)
18. Kohen A, Leibowitch G, Deutscher G (2003) Phys Rev Lett 90:207005
19. Srikanth H, Zhai Z, Sridhar S, Erb A, Walker E (1998) Phys Rev B 57:7986
20. Müller KA, Keller H (1997) In: Kaldis E, Liarokapis E, Müller KA (eds) High T_c superconductivity 10 years after the discovery, Series E. Kluwer Applied Sciences, vol 343, p 7
21. Zhang FC, Rice TM (1988) Phys Rev B 37:3759
22. Hirsch JE (1987) Phys Rev Lett 59:228
23. Anderson PW, Lee PA, Randeria M, Rice TM, Trivedi M, Zhang FZ (2004) J Phys Condens Matter 16:R755

24. Shen ZX, Dessau DS, Wells BO, Olson CG, Mitzi DB, Lombado L, List RS, Arko J (991) Phys Rev B 44:12098
25. Bussmann-Holder A (2000) J Supercond 13:2004
26. Pavarini E, Dasgupta I, Saha-Dasgupta T, Jepsen O, Andersen OK (2001) Phys Rev Lett 87:047003
27. Axe JD, Moudden A-H, Hohlwein D, Cox DE, Mohanty KM, Moudenbough AR, Xu Y (1989) Phys Rev Lett 62:2751
28. Bussmann A, Bilz H, Roenspiess R, Schwarz K (1980) Ferroelectrics 25:343
29. Rösch O, Gunnarson O (2004) Phys Rev Lett 92:146403
30. Ishihara S, Nagaosa N (2004) Phys Rev B 69:144520
31. Deveraux TP, Cook T, Shen Z-X, Nagaosa N (2004) Phys Rev Lett 93:117004
32. Kim Yu H, Levin K, Wentzcovitch R, Auerbach A (1991) Phys Rev B 44:5148
33. Rice TM, Scott GK (1975) Phys Rev Lett 35:120
34. Pytte E (1974) Phys Rev B 10:4637
35. Bahara SN, Mishra SG (1985) Phys Rev B 31:2773
36. Lang SG, Firsov Yu A (1963) Sov Phys JETP 16:1302
37. Micnas R, Robaszkiewicz S, Bussmann-Holder A (2005) (this volume)
38. Bussmann-Holder A, Keller H, cond-mat/0409738
39. Shen KM et al., cond-mat/0407002
40. Bussmann-Holder A, Müller KA, Micnas R, Büttner H, Simon A, Bishop AR ((2001) J Phys Cond Mat 13:L545
41. Choi HJ, Roundy D, Sun H, Cohen ML, Louie SG (2002) Nature 418:758
42. Sudbo A, Chakravarty S, Strong S, Anderson PW (1994) Phys Rev B 49:12245
43. Gweon GH et al. (2004) Nature 430:187
44. Zhao G-M, Condor K, Keller H, Müller KA (1996) Nature 381:676
45. Bill A, Kresin VZ, Wolf SA (1998) Phys Rev B 57:10814
46. Alexandrov AS (1992) Phys Rev B 46:14932
47. Grimaldi C, Cappeluti E, Pietronero L (1998) Europhys Lett 42:667
48. Schneider T, Keller H (2001) Phys Rev Lett 86:4899
49. Bussmann-Holder A, Micnas R, Bishop AR (2004) Phil Mag 84:1257
50. Uemura YJ et al. (1991) Phys Rev Lett 66:2665
51. Simon A (1987) Angew Chem 26:579
52. Müller KA (1999) J Supercond 12:3

Author Index Volumes 101–114

Author Index Vols. 1–100 see Vol. 100

The volume numbers are printed in italics

Subject Index